



**UNIVERSITY OF
CAMBRIDGE**

**Approaches Towards the
Inhibition of Anti-Apoptotic
Proteins**

Jessica Iegre

Trinity College

University of Cambridge

February 2019

Supervised by Prof. David R. Spring

This dissertation is submitted for the degree of Doctor of Philosophy

Declaration

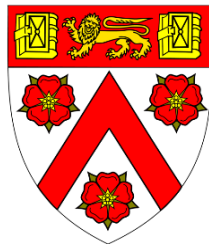
This dissertation is the result of my own work carried out between October 2015 and February 2019. It includes nothing which is the outcome of work done in collaboration except where specifically indicated in the text. It does not exceed the word limit specified by the Physics and Chemistry Degree Committee.

Signed,

Date:

Jessica Iegre

Trinity College, University of Cambridge



Acknowledgments

Firstly, I would like to thank Prof. David Spring for giving me the opportunity to work in his research group, for his help, advice, and encouragement throughout. Your trust and open-mindedness made my PhD a truly enjoyable and stimulating experience. Thanks to Trinity College for funding and for the opportunity to attend national, international conferences, and workshops.

I am very grateful to all the great people I collaborated with throughout my PhD, who taught me that projects are far more interesting when shared! In particular, my thanks go to Dr Paul Brear and Dr Marko Hyvönen for helping me with the biophysics and for letting me go over to their lab and destroy their equipment. I would also like to thank Dr Daniel O' Donovan, Dr David Baker, and all the wonderful people at AstraZeneca Cambridge for always going out of their way to help me. Thank you, Dr Nicholas Pugh and Niaz Ahmed, for bleeding people every time I wanted to play with platelets and for teaching me that cells can do amazing things even without a nucleus! I feel truly blessed to have been able to collaborate with you all.

My special thanks to Dr Gabriele Fumagalli for reading this whole thesis. His proof-reading has been invaluable, and I have learnt a lot from it. Many thanks to Josephine Gaynord, Stephen Walsh, Dr Kim Mortensen, Dr Naomi Robertson and Dr Thomas Osberger for reading parts of this dissertation. I am particularly grateful to Dr Hannah Sore for her guidance, positiveness, and for pushing me outside my comfort zone throughout my PhD. We, in the Spring group, are very fortunate to have you around.

I would like to thank all the past and present Spring group members for their good humour and for making the last years so enjoyable. A special thank goes to my bay-buddy Josie, for her kindnesses, friendship, and for joining the Jossy team. And thank you, Steve, for keeping me company during my whole PhD. We have gone through good and bad days together, but we managed to not kill each other: I guess that means we are real friends!

I would also like to thank my family who has always encouraged me to be the best that I can be. You have always given me the freedom to do what I wanted in life, even if that meant living in different countries – I am incredibly thankful for that, and I love you all.

Last but not least, my gratitude goes to Diego for following me everywhere I go and for his every-day support and tolerance especially in my moodiest days. None of this would have been possible without you by my side – I feel extremely lucky to have you in my life. I dedicate this thesis to you.

Abstract

Anti-apoptotic proteins play a fundamental role in cell survival. Under physiological conditions, such proteins trigger apoptosis in defective or damaged cells only; under pathological conditions, however, they can be dysregulated allowing the cells to survive despite being harmful. Considering the importance of anti-apoptotic proteins in many physio-pathological roles, their specific inhibition is an attractive strategy to develop safe therapeutics.

This thesis describes the inhibition of two classes of anti-apoptotic proteins:

1) Inhibition of the anti-apoptotic protein CK2 to develop novel anti-cancer molecules targeting pockets outside the well-conserved ATP-binding site:

-Using a Fragment-Based-Drug-Discovery (FBDD) approach twelve small molecule inhibitors of CK2 were developed. The lead molecule, **3I**, inhibited the catalytic activity of CK2 α by binding in the cryptic α D pocket with a K_d of 4 μ M. **3I** stopped proliferation of colorectal cancer cells with a GI_{50} of 10 μ M and presented improved drug-like properties and selectivity compared to previously reported inhibitors. Remarkably, **3I** has the potential to be developed into a potent and selective anticancer drug.

-Using a combination of rational-based approach and peptide stapling, twenty-two conformationally-constrained peptides were generated to target the protein-protein interaction (PPI) of CK2 and affect its function. The lead peptide, **P7-F1C5**, presented a novel, highly-functionalised constraint that allowed the molecule to become cell-permeable, exert its anti-proliferative activity in cancerous cells, and to become resistant to serum proteases. **P7-F1C5** is the first macromolecule reported in the literature that binds to CK2 α with sub-micromolar affinity (K_d 150 nM), and that can act as a chemical probe for targeting the PPI of CK2.

2) Inhibition of the anti-apoptotic Bcl-2 proteins to dissect their role in platelet activation and apoptosis.

Bcl-2 proteins regulate cell lifespan; however, their role in non-nucleated platelets is not fully understood. The elucidation of these pathways in platelets is crucial to the development of selective anti-platelet therapeutics.

To this end, this thesis describes the development and the first application of twenty-seven BH3-only peptides in human platelets highlighting how peptides can provide an alternative to conventional methodologies to study PPIs in platelets. The most promising peptide, **P9-F5C5**, engaged the anti-apoptotic protein Bcl-x_L with 26 nM affinity and revealed a new role for the protein Bim in platelet activation.

Abbreviations

1C-PS	one-component peptide stapling
2C-PS	two-component peptide stapling
Δ	heat
δ	chemical shift
μ	micro
v_{\max}	absorption maximum
\AA	angstrom(s)
A1	Bcl-2 related protein A1
Ac	acetyl
ADP	adenosine diphosphate
AH	all-hydrocarbon
Ahx	6-aminohexanoic acid
AKT/PKB	protein kinase B
APC	allophycocyanin
Ar	aryl
ASAP	atmosphere solids analysis probe
ATP	adenosine triphosphate
B-Raf	rapidly-accelerated fibrosarcoma protein kinase B
BACE1	beta-secretase 1
Bad	Bcl-2-associated death promoter
Bak	Bcl-2 associated k protein
Bax	Bcl-2 associated x protein
Bcl-2	B-cell lymphoma protein 2
Bcl-w	Bcl-2-like protein 2
Bcl-x _L	B-cell lymphoma extra-large protein
Bcr-Abl	breakpoint cluster region- <i>proto-oncogene</i> tyrosine-protein kinase
BET	bromodomain and extra-terminal domain
BH	Bcl-2 homology domain
Bid	BH3 interacting-domain death agonist
Bik	Bcl-2 interacting killer
Bim	Bcl-2-like protein 11
Bmf	Bcl-2-modifying factor
Boc	<i>tert</i> -butoxycarbonyl
BSA	bovine serum albumine
<i>n</i> butyl	normal (primary) butyl

^t butyl	tertiary butyl
°C	degrees Celsius
CAMK1	calcium/calmodulin-dependent protein kinase type 1
CAS	computational alanine scanning
CCHP	conformationally-constrained hybrid peptide(s)
CD	circular dichroism
CDK	cyclin-dependent kinase
CDKL	CDK-like kinase
Cft4	chromosome transmission fidelity 4
CK2	casein kinase II
CLIPS	chemical ligation of peptide into scaffolds
CLK	Cdc2-like kinase
cm ⁻¹	wavenumbers
COSY	correlation spectroscopy
CPP	cell penetrating peptide(s)
CSF1R	colony stimulating factor 1 receptor
CuAAC	copper-catalysed azido-alkyne click reaction
CVMD	cardiovascular and metabolic diseases
CXCL4	platelet factor 4
Cy	cyclohexyl
Cyt C	cytochrome C
d	deuterated
Da	dalton(s)
Dap	2,3-diaminopropionic acid
Db	dibenzylideneacetone
DBF	dibenzofulvene
DCE	1,2-dichloroethane
DEAD	diethyl azodicarboxylate
DEPT	distortionless enhancement polarisation transfer
DIC	<i>N,N'</i> -Diisopropylcarbodiimide
DIMAT	2-dimethylamino-4,5,6,7-tetrabromo-1H-benzimidazole
DIPEA	<i>N,N</i> -diisopropylethylamine
DISC	death-inducing signalling complex
DMAP	4-dimethylaminopyridine
Dmb	2,4-dimethoxybenzyl
DME	1,2-dimethoxyethane
DMF	<i>N,N</i> -dimethylformamide

DMSO	dimethyl sulfoxide
DMS	dimethylsulfide
DNA	deoxyribonucleic acid
dppf	1,1'-Bis(diphenylphosphino)ferrocene
DRB	5,6-dichloro-1- β -D-ribofuranosyl-benzimidazole
DTT	<i>DL</i> -dithiothreitol
Dvl	cytoplasmic dishevelled phosphoproteins family
DYRK	Down syndrome related kinase
EC ₅₀	half maximal effective concentration
EDC	1-ethyl-3-(3-dimethylaminopropyl)-carbodiimide
EDT	ethyldithiol
EDTA	ethylenediaminetetraacetic acid
EF2K	elongation factor 2 kinase
eIF2 β	eukaryotic initiation factor 2
EMA	European medicines agency
EPK	eukaryotic protein kinase
equiv	equivalent(s)
ER	endoplasmic reticules
Erk	extracellular-signal-regulated kinases
ESI	electron spray ionisation
Et	ethyl
FADD	Fas-associated death domain protein
FAF-1	Fas-associated factor-1
FAIM3	Fas apoptotic inhibitory molecule 3
FasL	cell-surface cell ligand
FBDD	fragment-based drug discovery
FBS	fetal bovine serum
FDA	food and drug authority
FGF-2	fibroblast growth factor-2
FGFR	fibroblast growth factor receptor
FITC	fluorescein 5-isothiocyanate
FLIP	(FADD-like IL-1 β -converting enzyme)-inhibitory protein
FP	fluorescent polarisation
FSC	forward scattering
FXa	coagulation factor Xa
FW	formula weight
g	gram(s)

G6PDH	glucose-6-phosphate dehydrogenase
GAFF	generalised AMBER force field
GB	generalised born
GCN4	general control protein N4
GI ₅₀	half maximal concentration to inhibit cell growth
GLP-1	glucagon-like peptide 1
GP $\alpha_{IIb}\beta_3$	glycoprotein platelet fibrinogen receptor
GPCR	G-protein coupled receptor(s)
G α	G _s alpha subunit
GSK	glycogen synthase kinase
GTP	guanosine triphosphate
h	hour(s)
HATU	1-[bis(dimethylamino)methylene]-1 <i>H</i> -1,2,3-triazolo[4,5- <i>b</i>]pyridinium 3-oxid hexafluorophosphate
HBA	hydrogen bond acceptor(s)
HBD	hydrogen bond donor(s)
HCT116	human colorectal cancer cells
Hepes	<i>N</i> -2-hydroxyethylpiperazine- <i>N'</i> -2-ethanesulfonic acid
HIV	human immunodeficiency virus
HMBC	heteronuclear multiple bond correlation
HNF1 β	transcription factor 2
HPLC	high performance liquid chromatography
Hrk	Harakiri, Bcl-2 interacting protein
HRMS	high resolution mass spectroscopy
HSP90	heat shock protein 90
HSQC	heteronuclear single quantum correlation
HTS	high-throughput screening
Hz	hertz
IAP	inhibitor of apoptotic protein
IC ₅₀	half maximum inhibitory concentration
IFD	induced fit docking
I κ β	inhibitor of kappa-light-chain enhancer of activated B-cells
ILGF1	insulin-like growth factor 1
IPTG	isopropylthio- β -D-galactopyranoside
IR	infrared
IRAK4	interleukin-1 receptor-associated kinase 4
ITC	isothermal titration calorimetry

ivDde	4,4-dimethyl-2,6-dioxocyclohex-1-ylidene)-3methylbutyl
<i>J</i>	coupling constant
JAK	Janus protein kinase
K_d	dissociation constant
KHK	ketoheokinase
KIT	mast/stem cell growth factor receptor
L	litre(s)
LCMS	liquid chromatography mass spectroscopy
LE	ligand efficiency
LLE	ligand lipophilicity efficiency
logP	logarithm of the octanol/water partition coefficient
LTA4H	leukotriene-A4 hydrolase
M	molar or mega
m	milli or metre
<i>m</i>	<i>meta</i>
MAPK	mitogen activated protein kinase
MBHA	methylbenzhydryl amine
Mcl-1	induced myeloid leukaemia cell differentiation protein
MD	molecular dynamic(s)
Me	methyl
MEP	molecular electrostatic potential
MES	2-Morpholinoethanesulfonic acid sodium salt
min	minute(s)
MM/GBSA	molecular mechanics/generalised born surface area
MMP	mitochondria membrane potential
MNK	MAPK-interacting kinase
mol	mole(s)
MOMP	mitochondria outer membrane permeabilisation
mp	melting point
mRNA	micro ribonucleic acid
<i>m/z</i>	mass-to-charge ratio
MW	microwave irradiation
n	nano
NBS	<i>N</i> -bromosuccinimide
NF- κ B	nuclear factor kappa-light-chain-enhancer of activated B-cells
NHS	<i>N</i> -hydroxysuccinimide
NLS	nuclear localisation sequence

NMR	nuclear magnetic resonance
Nopp140	nucleolar phosphoprotein 140
Noxa	phorbol-12-myristate-13-acetate-induced protein 1
NRB	number of rotatable bond(s)
NTA	nitrilotriacetic acid
<i>o</i>	<i>ortho</i>
<i>p</i>	<i>para</i>
p53	phosphoprotein 53
Pbf	2,2,4,6,7-pentamethyldihydrobenzofuran-5-sulfonyl
PBS	phosphate-buffered saline
PCD	programmed cell death
PDB	protein data bank
PDGF	platelet-derived growth factor(s)
PE	phycoerythrin
PE 30-40	petroleum ether (fractions with boiling point between 30-40 °C)
PE 40-60	petroleum ether (fractions with boiling point between 40-60 °C)
PFA	paraformaldehyde
PGE ₁	prostaglandin E1
Ph	phenyl
PI3K	phosphoinositol-3-kinase
PIFA	[bis(trifluoroacetoxy)iodo]benzene
PIP3	phosphoinositol-triphosphate
PK	pharmacokinetic
PLC	preparative liquid chromatography
PPAR	peroxisome proliferator-activated receptor(s)
PPI	protein-protein interaction
ppm	parts per million
PROTAC	proteolysis targeting chimera(s)
PRP	platelet rich plasma
<i>PS</i>	phosphatidylserine
PS	peptide stapling
PSA	molecular polar surface area
PTEN	protein phosphatase and tensin homolog
PTFE	polytetrafluoroethylene
Puma	p53 upregulated modulator of apoptosis
R	unspecified substituent
RCM	ring-closing metathesis

RESP	restrained electrostatic potential
R_f	retention factor
RIA	respiratory, inflammatory and autoimmune
RNA	ribonucleic acid
ROS	reactive oxygen species
rt	room temperature
RTK	receptor tyrosine kinase
s	second(s)
SAR	structure-activity relationship
SASA	solvent accessible surface area
SGK1	serum and glucocorticoid-regulated kinase 1
SICLOPPS	split-intein circular ligation of peptides
SmMLCK	calcium/calmodulin-dependent myosin light chain kinase
SMoC	small molecule carrier
S_N2	bimolecular nucleophilic substitution
S_NAr	nucleophilic aromatic substitution
SPPS	solid phase peptide synthesis
SPR	surface plasmon resonance
TAAB	<i>N,N,N'</i> -benzene-1,3,5-triyltrisprop-2-enamide
TAMRA	carboxytetramethylrhodamine
TAT	HIV-derived transactivator of transcription
TATA	1,3,5-triacryloyl-1,3,5-triazinane
TBAB	<i>N,N,N'</i> -(benzene-1,3,5-triyl)tris(2-bromoacetamide)
TBAF	tetrabutylammonium trifluoride
TBB	4,5,6,7-tetrabromobenzotriazole
TBI	4,5,6,7-1H-tetrabromobenzimidazole
TBMB	tris-(bromomethyl)benzene
TCEP	(tris(2-carboxyethyl)phosphine)
TEA	triethylamine
TEV	tobacco etch virus
Tf	trifluoromethanesulfonyl (triflyl)
TGF	transforming growth factor
THF	tetrahydrofuran
THPTA	tris(3-hydroxypropyltriazolylmethyl)amine
TIPS	triisopropylsilane
TLC	thin layer chromatography
TMS	trimethylsilyl

TNF	tumour necrosis factor
TNKS	tankyrase
TPSA	total polar surface area
TRAIL	TNF-related apoptosis-inducing ligand
Trt	trityl
TS	thermal shift
U2OS	human osteosarcoma cancer cells
UV	ultraviolet
VWF	Von Willebrand factor
Wnt	cysteine-rich glycoproteins
WT	wild-type

Standard one and three letter codes are used for amino acids.

Table of contents

SECTION I: Introduction

CHAPTER 1: Current Approaches in Drug Discovery	2
1.1 Fragment-Based Drug Discovery	4
1.1.1. State of the art of FBDD	7
1.2 Therapeutic peptides	9
1.2.1. Macrocyclised peptides	9
CHAPTER 2: Anti-Apoptotic Proteins	23
2.1. Inhibition of anti-apoptotic proteins	25
2.1.1. Anti-apoptotic CK2 protein kinase	26
2.1.2. Anti-apoptotic Bcl-2 proteins	35
2.1.3. Quick consideration on selectivity	42

SECTION II: Results and discussion

CHAPTER 3: A Fragment-Based Approach Towards the Inhibition of the Anti-Apoptotic Protein CK2	44
3.1. Summary	45
3.2. Project background	46
3.2.1. Preliminary work on fragment binding in the α D pocket	46
3.2.2. Preliminary work on fragment binding at the α/β interface	49
3.3. Project aim and overview	51
3.4. Results and discussion	53
3.4.1. Fragments exploring vacant parts of the α D pocket	53
3.4.2. Fragments growing towards the ATP binding site: second-generation CK2 inhibitors	68
3.5. Conclusions and future work	73
CHAPTER 4: Conformationally-Constrained Peptides Targeting the PPI of the Anti-Apoptotic Protein CK2	74
4.1. Summary	75
4.2. Project background	76
4.3. Project aim and overview	77

4.4. Results and discussion	78
4.4.1. Design of CK2 β -like peptides	78
4.4.2. Screening of constrained peptides	80
4.4.3. Attempts to develop Conformationally-Constrained Hybrid Peptides (CCHPs)	87
4.4.4. X-ray crystal structures of the constrained peptides	91
4.4.5. Further sequence modification: P6-C5, P7-C5, and P8-C5	93
4.4.6. Multi-functionalisation of the constraint C5	96
4.4.7. Cellular work on P7-C5 derivatives	98
4.5. Conclusions and future work	105
CHAPTER 5: Targeting of Anti-Apoptotic Bcl-2 Proteins in Platelets Using Stapled Peptides	107
5.1. Summary	108
5.2. Project background	109
5.3. Project aim and overview	110
5.4. Results and discussion	111
5.4.1. Uptake and bioactivity of model stapled peptides in human platelets	111
5.4.2. Investigation of the Bim/Bcl-x _L PPI in platelets using <i>i,i+4</i> stapled peptides	115
5.4.3. Dissecting the role of Bim, Bad, and Bid proteins in platelets using stapled peptides	124
5.5. Conclusions and future work	131
SECTION III: Experimental procedures	
CHAPTER 6: Chemistry Experimental	134
6.1. Experimental synthetic details	137
6.1.1. Small molecules	137
6.1.2. Peptides	168
CHAPTER 7: Computational Chemistry Experimental	174
7.1. Docking studies for CK2 fragments	175
7.2. Computational chemistry for CK2 peptides	175
7.3. Computational chemistry for BH3 peptides	178

CHAPTER 8: Biophysics Experimental	180
8.1. Biophysics experimental for CK2 fragments and peptides	181
8.1.1. Protein expression and purification	181
8.1.2. Fluorescent Polarisation	182
8.1.3. Isothermal Calorimetry Titration	182
8.1.4. Kinase assay	183
8.1.5. X-ray crystallography	183
8.2. Biophysics experimental for BH3 peptides	185
8.2.1. Protein exxpression and purification of Bcl-x _L	185
8.2.2. Surface Plasmon Resonance	185
8.2.3. Circular dichroism experiments	186
CHAPTER 9: Biology Experimental	187
9.1. Biology experimental for CK2 peptides	188
9.1.1. Serum stability test	188
9.1.2. Tissue culture	188
9.1.3. Proliferation assay	188
9.1.4. Viability assay	189
9.1.5. Co-localisation experiments	189
9.2. Biology experimental for BH3 peptides	190
9.2.1. Preparation of washed platelet suspension	190
9.2.2. Flow cytometry	190
9.2.3. Light transmission aggregometry	192
9.2.4. Confocal microscopy of live platelets	192
9.2.5. Serum stability test	193
CHAPTER 10: Bibliography	194
Appendices	
A.1: ¹ H, ¹³ C, ¹⁹ F NMR spectra	210
A.2: HPLC traces of selected compounds	265
A.3: Structures of additional CK2 fragments docked	271
A.4: Selected ITC binding curves	272
A.5: Unsuccessful crystallisation attempts of CK2 peptides	276
A.6: Papers published on this work	277

SECTION I

Introduction

CHAPTER 1:

Current Approaches in Drug Discovery

Until three decades ago, the high-throughput screening (HTS) of libraries of small organic molecules was the gold-standard approach used as a starting point in drug discovery. However, these multimillion-compound libraries were characterised by a high degree of structural similarity and included compounds targeted against known binding sites, hence limiting the chances of engaging previously unexplored biological space. When screened against well-established targets, HTS libraries were particularly effective, but when screened against new or difficult biological systems, they provided very few hits and several false positives.¹ In the last few decades, a deeper understanding of biotechnology and biology have expanded the number of '*druggable*' targets and pushed medicinal chemists to employ new molecular entities beyond traditional small molecules as well as new approaches to discover life-changing medicines.

Fragment-Based Drug Discovery (FBDD), for instance, has emerged as a complementary technique to discover new binding sites and new drugs more efficiently. The establishment of FBDD was made possible thanks to advances made in the field of biotechnology that allow detection of weak bindings such as those of fragments.²

Advances in biology, on the other hand, have led to the realisation that the majority of medically-relevant biological systems can rarely be targeted with traditional small molecules. Consequently, pharmaceutical industries have expanded their pipelines to accommodate previously uncharted chemical entities – hereinafter referred to as new modalities.³ New modalities – *e.g.* peptides, antisense oligonucleotides, proteins, synthetic mRNA, proteolysis targeting chimeras (PROTACs) – feature nowadays at any stage of the drug discovery programs and clinical studies and they are soon-to-become the medicines of tomorrow, able to engage targets considered '*undruggable*' until not long ago.

For the purpose of this dissertation, an overview of recent advances on both FBDD and therapeutic peptides will be presented in this chapter, since other new modalities fall beyond the scope of the work being described.

1.1. Fragment-Based Drug Discovery

FBDD is a structure-based approach that provides lead compounds to target biological systems.² FBDD allows the screening of fewer, low-molecular-weight molecules compared to other approaches employed to obtain chemical leads such as HTS.^a There are several advantages to using smaller fragment-sized libraries:

- the sampling of the chemical space is much more efficient due to the lower number of possible obtainable molecules;
- being less complex than traditional small molecules, fragments make fewer interactions with the proteins but can bind to a greater number of pockets, on a greater number of targets, resulting in higher hit rates;
- owing to their smaller size, libraries can be assembled and screened by small biotech companies and academic groups.¹

Although initial hits usually have lower potency, FBDD is considered to be more efficient in the optimisation phases of drug discovery, which are guided by the 3D information of fragment binding modes obtained by means of experimental techniques.^{2,4,5}

In a typical FBDD flow (Figure 1), firstly, a fragment library is assembled, and the fragments are then screened using biophysical techniques. Due to the low molecular weight and potency of the initial fragments, highly sensitive biophysical techniques are required for initial screening, such as Surface Plasmon Resonance (SPR), Isothermal Calorimetry (ITC), Thermal Shift (TS) and functional assays.^{6,7} X-ray or NMR techniques are used to investigate the binding modes of the fragment hits in the protein of interest and, therefore, to characterise the fragments.⁸⁻¹⁰ The third step in a FBDD approach is fragment elaboration. In this stage, the fragments to be progressed are selected according to different criteria such as potency, Ligand Efficiency (LE)^b, Ligand Lipophilicity Efficiency (LLE)^c and availability of X-ray or NMR structures.¹¹⁻¹³ The more drug-like fragments showing an IC₅₀ in the mM range and interesting binding modes to the target are selected to be optimised into leads (IC₅₀ in nM range). Such elaboration is achieved *via* iterative cycles of synthesis, structural analysis, and computer-aided design.⁵

^a FBDD screens thousands of compounds with a number of heavy atoms ≤ 20 ; HTS screens millions of compounds with ~ 30 heavy atoms each.¹

^b The LE is defined as the Gibbs free energy of binding (KJ·mol⁻¹ or Kcal·mol⁻¹) divided by the number of non-hydrogen atoms.²⁸⁴ LE normalises the potency with respect to the number of heavy atoms, and it is of great importance when comparing the potency of compounds with a variety of formula weight (FW).¹² At the fragment stage, an LE of approximately 0.3 or higher is preferred.¹¹

^c The introduction of lipophilic groups can provide a quick mean of improving the potency of a fragment, but it often leads to problems such as non-specific binding and poor bioavailability.¹¹ LLE (defined as $\text{pIC}_{50} - \text{cLogP}$) is a parameter that can be used to ensure that the generated fragments do not gain an excessive hydrophobic character during the elaboration. An LLE of ~ 5 or higher is advisable.¹³

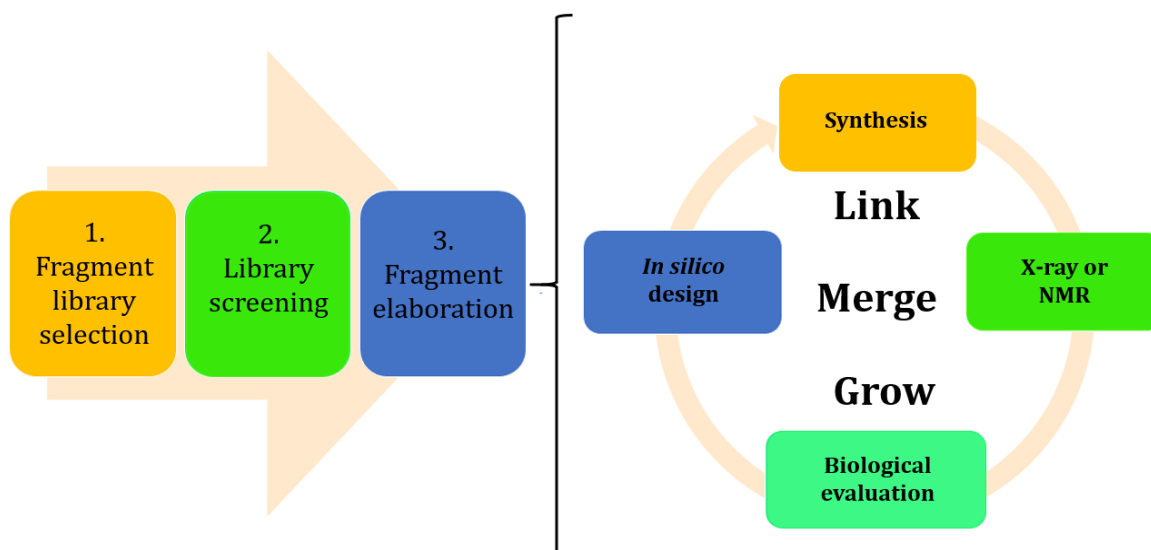


Figure 1 - Typical FBDD flow. The fragment hits generated by the screening of the library are further elaborated via linking, merging and/or growing strategies. The elaboration is the result of iterative cycles of chemical synthesis, biophysical assays and *in silico* design.

The fragment elaboration typically occurs *via* linking, growing and/or merging strategies. The growing strategy consists in using a single vector to grow the fragments to engage in additional interactions (Figure 2a). The merging strategy sees, instead, the best features of the original fragments merged into what is predicted to be a more potent and drug-like molecule (Figure 2b).¹¹ Alternatively, in the linking strategy fragments binding in different parts of the same pocket or in two adjacent pockets are linked together *via* linkers (Figure 2c).⁵ The linking of fragments has been considered to be the most difficult of the three methods: a linker should be introduced to maintain the optimal binding configurations that have been adopted by the individual fragments, should establish additional interactions with the protein to prevent a loss in LE, and should be synthetically accessible.^{11,14} However, when successful, the linking strategy can provide boosts in potency as high as 300-fold compared to the single fragments.¹⁵ The significant enhancement in binding affinity can be explained with the concept of ‘super-additivity’.^{14–17} Upon binding to the targeted protein, each fragment loses a significant part of its rigid body rotational and translational entropy resulting in an entropic penalty. The linked molecule would account for one entropic penalty only whilst two separate fragments would be affected by two unfavourable entropic terms.¹⁵ Consequently, the linked molecules can have a more favourable binding free energy (ΔG) than the sum of the ΔG values of the individual fragments.¹⁵

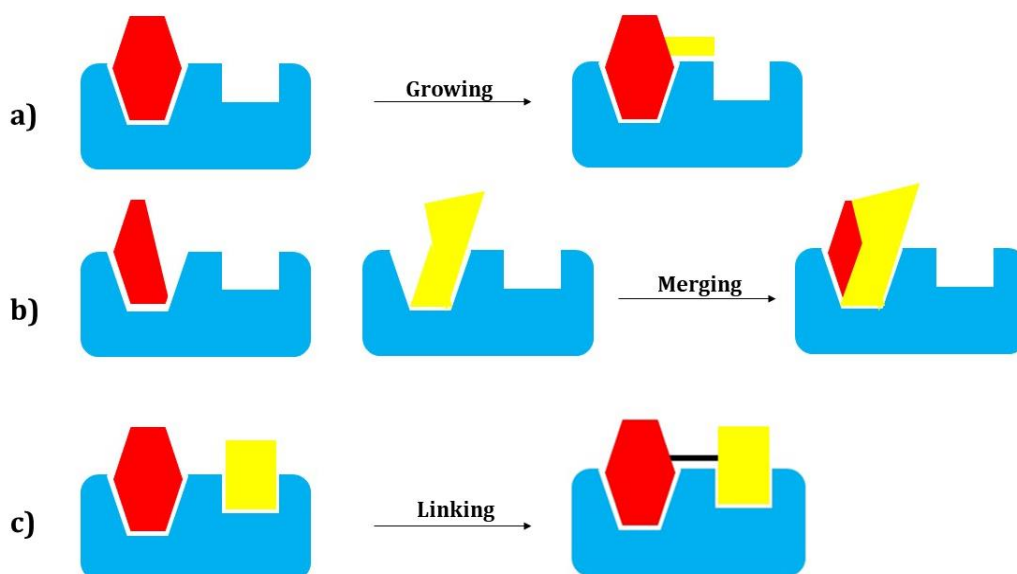


Figure 2 - Schematic representation of the different strategies that can be applied during fragment elaboration: (a) growing, (b) merging, (c) linking strategy. The protein is shown in light blue, fragments in red and yellow and the linker in black.

FBDD has shown some advantages with respect to more conventional drug discovery approaches. In particular:

- 1) Starting the optimisation with small compounds capable of making high-quality interactions with the protein means that the molecular weight, complexity and physicochemical properties of the molecule can be easily controlled during the elaboration.²
- 2) The high binding energy per atom can be maintained during the optimisation from hit to lead.^{16,17}
- 3) The ligand Efficiency (LE) and the Veber 'rule-of-three'^d allow easy comparison of lead-likelihood of fragments of different sizes.²
- 4) Compared to HTS, far fewer fragments are required in the initial screening to sample the chemical space (thousands vs millions of compounds).⁵

On the other hand, there are few disadvantages related to FBDD. However, these drawbacks are biotechnology-dependent and can be overcome with further advances in the field. In particular:

- 1) The low potency of the initial fragments requires the use of sensitive biophysical screening techniques and high fragment concentrations (up to 50 mM). Due to the high concentration, the fragments need to be highly soluble in the hydrophilic solvents used.⁵

^d According to the Veber 'rule of three' a fragment to be elaborated into an oral bioavailable lead should satisfy the following criteria: FW < 300 g·mol⁻¹, H-bond donor (HBD) ≤ 3; H-bond acceptor (HBA) ≤ 3, cLogP ≤ 3; Number of rotatable bonds (NRB) ≤ 3; Polar surface area (PSA) ≤ 60 Å².^{285,286}

2) Due to low potency, the fragments are also unsuitable for cell screening and kinetic assays where high concentration will likely lead to false positives.⁵

1.1.1. State of the art of FBDD

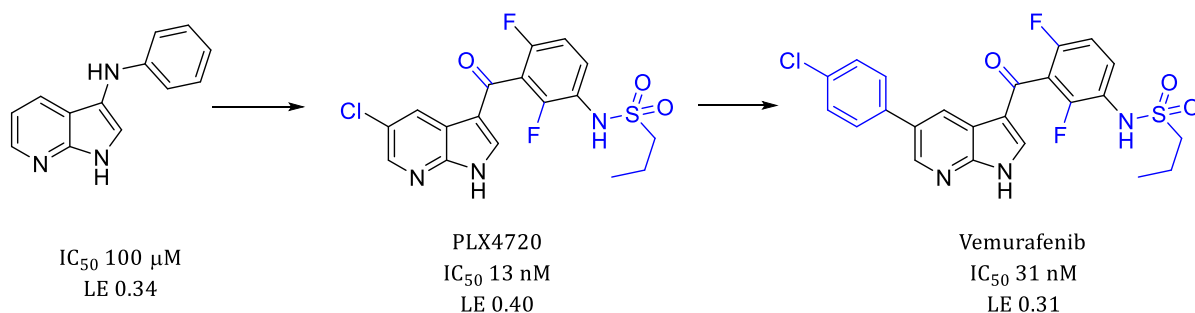
FBDD is currently widely used both in industry and academia as a powerful and complementary drug discovery approach. FBDD has proved to be efficient in delivering drug candidates for targets that have been regarded as ‘undruggable’ in the past, such as protein-protein interactions (PPIs).⁵ Currently, around 40 new molecular entities at different clinical stages have been developed using FBDD for a variety of targets. Table 1 lists some of the drug candidates discovered using FBDD currently in phase II, III and approved.¹⁸ In addition, it is estimated that at least 20 molecules are currently undergoing phase I studies.

Table 1 - List of selected drug candidates discovered using a FBDD approach currently in late-stage clinical studies.

Drug	Stage	Company	Target
Vemurafenib	Approved	Plexxikon	B-Raf
Venetoclax	Approved	AbbVie/Genentech	Bcl-2
Asciminib	Phase III	Novartis	Bcr-Abl
Erdafitinib	Phase III	Astex	FGFR1-4
Lanabecestat	Phase III	AstraZeneca/Lilly/Astex	BACE1
PLX3397	Phase III	Plexxikon	CSF1R, KIT
Verubecestat	Phase III	Merck	BACE1
AT7519	Phase II	Astex	CDK1,2,4,5,9
AT9283	Phase II	Astex	Aurora, JAK2
AUY-922	Phase II	Novartis	HSP90
AZD5363	Phase II	AstraZeneca/Astex/CRUK	AKT
CPI-0610	Phase II	Constellation	BET
DG-051	Phase II	deCODE	LTA4H
Eft508	Phase II	eFFECTOR	MNK1/2
Indeglitazar	Phase II	Plexxikon	Pan-PPAR
LY2886721	Phase II	Lilly	BACE1
LY517717	Phase II	Lilly/Protherics	FXa
Novitaclax	Phase II	Abbott	Bcl-2/Bcl-xL
Onalespib	Phase II	Astex	HSP90
PF-06650833	Phase II	Pfizer	IRAK4
PF-06835919	Phase II	Pfizer	KHK

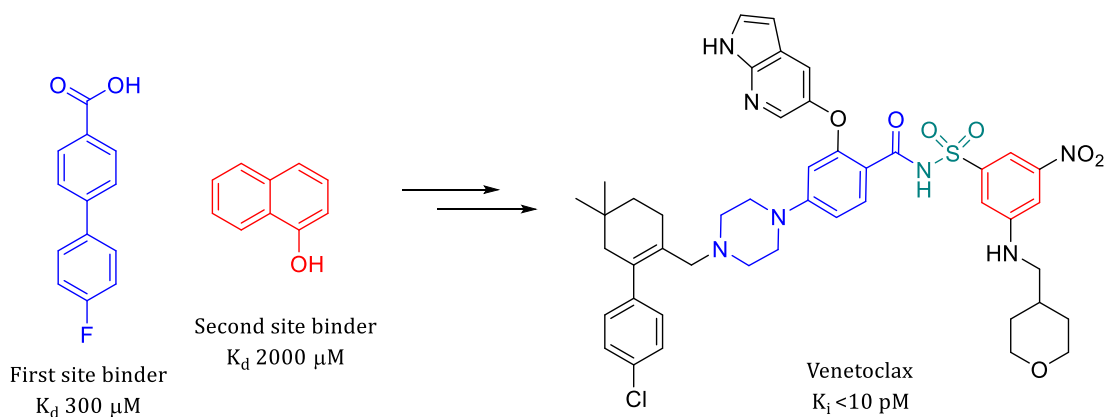
Highlighting the importance of FBDD in drug discovery, in 2011, the FDA approved the first fragment-based drug Vemurafenib (Zelboraf®) for the treatment of late-stage melanoma.¹⁹

Vemurafenib was developed from an azaindole derivative fragment (Scheme 1) and targets the ATP binding site of a mutant serine-threonine protein kinase B-Raf (V600E). Using a growing strategy, the initial fragment hit (IC_{50} 100 μ M) was elaborated into the 31 nM inhibitor Vemurafenib.



Scheme 1 - Growing strategy applied to the development of Vemurafenib, the first drug developed using a FBDD approach. The parts of the molecule that represent the growth of the initial fragment are shown in blue.

In 2015, Venetoclax (Venclexta®), a Bcl-2 antagonist, was approved for the treatment of chronic lymphocytic leukaemia, demonstrating the increasing success of the FBDD approach.²⁰ Venetoclax was developed adopting a linking strategy between two weakly binding fragments engaging two proximal pockets of Bcl-x_L (Scheme 2). The fragment elaboration was guided by an ‘SAR-by-NMR’ approach (Structure-Activity-Relationship guided by 2D protein-ligand NMR studies).²¹ Importantly, Venetoclax mimics the native BH3 domain of the pro-apoptotic Bcl-2 proteins, thereby acting as one of the first small molecules targeting a difficult PPI.



Scheme 2 - Chemical structures of Venetoclax and the initial fragments (blue and red) binding to two different binding sites. A linking strategy was adopted to link the two weakly binding fragments together via a sulfonamide (green).

Despite the fact that FBDD emerged only 30 years ago, two drugs have already been approved by the FDA, and there are a great number of molecules currently undergoing clinical studies. This evidence altogether makes FBDD a promising and efficient alternative to discover new drugs, especially those interacting with difficult biological systems.¹

1.2. Therapeutic peptides^e

Small molecules (FW < 500 Da) have traditionally been used to target deep and well-defined pockets of biological targets (*e.g.* proteins, enzymes, receptors, ion-channels *etc.*). Advances in biology, however, brought to light that 80% of the signalling pathways regulating important physio-pathological mechanisms are characterised by the interactions between proteins - often referred to as PPIs.²² Such interactions are characterised by the contacts between shallow and undefined pockets^{23,24,25} and, except for a few successful examples,²⁶⁻³¹ the failed attempts to target PPIs with small molecules are still numerous. Peptides are an ideal alternative to small molecules: they mimic the endogenous portions of the interacting proteins; they show low immunogenicity since they are made of proteinogenic amino acids; they can be easily synthesised; and they have lower production costs compared to other biologics.³² However, the development of peptide therapeutics is limited by their poor pharmacokinetic (PK) properties.³³ In particular, peptides suffer from poor membrane permeability, poor stability to plasma proteases and high renal excretion often resulting in a short half-life.³⁴ However, nature provides inspirational examples of a significant number of biologically-active peptides that validate their ability to interfere with both extra- and intra-cellular processes.³⁵ These successful examples have inspired scientists to develop new methodologies aimed at overcoming the PK limitations of this class of molecules.

1.2.1. Macrocyclised peptides

Peptide cyclisation is probably the most widely adopted strategy to ameliorate the PK properties of peptides, with at least 125 macrocyclic peptides being reported as orally bioavailable.³⁶ The macrocyclisation process on peptides, assuming it does not affect their secondary structure,³⁶ is performed to lock the macromolecules in their binding conformation preserving their function and reducing entropic costs.³⁷ Conversely, other methodologies applied to improve the PK properties of peptides, such as *N*-alkylation or the introduction of amide isosteres (peptidomimetics), may affect the peptide backbone resulting in changes that could compromise the peptide bioactivity. Peptide macrocyclisation can be achieved in different ways, and a schematic overview of the different techniques is shown in Figure 3.

^e The text of this paragraph has been adapted from Iegre *et al.*, *Advanced Therapeutics*, 2018.⁵⁹

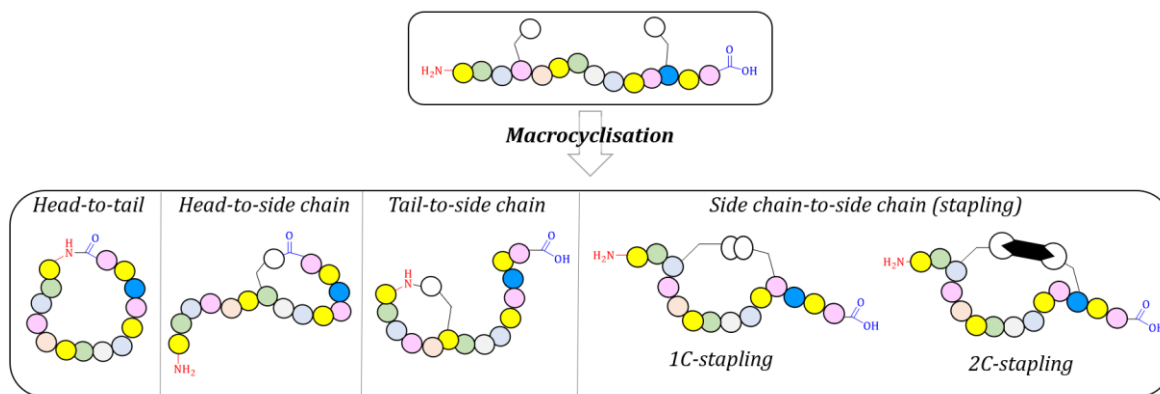


Figure 3 – Main classes of macrocyclisation techniques: head-to-tail, head-to-side chain, tail-to-side chain, side chain-to-side chain that can be divided into 1C- and 2C-stapling. Peptide head (C-terminus) is shown as a blue carboxylic acid, tail (N-terminus) as a red amine. Side chains involved in macrocyclisation are presented as white spheres and the linker in black.

The head-to-tail cyclisation generally involves the *N*-terminus and *C*-terminus of the peptide chain linked together *via* an amide bond; head-to-side chain and tail-to-side chain cross-link one of the terminus to a side chain of the peptide; side chain-to-side chain macrocyclisation, instead, involves the linkage of two side chains of the peptide sequence with or without the aid of a linker.^{37,38} The intramolecular reaction to cross-link two amino acids of the linear sequence is often referred to as one-component (1C) peptide stapling (PS).³⁸ On the other hand, intermolecular coupling involving a staple (or linker) and two amino acid side chains is referred to as two-component (2C) PS.^{37,39–41} It should be noted that the term *stapling* often refers to macrocyclisations that produce α -helical peptides. When a cyclisation reaction results in a non-helical peptide, the term *constraining* is generally accepted. In this dissertation, however, the terms *stapling* and *constraining* will be used interchangeably to describe macrocyclisations resulting in secondary structures beyond α -helices as well.

In this dissertation, the stapling methodologies only will be presented in detail in the following paragraphs.

1.2.1.1. One-component peptide macrocyclisation methodologies at a glance

1C-PS is the oldest and simplest of the two classes of peptide stapling methodologies. Disulfide bridge formation between two Cys residues is a common constraining methodology often adopted by nature to stabilise peptides and proteins. Disulfide bonds, however, are susceptible to being reduced in certain environments, such as those found intracellularly;⁴² therefore, alternative 1C stapling techniques have emerged to overcome this limitation. The most used 1C stapling technique is the all-hydrocarbon (AH) chemistry which involves a Ring-Closing Metathesis (RCM) reaction between two unnatural amino acids bearing terminal alkenes on the side chains. First reported by Grubbs and Blackwell in the 1990s, the RCM has been widely adopted to stabilise several biologically active and cell-penetrating peptides into helical

structures.^{43,44} The RCM has been thoroughly optimised and, when the appropriate stapling position and amino acids are used, it proved to be successful in enhancing the helicity of peptides, improve the stability to proteases and impart cell-permeability to otherwise impermeable peptides.⁴⁵⁻⁴⁷ Another widely used 1C-PS chemistry is lactam formation. Reported for the first time in the late 1980s, lactam cyclisation provided peptides with superior bioactivity compared to the linear analogues.⁴⁸ Lactam stapling has been mainly applied to peptides targeting extracellular or membrane-bound proteins, and its applicability to intracellular targets is yet to be determined.^{48,49} Even if more stable to proteolytic degradation than their linear counterparts, peptides stapled using this technique show inferior stability in respect to RCM-stapled peptides.⁵⁰ Since the advent of the pioneer 1C-PS methodologies, a plethora of alternative reactions have emerged in the literature, including: thiol-ene reactions between Cys and alkene amino acids,⁵¹ copper-catalysed azido-alkyne cycloaddition (CuAAC) between azido and alkyne groups,⁵²⁻⁵⁴ C-H activation reaction to cross-link aromatic side chains of natural amino acids,⁵⁵ thioether formation,⁵⁶ oxime formation,⁵⁷ and UV-promoted cycloaddition⁵⁸ among others (Figure 4).

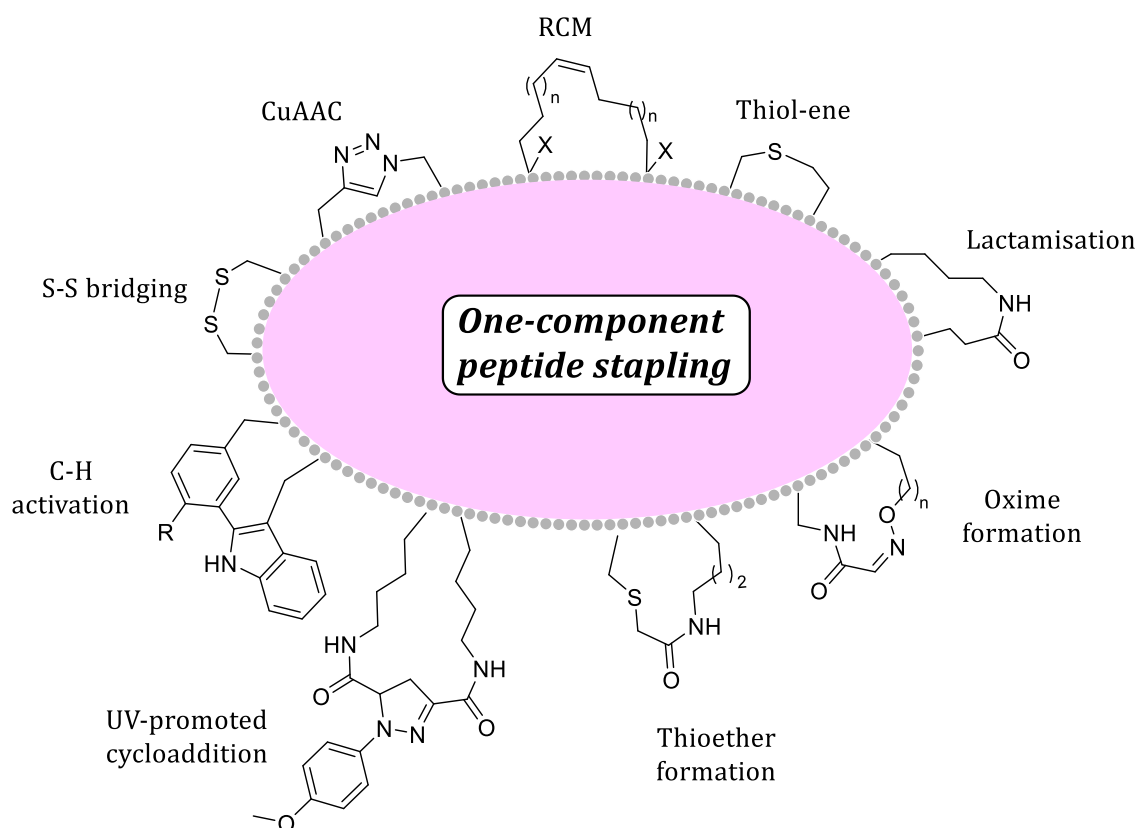


Figure 4 - Overview of selected one-component peptide stapling chemistries using side chains of natural and unnatural amino acids. Amino acids are represented as grey spheres.

General conclusions on the applicability of all the above-mentioned techniques to biologically-relevant targets cannot be drawn considering that a limited number of comparative examples are available in the literature for all these emerging techniques.

The well-established 1C-PS techniques offer the advantage of being carried out on resin, thus saving purification steps. However, 1C-PS methodologies present one main disadvantage: any changes to the staple or the sequence required for peptide optimisation involve the re-synthesis of the amino acid used for stapling, synthesis of the linear peptide sequence, and re-stapling.⁵⁹ Significant optimisation may be required for each of these steps, including the insertion of the new amino acid in solid-phase peptide synthesis (SPPS) procedures. To overcome these limitations, research groups have focused on the development of 2C macrocyclisation methodologies.

1.2.1.2. Two-component peptide macrocyclisation methodologies

Unlike the 1C stapling techniques, the 2C-PS offers a considerable advantage: the staple or constraint is optimised independently from the peptide sequence, and it can be used to introduce cell-permeable motifs, fluorescent tags, functionalities useful for biological assays or to improve the PK properties of the overall peptides in a combinatorial manner.⁵⁹ Most of the 2C-PS techniques derive from the 1C counterparts and involve both natural and unnatural amino acids. Unlike the 1C macrocyclisations, 2C stapling is often not performed on-resin due to site-isolation issues that penalise the desired intramolecular reaction in favour of the intermolecular reactions (Figure 5).⁵⁰

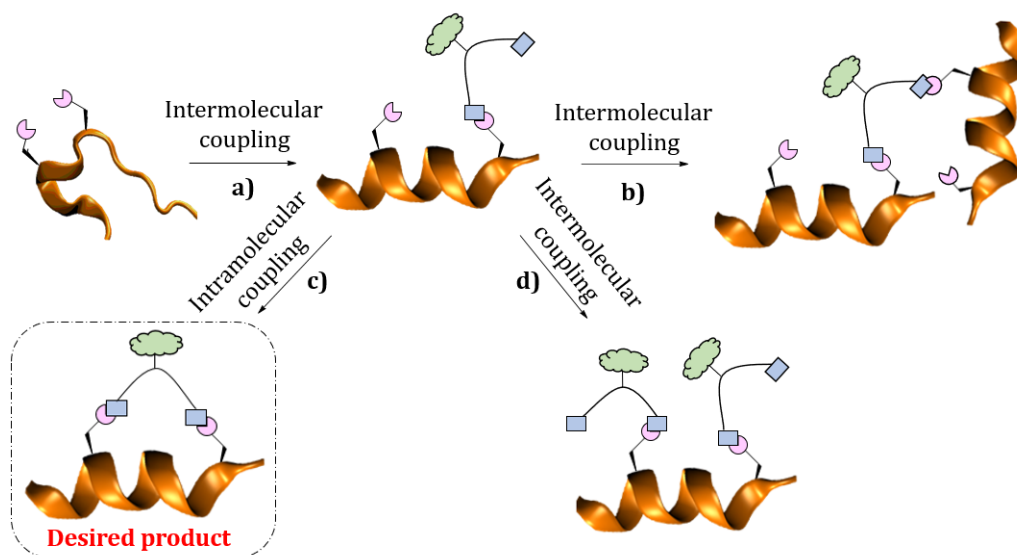


Figure 5 - Potential reaction pathways that can occur during the 2C-PS after the initial intermolecular coupling (a). Intramolecular coupling to give the desired product macrocycle (c), or a number of different undesired products due to multiple intermolecular coupling reactions (b, d). Taken from Iegre et al., *Advanced Therapeutics*, 2018.⁵⁹

The most reactive amino acid side chains are suitable for use in peptide macrocyclisation, with cysteine being the most used due to the high nucleophilicity of the sulfhydryl group.⁶⁰⁻⁶³ With respect to their unnatural counterparts, natural amino acids are cheap, widely available and hence simplify the synthesis of the linear peptide. However, the use of natural amino acids could lead to orthogonality and chemo-selectivity problems. Thiol-ene, in both radical and conjugate

addition, and S_N2 reactions are the most commonly used reactions for the application of Cys to peptide stapling with a limited number of reports on S_NAr .

Greenbaum and Waters pioneered the field with the use of aryl-halide linkers to cross-link two Cys side chains, whilst Timmerman *et al.* have recently modified the aryl-halide linkers into water-soluble staples to access functionalised stapled peptides (Figure 6).^{64–66} Importantly, the cross-linking between aryl-halides and the thiol groups of Cys residues has been renamed as CLIPS (Chemical Ligation of Peptide into Scaffolds) technology, and it is currently used by start-ups and pharmaceutical companies to access the so-called bicycle and tricycle peptides. Dawson *et al.* made use of 1,3-dichloroacetone to cross-link between Cys residues *via* an S_N2 reaction followed by oxime linkage to introduce functionalities.⁶⁷ Likewise, Cramer *et al.* exploited the S_N2 reaction between diiodomethane and Cys residues to convert labile disulfide bridges into stable methylene thioacetals (Figure 6). Bernardes *et al.* have recently reported a biocompatible and chemo-selective methodology which exploits the reaction between cysteine and dibromo-isobutylene to give cell-permeable grafted peptides.⁶⁸

Examples of thiol-ene reactions in peptide stapling are provided by Jiang *et al.* who used divinyl sulphonamides as linkers for 2C-PS with Cys.⁶⁹ Similarly, Chou *et al.* reported of a light-mediated thiol-ene 2C stapling method utilising bis-alkene linkers.⁷⁰ A similar method was developed by Keillor *et al.* using functionalised maleimides (Figure 6).⁷¹

S_NAr cysteine stapling chemistry has been reported by Pentelute *et al.* who exploited the reactivity of sulfhydryl groups towards perfluoroaryl compounds to access stabilised peptides,⁷² whilst Derda *et al.* utilised decafluoro-diphenylsulfone to the same end.⁷³ Remarkably, these stapling methodologies can be applied to Lys in addition to Cys residues (Figure 6).

Cys-mediated peptide stapling reactions have also been used to generate reversible systems which efficiently pass between rigid and flexible states in a biorthogonal manner, with the aim of elucidating the relationship between binding, biological activity, and secondary structure. To this end, Wilson *et al.* utilised the nucleophilic substitution reaction between dibromo maleimide linkers and Cys (Figure 6).⁷⁴ Similarly, Smith *et al.* employed an S_NAr reaction to staple the peptide *via* 3,6-dichloro-1,2,4,5-tetrazine: under UV radiation such a linker would open and provide the uncyclised peptide bearing cyano groups on the cysteine residues.⁷⁵ Treatment with an excess of cysteine would return the starting peptide (Figure 6). The 3,6-dichloro-1,2,4,5-tetrazine linker was functionalised *via* a reverse-electron demand Diels Alder.⁷⁵

A limited number of examples see natural amino acids other than Cys in 2C-PS; namely Trp and Glu (Figure 6). Johannes *et al.* have developed a method in which two tryptophan residues were reacted with a *para*-substituted benzaldehyde in a condensation reaction to form

conformationally constrained model peptides with improved proteolytic stability towards proteases compared to the linear analogue.⁷⁶ On the other hand, McDowell *et al.* reported an example of bis-lactamisation in peptide stapling utilising Glu amino acids that, after being protected, were reacted with diaminoalkanes to stabilise model helical peptides (Figure 6).⁷⁷

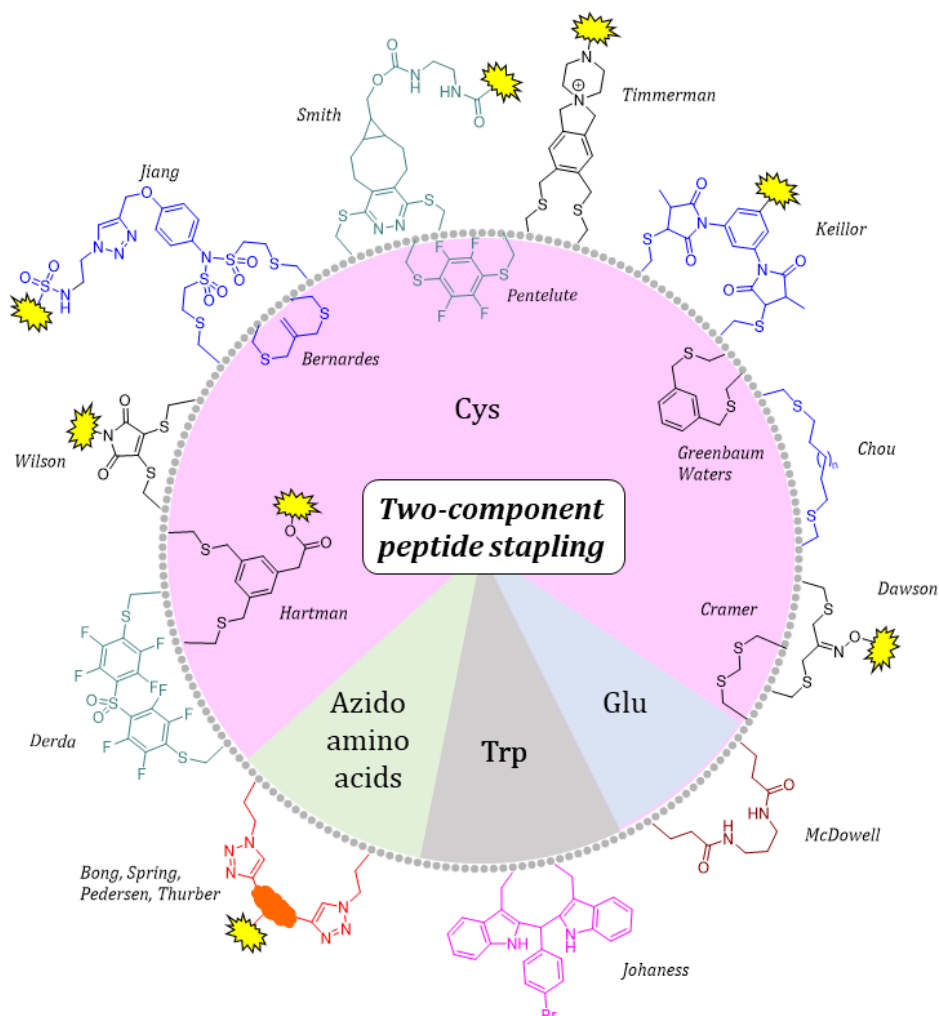


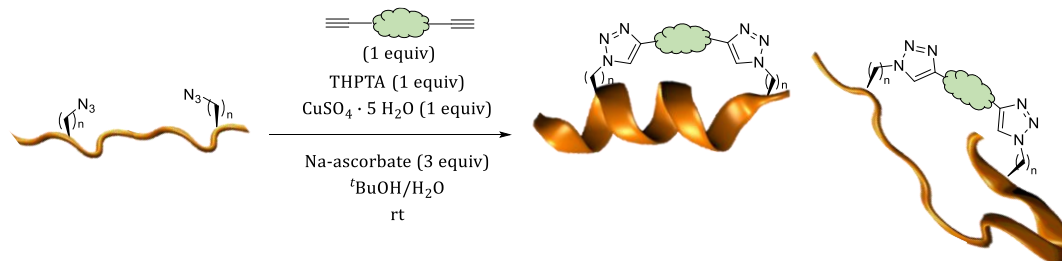
Figure 6 – Selected 2C-PS chemistries using Cys side (pink background), Trp (grey background), Lys (light blue background), and azido side chains (green background). Macrocycles obtained via thiol-ene reactions are shown in blue, in green stapling via S_NAr and in black S_N2 . Stapled peptides obtained via CuAAC are shown in orange and lactamisation in brown. The yellow cloud indicates that various functionalities have been added to the staple/constraint.

The only 2C-PS methodology that uses unnatural amino acids is the CuAAC (Figure 6), and it will be discussed in detail in the next paragraph.

1.2.1.2.1. Spotlight on 2C CuAAC peptide chemistry

Pioneer work carried out by Bong *et al.* reported azido-alanine residues being introduced at an $i,i+4$ distance to each other and clicked with aliphatic and aromatic dialkyne linkers to stabilise a peptide based on a GCN4 leucine zipper.⁷⁸ Inspired by this work, the Spring group expanded the 2C-PS methodology to include stapling positions beyond $i,i+4$ and, importantly, to introduce functionalisation on the linker. The CuAAC 2C stapling reaction involves an intermolecular

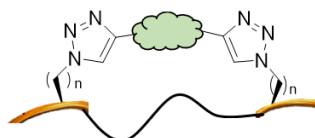
coupling between two azido side chains of a linear peptide and a bis-alkynyl linker to give the cyclised peptide. The optimised macrocyclisation reaction is carried out in aqueous conditions, at low concentrations of peptide (1 mg/mL) and with one equivalent of the linker (Scheme 3).³⁸



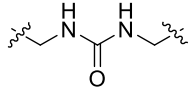
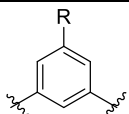
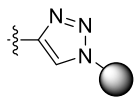
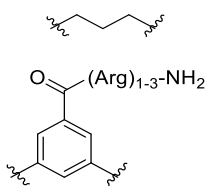
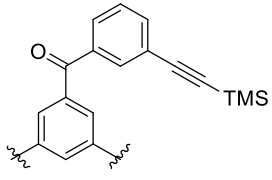
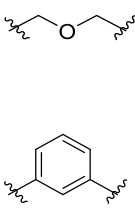
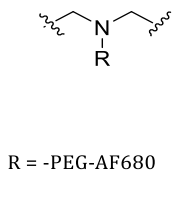
Scheme 3 - Schematic representation of the CuAAC 2C-PS. The peptide is shown in orange, the core of the constraint as a green cloud. THPTA = Tris(3-hydroxypropyltriazolylmethyl)amine. $n = 1$ to 4.

Among the disadvantages associated with the CuAAC 2C-PS technology there is the use of non-proteinogenic amino acids containing azido side chains, the use of a copper(II) catalyst which leads to air-sensitivity of the catalytic copper-complex, requiring all solvents to be degassed, and the risk of toxicity arising from any residual copper in the final stapled peptides.³⁸ On the other hand, there are a number of advantages that outbalance the drawbacks of this methodology. In particular, the use of azido side chains provides orthogonality with respect to the other amino acids, leading to the avoidance of chemo-selectivity issues. Furthermore, the azido amino acids can be readily synthesised in few steps, the conditions used in the stapling reaction are mild, and functionalisation of the linkers is relatively easy, allowing the quick and efficient generation of libraries of functionalised stapled peptides.³⁸ Peptides constrained using the CuAAC 2C-PS methodology have proved to be stable to proteolytic degradation, cell-permeable, biologically active in cells, and have led to the creation of a toolbox of functionalised staples that found application in different targets.⁷⁸⁻⁸⁴ A list of selected peptides macrocyclised using the CuAAC 2C-PS chemistry is shown in Table 2.

Table 2 – List of selected biologically active macrocyclic peptides obtained using the CuAAC 2C-PS methodology.



Position	n	Constraint	Structure	Sequence	Ref
$i, i+4$	2		Extended	TNKS REXGDGXE	84
	3		Helix	GNC4 Leucine Zipper RIKQLEEKIXGLGXKIEELEKK	78
$i, i+6$	3		Helix	Cft4 MDIXIDDILXELDKETTAV	82

2		Extended	HNF1β TAMRA-Ahx-TXKKMRRXR	83
2		Helix	Model peptide AAEAWAXAEAAEAXEA	81
3	R = H, 		Gsα RDIXQRNorLHLRXYELL	80
<i>i,i+7</i>		Helix	p53 LTFXHYWAQLSX	85
	3			p53 ETFXDLWRLLXEN
2		Helix	GLP-1 HAEGTFTSDVSSYXEGQAAKXFIAWLVKGR	87
			Exedin HGEGTFTSDLSKQXEEEEAVRXFIEWLKNGGPSS GAPPPS	

 = functionalities including biotin, PEGs, fluorescent tags, and cell-permeable motifs.

Considering the variety of 2C-PS methodologies developed to date, it is clear that the decision of which one to use depends mainly on the structure of the peptide to be constrained and on the availability of the starting materials. The CuAAC 2C-PS methodology is among the most widely applied 2C-PS chemistries.⁷⁸⁻⁸⁷ It proved itself compatible with various amino acid sequences, enhanced the activity and proteolytic stability of several biologically active peptides, and it is applicable to both helical and non-helical peptides.⁷⁹⁻⁸⁴ Therefore, the CuAAC 2C-PS technique presents itself as a feasible stapling methodology to use when the priority is to functionalise the constrained peptides or study novel functionalised staples since the macrocyclisation reaction itself is well-validated.

1.2.1.3. Discovery of therapeutic macrocyclised peptides

The strategies used to develop therapeutic macrocyclised peptides can be divided into three main groups: natural products, screening of peptide libraries, and target-based rational design (Figure 7).

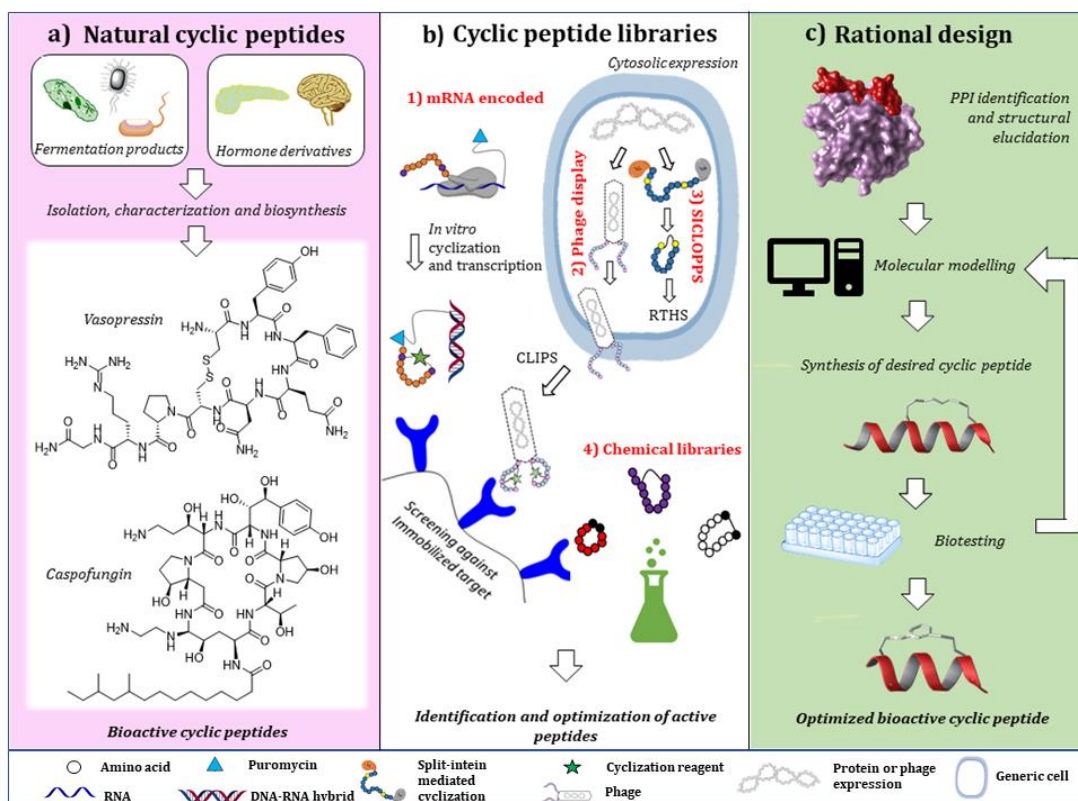


Figure 7 – Major approaches adopted by pharmaceutical industries and academic groups to discover cyclic peptides as therapeutics: a) Peptides derived from natural sources; b) biological and chemical peptide libraries; 1) mRNA encoded libraries expressed *in vitro* and cyclised using specific reagents; 2) phage-display libraries expressed by bacteriophages in host cells and cyclised after phage release either by disulfide bridge formation or by CLIPS technology; 3) genetically selected cyclic peptides expressed in bacteria, cyclised in cell using the SICLOPPS technology and tested in functional assays in cells (RTHS: reversed bacteria two-hybrid system); 4) chemical libraries of cyclic peptides synthesised in parallel or using combinatorial chemistry; c) Target-based rational design of cyclic peptides: a generic PPI is shown as pink and red surface, designed peptides as red helices, and staple in grey sticks. Taken from Iegre et al., *Advanced Therapeutics*, 2018.⁵⁹

Natural and semi-synthetic cyclic peptides (Figure 7a) pioneered the use of this class of macromolecules as therapeutics; indeed, nine natural product cyclic peptides were approved by the FDA and EMA between 2005 and 2015.⁸⁸ Examples of this class of molecules are fermentation products of microorganisms - Caspofungin,^{89,90} Cyclosporin A,⁹¹ Daptomycin,⁹² Anidulafungin,⁹³ Romidepsin,⁹⁴ Linaclotide and Pasireotide⁹⁵ among others - hormones and hormones derivatives - Vasopressin, Octreotide and Oxytocin.⁸⁸ These peptides find application as antifungal agents, antibiotics, chemotherapeutics, treatments for hormonal disorders and offer the advantage of being highly selective and stable *in vivo*.

Peptide libraries can be divided into biological and chemical libraries. Biological peptide libraries (Figure 7b) are synthesised with the aid of bacteriophages (phage-display) or using

cell-free display technologies (mRNA display) and cyclised using some of the methodologies listed herein:

- cysteine amino acids are added to the phage-displayed peptide in a random manner to allow successive disulfide bridge formation.^{96–100} The “CLIPS” cyclisation technology is a variant of this methodology, and it generates bicyclic peptides *via* conjugation between three cysteine residues and a tris-(bromomethyl)benzene (TBMB) core.¹⁰¹ More recently, alternative trivalent thiol-reactive linkers have been used to provide bicyclic peptides characterised by diverse conformations and include *N,N,N'*-(benzene-1,3,5-triyl)tris(2-bromoacetamide) (TBAB), *N,N,N'*-benzene-1,3,5-triyltrisprop-2-enamide (TAAB) and 1,3,5-triacryloyl-1,3,5-triazinane (TATA) (Figure 8a);¹⁰²
- head-to-tail cyclisation performed intracellularly exploiting the protein splicing capability of split inteins (the so-called SICLOPPS technology).^{103,104} This technology implements a reverse two-hybrid system to allow for functional and binding assays (Figure 8b);
- mRNA encoded libraries of linear peptides are translated *in vitro* in a cell-free system. Cyclisation is then performed using reagents like disuccinimidyl glutarate to connect the *N*-terminus and a side chain of a Lys residue or *via* disulfide bridges across Cys residues (Figure 8c).^{105,106}

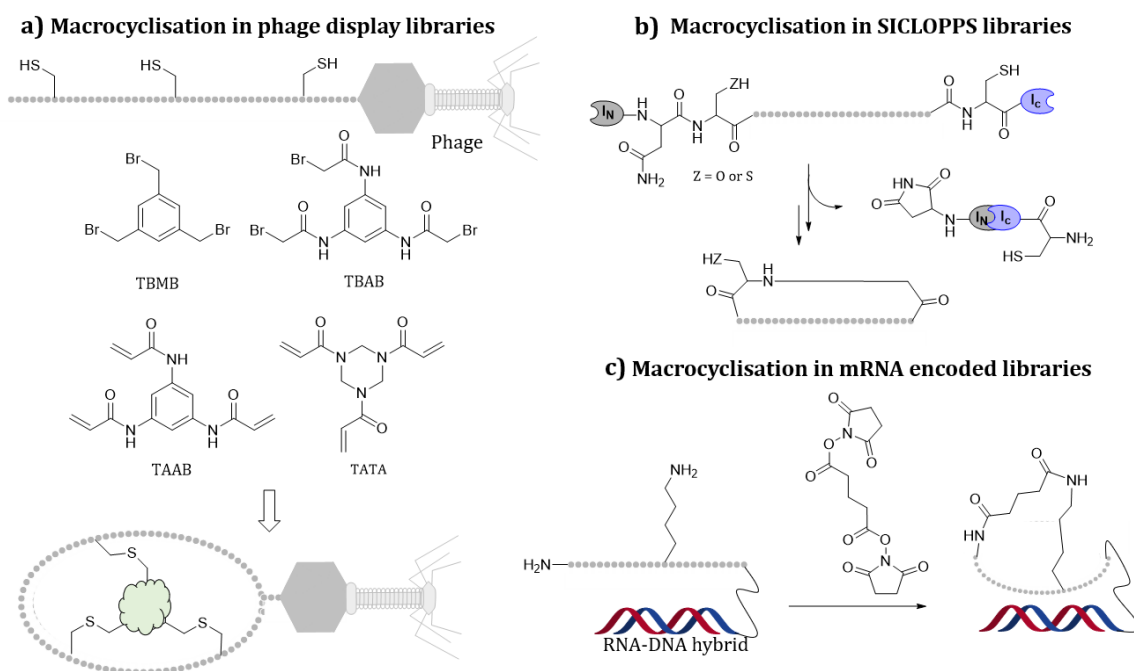


Figure 8 - Main types of cyclisation chemistries performed in the generation of biological libraries. a) CLIPS macrocyclisation used in phage display. The generic core is shown as a green cloud; b) Intein mediated SICLOPPS cyclisation; c) cyclisation done on mRNA encoded library. The DNA-RNA hybrid transcript is shown as blue and red helices, linkage of the peptide to the nucleic acid strand as a black, curved line. Generic amino acids are shown as white spheres.

Phage-display peptide libraries offer the advantage of providing highly diverse libraries. However, the peptides generated may have low affinity for the target and problems associated with the use of live cells and phages could arise. mRNA encoded libraries may overcome these limitations, therefore representing a valid alternative.¹⁰⁷ New genetic technologies have recently emerged to allow the incorporation of unnatural amino acids into biological libraries, providing more flexibility in the composition of the peptide sequence.¹⁰⁸⁻¹¹⁰ Of particular interest are the mRNA-encoded peptide libraries developed in the Suga group: thioether macrocyclic peptides are generated following spontaneous intramolecular reaction between Cys residues and the side chains of unnatural *N*-(chloroacetyl)-*D*-Trp or *N*-(chloroacetyl)-Tyr (Figure 9a).^{111,112} An alternative cyclisation has been achieved by the same group with the introduction of 5-hydroxytryptamine and benzylamine amino acid derivatives followed by fluorogenic oxidative coupling between the two side-chains to afford fluorescent cyclic peptides (Figure 9b).¹¹³

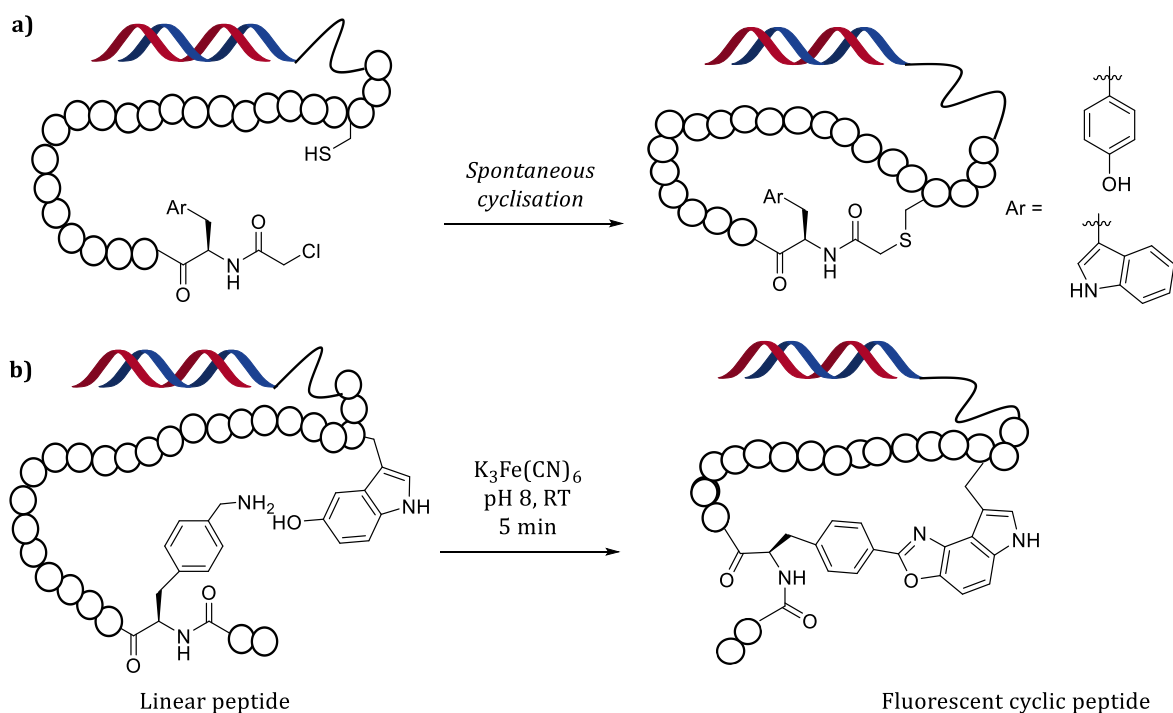


Figure 9 - Macrocyclisations performed using unnatural amino acids in peptide ribosomal synthesis. a) Macrocyclisation obtained using *N*-(chloro-acetyl) amino acid derivatives; b) Macrocyclisation performed using *N*-benzylamine and hydroxy tryptamine derivatives to obtain fluorescent cyclic peptides. The DNA-RNA hybrid transcript is shown as blue and red helices, linkage of the peptide to the nucleic acid strand as a black, curved line. Generic amino acids are shown as white spheres.

Chemical libraries of cyclic peptides, on the other hand, are synthesised using parallel or combinatorial chemistry. Parallel synthesis is limited in the number of macrocycles that can be simultaneously generated, whilst combinatorial methods allow the generation of a greater number of compounds. Once assembled, the chemical peptide libraries can be screened against a selected target before or after cleavage from the resin support.¹¹⁴

The target-based rational design approach aims to develop cyclic peptides for well-validated targets for which structural information of the protein of interest is available. This approach does not require the synthesis of many biomolecules since the peptides designed feature amino acid sequences that resemble portions of the native protein that is being mimicked. This approach allows for more flexibility for peptide modification and the amount of product synthesised. Furthermore, a target-based rational design approach can be used to optimise hit peptides coming from library screenings.⁵⁹

In a typical example (Figure 7c), an X-ray crystal structure of the target protein and ideally of the native PPI is desired. *In silico* molecular modelling can guide the design of the peptide and identify suitable residues for cyclisation to happen.¹¹⁵ Further changes in the peptide sequence are aimed at replacing amino acids to increase the binding affinity and optimise PK properties. Subsequently, the designed peptides are synthesised and assessed *in vitro*. Iterative cycles of enzymatic, cellular, structural assays and synthesis are performed to build an SAR and guide further modifications until the optimal peptide is developed prior to *in vivo* testing. This approach offers the advantages of knowing the target in advance, and the synthesis of a smaller number of peptides is required to generate novel synthetic peptides with a high affinity for the desired target and improved PK properties. The main drawback of the target-based rational design approach is the need for detailed structural information of target and natural PPI sequence to guide the design.⁵⁹

1.2.1.4. Cyclised peptides in advanced stages of the pipeline

Twenty-six cyclic peptide therapeutics have been approved by the FDA thus far.¹¹⁶ Of these, twenty were cyclised *via* intramolecular formation of disulfide bridges, four *via* intramolecular amide bonds and two *via* intramolecular formation of other types of chemical bonds (ester and carbamate).¹¹⁶ Vasopressin, the first cyclic peptide marketed, was approved in 1962 for the treatment of anti-diuretic hormone deficiency, and it is constrained *via* an intramolecular disulfide bridge. Macrocyclisation techniques besides disulfide bridging and lactamisation only became popular in the late 1990s, and it is therefore not surprising that the cyclic peptide drugs approved thus far do not feature more modern type of macrocycles, considering the long timelines of drug discovery and clinical studies. Noteworthy, most of the cyclic peptides with therapeutic applications approved to date derive from natural products. Thanks to the advances in biotechnology, the cyclic peptides that are currently undergoing clinical development feature both classic and modern cyclisation chemistries and have been discovered using directed-evolution techniques, rather than being inspired by natural products.¹¹⁷ An overview of some notable cyclic pharmaceutical peptides with public structures available currently in clinical studies and approved drugs is shown in Figure 10.

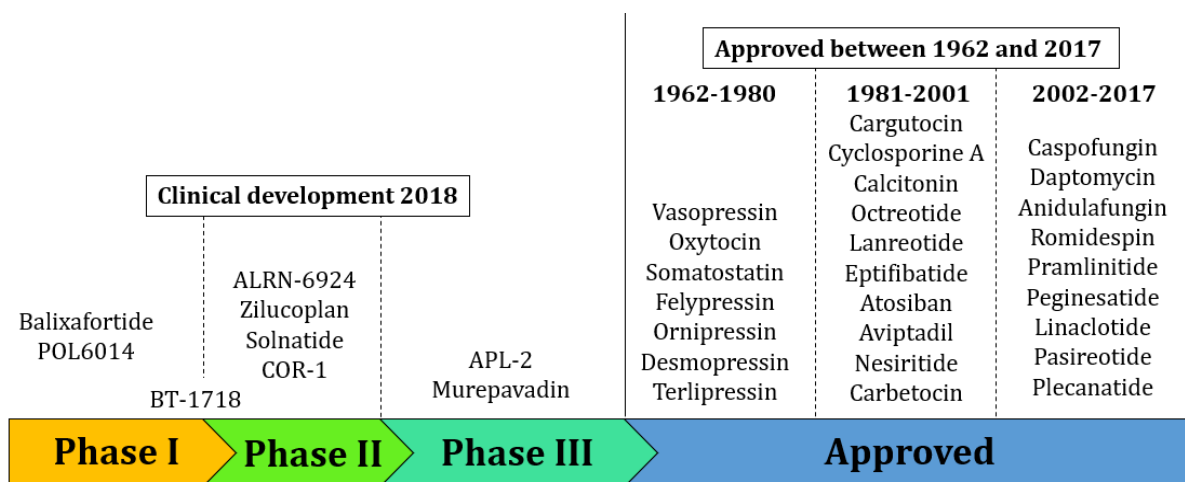


Figure 10 - Overview of cyclic peptide drugs currently under clinical development (2018) and cyclic peptide therapeutics approved between 1962 and 2017.^{116,118}

Historically, cyclic peptides found application in a wide variety of primary disease areas, with the majority of the drugs approved to treat infertility and obstetric/gynecologic disorders, cardiovascular and metabolic diseases (CVMD), and endocrinology-related diseases (Figure 11a).¹¹⁶ This fact has now been challenged by the cyclic peptides currently under clinical development, where oncology features as the main player in the therapeutic areas' field, closely followed by respiratory, inflammatory and autoimmune (RIA) diseases (Figure 11).¹¹⁸

Primary therapeutic areas

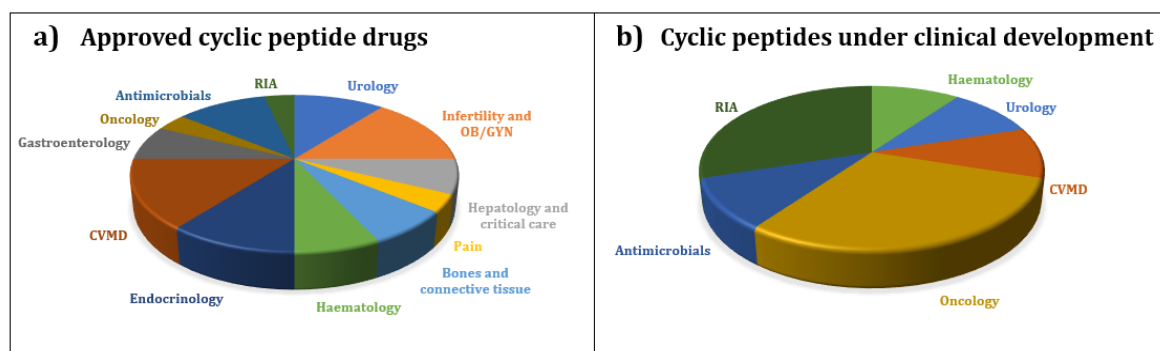


Figure 11 - Primary therapeutic areas of approved cyclic peptide drugs (a) and cyclic peptides currently under clinical studies (b). OB/GYN = obstetrics and gynaecology; CVMD = cardiovascular and metabolic diseases; RIA = respiratory, inflammatory, auto-immune diseases.

It should be noted that the interest of pharmaceutical companies working on cyclic peptides goes beyond oncology and RIA, with discovery pipelines focusing on the development of cyclic peptides for complement-mediated diseases (Ra Pharmaceuticals),¹¹⁹ CVMD, haematology, ophthalmology, and anti-infectives diseases (Bicycle Therapeutics),¹²⁰ and antimicrobials (Polyphor).¹²¹ It is therefore evident that in the next decades, the primary therapeutic area landscape is bound to change significantly again. In addition, considering that cyclic peptides are receiving the attention of an increasing number of pharmaceutical companies and academic groups, further therapeutic areas will most likely engage this new drug modality.

CHAPTER 2:

Anti-Apoptotic Proteins

Cellular-self destruction or programmed cell death (PCD) is a fundamental process that allows the cells to be eliminated should they become defective, old, and potentially harmful to the living organism.¹²² Apoptosis (type I PCD) is the major form of PCD, followed by autophagy (type II) and necrosis (type III). Considering that PCD is of crucial importance to homeostasis, the cells are equipped with a multitude of finely regulated mechanisms that allow them to escape apoptosis under physiological conditions and trigger it when potentially harmful alterations are detected.¹²² These mechanisms consist of complicated cross-signalling between proteins and messengers that occur both intracellularly and extracellularly. The pro- and anti-apoptotic signalling pathways are extremely complicated and, in some parts, not fully understood. The overall cascades can be divided into four major classes: tumour necrosis factor (TNF) pathway, survival pathway, DNA damage and stress pathway, and death ligands pathway as exemplified in Figure 12.^{123,124}

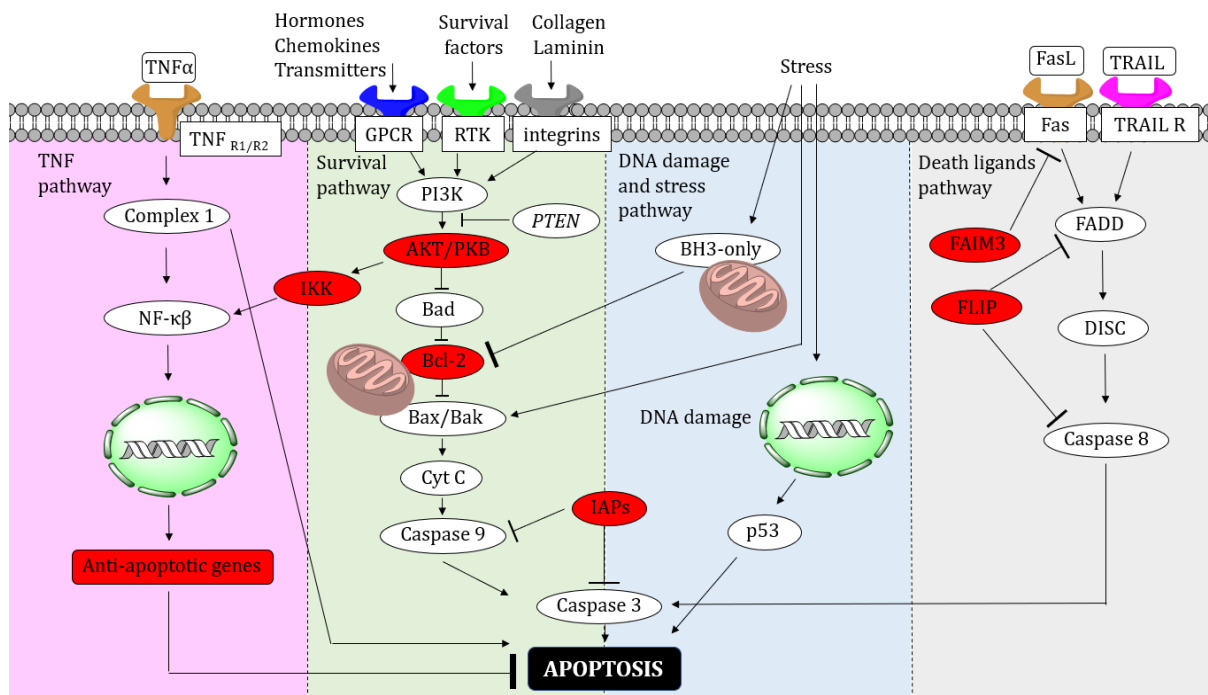


Figure 12 - Apoptotic and anti-apoptotic pathways divided by class. The figure does not intend to represent the pathways in full, and it provides an overview of the complexity of the cascades that regulate cell survival. Proteins and genes which play an anti-apoptotic role are shown in red. Activation is depicted as an arrow, inhibition as a dash at the end of the line.^{123,124}

The TNF pathway is considered an anti-apoptotic cascade: the cell signalling protein tumour necrosis factor α (TNF α) binds and activates the TNF receptors expressed on the cell membrane. The receptor, in turn, activates the complex-1 which triggers the NF- κ B protein complex initiating the transcription of anti-apoptotic genes.¹²⁵ The survival pathway is activated by a variety of extracellular ligands including hormones, chemokines, survival factors, collagen and laminin. Binding of these ligands to their receptors activates cytosolic kinases which all converge on the phosphorylation and activation of the AKT/PKB pathways resulting in the inhibition of the pro-apoptotic Bcl-2 proteins (such as Bad).¹²² When the pro-apoptotic Bcl-2 proteins are

inhibited, the anti-apoptotic proteins of the same family are activated and prevent the release of the cytochrome C with consequent activation of caspases, resulting in inhibition of apoptosis. The action of the survival pathway can be reinforced by the activation of the inhibitor of apoptosis proteins (IAPs) which inhibit the caspases, thereby preventing apoptosis from happening. Conversely, the phosphatase and tensin homolog protein PTEN can block the activation of the AKT/PKB pathways by PI3K kinase, inducing apoptosis.¹²² On the other hand, stress and DNA damage trigger apoptosis by activating the pro-apoptotic Bcl-2 proteins and by activating p53, among other effectors, in the nucleus.¹²⁶ Activation of pro-apoptotic Bcl-2 proteins (BH3-only proteins) means that mitochondria lose their outer membrane potential, the cytochrome C is released, and caspases are activated to exert apoptosis. Finally, apoptosis can be triggered by the so-called death ligands, namely FasL and TRAIL. The latter can indirectly stimulate the death-inducing signalling complex (DISC) to activate caspase 8 and therefore apoptosis.¹²⁶ Anti-apoptotic proteins such as FAIM3 and FLIP prevent the apoptosis by inhibiting components of this cascade. The death ligands pathway is often referred to as extrinsic apoptosis to differentiate it from the intrinsic apoptosis, which is mitochondria-associated.^{123,124}

Dysregulations that break the equilibrium between the activity of pro- and anti-apoptotic proteins are linked to the development and progression of pathological conditions, the most studied of which is cancer. Alterations that result in the cells becoming able to escape apoptosis include: activation or up-regulation of mitogenic signals (*i.e.* Erk1/2, AKT), inactivation or downregulation of pro-apoptotic proteins (*i.e.* Bax and Bak), and up-regulation of genes encoding for anti-apoptotic proteins (*i.e.* Bcl-2 proteins).¹²²

2.1. Inhibition of anti-apoptotic proteins

Considering the central role of anti-apoptotic proteins in regulating cell lifespan, it is not surprising that their dysregulation is implied in a variety of diseases. Restoring the naturally-occurring apoptotic activity in diseased organisms by acting on anti-apoptotic proteins has been reported to be a more successful strategy than targeting pro-apoptotic proteins.¹²² Anti-apoptotic proteins play important roles in neurodegenerative conditions including Alzheimer's and Parkinson's disease, as well as during heart attacks or ischemic strokes.¹²⁷⁻¹³⁰ Under these pathological conditions, there is a decreased activity of anti-apoptotic proteins in favour of a more pronounced apoptotic activity. On the contrary, in a number of physio-pathological conditions cells escape apoptosis to a much larger extent due to increased anti-apoptotic activity. Examples of such conditions include auto-immune diseases, inflammation, animal hibernation, and cancer.^{123,124,131,132}

Resistance to PCD is the hallmark of cancer cells, and inhibition of anti-apoptotic proteins is a well-exploited strategy in oncology. Such inhibition is achieved by targeting the apoptotic cascade at any level: mitochondrial outer membrane proteins (*i.e.* Bcl-2), proteasomes, nonproteolytic death effectors, death receptors, nuclear factors, stress kinases (Figure 12).¹³³ Depending on the desired target, apoptosis is induced utilising different approaches: for instance, anti-apoptotic gene transcription can be switched off; alternatively mRNA degradation can be induced using antisense oligonucleotides, then again small molecules, peptides, and antibodies can be developed to either inhibit the activity of a specific protein, or to prevent the cross-talk between proteins (PPIs).¹³³

The aforementioned pro- and anti-apoptotic pathways are the subject of intense study and scrutiny. Many of the proteins involved have been the subject of drug discovery campaigns, or probe-designing efforts, but several of their mechanisms still require elucidation. In an effort to analyse and comprehend these mechanisms better, two main proteins will be the focus of this dissertation: CK2 and Bcl-2.

2.1.1. Anti-apoptotic CK2 protein kinase

CK2 (formerly named protein Casein Kinase 2) is a protein kinase which plays crucial roles in multiple intracellular pathways including the regulation of cell proliferation and cell growth; it is also believed to be an anti-apoptotic protein in both healthy and cancer cells.^{134,135} It is, however, overexpressed in various cancer cell lines including breast, lung, prostate, colorectal, renal, leukaemia and glioblastoma brain tumours.^{136,137}

CK2 is a heterotetrameric enzyme composed of two catalytic subunits (α and/or α')^f and two regulatory subunits (β) (Figure 13).

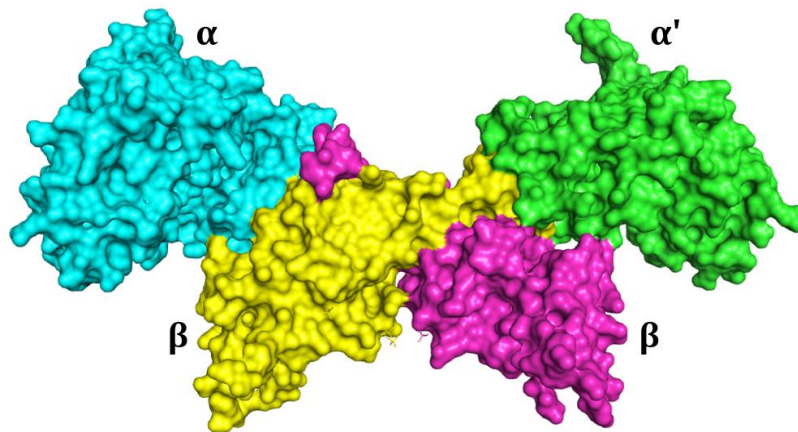


Figure 13 - Human CK2 holoenzyme (PDB code: 1JWH).¹³⁸ Catalytic subunits are shown in cyan (α) and green (α'), regulatory subunits in yellow and purple (β).

CK2 is constitutively active and uses ATP or GTP as co-substrate.¹³⁹ Interestingly, these characteristics are not common to other eukaryotic protein kinases (EPKs),¹³⁹ and the mechanisms that control its catalytic activity are unique to CK2.¹⁴⁰

Formation of the holoenzyme occurs *via* dimerisation of the β subunits followed by complexation with the *N*-terminal domain of CK2 α . The surface contact between the α and the β domains is relatively small compared to other PPIs (832 Å²). Thereby, the activity of the CK2 enzyme can be affected either by acting on the α subunits or by preventing the formation of the holoenzyme.

2.1.1.1. CK2 α subunit

CK2 α is composed of two domains, the *N*- and *C*-terminal domain with the ATP active site located between them (Figure 14).¹⁴⁰ The *N*-terminal domain (red-orange) contains five stranded β -sheets (β 1- β 5) and one α -helix (α C) situated next to the inter-domain cleft. The α C-helix contains basic lysine residues and has, therefore, a preference for acidic substrates.¹³⁸ The *N*- and *C*-terminal segments are linked *via* the hinge/ α D region, and the α D pocket that will be

^fThe α subunit presents 20 additional amino acids at the *C*-terminus that are absent in the α' subunit.¹⁴⁴

discussed in this work is located in close proximity to the α D helix. The C-terminal segment (green, blue and purple) is formed of α -helices and two double-stranded β -sheets at the inter-domain cleft and contains the activation loop. The conformation of the activation segment, as well as the glycine-rich loop (β 1 β 2-loop), is important for the catalytic activity of the protein.¹⁴⁰

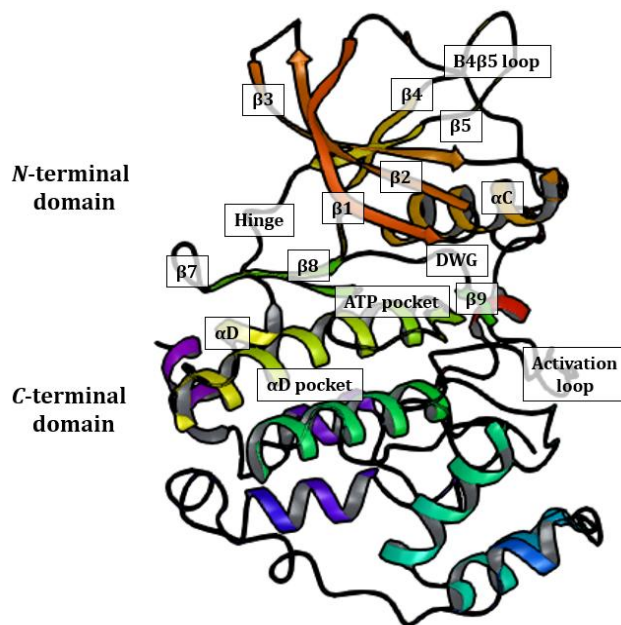


Figure 14 - Crystal structure of CK2 α subunit (PDB code 3NSZ).¹⁴¹ In orange-yellow the N-terminal domain and in green-blue the C-terminal domain of the catalytic subunit. The key parts of the protein are labelled in the figure.

The mechanisms that control the catalytic activity of CK2 are distinct from most other EPKs, namely the catalytic activity of CK2 is not controlled by phosphorylation (within the activation loop) or by interaction with regulatory proteins.¹⁴⁰ Instead, the conformation of the DWG motif (Asp175-Trp176-Gly177) in the activation segment and the adopted active conformation of the α C-helix make CK2 α constitutively active. In this conformation, the activation segment is open and allows for substrate binding and phosphor-transfer reactions. Specifically, the N-terminal segment establishes extensive contacts with the α C-helix and the activation loop, stabilising CK2 α in a constitutively active conformation.^{140,142} The ability of CK2 α to maintain the activation segment in this active form, unlike most EPKs, has also been attributed to differences in its sequence.¹⁴⁰ Most EPKs contain a DFG motif, whereas CK2 α feature a DWG motif. In EPKs, such as CK2's closest analogue CDK2, the central Phe is dynamic and variable between the active and inactive states (green in Figure 15). In CK2 (purple in Figure 15) an additional hydrogen bond between the indole-nitrogen of the Trp176 and the backbone carbonyl of Leu173 is established, thereby maintaining the active state conformation.¹⁴⁰

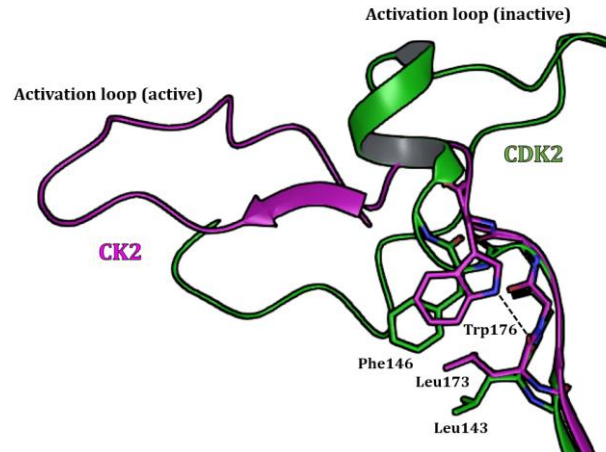


Figure 15 - Overlay of the activation segments of CK2 α (PDB: 1LP4, purple) and inactive form of CDK2 (PDB: 1HCK, orange). The DWG motif in CK2 α allows for an additional hydrogen bond to Leu173 as shown by the dashed black line.

Upon complexation with CK2 β , a major conformational change occurs in CK2 α : the β 4 β 5-loop of CK2 α , which is in the open form in X-ray crystal structures of the holoenzyme, switches to the closed form in the monomeric form.¹⁴³

2.1.1.2. CK2 β

The CK2 β subunit is smaller than the catalytic α domains (~28 kDa and ~48 kDa respectively) and, although it is not required to activate CK2 α , it regulates the activity of the kinase. In particular, CK2 β increases the thermostability of CK2 and enhances its catalytic activity. In addition, intracellular localisation of CK2 is influenced by the presence of CK2 β which is required for the protein shuttling between intracellular compartments. Moreover, CK2 β acts as a docking station for some CK2 substrates (*i.e.* Nopp140, p53, FAF-1, topoisomerase II, FGF-2, and eIF2 β)¹⁴⁴ by bringing the α subunit into proximity with them. In addition, CK2 β is needed to dock to and penetrate the nuclear membranes.¹⁴⁵ CK2 β is present as a homodimer in solution and comprises of a body and a tail (Figure 16). The body includes the *N*-terminus and the dimerisation domain, which comprises the zinc binding site. The zinc is anchored by three-stranded anti-parallel β sheets and four cysteine residues; The tail includes the *C*-terminus, and it is formed by a β -turn and a short α -helix.

The β -turn includes the hydrophobic hotspot residues which are essential for the docking to the CK2 α subunit. In particular, the lack of residues Arg186, Tyr188, Phe190, and His193 is detrimental to the holoenzyme formation. Unlike for CK2 α , no major conformational changes occur in CK2 β upon holoenzyme assembly, as documented by the X-ray structures of the subunit in isolation and complexed with CK2 α .¹³⁸

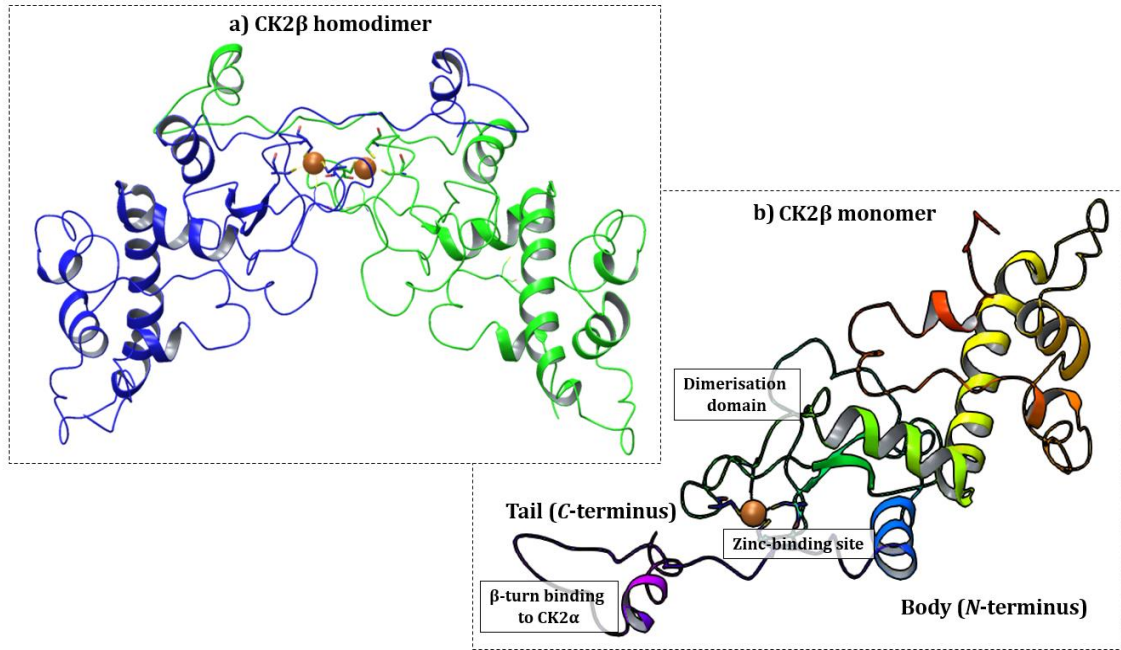


Figure 16 – Structure of CK2 β (PDB code: 1JWH).¹³⁸ a) CK2 β homodimer: the two CK2 β subunits are shown as blue and green ribbons, the zinc ions as orange spheres. b) Details of the CK2 β domain: N-terminal domain is shown as yellow-orange-green and contains the dimerisation domain; the C-terminal domain (purple) contains the portion of CK2 β that binds to CK2 α .

2.1.1.3. Signalling pathways involving CK2

CK2 is involved in a multitude of subcellular pathways at different levels and has a substantial impact on cell growth, proliferation, and apoptosis.¹⁴⁶ The importance of CK2 in cell proliferation and growth is evident considering the increase in its expression level in healthy cells during cell proliferation. Moreover, CK2 α -CK2 β knockout mice models led to mice death, emphasising the essential role of this protein in cell survival.¹³⁴ The mechanisms through which CK2 acts as an apoptosis-suppressor involve several signalling pathways, including the secreted cysteine-rich glycoproteins (Wnts), IAPs, reactive oxygen species (ROS), caspases, TNF pathway, and PI3K/AKT thereby acting on multiple pathways of the apoptotic cascades (Figure 17).¹⁴⁶ For example, CK2 promotes degradation of the NF- κ B-inhibitory-protein I κ B and consequent activation of the transcription factor NF- κ B.¹⁴⁷ In addition, CK2 activates different components of the Wnt pathway, such as the dishevelled protein (Dvl) *via* phosphorylation: it phosphorylates, stabilises, increases the transcriptional activity of β -catenin and recruits other Wnt regulators. When activated, Wnt signalling inhibits the so-called disruption-complex, preventing apoptosis.¹⁴⁸ As reported by Piazza *et al.*, PIP3 (phosphatidylinositol 3,4,5-triphosphate) is generated by the kinase PI3K and causes the activation of several downstream protein kinases of the survival pathway (*vide supra*), including AKT/PKB, which critically regulates cell survival, proliferation, and oncogenesis. Moreover, *PTEN* is a lipid and protein phosphatase able to dephosphorylate PIP3, and it is an essential tumour suppressor. CK2 phosphorylates *PTEN* in the C-terminal region, stabilising the protein against ubiquitin-mediated proteasomal

degradation, and enhancing *PTEN* activity. In addition to its direct regulation of *PTEN*, CK2 is able to activate AKT through direct phosphorylation and prevent dephosphorylation of its active form *via* an indirect mechanism.¹⁴⁸

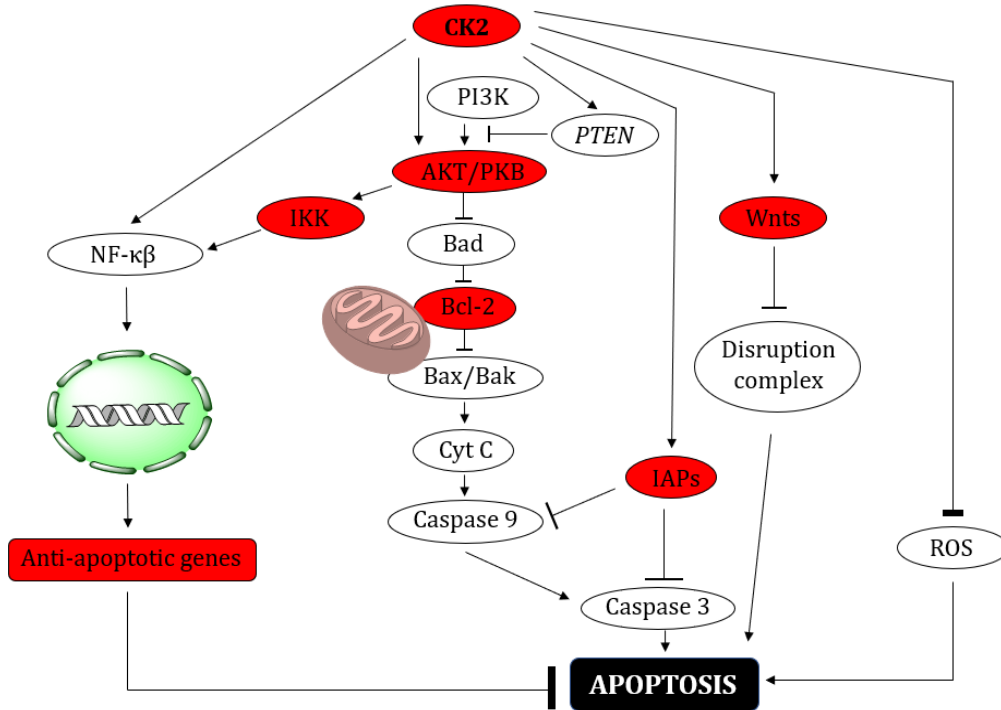


Figure 17 - Overview of the central role of CK2 in the apoptotic pathways. Anti-apoptotic proteins are shown in red. Activation is depicted as an arrow, inhibition as a dash at the end of the line.

The link between CK2 and ROS has been investigated by Ahmad *et al.* using various prostate cancer models.¹⁴⁹ The research group discovered that when CK2 is inhibited, the intracellular levels of H₂O₂ increased leading to the release of pro-apoptotic signals such as cytochrome c, activation of caspase 3, downregulation of Iκβ, translocation of NF-κB, and DNA fragmentations. Moreover, expression levels of the anti-apoptotic IAPs are diminished when CK2 is inhibited.¹⁴⁹

2.1.1.4. Approaches towards the inhibition of CK2 in oncology

Among other features, cancer cells present dysregulated proliferation and deregulated apoptotic activity, leading to uncontrolled cell growth.¹⁵⁰ The well-established overexpression of CK2 in cancer cells has been attributed to a new basal level of CK2 protein expression taking place when healthy cells morph into cancer cells. The new and dysregulated basal level disrupts the cell homeostasis and makes the cells more sensitive to CK2 inhibition.¹⁵⁰ In healthy cells, however, the level of CK2 expression increases only during controlled proliferation.¹⁴⁶ The ability of CK2 to affect cell proliferation and apoptosis in both normal and cancer cells has been validated using several *in vivo* and *in vitro* experimental models.^{134,135} Therefore, as reported by Trembley *et al.*,¹⁴⁶ the importance of targeting CK2 for anti-cancer purposes can be understood

considering:

- CK2 appears to be largely affected by mitogenic signals;
- Downregulation of CK2 expression has a strong influence on inflammation, angiogenesis, and drug efflux pathways to the benefit of cancer cell elimination;
- Dysregulated expression of CK2 in cancer cells is an index of the pathological status of the tumour;
- CK2 downregulation results in inhibition of cell growth, proliferation, and an increased apoptotic activity;
- CK2 is crucial for cell survival, and there appear to be no redundant pathways to compensate for its downregulation.

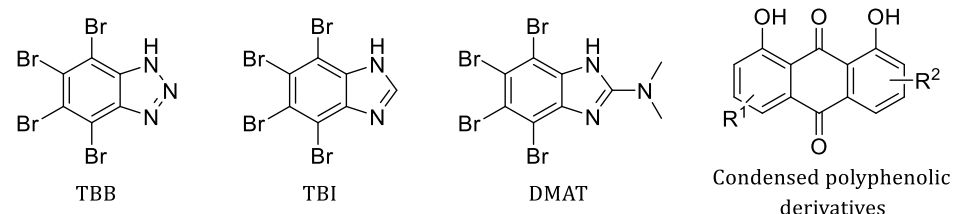
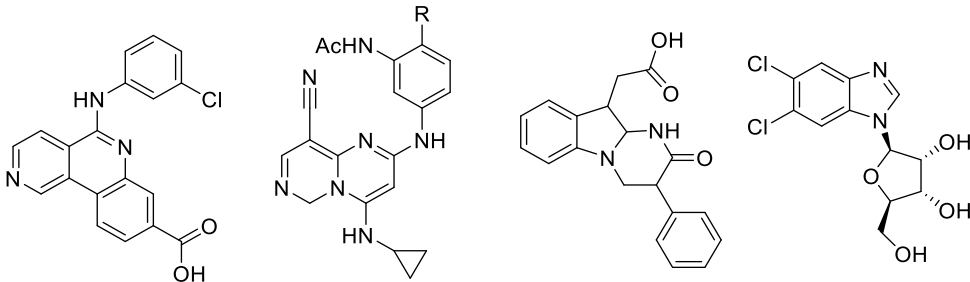
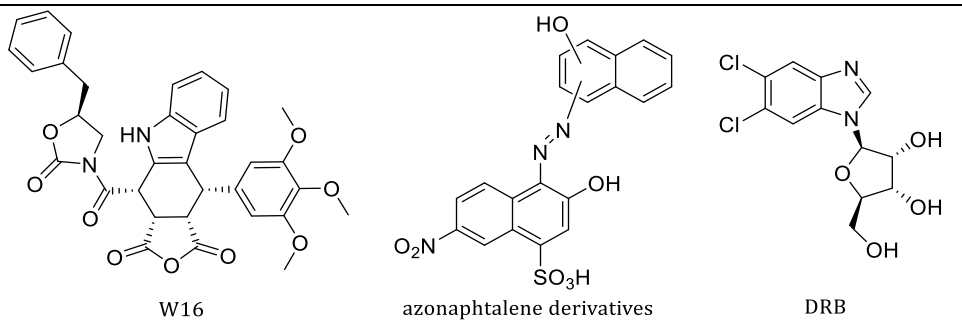
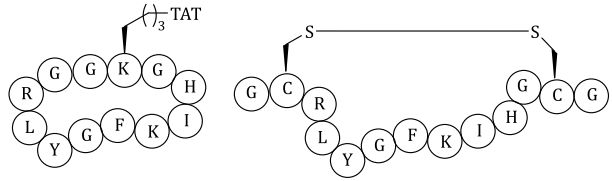
All this evidence together makes CK2 inhibition an attractive target for cancer therapy.¹⁴⁶

A wide variety of approaches have been used to inhibit CK2, and both RNA knockdown and small molecules strategies have been embraced. The first antisense oligonucleotide was developed by Faust *et al.*¹⁵¹ Although the oligodeoxynucleotide was able to cause an antisense-mediated disruption of CK2 leading to apoptosis, it proved less efficacious in reducing the expression level of the protein.¹⁵² Therefore, small molecules were preferred to induce CK2 inhibition as they have the potential to be more selective, with different strategies being applied and reported herein (Table 3).

The most common one is the inhibition of CK2 with small molecules that bind at the ATP-binding site; however, despite their efficiency in providing low nM-range inhibitors, they suffer the drawback of having off-target activity towards other kinases with a similar ATP-binding sites.^{135,152} Several ATP-competitive inhibitors showing a range of potency and selectivity have been developed either in industry or in academia – *e.g.* tetrabromobenzimidazole derivatives (TBB, TBI, DMAT),¹⁵³ condensed polyphenolic derivatives,¹⁵⁴ indoloquinazoline-based compounds¹⁵⁵ and pyrazolo[1,5-a]pyrimidine derivatives.¹⁵⁶ Among these, the ATP-competitive CK2 inhibitor CX4945, Silmitasertib, developed by Cyclene Pharmaceutical, represents the first orally bioavailable inhibitor of CK2 currently undergoing clinical trials.¹³⁹ CX4945 inhibits CK2 with an IC₅₀ of 1 nM, and its selectivity was screened against a panel of 238 kinases; 7 of these were inhibited at more than 90% showing that CX4945 is able to engage kinases other than CK2.

139

Table 3 - An overview of some inhibitors of CK2 grouped by type of inhibition.

Inhibition type	Inhibitor
	 <p>TBB TBI DMAT Condensed polyphenolic derivatives</p>
ATP competitive inhibitors	 <p>CX4945 Pyrazole[1,5-a]pyrimidine derivatives Indoloquinazoline-based compounds DRB</p>
Displacer of CK2α substrates	 <p>C W M S P R H L G T C Y P15</p>
Inhibitors of the PPI between CK2β and its substrates	 <p>G K M N G V L P L A W P S L Y L R L P1</p>
Allosteric inhibitors with unknown binding mode	 <p>D C R G L I V M I K L H B2</p>
Inhibitors of the α/β PPI	 <p>W16 azonaphtalene derivatives DRB</p>
	 <p>Pc-TAT Pc</p>

Due to potential selectivity issues linked to targeting the highly conserved ATP-binding site, an

increasing interest has arisen in the development of non-ATP-competitive and allosteric inhibitors.¹⁵⁷ CK2 inhibition exploiting binding sites outside the catalytic ATP pocket has been achieved using a variety of approaches (Table 3).

An interesting approach towards non-ATP-competitive inhibition is the one used by Perera *et al.* displacing the CK2 substrates. CK2 targets present an acidic phosphoro-acceptor site which allows for phosphorylation, and peptide P15 was designed to bind to these appendices to inhibit substrate phosphorylation in a non-ATP-competitive fashion.¹⁵⁸

Other approaches target the CK2 β regulatory subunit. For instance, peptide P1 binds to the N-terminal domain of the β subunit, triggering cell apoptosis by preventing key interactions of the α subunit with specific anti-apoptotic protein substrates.¹⁵⁹

An additional interesting non-ATP-competitive strategy is the disruption of the α/β subunit interaction. Inhibition of the PPI between the α catalytic subunit and the β regulatory subunit results in prevention of the holoenzyme assembly, with negative consequences on substrate recognition, protein shuttling between different intracellular compartments, and the stability of the catalytic subunit, thereby impacting the cell cycle and cell progression. The inhibition of the holoenzyme assembly by targeting the interface has been reported to be a more selective and elegant way of affecting the activity of CK2, especially in the light of the fact that the catalytic α subunit remains active towards some of its substrates and that the protein interface is not conserved among other kinases.¹⁶⁰

The interface of the isolated CK2 protein was successfully targeted using small molecules such as the podophyllotoxin indole analogue W16¹⁶⁰ or using the cyclic disulfide bridged peptide Pc.¹⁶¹ Interestingly, the small molecule W16 inhibited the catalytic activity of CK2 α in an allosteric manner whilst Pc resulted in an enhancement of the catalytic activity.^{160,161} The potency of these two compounds in a cellular context is unknown. Similarly, Raaf and *et al.* showed that the known CK2 inhibitor DRB was also able to bind at the interface although, with a low binding affinity insufficient to cause a biological response.¹⁶² Lately, a 12-mer peptide, named B2 was identified using phage-display technology. B2 is able to disrupt both the PPI and the catalytic activity with an identical IC₅₀ of 0.8 μ M; however, it is not clear how the 12-mer peptide binds to CK2 α and how it inhibits the catalytic activity of the protein.¹⁶³ Recently, a cyclic peptide analogue of Pc was reported in the literature: the Pc peptide was conjugated with a TAT cell-penetrating peptide to gain cell-permeability, and the disulfide bond in Pc was replaced with a

[§] Allosteric inhibition aims to develop a ligand for a site different from the active site, but able to cause a change in the protein structure which will impede catalysis.²⁸⁷

head-to-tail lactam. Although cell-permeable, there are no reports of the binding mode or target engagement of TAT-Pc^h.¹⁶⁴ Data on the stability of the complex under physiological conditions are also missing. It is therefore clear that, despite recent advances, selective, stable, and potent inhibitors acting at the CK2 PPI are still missing. The discovery of molecular probes able to disrupt the PPI of CK2 in cells and, potentially, *in vivo* would shed light on the regulatory mechanisms of the protein and the importance of the holoenzyme to cancer progression.

^h Cell-penetrating peptide derived from the transactivator of transcription domain (TAT) of human immunodeficiency virus. The sequence of TAT peptide is GRKKRRQRRRPQ.

2.1.2. Anti-apoptotic Bcl-2 proteins

Bcl-2 proteins are a family of proteins with well-established roles in apoptosis. The family comprises membrane-associated and cytosolic proteins with both pro- and anti-apoptotic functions acting on mitochondria outer membrane permeabilization (MOMP), thereby representing an essential component of the intrinsic apoptotic cascade.¹⁶⁵ The proteins of the Bcl-2 family can be divided as follows: pro-apoptotic (Bim, Bad, Bid, Bmf, Noxa, Puma, Hrk, Bik); anti-apoptotic (Bcl-x_L, Bcl-w, Bcl-2, Mcl-1, and A1); effectors of apoptosis (Bax and Bak).¹⁶⁵ They share the so-called Bcl-homology (BH) domains that can be grouped as follows: BH1, BH2, BH3, and BH4.¹⁶⁶ The Bcl-2 family members interact with each other *via* a series of PPIs made possible by the BHs. The BHs, in fact, are necessary for the formation of homo- and hetero-complexes. The pro-apoptotic proteins are often referred to as BH3-only proteins since they conserve the BH3 domain only. The anti-apoptotic proteins, on the other hand, can present all four homology domains, with BH1 and BH2 necessary to interact with the effectors of apoptosis Bax and Bak.¹⁶⁶ The exact mechanisms by which apoptosis is induced by the Bcl-2 family members is highly debated and not fully understood. It is widely accepted that the pro-apoptotic proteins form a heterodimer with the anti-apoptotic proteins thereby inducing conformational changes that displace the effectors of apoptosis from their complex with the anti-apoptotic proteins (Figure 18a). Once freed, Bax and Bak become able to trigger apoptosis by affecting the MOMP. Alternatively, the BH3-only proteins bind and activate Bax and Bak directly: proteins that can interact with the effectors of apoptosis directly are called activators (Bid, Bim, Puma), whereas proteins that bind to the anti-apoptotic proteins are called sensitisers (Bad, Bmf, Bik, Noxa, Hrk) (Figure 18a).

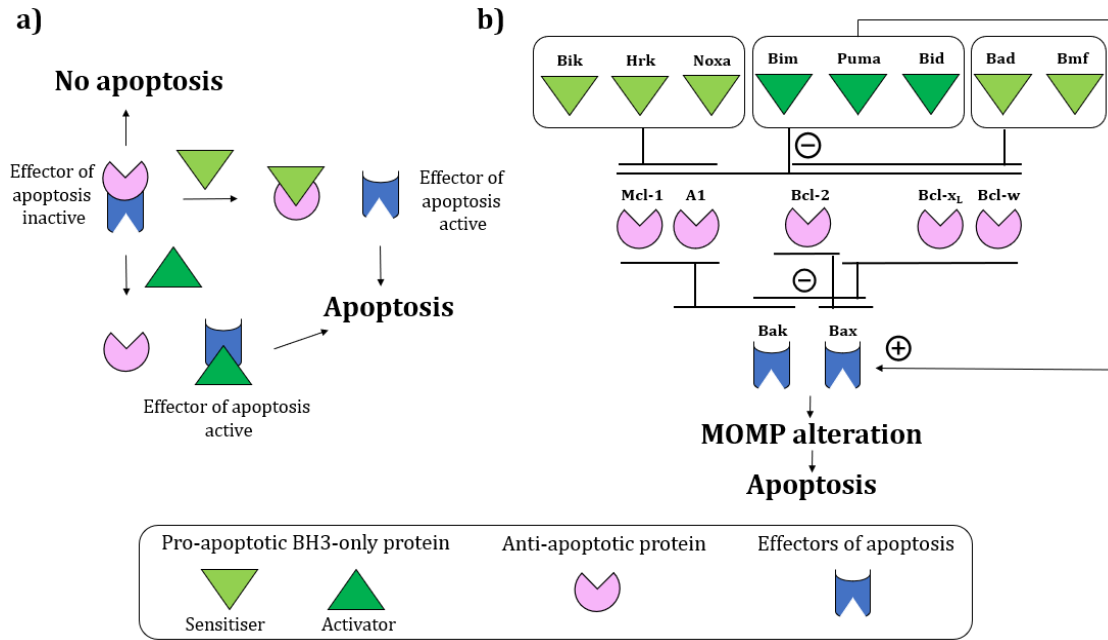


Figure 18 - Exemplified overview of the Bcl-2 pathways inducing apoptosis. a) Activation mechanisms within the Bcl-2 family: the pro-apoptotic proteins directly activate the effectors of apoptosis (blue) or can bind to the anti-apoptotic proteins (pink) and induce conformational changes that result in the anti-apoptotic protein releasing the effectors of apoptosis. Once Bax and Bak become active, they exert their apoptotic activity. b) PPIs between members of the Bcl-2 family.

It should be noted that the activators can also act as sensitisers, but sensitisers do not act as activators. When active, Bax and Bak oligomerise on the mitochondria membranes by means of the BH3-domain, resulting in the formation of pores, and hence triggering apoptosis.¹⁶⁵⁻¹⁶⁸ It should be noted that members of the Bcl-2 family may also interact with proteins outside of their group. In addition, the PPI between pro- and anti-apoptotic Bcl-2 proteins occur in a very selective manner, with BH3-only proteins interacting with specific Bcl-2 anti-apoptotic proteins only as exemplified in Figure 18b.

2.1.2.1. The function of Bcl-2 proteins in the survival of nucleated cells

As for all the anti-apoptotic proteins, the Bcl-2 family members act as guardians of cell death and survival; therefore, alteration in gene expression or activity of Bcl-2 proteins leads to pathological conditions. For example, the expression levels of Bcl-2 anti-apoptotic proteins have been found to be particularly elevated in a number of cancers.¹⁶⁹ Cancerous cells over-expressing anti-apoptotic Bcl-2 proteins can easily escape apoptosis and therefore are not eliminated by the organism. Elevated expression levels of Bcl-2 anti-apoptotic proteins can be attributed to the loss of endogenous mRNAs that represses Bcl-2 gene expression under physiological conditions, to changes to the gene structures, the number of copies, and gene hypomethylation.¹⁶⁹ It is not surprising that inhibition of anti-apoptotic proteins of the Bcl-2 family is an attractive, well-exploited strategy used in oncology to restore the physiological level of apoptosis, and hence allowing the organism to eliminate defected, cancerous cells *via* the PCD.

2.1.2.2. Approaches towards the inhibition of anti-apoptotic Bcl-2 proteins

The role of the anti-apoptotic Bcl-2 proteins (Bcl-2, Bcl-x_L, Bcl-w, Mcl-1, A1) is to sequester the effectors of apoptosis Bax and Bak, therefore, preventing their pro-apoptotic activity. Any molecules that can antagonise the action of the anti-apoptotic proteins by displacing or liberating the effectors of apoptosis are known as Bcl-2 inhibitor. Since the BH3 only proteins act as inhibitors of the anti-apoptotic Bcl-2 proteins, the majority, if not all of the Bcl-2 inhibitors known to date are BH3 mimetics: they bind to the hydrophobic groove of the anti-apoptotic proteins in the same way that BH3-only proteins do with their α -helical BH3 domain (Figure 19).¹⁷⁰

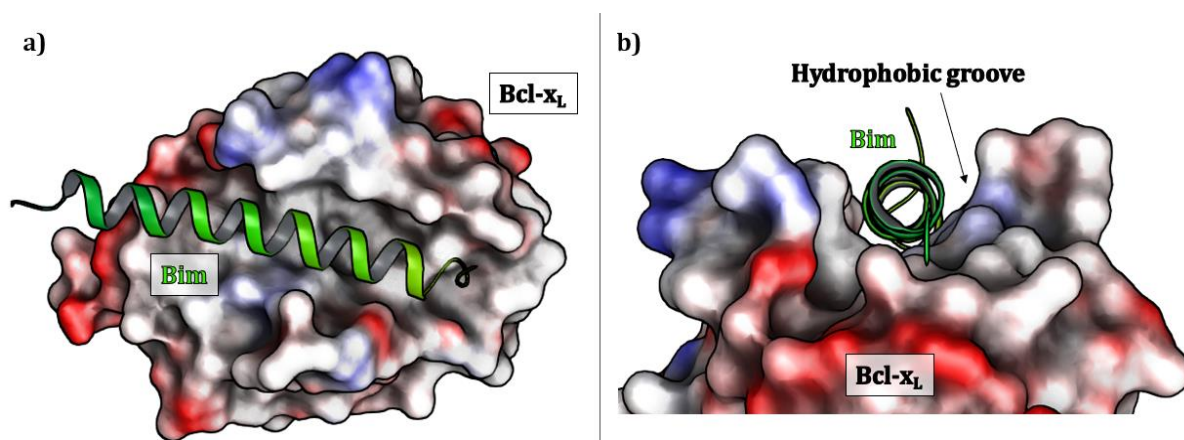
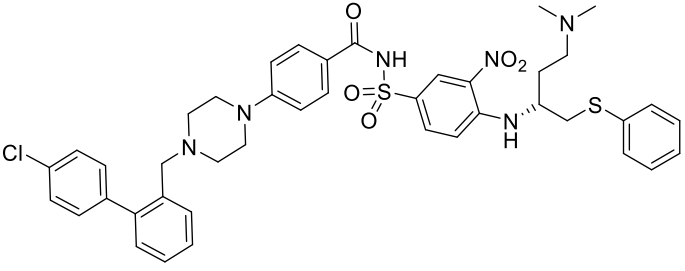
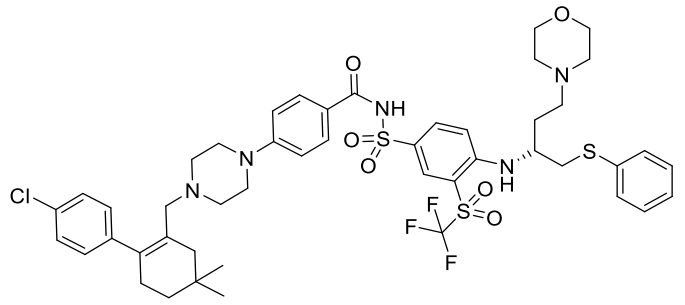
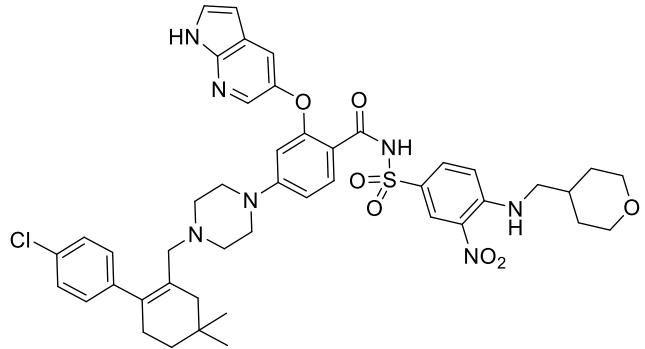
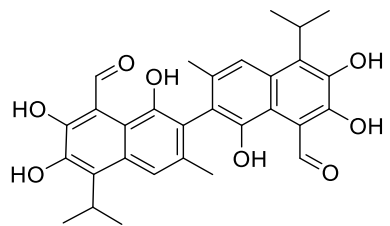
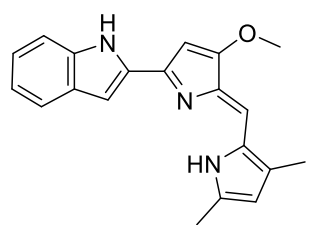
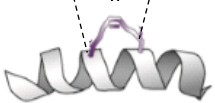


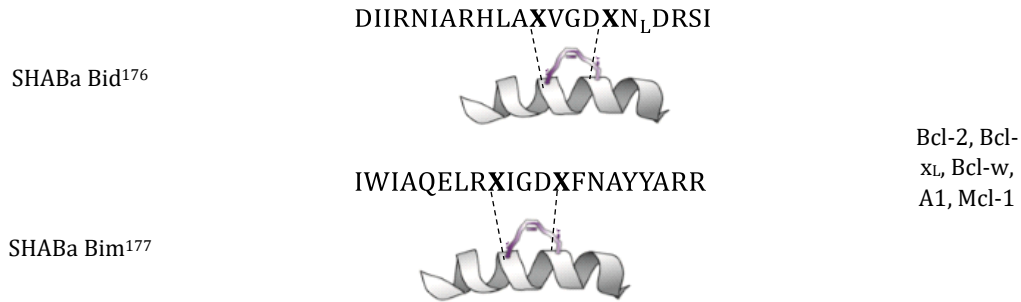
Figure 19 - Typical binding mode of BH3-only proteins to Bcl-2 anti-apoptotic proteins. The interaction between Bim and Bcl-2 is shown here (PDB: 1PQ1).¹⁷¹ a) View from the top of the BH3 domain of the Bim protein (green) complexing with Bcl-x_L. b) Side-view of the complex showing the binding of the helical Bim protein into the hydrophobic groove of Bcl-x_L. Protein surface is coloured according to the electrostatic potential: grey (hydrophobic), blue (negatively charged) and red (positively charged).

All the BH3 mimetics developed to date can be divided into two categories: true BH3 mimetics – characterised by high affinity for the target and no off-target effects – and putative BH3 mimetics – showing low affinity for the anti-apoptotic targeted protein and several off-target effects.¹⁷⁰ Although non-selective, putative BH3 mimetics are often used to investigate resistance mechanisms in cancer cells.¹⁷⁰ BH3 mimetic therapeutics comprise both small molecules and peptides, and they all find application as anti-cancer drugs. Table 4 lists some notable compounds inhibitors of the anti-apoptotic Bcl-2 proteins that were promoted to the late stages of the drug discovery process.

CHAPTER 2: Anti-apoptotic proteins – Bcl-2

Table 4 - Non-comprehensive list of notable Bcl-2 inhibitors in advanced phases of drug discovery.

Drugs	Structure	Target	Stage
ABT-737 ²¹		Bcl-2, Bcl-xL, Bcl-w	Stopped after pre-clinical studies
Navitoclax (ABT-263) ¹⁷²		Bcl-2, Bcl-xL, Bcl-w	Stopped after phase II studies
Venetoclax (ABT-199) ¹⁷³		Bcl-2	Approved
Gossypol ¹⁷⁴		Bcl-2, Bcl-xL, Bcl-w	Phase I/II
Obatoclax ¹⁷⁵		Bcl-2, Bcl-xL, Bcl-w, A1, Mcl-1	Stopped after phase II
SHABa Bad ¹⁷⁶	NLWAAQRYGRELR XN ₁ SDXFVDSFKK 	Bcl-2, Bcl-xL, Bcl-w	Preclinical



ABT-199 (Venetoclax) is the first marketed Bcl-2 inhibitor. ABT-737 and ABT-263 (Navitoclax) are analogues of Venetoclax whose clinical trials were stopped due to a dose-limiting thrombocytopenia. Venetoclax was developed to overcome this limitation by interacting with the anti-apoptotic Bcl-2 protein selectively. The thrombocytopenia caused by ABT-737 and Navitoclax inspired scientists to investigate the role of the Bcl-2 proteins in platelets.

2.1.2.3. The function of Bcl-2 proteins in platelets apoptosis and activation

Platelets are short-lived (8-10 days in humans), anucleated cells produced from megakaryocytes in the bone marrow, spleen, and foetal liver, and they constitute a key component of the blood.¹⁷⁸ Even though platelets do not have a nucleus, they contain the endoplasmic reticulum (ER), Golgi apparatus, mitochondria, and some mRNAs.¹⁷⁹ Platelets play essential roles in pathophysiological conditions including haemostasis, cardiovascular thrombotic events, cancer metastasis, inflammation and autoimmune diseases.¹⁸⁰⁻¹⁸² In particular, platelets maintain fluidity of the circulating blood and become active to trigger clot formation in the event of wounds, thereby preventing the organism from bleeding to death. During cardiovascular thrombotic events, the number of platelets in circulation increases and, in addition, platelets are considered responsible for the formation of atherosclerotic plaques, inflammatory processes, immune responses, and play a role in neurodegenerative conditions.¹⁸⁰⁻¹⁸² Similarly, platelets are important in cancer metastasis, where they help to tether circulating cancer cells, therefore increasing their invasiveness.¹⁸³

Platelet activation and lifespan are regulated by complex PPIs, the understanding of which has received increasing attention in recent years due to the relevance of this type of cell to many pathological conditions.^{184,185}

The proteins of the Bcl-2 family have a key role in regulating intrinsic apoptosis and the lifetime of platelets.^{167,178,186,187} The role of Bcl-2 proteins in platelet survival has been investigated using transgenic animal models, and more recently, BH3-only small molecule mimetics ABT-737, Navitoclax and ABT-199, that find application in oncology. Interested in the dose-limiting

thrombocytopenic side-effect of ABT-737 and its orally available analogue Navitoclax, Debrincat *et al.* investigated the effect of these Bad-like BH3 mimetics on platelet apoptosis.¹⁷⁸ They found that the anti-apoptotic protein Bcl-x_L is indispensable to platelet survival and its inhibition causes platelet death. On the contrary, ABT-199, a selective Bcl-2 inhibitor, does not cause platelet apoptosis. Similarly, concomitant depletion in mice of Bcl-2 and Mcl-1 was found not to be detrimental to platelet survival.¹⁷⁸

It is interesting to note that activated platelets go through apoptotic-like changes, and the apoptotic and activation pathways converge on the loss of mitochondrial membrane polarisation (MMP) and the occurrence of phosphatidylserine (PS) exposure (Figure 20). It is the essential roles of Bcl-2 proteins in regulating MMP that suggested they might have a central role in both platelet apoptosis and activation. However, the mechanistic differences between the apoptotic and activation signalling are poorly understood.^{179,188,189} The main divergences between the two pathways are described by Vogler *et al.*¹⁸⁸ as follows, and these conclusions derived from the use of ABT-737 in platelets:

- Bcl-2-mediated apoptosis is slower than Bcl-2-mediated platelet activation;
- Activation of caspases is essential for apoptosis but not for activation, at least in the first stages of platelet activation to a pro-coagulant phenotype;
- Platelet activation is a calcium-dependent mechanism, whilst apoptosis is not.

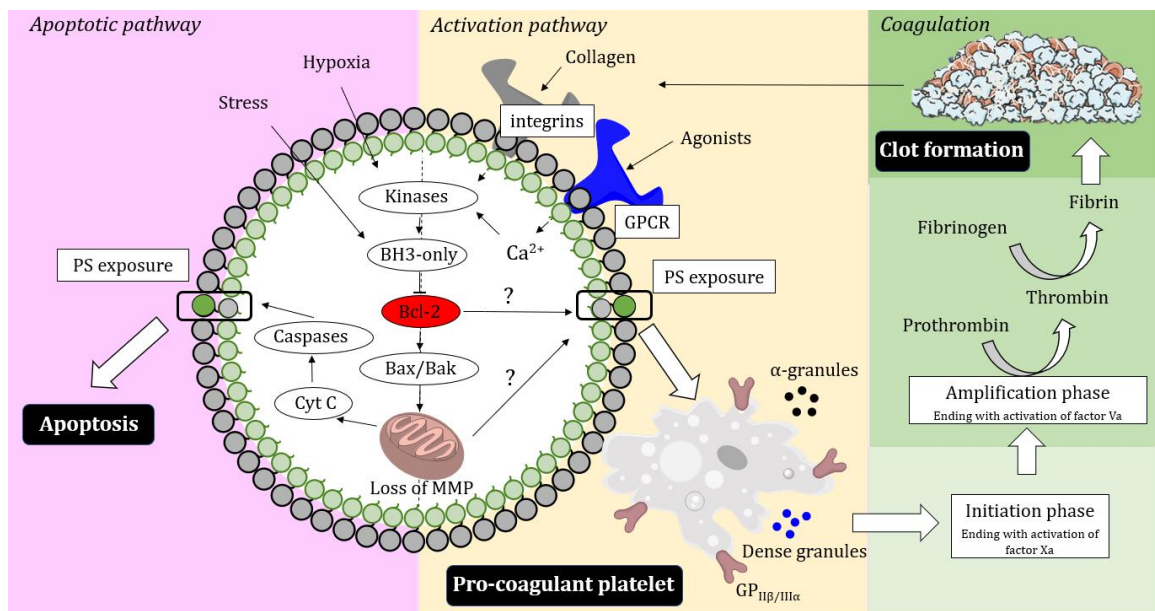


Figure 20 - Exemplified differences between apoptosis and activation in platelets. Apoptosis (pink) is induced by ageing, stress, hypoxia etc. and activates the intracellular intrinsic pathway that culminates with loss of MMP, the release of cytochrome c from the mitochondria, activation of caspases, PS exposure. Activation (yellow) in response to agonist or collagen overlaps to some degree with the apoptotic pathway. Once active, the platelets change shape, release granules and expose glycoprotein receptors to facilitate aggregation at a later stage. The factors released by pro-coagulant platelet trigger the coagulation phase (green) that culminates with the clot formation enabled by fibrin.

In addition, Vogler *et al.* have shown that inhibition of the anti-apoptotic proteins Bcl-2 and Bcl-x_L by the Bad mimetic ABT-737 inhibits platelet activation whilst resulting in platelet apoptosis, supporting the hypothesis of distinct roles for the Bcl-2 proteins in platelet activation and apoptosis.^{188,190}

Once platelets are activated by agonists or adhesion to the collagen exposed on the blood vessel following an injury, they secrete granules (*i.e.* α- and dense granules) necessary to trigger the coagulation cascade, change shape, and expose glycoproteins (*i.e.* GP_{IIb/IIIa}). All these events are necessary for the fibrinogen binding and clot formation (Figure 20).

Whilst the role of some Bcl-2 proteins in platelet survival and activation has been elucidated (Bad, Bcl-2), a deep understanding of the involvement of all the members of the Bcl-2 family in platelet apoptosis and activation is still missing.

The lack of a nucleus in platelets makes the use of conventional recombinant techniques ineffective and hampers the study of PPIs, and hence the elucidation of intracellular pathways. As for nucleated cells, the use of small molecules to study PPIs can lead to selectivity problems due to the lack of specificity among related proteins.²⁵ In addition, as highlighted earlier, the design and development of small molecules targeting a shallow protein-protein interface can be challenging.¹⁹¹ On the other hand, an alternative way to study PPIs in platelets is provided by the use of transgenic animal models. Nevertheless, the generation of such models is time-consuming, expensive, may be prone to side-effects during the development of the embryo, and may not be representative of the human situation.¹⁹²

The understanding of PPIs in human platelets could aid the discovery of selective and specific anti-platelet therapeutics which could find use in the treatment of cardiovascular diseases, inflammation and cancer therapy. Therefore, there is an unmet need for new, complementary and efficient approaches to study medically-relevant PPIs that can be used in human platelets directly overcoming the above-mentioned limitations. Macrocyclic peptides may be a suitable solution; however, there are no reports of their use in platelets.¹⁹³

2.1.3. Brief considerations on selectivity

The main problem associated with targeting anti-apoptotic proteins is selectivity. Whilst overexpressed in diseased cells, anti-apoptotic proteins are also present in healthy cells, and therefore, side-effects may be an issue. Off-target effects and unspecific cytotoxicity can be minimised by exploiting any small structural differences between the targeted protein in the diseased and healthy cells or by taking advantage of specific receptors on the surface of the targeted cell-type that may facilitate the entrance of the therapeutic agent. Biologics are often used to this end due to their high specificity, however, they suffer from poor PK properties, have high development costs, and can lead to immunogenicity;^{194,195} small molecules, on the other hand, can be more easily tuned to optimise their PK properties, but they often lack the high specificity of more complex macromolecules.²⁴ This can lead to off-target effects. Such off-target effects can be minimised by taking advantage of allosteric sites that are not well conserved in a family of proteins.¹⁵⁷ Short peptides sit in between these two categories of drugs, sharing the high specificity of biologics, and, if properly modified, the PK properties of small molecules. They can act at the interface of protein signalling, disrupting PPIs, thus targeting shallow and relatively large surfaces (800-2000 Å²), instead of deep binding pockets.^{3,25,40}

SECTION II

Results and discussion

CHAPTER 3:

A Fragment-Based Approach Towards the Inhibition of the Anti-Apoptotic Protein CK2

3.1. Summary

CK2 (formerly Casein Kinase II) protein kinase plays crucial roles in cell growth, cell proliferation, and apoptosis. It is overexpressed in a wide range of cancer cells, and due to the lack of compensatory mechanisms, CK2 inhibition is an attractive strategy used in oncology: the small molecule CX4945 is currently under phase II clinical studies.^{139,146}

This chapter describes the discovery of novel CK2 inhibitors targeting poorly-conserved binding sites within the α catalytic subunit to overcome the limitations of existing inhibitors namely, lack of specificity for CK2 and poor drug-like properties.

Using a fragment-based drug-discovery (FBDD) approach, **31** and **3g** were developed. **31** is the first selective CK2 α inhibitor, with drug-like properties, that engages the cryptic α D pocket of CK2 α and does not interact with the highly-conserved ATP-binding site (Figure 21). **3g** is the first fragment-sized molecule that binds at the interdomain surface of CK2 and that could act as a starting point for the development of novel inhibitors of the holoenzyme assembly (Figure 21).

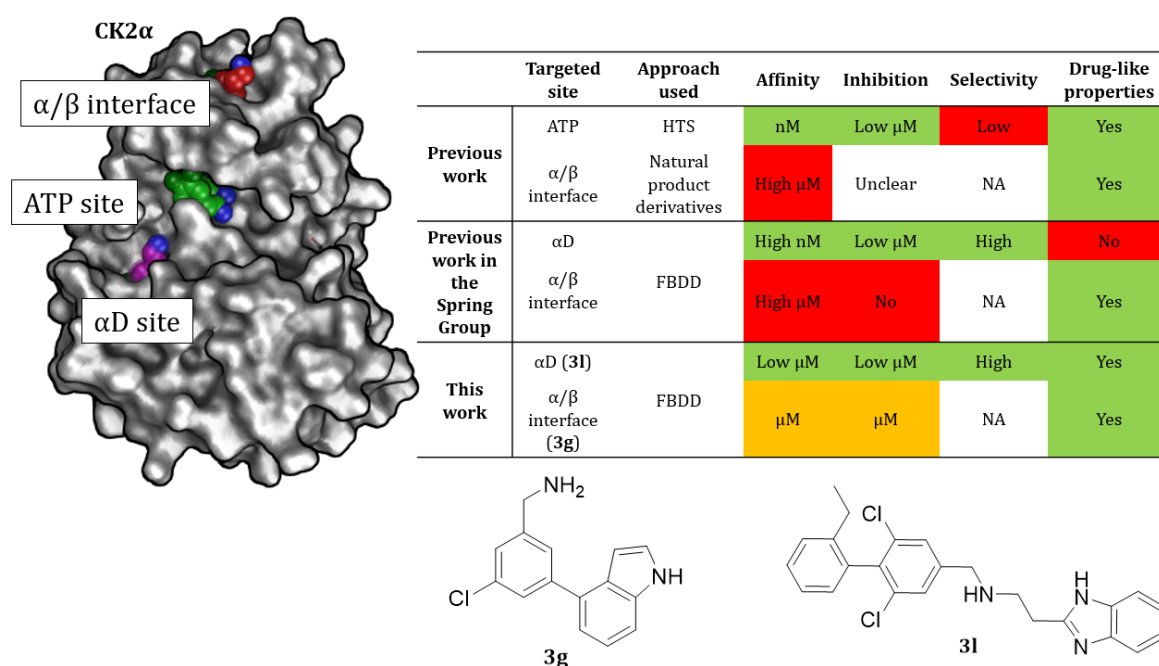


Figure 21 - Previous and current approaches to develop CK2 inhibitors. Structures of compounds **3g** and **31** are shown at the bottom of the figure.

3.2. Project background

The Spring group and collaborators at the University of Cambridge became interested in developing novel CK2 inhibitors acting outside the ATP-binding site to engage this exciting target. Prior to the work described in this thesis, pioneering studies on CK2 inhibition using a FBDD approach were conducted by Dr Chris Stubbs in the Abell Group (Department of Chemistry, University of Cambridge)¹⁹⁶ and Dr Paul Brear in the Hyvönen Group (Department of Biochemistry, University of Cambridge). An initial FBDD approach was adopted, and X-ray crystallography used to screen 400 fragments from the 'NMR¹ fragment library' developed in the Abell Group. The screening provided promising preliminary results, yielding several hits that showed promiscuity for several binding sites within the α catalytic subunit; interestingly, some fragments were found to bind at the α/β interface of the protein, whereas others revealed a new pocket in proximity to the α D helix, referred to as the α D pocket.^{197,198} It was therefore decided to optimise the fragments for the two above-mentioned binding sites in an independent manner in order to improve the binding affinity of the initial hits and, ultimately, avoid undesired promiscuity. Optimisation of the fragments binding at the protein interface was predominantly carried out by Dr Kathy Hadje Georgiou during her PhD in the Spring Group¹⁹⁷ whereas, optimisation of fragments binding in the hidden α D pocket was performed by Dr Claudia De Fusco and Dr Laura Carro, Postdoctoral fellows in the Spring Group.

3.2.1. Preliminary work on fragments binding in the α D pocket

Although the α D pocket was mentioned in work by Kinoshita and co-workers,¹⁹⁹ the full size of this pocket was only revealed upon binding of the fragments synthesised in the Spring Group (Figure 22). Considering the α D helix of CK2 α is less conserved than the ATP site amongst related protein kinases of the CMGC² family,⁴ it was thought that this pocket could be exploited further to develop selective CK2 α inhibitors.

¹ Library assembled for NMR screening of other targets. In this project, the library was screened by X-ray crystallography.

² Family of kinases including CDK, CDKL, CK2, CLK, DYRK, GSK, MAPK.

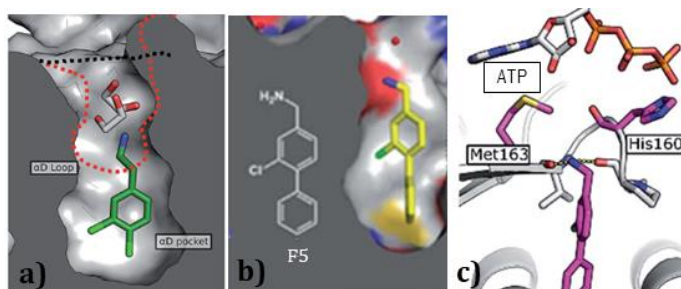


Figure 22 - X-ray crystallographic structures of fragments **NMR154L** and **F5** in complex with CK2 α . a) The opening of the α D pocket in the apo-structure (black dashed line), in the presence of glycerol (red dashed line) and **NMR154L** (grey surface). b) **F5** binding in the pocket. c) Met163 is not able to displace the ATP when **F5** binds. Figures adapted from Brear et al. *ChemSci*, 2016.¹⁹⁸

Following initial screening, the fragments that bound at the α D pocket, as confirmed by electron density seen in X-ray co-crystallography, were elaborated using iterative cycles of design, synthesis, and biological testing. The structure and binding affinity (K_d values obtained by ITC) of some of the fragments are shown in Figure 23.

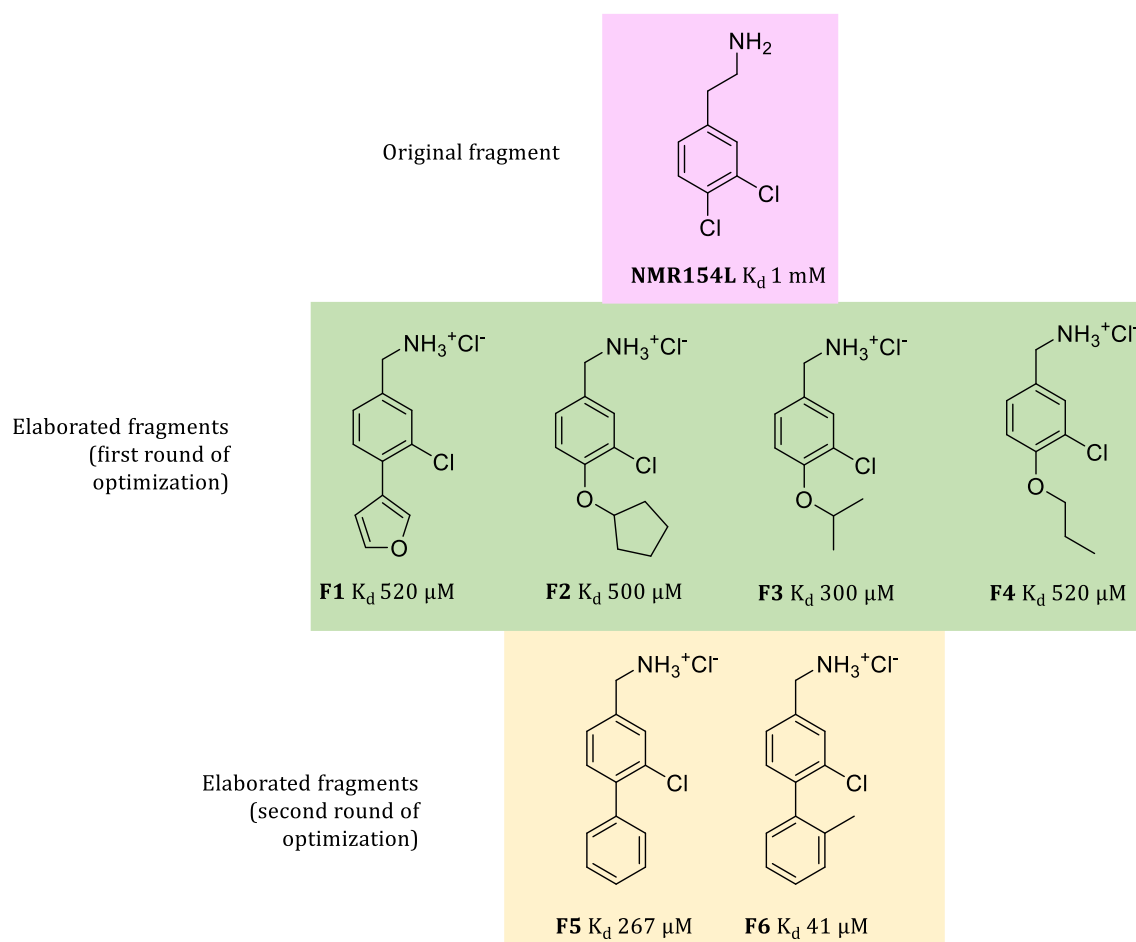


Figure 23 - Structure and binding affinity of some of the fragments synthesised prior to this work. The original hit fragment **NMR154L** is shown in pink, the highest affinity fragments obtained during the first round of elaboration are shown in green and the ones from the second round of optimisation are presented in yellow.

In summary, using a FBDD approach the initial hit **NMR154L** was successfully elaborated into **F6** with a K_d of 41 μ M and a ligand efficiency (LE) of 0.38 Kcal mol⁻¹ heavy atom⁻¹.

Although the optimisation of the fragments improved the affinity due to their ability to expand the α D pocket, inhibition of CK2 activity was not observed. X-ray crystal structures of the molecules bound to CK2 α showed that the residue Met163 did not flip to the 'out' conformation and did not displace the ATP from its binding site hence resulting in no inhibition of phosphorylation (Figure 22).^{198,200} Such a residue-flip is thought to be essential for the inhibition of the catalytic activity of CK2 α . It was envisioned that growing the fragments towards the ATP-binding site would allow for ATP displacement by triggering the Met163 flip while keeping the selectivity over other kinases by the interacting with the poorly-conserved α D pocket.¹⁹⁸ To this end, a series of compounds bearing aliphatic, aromatic and heteroaromatic moieties were synthesised and tested.^{k,200} The most promising compound, **CAM4066** inhibited phosphorylation of CK2 substrates by successfully linking fragment **F5** to a weakly binding ATP fragment *via* a flexible linker (Figure 24).^{198,200}

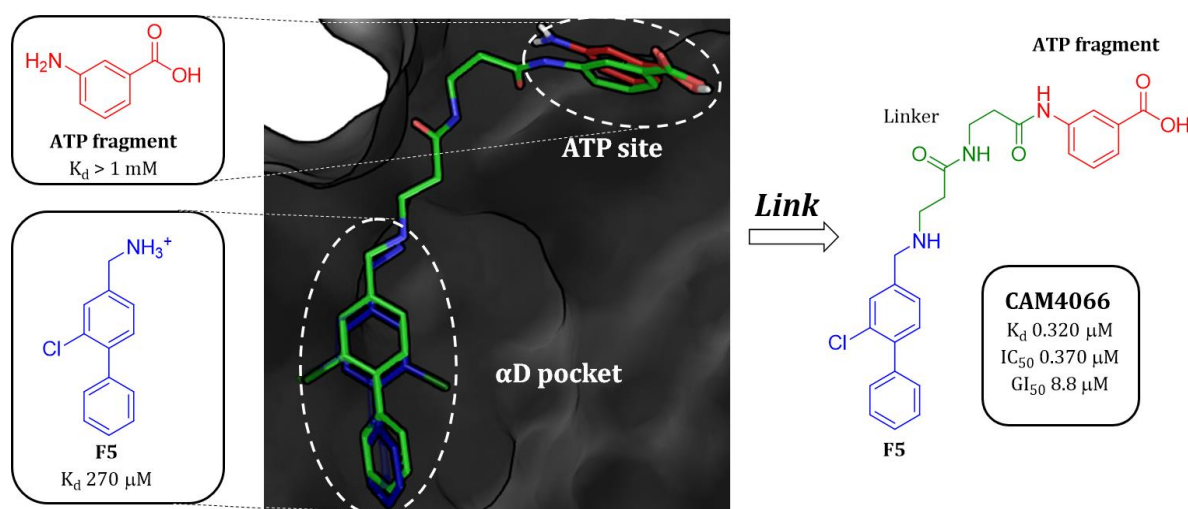


Figure 24 – Structure of **CAM4066**: the first CK2 inhibitor targeting the α D pocket and its biological evaluation. Initial fragments (**F5** in blue and an ATP fragment in red), their biological data and X-ray structures are also shown. The linker used to link the two fragments together is shown in dark green in **CAM4066**.

The ability of **CAM4066** to arrest cell proliferation in cancer cells was comparable to that of the clinical candidate CX4945 (GI_{50} 8.8 μM vs 4.8 μM respectively).^{139,198} However, **CAM4066** proved to be more selective than the ATP-competitive inhibitors reported in literature: unlike CX4945, none of the closely related kinases of the CMGC family were inhibited by **CAM4066**.¹⁹⁸

Although **CAM4066** was the first CK2 inhibitor to bind to the cryptic α D pocket, the compound presented several limitations. In particular, the molecule featured a high number of amide bonds, rotatable bonds, hydrogen-bond donors (HBDs) and acceptors (HBAs), and a drop-off of activity in cells which required the formulation as a methyl ester pro-drug (pro-**CAM4066**) to

^k Synthesis performed by Dr Claudia De Fusco, Dr Kathy Hadje Georgiou, Dr Laura Carro; biological evaluation performed by Dr Paul Brear.

gain cell entry due the presence of the carboxylic acid. In addition, the compound still included a weakly-binding portion interacting with the highly-conserved residues of the ATP binding site.

3.2.2. Preliminary work on fragments binding at the α/β interface

It emerged from a literature search at the time that only three classes of molecules are reported to bind at the α/β CK2 interface¹:

- DRB, a small molecule binding at the interface and at the ATP binding site;¹⁶²
- W16 and azonaphthalene derivatives for which no x-ray structural information is available;^{160,201}
- Pc peptide and its analogues, cyclic peptides with poor drug-like properties that can disrupt the interaction between the α and β subunits.^{161,164}

The limitations of these molecules regarding activity and drug-likeness led the Spring group to further elaborate on **NMR154L**. Such a fragment was identified as hit from the initial X-ray screening and it was found to bind at the protein interface as well as in the α D pocket. The ultimate goal was to deliver drug-like chemical tools to study regulatory mechanisms of CK2 by acting at the interface. This fragment elaboration was carried out prior to the work described in dissertation, and in parallel to the optimisation of the α D fragments. Seventy fragments were synthesised^m elaborating from the initial molecule **NMR154L**, and some of them are represented in Figure 25.²⁰²

¹ For chemical structures *vide* 2.1.1.4

^m Synthesis carried out by Dr Kathy Hadje Georgiou and part III students Alexandra Lubin and William Green

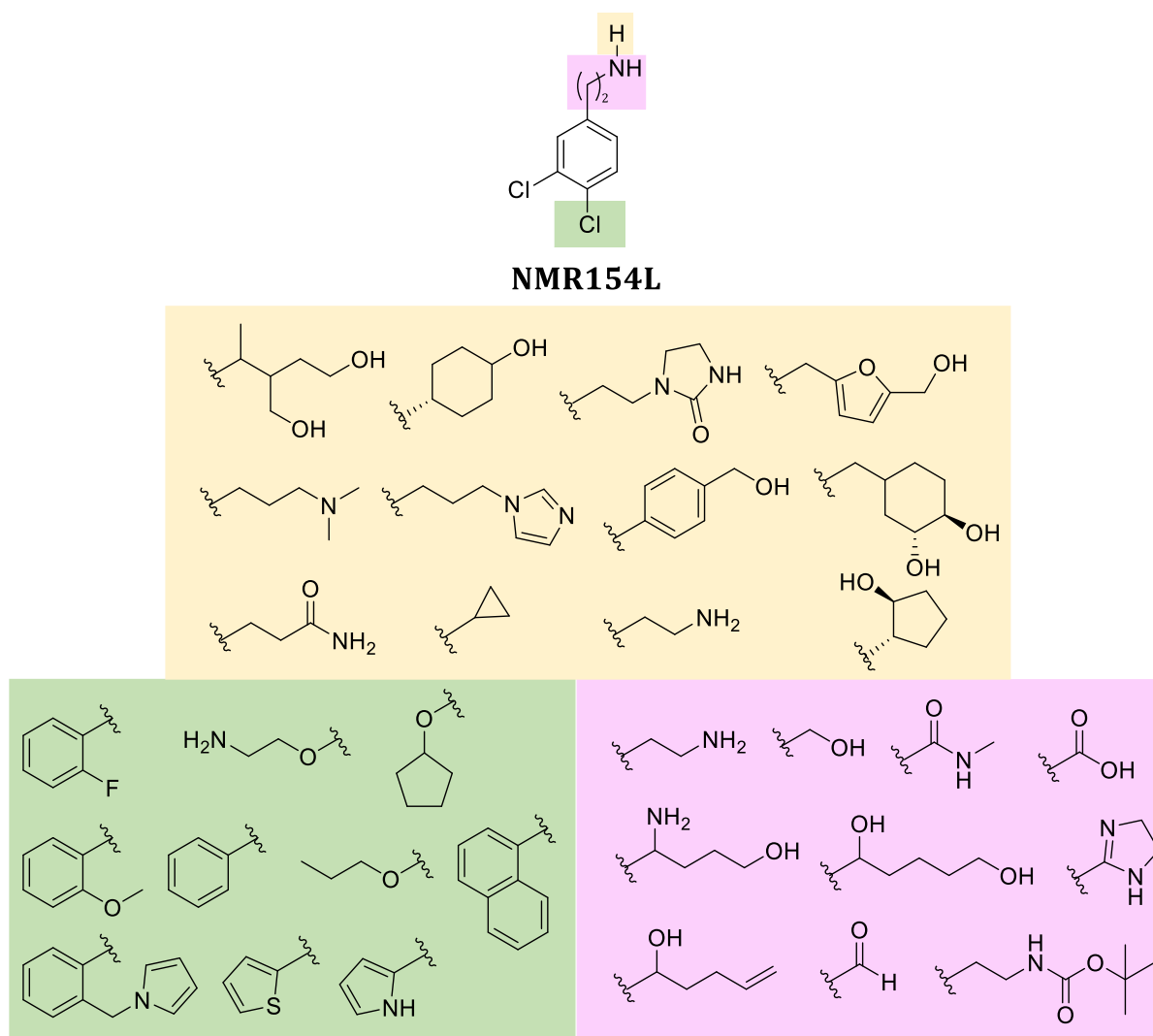


Figure 25 - Some of the elaborated fragments made by previous members of the Spring group to develop CK2 inhibitors of the α/β interface. In yellow, substituents on the amine motif of NMR154L, in green substituents of the 4-chlorine atom, in pink substituents of the ethylamine group.

Unfortunately, despite the many fragment elaboration steps carried out in the group, none of the molecules showed affinity below the high μM range.

3.3. Project aim and overview

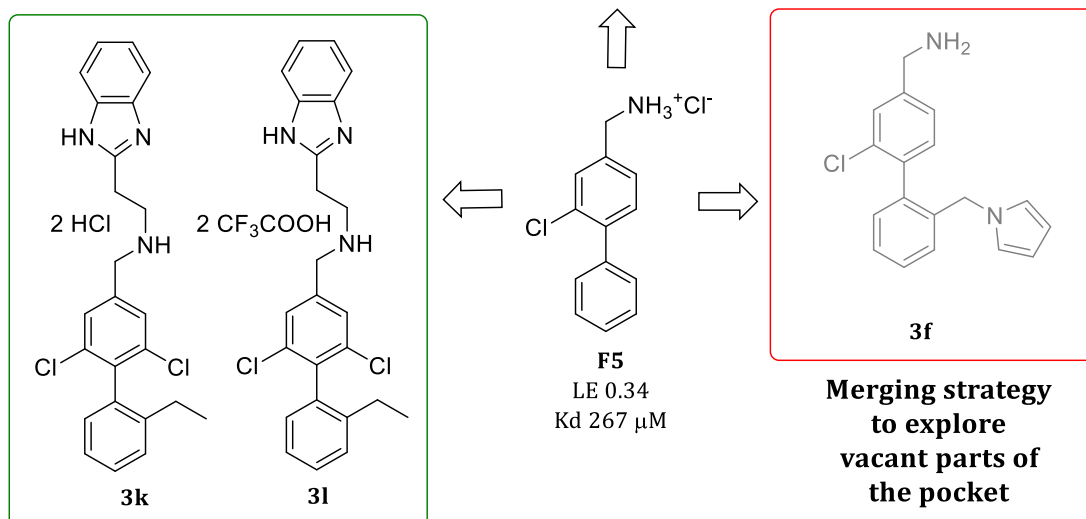
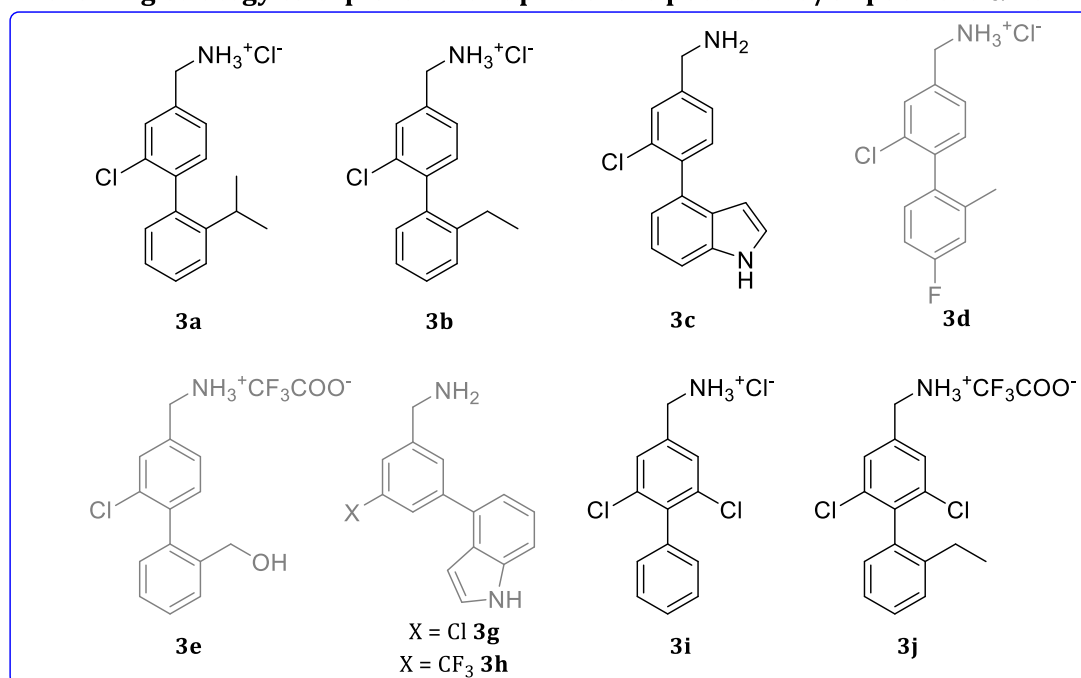
In this dissertation, the FBDD approach towards CK2 project aimed to overcome the limitations of **CAM4066** to develop selective second-generation CK2 inhibitors targeting the α D pocket. In particular, the project aimed to develop drug-like molecules with a reduced number of rotatable bonds, HBDs, HBAs, able to inhibit CK2 α without interacting with the well-conserved ATP binding pocket and that could exert their biological activity without needing to be administered as a pro-drug.

This chapter describes the rational design, synthesis, and biological testing of the elaborated fragments binding to the α D pocket of CK2. We envisioned that the need for the interaction with the ATP binding site could be avoided and selectivity enhanced by increasing the affinity of the α D-binding motif of **CAM4066**. To this end, various substituents on the lower and upper aromatic rings of **F5** were explored to interact with vacant parts of the α D pocket. The combination of the best substitution patterns and a fragment merging strategy resulted in the development of a second-generation CK2 inhibitor (**3I**) with improved drug-like properties.

During the initial optimisation of the fragments for the α D pocket, some molecules were found to bind predominantly at the α/β interface of the CK2 protein. Their synthesis, biological testing, and X-ray crystallographic structures are described in this chapter.

An overview of the molecules subject of this chapter is provided in [Scheme 4](#).

Growing strategy to explore vacant part of the pocket and/or push the α helix



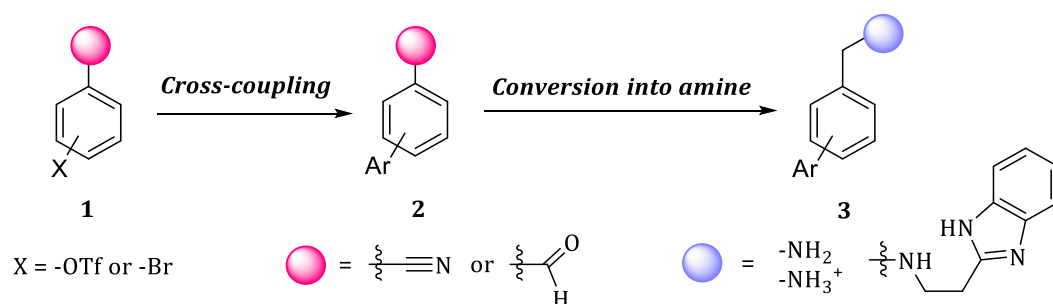
Growing towards the ATP binding site

Scheme 4 - Overview of the molecules discussed in this chapter. Compounds shown in black were found to bind in the α D site, compounds in grey were found to bind predominantly at the protein interface. The compounds are grouped according to the rationale behind their design and synthesis.

3.4. Results and discussionⁿ

All of the compounds were synthesised and co-crystallised with CK2 α , and the results are reported in this section. The fragments that showed electron density in the α D pocket or at the α/β interface were further tested in assays to determine their affinity for the protein as well as a phosphorylation assay to assess their ability to inhibit the catalytic activity of the protein. Ligand Efficiency (LE) was also calculated in order to assess the relative-quality of the fragments. Biological testing and X-ray crystallography were carried out by our collaborator Dr Paul Brear in the Hyvönen group, Biochemistry Department, University of Cambridge.

The molecules whose synthesis and biological evaluation are described in the following paragraphs were synthesised according to the generic synthetic route adapted from previous reports¹⁹⁸ and outlined in Scheme 5.



Scheme 5 – Generic synthetic route leading to the molecules synthesised in this project.

The appropriately substituted aryl derivative **1** underwent a Suzuki cross-coupling reaction with the desired aryl boronic acid or ester to afford the biaryl of generic structure **2**. Intermediate **2** was reduced in its nitrile or aldehyde functionality to afford the desired final amine of generic structure **3**.

3.4.1. Fragments exploring vacant parts of the α D pocket

3.4.1.1. 1-Methanamine, 3-chloro biaryl fragments: 3a-3e

The X-ray structure of **F5** and **F6** (synthesised by Dr Kathy Hajde Georgiou and Dr Laura Carro prior to this work) co-crystallised with CK2 α provided the basis for the design of compounds **3a-3e**. In particular, functional groups with different properties were employed with the aim of exploring the vacant part of the α D pocket (Figure 26). It was envisioned that the affinity of the

ⁿ The work described in this chapter has been published in scientific journals. In particular, the synthesis and biological evaluation of compounds **3a-3d** and **3i-3l** have been reported in Iegre *et al.*, ChemSci, 2018²⁰⁶ and the synthesis and biological evaluation of compound **3g** has been published in Brear *et al.*, BMC, 2018.²⁰² Part of the text and figures presented in this chapter has been adapted from the above-mentioned publications.

fragments could be enhanced by engaging additional interactions within the said pocket. The availability of the starting materials was also a factor influencing the design.

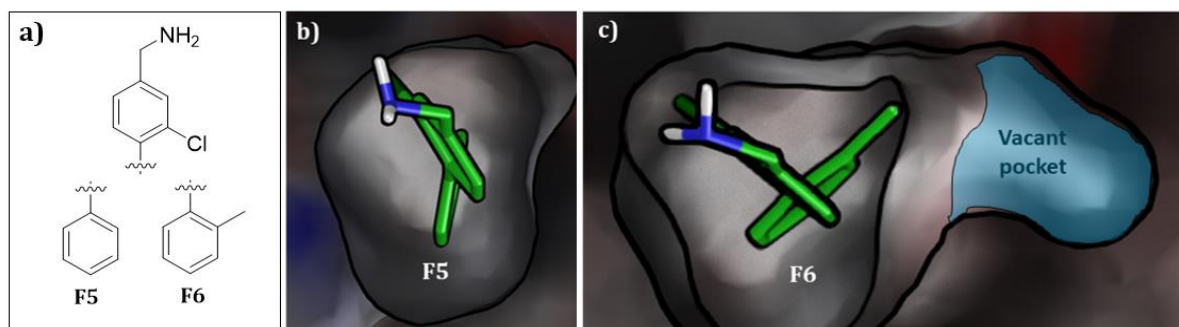
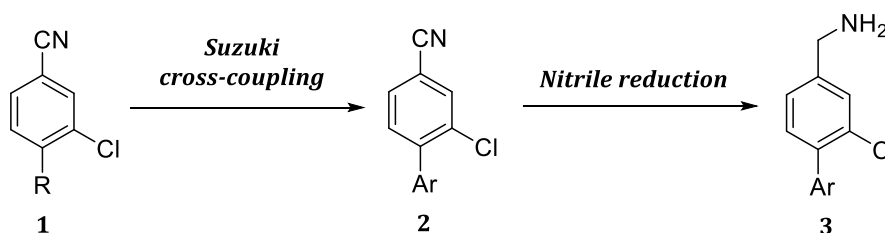


Figure 26 – Chemical structures (a) and co-crystal structures of F5-F6 in the αD pocket showing the pocket expansion going from F5 (b) to F6 (c).

The first step of the synthetic route leading to the 1-methanamine, 3-chloro biaryl fragments was envisioned to be a Suzuki-Miyaura cross-coupling between 2-chloro benzonitrile of generic structure **1** and the appropriate boronic acid to afford the biaryl derivative **2**. Nitrile reduction of **2** would yield the desired amine **3** (Scheme 6).¹⁹⁸

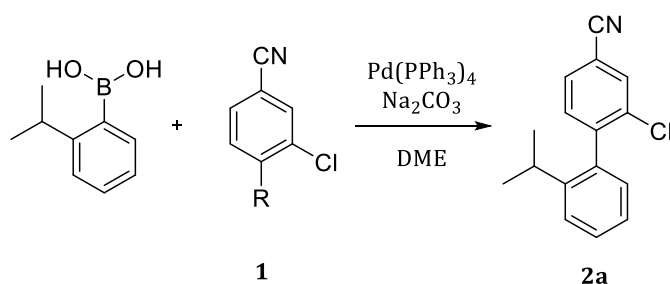


Scheme 6 – Generic synthesis of 1-methanamine, 3-chloro biaryl fragments of generic structure **3**.

The Suzuki-Miyaura step required optimisation as initial attempts to synthesise the first biaryl intermediate **2a** following previously reported procedures¹⁹⁸ resulted in low yields (Table 5).

3-chloro-4-bromo-benzonitrile and 2-isopropylphenyl boronic acid were employed as substrates in the presence of $\text{Pd}(\text{PPh}_3)_4$, Na_2CO_3 , and DME according to literature precedent.²⁰³ However, the reaction did not proceed to complete conversion, and several unidentified impurities were formed, which proved inseparable from the desired product *via* column chromatography. We attempted to reduce the amount of by-products by varying reaction time (between 1 and 3 h), catalyst equivalents (0.005 and 0.010) or type of heating (microwave irradiation and thermal). Pleasingly, the desired product **2a** was obtained in good yield (85%) when the reaction was performed using the triflate derivative of **1** (**1a** hereinafter) and thermal heating (entry 6, Table 5). The same reaction performed under MW irradiation gave the desired product **2a** in poorer yield (entry 4, Table 5).

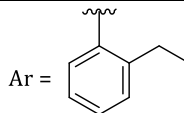
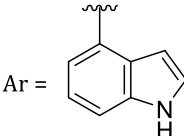
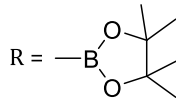
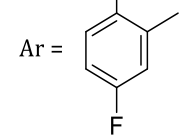
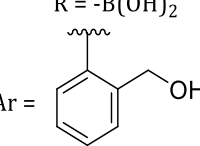
Table 5 - Optimisation of Suzuki coupling conditions to obtain compound **2a**.



Entry	R	Catalyst equivalents	Heating	Temperature	Reaction time	Results
1	-Br	0.01	MW	130 °C	3 h	Aryl bromide/ unidentified impurity
2	-Br	0.005	MW	130 °C	1 h	Aryl bromide/ unidentified impurity
3	-Br	0.005	MW	110 °C	2 h	Unidentified impurities
4	-OTf	0.005	MW	130 °C	2 h	20% conversion to 2a
5	-Br	0.005	Thermal	90 °C	3 h	Unidentified impurities
6	-OTf	0.005	Thermal	90 °C	3 h	85% conversion to 2a

These optimised cross-coupling conditions employing **1a** were successfully applied to the synthesis of the biaryl fragments shown in Table 6. Compound **1a** was obtained in 91% yield by treating the commercially available 4-hydroxy-3-chloro-benzonitrile with Tf₂O in pyridine (Table 6).²⁰⁴

Table 6 - Compounds obtained using the same Suzuki-Miyaura reaction conditions shown in entry 6, Table 5.

Entry	Compound number	Ar, R	Yield (%)
1	2b	Ar =  R = -B(OH) ₂	61
2	2c	Ar =  R = 	67
3	2d	Ar =  R = -B(OH) ₂	97
4	2e	Ar =  R = -B(OH) ₂	90

Nitrile precursor **2c** was obtained via Suzuki cross-coupling using the same conditions as described above with the exception that the corresponding pinacol boronic ester was used instead of the boronic acid for commercial availability reasons. In all Suzuki couplings described in Table 6, by-products tentatively assigned to be the result of incorporation of phenyl groups from PPh₃ in the products were obtained in small amounts, as previously reported.²⁰⁵ Traces of the de-boronated derivative of the boronic acid were also found in most cases.

The nitrile groups of the obtained biaryl fragments (generic structure **2**, Scheme 6) were reduced to the corresponding primary amines **3** by treatment with LiAlH₄ and AlCl₃ in Et₂O.¹⁹⁷ For compounds stable in acidic conditions, the corresponding amines were converted into hydrochloride salts using 4 M HCl in 1,4-dioxane. The salt proved to have greater kinetic solubility in the aqueous buffer used in biological testing than the corresponding free amines (Table 7).

Table 7 - Results of the nitrile reduction steps (entries 3 and 5) and treatment with HCl (entries 1, 2 and 4).

2
3

Entry	Compound number	Ar	R	Yield (%)
1	3a		-NH ₃ ⁺ Cl ⁻	77 ^a
2	3b		-NH ₃ ⁺ Cl ⁻	43 ^a
3	3c		-NH ₂	55 ^b
4	3d		-NH ₃ ⁺ Cl ⁻	32 ^a
5	3e		-NH ₃ ⁺ CF ₃ COO ⁻	54 ^b

^a overall yield of nitrile reduction and salt formation; ^b yield of the nitrile reduction only

Moderate yields could be attributed to the formation of the de-chlorinated analogues as observed by ¹H-NMR analysis of the crude reaction mixture, as well as a small amount of unreacted starting material and loss of mass during the purification step.^o

Treatment of **3c** with HCl led to degradation of the compound, most likely by polymerisation at the indole 3-position as shown by the lack of signal of the corresponding proton of the indole (NMR analysis of crude mixture).

^o The amines synthesised were purified either on silica gel or aluminium oxide gel by flash chromatography. Silica gel was chosen over aluminium oxide due to its better separation potential. When this purification method was chosen, silica was deactivated using various percentages of 7 M NH₃ in MeOH in the eluent. However, due to the nature of silica gel and the polarity of the amine, an amount of product was inevitably lost in the purification due to the streaking of the compound through the column. For purifications where the difference between R_f of the impurities and the product was greater than 0.05, aluminium oxide was used as stationary phase and the streaking of the compounds was minimal.

Compound **3e** was submitted for crystallisation as a trifluoroacetate salt since its corresponding amine was purified *via* preparative HPLC using acidic conditions (0.05-0.1% TFA). Purification of this compound using reversed-phase preparative HPLC was possible due to its increased polarity.

The so-obtained compounds were co-crystallised with CK2 α . The electron density for compound **3a** was observed at both the α D pocket and at the α/β interface showing promiscuity and partial occupancy of each site (Figure 27a-b). However, its binding mode in the α D pocket suggested the possibility of exploiting a space that opened up around the 6' position of the bottom ring in addition to the usual 2' position (Figure 27a).

The X-ray structures of **3b** and **3d** showed the compounds adopting the typical binding modes for these fragments in the α D pocket. Unlike the other fragments, the top aromatic ring of **3d** seems to rotate as shown by the electron density for the chlorine atom observed at both the 3 and 5 positions (Figure 27c).

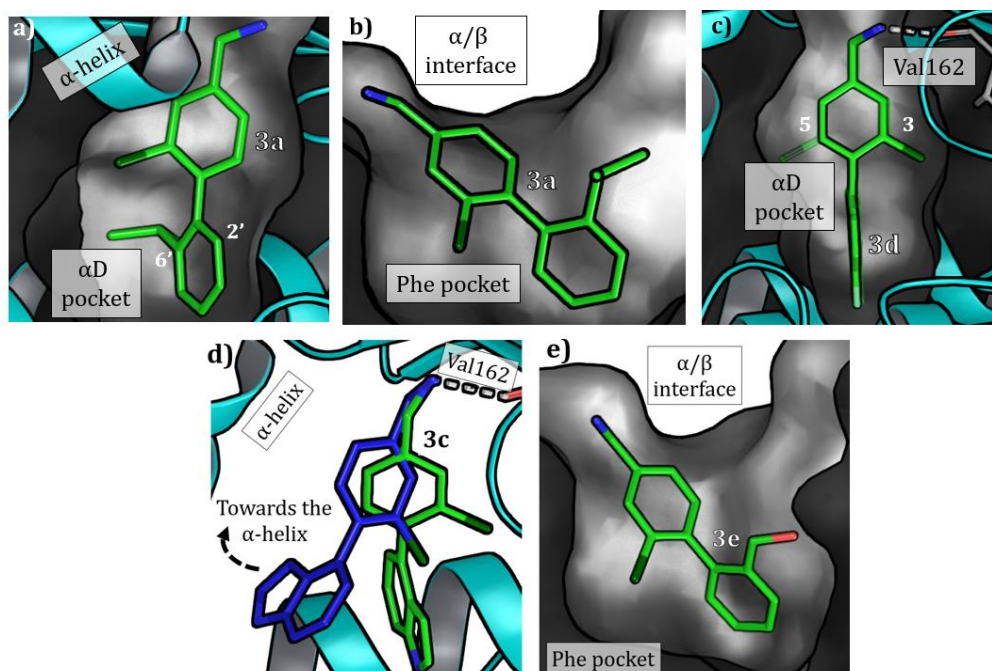


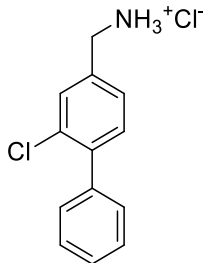
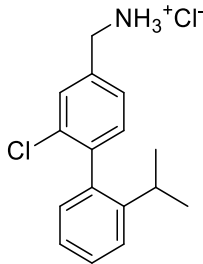
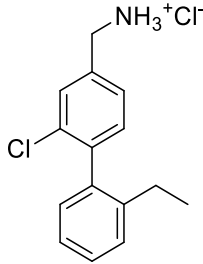
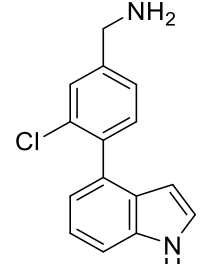
Figure 27 - Crystallographic structure of **3a** (PDB code: 5OS7),²⁰⁶ **3c**, **3d** (PDB code: 5OS8),²⁰⁶ and **3e** binding to CK2 α . a) **3a** in the α D pocket; b) **3a** at the interface; c) **3d** in the α D pocket; d) **3c** showing two different binding modes (blue and green) in the α D pocket; e) Fragment **3e** binding at the interface. The protein surface is represented in grey, secondary structure as cyan ribbons and ligand in green or blue. The H-bonds between the ligands and the Val162 are represented as white dashed lines.

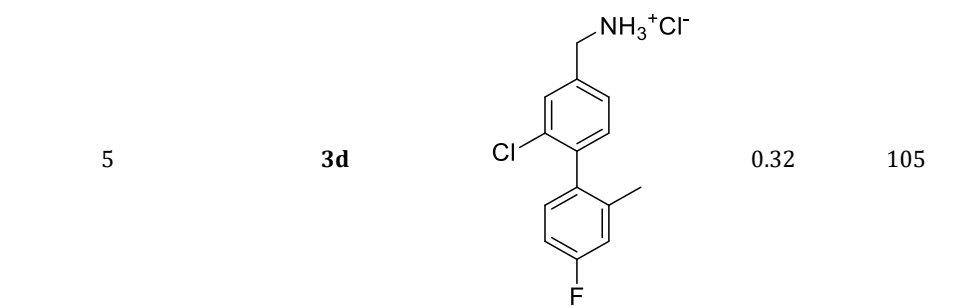
The amine remains in the same position as the other fragments creating an H-bond interaction with the carbonyl of Val162 indicating that this is a strong interaction and an anchor point for all the fragments (Figure 27c). Interestingly, the X-ray structure of **3c** showed two different binding modes in the α D site (Figure 27d). One of these poses (blue, Figure 27d) sees the indole motif closer to the α D helix while the other (green, Figure 27d) resembles the binding mode

characteristic of the biphenyl fragments previously synthesised in the Spring group. The combination of these two poses suggested that exploring different aromatic substituent patterns on the benzylamine core such as 3-indole-phenyl-methanamine derivatives might be beneficial (*vide infra* 3.4.1.3).

Biaryl fragments bearing H-bond donor/acceptor substituents at the 2' methyl position such as **3e** appeared to bind weakly at the α/β interface, and no electron density was observed at the α D site (Figure 27e). X-ray crystallography for compounds **3a-3d** showed electron density in the α D pocket, and therefore, their binding affinity was determined *via* isothermal titration calorimetry (ITC). The results are shown in Table 8.

Table 8 - ITC and LE of the biaryl fragments **F5**, **3a-3d**.

Entry	Compound number	Fragment	LE	K _d (μM)
1	F5		0.32	267
2	3a		0.27	300
3	3b		0.38	17
4	3c		>0.25	> 500



Pleasingly, fragment **3b** showed a significant enhancement in binding affinity compared to **F5** with a K_d of 17 μM representing the fragment with the highest binding affinity and LE of the whole series. Unfortunately, fragments **3a** and **3c** did not show improved binding affinity compared to **F5** whilst **3d** provided a slight improvement. However, their binding modes proved to be useful for the design of other fragments. The binding affinity of **3e** for CK2 α was not measured due to the weak electron density observed in the X-ray structure.

3.4.1.2. Biaryl compound bearing a 5-membered heterocyclic substituent: **3f**

X-ray structures of commercially available and previously synthesised fragments – *i.e.* **3b** and **F7** – led to the proposal of a new biphenyl fragment bearing a 2-methyl-5-membered heterocycle on the bottom aromatic ring (Figure 28). By merging the two classes of compounds, it was envisioned that new interactions with the protein could be engaged. Docking studies were performed to establish the likelihood of these compounds to bind in the αD pocket.^p The results showed that the proposed compound **3f** may lead to the heterocyclic ring expanding the αD pocket.

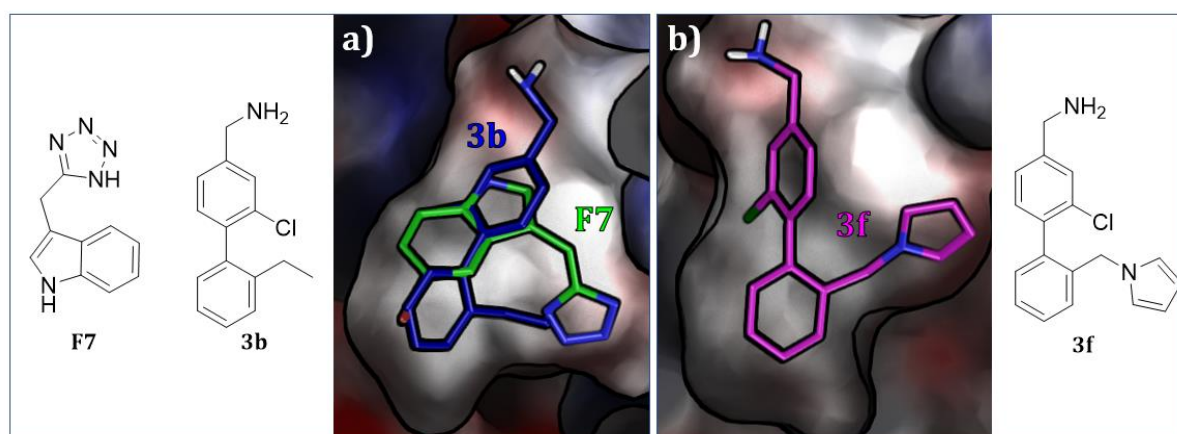
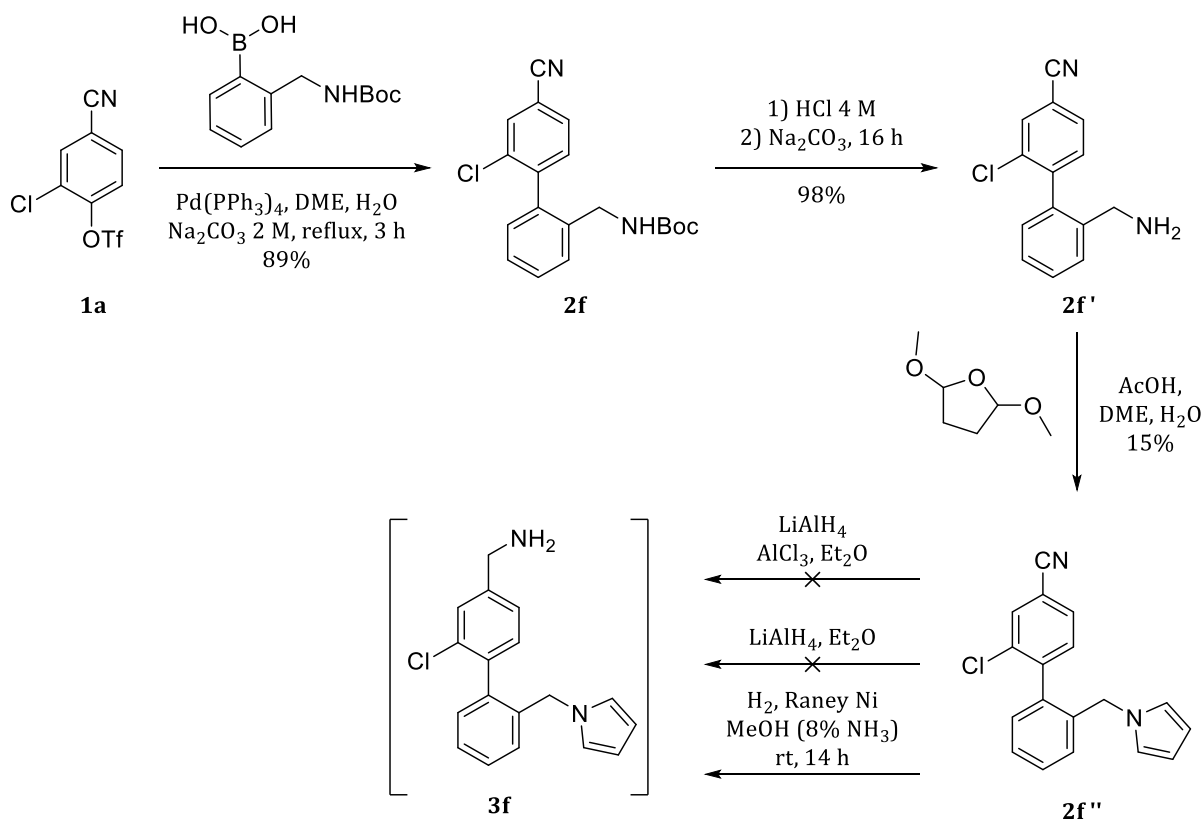


Figure 28 – Fragment merging strategy. a) Overlap of compound **3b** (blue) and **F7** (green) made by Dr C. De Fusco. b) Docking pose of **3f** (purple) as a result of the merging of the previously mentioned fragments. CK2 α is shown as a cross-section of the αD pocket. Protein surface is shown in grey.

^p Structures of the other compounds docked can be found in the appendix A.3.

With the docking study in hand, synthesis of **3f** was commenced. In the first synthetic route attempted (Scheme 7) the synthesis of **3f** started from a cross-coupling reaction between the commercially available 2-*N*-Boc-methanaminebenzeneboronic acid and compound **1a** to afford biaryl nitrile intermediate **2f**.

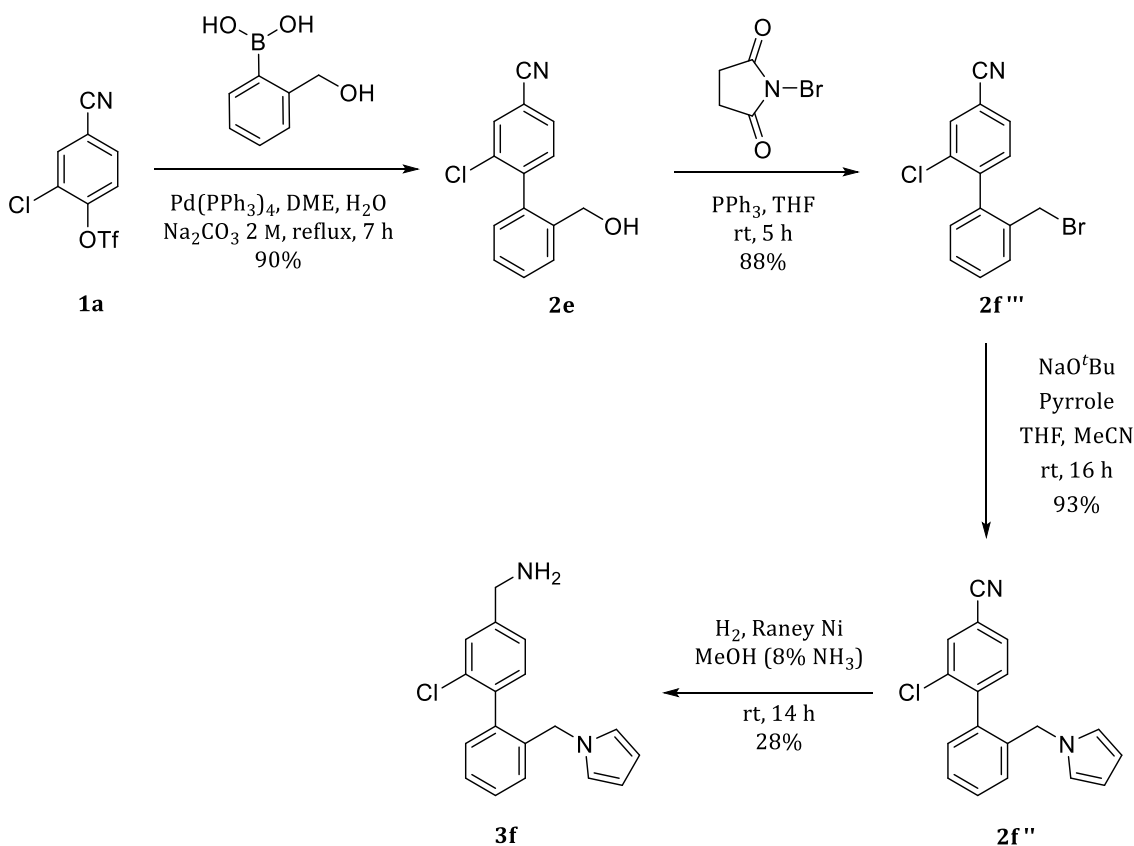


Scheme 7 - Synthetic route attempted to the synthesis of the heterocycle derivative 3f.

Compound **2f** was then treated with HCl to remove the Boc group, and the reaction mixture was basified to obtain compound **2f'** as the free amine. The biphenyl compound was subjected to Clauson-Kaas reaction²⁰⁷ in the presence of 2,5-dimethoxytetrahydrofuran and glacial acetic acid to afford the corresponding pyrrole derivative **2f''** in a 15% yield. Unfortunately, this proved to be unstable in the presence of AlCl_3 , which was used as a Lewis acid catalyst in the subsequent attempted nitrile reduction. Reduction in the absence of the Lewis acid also failed to yield the desired product **3f** and only starting material was returned. An alternative nitrile reduction was carried out using H_2 in the presence of Raney Nickel to afford trace amounts of impure **3f**.

Considering the elevated cost of the boronic acid required and the low yield of the final two steps of the synthetic route, an alternative pathway was used to introduce a 5-membered heterocycle into the 2' position of biphenyl fragments (Scheme 8). The new synthetic pathway commenced with a Suzuki coupling between **1a** and (2-(hydroxymethyl)phenyl)boronic acid to afford biaryl compound **2e**, which was subjected to nucleophilic substitution in the presence of *N*-bromosuccinimide.²⁰⁸ The corresponding bromide derivative **2f'''** was synthesised in large

amounts to allow for potential subsequent diversification. Compound **3f** was obtained from **2f''** upon reaction of **2f'''** with pyrrole in the nucleophilic substitution, followed by nitrile reduction using Raney Nickel.²⁰⁹ Due to the potential instability of pyrrole product **3f** under acidic conditions, the compound was submitted for testing as the free amine.



Scheme 8 - Synthetic route to compound **3f**.

Unexpectedly, X-ray crystallography of compound **3f** revealed that only weak electron density was observed at the interface and no binding was detected in the αD pocket. Considering these results, the biological evaluation of compound **3f** was not pursued, and the synthesis of analogues not attempted.

3.4.1.3. 3-Indole-phenyl-methanamine derivatives: **3g** and **3h**

The two poses found in the X-ray structure of **3c** (Figure 27d) suggested investigating a new design set. Docking studies were performed to explore different aromatic substituent patterns on the benzylamine core and their ability to push the αD helix outwards.⁹ This strategy was regarded as promising since the flexibility of the α -helix is unique to CK2,¹⁹⁸ and therefore this may help improve the selectivity of the compounds. For compound **3g** docking gave promising

⁹ Structures of the other compounds docked can be found in the Appendix A.3.

results, the docked compound overlapped with the X-ray structure of compound **3c**, and the nitrogen of the indole was able to H-bond the carbonyl of the Met255 *via* a water molecule (Figure 29).

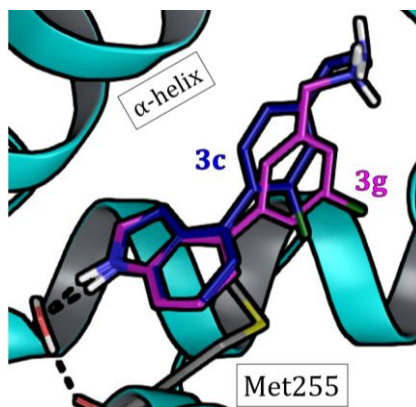
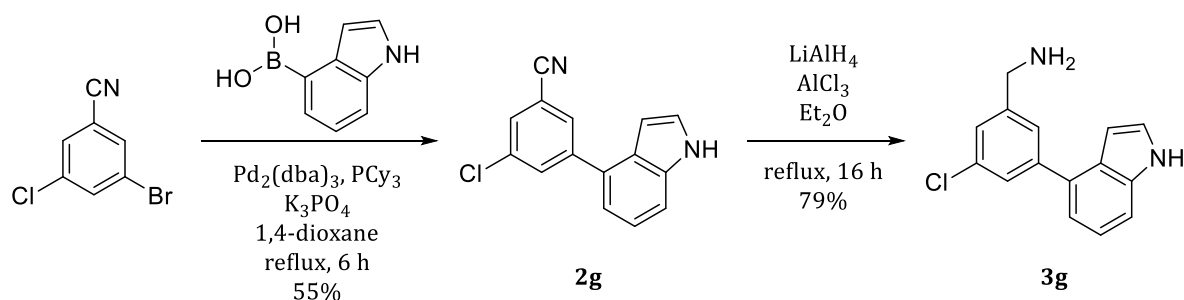


Figure 29 - Docked **3g** (purple) and X-ray structure of **3c** (ligand in blue and protein in cyan).

Compound **3g** was synthesised in the hope that this could give information on the tolerability of the indole in the 5-position of the aryl ring prior to synthesis of more hindered compounds.

The synthesis of **3g** (Scheme 9) commenced with a Suzuki-Miyaura cross-coupling between indole-3-boronic acid pinacol ester and 3-chloro-5-bromobenzonitrile to afford **2g** in 48% yield. A slightly higher yield (55%) was achieved when the corresponding boronic acid was used in the presence of $\text{Pd}_2(\text{dba})_3$, PCy_3 and K_3PO_4 . The choice of reaction conditions was determined on the basis of substrate similarity with literature procedures.²¹⁰ The nitrile group in **2g** was then reduced with LiAlH_4 and AlCl_3 to yield the desired product **3g** in 79% yield.



Scheme 9 - Synthesis of compound **3g** commencing from the commercially available starting material.

Attempted purification using silica gel on flash chromatography or preparative HPLC of the final compound led to degradation of the molecule. It was hypothesised that the degradation was due to the acidic nature of the silica gel and mobile phases of the HPLC respectively. Therefore, purification was successfully performed *via* flash chromatography on aluminium oxide under basic conditions. The methylamine **3g** was submitted for testing as the free-base because, as seen for **3c**, treatment with acidic solution led to polymerisation at the 3-position of the indole

as shown by lack of signal of the proton at the 3-position of the indole (NMR analysis of the crude mixture).

Unexpectedly, co-crystallisation of compound **3g** with CK2 α showed electron density at the interface, with the chlorine atom buried in the lipophilic Phe pocket, much deeper than the fragments binding at the interface studied thus far (Figure 30). Weak electron density only was observed in the α D pocket.

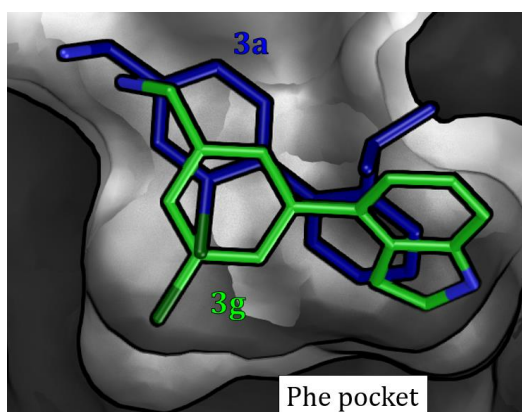
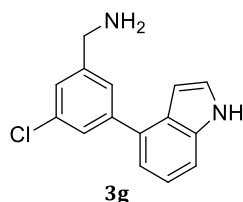


Figure 30 -Overlay of the X-ray structures of **3g** (green, PDB code: 6GIH)²⁰² and **3a** (blue, PDB code: 5OS7)²⁰⁶ showing how **3g** binds deeper into the Phe pocket.

The fact that the chlorine atom of **3g** bound deeply in the Phe pocket resulted in a considerable boost in potency. In addition, the compound was able to displace a CK2 β -like probe in a Fluorescent Polarisation assay (FP) with an IC₅₀ of 44 μ M. Pleasingly, compound **3g** represented the highest affinity fragment binding at the α/β interface developed during our FBDD research.

3g appeared to be the first CK2 inhibitor acting at the α/β interface with fragment-like properties reported in the literature, and therefore, it could be further developed into a drug-like molecule with high potency and selectivity against CK2 (Table 9).²⁰²

Table 9 - Fragment-like properties of **3g** and other known small molecules acting at the α/β interface of CK2. Adapted from Brear et al., BMC, 2018.²⁰²

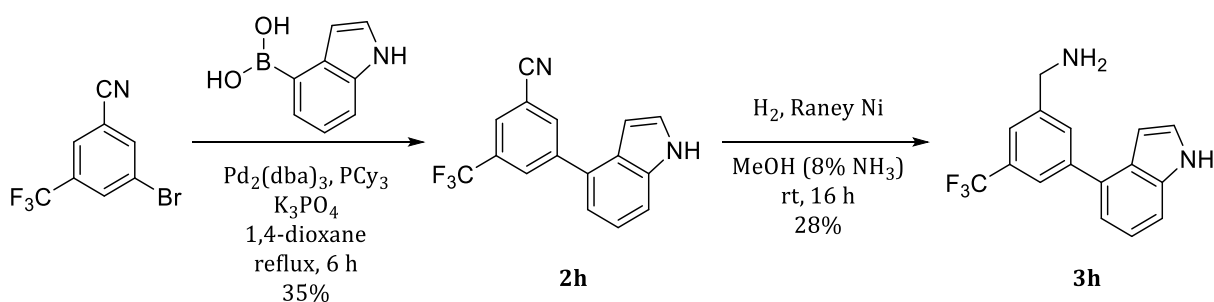


Property	Ideal Range	DRB ¹⁶²	W16 ¹⁶⁰	3g
FW	<300	319	611	257
TPSA	≤ 60	87.7	133	41.8
HBA	≤ 3	6	11	2
HBD	≤ 3	3	1	3
NRB	≤ 3	5	7	3
ATP	No	Yes	No	No

FW: formula weight in g/mol, TPSA: polar surface area in \AA^2 , HBA: hydrogen-bond acceptors, HBD: hydrogen-bond donors, NRB: number of rotatable bonds, ATP: does the compound bind in the ATP pocket of CK2. Green is within the ideal range; amber is within 15% of ideal range; red is over 15% from ideal range.²¹¹

Considering the binding mode of **3c** showed the potential of **3g** pushing the α D helix outwards, it was decided to synthesise compound **3h** – analogue of compound **3g** bearing a trifluoromethyl group as replacement of the chlorine. In addition, compound **3g** showed weak electron density in the α D pocket, and it was envisioned that the chlorine-to-trifluoromethyl in **3h** would abrogate the binding of the molecule at the interface in favour of an enhanced binding in the α D pocket considering previous reports.¹⁹⁷

As reported in Scheme 10, synthesis of **3h** followed the same synthetic steps and conditions as **3g** except for the nitrile reduction which was performed using hydrogenation with Raney Nickel²¹² due to $-\text{CF}_3$ lability in the presence of LiAlH_4 and AlCl_3 .



Scheme 10 - Synthesis of compound **3h** starting from the commercially available starting material.

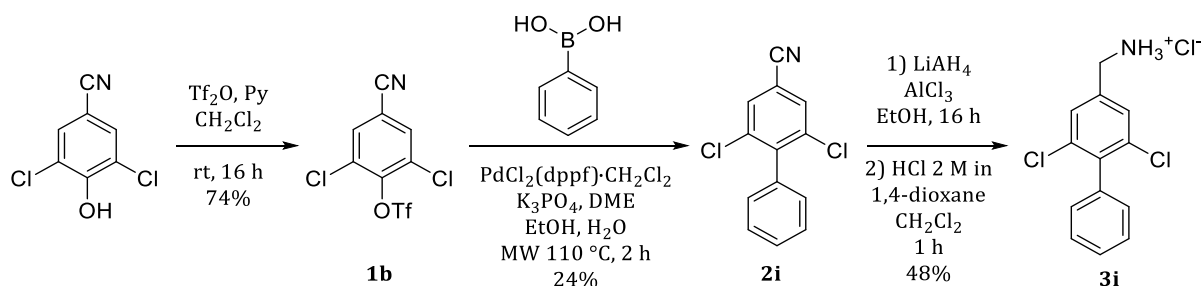
Suzuki cross-coupling between the commercially available 3-bromo-5-(trifluoromethyl)benzonitrile and indole-3-boronic acid in the presence of $\text{Pd}_2(\text{dba})_3$ and PCy_3 afforded intermediate **2h** in 35% yield; **2h** was then reduced to the desired compound **3h** using H_2 and Raney Ni (28% yield).

The introduced trifluoromethyl group decreased the binding affinity for the α/β interface, as shown by the poor electron density observed in the X-ray structure, yet, no electron density for the compound was observed in the α D pocket. Other compounds binding in the α D pocket gave more promising results than the 3-indole-phenyl-methanamine derivatives, and therefore, it was decided not to pursue the synthesis of this series of compounds further.

3.4.1.4. Dichloro-biaryl derivatives: **3i** and **3j**

The crystal structures of fragments **F5**, **F6** and **3d** binding to the α D pocket showed two binding poses that only differ by the position of the chlorine atom, suggesting that slow rotation of the biaryl bond occurs. It was envisioned that 3,5-dichloro-biphenyl fragments might result in a reduction of the entropy of binding by preventing free rotation around the biaryl bond and therefore a decrease in binding energy.

The first dichloro derivative synthesised was **3i**, an analogue of **F5**, whose synthesis was achieved as shown in Scheme 11.



Scheme 11 - Steps leading to the dichloro derivative **3i**.

Compound **1b** was obtained from the commercially available phenol derivative using Tf_2O and pyridine; the same conditions successfully used to synthesise compound **1a**.²⁰⁴ However, the yield of the phenol triflation (74%) was lower than for **1a** (91%) probably due to the steric bulk around the hydroxyl group. The cross-coupling of **1b** with phenylboronic acid to produce the essential precursor **2i** proved challenging, and a few Suzuki coupling conditions were screened as reported in Table 10.

Table 10 - Suzuki coupling conditions screened to obtain **2i**.

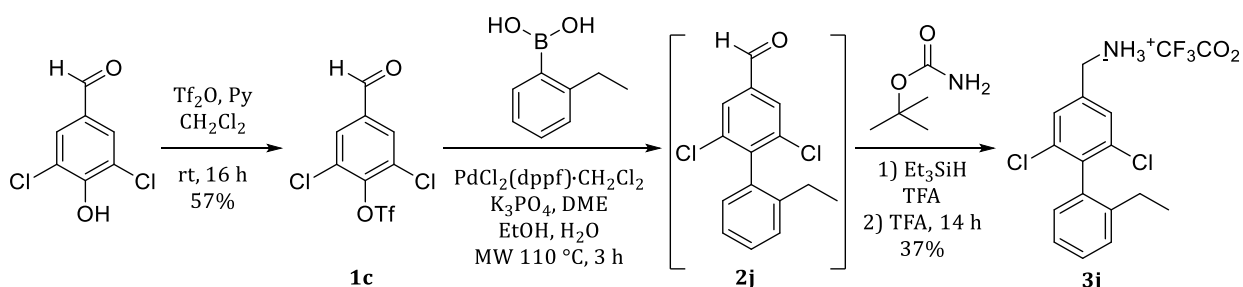
Entry	Starting material	Catalyst	Base	Reaction time	Outcome	Yield
1	Boronic acid	$\text{Pd}(\text{PPh}_3)_4$	Na_2CO_3	16 h	Very little desired product, 3 unknown impurities	<5%
2	Pinacol boronic ester	$\text{Pd}(\text{PPh}_3)_4$	Na_2CO_3	30 min	2 unknown aromatic by-products	0%
3	Boronic acid	$\text{PdCl}_2(\text{dppf})$	K_3PO_4	2 h (MW)	Desired product, aromatic impurity	24%

The use of $\text{PdCl}_2(\text{dppf})\cdot\text{CH}_2\text{Cl}_2$ in the presence of K_3PO_4 in DME, EtOH and H_2O (entry 3, Table 10) appeared to be the best set of conditions.²¹³ The low yield observed was attributed to the loss of the desired product during purification. The R_f of the desired product was very similar to an unidentified impurity formed during the reaction. Flash chromatography using different solvent systems failed to separate the two molecules, which were partially separated using preparative TLC.

Nitrile reduction of **2i** with LiAlH_4 and AlCl_3 , followed by treatment with HCl afforded **3i** in 48% yield (Scheme 11).

In parallel, it was decided to synthesise the dichloro analogue of the highest affinity fragment **3b**. The synthesis of **3j** started from the 3,5-dichloro-4-hydroxybenzaldehyde which underwent treatment with Tf_2O and pyridine in CH_2Cl_2 to afford **1c** in 57% yield. Attempts using the corresponding nitrile in the Suzuki coupling failed. Coupling using **1c** and 2-ethyl-phenylboronic acid afforded the intermediate **2j** that could not be isolated due to its R_f similar to that of unidentified impurities formed. The so-obtained crude compound underwent a reductive Boc

amination in the presence of *t*butylcarbamate and Et₃SiH in TFA to afford **3j** in 37% overall yield (Scheme 12).



Scheme 12 - Synthetic steps leading to the dichloro derivative **3j**.

Pleasingly, in crystallisation studies compounds **3i** and **3j** were the first fragments able to open the α D pocket of the more rigid construct of the protein.^r In the X-ray structures (Figure 31), the bottom ring is twisted 90° relative to the upper aromatic ring. As expected, only one binding mode was detected for these compounds suggesting that the two chlorine atoms help to lock the molecule in a twisted conformation reducing the rotational freedom of the aromatic rings.

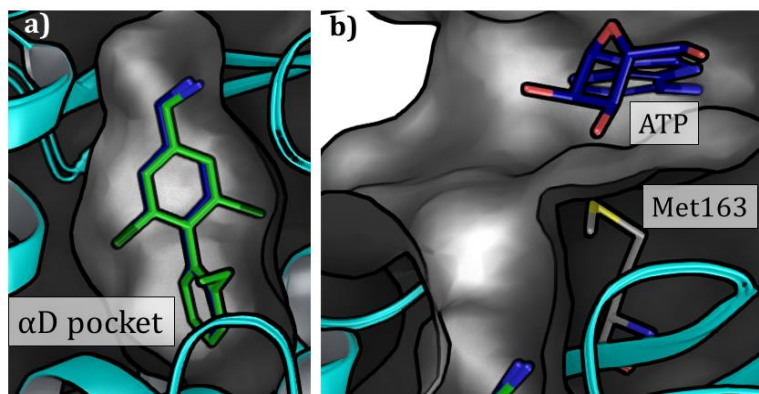
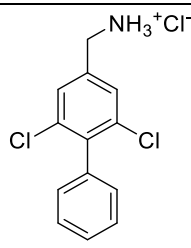
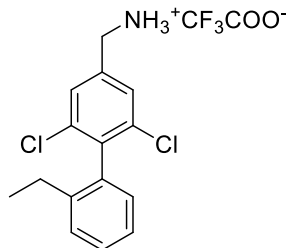


Figure 31 – a) X-ray structures of compound **3i** (blue, PDB code: 5OTR)²⁰⁶ and **3j** (green, PDB code: 5OTZ)²⁰⁶ co-crystallised with CK2 α . b) Zoomed-in section showing the fragments are not able to flip the Met163 and displace the ATP (blue) from its binding site. Protein is shown as cyan ribbon and grey surface.

Pleasingly, the biological evaluation of compounds **3i** and **3j** showed a remarkable boost in binding affinity compared to the fragments tested thus far (Table 11). Moreover, the LE was also improved.

^r For more details about the different constructs used *vide* 8.1.1. CK2 α _KA presents a more flexible β 4- β 5 motif and α D helix whereas CK2 α _FP is more rigid.

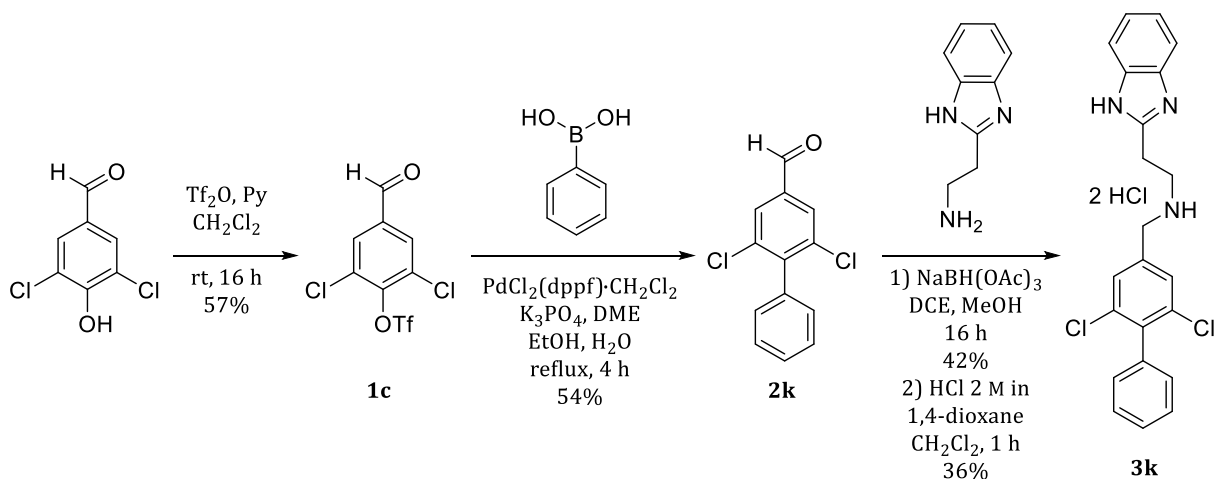
Table 11 - LE and K_d of dichloro derivatives **3i** and **3j**.

Compound	Structure	LE	K_d (μM)
3i		0.42	12
3j		0.39	6.5

3.4.2. Fragments growing towards the ATP binding site: second-generation CK2 inhibitors

Compounds **3i** and **3j** showed the highest binding affinity and the best LE for the αD pocket over the fragments synthesised in the Spring group during the fragment elaboration phase. These molecules were not able to inhibit the catalytic activity of CK2 as they did not flip the Met163 and hence displace the ATP; therefore, they were used as the bottom part of the second-generation inhibitors. The αD fragments were merged with a benzimidazole fragment that binds at the ATP mouth without interacting with conserved residues within the ATP binding site to achieve inhibition.²⁰⁶ Optimisation of the benzimidazole fragment was carried out by Dr Claudia De Fusco in the Spring group. Unlike **CAM4066**, it was envisioned that CK2 inhibition could be achieved without the need of a fragment binding at the ATP pocket considering the affinity of the αD fragment was significantly improved respect to fragment used in **CAM4066** (**F5** $K_d = 267 \mu\text{M}$ vs $K_d = 6.5$ and $12 \mu\text{M}$ for **3j** and **3i** respectively).¹⁹⁸ It was decided to merge compounds **3i** and **3j** with the benzimidazole motif as an attempt to achieve CK2 inhibition.

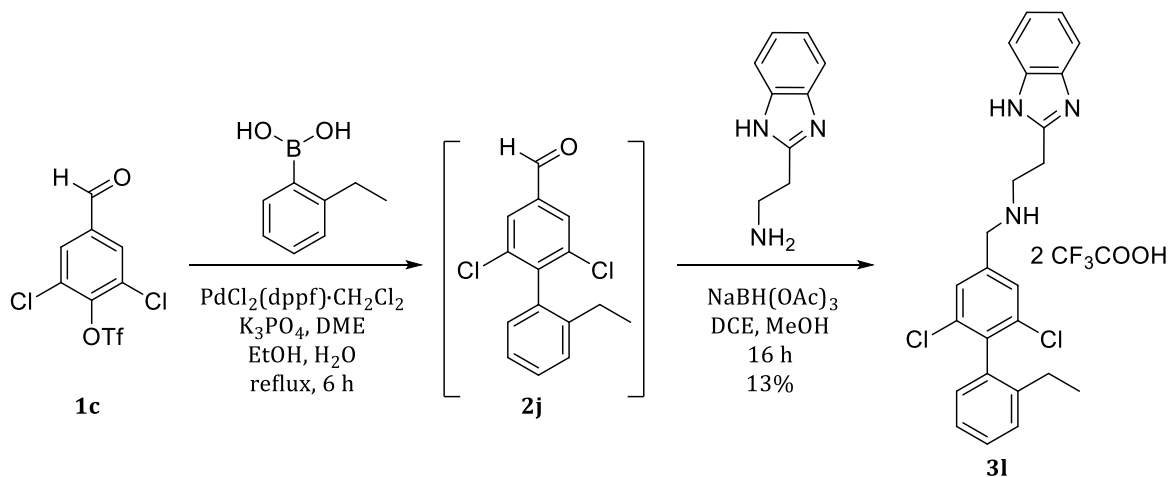
Synthesis of **3k** followed the synthetic route reported in Scheme 13. We were gratified to find that when **1c** was reacted with phenylboronic acid under thermal heating using $\text{PdCl}_2(\text{dppf})$, CH_2Cl_2 , K_3PO_4 , DME, EtOH, and H_2O compound **2k** was obtained in a superior yield of 54% compared to the 24% obtained when the corresponding nitrile (**1b**) was used (Scheme 11).



Scheme 13 – Synthetic route to compound **3k**.

Intermediate **2k** underwent a reductive amination in the presence of commercially-available 2-benzimidazolyl-ethylamine and $\text{NaBH}(\text{OAc})_3$, followed by acidification, to afford compound **3k**.²¹⁴

Compound **3l** was synthesised in a similar way to compound **3k** with the exception that isolation of the biaryl aldehyde intermediate **2j** was not possible, as observed in the synthesis of **3j**. The crude was therefore carried onto the reductive amination step, and the resulting amine purified *via* preparative HPLC to afford **3l** as TFA salt with 13% overall yield (Scheme 14).



Scheme 14 - Synthesis of Second-generation inhibitor **3l**.

The crystallographic structure of **3k** and **3l** confirmed the expected binding mode with Met163, whose position is thought to be essential for the inhibition, flipped into the 'out' conformation to displace the ATP. As hoped, the benzimidazole motif binds at the mouth of the ATP binding site without interacting with residues in the ATP binding site (Figure 32).

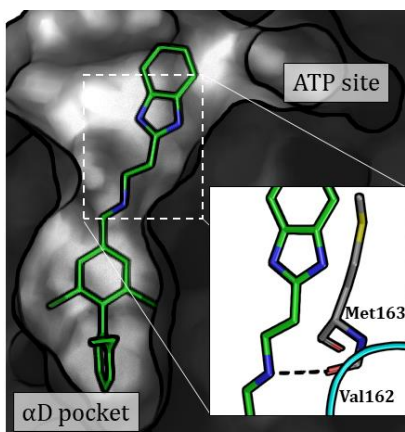


Figure 32 - Binding mode of **3l** as detected in the X-ray crystal structure (PDB code: 5OTZ).²⁰⁶ The molecule occupies the α D pocket and the channel connecting it to the ATP binding site. A zoomed-in section of the Met163 in the flipped-out position is shown on the right.

Compound **3k** proved to be insoluble under ITC assays condition and in the cell growth media, and therefore its biological evaluation was not possible.

Compound **3l** showed improved solubility compared to **3k**, but it was still not soluble enough to perform ITC direct binding experiments which require a high concentration of the compound. Therefore, ITC competition studies were performed (by Dr Paul Brear) to confirm the binding mode and to estimate the affinity of **3l** for the α D site. Probe molecules that have well characterised binding modes and affinities were titrated into CK2 α in the presence of **3l**. In particular, the following experiments were performed, and the following observations were made:

- 20 μ M **3l** inhibited the binding of **CAM4066** (first-generation inhibitor) to CK2 α .
- Compound **3j** was titrated into CK2 α in the presence of 20 μ M **3l**. This showed that **3l** inhibited the binding of **3j** to CK2 α confirming that the binding site of **3l** is the α D pocket.
- 2-hydroxyl-5-methyl benzoic acid is a fragment that binds to the conserved Lys68 in the ATP site and occupies the right-hand side of the pocket. The binding of this compound was not inhibited by **3l** confirming that the benzimidazole ring does not interact with the right-hand side of the ATP pocket and validates the binding mode derived from the crystal structure.
- CX4945, which from the analyses of crystal structures would clash with **3l** in the hinge region, was titrated into CK2 α in the presence of **3l**. **3l** was able to inhibit the binding of CX4945 to CK2 α . This confirmed that the benzimidazole ring flips the Met163 channel and blocks access to the ATP site inhibiting the binding of CX4945.

These competition experiments suggested that the K_d of **3l** towards CK2 α is approximately 4 μ M and confirmed that the binding mode of **3l** in the α D pocket and mouth of the ATP site corresponds to that seen in the crystal structure.²⁰⁶

Compound **31** was able to inhibit the CK2 catalytic activity with an IC_{50} of 7 μM (*in vitro* phosphorylation assay) and a GI_{50} of $10.0 \pm 3.6 \mu M$ (cellular assay using HCT116 cells). Pleasingly, **31** was able to inhibit the phosphorylation of specific CK2 substrates in a cellular context as shown in Figure 33.

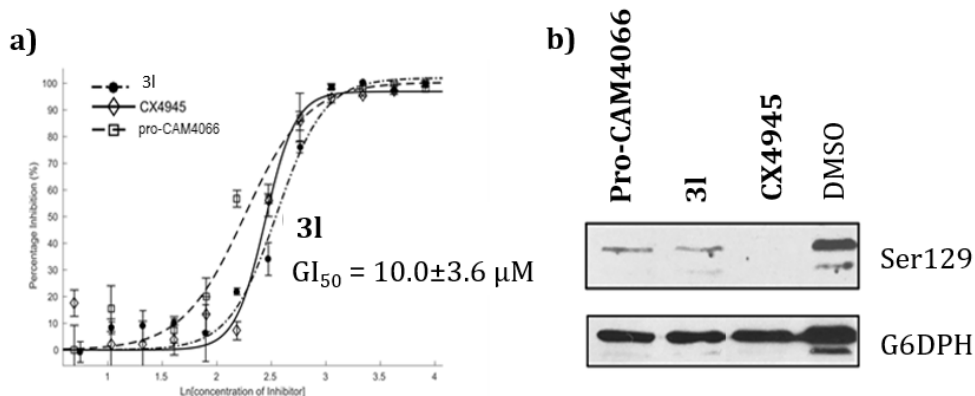


Figure 33 – Bioactivity of **31** in cancer cells. a) Dose-response curve for the inhibition of growth of HCT116 cells by **31**, pro-CAM4066 and CX4945. Compound concentrations on the x-axis are shown as natural logarithm. All graphs show the mean \pm SEM of not less than three independent experiments with each in triplicate. b) Western blot analysis showing the specific CK2 phosphorylation targets: AKT1 Ser129 and G6DPH. HCT116 cells were treated with $2 \times GI_{50}$ of CX4945 (20 μM), **31** (20 μM) or pro-CAM4066 (20 μM) for 72 hours. Adapted from Iegre et al., ChemSci, 2018.²⁰⁶

31 was subjected to a kinase selectivity panel (Dundee Kinase panel) at 30 μM concentration ($4 \times IC_{50}$) to prove that CK2 inhibition from the αD pocket can lead to a more selective inhibitor than ATP-competitive compounds. Pleasingly, despite the relatively high concentration used, **31** showed good selectivity against 20 closely related kinases (CMGC family, Figure 34a). Even though for 4 kinases – CAMK1, SmMLCK, EF2K, SGK1 – out of 140 **31** causes more than 50% inhibition, the compound showed a more selective profile compared to known CK2 ATP-competitive inhibitors (Figure 34b).

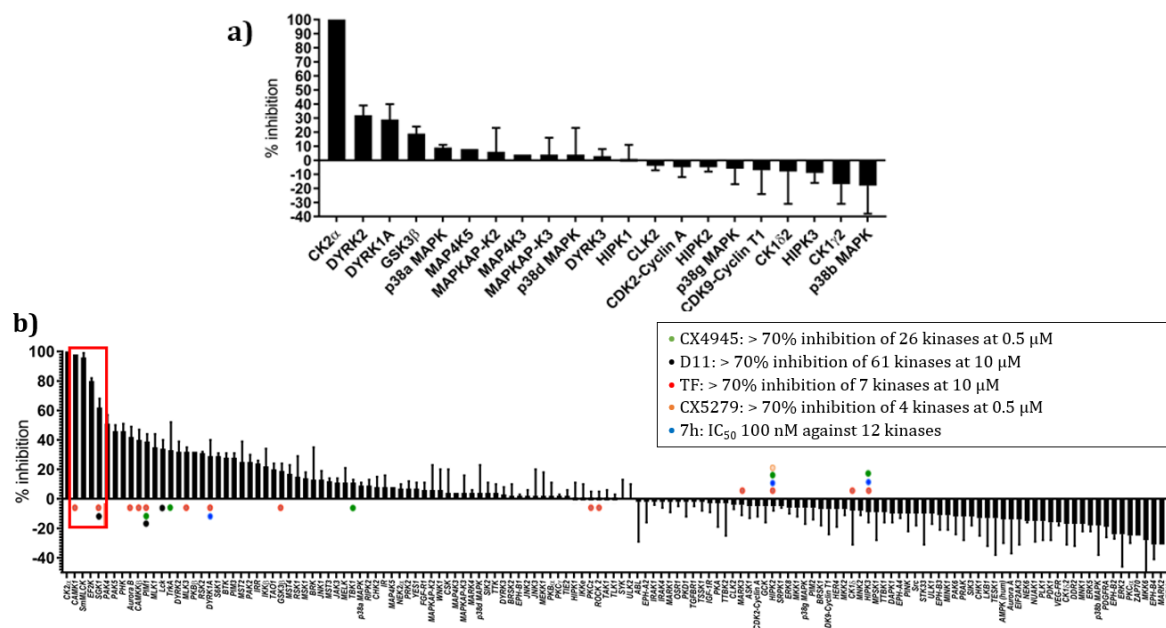


Figure 34 - Kinase selectivity panel for **31**. a) Selectivity profile of **31** at 30 μM concentration against closely related CMGC family members; b) Selectivity profile of **31** at 30 μM against a panel of 140 kinases. Kinases inhibited by **31** by more than 50% are highlighted in red. Kinases inhibited by more than 70% by previously reported CK2 kinase inhibitors (namely CX4945, D11, TF, CX5279, 7h) are shown as coloured dots. Adapted from Iegre et al., ChemSci, 2018.²⁰⁶

The ultimate goal of this project was to develop second-generation CK2 inhibitor with improved properties in respect to **CAM4066**. Compound **31** was successful in that as it overcame the limitation of the first-generation inhibitor as shown in Table 12.

Table 12 - Properties and structural features of compound **31** compared to **CAM4066**. Taken from Iegre et al., ChemSci 2018.²⁰⁶

31

Property	Ideal range	CAM4066	31
FW	<500	494	453
TPSA	<140	101	41
NRB	<10	12	8
HBA	<10	4	2
HBD	<5	3	2
Conserved interaction	No	Yes	No
Need of a pro-drug	No	Yes	No
Amide bonds	No	Yes	No
Drop in potency*	No	~10 fold	No

FW = formula weight in g/mol; TPSA = topological polar surface area in Å² NRB = number of rotatable bonds; HBA = number of hydrogen bond acceptors; HBD = number of hydrogen bond donors.²¹¹ * Drop in potency between enzymatic and cellular assays.

3.5. Conclusions and future work

The work described in this chapter led to the development of **3l**: the first CK2 inhibitor that targets the allosteric α D pocket and that does not interact with highly conserved residues located in the ATP site hence providing selectivity.

3l was developed using a FBDD approach starting from **F5**, a fragment with 267 μ M affinity for the α D pocket. Through iterative cycles of design, synthesis, X-ray crystallography and biophysical evaluation the initial fragment was first elaborated into **3j** (K_d 6.5 μ M) and subsequently linked to a benzimidazole-like motif to reach the mouth of the ATP binding site and flip the Met163 - a residue seen as important for the catalytic activity. The merging strategy adopted in this work led to **3l** which was able to bind to CK2 α with a K_d of 4 μ M, inhibit CK2 *in vitro* (IC_{50} 7 μ M), inhibit growth of colorectal cancer cells (GI_{50} 10 μ M) and showed promising selectivity for CK2 versus 140 other kinases.

This work showcases the successful application of FBDD to overcome the limitation of the first-generation inhibitor **CAM4066**. Compared to **CAM4066**, **3l** presents a reduced number of rotatable bonds, HBDS, HBAs, does not contain amide bonds, and it maintains its activity in cells without the need of being formulated as a pro-drug.

In conclusion, **3l** present itself as an ideal chemical tool that can be further elaborated into a drug molecule. Pleasingly, APOLLO therapeutics became interested in the project and are now running a drug-discovery programme to pursue this project further.

In addition, during the fragment optimisation carried out in this study, a few fragments were found to bind at the protein interface predominantly. One of them, **3g** was found to bind deep in the Phe pocket - the only pocket present at the shallow interface - and it proved to be able to displace the CK2 β -like probe with an IC_{50} of 44 μ M. **3g** is, therefore, the most promising fragment binding at the interface with structural information available reported in the literature. Due to its fragment-like properties, **3g** is an ideal starting point to develop small molecule modulators of the CK2 interface. Considering the high number of attempts in the Spring group prior to this work to develop high-affinity fragments binding at the interface, it was decided not to optimise **3g** further.

Instead, as a continuation of this project, Chapter 4 describes the development of conformationally-constrained peptides binding at the α/β interface.

Furthermore, additional fragment screenings of Diversity-Oriented-Synthesis (DOS) libraries are underway in the Spring group to identify novel sp^3 rich molecules to disrupt the CK2 PPI.

CHAPTER 4:

Conformationally-Constrained Peptides Targeting the PPI of the Anti-Apoptotic Protein CK2

4.1. Summary

The development of molecules able to disrupt the protein-protein interaction (PPI) between the α and the β subunits of the protein kinase CK2 has received increasing interest in the last few decades.¹⁶⁰⁻¹⁶⁴ However, the discovery of a selective, tissue permeable, and stable chemical tool that could act at the protein interface and that could be used *in vivo* is still missing.

This chapter describes the approach used to efficiently develop peptides acting at the CK2 α/β interface that are highly functionalised, cell-permeable, stable in serum, and with structural information available (Figure 35). The lead probe developed in this work, **P7-F1C5**, should be of great help in understanding the regulatory mechanisms behind CK2 and their implication in oncogenesis.

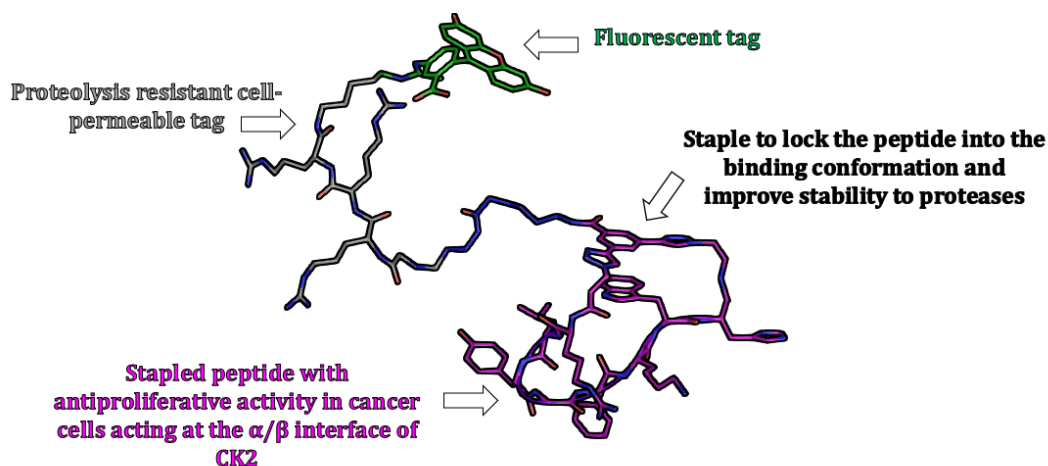
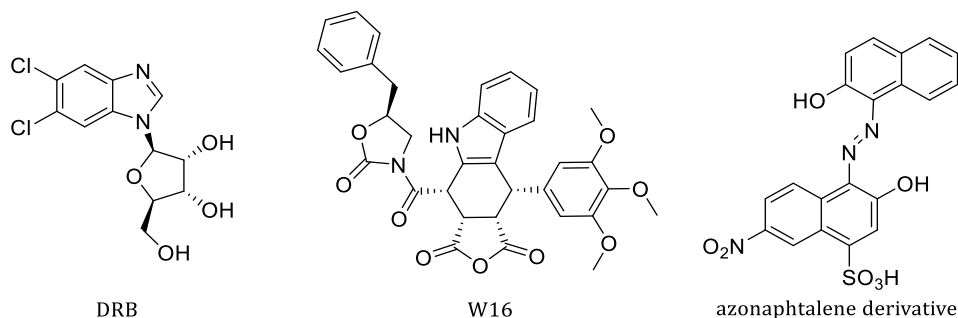


Figure 35 – Functionalised stapled peptide P7-F1C5 described in this chapter.

Whilst the approach described herein is specific to CK2, a similar strategy could be applied to any target needing the fast development of highly functionalised peptide modulators of PPIs.

4.2. Project background

A limited number of small molecules have been developed before this work - namely DRB, W16, and azonaphthalene derivatives (structures shown below)^{160, 162, 201} - with the aim of inhibiting CK2 by acting at the protein interface.



However, due to the nature of these small molecules and the characteristics of the interface, none of the compounds developed to date is selective for the interface. In some cases, structural evidence of the binding at the protein interface is also missing.

In the Spring group efforts have focused on the development of inhibitors of the CK2 α/β interface using a Fragment-Based Drug Discovery approach (FBDD) approach. However, the best fragment **3g**, whose development is described in Chapter 3, needs to be elaborated further in order to identify a higher affinity molecule to act as a useful chemical tool.

On the other hand, Cochet *et al.* have used the sequence of the tail of the regulatory CK2 β domain to design a cyclic peptide that could displace the native CK2 β subunit and prevent the assembly of the holoenzyme.¹⁶¹ The disulfide-bridged peptide, hereafter known as Pc, showed a sub-micromolar affinity for CK2 α and displaced CK2 β *in vitro*. However, due to the inherent low stability of disulfide bonds under reducing conditions, its cellular activity could not be investigated.¹⁶¹ Fast forward ten years and the same research group developed a lactam head-to-tail cyclised variant of Pc that was conjugated to a TAT peptide to gain cell-entry ($IC_{50} = 5 \mu M$).¹⁶⁴ Although cell permeable, no structural information on the new macrocyclic peptide or data on the stability of the latter molecule in physiological fluids were reported, and therefore, such molecule could not serve as a chemical probe without further validation.

4.3. Project aim and overview

The aim of this project was to develop conformationally-constrained peptide CK2 inhibitors targeting the protein interface and that have the potential to act as valuable chemical probes *in vivo*.

Initially, molecular modelling was carried out using the structural information available on Pc²¹⁵ and on the portion of CK2 β interacting with the catalytic domain to identify a suitable position to place the covalent constraint. It was envisioned that a constraint was necessary to improve the peptide affinity for the target by locking it into the binding conformation and simultaneously enhance the stability to proteases. Consequently, a series of constrained peptides were synthesised and tested *in vitro* to assess their ability to engage CK2 α . The most promising peptide was then modified to incorporate fragment-like amino acids to boost the potency. Successively, X-ray crystallography revealed insights into the peptide binding mode and guided the design further. Lastly, the higher affinity peptide, **P7-C5** was efficiently functionalised employing a novel multi-functional constraint.

In total, twenty-two macrocyclic peptides were synthesised; the most promising one, **P7-F1C5** engaged CK2 α with sub-micromolar affinity, it is stable in serum, cell-permeable, and active in cancer cells. An overview of the workflow is shown in Figure 36.

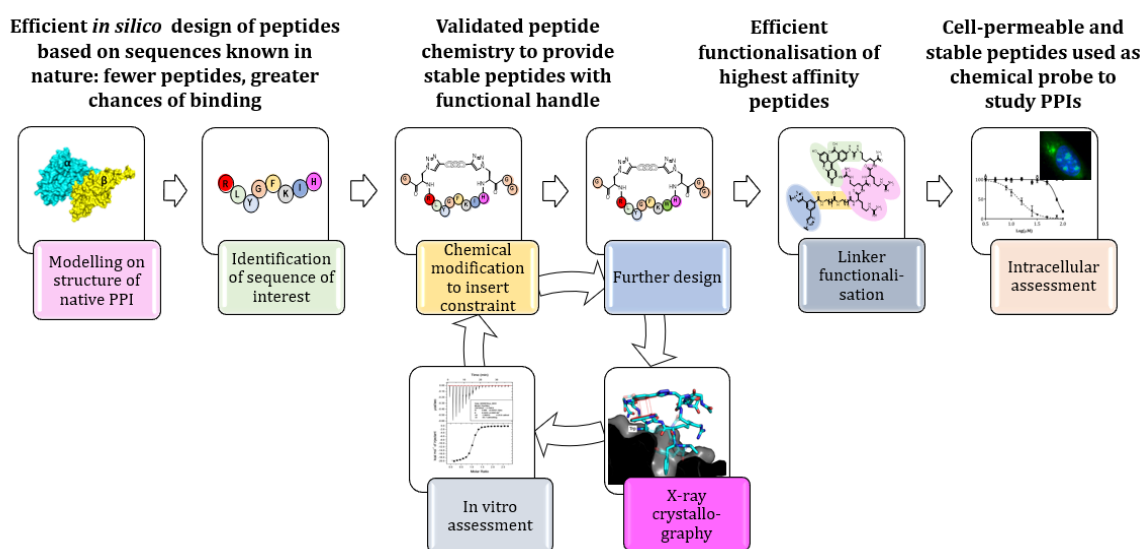


Figure 36 - Workflow of the project described in Chapter 4.

4.4. Results and discussion^s

Unless otherwise stated, the peptides described in this chapter were synthesised using standard procedures for solid-phase peptide synthesis (SPPS) and peptide macrocyclisation was achieved by following standard procedures for two-component copper-catalysed azido-alkyne cycloaddition peptide stapling (2C CuAAC PS).³⁸

Biophysics experiments such as fluorescent polarisation (FP), isothermal titration calorimetry (ITC), kinase assays, and X-ray crystallography were performed under the supervision of Dr Paul Brear (Hyvönen group, Biochemistry, University of Cambridge). Cellular experiments such as cell culture, confocal microscopy, anti-proliferation assay, and cell-viability assay were performed under the supervision of Dr David J. Baker (Discovery Sciences, AstraZeneca, Cambridge). Molecular dynamics simulations were conducted by our collaborator Dr Yaw Sing Tan (A*STAR, Singapore).

4.4.1. Design of CK2 β -like peptides

Analysis of the portion of CK2 β interacting with CK2 α has suggested that only a cluster of 8 amino acid (186-193) contribute to the binding significantly: RLYGFKIH. All of the amino acids mentioned above are included in the sequence of the disulfide-bridged Pc peptide developed by Cochet *et al.*¹⁶¹ Therefore, the X-ray crystallographic structure of Pc bound to CK2 α (PDB code: 4I5B)²¹⁵ was used to understand which of those residues could be replaced by amino acids amenable to side-chain cross-linking to form stable cyclic peptides. Computational alanine scanning (CAS) and energetic decomposition suggested that any of the terminal residues introduced in Pc – namely G1, C2, G11, C12, G13 – could be replaced to introduce the constraint as they did not contribute to the binding (Figure 37).

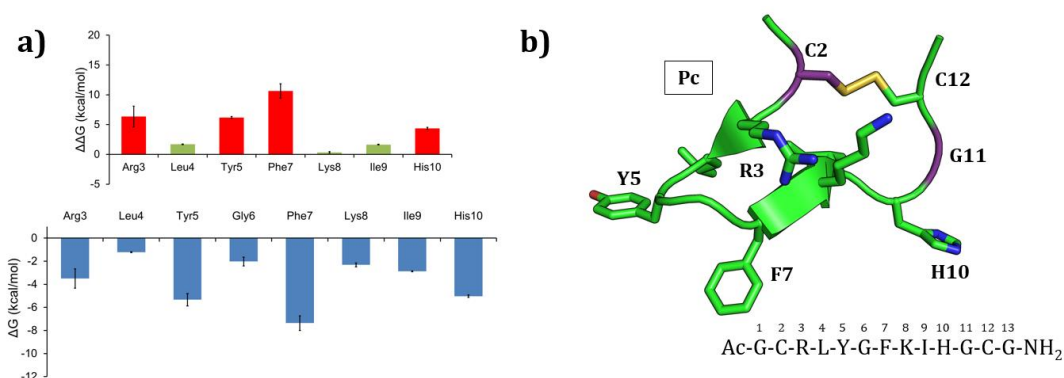


Figure 37 – Molecular modelling done on Pc peptide. a) CAS (top) and energetic decomposition (bottom) of the amino acids of Pc. Residues whose mutation to Ala negatively affected the binding significantly are shown in red, residues non-

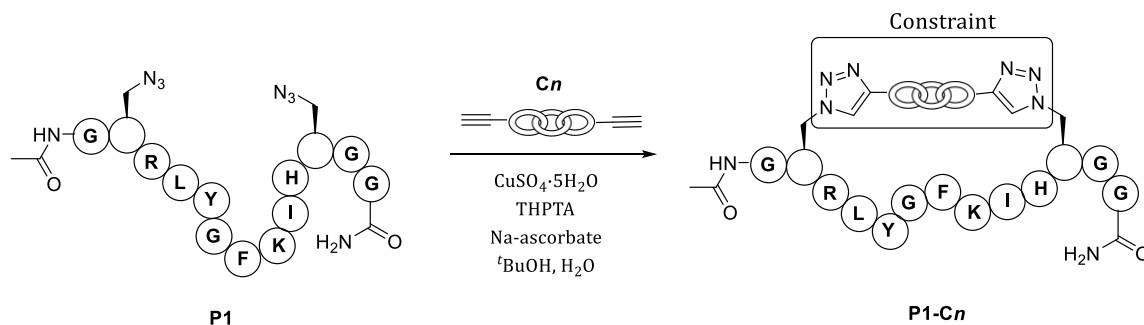
^s The work described in chapter has been published in Iegre *et al.* ChemSci, 2019.²⁸⁸ Part of the text and figures have been adapted from this publication.

CHAPTER 4: Conformationally-constrained peptides targeting the protein-protein interaction of the anti-apoptotic proteins CK2

contributing to the binding are shown in green; b) Structure of Pc peptide (from PDB: 415B).²¹⁵ Residues coloured in purple (C2 and G11) are the ones chosen to place the constraint in this study.

It was decided to employ the 2C CuAAC peptide macrocyclisation chemistry to constrain the peptides as this cross-linking technology has been successfully used in the past to constrain peptides into their binding conformation, improve PK properties and simultaneously allow for functionalisation *via* the constraint rather than *via* the linear sequence.^{79,83,84,86,87,216}

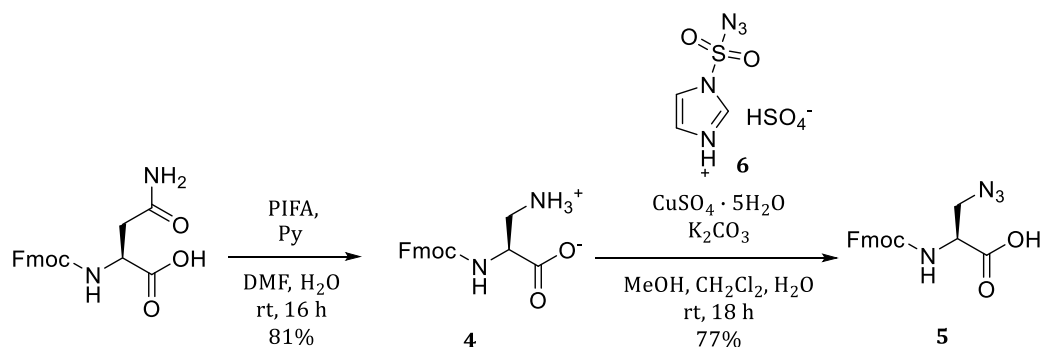
C2 and G11 were positioned at a suitable distance from each other to accommodate a 2C double-click constraint (Figure 37). Consequently, the 13-mer linear peptide would feature the sequence Ac-GXRLYGFKIHGG-NH₂ where X indicates the azido amino acids incorporated for constraining. The peptide sequence mentioned above will be referred to as **P1** hereinafter. It was envisioned that the constraint should be rather rigid to minimise entropic penalties upon binding that may occur as the result of excessive flexibility. Therefore, the azido amino acid selected for cross-linking was azido-alanine (**5**) which, once reacted with the appropriate dialkyne linkage, would generate a cyclic peptide of a generic structure **P1-Cn** shown in Scheme 15.



Scheme 15 - Generic structure of the linear and cyclic peptides that are the subject of this work.

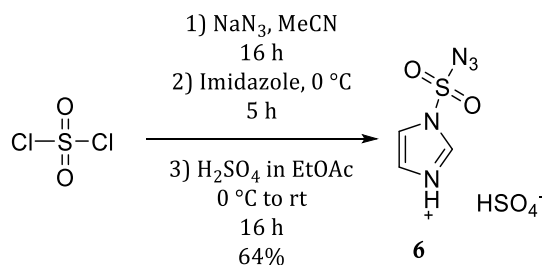
4.4.1.1. Synthesis of Fmoc-azido-alanine 5

The synthesis of Fmoc-azido-alanine **5** was performed following literature precedent (Scheme 16).²¹⁷ The synthetic route commenced from the commercially available Fmoc-Asn-OH that underwent a Hofmann rearrangement in the presence of [bis(trifluoroacetoxy)iodo]benzene (PIFA) to afford Fmoc-Dap-OH (**4**) in 81% yield. The amino acid was then treated with the azido transfer reagent imidazole-1-sulfonyl-azide hydrogen sulfate **6** to obtain **5** in 77% yield.



Scheme 16 - Synthesis of Fmoc-azido alanine **5** from commercially available Fmoc-Asn-OH. Fmoc = Fluorenylmethyloxycarbonyl

The azido transfer reagent **6** was synthesised in a one-pot procedure from the cheaply available starting materials sulfuryl chloride, imidazole, and NaN₃ (Scheme 17).²¹⁸



Scheme 17 - One-pot synthesis of azido transfer reagent **6**.

The Fmoc protected azido amino acid **5** was used to synthesise the linear peptide **P1** by SPPS.

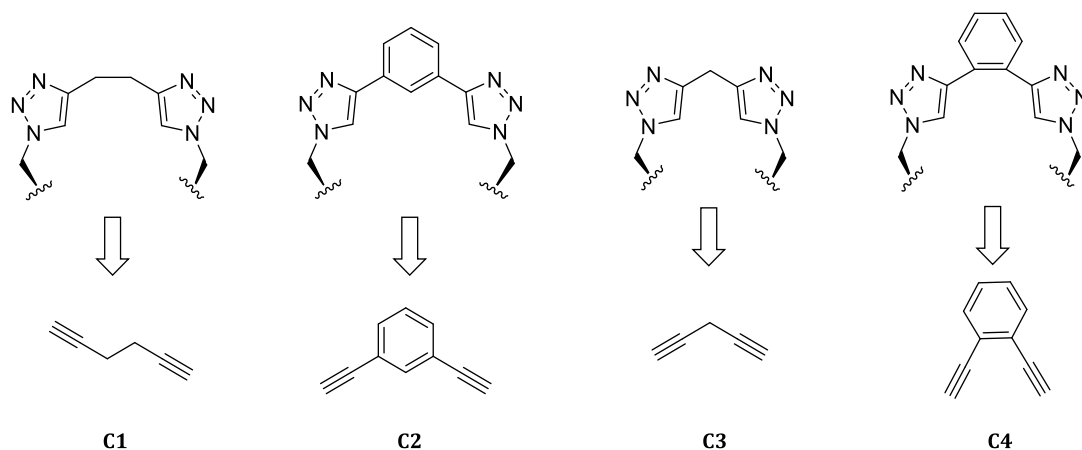
4.4.2. Screening of constrained peptides

Once the linear sequence was identified and synthesised, the next step aimed to constrain the peptide into a conformation that resembles the portion of CK2β binding to CK2α.

The ultimate goal of this project was to develop highly functionalised peptides in which the functionalisation feature was on the constraint rather than the linear sequence itself. This strategy was considered advantageous as it requires the synthesis of one linear bioactive peptide only, whereas peptidic functionalities such as CPPs and fluorescent tags are added onto the constraint *via* amide coupling. To this end, a functional handle on the constraint would be required. However, it was decided to commence the screening of the constraints from commercially available materials or easily synthesised plain dialkynes. The plain cyclised peptides would then be tested to investigate their ability to displace a CK2β-like probe in an FP assay and the most promising ones re-synthesised using constraints bearing a functional handle.

4.4.2.1. Plain constraints: C1-C4

Molecular modelling performed on the X-ray structures of Pc²¹⁵ suggested that four possible constraints could be used to constrain the peptide into a CK2 β -like conformation (Scheme 18).



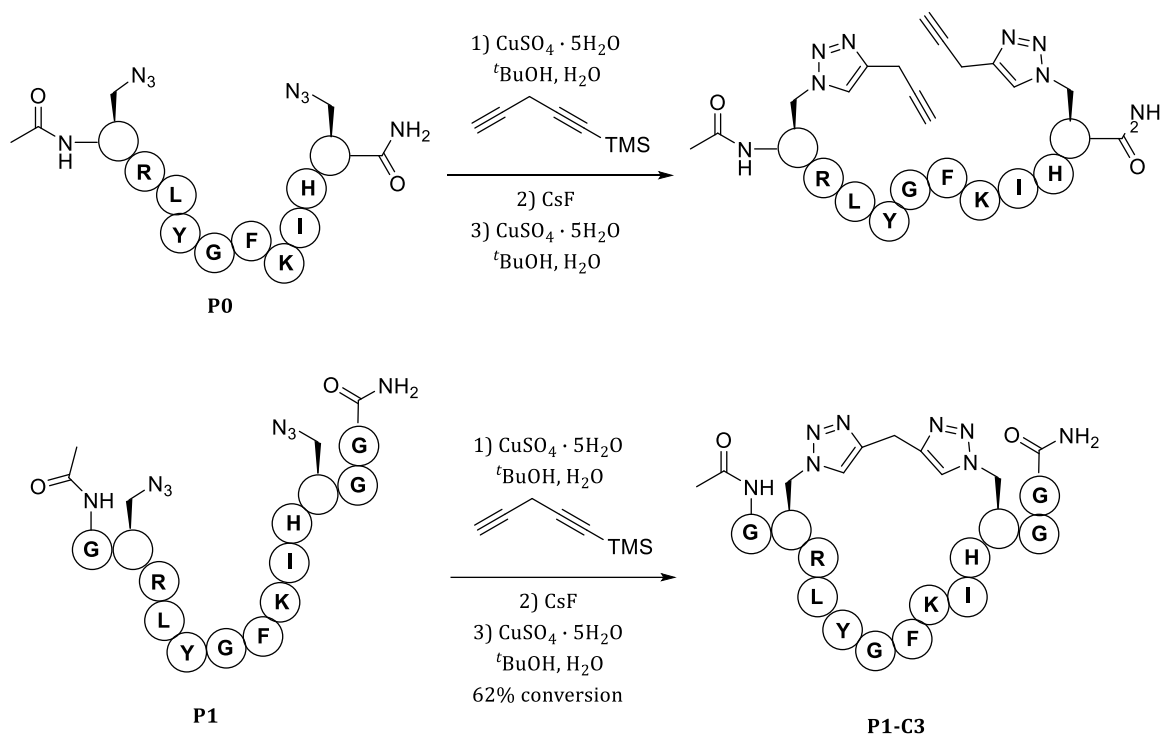
Scheme 18 - Proposed constraints for peptide macrocyclisation (top) and their corresponding dialkyne precursors (bottom).

Constraints **C1** and **C2** were commercially available and were used as such in the CuAAC 2C macrocyclisation reaction. Initially, it was decided to use a shorter version of the linear peptide **P1** by removing the three terminal glycine residues (**P0**, Ac-XRLYGFKIHX-NH₂). Molecular dynamic simulations (MDs, performed by Dr Yaw Sing Tan, A*STAR, Singapore) showed that the terminal glycine residues did not contribute to the binding significantly (calculated ΔH -50.6 ± 1.7 and -56.6 ± 1.2 Kcal·mol⁻¹ for Pc and shorter Pc respectively). In addition, by removing the terminal residues, three coupling and deprotection steps could be avoided. Whilst constraining of **P0** with **C1** successfully provided **P0-C1** (82% conversion)[†], cyclisation with **C2** was not achieved, with only the addition of two equivalents of the linker **C2** per equivalent of the linear sequence **P0**, as observed by LCMS of the crude mixture. By changing the linear sequence to **P1**, the desired product **P1-C2** was obtained (65% conversion) suggesting that the terminal glycine residues may help cyclisation.

Constraints **C3** and **C4** were not commercially available, and their synthesis is discussed below. It was envisioned that **C3** could be obtained by TMS deprotection of the commercially available TMS-mono-protected analogue by treatment with TBAF for 14-16 h. However, due to the high volatility of the product, its isolation was not achieved. It was decided to perform a first CuAAC reaction in the presence of the commercially available trimethyl(penta-1,4-diyn-1-yl)silane and **P0**, followed by addition of CsF to remove the TMS group and a second CuAAC reaction (Scheme 19). Unfortunately, only the addition of two deprotected constraints was detected in the crude

[†] LCMS conversions are given for peptide macrocyclisation reactions instead of yield due to loss of material during the purification on preparative HPLC.

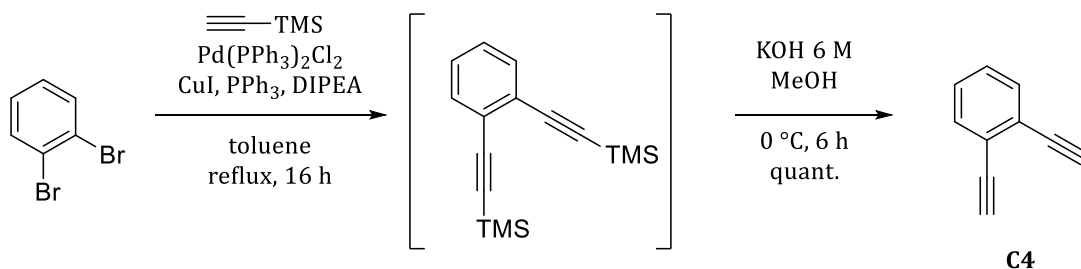
mixture. Pleasingly, the same procedure repeated with **P1** afforded the desired product **P1-C3** (62% conversion) as shown in Scheme 19.



Scheme 19 - Attempts of cyclising **P0** into **P0-C3** and **P1** into **P1-C3** using CuAAC peptide chemistry.

Considering that the terminal residues were required to obtain the desired cyclisation products with **C2** and **C3**, it was decided to use the sequence of **P1** for all the successive reactions described hereafter.

Constraint **C4** was obtained from the commercially available 1,2-dibromobenzene. The latter molecule underwent a Sonogashira coupling in the presence of trimethylsilylacetylene, $\text{Pd}(\text{PPh}_3)_2\text{Cl}_2$, CuI, PPh_3 , and DIPEA followed by TMS deprotection in the presence of KOH and MeOH to afford **C4** as a 42% w/v solution in PE 40-60 (Scheme 20).



Scheme 20 - Synthesis of **C4** from commercially available 1,2 dibromo-benzene.

2C CuAAC peptide macrocyclisation between **C4** and **P1** afforded **P1-C4** in 79% conversion.

CHAPTER 4: Conformationally-constrained peptides targeting the protein-protein interaction of the anti-apoptotic proteins CK2

With the four cyclic peptides in hand, their biological activity was investigated using an FP assay. In this study, FP was used to determine the ability of the peptide to displace a commercially available fluorescent probe meant to mimic the CK2 β subunit.^u The assay looked at the anisotropy resulting from the interaction of CK2 α and the fluorescent probe in the presence of 15 μ M peptide concentration. The results included Pc, its shorter analogue, and the linear Pc peptides for comparison (synthesised according to previous reports)^{161, 215}. The results are expressed as % inhibition and indicate the inhibition of the assembly of CK2 α with the fluorescent probe (Table 13). The corresponding calculated binding energies are also shown in the table.

Table 13 - % inhibition of the assembly between CK2 α and the FP probe at 15 μ M peptide concentration.

Entry	Peptide	Structure	% inhibition (at 15 μ M)	Calculated Δ H (Kcal/mol)
1	Pc	GCRLYGFKIHGCG (S-S)	79.0 \pm 7.0	-50.6 \pm 1.7
2	Short Pc	GCRLYGFKIHGC (S-S)	73.8 \pm 2.5	-56.6 \pm 1.2
3	Linear Pc	GCRLYGFKIHGCG	13.1 \pm 2.3	NA
4	P0-C1	X _{C1} LYGFKIH X _{C1}	0.6 \pm 0.1	-50.3 \pm 0.6
5	P1	G X LYGFKIH X GG	12.6 \pm 1.7	NA
6	P1-C2	G X _{C2} LYGFKIH X _{C2} GG	NA	-57.1 \pm 2.1
7	P1-C3	G X _{C3} LYGFKIH X _{C3} GG	58.4 \pm 4.0	-54.1 \pm 2.1
8	P1-C4	G X _{C4} LYGFKIH X _{C4} GG	21.1 \pm 1.9	NA

All the peptides feature an amide at the C-terminus and an acetyl capping at the N-terminus. X = Fmoc-Aza-OH (5).

The results confirmed that the terminal Gly residues did not contribute significantly to the binding as predicted by the molecular modelling (entries 1 and 2, Table 13). **P1-C3** appeared to be the most promising of the cyclised peptides synthesised so far, and therefore, it was the one brought forward. Unfortunately, **P1-C2** proved to be insoluble in the assay conditions and its evaluation was not possible at that stage.

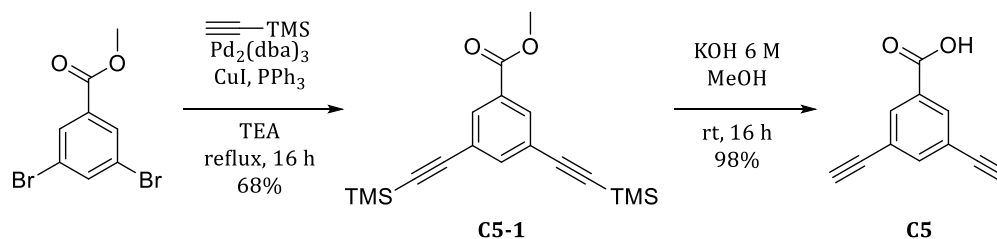
^u Fluorescent probe of sequence FITC- β Gly-RLYGFKIHMPAYQLQ.

4.4.2.2. Constraints with a functional handle: C5 and C6

Although the ability of **P1-C2** to displace the CK2 β -like probe from CK2 α could not be studied due to solubility issues, MDs suggested that the peptides **P1-C2** and **P1-C3** may have a more favourable enthalpy of binding than Pc (-57.1 ± 2.1 Kcal \cdot mol $^{-1}$ for **P1-C2**, -54.1 ± 2.1 Kcal \cdot mol $^{-1}$ for **P1-C3** and -50.6 ± 1.7 Kcal \cdot mol $^{-1}$ for Pc, Table 13) and hence it was decided to consider them both for further evaluation.

It was envisioned that by introducing a suitable functional group – such as carboxylic acid or amine – the solubility of peptide **P1-C2** in aqueous buffers could be improved and would simultaneously set up for the introduction of peptidic functionalities at a later stage.

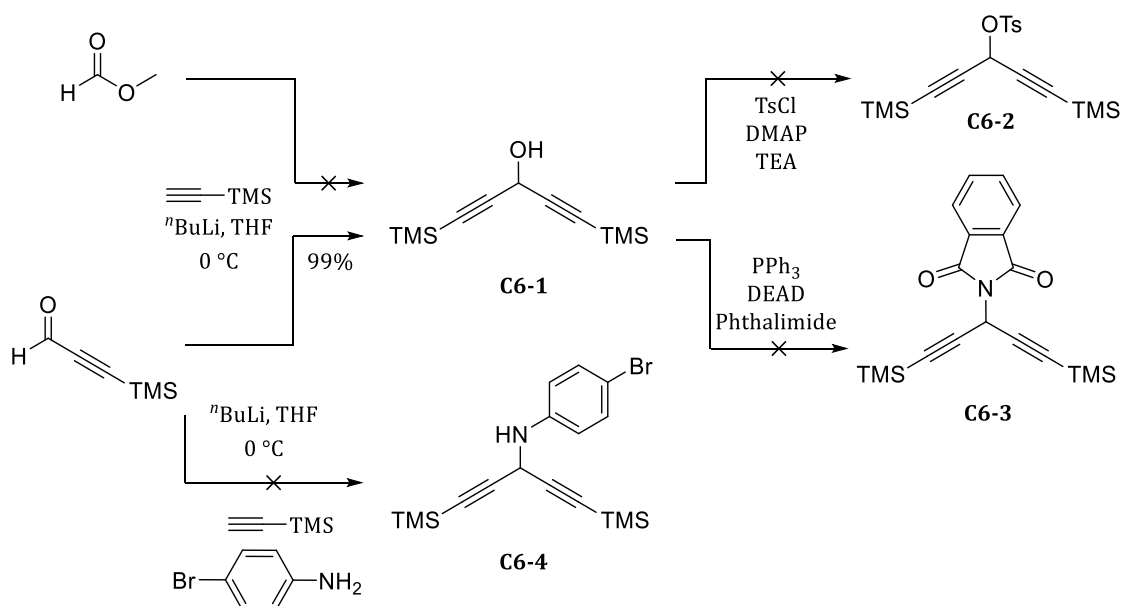
Consequently, **C2** was modified into the corresponding carboxylic acid arylalkyne **C5**. The synthesis followed previous reports^{219,220} and commenced from a Sonogashira reaction between the commercially available methyl 3,5-dibromobenzoate and trimethylsilylacetylene in the presence of Pd₂(dba)₃, PPh₃, CuI in TEA to afford **C5-1** in 68% yield (Scheme 21). The intermediate was then subjected to ester hydrolysis and TMS deprotection in the presence of MeOH and KOH to afford the constraint **C5** in 98% yield.



Scheme 21 - Synthesis of constraint C5 from the commercially available 3,5-dibromobenzoate.

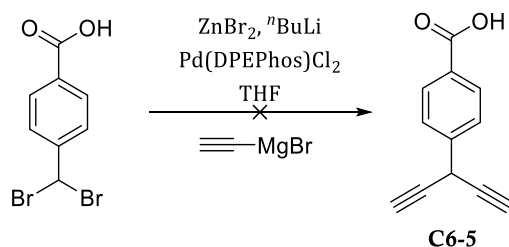
Functionalisation of constraint **C3** presented some difficulties. Initially, it was envisioned that the desired one-carbon atom linker could be accessed from the cheap methyl formate (Scheme 22). It was proposed that the treatment of this ester with TMS-acetylene in the presence of ⁿBuLi could afford **C6-1**. However, the reaction did not proceed as expected, and no desired product could be isolated. It was thus decided to perform the same reaction starting from 3-(trimethylsilyl)propionaldehyde. Pleasingly, the addition onto the aldehyde afforded **C6-1** in quantitative yield. It was envisioned that the hydroxyl group in **C6-1** could be converted into a good leaving group that would then allow for the introduction of a carboxylic acid or an amine. However, attempts to convert **C6-1** into tosyl (**C6-2**) or into a phthalimide *via* aza-Mitsunobu reaction (**C6-3**) failed, probably due to polymerisation as suggested by the formation of black, insoluble products (Scheme 22). A final attempt started from 3-(trimethylsilyl)propionaldehyde and *p*-bromo-aniline followed by addition of TMS-acetylene to obtain **C6-4** (Scheme 22). As observed for **C6-2** and **C6-3** only black and insoluble products were obtained. If this reaction

had been successful, 4-aminobenzoic acid would have been used instead of *p*-bromo-aniline. The latter was used only to test the outcome of the reaction on a simplified substrate.



Scheme 22 - Attempts to synthesise a one-carbon atom linker bearing a functional handle.

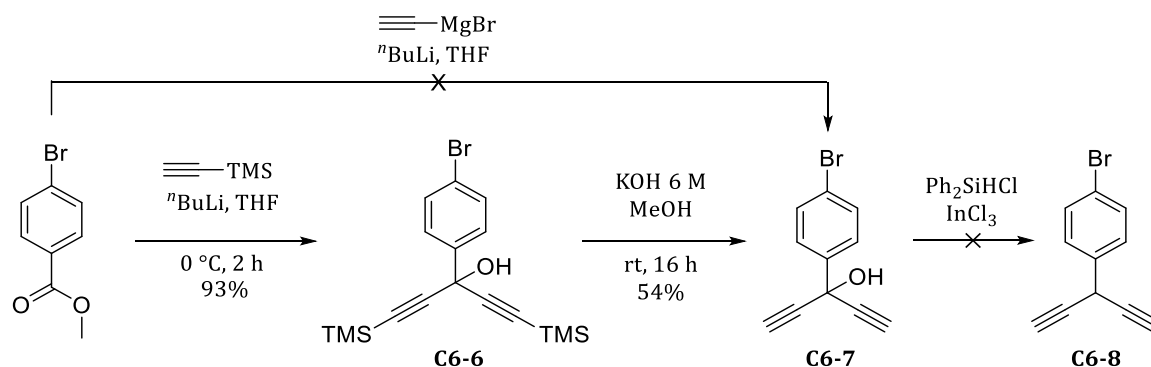
It was proposed to change strategy, and a double Negishi cross-coupling reaction was attempted starting from the commercially available 4-(dibromomethyl)benzoic acid and ethynylmagnesium bromide to obtain linker **C6-5** (Scheme 23). Unfortunately, only unidentified by-products were observed.



Scheme 23 - Double Negishi reaction attempted to synthesise C6-5.

Finally, it was decided to follow an alternative route using a substrate without a functional group that may complicate the synthesis. In particular, it was envisioned to start the synthesis from methyl 4-bromobenzoate (Scheme 24). The starting material was reacted with TMS-acetylene in the presence of *n*-BuLi to afford **C6-6** in 93% yield. The TMS protecting groups on the intermediate were then removed in the presence of KOH and MeOH to afford **C6-7** in 54% yield. An attempt to react methyl 4-bromobenzoate with ethynylmagnesium bromide to obtain **C6-7** in one step failed. It was proposed that the tertiary alcohol in **C6-7** could be removed *via* a deoxygenation reaction. However, only unidentified by-products were detected. This result, in combination with the failures encountered in the previous routes, suggested that the

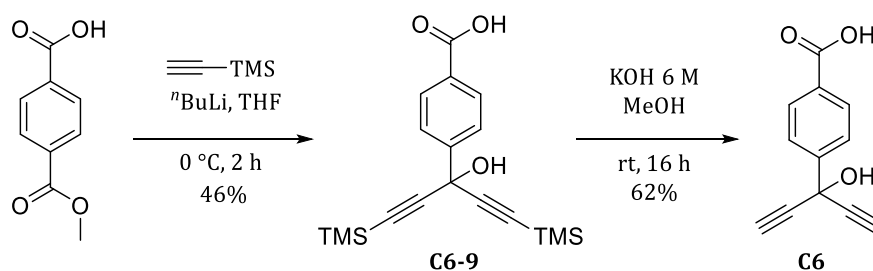
intermediates deriving from the modifications of the tertiary alcohol group were extremely unstable.



Scheme 24 - Synthetic route to access C6-7.

To see whether the steric hindrance of constraint C6-7 would be tolerated in the 2C-CuAAC reaction, C6-7 was reacted with P1. Pleasingly, P1-C6-7 was obtained with 52% conversion. It was decided to repeat the reactions that led to C6-7 with a substrate carrying a carboxylic acid that could be used as a functional handle.

The synthetic route proceeded from the commercially available 4-(methoxycarbonyl)benzoic acid that underwent a double TMS-acetylene addition onto the ester to afford C6-9 in 46% yield (Scheme 25). The yield for this reaction was considerably lower than the analogue that led to C6-6 (93%) potentially due to the different electronics of the aromatic rings. The TMS protecting groups of C6-9 was removed in the presence of KOH and MeOH to yield C6 in 62% yield.



Scheme 25 - Synthetic route leading to C6.

Constraints C5 and C6 were used in the 2C-CuAAC peptide macrocyclisation in the presence of P1 to afford P1-C5 and P1-C6 with 92% and 85% conversion respectively.

The affinity of the newly synthesised peptides for CK2 α was measured using an ITC assay. ITC provides a more accurate measurement of the binding affinity than FP as it measures the direct binding to the protein of interest. However, ITC is not high-throughput and, consequently, was not used for the lower affinity peptides. P1-C5 and P1-C6 were soluble in the assay conditions and showed a K_d for CK2 α of 460 nM and 58 μ M respectively. Whilst P1-C6 showed a decreased

affinity for the protein compared to the reference Pc peptide (K_d 1 μ M), **P1-C5** showed higher affinity than Pc (Figure 38).

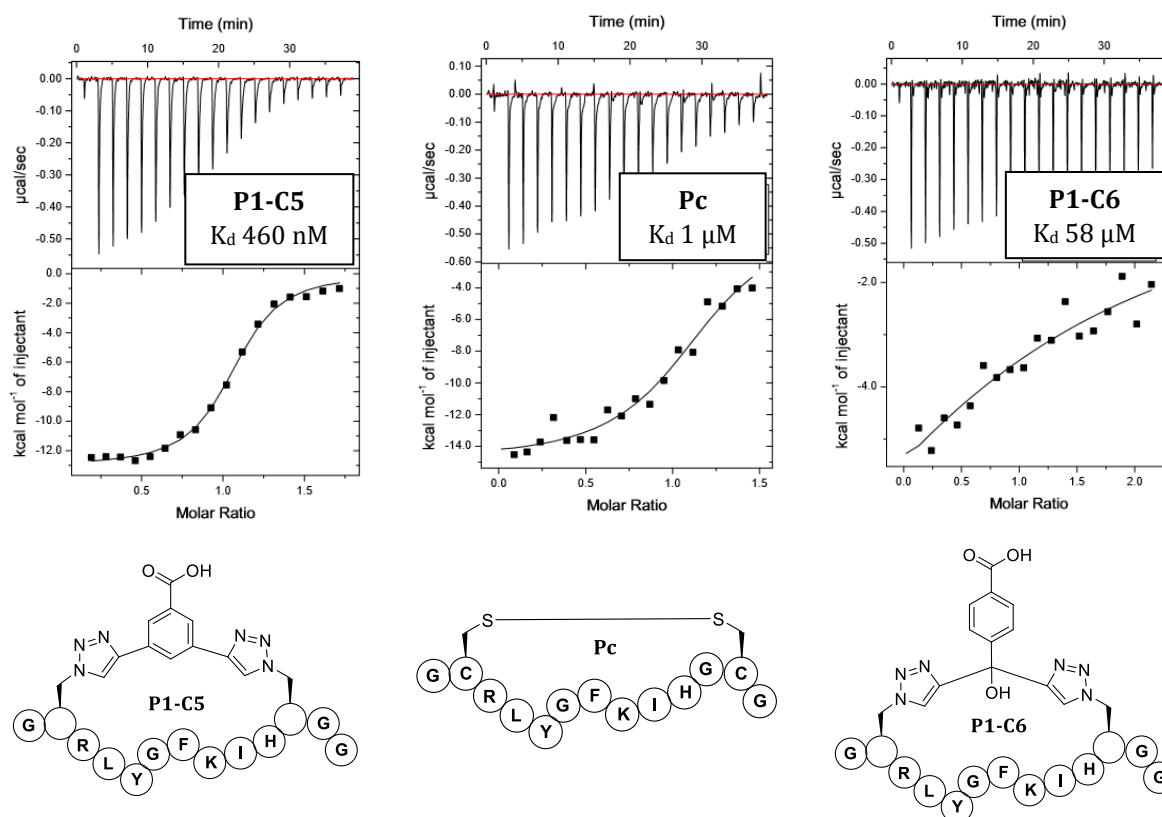


Figure 38 - ITC binding curves of **P1-C5**, **P1-C6**, and **Pc** binding to **CK2 α** . The peptides shown feature an acetyl capping at the N-terminus and an amide at the C-terminus.

With this promising result in hand, the ability of **P1-C5** to disrupt the interaction between the α and the β subunits of CK2 was investigated using an ITC competition assay. The affinity of the CK2 β domain for the α was measured using a direct ITC assay and was found to be 9 nM (literature value 4 nM).²¹⁵ The binding was then investigated in the presence of the peptide at 100 μ M concentration.^v Pleasingly, no binding of CK2 β to α was detected under these conditions.

Therefore, constraint **C5** proved to be the most effective at constraining the peptide in its binding conformation, and the resulting cyclic peptide **P1-C5** was able to disrupt the PPI of CK2.

4.4.3. Attempts to develop Conformationally-Constrained Hybrid Peptides (CCHPs)

Chapter 3 described the FBDD approach used in the Spring group to develop CK2 inhibitors binding in the cryptic α D pocket and at α/β interface. Fragment optimisation of the molecules binding at the interface did not result in significant improvement of the binding affinity

^v Concentration in the ITC titrant and ITC syringe.

compared to the initial hit fragment **NMR154L**, except for **3g**. Considering that the initial hit fragment overlaps with the Phe7 hotspot residue of the CK2 α (Figure 39a), it was decided to merge fragment **NMR154L** with peptide **P1-C5** (CCHPs) with the aim of increasing the binding affinity of the overall peptides and impart selectivity to the fragments. Fragments of bigger size, such as the more active **3g**, were not considered at this stage as their introduction could lead to clashes with other residues within the peptide.

4.4.3.1. Chloro-phenylalanine containing peptides: **P2'-C5**, **P2''-C5**, **P3-C5**

Molecular modelling to design the CCHPs was performed using the X-ray structure of Pc (PDB: 4IB5)²¹⁵ and **NMR154L** (PDB: 5CLP)¹⁹⁸ due to the absence of X-ray crystal structures for the newly developed **P1-C5** peptide (Figure 39). Chlorobenzene probes in ligand-mapping simulations indicated that a chlorine atom in the 3 position of Phe7 residue (peptide **P2-C5**) could be introduced without compromising the binding affinity of the peptide (ΔH -58.07 ± 2.92 Kcal \cdot mol $^{-1}$ for **P2-C5** vs -57.1 ± 2.4 Kcal \cdot mol $^{-1}$ for **P1-C5**). The introduction of a chlorine atom in the 4 position of Phe7 was also proposed (**P3-C5**) as the newly inserted atom should not affect the binding affinity significantly (ΔH -55.6 ± 2.2 Kcal \cdot mol $^{-1}$).

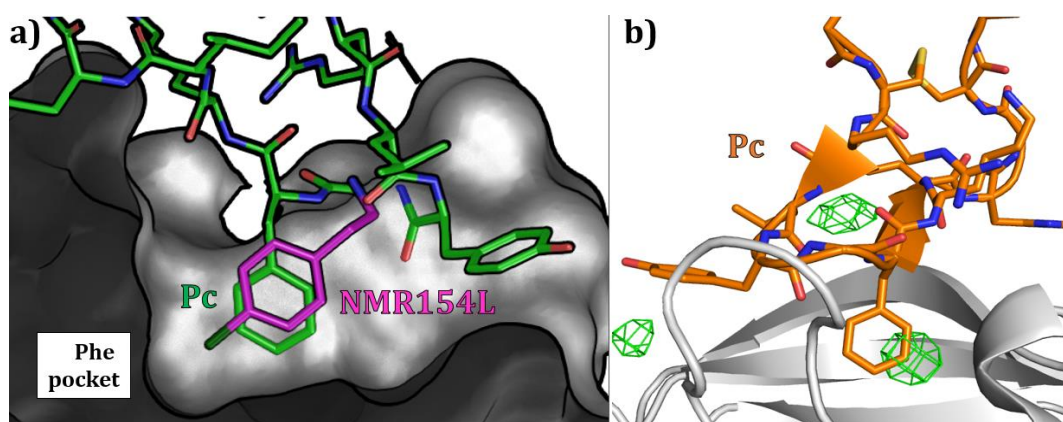
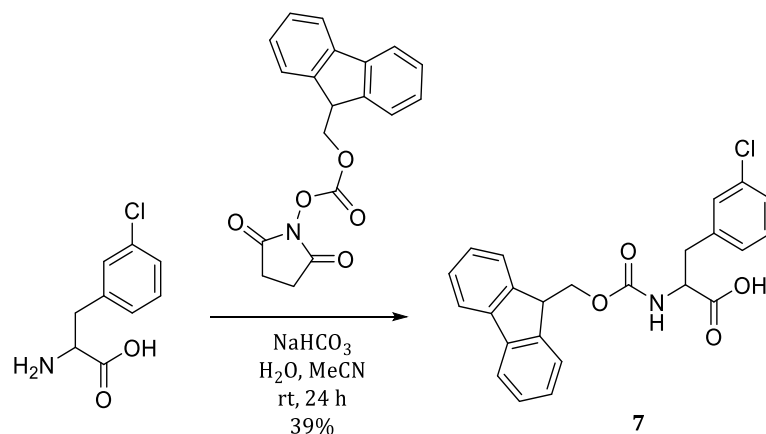


Figure 39 – Structure-based design of CCHPs. a) Overlay of the X-ray structures of **NMR154L** (purple, PDB code: 5CLP)¹⁹⁸ and Pc peptide (green, PDB: 4IB5)²¹⁵ binding at the CK2 interface. b) Chlorobenzene probe used in MD shows the chlorine occupying a region (green mesh) corresponding to the 3-position of the Phe7 of Pc (orange).

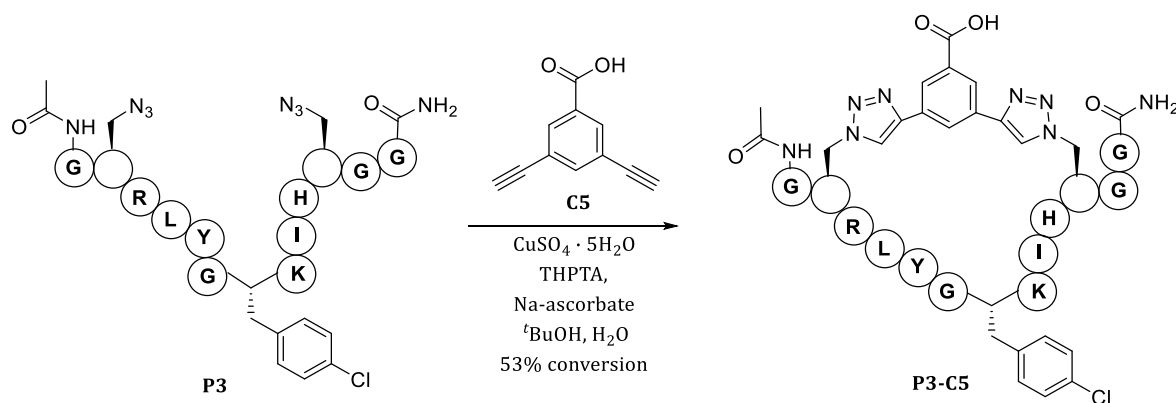
The Fmoc-3-chloro-Phe-OH amino acid (**7**) required for the synthesis of **P2-C5** was synthesised from the racemic, unprotected amino acid 3-chloro phenylalanine for availability reasons. The free amine was protected using N-(9-fluorenylmethoxycarbonyloxy)succinimide and NaHCO₃ (Scheme 26).



Scheme 26 - Synthesis of the amino acid 7.

As expected, incorporation of **7** in the peptide afforded two diastereomers **P2'** and **P2''** which were separated by preparative HPLC and cyclised with **C5** to afford **P2'-C5** and **P2''-C5** respectively. It was envisioned that X-ray crystallography of the peptides in complex with the protein would elucidate the stereochemistry.

The synthesis of **P3** required the amino acid L-Fmoc-4-chloro-Phe-OH that was commercially available. Cyclisation of linear peptide **P3** with **C5** afforded **P3-C5** in 53% conversion (Scheme 27).



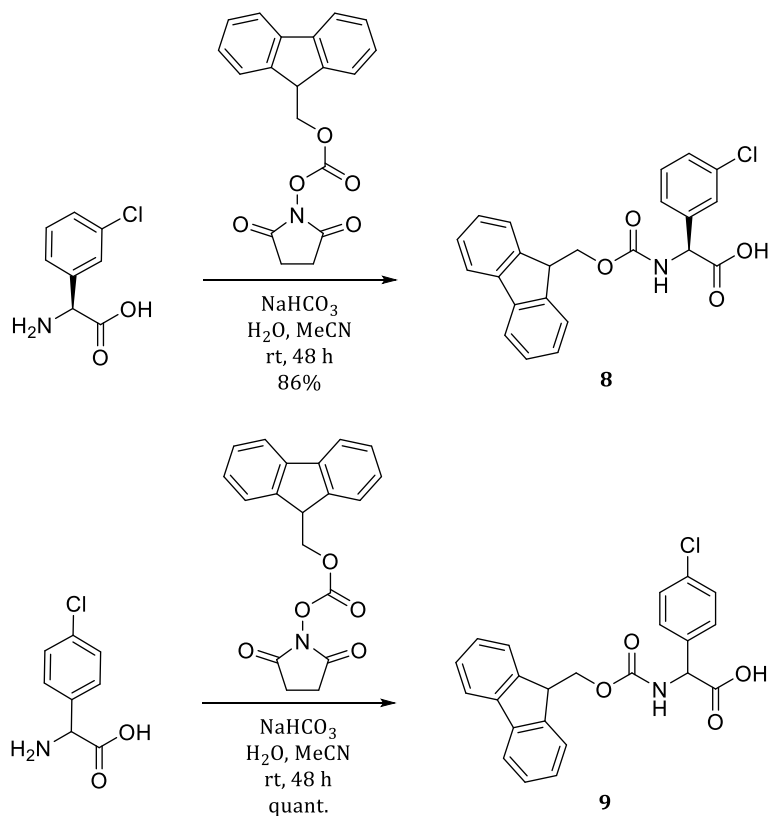
Scheme 27 - CuAAC PS of **P3** with **C5** to afford **P3-C5**.

ITC was performed to measure the binding affinities of **P2'-C5**, **P2''-C5** and **P3-C5** for CK2 α . Unfortunately, none of the CCHPs showed improved binding affinity compared to **P1-C5** (K_d of 460 nM): peptide **P2'-C5** was found to have a K_d of 2 μ M, **P2''-C5** did not show binding to the protein at a concentration below 125 μ M whilst **P3-C5** was found to have a K_d of 56 μ M.

4.4.3.2. Chloro-phenylglycine containing peptides: P4-C5, P5'-C5, P5''-C5

Considering the lack of structural information available for the first set of CCHPs, it was hypothesised that the chloro-Phe residues in the peptides might bind deeper than expected making the interactions of the peptide with CK2 α less optimal. Consequently, it was decided to shorten the Phe side chain of the amino acid residue by one carbon atom, introducing chloro-phenylglycine derivatives as the Phe7 replacements.

As for **P2-C5**, the synthesis of the peptides containing 3-chloro-phenylglycine (contained in peptide **P4**) and 4-chloro-phenylglycine (included in peptide **P5**) required the protection of the commercially available corresponding amines to Fmoc-protected amino acids **8** and **9** respectively. The 3-chloro-phenylglycine was provided enantiopure whereas the 4-chloro analogue was available as a racemic mixture. For both amino acids, Fmoc protection was performed using *N*-(9-fluorenylmethoxycarbonyloxy)succinimide and NaHCO₃ (Scheme 28). Fmoc protection of 3-chloro-phenylglycine afforded **8** in 86% yield, and **9** was obtained from 4-chloro-phenylglycine quantitatively.



Scheme 28 - Fmoc protection of 3- and 4- chloro-phenylglycine amino acids **8** and **9**.

The linear peptides **P4**, **P5'** and **P5''** were clicked with **C5** to obtain the corresponding cyclic peptides **P4-C5** (60% conversion), **P5'-C5** (53% conversion) and **P5''-C5** (47% conversion).

Unfortunately, all the chloro-phenylglycine containing peptides showed no detectable binding to CK2 α on ITC. The lack of structural information at that stage made it impossible to build any SAR. If X-ray structures of the hybrid peptides bound to CK2 α can be obtained, the design of further CCHPs could be adjusted.

4.4.4. X-ray crystal structures of the constrained peptides

Due to the crucial importance of structural information to guide the design further, priority was given to X-ray crystallography.

After several attempts of soaking and co-crystallisation with different commercially available and custom-made screens, as well as different constructs of the protein, we were pleased to find conditions that yielded crystals of **P1-C5** bound to CK2 α .^w The X-ray structure showed **P1-C5** binding in a conformation that resembles the portions of CK2 β and Pc binding to CK2 α with the hotspot residues occupying their respective pockets (Figure 40a-b). The backbone residues of **P1-C5** are all slightly shifted compared to Pc especially closer to the constraint. This difference can be explained considering that **C5** is larger and more rigid than the disulfide bridge in Pc and therefore, it holds the two ends of the peptide further apart (12.6 Å vs 9.8 Å, Figure 40c-d).

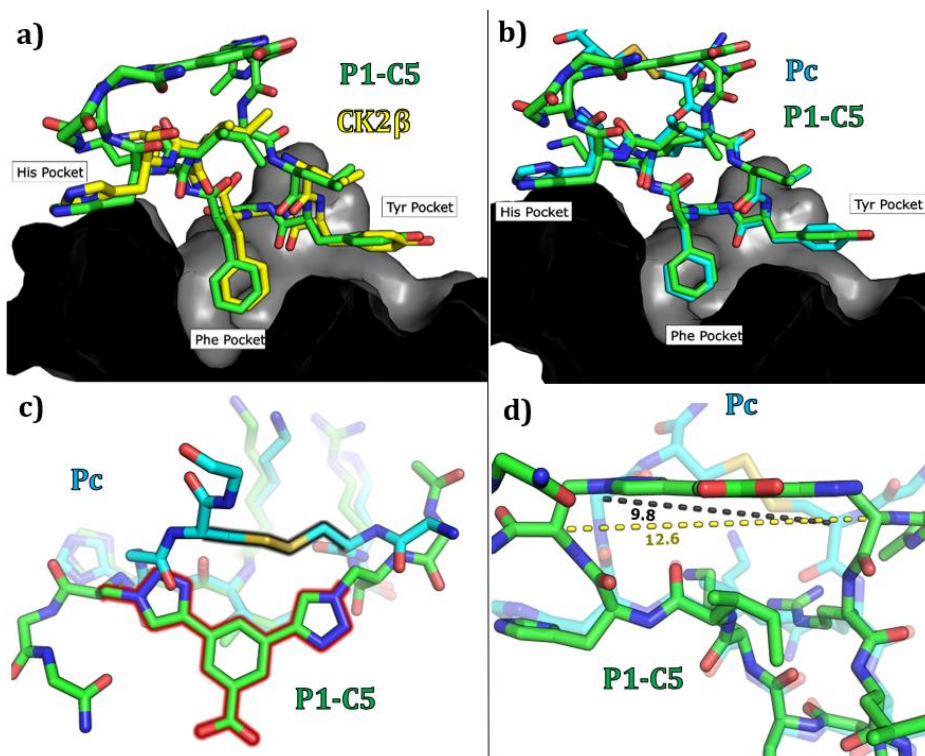


Figure 40 - X-ray crystal structure of **P1-C5** (PDB: 6Q38). a) Overlay of **P1-C5** (green) and CK2 β (yellow). b) Overlay of **P1-C5** (green) and Pc (PDB: 4IB5,²¹⁵ cyan). c) Comparison of binding modes of **P1-C5** (green) and Pc (cyan). d) Differences between the triazole constraint and the disulfide bridge.

^w Details of the crystallisation attempts can be found in the Appendix A.5.

Using similar conditions as for **P1-C5** and matrix seeding from the co-crystals grown of the peptide, **P2'-C5** was crystallised with CK2 α . The X-ray structure showed that **P2'-C5** contained the *L*-enantiomer of the 3-chloro-phenylalanine residue **7** (Figure 41a) and that the modified Phe7 did not overlay with the fragments that the modifications and MDs were based upon. Indeed, the binding mode of **P2'-C5** forces the 3-Cl Phe to sit deeper in the pocket than the fragment which potentially leads to a clash with Tyr5 and accounts for the reduction in affinity. The structure shows that whilst chlorine in the 3-position could partially be accommodated in the Phe pocket (**P2'-C5** K_d 2 μ M), a chloro atom in the 4-position would disrupt the binding of the peptide as confirmed by the ITC experiments (**P3-C5** K_d 56 μ M). Even though the CCHP strategy did not result in an improvement in binding affinity of the peptides, the X-ray crystal structure of **P2'-C5** with CK2 α revealed the protein in complex with a peptide substrate (Figure 41b).^x

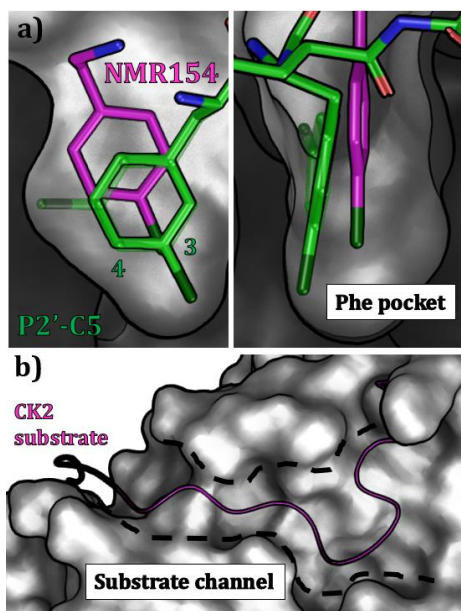


Figure 41 - X-ray crystal structure of **P2'-C5**. a) Overlay of **NMR154L** (purple) and **P2'-C5** (green) showing how the 3-chlorophenylalanine residue in **P2'-C5** binds deeper than **NMR154L** resulting in no space to accommodate a chlorine in the 4-position. b) CK2 substrate (purple) occupying the substrate channel (highlighted by black dashed lines).

This unprecedented result is of crucial importance to the CK2 kinase community as the structural information obtained opens opportunities to develop a novel class of substrate-competitive CK2 inhibitors and will help to elucidate the phosphorylation mechanism of the protein.

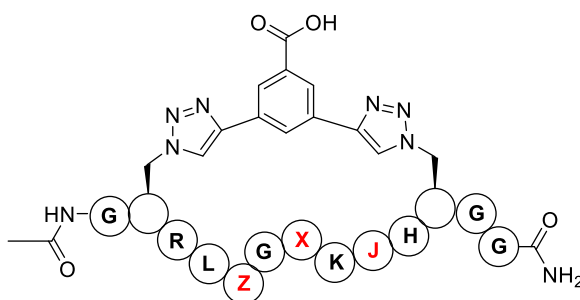
^x Peptide substrate mimicked by the N-terminal extension of CK2 α (GSMDFEFDDDDDDGSGSGSGSGS) in the protein construct used CK2 α _FP10.

4.4.5. Further sequence modification: P6-C5, P7-C5, and P8-C5

Molecular modelling and rational design based on the available crystal structures of **P1-C5** and **P2'-C5**, suggested that further modification of the sequence may result in enhancement of the binding affinity of the peptides.

The first variation of interest involves the substitution of Tyr5 residue (Table 14). This residue is located on the portion of the peptide that forms the β -turn in Pc, and it makes hydrophobic interactions with the so-called Tyr pocket. Therefore, it was decided to vary the Tyr5 to Pro, a residue known to help β -turn formation²²¹ that could make the overall peptide more rigid, reducing the entropic penalty upon binding. With this in mind, peptide **P6** was synthesised and constrained into the cyclic peptide **P6-C5** with 88% conversion.

Table 14 – Sequences modification of peptides P6-, P7-, P8-C5 respect to P1-C5.



Peptide	Sequence modification
P1-C5	Z = Y; X = F; J = I
P6-C5	Z = P; X = F; J = I
P7-C5	Z = Y; X = F; J = W
P8-C5	Z = Y; X = W; J = I

The second sequence modification concerned the Ile9 residue (Table 14). The X-ray crystal structure of **P1-C5** (Figure 42a) shows that the Ile9 could be replaced by an amino acid capable of π - π stacking with the aromatic ring of **C5**. Likewise, chlorobenzene probes in ligand-mapping simulations indicated an unfilled hydrophobic region around Ile9 (Figure 42b) suggesting that a larger, nonpolar side chain could be introduced (ΔH -59.7 ± 1.2 Kcal·mol⁻¹ for **P7-C5** compared to -57.0 ± 2.1 Kcal·mol⁻¹ for **P1-C5**, as calculated from MD simulations).

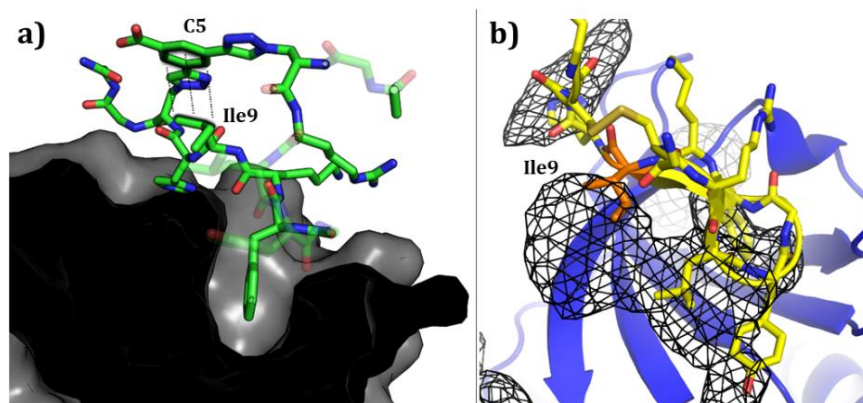


Figure 42 – Peptide design guided by the X-ray structure of **P1-C5** bound to CK2 α . a) X-ray structure of **P1-C5** showing Ile9 oriented in the right direction to stack with the constraint **C5**. b) Chlorobenzene mapping on Pc showing a high occupancy region by the aromatic carbon atoms of the probe around Ile9. Areas shown as black mesh represent regions around the CK2 α protein (blue) occupied by the hydrophobic chlorobenzene probe during the MD simulation. Peptide **P1-C5** is shown in yellow to show which residues of the peptide correspond to the regions occupied by the probe during the MD. Ile9 of **P1-C5**, which is mutated to Trp in **P7-C5**, is shown in orange.

The sequence of **P1** was modified to **P7** to accommodate the largest aromatic residue Trp. Automated MW-assisted SPPS of **P7** using standard Fmoc protected amino acids led to on-resin aggregation after the attachment of the first five amino acids as suggested by poor Fmoc deprotection of the amino acids.^y On-resin aggregation was successfully prevented by replacing standard Fmoc-Gly-OH with backbone protected Fmoc-(Dmb)Gly-OH residues at the 2- and 8-position of the peptide.²²² The resulting peptide **P7** was macrocyclised with **C5** as the linker to afford **P7-C5** (83% conversion).

Finally, the last modification was performed to generate a peptide that could be used as negative control in the functional and cellular assays. Such peptide (**P8**) featured a Trp residue as replacement of the Phe7 (Table 14). The Trp was chosen as it is the biggest natural amino acid and therefore should not be able to fit in the Phe pocket.

Disappointedly, peptide **P6-C5** (Y5P) showed no binding to CK2 α as measured by ITC. On the other hand, **P7-C5** (I9W) appeared to be the highest affinity peptide developed thus far with a K_d of 150 nM. In favour of the hypothesis that a suitable constraint may enhance the binding of the peptide significantly, the constrained peptide showed a 300-fold improvement compared to the linear variant (K_d 44 μ M, Figure 43). As for **P1-C5**, the ability of the peptide to prevent CK2 β binding to CK2 α was investigated using an ITC competition assay. No binding of the regulatory β subunit to the catalytic subunit was observed in the presence of 100 μ M of the peptide.^z

^y Fmoc deprotection in automated MW-assisted SPPS is monitored by UV absorbance of the dibenzofulvene (DBF) intermediate formed during DIPEA-mediated Fmoc removal.²⁸⁹

^z Peptide concentration in the ITC titrant and syringe.

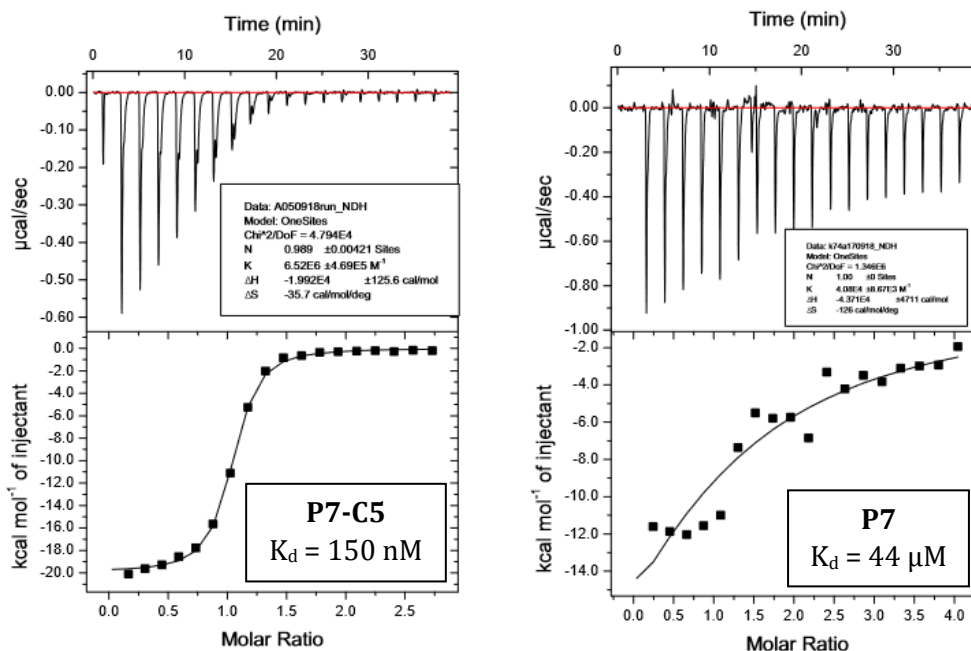


Figure 43 - ITC binding curves of P7-C5 and P7 binding to CK2α.

X-ray crystal structure of **P7-C5** allowed rationalisation of the improved binding affinity of the peptide compared to **P1-C5**. The structure shows the introduced Trp residue π - π stacking with the benzene ring of the constraint. No other additional interactions with CK2α were observed. Therefore, the increased binding affinity of **P7-C5** for CK2 may be rationalised with a reduced entropic penalty upon binding due to the rigidifying interaction occurring between the constraint and the Trp residue (Figure 44).

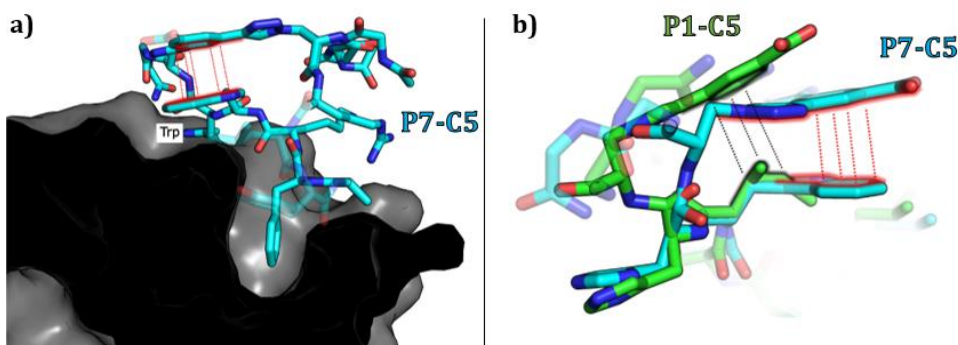


Figure 44 – Comparison of **P1-C5** and **P7-C5** bound to CK2α. a) X-ray crystal structure of **P7-C5** bound to CK2α (PDB: 6Q4Q). b) A comparison of the stacking with C5 in **P1-C5** (green) and **P7-C5** (green).

As expected, no binding of the negative peptide **P8-C5** was detected in the ITC direct binding assay.

The effect of PPI inhibition on substrate phosphorylation was also studied using CK2β dependent and independent substrates. It was shown that **P7-C5** was able to inhibit the

phosphorylation of a β -dependent substrate^{aa} with an IC_{50} of 206 ± 29 nM. Pleasingly, the negative peptide **P8-C5** did not cause inhibition of the phosphorylation of the β -dependent substrate (Figure 45). The peptide did not affect the phosphorylation of a β -independent substrate peptide (RRRADDSDDDD) suggesting that the binding of the peptide at the interface site does not displace the ATP.

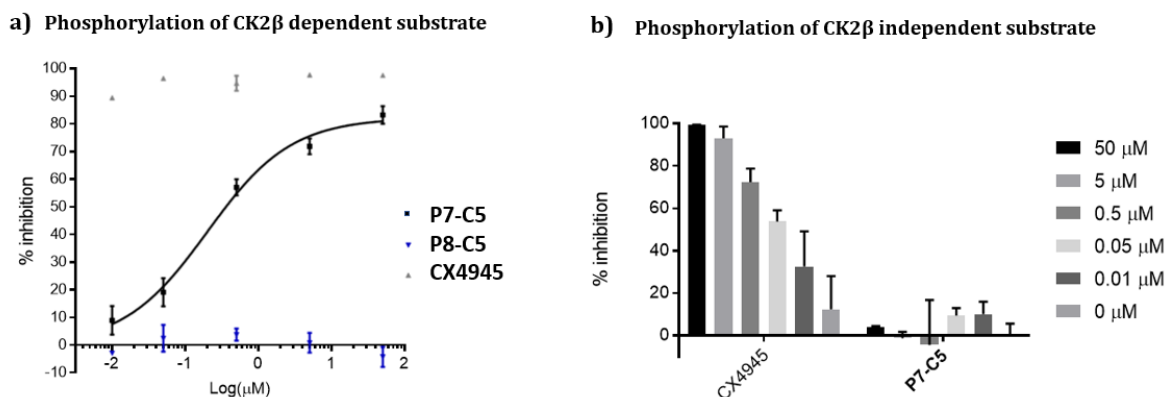


Figure 45 - Inhibition of phosphorylation of a β -dependent substrate (a) and a β -independent substrate (b). CX4945 was used as positive control for its documented ability to inhibit the catalytic activity of CK2 α .

4.4.6. Multi-functionalisation of the constraint C5

Preliminary confocal microscopy experiments carried out with FITC-labelled peptide **P1-C5** (FITC-P1-C5)^{bb} showed that the peptide was not able to permeate the membrane of human colorectal cancer cells (HCT116). Z-stacks of fixed cells showed no green emission (corresponding to the FITC signal) whilst only the blue signal corresponding to the nuclei stain was observed (Figure 46).

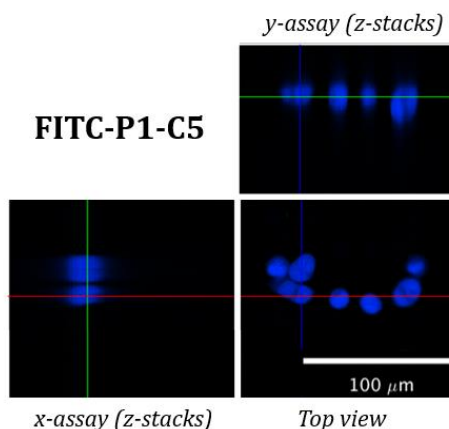


Figure 46 - Cellular uptake of the cell impermeable FITC-P1-C5 using HCT116 cells. Composite of z-stacks obtained on confocal microscopy using a 20X objective showed that no FITC-labelled peptide is internalised by the cells. Nuclei are stained in blue.

^{aa} β -dependent substrates rely on the CK2 β subunit to be bound to CK2 α to be phosphorylated. Whilst CK2 β does not phosphorylate the substrate itself, it acts as a docking station, and it is therefore crucial for substrate recognition. The CK2 β -dependent substrate used in this work is the transcription factor eIF2 β .

^{bb} Sequence FITC-Ahx-P1 cyclised with C5 to obtain FITC-Ahx-P1-C5 in 56% conversion.

Therefore, since both cell-penetrating motifs and fluorescent tags were necessary for the cellular assays, it was decided to develop a novel multi-functional constraint that would simultaneously constrain the peptide in its binding conformation, enhance stability to proteases, provide cell-permeability to the CK2 peptide and act as a fluorophore (Figure 47).

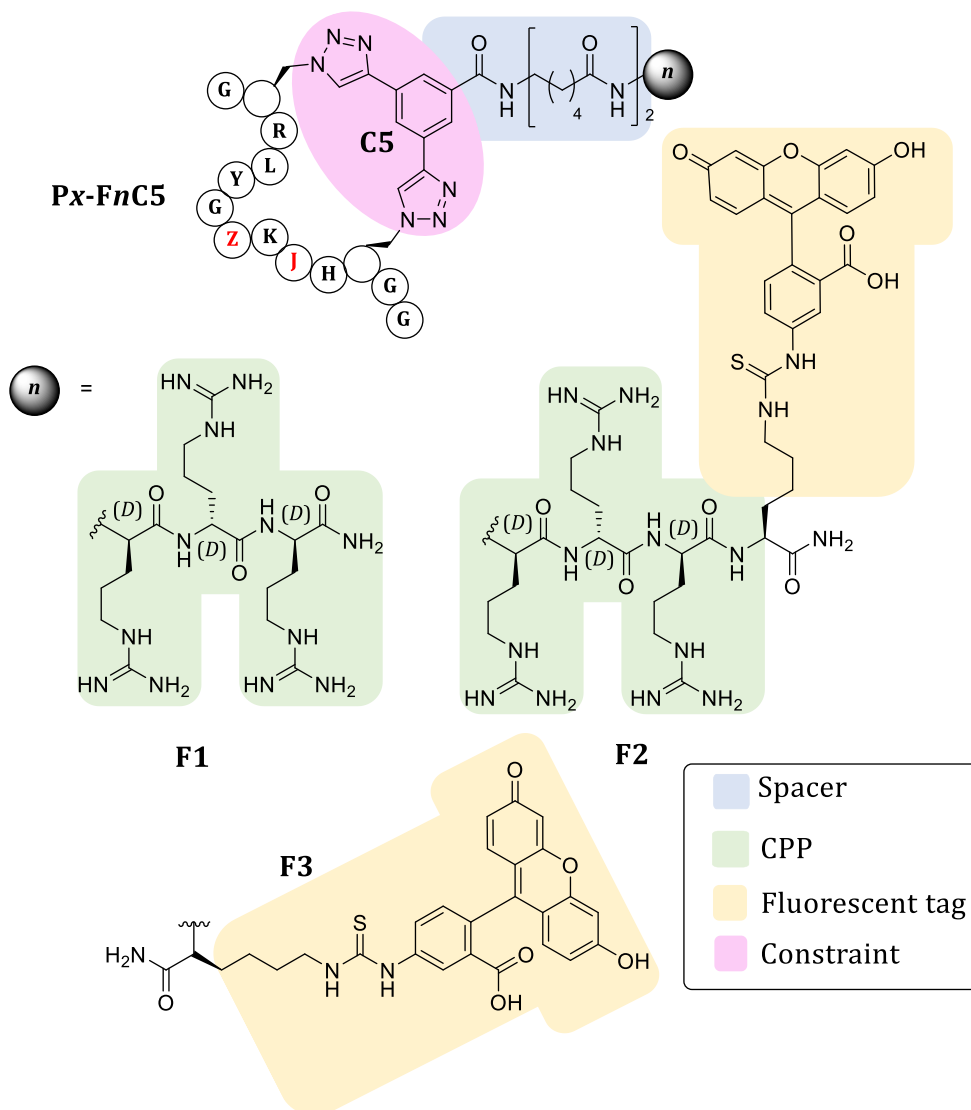


Figure 47 - Structures of multi-functional constraints developed in this work. Different functionalities are color-coded as shown in the figure legend. **P1**: Z = F, J = I; **P7**: Z = F, J = W; **P8**: Z = W, J = I.

In addition, it was proposed that the functionalised constraints could be entirely synthesised in an automated manner using SPPS and independently from the CK2 peptide. The benzoic acid derivative linker was attached on-resin to a cell-penetrating peptide (CPP) *via* two molecules of aminohexanoic acid to avoid steric clashes with the CK2 peptide and the CK2 α domain. Several reports make use of a poly-arginine tripeptide as a useful CPP to carry peptide cargos into cells.^{81,193} The previously used *L*-arginine was replaced with the *D*-arginine isomer to confer cell-permeability to the CK2 peptide and provide a proteolysis resistant alternative (**F1C5**,

Figure 47). The CPP was in turn attached to the fluorescent tag FITC via an orthogonally-protected Lys – namely Lys(ddve)- to monitor peptide uptake into the cells (**F2C5**). FITC was also directly attached to the spacer via the Lys to provide a cell-impermeable fluorescent tag (**F3C5**) to use as a negative control. The functionalised linkers were then reacted with the linear peptides to obtain highly functionalised peptides and study their biological activity in cells was subsequently studied.

The ability of the functionalised constraint to improve the overall stability of the peptide to proteases was investigated using human serum. Importantly, the cell-permeable lead peptide (**P7-F1C5**) displayed significant stability in human serum (47% intact peptide after 24-hour incubation, Figure 48) whilst the linear analogue **P7** was degraded entirely after 8-hour incubation.

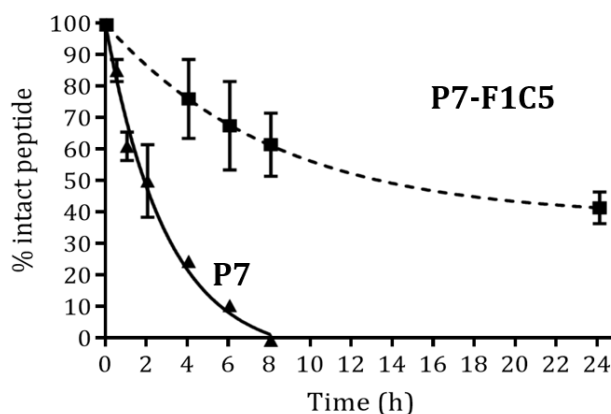


Figure 48 - Serum stability test of **P7** (black line) and **P7-F1C5** (dashed-black line) in the presence of 20% serum. The results shown are the average of two-independent repeats.

4.4.7. Cellular work on **P7-C5** derivatives

The ultimate goal of this project was to investigate the activity of the peptide in cancer cells. Therefore, further cellular experiments were carried out using two cell-lines: HCT116 and U2OS. The HCT116 cell line was chosen to study the activity of the peptides in cells due to its documented high expression levels of CK2.¹³⁹ U2OS, on the other hand, was chosen to perform intracellular localisation experiments due to its great cytosol/nucleus ratio.

4.4.7.1. Intracellular localisation experiments

The ability of the functionalised constraint **F2C5** to impart cell-permeability to the peptide was initially investigated using the FITC-labelled peptide **P1-C5** which was previously found to be cell-impermeable in preliminary experiments (Figure 46). To this end, **P1** was constrained with the FITC-labelled penetrating constraint **F2C5** and with the FITC-labelled impermeable constraint **F3C5** (Figure 49).

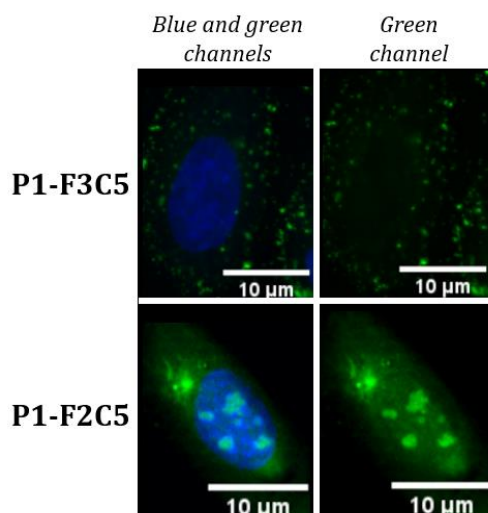


Figure 49 - Cellular uptake of **P1-F3C5** and **P1-F2C3** using osteosarcoma cancer cells (U2OS). Fixed cells were imaged using a 40 X objective. Peptides are shown in green, nuclei in blue.

The results showed that **F2C5** was effective at transporting peptide **P1** into cells whilst **F3C5** was not. Consequently, **F2C5** was used to constrain the lead peptide **P7** and investigate its intracellular localisation. Confocal microscopy of U2OS osteosarcoma cancer cells treated with **P7-F2C5** showed the peptide localising to the cell nucleus and also accumulating in proximity to the nuclear membrane at different time points (5 minutes to 6 hours) as shown in **Figure 50**. Thus, further studies were undertaken to elucidate the exact intracellular localisation of the peptide.

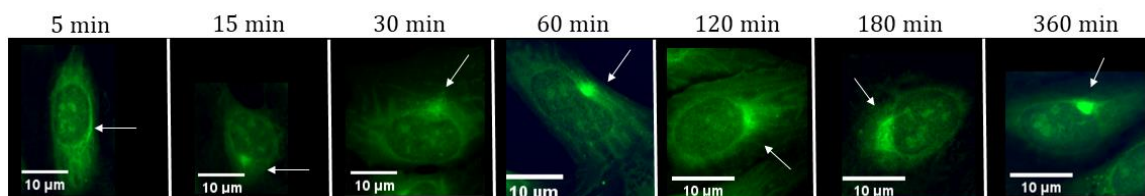


Figure 50 - Uptake of **P7-F2C5** by U2OS cells. Cells were incubated with 1.25 μM^{cc} of the peptide at 37 °C for the designated time point and then fixed using 4% PFA. Images were recorded on a confocal microscope using 40 X magnification.

There are several reports of positively charged peptides being unable to escape the endosomes and ending up in the lysosomes,²²³ and therefore, imaging experiments were carried out to look at co-localisation with endosomal and lysosomal markers. Surprisingly, no co-localisation with endosomal markers was detected at any time-point (first and second row, **Figure 51**). On the other hand, partial co-localisation was detected with the lysosome stain (third row, **Figure 51**).

^{cc} 1.25 μM concentration was chosen for its optimal signal/background ratio compared to the other concentrations screened (between 20 μM and 0.2 μM).

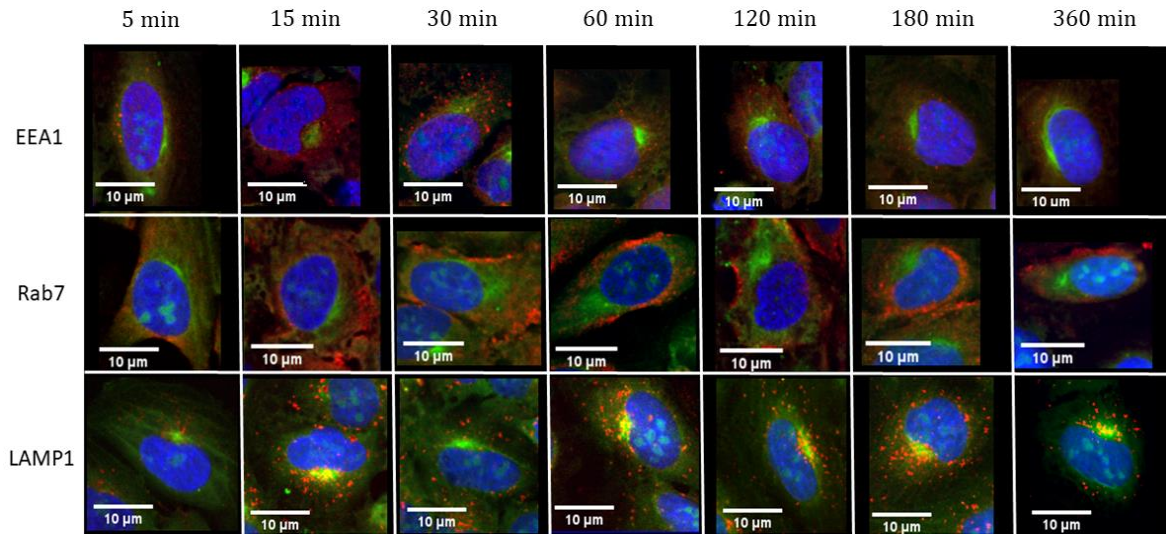


Figure 51 - Co-localisation experiments of P7-F2C5 with trafficking antibodies: EEA1 marker for early endosomes, Rab7 marker for late endosomes, LAMP1 marker for lysosomes. Nuclei are stained in blue, antibodies in red and peptide in green.

Despite partial co-localisation of the peptide with the lysosome stain, there was still a significant portion of the FITC signal that did not co-localise with any of the markers used thus far. It was decided to look at the co-localisation with Trans and Cis Golgi stains and markers for the endoplasmic reticulum (ER). These organelles are in proximity to the nuclear membranes and are involved with the trafficking of vesicles going in and out the lysosomes. It was envisioned that the peptide might co-localise with some of these organelles. Whilst minimal co-localisation was observed with the trans-Golgi (TNG46) at the early time-points, the peptide was found to co-localise with Cis-Golgi (ZFLP1) and ER markers (Calnexin) as shown in Figure 52.

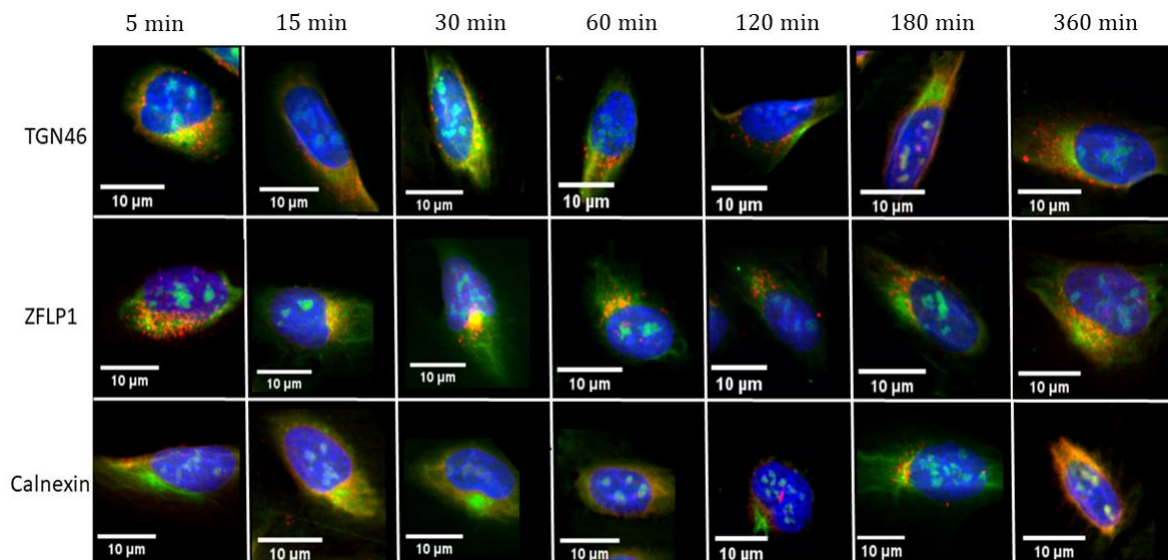


Figure 52 - Co-localisation experiment of P7-F2C5 with Golgi and ER antibodies: TGN46 marker for trans Golgi, ZFLP1 marker for Cis Golgi, Calnexin marker for ER. Nuclei are stained in blue, antibodies in red and peptide in green.

This is an unexpected and unprecedented result that would need further investigation to understand ways of preventing the peptide from becoming trapped in the Golgi and ER. Despite this event, the peptide was detected in the nuclei at all time points. CK2 is a protein that shuttles between the cytosol and the nucleus; therefore, we proposed that the peptide present in the nucleus would be able to interact with CK2 and exert its bioactivity.

4.4.7.2. Anti-proliferative activity on colorectal cancer cells treated with P7-F1C5

Disruption of the PPI of CK2 has been reported to arrest cell cycle progression, induce apoptosis and slow cell proliferation in a variety of cell lines including human colorectal cancer cells (HCT116).¹⁴⁴ To this end, the bioactivity of **P7-F1C5** in HCT116 was investigated.

The effect of the peptide on cell proliferation was studied in two ways: (1) monitoring the rate of growth of the cells in the presence of increasing concentration of the peptide over 4 days; (2) using a Sytox Green™ assay to quantify the cells after 4-day incubation with the peptides. In the first case, the cells were treated with the peptide, and their rate of growth monitored at 37 °C. Scans of the cell confluency were recorded every 2 hours to give a percentage of the cell confluency at each scan (Figure 53).

The scans showed that **P7-F1C5** slows down the proliferation of the cells at a concentration of 32 µM with 80% inhibition at 100 µM. For this experiment, two types of controls were used: CX4945 (positive control), **P7-C5** (cell impermeable constrained peptide) and the functionalised cell-penetrating constraint **F1C5** (cell-penetrating constraint without the peptide). CX4945 is a clinical candidate CK2α inhibitor inhibiting CK2 in an ATP-competitive manner.¹³⁹ It is known to inhibit proliferation in HCT116 cells, and it was therefore used as positive control. Due to the mechanistic differences between CX4945 and **P7-F1C5** a difference in the outcome of the assay was expected; whilst inhibition of the CK2α catalytic subunit is known to cause drastic effects in cells, inhibition of the holoenzyme assembly has been reported to have less severe consequences due to the fact that the activity of the catalytic α subunit is not affected.¹⁶⁴ In addition, CX4945 is known to inhibit other kinases, and therefore, its more pronounced cytotoxic activity could be attributed to off-target effects.¹⁹⁸ The constraint **F1C5** was used as negative control to ensure that the positive charges on it would not cause any unspecific cytotoxicity while **P7-C5** was used as negative control considering its limited cell-permeability.

CHAPTER 4: Conformationally-constrained peptides targeting the protein-protein interaction of the anti-apoptotic proteins CK2

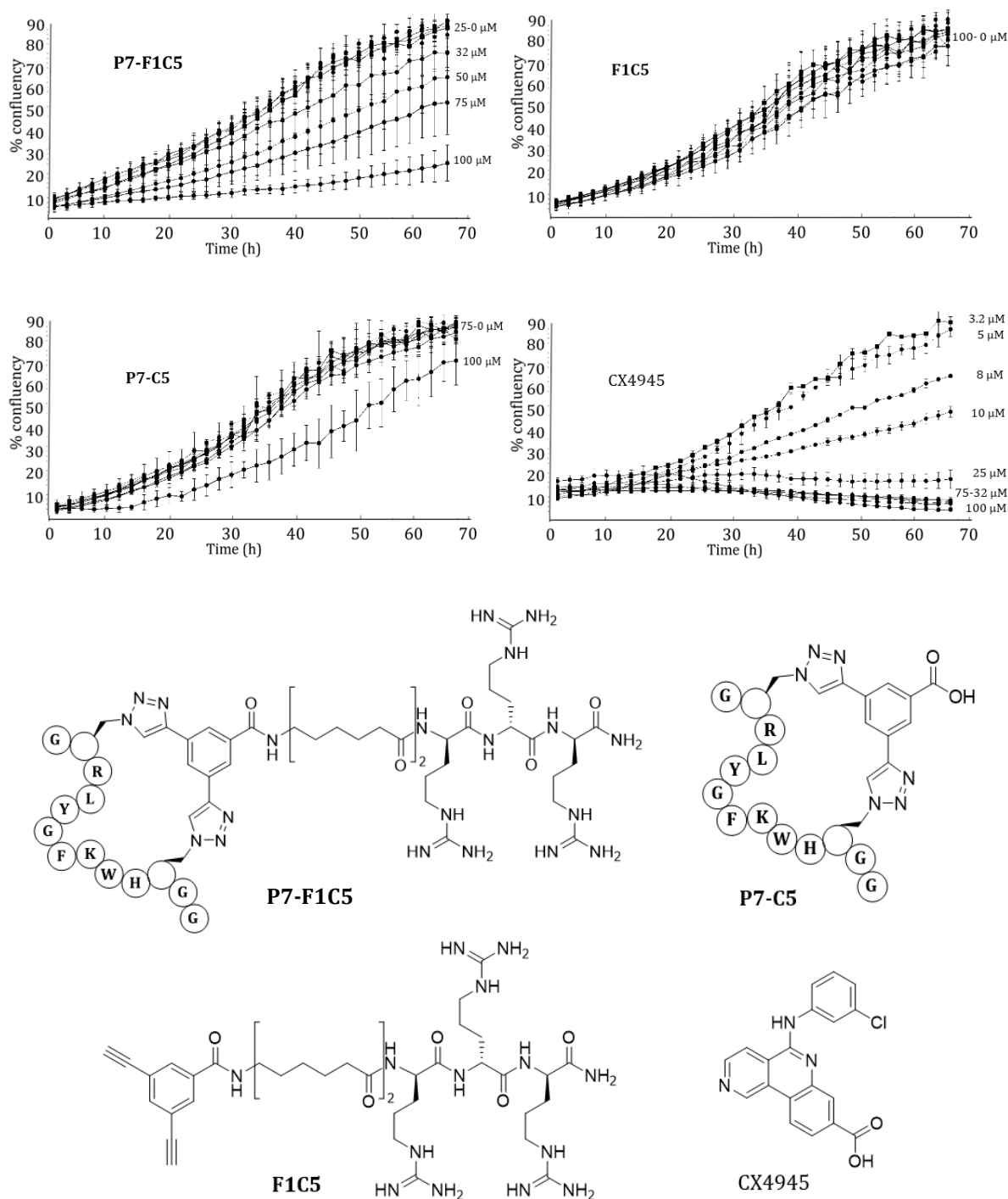


Figure 53 - Rate of cell growth over 70 hours. HCT116 were treated with increasing concentration of compounds and incubated at 37 °C for 70 hours. Results are shown as the average of 4 independent repeats.

Once it was verified that **P7-F1C5** slowed down the proliferation of HCT116 cells, it was decided to determine its GI_{50} using the Sytox Green™ assay. Sytox Green™ is a reagent that would generally stain nucleic acids of dead cells. If the detergent Saponin is added to the assay, cellular membranes become permeable, and the stain permeates both viable and dead cells and therefore gives an indication of the total number of cells. Consequently, the reagents were added straight after the peptide addition and after 4-day incubation to provide the number of cells in

the plate. In this assay, CX4945 was used as a positive control whereas **F1C5**, the cell impermeable **P7-C5** and the cell-permeable negative peptide **P8-F1C5** were used as negative controls. The results are shown in Figure 54.

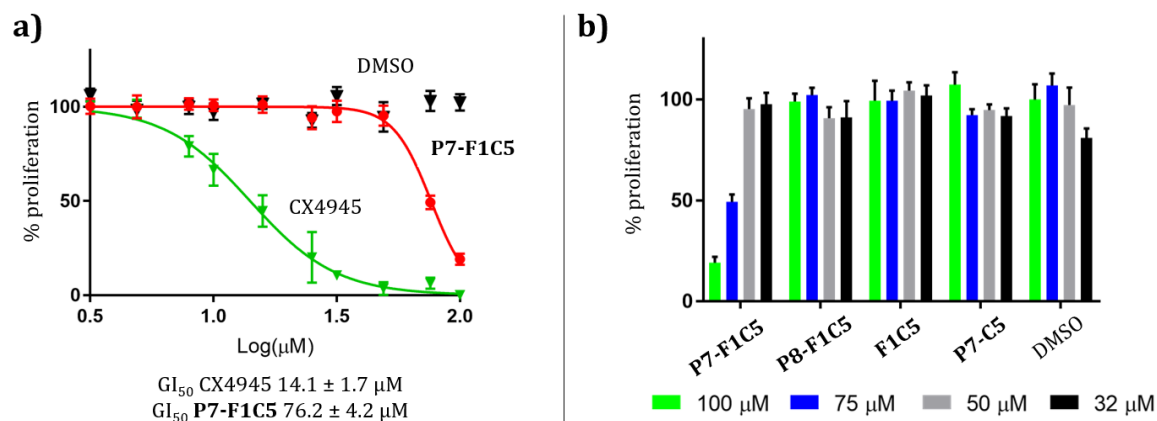


Figure 54 – Percentage of the proliferation of HCT116 cells after 70-hour incubation with the compounds. a) GI_{50} curves for and CX4945. b) Percentage proliferation of HCT116 cells treated with **P7-F1C5** and negative peptides at the top concentrations (100, 75, 50, 32 μM).

P7-F1C5 was able to inhibit cell proliferation with a GI_{50} of $76 \pm 4.1 \mu\text{M}$ whilst the negative peptides did not show inhibition. However, the activity drop-off in the cellular assay was significant with respect to the enzymatic assays (K_d 170 nM, IC_{50} 370 nM). This result could be speculatively rationalised with the fact that the organelle trapping causes a drop-off in the concentration of peptide able to interact with CK2 intracellularly. It is also possible that the effect of the inhibition of the phosphorylation of CK2 β -dependent substrates is outbalanced by the phosphorylation of CK2 β -independent substrates.

4.4.7.3. Cell viability of colorectal cancer cells treated with P7-F1C5

We went on to investigate the ability of **P7-F1C5** to induce apoptosis in cancer cells using the CytoTox-Glo™ Cytotoxicity Assay (Promega). As for the proliferation assays, several peptides were used as negative controls. Unlike the proliferation assay, the outcome of the cell viability assay was determined after 5-hour incubation with the peptides. The results are shown in Figure 55.

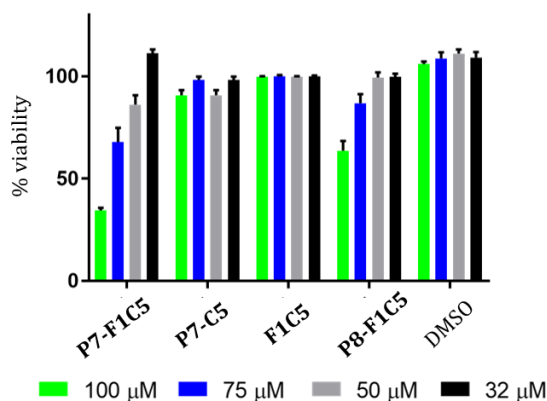


Figure 55 - HCT116 cell viability in the presence of a high concentration of compounds.

Once again, the EC_{50} ($87.5 \pm 6.8 \mu\text{M}$) of **P7-F1C5** was considerably higher than expected. Pleasingly, no cytotoxic effect was detected for **P7-C5** and **F1C5** whilst 60% viability was observed when the top concentration of the negative peptide **P8-F1C5** was used. It should be noted that no inhibition of the proliferation was observed when the same concentration was used in the anti-proliferation assay. Whilst the outcome of the viability assay is determined after 5-hour incubation, the anti-proliferative effect is measured after 70-hour incubation. Therefore, the initial unspecific cytotoxic effect of **P8-F1C5** is somehow overcome by the viable cells whose long-term proliferation is not affected.

4.5. Conclusions and future work

In this work, conformationally-constrained peptides that act as CK2 α/β PPI inhibitors were developed. The lead peptide, **P7-C5**, presents an enhanced binding affinity for CK2 α with respect to the previously developed Pc (K_d 150 vs 1000 nM) and it is stable under conditions mimicking physiological fluids. Due to the lack of intrinsic cell-permeability of the peptides, an easily-synthesised multi-functional constraint was developed giving **P7-F1C5** which allowed the investigation of the intracellular activity. **P7-F1C5** was found to arrest cancer cell proliferation and induce apoptosis in a dose-dependent manner. Importantly, the multi-functional constraint developed herein could be used to lock other peptides into their binding conformation and simultaneously functionalise them.

P7-F1C5 is the first inhibitory peptide of the CK2 α/β PPI that is stable in serum, cell-permeable, active in cells, able to engage the target and with structural information available. Such a peptide could act as a chemical probe allowing study of the CK2 PPI using endogenous levels of proteins and could, therefore, be a powerful tool for validating and dissecting biological processes associated with CK2.

The downside of **P7-F1C5** is its accumulation in some cytosolic organelles – namely lysosomes, Golgi and ER. Future work will focus on understanding the causes of this effect by introducing mutations in the peptide sequence or by changing the cell-penetrating tag. In addition, further attempts to investigate the ability of **P7-F1C5** to engage CK2 intracellularly will be carried out.

Shorter peptides with improved ligand efficiency will be developed using the X-ray structures obtained in this work as a starting point. The ultimate goal is to develop peptides that are cell-permeable without the introduction of cell-penetrating motifs. Considering that the peptide hotspots are known, the shorter peptides will have a sequence based around them (RLYGFK), and new constraints will be screened to lock the shorter peptides in their binding conformation. At a later stage, the peptides could be merged with fragments found to bind in the Tyr pocket in FBDD screening campaigns carried out by collaborators in the Hyvönen group (Biochemistry, University of Cambridge). Whilst the CCHP strategy around the Phe7 residue failed in this study, shorter peptides should allow more flexibility around the Tyr pocket, and therefore, it is envisioned that the CCHP strategy would work with the shorter peptides.

CK2 is overexpressed in cancer cells but it is also present in healthy cells. Selective cancer-cell targeting would improve the therapeutic window of CK2 inhibitors therefore reducing side effects. Selective cancer-cell targeting may be achieved with the use of homing peptides – short amino acid sequences that recognise the receptor exposed on the membrane of cancer cells.

*i*RGD, for instance, is a homing peptide that targets colorectal cancer cells, and it could be attached to the CK2 peptides for CK2 targeting in selected cells. Stapling of the homing peptide will be considered to avoid its degradation in the bloodstream.

Finally, in this work **P2'-C5** provided the first X-ray structure of the CK2 substrate binding in the substrate channel. Such information will be used to develop high-affinity peptides that could displace the native CK2 α substrates, and therefore the structural information obtained in this work opens up the possibility to develop a novel class of CK2 inhibitors and to fully understand the phosphorylation mechanisms of CK2.

CHAPTER 5:

Targeting of Anti-Apoptotic Bcl-2 Proteins in Platelets Using Stapled Peptides

5.1. Summary

Platelets are blood cells with numerous crucial pathophysiological roles in haemostasis, inflammation, cardiovascular thrombotic events, and cancer metastasis.¹⁸⁰⁻¹⁸² Platelet activation and survival require the engagement of intracellular signalling pathways that involve protein-protein interactions (PPIs), and a better understanding of these pathways is crucial for the development of selective antiplatelet drugs. Conventional platelet research methods present several limitations. For example, small molecule inhibitors can lack selectivity and are often challenging to design and synthesise; the development of transgenic animal models is costly and time-consuming; and conventional recombinant techniques are ineffective due to the lack of a nucleus in platelets.¹⁹³

In order to overcome the limitations of conventional research methods, this chapter describes the first application of stapled peptides in human platelets to study PPIs of the Bcl-2 protein family (Figure 56).

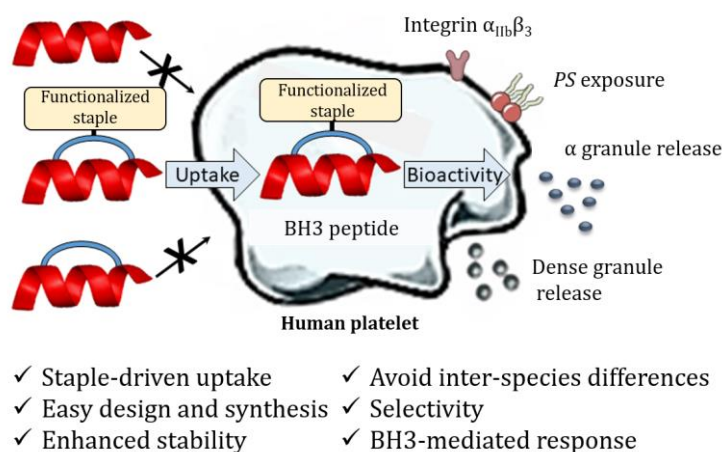


Figure 56 - First application of stapled peptides in platelets to study PPIs.

This work shows that stapled peptides have the potential to unlock the number of PPIs that can be studied in human platelets, and they could help in the development of safer platelet-targeting drugs for treatment of a variety of diseases.

5.2. Project background

Of interest is the investigation of the Bcl-2 proteins, in particular, the BH3-only proteins which play a crucial role in regulating intrinsic apoptosis and the lifetime of platelets.^{167,178,186,187} Whilst all-hydrocarbon stapled peptides corresponding to the BH3 domains of the BH3-only protein family members have previously been used in haematological cancer cells, the efficacy of these molecules for use in platelets has yet to be examined. On the other hand, the small molecule Bad-BH3 mimetic ABT-737²¹ has been employed in platelets where it was found to cause platelet apoptosis but no platelet activation.^{188,224} The pathways that lead to intrinsic apoptosis in platelets overlap to some degree with those leading to platelet activation and clot formation as described previously (Figure 20), and it is believed that the different BH3-only proteins may trigger activation or apoptosis selectively (Figure 57). The elucidation of these pathways could have a remarkable impact on the development of selective platelet-targeting therapy.

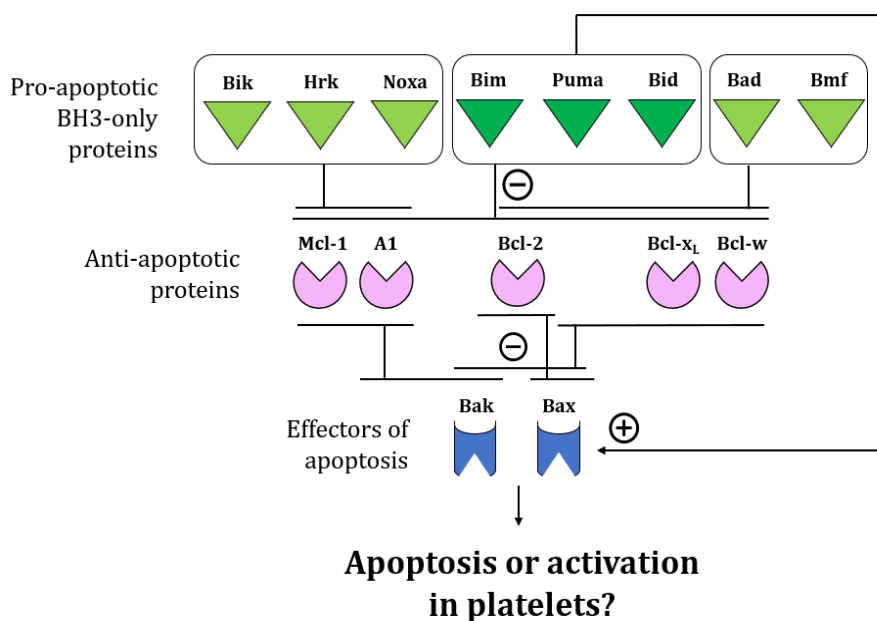


Figure 57 – Schematic representation of the Bcl-2 family members and their relationship with each other. Pro-apoptotic BH3-only proteins are shown in green (light green for sensitiser and dark green for activator), anti-apoptotic proteins in pink and effectors of apoptosis in blue. BH3-only proteins can inhibit one class or both classes of anti-apoptotic proteins, and the effect of inhibiting one class or another on platelet activation and apoptosis is not known.

5.3. Project aim and overview

This project aimed to develop stapled peptides able to mimic the BH3-only proteins of the Bcl-2 family and utilise these to dissect their role in platelet apoptosis and activation.

Initially, uptake experiments were carried out using model peptides with different tags on the staple. This showed how the nature of the tags impacted on the ability of the stapled peptides to permeate the membrane of the platelets. The model peptides were based on the p53 sequence and did not affect platelet activation or apoptosis: platelets are anucleated cells, and p53 is a nuclear protein. Successively, the tags that allowed the p53-based model peptides to enter the cytosol of platelets were used to staple Bim-BH3-based peptides at an $i,i+4$ position, and their effect on platelet activation and apoptosis studied. At a later stage, the ability of the peptides to engage with their target was investigated *in vitro*. Mechanistic differences between the Bim-BH3 peptide and the small molecule Bad-BH3 mimetic ABT-737²¹ utilised as positive control inspired us to investigate the effects of all the other BH3-only proteins on platelet activation and apoptosis. Initially, we intended to employ an $i,i+11$ stapling strategy to constrain the BH3 peptides; however, due to problematic functionalisation of the linker, an $i,i+7$ stapling chemistry was applied instead. The workflow described in this chapter is summarised in Figure 58.

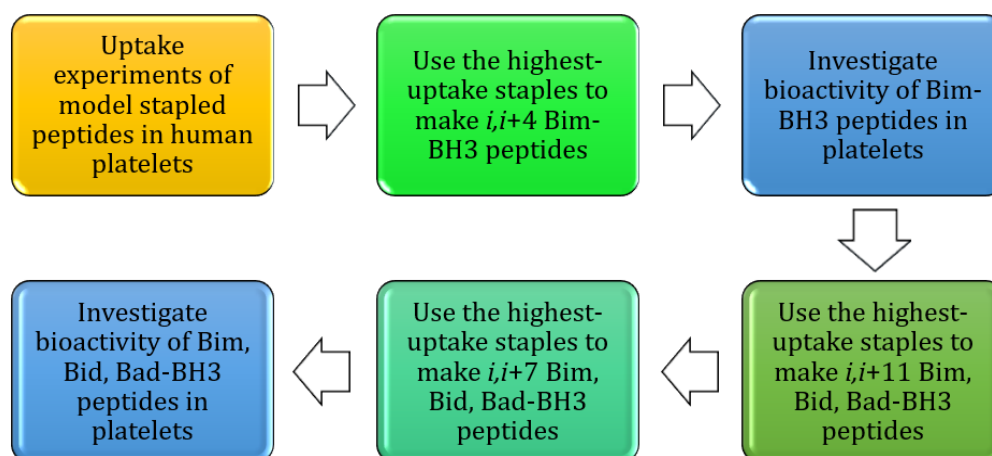


Figure 58 - Overview of the work described in this chapter.

5.4. Results and discussion^{dd}

Unless otherwise stated, the peptides described in this chapter were synthesised using standard procedures for solid phase peptide synthesis (SPPS) and peptide macrocyclisation was achieved by following previously reported procedures for two-component copper-catalysed azido-alkyne cycloaddition peptide stapling (2C CuAAC PS).³⁸

The cellular experiments reported in this chapter were performed at Anglia Ruskin University, Cambridge, under the supervision of Dr Nicholas Pugh. The Surface Plasmon Resonance (SPR) assay was performed at AstraZeneca, Cambridge, under the supervision of Dr Kara Herilhy.

5.4.1. Uptake and bioactivity of model stapled peptides in human platelets

Since no reports existed in the literature on using stapled peptides in platelets, we started investigating cell permeability. To this end, a panel of sixteen model stapled peptides (synthesised by Dr Yuteng Wu) was used.²²⁵ The model peptides were TAMRA labelled to allow for fluorescent visualisation on flow cytometry, and their sequence was based on the p53 protein (a nuclear effector) and should have no effect on anucleated platelets. In addition, the model peptides were stapled with functionalised peptidic and non-peptidic groups providing enough variety to understand which groups are more effective at carrying the cargo peptides into platelets (Figure 59). Functionalised groups included: polycationic peptidic chains,⁸¹ the nuclear localisation sequences PKKKRKV (NLS) and a polyguanidine small molecule carrier (SMoC)²²⁶⁻²³⁰. Moreover, a panel of anionic and polar peptidic chains was also screened.

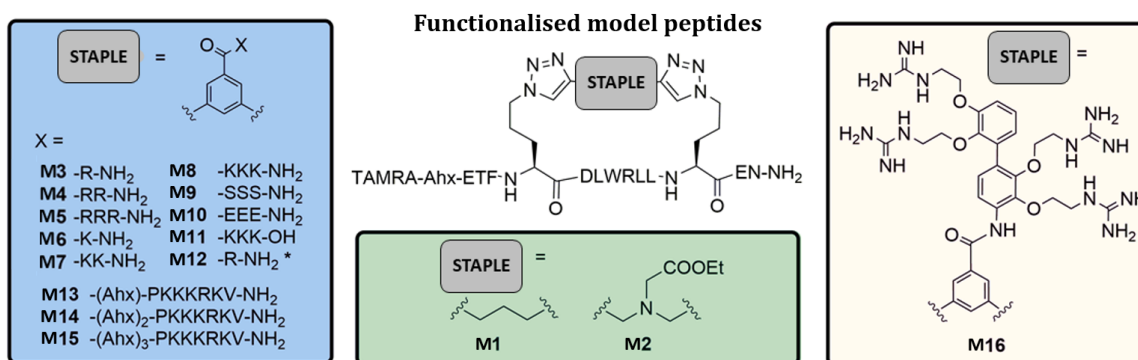


Figure 59 - TAMRA-labelled functionalised stapled peptides synthesised by Dr Yuteng Wu used to analyse platelet uptake of peptides. Schematics of the different peptidic (blue), non-peptidic functionalised staples (green) and a SMoC staple (yellow). * indicates unlabelled peptides (N-terminus capped as acetyl). Adapted from Iegre *et al.*, *ChemSci*, 2018.¹⁹³

^{dd} The work described in paragraphs 5.4.1 and 5.4.2 have been published in a scientific journal prior to publication of this PhD thesis and some text and figures reported herein have been adapted from the publication Iegre *et al.*, *ChemSci*, 2018.¹⁹³

Flow cytometry was employed to assess the uptake of the peptides into platelets at different time points: internalisation of the TAMRA labelled peptides resulted in fluorescent platelets with emission at 550 nm (Figure 60a).^{ee} Treatment with **M13-M15** (carrying NLS) or **M16** (bearing the SMOc motif) showed the highest platelet fluorescence after a 3-hour incubation ($96.1 \pm 0.8\%$, $98.1 \pm 1.1\%$, $97.5 \pm 1.4\%$ and $96.1 \pm 2.2\%$ respectively) indicating a substantial association of the platelets with the stapled peptide. Similarly, **M2** (ethyl ester) and the poly-arginine stapled peptides **M4** and **M5** showed significant uptake ($88.8 \pm 5.6\%$, $73.0 \pm 13.3\%$ and $87.0 \pm 7.3\%$ respectively) whereas only $34.9 \pm 7.8\%$ of platelets were fluorescent following treatment with **M8** (poly-lysine). No changes in fluorescence were observed with the other peptides, indicating that the other tags were ineffective as cell-penetrating peptides (CPPs).

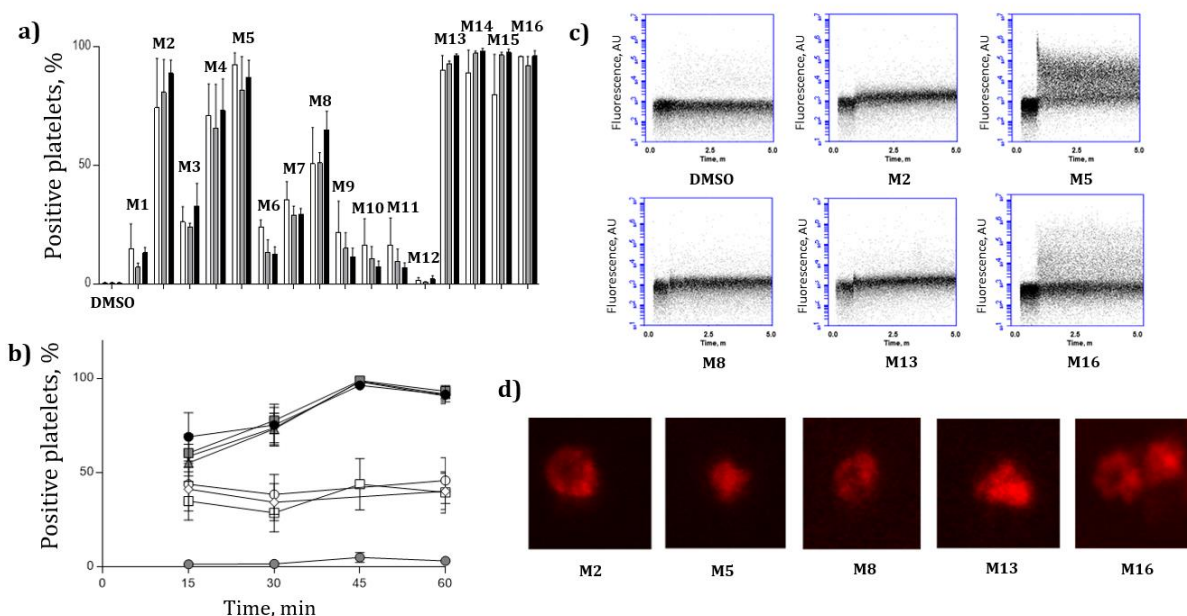


Figure 60 – Uptake experiments using model peptides **M1-M16**. a) Platelets fluorescence after 1 h (white), 2 h (grey) and 3 h incubation (black). b) Peptide uptake of model peptides monitored during the first 60 minutes of treatment. ●: vehicle (DMSO), ●: **M16**, ■: **M15**, ▲: **M14**, ▼: **M13**, ◇: **M8**, □: **M5**, ○: **M2**. c) Five-minute real-time measurement of peptide uptake. Unlabelled platelets were recorded for 30 sec prior to addition of the given peptide. d) Confocal microscopy images of live platelets incubated with the TAMRA-model peptides. Adapted from Iegre et al., *ChemSci* 2018.¹⁹³

For the peptides that showed maximum fluorescence after 3-hour incubation, the uptake was monitored after 15, 30, 45, and 60 minutes (Figure 60b). More than 50% of platelets became fluorescent during the first 15 minutes of incubation with **M13-M16** with a further increase after the first 45 minutes. Some 40-50% of platelets were fluorescent after 15 minutes following treatment with **M2**, **M5** or **M8**, and no further increase was detected thereafter. Continuous

^{ee} In all the flow cytometry experiments described in this chapter, the fluorescence associated with untreated platelets (no compounds, no fluorescently-labelled markers) was recorded and used to normalise the results. In particular, the peak corresponding to the untreated platelet signal read on the laser of interest was considered as zero. Shift of such peak towards the right was considered as positive platelet and quantify accordingly (vide 9.2.2, Figure 72 for more details).

assessment of platelet fluorescence in the first 5 minutes of treatment demonstrated that peptides **M5** and **M16** were instantly internalised by a fraction of the cells (Figure 60c).

Peptide uptake experiments of the most permeable model peptides **M5**, **M13-M16** were repeated in the presence of platelet-rich plasma (PRP) to ensure realistic conditions. The results showed only a small reduction in peptide uptake between 10 and 20% compared to buffer, indicating that the uptake is not prevented by the interaction of the peptides with the other components of the plasma.

Whilst flow cytometry quantifies the fluorescence of the platelet population, is not indicative of whether the fluorescence is a result of peptide internalisation or association with the membranes. Consequently, confocal microscopy of live platelets was carried out to elucidate the peptide localisation. It should be noted that platelets are small-sized ($\varnothing \sim 2 \mu\text{m}$); therefore, confocal microscopy cannot assign pixel localisation unequivocally but can, nonetheless, indicate whether the fluorescence comes from the platelet membrane or cytosol. Live platelets were imaged after 1-hour incubation with the TAMRA-labelled model peptides, and the results suggested that peptides **M5** and **M13** permeated into the platelet cytosol. On the contrary, **M2**, **M8**, and **M16** localised predominantly on the platelet membrane (Figure 60d).

Conventional platelet apoptosis and activation responses were assessed to investigate potential off-target effects following treatment with the platelet-permeable model peptides. As a response to external stimuli, platelets expose phosphatidylserine (*PS*) on the plasma-oriented surface of their membrane. It is widely recognised that plasma-exposed *PS* plays a regulatory part in blood coagulation acting as a secondary messenger and is an index of apoptosis (in both platelets and nucleated cells).²³¹ When exposed on the platelet surface, *PS* binds the marker Annexin V in the presence of Ca^{+2} ions. If the marker is fluorescently labelled (*i.e.* with a FITC group^{ff}), its signal can be used in flow cytometry to detected *PS* exposure (Figure 61). Similarly, other platelet activation markers (dense and α granules release, integrin $\alpha_{\text{IIb}}\beta_3$) can be detected using flow cytometry when specific fluorescently-labelled antibodies are used. For instance, exposure of integrin $\alpha_{\text{IIb}}\beta_3$ on the platelet surface can be detected by the antibody PAC-1 (Figure 61). When platelets become activated, they expose integrin $\alpha_{\text{IIb}}\beta_3$ to bind substrates that once complexed, promote platelet aggregation and clot formation.

^{ff} Different excitation/emission wavelengths for TAMRA (Ex-max 546 nm/Em-max 579 nm) and FITC (Ex-max 494 nm/520 nm Em-max) allowed selective detection of a fluorescent signal over the other.

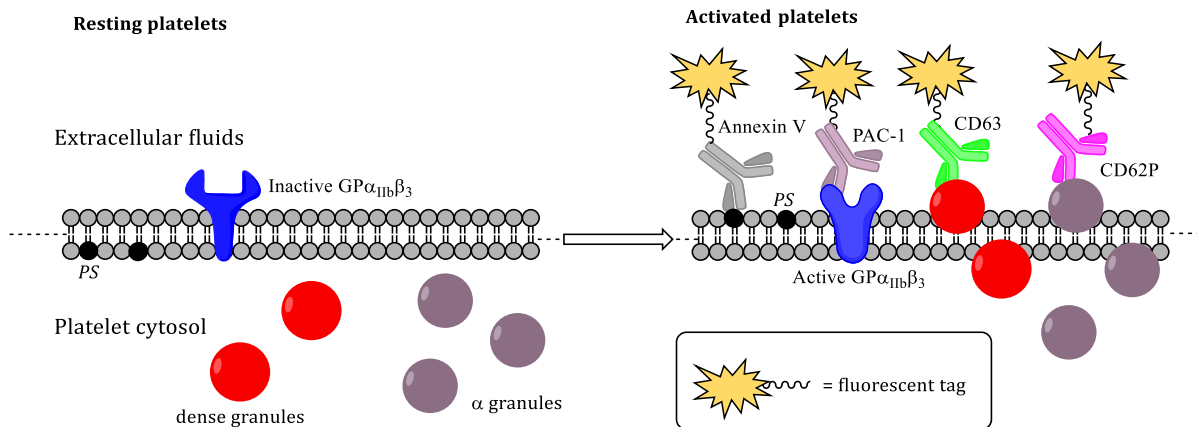


Figure 61 - Schematic of the detection of PS exposure and platelet activation using fluorescently labelled antibodies. PS is represented in black, dense granules in red, α granules in aubergine, integrin $GP\alpha_{IIb}\beta_3$ in blue.

Since the model peptides used were based on the sequence of the nuclear effector p53, and platelets have no nucleus, no biological effect was expected after treatment with the peptides. As expected, only low activation changes were observed following treatment with NLS-bearing peptides **M13-M15** and SMOc peptide **M16** (Figure 62a and b). No change in platelet activation markers was found for the other peptides, indicating that the treatment of platelets with the model peptides did not cause unspecific responses. Undesired platelet aggregation - as noted by analysis on the aggregometer - was detected in response to treatment with peptide **M16**, but not for the other peptides (Figure 62c). Thus, peptide **M16** was excluded from further studies.

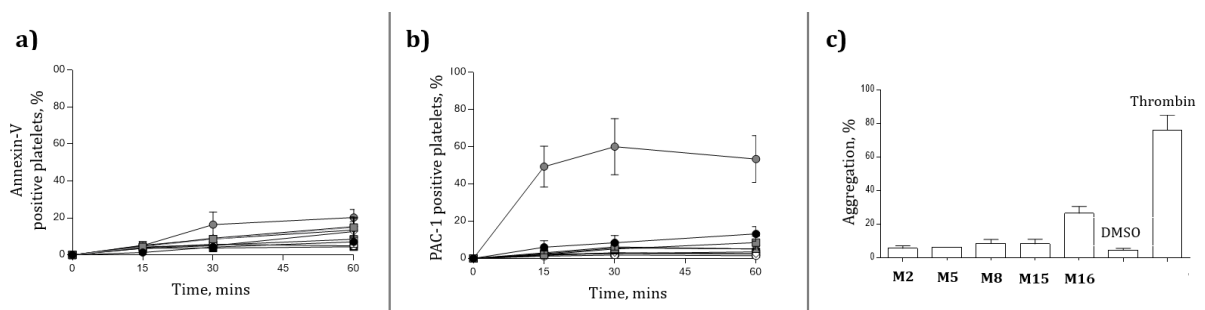


Figure 62 - a) Annexin V binding for model platelet-permeable peptides; b) PAC-1 binding: ● : Thrombin 1U/mL, ■ : vehicle (DMSO), ● : M16, ■ : M15, ▲ : M14, ▼ : M13, ◇ : M8, □ : M5, ○ : M2. c) Platelet aggregatory responses to treatment with model peptides. Vehicle control (DMSO) and thrombin were used as negative and positive control respectively.

This data set provides evidence that functionalisation of stapled peptides is required for the uptake of peptides into platelets, with the NLS sequence (**M13-M15**) and poly-arginine staple (**M5**) being the most effective. In addition, these preliminary experiments showed that the staples themselves do not exert any unspecific activity in platelets.

5.4.2. Investigation of the Bim/Bcl-x_L PPI in platelets using *i,i+4* stapled peptides

Once it was confirmed that platelets were able to uptake stapled peptides, further experiments were performed to investigate whether peptides based on biologically relevant sequences could elicit a relevant intracellular response in platelets.

The role of BH3-only proteins in the development of a pro-coagulant platelet phenotype has been investigated using the Bad-BH3 mimetic small molecule ABT-737.²¹ This induces mitochondrial membrane depolarisation, activation of caspases -9, -8 and -3, PS exposure, and causes inhibition of the platelet activation process by interacting with the pro-survival Bcl-2 proteins.^{188,189,224,232} However, the role of the other BH3-only proteins (Bid, Bim, Bmf, Noxa, Puma) in platelet activation and apoptosis is not fully understood. Previous work has demonstrated that an all-hydrocarbon (AH) Bim sequence-based peptide (denoted Bim SAHBa, Table 15) induces Bax mediated apoptotic responses in nucleated cancerous cells.^{177,233,234} To the best of our knowledge, the implication of the interaction of Bim-BH3 mimetics with the anti-apoptotic Bcl-2 proteins in platelets is unknown. Hence, CuAAC 2C stapled peptides based on the Bim-BH3 sequence were synthesised and utilised to investigate their effects on platelet processes. The CuAAC 2C peptide stapling methodology was chosen as it allows to access multiple stapled peptides from one linear sequence in a combinatorial manner. This results in a more efficient access to libraries of functionalised peptides.

5.4.2.1. Design and synthesis of *i,i+4* Bim-BH3 stapled peptides

Inspired by the work of Walensky *et al.*,¹⁷⁷ we decided to synthesise *i,i+4* stapled peptides based on the SAHBa sequence. Molecular dynamic simulations (MDs) were performed by Dr Yaw Sing Tan on the complex form by the Bcl-x_L protein⁸⁸ and the peptide mimicking the BH3-only domain of the protein Bim to suggest amino acid and staple combination to use to retain the binding affinity of the native Bim peptide. MDs simulations suggested employing the azido ornithine amino acid (**12**) as the unnatural amino acid to perform the 2C CuAAC stapling. This would facilitate the synthesis of different stapled peptides from one linear precursor (**P9**, Figure 63a). 3,5 dialkyne benzoic acid (**C5**) was used as the linker for stapling. MDs simulations of the peptide complexed with Bcl-x_L suggested that the stapled peptide **P9-C5** (Figure 63b) would retain an α -helical conformation upon binding and that its binding affinity would be comparable to that of the unstapled wild-type (WT) peptide (**P10**) (ΔH -107.6 \pm 4.9 Kcal·mol⁻¹ vs -108.3 \pm 1.5 Kcal·mol⁻¹, Figure 63).

⁸⁸ An anti-apoptotic Bcl-2 protein which is known to be expressed in platelets.¹⁷⁸

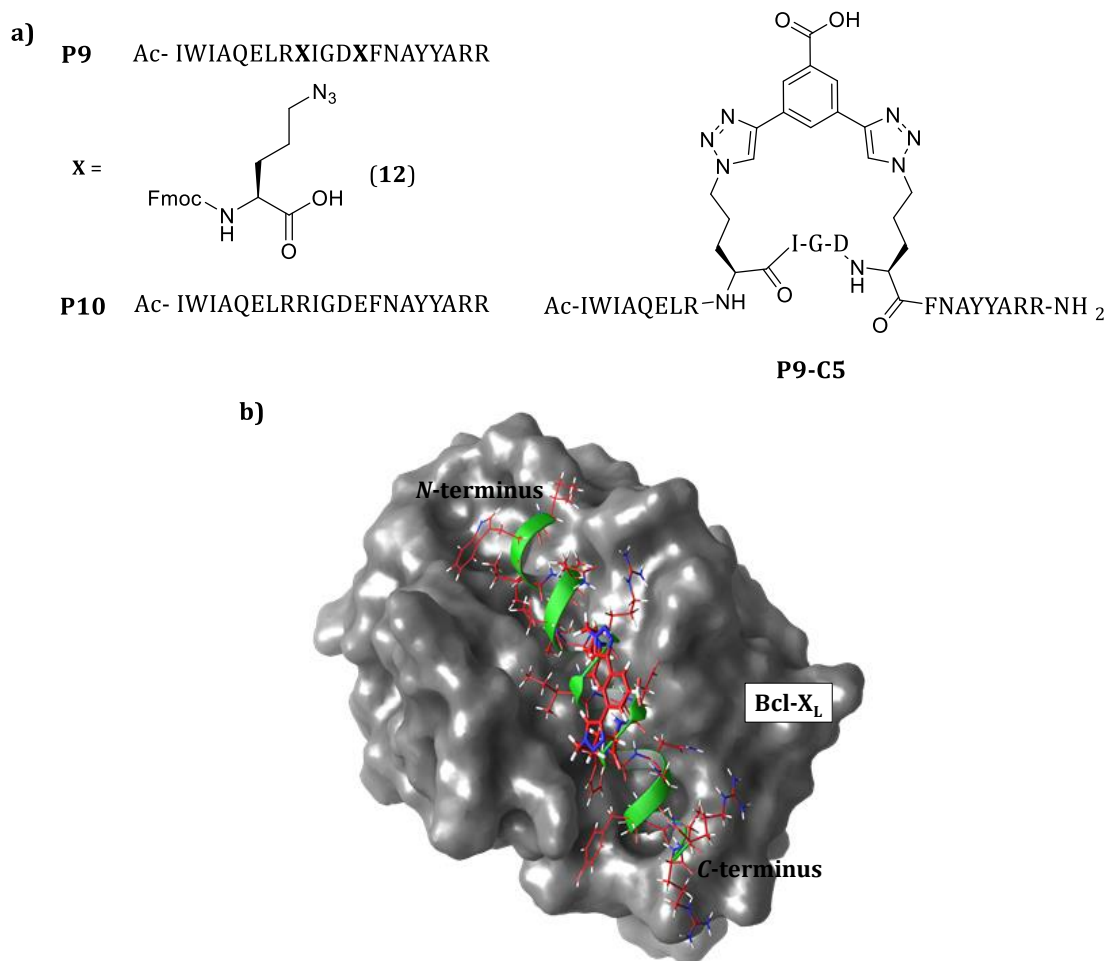
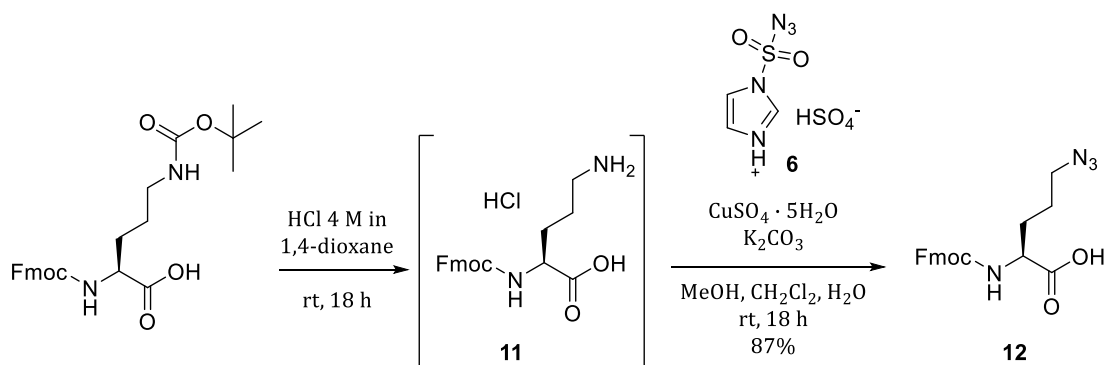


Figure 63 – a) Structures of **P9**, **P10** and **P9-C5**. b) Snapshot taken from the end of the MD simulation of **P9-C5** in complex with **Bcl-X_L**. The surface of **Bcl-X_L** protein is shown in grey, peptide secondary structure in green and peptide residues in orange.

Synthesis of peptide **P9** required Fmoc-azido ornithine amino acid **12** which was synthesised according to literature precedent.²³⁵ The synthesis commenced from the commercially available Fmoc-Ornithine(Boc)-OH that underwent Boc deprotection in the presence of 4 M HCl in 1,4-dioxane to afford Fmoc-Ornithine-OH **11**. The crude product was then subjected to treatment with azido-transfer reagent imidazole-1-sulfonyl azide hydrogen sulfate (**6**) in the presence of $\text{CuSO}_4 \cdot 5\text{H}_2\text{O}$ to yield the desired product **12** in 78% yield (Scheme 29).



Scheme 29 - Synthesis of azido amino acid **12** starting from commercially available Fmoc-Ornithine(N-Boc)-OH.

Synthesis of the azido-transfer reagent **6** and constraint **C5** are described in Chapter 4.

Synthesis of staples **F4C5** and **F5C5** was achieved using the standard procedure for SPPS (Figure 64). The *N*-terminus of the peptides were capped with **C5** before peptide cleavage from the resin, trituration with Et₂O and purification.

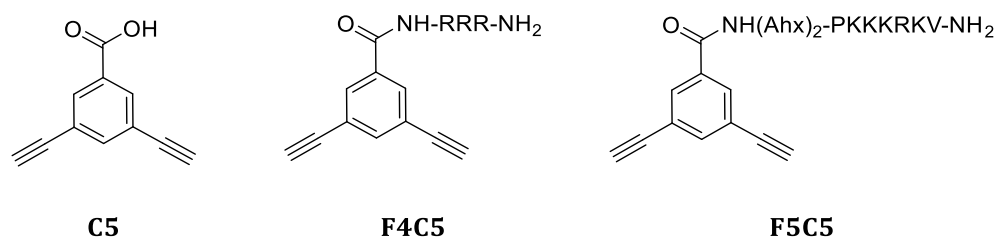
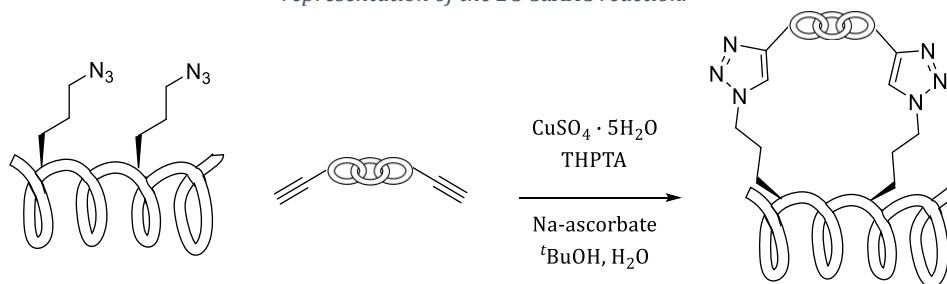


Figure 64 - Structures of constraints **C5**, **F4C5** and **F5C5**.

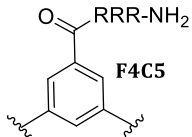
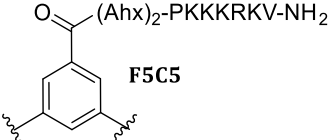
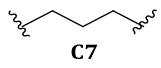
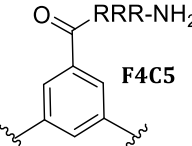
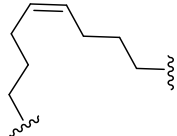
Based on the platelet permeability results of the model peptides, **P9** was then stapled with **C7** (non-functionalised staple to be used as negative control), **F4C5** (poly-arginine staple) and **F5C5** (NLS staple) where **F4C5** and **F5C5** are the same functionalised staples as the model peptides with the highest cytosolic platelet uptake **M5** and **M14**. A list of all the peptides used in this study and conversions of the CuAAC 2C-PS reactions can be found in Table 15.

Additionally, a negative cell-permeable peptide was synthesised and used as a negative control. The negative peptide (**P11-F4C5**) presented an R153D mutation in its sequence which was found not to exert the Bim-BH3 biological effect in nucleated cells.¹⁷⁷ FITC-labelled analogues of all the stapled peptides were also synthesised to monitor their uptake into platelets. In this study, FITC was attached to the *N*-terminus of the peptides by treating the on-resin Fmoc-deprotected peptide with FITC and DIPEA in the dark for 14-16 hours. An aminohexanoic acid spacer (Ahx) was placed between the *N*-terminal peptide residue and the FITC group to avoid steric clashes. The SAHBa peptide, which inspired this work, and its FITC-labelled analogue, were also synthesised for comparison.

Table 15 - Names and structures of the peptides used in this study, conversions of the 2C-PS stapling and schematic representation of the 2C CuAAC reaction.



Peptide	Sequence	Staple	Conversions
P9	Ac-IWIAQELRXIGDXFNAYYARR	NA	-

P9-F4C5	Ac-IWIAQELRX _{F4C5} IGDX _{F4C5} FNAYYARR		59
FITC-Ahx-P9-F4C5	FITC-Ahx-IWIAQELRX _{F4C5} IGDX _{F4C5} FNAYYARR		74
P9-F5C5	Ac-IWIAQELRX _{F5C5} IGDX _{F5C5} FNAYYARR		87
FITC-Ahx-P9-F5C5	FITC-Ahx-IWIAQELRX _{F5C5} IGDX _{F5C5} FNAYYARR		90
P9-C7	Ac-IWIAQELRX _{C7} IGDX _{C7} FNAYYARR		81
FITC-Ahx-P9-C7	FITC-Ahx-IWIAQELRX _{C7} IGDX _{C7} FNAYYARR		NA
P10	Ac-IWIAQELRRIGDEFNAYYARR		-
FITC-Ahx-P10	FITC-Ahx-IWIAQELRRIGDEFNAYYARR	NA	-
P11-F4C5	Ac-IWIAQELDX _{F4C5} IGDX _{F4C5} FNAYYARR		NA
FITC-Ahx-P11-F4C5	FITC-Ahx-IWIAQELDX _{F4C5} IGDX _{F4C5} FNAYYARR		79
SAHBa	Ac-IWIAQELRZIGDZFNAYYARR		-
FITC-Ahx-SAHBa	FITC-Ahx-IWIAQELRZIGDZFNAYYARR		-

All the peptides have an amide at the C-terminus. X = azido ornithine; The schematic structure showed above the table does not represent one of the SAHBa peptides which were cyclised using a RCM reaction. Z = (S)-2-(pent-4-enyl) alanine and the AH staple is shown in the column "Staple". ^a Conversion of stapling reactions as determined by LCMS of the crude reaction mixture. NA = not available due to complicated LCMS chromatogram.

Synthesis of peptide **P9** proved challenging. Standard microwave-assisted SPPS procedure using MBHA Rink Amide (0.35 meq/g resin loading) resulted in some impurities with a similar retention time to the desired product hence preventing its purification. The use of lower loading resin (0.19 meq/g) did not resolve the issue, and neither did room temperature peptide synthesis. Pleasingly, a double coupling for each of the amino acids afforded the desired product **P9**. The latter crude peptide presented solubility issues in the solvents used for HPLC purification (MeCN, H₂O, TFA) and in DMSO. High dilution of the crude material followed by several filtrations using 0.45 µm PTFE syringe filters resulted in a clear solution that underwent purification successfully. Similarly, synthesis of **P10** was achieved on a microwave-assisted peptide synthesiser using double coupling for all the amino acid. Unlike **P9**, **P10** did not present solubility issues

5.4.2.2. The uptake of Bim peptides into platelets

As with the model peptides, flow cytometry was used to detect fluorescent platelets in the presence of the FITC-labelled Bim-BH3 peptides. The PRP was incubated with the FITC-labelled peptides, and the uptake monitored after 15, 30 and 60-minute incubation (Figure 65a).

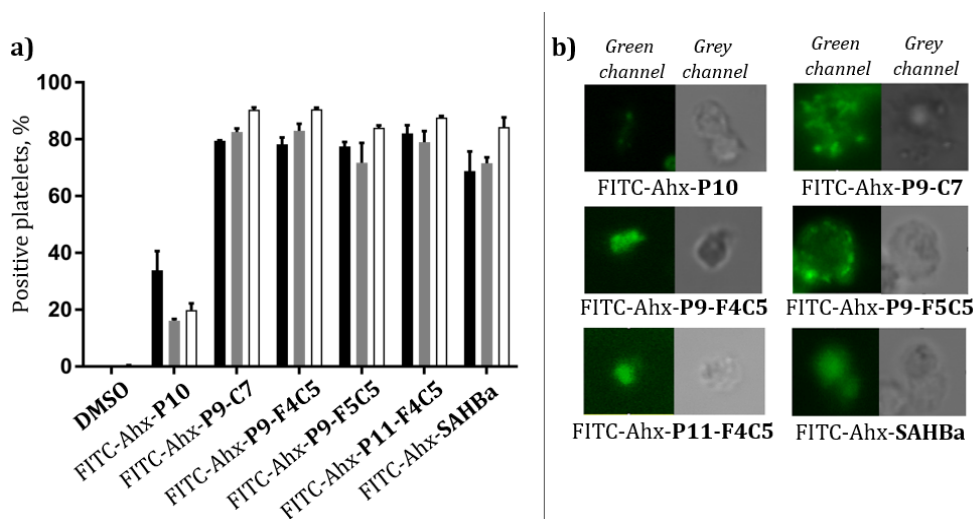


Figure 65 - Uptake experiments in the presence of FITC-labelled Bim-BH3 peptides. a) Uptake of Bim-BH3 peptides and SAHBa in PRP after 15 minutes (black), 30 (grey), 1 h (white). The results shown are the average of two independent repeats and error shown as SEM. b) Images of live platelets incubated with Bim-BH3 FITC-labelled peptides. For each peptide, the green channel is shown on the left and the grey on the right.

The uptake experiment showed that all the peptides tested associated rapidly with platelets except for the WT peptide FITC-Ahx-**P10**.

Successively, confocal microscopy was used to understand whether the fluorescence observed by flow cytometry was cytosolic or associated with the platelet membranes (Figure 65b). Consistently with the behaviour of the non-functionalised model peptide **M1**, the images showed poor membrane permeability of peptide FITC-Ahx-**P10**. Even though flow cytometry of FITC-

Ahx-**P9-C7** suggested high platelet fluorescence in plasma, confocal imaging showed the peptide forming aggregates outside the platelet cytosol and hence being unable to reach the target protein. Peptide FITC-Ahx-**P9-F4C5** was the most effective at localising into the platelet cytosol: FITC-Ahx-**P9-F5C5**, in fact, aggregates partially with the platelet membrane. Both the positive and negative control peptides (SAHBa and FITC-Ahx-**P11-F4C5** respectively) were successfully internalised in the platelet cytosol.

5.4.2.3. Phosphatidylserine exposure induced by Bim-BH3 peptides: a sign of apoptosis or platelet activation

Once it was confirmed that Bim-BH3 peptide uptake is dependent on a functionalised staple, the influence of these peptides on activating processes in washed platelet suspensions was studied. The activity of the peptides was compared with ABT-737, the previously reported Bad-BH3 small molecule mimetic.^{21,188} Initially, the ability of the peptides to cause *PS* exposure was investigated on flow cytometry using FITC-labelled Annexin V.

Treatment of platelets with **P9-F4C5** or **P9-F5C5** resulted in *PS* exposure (with $78 \pm 1.3\%$ and $42.9 \pm 6.0\%$ Annexin V binding after 3-hour incubation), consistent with the generation of a pro-coagulant phenotype. Of note, **P9-F4C5** showed a similar profile to ABT-737 and appeared to be more potent than the AH stapled Bim peptide SAHBa (Figure 66). No Annexin-V binding was observed following treatment with the WT peptide **P10** nor with the non-functionalised stapled peptide **P9-C7**, consistent with their cell-impermeable nature. Pleasingly, the negative peptide **P11-F4C5** did not result in *PS* exposure in platelets despite being platelet-permeable, suggesting that the effects of the BH3 stapled peptide are specific to biologically relevant processes.

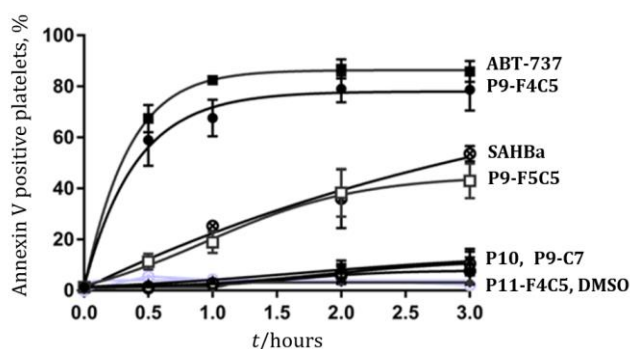


Figure 66 - Functionalised, stapled Bim-BH3 peptides induce *PS* exposure in platelets. Platelets were treated with $10 \mu\text{M}$ compounds, and changes in Annexin-V binding were quantified using flow cytometry at different time points. ●: **P9-F4C5**, □: **P9-F5C5**, ▲: **P9-C7**, ○: **P10**, ■: **ABT-737**, ◆: vehicle (DMSO), ●: **P11-F4C5**, θ: **SAHBa**.

5.4.2.4. Activation marker binding induced by Bim-BH3 peptides: a sign of platelet activation

We then assessed the effect of permeable stapled peptides **P9-F4C5** and **P9-F5C5** on platelet activation markers since previous work has indicated that the small molecule Bad-mimetic ABT-737 induces apoptosis without causing platelet activation.²³⁶⁻²³⁸ As in the previous experiments, **P11-F4C5** peptide was employed as the negative control.

In addition to the previously described PAC-1 (*vide supra* 5.4.1), two other platelet activation markers were used in this experiment: CD62P and CD63. CD62P indicates secretion of α granules while CD63 is an index of secretion of dense granules.^{236,238} α granules are secreted by activated platelets into the plasma and contain several growth factors - such as IGF-1, PDGFs, TGF β , CXCL4 - and clotting proteins - including thrombospondin, fibronectin, factor V, and the VWF - which trigger clot formation. On the other hand, dense granules contain ADP, ATP, calcium ions and serotonin; all cofactors required to prompt the coagulation cascade. α and dense granules express the adhesion molecules CD62P and CD63 respectively and, when exposed on the platelet surface, can be recognised by the corresponding fluorescently labelled-antibodies.

Initially, it was decided to use the three antibodies (anti-PAC1, anti-CD63 and anti-CD62P) simultaneously as the markers carried different fluorophores that could be detected at three different wavelengths by the flow cytometer.^{hh} However, assessment of the three activation markers together was not possible as the readings generated inconclusive results with the DMSO control giving high response for all the markers. Therefore, the activation markers were assessed separately.

As shown in Figure 67, after 1-hour incubation both Bim-BH3 peptides induced integrin $\alpha_{IIb}\beta_3$ activation (as measured by PAC-1 binding), whilst ABT-737 was ineffective. In particular, treatment with **P9-F4C5** or **P9-F5C5** resulted in $24.1 \pm 2.4\%$ and $50.8 \pm 0.3\%$ PAC1-positive platelets, respectively.ⁱⁱ Treatment with both peptides resulted in similar levels of CD62P expression ($53.7 \pm 2.5\%$ and $62.1 \pm 7.8\%$, respectively), indicating peptide-induced α granule secretion. Additionally, both peptides increased CD63 expression (correlated with dense granule release), with peptide **P9-F4C5** being more effective than **P9-F5C5** ($72.9 \pm 5.3\%$ vs $34.4 \pm 6.7\%$ respectively). Pleasingly, unspecific activation was not observed when the mutant **P11-F4C5** was used.

^{hh} FITC-labelled PAC-1 (Ex-max 482 nm/Em-max 520 nm); PE-labelled CD62P (Ex-max 496 nm/Em-max 478 nm); APC-labelled CD63 (Ex-max 650 nm/Em-max 660).

ⁱⁱ Positive platelets are ones that showed greater fluorescence than any platelets in the untreated control sample. *Vide* Figure 72, section 9.2.2 for more details.

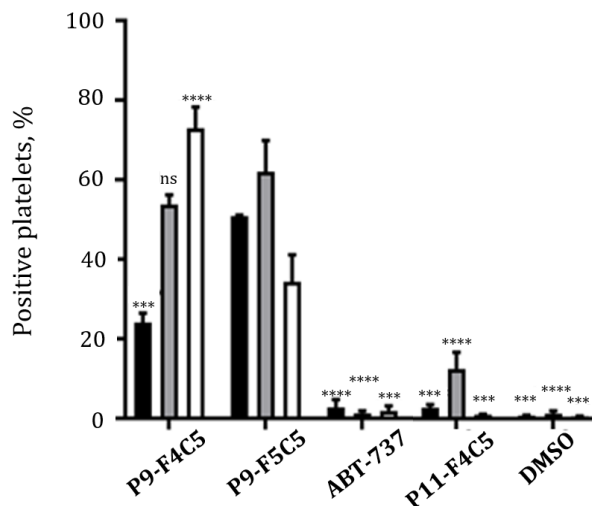


Figure 67 – Induction of activation markers by Bim-BH3 peptides and ABT-737. Platelet activation markers (% positive platelets) were investigated following 1 h of peptide treatment. ■ PAC-1, ■ CD62P and □ CD63 binding. Statistic significance compared to **P9-F5C5**: **** = $P < 0.0001$, *** = P between 0.0001 and 0.0005, ns = non-significant.

In conclusion, despite having similar effects on PS exposure with respect to the clinical candidate ABT-737, our Bim BH3 peptides showed a pronounced increase in activation markers. These results highlight that Bim and Bad have different effects on platelet activation, thus pointing to a difference in the roles and mechanisms of these two proteins. Further investigation dissecting the roles of each BH3-only protein in platelets would help to understand these mechanistic differences.

5.4.2.5. *In vitro* target engagement using an SPR assay

Surface Plasmon Resonance (SPR) assay was used to understand whether the peptides were able to bind to the anti-apoptotic proteins of the Bcl-2 family (Bcl-x_L, Mcl-1, A1, Bcl-2, Bcl-w). In particular, the ability of **P10**, **P9-F4C5**, **P11-F4C5** and SAHBA to bind to Bcl-x_L was investigated. Bcl-x_L was chosen among the other members of the anti-apoptotic family for its well-documented presence in platelets.¹⁷⁸

In the SPR assay performed in this study, the Bcl-x_L protein was immobilised on a flexible dextran matrix, and the peptides were allowed to flow across that surface. The SPR assay was configured to examine the direct binding of peptides to Bcl-x_L derivatised sensor surfaces and generate apparent affinity values (K_{dapp}) to provide ranking data for the series of peptides under examination.

The results confirm that the WT peptide **P10** and platelet-permeable stapled peptide **P9-F4C5** were able to engage with Bcl-x_L protein (K_{dapp} 7.3 ± 0.2 and 26 ± 0.3 nM respectively) supporting the hypothesis that **P10** does not exert a biological response in platelet due to the lack of cell-permeability. Interestingly, the AH stapled Bim-BH3 peptide SAHBA showed a reduced binding

affinity compared to the WT and peptide **P9-F4C5** ($K_{dapp} > 33$ nM).^{jj} No binding was observed for the negative peptide **P11-F4C5**.

5.4.2.6. Effect of stapling on the peptide secondary structure and stability to serum proteases

Circular dichroism (CD)^{kk} was used to elucidate the effect of the *i,i+4* stapling on the secondary structure of the Bim peptides. To this end, the functionalities that **P9-F4C5** and **P9-F5C5** carry on the staples were removed to avoid interference, and **P9** was stapled with **C5** (3,5-dialkyne benzoic acid, 58% conversion). The secondary structure of **P9-C5** was measured in a 50:50 mixture of MeCN and H₂O at a concentration of 50 μ M. For comparison, the structure of the WT Bim-BH3 peptide **P10** in solution was determined using the same conditions (Figure 68).

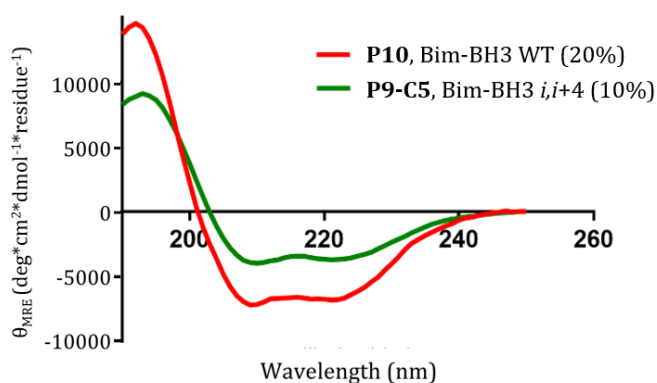


Figure 68 - Mean Residue Ellipticity of the Bim-BH3 peptides **P9-C5** (green) and **P10** (red).

The spectra showed that **P9-C5** was able to maintain a helical structure although its % helicity (at 222 nm) was reduced compared to the WT peptide **P10** (10% vs 20%, respectively).

In order to understand whether stapling *via* 2C CuAAC enhanced the proteolytic stability of the peptides to proteases, serum stability tests were undertaken for the stapled peptide **P9-C5** and the WT linear peptide **P10**.

^{jj} Exact quantification of the K_{dapp} for SAHBA was not possible due to solubility issues encountered when concentrations higher than 33 nM were used.

^{kk} Circular dichroism (CD) is a technique used to investigate the peptide secondary structure in solution. For α -helical peptides, a typical CD spectrum shows a characteristic double minimum at 208 and 222 nm. CD provides a simple method for estimating α -helical content of peptides and proteins but should not be considered definitive.

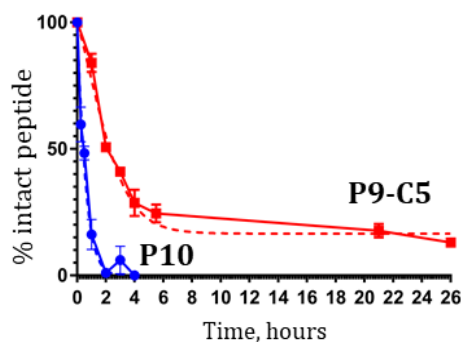


Figure 69 - Stability of Bim-BH3 peptides **P10** (blue) and **P9-C5** (red) in human serum. The results are the average of three independent repeats, and the error is shown as SEM.

The staple was effective at improving the stability of the peptide to the serum proteases: the WT peptide **P10** was fully degraded after 4 hours while 20% of the stapled peptide was still detected after 26-hour incubation.

5.4.2.7. Considerations on the use of *i,i+4* Bim-BH3 peptide in platelets

The results obtained thus far showed that platelets are amenable to treatment with stapled peptides. In particular, a functionalised staple was required to translocate p53 and Bim-based 2C CuAAC stapled peptides into the platelet cytosol. The *i,i+4* stapled peptides developed in this work proved to be more stable than the WT peptide to serum proteases. Besides, the peptides engaged the Bcl-x_L target with nM affinity and were able to cause platelet activation.

5.4.3. Dissecting the role of Bim, Bad, and Bid protein in platelets using stapled peptides

Intrigued by the results obtained when comparing Bim to Bad mimetics, we decided to investigate the effect of mimics of each member of the pro-apoptotic proteins of the Bcl-2 family on platelet activation and apoptosis. In nucleated cells, Noxa-BH3 antagonises exclusively the anti-apoptotic proteins Mcl-1 and A1. Bim, Puma, and Bid inhibit all of the anti-apoptotic proteins whereas Bad, and Bmf engage Bcl-2, Bcl-x_L, and Bcl-w (Figure 57).¹⁶⁸ To this aim, Bim, Bad and Bid-BH3 mimetics were synthesised, and their characterisation is described in this work; Noxa, Puma, and Bmf-BH3 peptides were synthesised by Josephine Gaynord, PhD student in the Spring group.

5.4.3.1. Looking at *i,i+11* stapling

The *i,i+4* stapling of the Bim-BH3 peptides synthesised in the first part of this study did not enhance the helicity of the WT peptide (Figure 68). It is highly debatable whether the

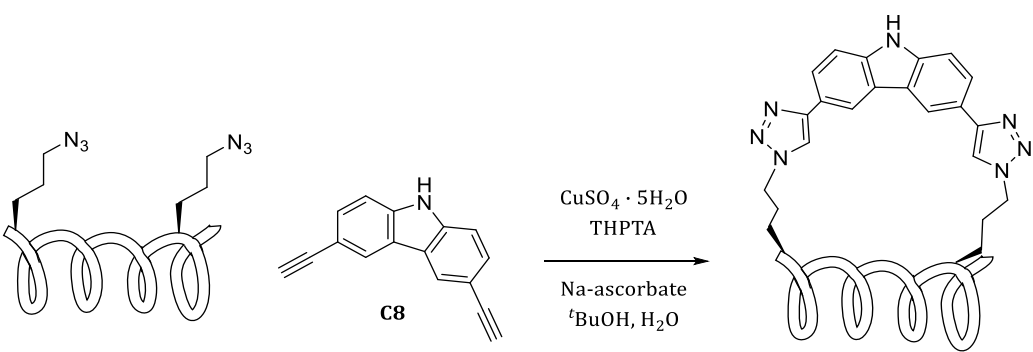
enhancement of helicity results in an improved binding affinity for the BH3 peptides; however, the majority of reports indicate that greater helicity results in greater binding.^{176,186,239}

Consequently, alternative stapling positions to the *i,i+4* were considered to impart greater helicity on the peptides. The use of *i,i+11* stapling in 2C CuAAC is highly underexplored with only one study done on one model peptide sequence: a 3,6-diethynyl-9H-carbazole used in combination with azido-ornithine amino acids was the most effective, among other stapling combinations explored, at inducing α -helical structures.²⁴⁰ In addition, the proteolytic stability as a result of constraining 11 residues instead of 4 may be improved further. Encouraged by this evidence, we decided to synthesise *i,i+11* Bim, Bad, and Bid BH3 peptides using a carbazole linker as the staple.

5.4.3.1.1. Design and synthesis of *i,i+11* stapled peptides

The *i,i+11* stapled peptides were designed from the X-ray structures available. The staple was placed on those residues that did not contribute to the binding and that are solvent exposed to avoid clashes with other residues on the peptide or the target proteins. A summary of the *i,i+11* stapled peptides proposed, their corresponding WT peptides, a schematic representation of the stapling reaction, and the reference PDB codes can be found in Table 16.

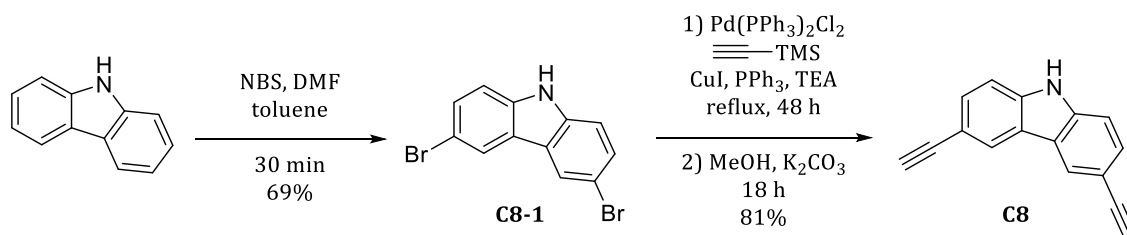
Table 16 – WT and *i,i+11* Bim, Bad, Bid stapled peptides subject of this work.



Protein	PDB	WT peptide	Azido-linear peptide	Stapled peptide	Conversions ^a
Bim	2YQ7 ²⁴¹	IAQELRRIGDEFNAYYARR (P10)	IAXELRRIGDEFNXYXA (P14)	P14-C8	NA
Bad	1G5J ²⁴²	RYGRELRRMSDEFVDSF (P12)	XYGRELRRMSDXFVDSF (P15)	P15-C8	90%
Bid	5C3F ²⁴³	IIRNIARHLAQVGDSDRS (P13)	IIRNIAXHLAQVGDSDXS (P16)	P16-C8	60%

All the peptides present an amide at the C-terminus and are capped with an acetyl group at the N-terminus. X in the linear peptides refers to the azido-ornithine (12). ^a Conversion of stapling reactions as determined by LCMS of the crude reaction mixture. NA = conversions of stapling reaction not available due to complicated LCMS chromatogram

Synthesis of the a 3,6-diethynyl-9*H*-carbazole staple (**C8**) required for peptide stapling was carried out according to literature reports.²⁴⁴ The synthetic route commenced from the bromination of the commercially available carbazole in the presence of NBS (Scheme 30). The reaction afforded the desired intermediate **C8-1** which was then subjected to a Sonogashira coupling in the presence of TMS-acetylene, Pd(PPh₃)₂Cl₂, PPh₃, and CuI to afford the TMS-protected analogue of **C8**. The latter compound underwent basic treatment in the presence of K₂CO₃ and MeOH to afford the desired staple **C8** in 81% yield.



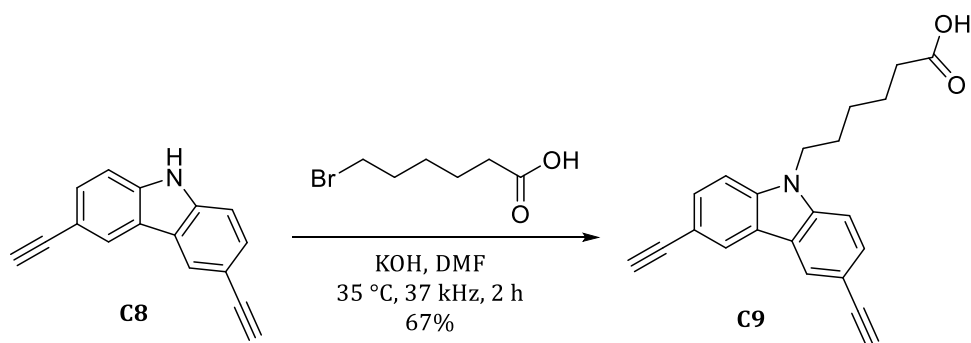
Scheme 30 - Synthetic route leading to the carbazole staple C8.

The synthesis of **12** was described in section 5.4.2.1.

Peptides were assembled using microwave-assisted SPPS performing double coupling for all amino acids with the exception of azido amino acid (**12**), which was coupled using longer, single coupling under MW.

The crude mixture of Bim-derived peptide **P14** presented solubility issues prior to purification as observed for its analogue **P9**. High dilution and multiple filtrations resolved the issue with loss of crude material.

Assessment of the *i,i+4* Bim-BH3 stapled peptides in platelets showed that the peptides required a functionalised staple (preferably a tri-arginine tag) to gain cytosolic entry. It was decided to functionalise the staple **C8** using SPPS, so as to make it easily accessible. To achieve that, a chemical handle in the form of carboxylic acid was introduced. It was decided to employ 6-bromo hexanoic acid so that it would act as a functionalisable spacer. Reaction of **C8** with KOH under ultrasonic waves at 35 °C for 2 hours afforded the title staple **C9** bearing a carboxylic acid as a functional handle (Scheme 31).



Scheme 31 - Synthesis of functionalisable staple **C9** starting from **C8**.

In a similar method for functionalising the CK2 peptides described in Chapter 4, a tri-D-arginine tag was chosen as the tag to attach to **C9** to improve cell permeability and stability to proteases of the overall construct. However, **C9** appeared to be unstable under the acidic conditions used to cleave the peptide from the resin. After capping the tri-peptide with **C9**, the TFA cleavage cocktail was added to the resin either at room temperature or 42 °C: the resin instantly turned black, and LCMS could detect no desired product once the crude reaction mixture was concentrated and triturated with Et₂O. To confirm whether the instability could be attributed to the staple itself, **C9** was subjected to treatment with TFA in solution leading to the same problem: formation of a black product that was insoluble in any NMR solvents preventing its characterisation. An alternative, milder cleavage cocktail was used to cleave the peptide from the resin.²⁴⁵ However, the TFA-free cocktail (containing 0.1 M HCl in hexafluoroisopropanol) led to the same issue. Before attempting the time-consuming synthesis of the functionalised staple in solution, it was decided to investigate the secondary structure of the *i,i+11* stapled peptides using CD.

5.4.3.1.2. Helicity of *i,i + 11* stapled peptides

CD spectra for all the *i,i+11* stapled peptides and their corresponding linear WT peptides were recorded in a 50:50 mixture of H₂O/MeCN at a concentration of 100 μM and the results are shown in Figure 70.

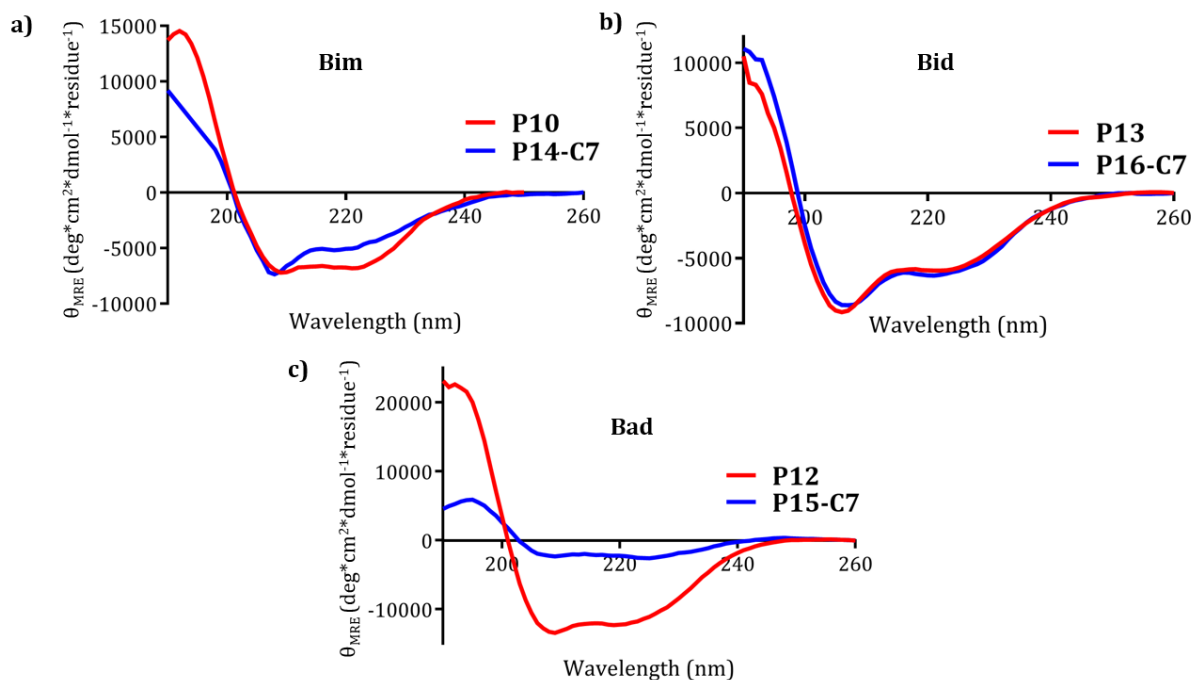


Figure 70 - Mean Residue Ellipticity (θ_{MRE}) of $i,i+11$ stapled BH3 peptides (blue) and corresponding linear WT peptides (red). a) Spectra of Bim-BH3 peptides; b) Spectra of Bid-BH3 peptides; c) Spectra of Bad-BH3 peptides.

The staple significantly disrupted the helicity of the Bad peptide (7% compared to 54% of the WT) whilst it did not affect the helicity of the Bid-BH3 peptide (17% compared to 18% of the WT). The $i,i+11$ stapling negatively affected the structure of the Bim-BH3 peptide even more than the previously used $i,i+4$ stapling (20% helicity for the WT, 10% for the $i,i+4$ and 7% for the $i,i+11$).

Considering the difficulties associated with the staple functionalisation and the fact that the $i,i+11$ stapling did not enhance the helicity of the peptides, it was decided not to pursue this strategy further.

5.4.3.2. Looking at $i,i+7$ stapling

The use of the $i,i+7$ stapling is well-established, and the combination of azido-ornithine amino acids (**12**) and 3,5-dialkyne benzene derivatives has been used on several occasions to induce α -helical structures to peptides with helical propensity.^{81,86,87} In addition, the 3,5-dialkyne benzoic acid staple (**C5**) has been straightforwardly functionalised on-resin in a variety of different ways.^{81,84,86,87} Taking into account the problems encountered with the $i,i+11$ stapling, it was decided to staple the BH3 peptides using the $i,i+7$ stapling technique to cross-link the side chains of azido-ornithine amino acids with the staple **C5**.

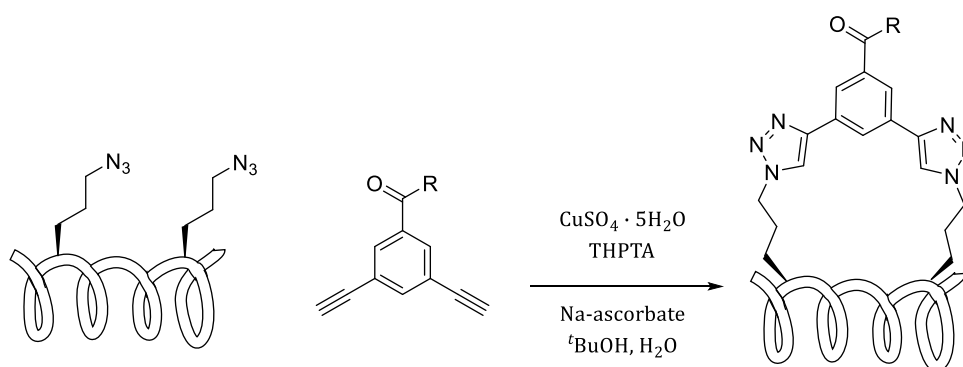
5.4.3.2.1. Design and synthesis of $i,i+7$ BH3 stapled peptides

In a similar method described for the $i,i+11$ stapled peptides, the design of the new peptides was based on the available X-ray structures of the proteins of interest. The staple was placed in a way

to avoid clashes with other residues on the peptide or the target proteins. A list of the $i,i+7$ stapled peptides synthesised, their corresponding linear peptides, the reference PDB codes, and a schematic representation of the stapling reaction can be found in Table 17.

The synthesis of the peptides presented in the table was achieved using double coupling for all amino acids. Solubility problems were encountered with the crude **P17-C5** peptide which, as previously, required high dilution and filtrations before purification. Percentage conversion of the stapling reactions are reported in Table 17.

Table 17 – $i,i+7$ stapled and linear Bim, Bad, Bid peptides subject of this work.



Protein	PDB	Azido-linear peptide	Staple	Conversion
			R = -OH (P17-C5)	92%
Bim	2YQ7 ²⁴¹	IAQXLRRIGDXFNAYYA (P17)	R = -NH-(Ahx) ₂ -[(D)R] ₃ -NH ₂	92%
			(P17-F1C5)	
			R = -OH (P18-C5)	68%
Bad	1G5J ²⁴²	YGRXLRRMSDXFVDSF (P18)	R = -NH-(Ahx) ₂ -[(D)R] ₃ -NH ₂	77%
			(P18-F1C5)	
			R = -OH (P19-C5)	97%
Bid	4QVE ²⁴⁶	IIRXIARHLAXVGDSMDRS (P19)	R = -NH-(Ahx) ₂ -[(D)R] ₃ -NH ₂	72%
			(P19-F1C5)	

All the peptides present an amide at the C-terminus and are capped with an acetyl group at the N-terminus. X in the azido-linear peptides refers to azido-ornithine as shown in the reaction scheme. R on the 3, 5 dialkyne benzene ring is a functional group as specified in the column "Staple".^a Conversion of stapling reactions as determined by LCMS of the crude reaction mixture.

5.4.3.2.2. Helicity of $i,i+7$ stapled peptides

As for the other peptides, the secondary structure of the $i,i+7$ stapled BH3 peptides was investigated using CD spectrometry. Only the structure of the peptides without a functional tag was analysed as it was envisioned that the tag would interfere with the analysis. The results are shown in Figure 71.

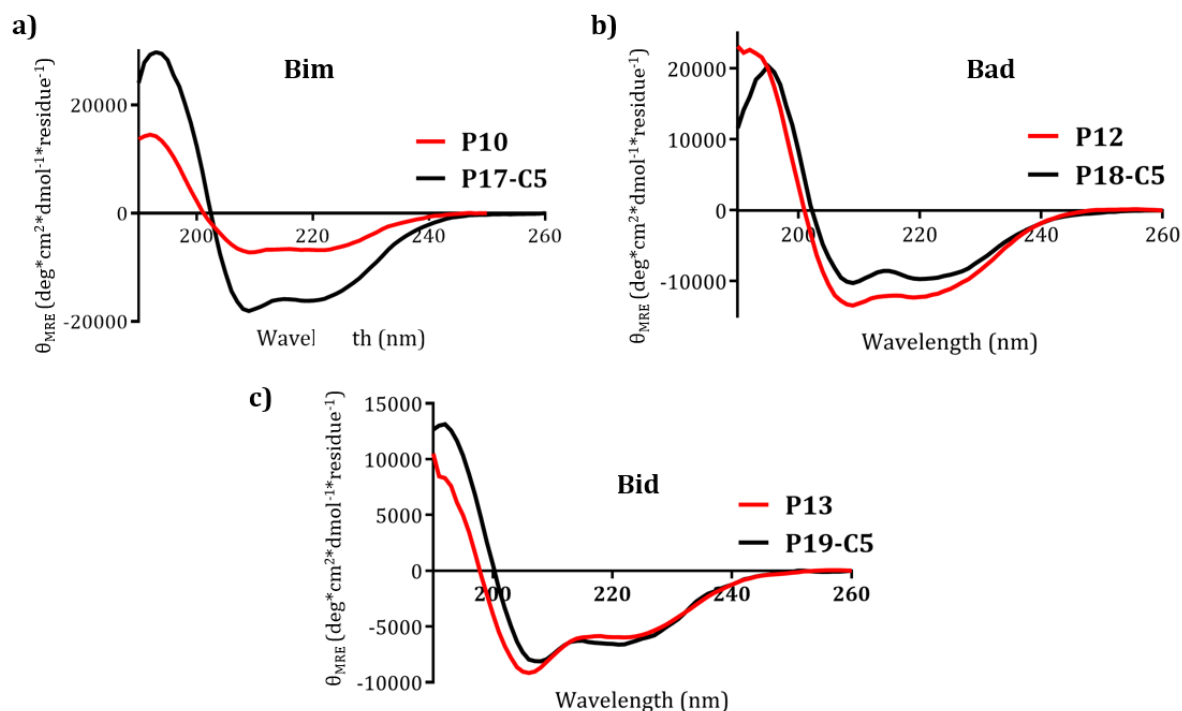


Figure 71 - CD spectra of *i,i+7* stapled BH3 peptides (black) and corresponding linear wild-type peptides (red). a) Spectra of Bim-BH3 peptides; b) Spectra of Bad-BH3 peptides; c) Spectra of Bid-BH3 peptides.

The results showed that the *i,i+7* stapling was effective at enhancing the helicity of the Bim-BH3 peptide (47% helicity for the stapled peptide and 20% for the WT) whilst did not affect the structures of the Bad (35% vs 28%) and Bid peptides (22% vs 17%) significantly.

With these peptides in hand, their effect on platelet activation and apoptosis will be investigated in a similar manner to that reported for the *i,i+4* Bim-BH3 peptides (*vide supra*, 5.4.2.3, 5.4.2.4).

5.5. Conclusions and future work

This work is the first to describe the use of functionalised stapled peptides to perturb and investigate signalling pathways in human platelets. Using a panel of model stapled peptides, it was found that the nature of the motif incorporated onto the staple impacts the ability of the peptides to enter the platelet cytosol and modulate activity. Utilising the functionalised staples that allowed the model peptide to permeate the platelet membranes, stapled *i,i+4* Bim peptides were synthesised to investigate *PS* exposure in platelets. The most promising peptide, **P9-F4C5**, showed a binding affinity of 26 nM for Bcl-x_L, and its bioactivity in platelets was comparable to that of the small molecule Bad mimetic ABT-737. Importantly, unlike ABT-737, stapled peptide Bim-BH3 mimetics caused platelet activation, demonstrating a differential activation of signalling pathways.

In order to dissect the role of each BH3-only protein in platelet apoptosis and activation, *i,i+7* Bad, Bim and Bad peptides have been synthesised, and their bioactivity in platelets will be studied.

Perturbation of the Bcl-2 pathway demonstrates the considerable potential of functionalised stapled peptides to investigate other PPIs in human platelets and for future development of new antiplatelet drugs. One of the advantages of this technology over small molecule use is the ease of design and synthesis of the peptides, as they are a mimetic of the natural components. Moreover, limitations such as the lack of membrane permeability and poor serum stability are overcome by the presence of the staple. The double click approach only requires one linear peptide to enable the generation of a variety of functionalised stapled peptides, which facilitates the exploration of various functionalities on the linker and thus the properties of the overall peptide. Most importantly, this methodology allows testing in human platelets directly, avoiding the inter-species difference, cost and time limitations of transgenic animal models.

Further work on the peptides developed in this project would involve co-immunoprecipitation assays to elucidate intraplatelet target engagement and rationalise the biological results obtained. In addition, Bcl-2 proteins are present in nucleated cells and therefore a way of targeting platelets selectively or under specific pathological conditions would be investigated to develop novel therapeutics. During this project, it was observed that the peptides require a cell-penetrating tag to gain platelet entrance. Consequently, a homing-peptide that recognises membrane receptors expressed on the membrane of platelets but not on the membrane of nucleated cells could be incorporated on the staple to gain selectivity for the desired cell type. An alternative approach could see the use of a thrombin-sensitive tag attached to a cell-impermeable sequence. When the thrombin levels increase, such as during cardiovascular

thrombotic event, the thrombin-sensitive tag is recognised by the thrombin protease, which will cleave the cell-impermeable tag off. This will reveal the stapled cell-permeable peptide, which would be able to exert its bioactivity under pathological conditions only.

SECTION III

Experimental

CHAPTER 6:

Chemistry Experimental

All experiments were carried out in oven-dried glassware under an atmosphere of N₂ using distilled solvents unless otherwise stated.

Reagents: Chemicals were purchased from commercial sources and used without further purification.

Yield: refer to chromatographically and spectroscopically pure compounds unless otherwise stated and are reported as follows: mass, moles, percentage.

Temperature: Reaction temperatures of 0 °C were maintained using an ice-water bath and those of -78 °C using dry-ice and acetone; room temperature (rt) refers to 20-25 °C.

Flash chromatography: Analytical thin layer chromatography was carried out on SiO₂ Merck Kieselgel 60 F254 plates with visualisation either by ultraviolet light or staining with potassium permanganate or ninhydrin dips made using standard procedures. Retention factors (*R_f*) are quoted to 0.01. Flash column chromatography was performed using silica gel 60 (230-400 mesh), or standardised aluminium oxide 90 (150 mesh), under a positive pressure of N₂. Eluent systems are expressed in % v/v. NH₃ used in flash chromatography is a 7 N solution in MeOH.

Nuclear Magnetic Resonance (NMR): ¹H, ¹³C and ¹⁹F NMR spectra were recorded using an internal deuterium lock at ambient probe temperatures on the following instruments: Bruker Avance III 400 MHz HD Smart Probe Spectrometer, Bruker Avance III 400 MHz HD Spectrometer, Bruker 400 MHz QNP Cryoprobe Spectrometer, Bruker 500 MHz DCH Cryoprobe Spectrometer, Bruker Avance III 500 MHz HD Smart Probe Spectrometer. The following deuterated solvents were used: chloroform (CDCl₃), dimethylsulfoxide (DMSO-d₆) and methanol (CD₃OD). ¹H-NMR chemical shifts (δ) are quoted in ppm to the nearest 0.01 ppm, relative to the residual non-deuterated solvent peak and coupling constants (*J*) are quoted to the nearest 0.1 Hertz (Hz). ¹³C-NMR chemical shifts are quoted to the nearest 0.1 ppm, relative to the solvent peak and coupling constants are quoted to the nearest 0.1 Hz. ¹⁹F-NMR chemical shifts are quoted to the nearest 0.1 ppm. Spectral data is reported as follows: chemical shift, integration, multiplicity (s, singlet; d, doublet; t, triplet; q, quartet; sept, septet; m, multiplet; br, broad; or as a combination of these *e.g.* br s, dd, dt), coupling constant(s) and assignment. The numbering system used in the assignments does not necessarily follow the IUPAC convention. Assignment of all spectra is supported by DEPT, COSY, HSQC and HMBC or done by analogy to fully assigned spectra of closely related compounds.

Infra-red spectroscopy (IR): Infra-red spectra were recorded neat on a Perkin Elmer Spectrum One FT-IR spectrometer fitted with an Attenuated Total Reflectance (ATR) sampling accessory. Selected absorption maxima (ν_{\max}) are quoted in wavenumbers (cm⁻¹) with the following abbreviations: w, weak; m, medium; s, strong; vs, br, broad.

Liquid chromatography-mass spectrometry (LCMS): LCMS was carried out using a Waters ACQUITY H-Class UPLC with an ESCi Multi-Mode Ionisation Waters SQ Detector 2 spectrometer using MassLynx 4.1 software; ESI refers to the electrospray ionisation technique; LC system: solvent A: 2 mM NH₄OAc in H₂O/MeCN (95:5); solvent B: MeCN; solvent C: 2% formic acid; column: ACQUITY UPLC® CSH C18 (2.1 mm × 50 mm, 1.7 μm, 130 Å) at 40 °C; gradient: 5 – 95% B with constant 5% C over 1 min at flow rate of 0.6 mL/min; Injection volume: 5 μL. Chromatographs were monitored by absorbance using diode array detection at a wavelength range of 190-600 nm, interval 1.2 nm.

High resolution mass spectrometry (HRMS): HRMS was carried out using a Waters LCT Premier® Time of Flight (ToF) mass spectrometer or the ThermoFinnigan Orbitrap Classic mass spectrometer. Reported mass values are within the error limits of ± 5 ppm mass units. ESI refers to the electrospray ionisation technique. ASAP refers to the atmospheric solids analysis probe ionisation technique.

Analytical HPLC: Chromatographs were obtained on an Agilent 1260 Infinity® using a reversed-phase Supelcosil ABZ+PLUS column (150 mm x 4.6 mm, 3 μm) eluting with a linear gradient system (solvent A: 0.05% (v/v) TFA in water, solvent B: 0.05% (v/v) TFA in MeCN) over 15 min, unless otherwise stated, at a flow rate of 1 mL/min. HPLC was monitored by UV absorbance at 220 and 254 nm.

Preparative HPLC: Preparative HPLC was carried out on an Agilent 1260 Infinity® using a reversed-phase Supelcosil ABZ+PLUS column (250 mm x 21.2 mm, 5 μm) eluting with a linear gradient system (solvent A: 0.1% (v/v) TFA in water, solvent B: 0.05% (v/v) TFA in MeCN) over 20 min at a flow rate of 20 mL/min. HPLC was monitored by UV absorbance at 220 and 254 nm.

Automated Solid Phase Peptide Synthesis (SPPS): automated SPPS was carried out on solid-phase using a Fmoc-protecting group strategy on a CEM Liberty Blue® automated microwave peptide synthesiser.

Microwave irradiation: Microwave irradiation was performed in a Biotage® microwave reactor.

Melting points: Melting points were measured using a Büchi melting point B545 apparatus and are uncorrected.

6.1. Experimental synthetic details

6.1.1. Small molecules

General method 1: Phenol triflation.²⁰⁴

To a solution of phenol (1.0 equiv) in anhydrous CH_2Cl_2 (reaction molarity 3.00 mM) was added anhydrous pyridine (1.6 equiv). The solution was cooled to 0 °C and trifluoromethanesulfonic anhydride (1.4 equiv) was added dropwise over 30 minutes. The reaction was allowed to warm to rt and stirred for 16 hours. CH_2Cl_2 was removed under reduced pressure, the residue was diluted with H_2O and extracted with EtOAc. The organic layer was washed successively with 10% aqueous HCl, 5% aqueous NaHCO_3 , brine, dried (MgSO_4), and concentrated under reduced pressure. The crude residue was purified by column chromatography to yield the desired product.

General method 2a: Suzuki-Miyaura coupling.²⁰³

To a solution of aryl triflate (1.6 equiv) and the appropriate boronic acid (1.0 equiv) in anhydrous DME (0.16 M) was added 2 M aqueous Na_2CO_3 solution (1.6 equiv). The reaction mixture was degassed by bubbling N_2 through the solution for 15 minutes before the addition of $\text{Pd}(\text{PPh}_3)_4$ (2.0-2.5 mol%). The solution was refluxed for 3-7 hours. The reaction was allowed to cool to room temperature and then diluted with EtOAc and H_2O . The aqueous phase was extracted with EtOAc (3 ×). The combined organic extracts were washed with brine, dried (MgSO_4), concentrated under reduced pressure, and purified by column chromatography to yield the desired product.

General method 2b: Suzuki-Miyaura coupling.²¹⁰

To a solution of the appropriate boronic acid (1.5 equiv) and the appropriate aryl bromide (1.0 equiv) in 1,4-dioxane was added 1.75 M aqueous K_3PO_4 solution (1.7 equiv). The mixture was degassed by bubbling N_2 for 10 minutes before PCy_3 (0.5 mol%) and $\text{Pd}_2(\text{dba})_3$ (0.25 mol%) were added. The mixture was refluxed for 4-8 hours. The crude mixture was diluted with EtOAc and filtered through Celite. The organic phase was washed with H_2O and dried (MgSO_4). The solvent was evaporated, and the product purified by column chromatography to yield the desired product.

General method 2c: Suzuki-Miyaura coupling.²¹³

A mixture of the aryl triflate (1.0 equiv), appropriate boronic acid (1.2 equiv), $\text{PdCl}_2(\text{dppf})\cdot\text{CH}_2\text{Cl}_2$ (1 mol%) and K_3PO_4 (2.0 equiv) were solvated with DME (0.2 M), EtOH (1.7 M) and

H₂O (2.5 M). The reaction mixture was degassed by bubbling N₂ through the solution for 15 minutes and then heated in the MW to 110 °C (2-3 hours) or refluxed (1-6 hours). The reaction was allowed to cool to room temperature, filtered through Celite™, washed with Et₂O and the solvent removed under reduced pressure. The residue was dissolved in Et₂O and H₂O, the phases were separated, and the organic layer was extracted with Et₂O (3 ×). The combined organic extracts were washed with brine, dried (MgSO₄), filtered, and concentrated under reduced pressure. The crude product was then purified by flash column chromatography or preparative TLC to yield the desired product.

General method 3: Nitrile reduction using LiAlH₄.¹⁹⁷

To a suspension of LiAlH₄ (2.0 equiv) in Et₂O (0.27 M) at 0°C was added AlCl₃ (1.0 equiv) and the mixture stirred for 10 minutes. The appropriate benzonitrile (1.0 equiv) was added and the reaction mixture stirred at rt for 30 minutes and then refluxed for 16 hours. The mixture was cooled to 0 °C, diluted with EtOAc and a saturated aqueous solution of potassium sodium tartrate tetrahydrate was added. The suspension was stirred for 1 hour and then poured into a 2 M aqueous solution of Na₂CO₃. The aqueous phase was extracted with EtOAc (3 ×). The combined organic phases were washed with brine and dried (MgSO₄). The product was purified by column chromatography to yield the desired product.

General method 4: Nitrile reduction using Raney Nickel and H₂.²¹²

To a solution of the appropriate nitrile in NH₃ (8% in MeOH, 0.15 M) was added a spatula of Raney Nickel (slurry solution). An atmosphere of H₂ was applied and the reaction mixture was vigorously stirred at rt for 16 hours. After this time, EtOAc was added and the suspension filtered under gravity. The filtrate was concentrated under reduced pressure, and the crude material purified by column chromatography to yield the desired product.

General method 5: Formation of hydrochloric amine salts.²⁴⁷

The appropriate amine (1.0 equiv) was dissolved in the minimum amount of anhydrous CH₂Cl₂ and HCl (2 M in 1,4-dioxane, 10 equiv) was added dropwise. The reaction mixture was stirred at rt for 1 hour. The resulting precipitate was filtered and washed with cold Et₂O to afford the desired salt.

General method 6: Reductive amination.²¹⁴

Anhydrous DCE (0.33 M) was added to a flask charged with the appropriate aldehyde (1.0 equiv), the amine (1.5 equiv) and molecular sieves (4 Å). The mixture was stirred at rt for 2.5 hours. After this time NaBH(OAc)₃ (1.4 equiv) was added in three portions over 15 minutes and the mixture stirred at rt for 16 hours. The reaction was quenched with a NaHCO₃ aqueous

solution and the product extracted with EtOAc (3 ×). The combined organic phases were dried (Mg₂SO₄), and the solvent evaporated under reduced pressure. The residue was purified by column chromatography to afford the free amine.

General method 7: Fmoc protection of primary amine.²⁴⁸

Solid NaHCO₃ (4.0 equiv) was dissolved in H₂O (0.2 M) and the solution was diluted with MeCN (0.2 M). To the solution were added the amine (1.0 equiv) and N-(9-fluorenylmethoxycarbonyloxy)succinimide (1.5 equiv). The mixture was stirred at rt for 24-48 hours. The organic solvent was removed under reduced pressure, and the aqueous phase was washed with CH₂Cl₂ (3 ×). The aqueous phase was adjusted to pH 2 with concentrated HCl to form a white precipitate. The precipitate was filtered, and the aqueous phase extracted with EtOAc (3 ×). The organic phases were combined with the precipitate, dried (MgSO₄), and the solvent evaporated under reduced pressure. The crude material was purified by column chromatography to yield the desired product.

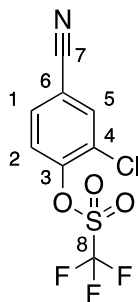
General method 8: TMS deprotection.²²⁰

Aqueous 6 M KOH (10 equiv) was added to a stirred solution of the TMS-protected alkyne (1 equiv) in MeOH (0.45 M). The mixture was stirred at rt for 18 hours. MeOH was removed under a stream of N₂ and the aqueous phase was acidified to pH 4 with HCl (6 N) and extracted with EtOAc (3 ×). The combined organic phases were dried (MgSO₄), and the solvent evaporated under reduced pressure to yield the desired compound.

General method 9: Addition of TMS-alkyne to esters and anhydride.²⁴⁹

Trimethylsilylacetylene (1.5-3 equiv) in anhydrous THF (1.2 M) was cooled down to -78 °C. ⁿBuLi 1.6 M in hexane (3 equiv) was added dropwise and the reaction mixture was stirred at -78 °C for 1 hour. After this time, the reaction was warmed to 0 °C for 10 minutes and then cooled down to -78°C. The appropriate benzoate or aldehyde (1 equiv) in anhydrous THF (1.1 M) was added over 10 minutes and the mixture stirred at rt for 2 hours. After this time, the reaction was quenched with NH₄Cl (saturated aqueous) solution, THF removed under a stream of N₂ and the product extracted with Et₂O (3 ×). The combined organic phases were dried (MgSO₄), and the residue purified by flash chromatography to give the desired product.

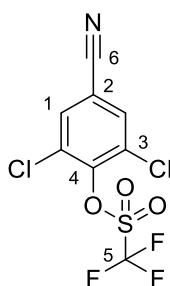
6.1.1.1. Fragment-based drug design

2-Chloro-4-cyanophenyl trifluoromethanesulfonate (**1a**)

Prepared following *general method 1* using 3-chloro-4-hydroxybenzonitrile (2.00 g, 13.0 mmol), CH_2Cl_2 (40.0 mL), pyridine (3.20 mL, 39.6 mmol) and trifluoromethanesulfonic anhydride (2.84 mL, 16.9 mmol). After work-up, the crude residue was purified by column chromatography on silica gel (5% EtOAc/hexane) to yield **1a** as a white crystalline solid (3.37 g, 11.8 mmol, 91%).

R_f = 0.68 (20% EtOAc/hexane); M_p = 61-62 °C; δ_H (400 MHz, CDCl_3): 7.88 (1H, d, J = 2.0 Hz, H5), 7.70 (1H, dd, J = 8.6, 2.0 Hz, H1), 7.53 (1H, d, J = 8.6 Hz, H2); δ_C (101 MHz, CDCl_3): 148.5 (C3), 134.9 (C5), 132.2 (C1), 128.9 (C4), 124.2 (C2), 118.5 (q, J = 227.3 Hz, C8), 116.0 (C7), 114.9 (C6); δ_F (376 MHz, CDCl_3): -74.1 ν_{max} : 2245 (C≡N, m), 1575 (C=C, w), 1478 (C=C, m); **LCMS**: R_t = 1.56 min, [M-H]⁻: 284.0.

Characterisation data in accordance with literature.¹⁹⁸

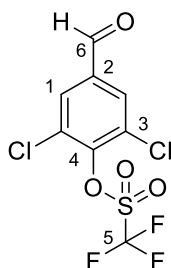
2,6-Dichloro-4-cyanophenyl trifluoromethanesulfonate (**1b**)

Prepared following *general method 1* using 3,5-dichloro-4-hydroxybenzonitrile (500 mg, 2.66 mmol), CH_2Cl_2 (2.40 mL), pyridine (300 μL , 4.26 mmol) and trifluoromethanesulfonic anhydride (600 μL , 3.46 mmol). After work-up, the crude residue was purified by column chromatography on silica gel (10% EtOAc/hexane) to yield **1b** as white solid (630 mg, 1.97 mmol, 74%).

R_f = 0.40 (10% EtOAc/hexane); M_p = 93-96 °C; δ_H (400 MHz, DMSO-d_6): 8.50 (2H, s, H1); δ_C (101 MHz, DMSO-d_6): 144.7 (C4), 134.4 (C1), 129.2 (C3), 117.3 (q, J = 225.3 Hz, C5), 115.6 (C6), 113.9

(C2); δ_{F} (376 MHz, CDCl_3): -71.7; ν_{max} : 2238 ($\text{C}\equiv\text{N}$, m), 1204 ($=\text{C}-\text{H}$, s); LCMS Rt = 4.07 min, $[\text{M}+\text{K}]^+$ 358.21.

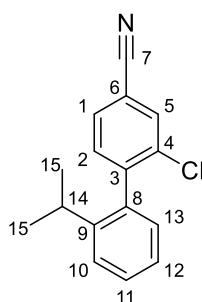
2,6-Dichloro-4-formylphenyl trifluoromethanesulfonate (**1c**)



Prepared following *general method 1* using 3,5-dichloro-4-hydroxybenzaldehyde (200 mg, 1.05 mmol), trifluoromethanesulfonic anhydride (260 μL , 1.52 mmol), pyridine (150 μL , 1.88 mmol) and CH_2Cl_2 (1.50 mL). After work-up, the crude material was purified by column chromatography on silica gel (10% EtOAc/hexane) to yield **1c** as a colourless oil (191 mg, 600 μmol , 57%).

R_{f} = 0.19 (10% EtOAc/hexane); δ_{H} (500 MHz, CDCl_3): 9.95 (1H, s, H6), 7.95 (2H, s, H1); δ_{C} (126 MHz, CDCl_3): 187.8 (C6), 146.2 (C4), 136.1 (C2), 130.8 (C3), 130.2 (C1), 117.0 (q, J = 320 Hz, C5); δ_{F} (376 MHz, CDCl_3): -71.3; ν_{max} : 1706 ($\text{C}=\text{O}$, s), 1429 ($\text{H}-\text{C}=\text{O}$, s), 1210 ($\text{C}-\text{F}$), 1129 (SO_2 , s); HRMS (ESI+): m/z found $[\text{M}+\text{H}]^+$ 322.9153, $\text{C}_8\text{H}_4\text{O}_4^{35}\text{Cl}_2\text{F}_3\text{S}$ required 322.9159 (Δ -1.9 ppm).

2-Chloro-2'-isopropyl-[1,1'-biphenyl]-4-carbonitrile (**2a**)

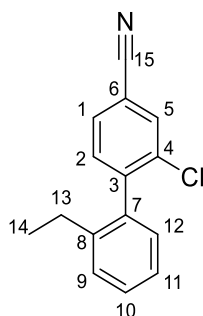


Prepared following *general method 2a* using (2-isopropylphenyl)-boronic acid (50.0 mg, 230 μmol), 2 M aqueous Na_2CO_3 solution (300 μL , 530 μmol), DME (5.00 mL) and $\text{Pd}(\text{PPh}_3)_4$ (10.5 mg, 10.0 μmol). The reaction was refluxed for 3 hours. After work-up, the crude material was purified by column chromatography on silica gel (20% EtOAc/hexane) to yield **2a** as a colourless oil (40.0 mg, 150 μmol , 85%).

R_{f} = 0.25 (20% EtOAc/hexane); δ_{H} (400 MHz, CD_3OD): 7.94 (1H, dd, J = 1.6, 0.3 Hz, H5), 7.74 (1H, dd, J = 7.9, 1.6 Hz, H1), 7.45-7.40 (3H, m, H2, H11, H12), 7.27-7.25 (1H, m, H13), 7.03 (1H, ddd, J = 7.2, 1.8, 0.7 Hz, H10), 2.58 (1H, sept, J = 6.7 Hz, H14), 1.20 (3H, d, J = 6.7 Hz, H15), 1.07 (3H, d, J

= 6.7 Hz, H15); δ_c (101 MHz, CD₃OD): 147.5 (C3 or C8), 147.3 (C3 or C8), 138.0 (C9), 135.9 (C4), 133.9 (C5), 133.7 (C2), 131.6 (C1), 130.2 (C11 or 12), 130.0 (C10), 126.8 (C13), 126.6 (C11 or 12), 118.4 (C7), 113.9 (C6), 31.7 (C14), 24.8 (C15), 23.4 (C15); ν_{\max} : 2962 (=C-H, m), 2326 (C≡N, m), 1473 (CH₃, m), 1383 (CH₃, m); **HRMS** (ESI+): m/z found [M]⁺ 256.0893, C₁₆H₁₄N³⁵Cl required 256.0893 (Δ 0.0 ppm).

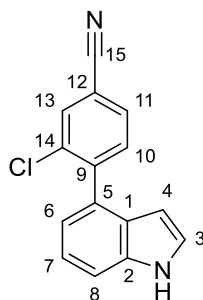
2-Chloro-2'-ethyl-[1,1'-biphenyl]-4-carbonitrile (**2b**)



Prepared following *general method 2a* using 3-chloro-4-bromobenzonitrile (300 mg, 1.39 mmol), 2-ethylphenylboronic acid (208 mg, 1.39 mmol), Pd(PPh₃)₄ (80 mg, 0.07 mmol), K₂CO₃ (383 mg, 2.77 mmol), DME (3.0 mL) and H₂O (1.0 mL). The reaction was refluxed for 4 hours. After work-up, the crude product was purified by flash column chromatography (10% EtOAc/PE 40-60) to yield **2b** as a clear oil (206 mg, 0.85 mmol, 61%).

R_f = 0.40 (10% EtOAc/PE 40-60); δ_H (400 MHz, CDCl₃): 7.79 (1H, d, J = 1.5 Hz, H5), 7.62 (1H, dd, J = 7.9, 1.5 Hz, H1), 7.45-7.36 (3H, m, H2, H10, H11), 7.30 (1H, app. td, J = 7.5, 1.7 Hz, H12), 7.10 (1H, dd, J = 7.5, 0.9 Hz, H9), 2.56-2.33 (2H, m, H13), 1.10 (3H, t, J = 7.6 Hz, H14); δ_c (101 MHz, CDCl₃): 145.8 (C8), 141.7 (C3), 137.1 (C4), 134.8 (C7), 132.8 (C5), 132.2 (C1), 130.2 (C2), 129.1 (C9), 129.0 (C10), 128.6 (C11), 125.9 (C12), 117.6 (C15), 112.7 (C6), 26.2 (C13), 15.1 (C14); ν_{\max} : 2967 (=C-H, m), 2232 (C≡N, m), 1472 (CH₃, m), 1445 (CH₃, m); **HRMS** (ESI+): m/z found [M+H]⁺ 242.0735, C₁₅H₁₃N³⁵Cl required 242.0737 (Δ -0.8 ppm).

3-Chloro-4-(1H-indole-4-yl)benzonitrile (**2c**)

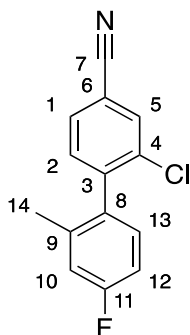


Prepared following *general method 2a* using 4-(1H-indole)-boronic acid pinacol ester (150 mg,

620 μmol), **1a** (125 mg, 440 μmol), 2 M aqueous Na_2CO_3 solution (700 μL , 1.32 mmol), DME (15.0 mL) and $\text{Pd}(\text{PPh}_3)_4$ (25.4 mg, 20.0 μmol). The mixture was refluxed for 3 hours. After work-up, the crude material was purified by column chromatography on silica gel (20% EtOAc/hexane) to yield **2c** as a dark orange oil (104 mg, 410 μmol , 67%).

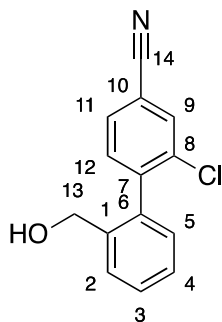
R_f = 0.44 (20% EtOAc/hexane); δ_{H} (400 MHz, CD_3OD): 7.94 (1H, d, J = 1.6 Hz, H13), 7.73 (1H, dd, J = 8.0, 1.6 Hz, H11), 7.61 (1H, d, J = 8.0 Hz, H10), 7.46 (1H, dd, J = 7.3, 0.8 Hz, H8), 7.27 (1H, d, J = 3.2 Hz, H3), 7.20 (1H, t, J = 7.3 Hz, H7), 6.99 (1H, dd, J = 7.3, 0.8 Hz, H6), 6.15 (1H, dd, J = 3.2, 0.8 Hz, H4); δ_{C} (101 MHz, CD_3OD): 146.8 (C2), 137.9 (C5), 135.4 (C14), 134.3 (C13), 134.0 (C10), 131.4 (C11), 130.9 (C3), 128.0 (C1), 126.5 (C12), 121.9 (C7), 121.0 (C6), 118.8 (C15), 113.4 (C8), 112.8 (C9), 101.5 (C4); ν_{max} : 3402 (N-H, br), 2231 ($\text{C}\equiv\text{N}$, m); **HRMS** (ESI+): m/z found $[\text{M}+\text{H}]^+$ 253.0545, $\text{C}_{15}\text{H}_{10}\text{N}_2^{35}\text{Cl}$ required 253.0533 (Δ 4.7 ppm).

2-Chloro-4'-fluoro-2'-methyl-[1,1'-biphenyl]-4-carbonitrile (**2d**)



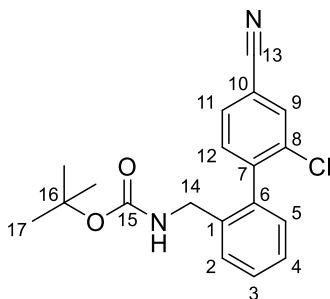
Prepared following *general method 2a* using compound **1a** (66.0 mg, 230 μmol), 4-fluoro-2-methylphenyl boronic acid (50.0 mg, 320 μmol), $\text{Pd}(\text{PPh}_3)_4$ (13.0 mg, 10.0 μmol), 2 M aqueous Na_2CO_3 solution (300 μL) and DME (5.00 mL). The reaction mixture was refluxed for 4 hours. After work-up, the crude product was purified by flash column chromatography on silica gel (0 to 5% EtOAc/hexane) to yield **2d** as a colourless oil (55.0 mg, 220 μmol , 97%).

R_f = 0.37 (20% EtOAc/hexane); δ_{H} (500 MHz, CDCl_3): 7.80 (1H, d, J = 1.4 Hz, H5), 7.64 (1H, dd, J = 7.8, 1.4 Hz, H1), 7.36 (1H, d, J = 7.8 Hz, H2), 7.11-6.97 (3H, m, H10, H12, H13), 2.12 (3H, s, H14); δ_{C} (126 MHz, CDCl_3): 163.8 (d, J = 242.5 Hz, C11), 144.9 (C3), 138.4 (d, J = 8.1 Hz, C9), 134.8 (C4), 133.5 (d, J = 3.3 Hz, C8), 132.9 (C5), 132.1 (C2), 130.5 (d, J = 8.6 Hz, C13), 130.3 (C1), 117.4 (C7), 116.9 (d, J = 21.3 Hz, C10), 112.9 (C6), 112.8 (d, J = 21.4 Hz, C12), 19.8 (d, J = 1.8 Hz, C14); δ_{F} (375 MHz, CDCl_3): 114.3; ν_{max} : 2233 ($\text{C}\equiv\text{N}$, w), 1383 (CH_3 , s); **HRMS** (ESI+): m/z found $[\text{M}+\text{H}]^+$ 246.0486, $\text{C}_{14}\text{H}_{10}\text{N}^{35}\text{ClF}$ required 246.0493 (Δ 2.8 ppm).

2-Chloro-[2'-(hydroxymethyl)-1,1'-biphenyl]-4-carbonitrile (**2e**)

Prepared following *general method 2a* using 2-hydroxymethyl-benzeneboronic acid (432 mg, 2.84 mmol), compound **1a** (600 mg, 2.20 mmol), Pd(PPh₃)₄ (128 mg, 110 μmol), 2 M aqueous Na₂CO₃ solution (2.80 mL) and DME (73.0 mL). The reaction was refluxed for 7 hours. After work-up, the crude material was purified by column chromatography on silica gel (20 to 30% EtOAc/hexane) to yield **2e** as a colourless oil (490 mg, 1.99 mmol, 90%).

R_f = 0.25 (20% EtOAc/hexane); **δ_H** (400 MHz, CDCl₃): 7.78 (1H, d, *J* = 1.6 Hz, H9), 7.63-7.60 (2H, m, H3 or H4, H11), 7.51 (1H, app. td, *J* = 7.8, 1.6 Hz, H3 or H4), 7.42 (1H, d, *J* = 7.8 Hz, H12), 7.39 (1H, app. td, *J* = 7.8, 1.0 Hz, H2 or H5), 7.14 (1H, dd, *J* = 7.8, 1.0, H2 or H5), 4.51 (1H, d, *J* = 12.9 Hz, H13), 4.38 (1H, d, *J* = 12.9 Hz, H13); **δ_C** (101 MHz, CDCl₃): 144.6 (C7), 138.3 (C1), 136.5 (C8), 134.5 (C6), 132.8 (C9), 132.1 (C12), 130.2 (C11), 129.3 (C3 or 4), 129.2 (C2 or 5), 128.2 (C3 or 4), 127.8 (C2 or 5), 117.4 (C14), 113.1 (C10), 62.9 (C13); **v_{max}**: 2988 (OH, br), 2226 (C≡N, w); **HRMS** (ESI⁺): *m/z* found [M+H]⁺ 244.0537, C₁₄H₁₁NO³⁵Cl required 244.0529 (Δ -3.3 ppm).

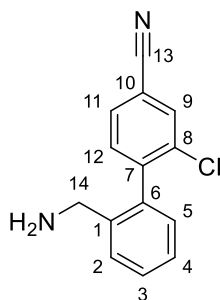
tert-Butyl ((2'-chloro-4'-cyano-[1,1'-biphenyl]2-yl)methyl)carbamate (**2f**)

Prepared following *general method 2a* using **1a** (131 mg, 460 μmol), 2-(((tert-butoxycarbonyl)amino)methyl)phenyl)boronic acid (150 mg, 590 μmol), 2 M aqueous Na₂CO₃ solution (700 μL, 1.38 mmol), DME (15.0 mL) and Pd(PPh₃)₄ (26.5 mg, 20.0 μmol). The reaction was refluxed for 3 hours. After work-up, the crude material was purified by column chromatography on silica gel (30% Et₂O/hexane) to yield **2f** as a colourless oil (140 mg, 410 μmol, 89%).

R_f = 0.22 (30% Et₂O/hexane); **δ_H** (400 MHz, CDCl₃): 7.77 (1H, d, *J* = 1.2 Hz, H9), 7.61 (1H, dd, *J* =

7.9, 1.2 Hz, H11), 7.44-7.43 (2H, m, H2, H3), 7.39-7.36 (2H, m, H4, H12), 7.11 (1H, d, $J = 7.3$ Hz, H5), 4.60 (1H, br s, NH), 4.10-4.08 (2H, m, H14), 1.39 (9H, s, H17); δ_c (101 MHz, CDCl_3): 155.6 (C15), 144.6 (C7), 136.9 (C6 or C8), 136.5 (C6 or C8), 134.5 (C10), 132.9 (C9), 131.9 (C12), 130.3 (C11), 129.3 (C2), 129.2 (C3), 128.2 (C4), 127.5 (C5), 117.3 (C13), 113.0 (C1), 80.0 (C16), 42.3 (C14), 28.4 (C17); ν_{max} : 3369 (N-H, br), 2978 (C-H, m), 2233 ($\text{C}\equiv\text{N}$, m), 1696 (C=O, s), 1247 (C-O, s); **HRMS** (ESI+): m/z found $[\text{M}+\text{H}]^+$ 265.0493, $\text{C}_{14}\text{H}_{11}^{35}\text{ClN}_2\text{Na}$ required 265.0503 (Δ -3.6 ppm).

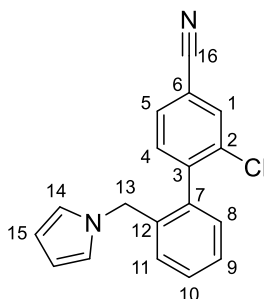
2'-(Aminomethyl)-2-chloro-[1,1'-biphenyl]-4-carbonitrile (**2f'**)



Prepared following a literature procedure.²⁵⁰ Compound **2f** (60.0 mg, 180 μmol) was dissolved in CH_2Cl_2 (600 μL) and treated with HCl (2 M in Et_2O , 1.80 mL, 3.70 mmol). The reaction was refluxed for 16 hours. The solvent was removed under reduced pressure, the residue diluted with cold Et_2O and the white solid collected by filtration. The salt was suspended in EtOAc and the free base obtained by addition of 2 M aqueous Na_2CO_3 solution (2 mL). The solvent was evaporated and the residue purified by column chromatography on silica gel (1:9:90 NH_3 : MeOH : CH_2Cl_2) to afford the product as an orange oil (45.0 mg, 170 μmol , 98%).

$R_f = 0.12$ (1:9:90 NH_3 : MeOH : CH_2Cl_2); δ_H (400 MHz, CDCl_3): 7.80 (1H, d, $J = 1.5$ Hz, H9), 7.64 (1H, dd, $J = 7.9, 1.5$ Hz, H11), 7.56 (1H, d, $J = 7.5$ Hz, H5), 7.47 (1H, td, $J = 7.5, 1.0$ Hz, H4), 7.40 (1H, d, $J = 7.9$ Hz, H12), 7.36 (1H, td, $J = 7.5, 1.0$ Hz, H3), 7.12 (1H, d, $J = 7.5$ Hz, H2), 3.69 (1H, d, $J = 14.6$ Hz, H14), 3.58 (1H, d, $J = 14.6$ Hz, H14); δ_c (101 MHz, CDCl_3): 145.1 (C7), 141.2 (C10), 136.5 (C8), 134.6 (C6), 132.9 (C9), 132.1 (C12), 130.2 (C11), 129.2 (C4), 129.2 (C5), 127.8 (C2), 126.9 (C3), 117.4 (C13), 112.9 (C1), 43.9 (C14); ν_{max} : 3373 (N-H, w), 2232 ($\text{C}\equiv\text{N}$, m); **HRMS** (ESI+): m/z found $[\text{M}+\text{Na}]^+$ 265.0493, $\text{C}_{14}\text{H}_{11}\text{N}_2^{35}\text{ClNa}$ required 265.0503 (Δ -3.6 ppm).

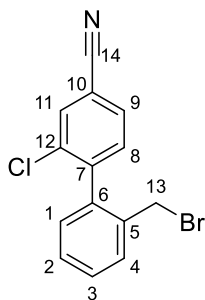
2'-((1*H*-Pyrrol-1-yl)methyl)-2-chloro-[1,1'-biphenyl]-4-carbonitrile (**2f''**)



Prepared following a literature procedure.²⁰⁹ NaO^tBu (47.0 mg, 490 μ mol) was added slowly to a solution of pyrrole (28.0 μ L, 410 μ mol) in MeCN (5.00 mL). The reaction mixture was stirred for 5 minutes before compound **2f'''** (150 mg, 490 μ mol) was added dropwise. The reaction was stirred at rt 16 hours. The solvent was then removed under reduced pressure, the reaction mixture was diluted with CH₂Cl₂ and washed with water (2 x 10 mL). The combined organic phases were washed with brine and dried (MgSO₄). The crude material was purified by column chromatography on silica gel (0 to 2% EtOAc/hexane) to yield **2f''** as a white film (132 mg, 453 μ mol, 93%).

R_f = 0.39 (10% EtOAc/hexane); **δ _H** (500 MHz, CDCl₃): 7.78 (1H, d, *J* = 1.5 Hz, H1), 7.55 (1H, dd, *J* = 7.9, 1.5 Hz, H5), 7.47-7.38 (2H, m, H8, H10), 7.18 (1H, d, *J* = 7.9 Hz, H4), 7.18-7.12 (2H, m, H9, H11), 6.38 (2H, app. t, *J* = 2.1 Hz, H14), 6.07 (2H, app. t, *J* = 2.1 Hz, H15), 4.88 (1H, d, *J* = 15.0 Hz, H13), 4.76 (1H, d, *J* = 15.0 Hz, H13); **δ _C** (126 MHz, CDCl₃): 144.1 (C7), 136.8 (C12), 135.8 (C3), 134.3 (C2), 132.7 (C1), 131.9 (C4), 130.4 (C5), 129.4 (C8), 129.3 (C9), 128.4 (C10), 128.0 (C11), 120.9 (C14), 117.3 (C16), 113.1 (C6), 108.5 (C15), 51.2 (C13); **ν _{max}**: 2359 (C≡N, w); **HRMS** (ESI+): *m/z* found [M+H]⁺ 293.0835, C₁₈H₁₄N₂³⁵Cl required 293.0846 (Δ -3.8 ppm).

2'-(Bromomethyl)-2-chloro-[1,1'-biphenyl]-4-carbonitrile (**2f'''**)

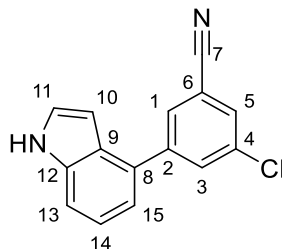


Prepared following a literature procedure.²⁰⁸ A solution of compound **2e** (100 mg, 410 μ mol) in anhydrous THF (2.50 mL) was cooled down to 0 °C. *N*-bromosuccinimide (153 mg, 860 μ mol) was added followed by PPh₃ (215 mg, 820 μ mol). The mixture was allowed to stir at room temperature for 5 hours. The reaction was quenched with saturated aqueous NaHCO₃ and the solvent removed under a stream of N₂. The residue was diluted with Et₂O and washed with water (2 x 10 mL). The combined organic phase was dried (MgSO₄), filtered and the solvent removed under reduced pressure. The crude material was purified by column chromatography on silica gel (20% EtOAc/hexane) to yield **2f'''** as a white solid (110 mg, 360 μ mol, 88%).

R_f = 0.30 (20% EtOAc/hexane); **Mp** = 73-76 °C; **δ _H** (400 MHz, CDCl₃): 7.80 (1H, d, *J* = 1.5 Hz, H11), 7.66 (1H, dd, *J* = 7.9, 1.5 Hz, H9), 7.53 (1H, dd, *J* = 7.6, 1.4 Hz, H1), 7.53 (1H, d, *J* = 7.9 Hz, H8), 7.46 (1H, td, *J* = 7.5, 1.4 Hz, H3), 7.41 (1H, app. td, *J* = 7.5, 1.4 Hz, H4), 7.15-7.13 (1H, m, H2), 4.39 (1H, d, *J* = 10.4 Hz, H13), 4.13 (1H, d, *J* = 10.4 Hz, H13); **δ _C** (101 MHz, CDCl₃): 143.7 (C7), 137.5 (C5), 135.4 (C12), 134.5 (C6), 132.9 (C11), 132.2 (C9), 130.7 (C3), 130.2 (C8), 129.8 (C1),

129.5 (C4), 128.8 (C2), 117.3 (C14), 113.4 (C10), 30.9 (C13); ν_{\max} : 2232 (C≡N, m), 1447 (C=C, m), 1384 (C-N, m); **HRMS** (ESI+): m/z found [M+H]⁺ 305.9683, C₁₄H₁₀N³⁵Cl⁷⁹Br required 305.9685 (Δ -0.7 ppm).

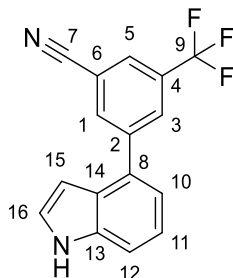
3-Chloro-5-(1H-indol-4-yl)benzonitrile (**2g**)



Prepared following *general method 2b* using 1-H-indole boronic acid (250 mg, 1.55 mmol), 3-bromo-5-chloro-benzonitrile (167 mg, 1.03 mmol), Pd₂(dba)₃ (9.50 mg, 10.0 μ mol), PCy₃ (7.00 mg, 20.0 μ mol), 1.75 M aqueous K₃PO₄ solution (1.00 mL) and dioxane (3.50 mL). The reaction was refluxed for 6 hours. After work-up, the crude material was purified by column chromatography on aluminium oxide gel (0 to 20% EtOAc/hexane) to yield **2g** as white solid (155 mg, 570 μ mol, 55%).

R_f = 0.24 (20% EtOAc/hexane); **Mp** = 134-137 °C; δ_{H} (500 MHz, CDCl₃): 8.41 (1H, br s, NH), 7.92 (1H, t, J = 1.6 Hz, H3), 7.88 (1H, t, J = 1.6 Hz, H5), 7.63 (1H, t, J = 1.6 Hz, H1), 7.48 (1H, d, J = 8.2 Hz, H15), 7.33-7.29 (2H, m, H11, H14), 7.15 (1H, d, J = 8.2 Hz, H13), 6.65-6.64 (1H, m, H10); δ_{C} (126 MHz, CDCl₃): 144.4 (C2), 136.3 (C12), 135.3 (C4), 133.2 (C3), 130.5 (C9), 130.4 (C5), 129.9 (C1), 125.7 (C8), 125.5 (C14), 122.4 (C11), 120.0 (C15), 117.8 (C7), 114.0 (C6), 111.9 (C13), 101.2 (C10); ν_{\max} : 3429 (N-H, m), 2236 (C≡N, w), 1566 (C=C, m); **HRMS** (ESI+): m/z found [M+H]⁺ 253.0524, C₁₅H₁₀N₂³⁵Cl required 253.0527 (Δ -1.0 ppm).

3-(1H-Indol-4-yl)-5-(trifluoromethyl)benzonitrile (**2h**)

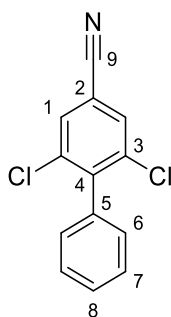


Prepared following *general method 2b* using 3-bromo-5-trifluoride benzonitrile (257 mg, 1.03 mmol), 1H-indole-4-boronic acid (250 mg, 1.55 mmol), Pd₂(dba)₃ (9.50 mg, 10.0 μ mol), PCy₃ (7.00 mg, 20.0 μ mol), 1.75 M aqueous K₃PO₄ solution (1.00 mL) and 1,4-dioxane (3.50 mL). The mixture was refluxed for 5 hours. After work-up, the residue was purified by column

chromatography on silica gel (0 to 10% EtOAc/hexane) to yield **2h** as a sticky, clear oil (110 mg, 360 μmol , 35%).

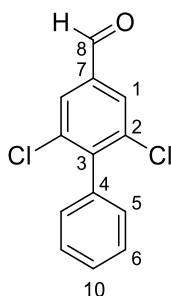
R_f = 0.24 (10% EtOAc/hexane); δ_H (500 MHz, DMSO- d_6): 11.42 (1H, br s, NH), 8.39 (1H, s, H3), 8.32 (1H, app. s, H5), 8.24 (1H, app. s, H1), 7.53-7.50 (1H, m, H12), 7.50-7.49 (1H, m, H10), 7.24-7.21 (2H, m, H11, H16), 6.75-6.54 (1H, m, H15); δ_C (126 MHz, DMSO- d_6): 143.8 (C2), 136.9 (C13), 136.0 (C1), 131.1 (q, J = 32.9 Hz, C4), 129.5 (C14), 129.4 (q, J = 3.6 Hz, C5), 127.9 (q, J = 3.6 Hz, C3), 127.4 (C10), 125.7 (C8), 124.0 (q, J = 273.0 Hz, C9), 121.9 (C11), 120.0 (C16), 118.1 (C7), 113.8 (C6), 113.0 (C12), 99.7 (C15); δ_F (376 MHz, DMSO- d_6): -63.0; ν_{max} : 3378 (N-H, m), 2235 (C \equiv N, w), 1105 (C-F, s); **HRMS** (ESI+): m/z found $[M+H]^+$ 287.0789, $C_{16}H_{10}N_2F_3$ required 287.0796 (Δ -2.4 ppm).

2,6-Dichloro-[1,1'-biphenyl]-4-carbonitrile (**2i**)



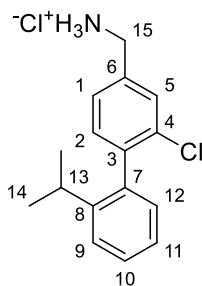
Prepared following *general method 2c* using **1b** (300 mg, 940 μmol), phenylboronic acid (160 mg, 1.31 mmol), K_3PO_4 (239 mg, 1.13 mmol), DME (800 μL), EtOH (600 μL), H_2O (150 μL), $PdCl_2(dppf)\cdot CH_2Cl_2$ (48.0 mg, 60.0 μmol). The mixture was heated to 110 $^\circ\text{C}$ in the MW for 2 hours. After work-up, the crude material was purified by flash chromatography on silica gel (0 to 2% EtOAc/hexane) followed by preparative TLC (100% Hexane) to yield **2i** as a white film (55.0 mg, 220 μmol , 24%).

R_f = 0.37 (100% hexane); Mp = 100-103 $^\circ\text{C}$; δ_H (500 MHz, $CDCl_3$): 7.71 (2H, s, H1), 7.52-7.47 (3H, m, H6, H8), 7.24-7.22 (2H, m, H7); δ_C (126 MHz, $CDCl_3$): 144.6 (C3), 136.2 (C4 or C5), 135.3 (C4 or C5), 131.2 (C1), 128.9 (C7), 128.9 (C6), 128.5 (C8), 116.3 (C9), 113.3 (C2); ν_{max} : 2236 (C \equiv N, m), 1532, 1444 (C=C, m), 1207 (=C-H, m); **HRMS** (ESI+): m/z found $[M+H]^+$ 248.0022, $C_{13}H_8N^{35}Cl_2$ required 248.0028 (Δ -2.4 ppm).

2,6-Dichloro-1[1,1'-biphenyl]-4-carbaldehyde (**2k**)

Prepared following *general method 2c* using compound **1c** (162 mg, 50.0 μmol), phenylboronic acid (73.3 mg, 600 μmol), and K_3PO_4 (213 mg, 1.00 mmol), DME (1.00 mL), EtOH (700 μL) and H_2O (150 μL), $\text{PdCl}_2(\text{dppf})\cdot\text{CH}_2\text{Cl}_2$ (20.5 mg, 30.0 μmol). The mixture was refluxed for 4 hours. After the workup, the crude material was purified by column chromatography on silica gel (0 to 1% EtOAc/hexane) to yield **2k** as a white solid (68.0 mg, 270 μmol , 54%).

R_f = 0.30 (10% EtOAc/hexane); **Mp** = 95-97 $^\circ\text{C}$; δ_{H} (500 MHz, CDCl_3): 9.97 (1H, s, H8), 7.91 (2H, s, H1), 7.52-7.44 (3H, m, H10, H5 or H6), 7.28-7.25 (2H, m, H5 or H6); δ_{C} (126 MHz, CDCl_3): 189.3 (C8), 145.2 (C3), 136.8 (C7), 136.3 (C2), 136.0 (C4), 129.0 (C1), 128.8 (C5 or C6 or C10), 128.7 (C5 or C6 or C10), 128.4 (C5 or C6 or C10); ν_{max} : 1707 (C=O, s); **HRMS** (ESI+): m/z found $[\text{M}+\text{H}]^+$ 251.0029, $\text{C}_{13}\text{H}_9\text{O}^{35}\text{Cl}_2$ required 251.0030 (Δ -0.4 ppm).

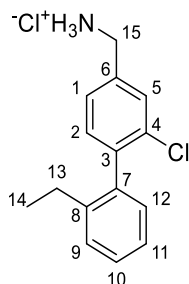
(2-Chloro-2'-isopropyl-[1,1'-biphenyl]-4-yl)methanaminium chloride (**3a**)

Prepared following *general method 3* using compound **2a** (40.0 mg, 150 μmol), LiAlH_4 (11.4 mg, 300 μmol), AlCl_3 (20.0 mg, 150 μmol) and Et_2O (3.00 mL). The amine product (35.0 mg, 130 μmol , 87%) was subjected to *general method 5* using 2 M HCl solution in 1,4-dioxane (0.700 mL) to yield **3a** as a white solid (35.0 mg, 120 μmol , 77%).

Mp = 218-220 $^\circ\text{C}$; δ_{H} (500 MHz, CD_3OD): 7.68 (1H, d, J = 1.5 Hz, H5), 7.50 (1H, dd, J = 7.8, 1.5 Hz, H1), 7.42-7.36 (2H, m, H10, H11), 7.35 (1H, d, J = 7.8 Hz, H2), 7.25 (1H, app. td, J = 6.9, 1.7 Hz, H12), 7.03 (1H, dd, J = 6.9, 1.7 Hz, H9), 4.21 (2H, s, H15), 2.65 (1H, sept, J = 7.4 Hz, H13), 1.20 (3H, d, J = 7.4 Hz, H14), 1.06 (3H, d, J = 7.4 Hz, H14); δ_{C} (126 MHz, CD_3OD): 146.4 (C6), 141.5 (C3 or 7), 137.4 (C3 or 7), 134.1 (C4), 132.0 (C8), 131.9 (C2), 129.6 (C9), 129.0 (C5), 128.4 (C10 or 11), 127.1 (C1), 125.3 (C12), 125.0 (C10 or 11), 42.1 (C15), 30.1 (C13), 23.4 (C14), 22.1 (C14);

ν_{\max} : 2960 (N-H, br), 1478 (CH₃, m), 1403 (CH₃, m); **HRMS** (ASAP): m/z found [M]⁺ 260.1196, C₁₆H₁₉N₂³⁵Cl required 260.1206 (Δ -3.8 ppm).

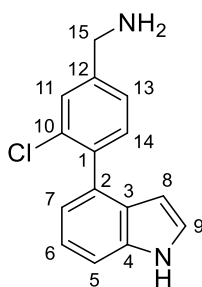
(2-Chloro-2'-ethyl-[1,1'-biphenyl]-4-yl)methanaminium chloride (**3b**)



Prepared by *general method 3* using LiAlH₄ (42 mg, 1.1 mmol), Et₂O (5.0 mL), AlCl₃ (147 mg, 1.10 mmol) and **2b** (132 mg, 0.550 mmol). The crude product was purified by flash column chromatography on silica gel (1:5:14 NH₃:MeOH:CH₂Cl₂) to provide the free amine. The free amine was then subjected to *general method 5* using 2 M HCl solution in 1,4-dioxane (2.75 mL) to yield **3b** as a white solid (65.0 mg, 0.230 mmol, 43%).

R_f (amine) = 0.18 (10% MeOH/CH₂Cl₂); **Mp** = 181-183 °C; **δ_{H}** (500 MHz, DMSO-d₆): 8.63 (3H, s, NH), 7.78 (1H, d, J = 1.6 Hz, H5), 7.55 (1H, dd, J = 7.8, 1.6 Hz, H1), 7.39-7.33 (3H, m, H10, H11, H12), 7.28-7.24 (1H, m, H2), 7.04 (1H, d, J = 7.3 Hz, H9), 4.09 (2H, s, H15), 2.47-2.24 (2H, m, H13), 0.98 (3H, t, J = 7.6 Hz, H14); **δ_{C}** (126 MHz, DMSO-d₆): 141.4 (C6), 139.7 (C3), 137.7 (C7), 135.4 (C4), 132.4 (C8), 131.5 (C2), 129.7 (C9), 129.4 (C5), 128.3 (br s, C10, C11), 127.8 (C1), 125.7 (C12), 41.3 (C15), 25.7 (C13), 15.1 (C14); ν_{\max} : 3300 (N-H, m), 1476 (CH₃, m), 1401 (CH₃, m); **HRMS** (ESI⁺): m/z found [M+H]⁺ 246.1061, C₁₅H₁₇N³⁵Cl required 246.1049 (Δ 4.8 ppm).

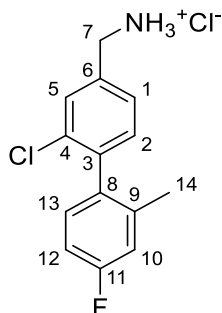
(3-Chloro-4-(1H-indol-4-yl)phenyl)methanamine (**3c**)



Prepared following *general method 3* using compound **2c** (95.0 mg, 380 μ mol), LiAlH₄ (29.0 mg, 750 μ mol), AlCl₃ (50.0 mg, 370 μ mol) and Et₂O (7.00 mL). After work-up, the crude material was purified by column chromatography on silica gel (0:2:98 to 1:4:95 NH₃:MeOH:CH₂Cl₂) to yield **3c** as a white solid (55.0 mg, 210 μ mol, 55%).

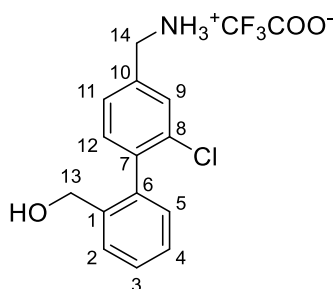
R_f = 0.20 (0.2:1.8:98 NH₃:MeOH:CH₂Cl₂); **Mp** 150-152 °C; δ_H (400 MHz, CD₃OD): 7.55 (1H, d, J = 1.5 Hz, H11), 7.43-7.41 (2H, m, H5, H14), 7.34 (1H, dd, J = 7.8, 1.5 Hz, H13), 7.23 (1H, d, J = 3.2 Hz, H9), 7.17 (1H, t, J = 7.3 Hz, H6), 6.96 (1H, dd, J = 7.3, 0.7 Hz, H7), 6.16 (1H, dd, J = 3.2, 0.7 Hz, H8), 3.88 (2H, s, H15); δ_C (101 MHz, CD₃OD): 142.3 (C4), 138.8 (C1), 136.3 (C12), 132.9 (C10), 131.7 (C14), 131.1 (C2), 128.4 (C11), 127.1 (C3), 125.4 (C13), 124.4 (C9), 120.5 (C6), 119.8 (C7), 110.4 (C8), 100.5 (C5), 44.4 (C15); ν_{max} : 2983 (N-H, br), 1373 (C-N, s); **HRMS** (ESI+): m/z found $[M+H]^+$ 257.0834, C₁₅H₁₄N₂³⁵Cl required 257.0840 (Δ -2.5 ppm).

(2-Chloro-4'-fluoro-2'-methyl-[1,1'-biphenyl]-4-yl)methanaminium chloride (**3d**)



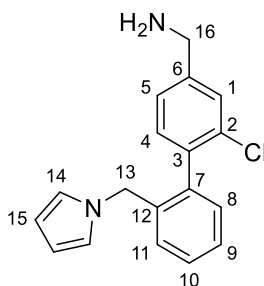
Prepared following *general method 3* using compound **2d** (70.0 mg, 280 μ mol), LiAlH₄ (32.0 mg, 840 μ mol), AlCl₃ (56.0 mg, 480 μ mol) and Et₂O (7.20 mL). After work-up, the crude material was purified by column chromatography on silica gel (1:4:95 NH₃:MeOH:CH₂Cl₂) to afford the desired amine as a colourless oil (28.0 mg, 110 μ mol, 39%). The amine (23.0 mg, 92.0 μ mol) was converted to its hydrochloride salt *via general method 5* with HCl (2 M solution in 1,4-dioxane, 500 μ L) and CH₂Cl₂ (100 μ L) to yield **3d** as a white solid (8.00 mg, 30.0 μ mol, 32%).

R_f (amine) = 0.70 (2:8:90 NH₃:MeOH:CH₂Cl₂); **Mp** = 189-193 °C; δ_H (500 MHz, CD₃OD) 7.52 (1H, d, J = 1.5 Hz, H5), 7.35 (1H, dd, J = 7.8, 1.5 Hz, H1), 7.19 (1H, d, J = 7.8 Hz, H2), 7.08-7.05 (1H, m, H10), 7.03-7.01 (1H, m, H13), 6.96 (1H, app. td, J = 8.5, 2.6 Hz, H12), 3.87 (2H, s, H7), 2.07 (3H, s, H14); δ_C (126 MHz, CD₃OD): 163.2 (d, J = 244.5 Hz, C11), 144.1 (C6), 139.9 (d, J = 8.0 Hz, C9), 136.6 (C3), 134.7 (C4), 132.5 (C8), 132.2 (C5), 132.1 (d, J = 8.4 Hz, C13), 129.6 (C1), 127.3 (C2), 117.2 (d, J = 21.5 Hz, C10), 113.3 (d, J = 21.5 Hz, C12), 45.6 (C7) 20.0 (d, J = 1.6 Hz, C14); δ_F (376 MHz, d₆-DMSO): -115.0; ν_{max} : 2981 (N-H, s, br), 1481 (C-F, s); **HRMS** (ASAP): m/z found $[M]^+$ 250.079, C₁₄H₁₄³⁵ClFN required 250.0793 (Δ 1.6 ppm).

(4'-((Aminomethyl)-2'-chloro-[1,1'-biphenyl]-2-yl)methanol) (**3e**)

Prepared following *general method 3* using compound **2e** (50.0 mg, 200 μ mol), LiAlH₄ (15.0 mg, 400 μ mol), AlCl₃ (27.0 mg, 200 μ mol) and Et₂O (3.70 mL). After work-up, the crude material was purified by preparative HPLC (5-95% B over 30 mins) to yield **3e** as a white solid (27.0 mg, 110 μ mol, 54%).

R_t (HPLC) = 8.76 mins (5-95% B over 15 mins); **Mp** = 205-211 °C; **δ_{H}** (500 MHz, CD₃OD): 7.66 (1H, dd, J = 7.0, 1.5 Hz, H12), 7.62 (1H, d, J = 1.5 Hz, H9), 7.47 (1H, app. td, J = 7.7, 1.2 Hz, H4), 7.40-7.38 (2H, m, H3, H11), 7.35 (1H, d, J = 7.7 Hz, H5), 7.12 (1H, dd, J = 7.7, 1.2 Hz, H2), 4.46 (1H, d, J = 13.6 Hz, H13), 4.32 (1H, d, J = 13.6 Hz, H13), 4.20 (2H, s, H14); **δ_{C}** (126 MHz, CD₃OD): 140.3 (C10), 139.0 (C1), 137.1 (C7), 134.4 (C8), 133.6 (C6), 131.8 (C12), 129.6 (C9), 129.1 (C5), 128.1 (C4), 127.1 (C11), 127.0 (C3), 126.8 (C2), 61.3 (C13), 42.1 (C14); **δ_{F}** (376 MHz, CD₃OD): -76.9; **ν_{max}** : 3380 (N-H, br), 2977 (O-H, br); **HRMS** (ESI+): m/z found [M+H]⁺ 248.0834, C₁₄H₁₅NO³⁵Cl required 248.0837 (Δ -1.0 ppm).

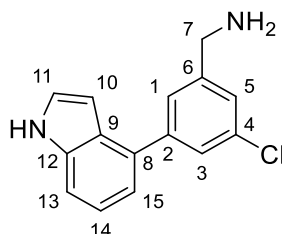
(2'-((1H-Pyrrol-1-yl)methyl)-2-chloro-[1,1'-biphenyl]-4-yl)methanamine (**3f**)

Prepared following *general method 4* with compound **2f''** (30.0 mg, 100 μ mol), Raney Ni and NH₃ (8% in MeOH, 2.00 mL). After the work-up, the crude product was purified by column chromatography on silica gel (0:5:95 to 0.5:4.5:95 NH₃:MeOH:CH₂Cl₂) to yield **3f** as a colourless viscous oil (8.50 mg, 29.0 μ mol, 28%).

R_f = 0.51 (2:18:80 NH₃:MeOH:CH₂Cl₂); **δ_{H}** (400 MHz, CD₃OD): 7.56 (1H, s, H1), 7.35-7.33 (3H, m, H5, H9, H10), 7.16 (1H, d, J = 7.5 Hz, H4), 7.14-7.13 (1H, m, H8), 7.03-7.01 (1H, m, H11), 6.48 (2H, app. t, J = 2.0 Hz, H14), 6.01 (2H, app. t, J = 2.0 Hz, H15), 4.90 (1H, d, J = 17.0 Hz, H13), 4.80 (1H, d, J = 17.0 Hz, H13), 3.86 (2H, s, H16); **δ_{C}** (101 MHz, CD₃OD): 142.2 (C6), 138.0 (C12), 138.0 (C3),

136.6 (C7), 133.0 (C2), 131.3 (C4), 129.5 (C8), 128.3 (C1), 128.1 (C5), 127.5 (C11), 127.1 (C9), 126.1 (C10), 120.6 (C14), 107.7 (C15), 50.4 (C13), 44.4 (C16); ν_{\max} : 2989 (N-H, br), 1264 (C-N, s); **HRMS** (ESI+): m/z found $[M+H]^+$ 297.1194, $C_{18}H_{18}N_2^{35}Cl$ required 297.1153 (Δ -1.2 ppm).

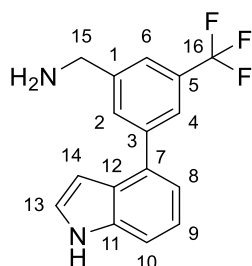
(3-Chloro-5-(1*H*-indol-4-yl)phenyl)methanamine (**3g**)



Prepared following *general method 3* using compound **2g** (77.5 mg, 280 μ mol), $LiAlH_4$ (22.0 mg, 570 μ mol), $AlCl_3$ (38.0 mg, 285 μ mol) and Et_2O (5.25 mL). After work-up, the crude mixture was purified by flash column chromatography on aluminium oxide (2:18:80 NH_3 : $EtOAc$:hexane) to yield **3g** as a white film (57.0 mg, 220 μ mol, 79%).

R_f = 0.40 (0.2:8.2:7 NH_3 : $EtOAc$:Hexane); δ_H (500 MHz, CD_3OD): 7.56-7.54 (2H, m, H3, H5), 7.42 (1H, app. td, J = 8.1, 0.8 Hz, H15), 7.36 (1H, t, J = 1.7 Hz, H1), 7.30 (1H, d, J = 3.2 Hz, H11), 7.21-7.18 (1H, m, H14), 7.10 (1H, dd, J = 7.4, 0.8 Hz, H13), 6.60 (1H, dd, J = 3.2, 0.8 Hz, H10), 3.85 (2H, s, H7); δ_C (126 MHz, CD_3OD): 144.5 (C6), 143.9 (C2), 136.7 (C12), 134.0 (C4), 132.0 (C9), 126.6 (C3), 123.5 (C5), 125.7 (C1), 125.3 (C14), 125.0 (C11), 121.2 (C15), 118.6 (C13), 110.8 (C8), 99.9 (C10), 44.8 (C7); ν_{\max} : 3437 (N-H, m), 679 (=C-H, s); **HRMS** (ESI+): m/z found $[M+H]^+$ 257.0831, $C_{15}H_{13}N_2^{35}Cl$ required 257.0840 (Δ -3.4 ppm).

(3-(1*H*-Indol-4-yl)-5-(trifluoromethyl)phenyl)methanamine (**3h**)

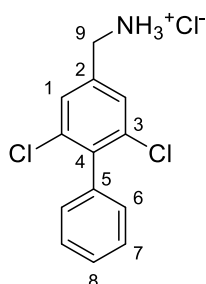


Prepared following *general method 4* using **2h** (100 mg, 360 μ mol), NH_3 (8% in MeOH, 2.00 mL) and Raney Nickel. The crude material was purified by column chromatography on silica gel (1:5:95 NH_3 :MeOH: CH_2Cl_2) to yield **3h** as a sticky, clear oil (29.0 mg, 100 μ mol, 28%).

R_f = 0.09 (1:5:95 NH_3 :MeOH: CH_2Cl_2); δ_H (400 MHz, CD_3OD): 7.92 (1H, s, H2), 7.84 (1H, s, H4), 7.68 (1H, s, H6), 7.46 (1H, d, J = 8.0 Hz, H8), 7.34 (1H, d, J = 3.2 Hz, H13), 7.23 (1H, t, J = 8.0 Hz, H9), 7.15 (1H, dd, J = 8.0, 0.9 Hz, H10), 6.59 (1H, dd, J = 3.2, 0.7 Hz, H14), 3.97 (2H, s, H15); δ_C

(101 MHz, CD₃OD): 143.8 (C1), 143.0 (C11), 136.8 (C3), 131.9 (C7), 130.9 (C2), 130.5 (q, $J = 32.0$ Hz, C5), 125.9 (C12), 125.1 (C13), 123.2 (q, $J = 260.6$ Hz, C16), 122.0 (q, $J = 3.6$ Hz, C4), 121.2 (C10), 118.7 (C9), 110.9 (C8), 99.7 (C14), 44.9 (C15); δ_{F} (376 MHz, CD₃OD): -64.8; ν_{max} : 2921 (N-H, br), 1257 (C-F, m); **HRMS** (ESI+): m/z found $[M+H]^+$ 291.1101, C₁₆H₁₄F₃N₂ required 291.1104 (Δ -0.8 ppm).

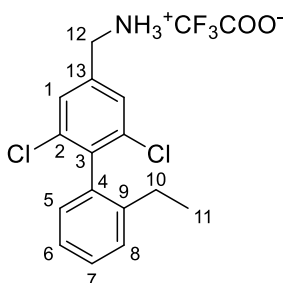
(2,6-Dichloro-[1,1'-biphenyl]-4-yl)methanaminium chloride (**3i**)



The free amine of compound **3i** was prepared following *general method 3* using nitrile **2i** (22.0 mg, 90.0 μmol), LiAlH₄ (7.00 mg, 180 μmol), AlCl₃ (12.0 mg, 90.0 μmol) and Et₂O (1.70 mL). After work-up, the crude material was purified by flash column chromatography on silica gel (1:9:90 NH₃:MeOH:CH₂Cl₂) to afford the amine (20.0 mg, 80.0 μmol , 88%). The amine underwent *general method 5*, using HCl (2 M in 1,4-dioxane, 500 μL , 870 μmol) and CH₂Cl₂ (1.00 mL). Compound **3i** was obtained as a white solid (12.0 mg, 40.0 μmol , 48%).

R_{f} (amine) = 0.44 (1:9:90 NH₃:MeOH:CH₂Cl₂); M_{p} = 246-250 °C; δ_{H} (500 MHz, CD₃OD): 7.62 (2H, s, H1), 7.50-7.41 (3H, m, H6, H8), 7.22-7.19 (2H, m, H7), 4.17 (2H, s, H9); δ_{C} (126 MHz, CD₃OD): 141.7 (C4), 137.7 (C2), 136.6 (C3), 136.4 (C5), 131.7 (C1), 130.7 (C7), 129.8 (C6), 129.5 (C8), 43.0 (C9); ν_{max} : 3332 (N-H, br), 892, 879 (=C-H, m); **HRMS** (ASAP): m/z found $[M]^+$ 252.0337, C₁₃H₁₂N³⁵Cl₂ required 252.0341 (Δ -1.7 ppm).

(2,6-Dichloro-2'-ethyl-[1,1'-biphenyl]-4-yl)methanamine trifluoroacetic salt (**3j**)

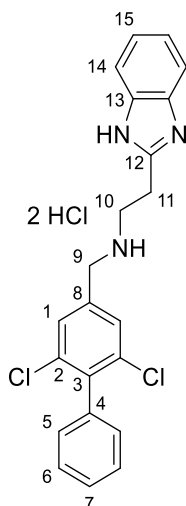


Prepared following *general method 2c* using **1c** (771 mg, 2.40 mmol), 2-ethyl-phenylboronic acid (430 mg, 2.87 mmol), PdCl₂(dppf)·CH₂Cl₂ (98.0 mg, 0.12 mmol), K₃PO₄ (1.02 g, 4.80 mmol), DME (5.60 mL), EtOH (0.35 mL) and H₂O (0.06 mL) and refluxed for 3 hours. A solution of crude 2,6-dichloro-2'-ethyl-[1,1'-biphenyl]-4-carbaldehyde (200 mg), ^tbutylcarbamate (170 mg, 4.30

mmol), Et₃SiH (0.66 mL, 4.30 mmol) and TFA (0.21 mL, 2.72 mmol) in MeCN (3.20 mL) was stirred at room temperature for 14 h. The mixture was diluted with Et₂O and washed with an aqueous solution of NaHCO₃ and brine. The combined organic layers were dried (MgSO₄), filtered and concentrated under reduced pressure. TFA (4.5 mL) was added to the *N*-Boc derivative and the mixture stirred at room temperature for 15 minutes. The excess TFA was blown off under a stream of nitrogen to give **3j** as a white solid (240 mg, 0.900 mmol, 37%).

R_f(amine) = 0.05 (10% CH₂Cl₂/MeOH); **Mp** = 218-222 °C; **δ_H** (500 MHz, CD₃OD): 7.62 (2H, s, H1), 7.39-7.35 (2H, m, H5, H6), 7.28-7.24 (1H, m, H7), 6.97 (1H, d, *J* = 7.4 Hz, H8), 4.17 (2H, s, H12), 2.33 (2H, q, *J* = 7.6 Hz, H10), 1.04 (3H, t, *J* = 7.6 Hz, H11); **δ_C** (126 MHz, CD₃OD): 141.7 (C13), 139.9 (C9), 135.6 (C2), 135.2 (C3), 128.9 (C4), 128.7 (C8), 128.4 (C6), 128.2 (C5), 125.7 (C1), 125.7 (C7), 41.8 (C12), 26.0 (C10), 13.8 (C11); **δ_F** (376 MHz, CD₃OD): -76.2; **v_{max}**: 3373 (N-H, m), 1674 (N-H, m), 1118 (C-N, m); **HRMS** (ESI): *m/z* found [M+H]⁺ 280.0641, C₁₅H₁₆³⁵Cl₂N required 280.0654 (Δ - 4.6 ppm).

N-(2-(1*H*-Benzo[d]imidazol-2-yl)ethyl)-2,6-dichloro-[1,1'-biphenyl]-4-aminium chloride (**3k**)

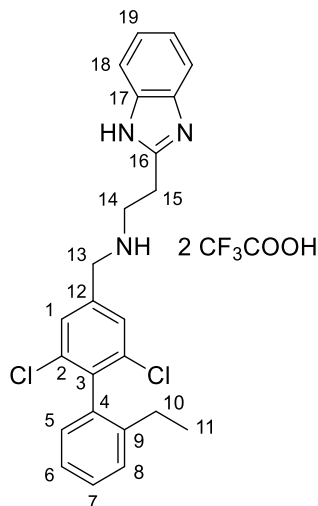


Prepared following *general method 6* using DCE (1.60 mL), **2k** (54.0 mg, 210 μmol), 2-(1*H*-benzo[d]imidazol-2-yl)ethan-1-amine (50.8 mg, 320 μmol), 4Å molecular sieves (50 mg), NaBH(OAc)₃ (62.3 mg, 290 μmol). After work-up, the crude material was purified by column chromatography on aluminium oxide gel (5 to 10% MeOH/CH₂Cl₂) to yield the free amine (32.0 mg, 90.0 μmol, 42%). The amine underwent *general method 5* using HCl (2 M in dioxane, 450 μL) to yield **3k** as a white solid (14.0 mg, 32.0 μmol, 36%).

R_f(amine) = 0.48 (10% MeOH/CH₂Cl₂); **δ_H** (500 MHz, DMSO-*d*₆): 7.87 (2H, s, H1), 7.75-7.73 (2H, m, H5), 7.52-7.43 (5H, m, H6, H7, H14), 7.24-7.22 (2H, m, H15), 4.32 (2H, s, H9), 3.62-3.59 (4H, m, H10, H11); **δ_C** (126 MHz, CDCl₃): 154.0 (C12), 141.4 (C13), 141.3 (C8), 138.4 (C4), 136.7 (C3), 135.1 (C2), 129.6 (C6), 128.2 (C5 or C7), 128.1 (C5 or C7), 127.7 (C14 or C15), 122.3 (C14 or

C15), 114.9 (C1), 52.8 (C9), 47.0 (C10), 28.9 (C11); ν_{\max} : 2720 (N-H, s); **HRMS** (ESI+): m/z found $[M+H]^+$ 396.1035, $C_{22}H_{20}N_3^{35}Cl_2$ required 396.1029 (Δ 1.6 ppm).

2-(1*H*-Benzo[d]imidazol-2-yl)-*N*-((2,6-dichloro-2'-ethyl-[1,1'-biphenyl]-4-yl)methyl)ethan-1-amine (**3I**)

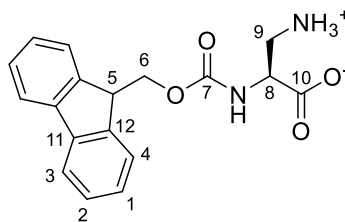


Prepared by *general method 2c* using **1c** (250 mg, 0.770 mmol), 2-ethylphenylboronic acid (139 mg, 0.930 mmol), $PdCl_2(dppf) \cdot CH_2Cl_2$ (32.0 mg, 0.390 mmol), K_3PO_4 (329 mg, 1.55 mmol), DME (2.00 mL), EtOH (0.300 mL) and H_2O (0.150 mL) and refluxed for 6 hours. The crude material (80.0 mg, 0.290 mmol) was then subjected to *general method 6* using 2-(1*H*-benzimidazol-2-yl)ethan-1-amine (69.0 mg, 0.430 mmol), 4Å molecular sieves (50 mg), DCE (1.00 mL) and sodium triacetoxyborohydride (86.0 mg, 0.410 mmol). The crude amine was purified by preparative HPLC (5-95% B over 20 mins) to yield **3I** as a sticky film (26.0 mg, 0.0400 mmol, 13%).

R_t (HPLC) = 9.43 mins (5-95% B over 15 mins); δ_H (500 MHz, CD_3OD): 7.76-7.71 (2H, m, H18), 7.70 (2H, s, H1) 7.53-7.49 (2H, m, H5, H6), 7.40-7.35 (2H, m, H19), 7.29-7.25 (1H, m, H7), 6.97 (1H, d, $J = 7.4$ Hz, H8), 3.75-3.63 (4H, m, H13, H14), 3.31-3.29 (2H, m, H15), 2.34 (2H, q, $J = 7.6$ Hz, H10), 1.05 (3H, t, $J = 7.6$ Hz, H11); δ_C (126 MHz, CD_3OD): δ 150.8 (C16), 143.0 (C9), 141.9 (C17), 137.1 (C12), 136.7 (C2), 134.4 (C3), 134.3 (C4), 130.7 (C8), 130.2 (C7), 130.1 (C6), 129.6 (C1), 127.1 (C5), 126.7 (C19), 115.2 (C18), 51.2 (C13), 45.6 (C14), 27.2 (C15), 25.1 (C10), 15.1 (C11); δ_F (376 MHz, CD_3OD): -76.9, -77.1; ν_{\max} : 2975 (N-H, s), 1667 (C-Cl, m); **HRMS** (ESI): m/z found $[M+H]^+$, 424.1346, $C_{24}H_{25}N_3^{35}Cl_2$ required 424.1347 (Δ -0.2 ppm).

6.1.1.2. Unnatural amino acids

Fmoc-Dap-OH (4)

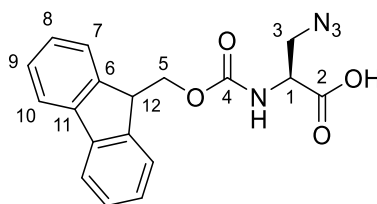


Fmoc-Asn-OH (4.00 g, 11.3 mmol) was added to a solution of [bis(trifluoroacetoxy)iodo]benzene (5.40 g, 16.9 mmol) in DMF/H₂O (2:1 53.2 mL: 26.4 mL). After 15 minutes, pyridine (2.10 mL) was added and the mixture was stirred at rt for 16 hours. The solvent was removed under reduced pressure and the oily residue was dissolved in H₂O (60.0 mL). Concentrated HCl (2 mL) was added and the acidified solution was washed with Et₂O (3 x 40 mL). The aqueous phase was adjusted to pH 6 with 2 M NaOH solution and the resulting precipitate was filtered, washed with H₂O, ice-cold EtOH, Et₂O and the residual solvent removed under reduced pressure to yield Fmoc-Dap-OH as a beige powder (2.99 g, 9.16 mmol, 81%).

δ_{H} (400 MHz, DMSO-*d*₆): 7.89 (2H, d, *J* = 7.5 Hz, H3), 7.70 (2H, d, *J* = 6.3 Hz, H4), 7.41 (2H, d, *J* = 7.4 Hz, H2), 7.35 (2H, *J* = 7.3 Hz, H1), 6.77 (1H, d, *J* = 6.1 Hz, CONH), 4.32-4.24 (3H, m, H5, H6), 3.69-3.44 (1H, m, H8), 3.00 (1H, dd, *J* = 10.8, 4.8 Hz, H9), 2.75 (1H, app t, *J* = 10.8 Hz, H9); δ_{C} (101 MHz, DMSO-*d*₆): 169.1 (C10), 156.3 (C7), 144.4 (C11), 141.2 (C12), 128.1 (C2), 127.8 (C1), 125.8 (C3), 120.6 (C4), 66.2 (C6), 52.4 (C8), 47.1 (C9), 41.1 (C5); **HRMS** (ESI⁺): *m/z* found [M+H]⁺ 327.1343, C₁₈H₁₉O₄N₂ required 327.1339 (Δ 1.2 ppm).

Characterisation data in accordance with literature.²³⁵

Fmoc-Aza-OH (5)



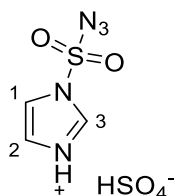
Compound **4** (4.04 g, 12.4 mmol) was added to a mixture of H₂O (60.0 mL), MeOH (180 mL), and CH₂Cl₂ (120 mL). CuSO₄·5H₂O (20.0 mg, 0.0800 mmol) and **6** (8.08 g, 29.9 mmol) were added, the mixture adjusted to pH 9 with saturated K₂CO₃ and stirred for 18 hours. The mixture was then diluted with CH₂Cl₂ (120 mL), and the aqueous phase isolated. The organic phase was extracted with saturated NaHCO₃ (2 x 200 mL). The aqueous extract was washed with Et₂O (2 x 200 mL), acidified to pH 2 with conc. HCl, and extracted with Et₂O (3 x 240 mL). The organic extracts were dried (MgSO₄) and the solvent removed under reduced pressure. The oily

residue was re-dissolved in EtOAc and the solvent removed under a stream of N₂ to yield **5** as a beige, amorphous solid (3.58 g, 9.53 mmol, 77%).

δ_{H} (400 MHz, DMSO-d₆): 7.94-7.89 (2H, m, H10), 7.74 (2H, d, $J = 7.4$ Hz, H7), 7.43 (2H, app t, $J = 7.4$ Hz, H9), 7.33 (2H, app t, $J = 7.4$ Hz, H8), 4.34-4.27 (2H, m, H5), 4.24-4.22 (2H, m, H1, H12), 3.64-3.62 (2H, m, H3); δ_{C} (101 MHz, DMSO-d₆): 171.5 (C2), 156.5 (C4), 144.2 (C6), 141.2 (C11), 128.1 (C9), 127.5 (C8), 125.7 (C7), 120.6 (C10), 66.3 (C5), 54.2 (C1), 51.4 (C3), 47.1 (C12); $[\alpha]_{\text{D}}^{25}$ -9.9 ($c = 1$, DMF); **HRMS** (ESI+): m/z found $[\text{M}+\text{H}]^+$ 353.1248, C₁₈H₁₇O₄N₄ required 353.1244 (Δ 1.0 ppm).

Characterisation data in accordance with literature.²¹⁷

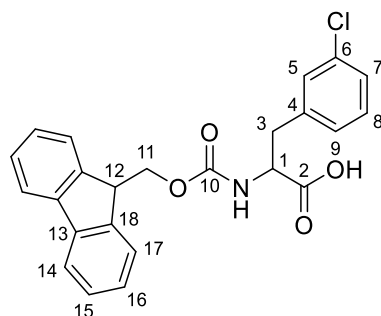
Imidazole-1-sulfonyl azide hydrogen Sulfate (**6**)



Sulfonyl chloride (16.1 mL, 200 mmol) was added dropwise to an ice-cold suspension of NaN₃ (13.0 g, 200 mmol) in MeCN (200 mL) and the mixture stirred for 16 hours. Imidazole (25.9 g, 380 mmol) was added and the pink mixture stirred at 0 °C for 5 hours. The mixture was then diluted with EtOAc (400 mL) and H₂O (400 mL). The organic fraction was isolated and washed with H₂O (400 mL) and saturated NaHCO₃ (2 x 200 mL) and then dried (MgSO₄). The solvent was reduced to 200 mL under reduced pressure. A solution of conc. H₂SO₄ (11.0 mL) in EtOAc (100 mL) was added to the ice-cold reaction mixture over 30 min. The reaction mixture was warmed to room temperature and stirred for 16 hours. The precipitate was filtered, washed with EtOAc (3 x 60 mL), and dried under reduced pressure to yield **6** as a white powder (34.9 g, 129 mmol, 64%).

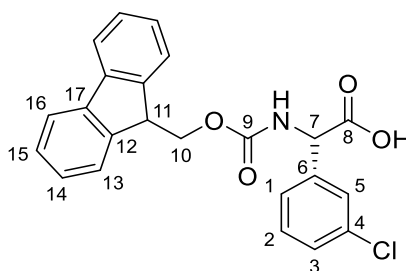
δ_{H} (500 MHz, DMSO-d₆): 8.64 (1H, s, H3), 7.97 (1H, app t, $J = 1.6$ Hz, H1), 7.35 (1H, app q, $J = 0.8$ Hz, H2); δ_{C} (101 MHz, DMSO-d₆): 138.2 (C3), 130.9 (C1), 119.4 (C2); **HRMS** (ESI+): m/z found $[\text{M}+\text{H}]^+$ 174.0073, C₁₈H₁₉O₄N₂ required 174.0080 (Δ 4.2 ppm).

Characterisation data in accordance with literature.²¹⁸

Fmoc-3-Chloro-phenylalanine (**7**)

Prepared following *general method 7* using NaHCO_3 (1.59 g, 19.0 mmol), H_2O (109 mL), MeCN (109 mL), 3-chloro-DL-phenylalanine (1.00 g, 5.00 mmol) and *N*-(9-fluorenylmethoxycarbonyloxy)-succinimide (1.86 g, 5.50 mmol). The mixture was stirred at rt for 24 hours. After work-up, the crude mixture was purified by flash chromatography on silica gel (0 to 20% MeOH in CH_2Cl_2) to yield **7** as a white solid (650g, 1.96 mmol, 39%).

R_f = 0.1 (20 % MeOH/ CH_2Cl_2); M_p = 78.6-87.5°C; δ_H (400 MHz, DMSO-d_6): 7.87 (2H, d, J = 7.5, 14H), 7.64-7.61 (2H, m, H17), 7.42-7.19 (8H, m, H5, H7, H8, H9, H15, H16), 4.24-4.10 (4H, m, H1, H11, H12), 3.13 (1H, app dd, J = 13.6, 3.9 Hz, H3), 2.91-2.85 (1H, m, H3); δ_C (101 MHz, DMSO-d_6): 174.1 (C2), 156.1 (C10), 144.4 (C18), 141.7 (C13), 141.3 (C4), 133.2 (C6), 130.4 (C8), 129.6 (C5), 128.6 (C15), 128.2 (C16), 127.6 (C9), 126.7 (C7), 125.7 (C14), 120.5 (C17), 66.0 (C11), 56.4 (C1), 47.1 (C12), 36.9 (C3); ν_{max} : 1707 (C=O, s), 757 (C=C, s), 737 (C=C, s); **HRMS** (ESI+): m/z found $[\text{M}+\text{Na}]^+$ 444.0964, $\text{C}_{24}\text{H}_{20}\text{O}_4\text{N}^{35}\text{ClNa}^+$ required 444.0973 (Δ -1.9 ppm).

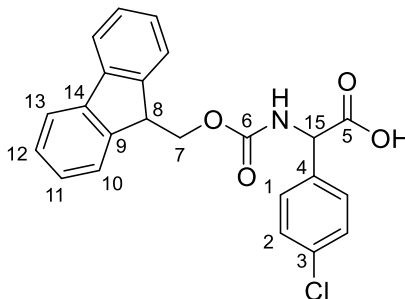
(S)-2-(((9*H*-Fluoren-9-yl)methoxy)carbonyl)amino)-2-(3-chlorophenyl)acetate (**8**)

Prepared following *general method 7* using NaHCO_3 (903 mg, 10.8 mmol), H_2O (60 mL), MeCN (60 mL), *(S)*-2-(3-chlorophenyl)glycine (500 mg, 2.69 mmol) and *N*-(9-fluorenylmethoxycarbonyloxy)succinimide (998 mg, 2.96 mmol). The mixture was stirred at rt for 48 hours. After the work-up, the crude product was purified by flash chromatography on silica gel (0 to 15% MeOH in CH_2Cl_2) to yield **8** as a white solid (940 mg, 2.31 mmol, 86%).

R_f = 0.54 (10% MeOH/ CH_2Cl_2); M_p = 241.0-242.4 °C; δ_H (400 MHz, DMSO-d_6): 7.89 (2H, d, J = 7.1 Hz, H16), 7.71 (2H, d, J = 7.1 Hz, H13), 7.44-7.39 (3H, m, H5, H15), 7.35-7.28 (4H, m, H1, H2, H3, H14), 4.87 (1H, d, J = 7.1 Hz, H7), 4.29-4.22 (3H, m, H10, H11); δ_C (101 MHz, DMSO-d_6): 171.4 (C8), 155.6 (C9), 144.4 (C12), 144.2 (C17), 141.2 (C6), 133.0 (C4), 130.1 (C2), 128.1 (C5), 127.5

(C1 or C3), 127.3 (C1 or C3), 127.0 (C15), 126.3 (C16), 125.7 (C14), 120.6 (C13), 66.1 (C10), 49.1 (C7), 47.1 (C11); ν_{\max} : 3387 (OH, br), 1666 (C=O, m); $[\alpha_D]^{20} + 79.00$ ($c = 0.22$, MeOH); **HRMS** (ESI+): m/z found $[M+H]^+$ 408.0997, $C_{23}H_{19}O_4N_1^{35}Cl_1$ required 408.0990 ($\Delta -1.8$ ppm).

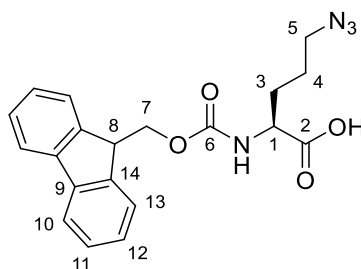
2-((((9*H*-Fluoren-9-yl)methoxy)carbonyl)amino)-2-(4-chlorophenyl)acetic acid (**9**)



Prepared following *general method 7* using $NaHCO_3$ (1.80 g, 21.5 mmol), H_2O (120 mL), MeCN (120 mL), 4-chloro-DL-phenylglycine (1.00 g, 5.39 mmol) and *N*-(9-fluorenylmethoxycarbonyloxy)succinimide (2.00 g, 5.93 mmol). The mixture was stirred at rt for 48 hours. After the work-up, the crude product was purified by flash chromatography on silica gel (0 to 20% MeOH in CH_2Cl_2) to yield **9** as a white solid (2.20 g, 5.39 mmol, quantitative).

$R_f = 0.47$ (20% MeOH/ CH_2Cl_2); **Mp** = 213.0-216.7 °C; δ_H (400 MHz, DMSO- d_6): 7.89 (2H, d, $J = 7.4$ Hz, H13), 7.72-7.70 (2H, m, H10), 7.41-7.29 (8H, m, H1, H2, H11, H12), 4.89 (1H, d, $J = 6.8$ Hz, H8), 4.28-4.22 (3H, m, H7, H15); δ_C (101 MHz, DMSO- d_6): 171.7 (C5), 155.8 (C6), 144.4 (C9), 144.2 (C14), 141.2 (C4), 129.5 (C1 or C2), 128.3 (C1 or C2), 128.0 (C13), 127.6 (C11 or C12), 125.7 (C3), 125.7 (C11 or C12), 120.5 (C10), 66.0 (C7), 59.2 (C15), 47.2 (C8); ν_{\max} : 3303 (OH, br), 1677 (C=O, m); **HRMS** (ESI+): m/z found $[M+Na]^+$ 430.0817, $C_{23}H_{18}O_4N^{35}Cl^{23}Na$ required 430.0817 ($\Delta 0.2$ ppm).

Fmoc-Azido ornithine (**12**)



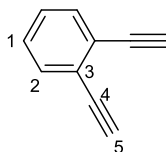
HCl in (4 M in 1,4-dioxane, 14 mL) was added to a solution of Fmoc-Orn(Boc)-OH (2.00g, 4.39 mmol) in 1,4-dioxane (14 mL). After stirring at rt for 16 h, the solvent was removed under a stream of N_2 and the resulting residue was suspended in Et_2O (70 mL). The solid was filtered and washed with Et_2O (70 mL) to give the Fmoc-Orn-OH HCl as a white solid (1.70 g, 99%). Fmoc-Orn-OH HCl (2.96 g, 7.54 mmol) was dissolved in a biphasic mixture of H_2O (44 mL), MeOH (87 mL) and CH_2Cl_2 (72 mL). $CuSO_4 \cdot 5H_2O$ (14.5 mg, 0.0580 mmol) and imidazole-1-

sulfonyl azide hydrogen sulfate **6** (5.80 g, 22.7 mmol) were added. The mixture was adjusted to pH 9 with K₂CO₃ aqueous solution. After stirring vigorously for 18 hours, the organic solvents were removed under reduced pressure. The remaining aqueous phase was washed with Et₂O (2 x 50 mL), acidified to pH 2 with concentrated HCl and extracted with Et₂O (3 x 50 mL). The organic extracts were dried (MgSO₄) and concentrated under reduced pressure. The oily residue was dissolved in EtOAc and the solvent removed under a stream of N₂ to give **12** as a white solid (2.25 g, 5.91 mmol, 78%).

δ_{H} (400 MHz, DMSO-d₆): 7.79 (2H, d, $J = 7.6$ Hz, H10), 7.62-7.60 (2H, m, H13), 7.43 (2H, app t, $J = 7.5$ Hz, H11), 7.33 (2H, app tt, $J = 7.4, 1.1$ Hz, H12), 5.39 (1H, d, $J = 8.1$ Hz, CONH), 4.60-4.45 (3H, m, H1, H7), 4.23 (1H, t, $J = 6.7$ Hz, H8), 3.35-3.16 (2H, m, H5), 2.07-1.46 (4H, m, H3, H4); δ_{C} (126 MHz, DMSO-d₆): 175.6 (C2), 156.1 (C6), 143.7 (C14), 141.3 (C9), 127.8 (C11), 127.1 (C12), 125.0 (C13), 120.1 (C10), 67.2 (C7), 53.2 (C8), 50.8 (C1), 47.2 (C5), 29.6 (C4), 29.5 (C3); $[\alpha]_{\text{D}}^{20} -2.02$ ($c = 1.0$, MeOH).

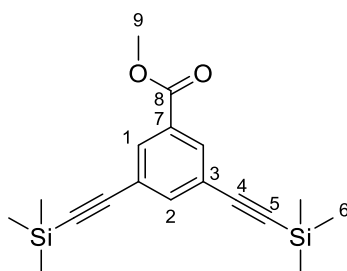
Characterisation data in accordance with literature.²⁵¹

6.1.1.3. Constraints

1,2-Diethynylbenzene (**C4**)

1,2-dibromobenzene (200 mg, 0.850 mmol), Pd(PPh₃)₂Cl₂ (23.8 mg, 0.0340 mmol), CuI (6.50 mg, 0.0340 mmol), PPh₃ (18.0 mg, 0.0680 mmol) were dissolved in DIPEA (283 μ L) and anhydrous toluene (1.41 mL). The mixture was stirred at rt for 5 minutes and TMS-acetylene was added. The mixture was refluxed under N₂ for 16 hours. The solution was cooled down to 0 °C and KOH (6N in MeOH, 1.30 mL, 3.40 mmol) was added and the mixture was stirred at rt for 6 hours. The reaction was quenched with saturated NH₄Cl and the volatiles removed under a stream of N₂. The aqueous phase was acidified to pH 5 and extracted with CH₂Cl₂ (3 x 5 mL). The combined organic layers were dried (MgSO₄), filtered, and the solvent evaporated under reduced pressure. The crude mixture was purified by flash chromatography on silica gel (100 % PE 30-40). To yield **C4** as a 42% w/v solution in PE 30-40 (107 mg, 0.850 mmol, quantitative).

R_f = 0.4 (100% hexane); **δ_{H}** (400 MHz, CDCl₃): 7.55-7.53 (2H, m, H₂), 7.34-7.32 (2H, m, H₁), 3.35 (2H, s, H₅); **δ_{C}** (101 MHz, CDCl₃): 132.6 (C₂), 128.5 (C₁), 125.1 (C₃), 81.8 (C₄), 81.1 (C₅); **ν_{max}** : 3287 (C \equiv C), 756 (C=C), 731 (C=C); **HRMS** (ASAP): *m/z* found [M]⁺ 126.0465, C₁₀H₆ required 126.0470 (Δ -4.0 ppm).

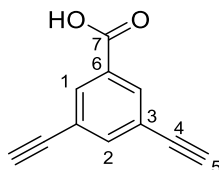
Methyl 3,5-bis((trimethylsilyl)ethynyl)benzoate (**C5-1**)

Trimethylsilylacetylene (6.00 mL, 42.2 mmol) was added to a stirring mixture of methyl 3,5-dibromobenzoate (900 mg, 3.10 mmol), Pd₂(dba)₃ (54.0 mg, 0.0590 mmol), CuI (11.4 mg, 0.00600 mmol) and PPh₃ (77.4 mg, 0.290 mmol) in dry triethylamine (15.0 mL). The reaction mixture was refluxed for 16 hours under N₂. The solvent was removed under reduced pressure, the residue was diluted with EtOAc and washed with H₂O. The organic phase was dried (MgSO₄) and the crude residue was purified by flash chromatography on silica gel (0-5% EtOAc in PE 40-60) to give **C5-1** as a yellow oil (693 mg, 2.11 mmol, 68%).

R_f = 0.4 (5% EtOAc/PE 40-60); M_p = 73-75 °C; δ_H (400 MHz, $CDCl_3$): 8.07 (2H, app d, J = 1.4 Hz, H1), 7.74 (1H, app t, J = 1.4 Hz, H2), 3.93 (3H, s, H9), 0.26 (18H, s, H6); δ_C (101 MHz, $CDCl_3$): 165.7 (C8), 139.0 (C2), 132.6 (C1), 130.5 (C3), 123.9 (C7), 102.9 (C4), 96.1 (C5), 52.4 (C9), -0.2 (C6); ν_{max} : 2956 (C≡C, m), 2157 (C≡C-H, m), 1729 (C=O, s); **HRMS** (ESI+): m/z found $[M+H]^+$ 329.1378, $C_{18}H_{25}O_3Si_2$ required 329.1388 (Δ 3.0 ppm).

Characterisation data in accordance with literature.²¹⁹

3,5-Diethylbenzoic acid (C5)

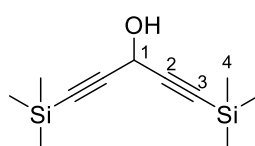


Prepared following *general method 8* using aqueous 6 M KOH (3.00 mL, 17.9 mmol), **C5-1** (590 mg, 1.79 mmol), MeOH (4.00 mL). After the work-up, **C5** was obtained as an orange solid (300 mg, 1.76 mmol, 98%).

R_f = 0.40 (20% MeOH/ CH_2Cl_2); δ_H (400 MHz, CD_3OD): 8.05 (2H, app d, J = 1.32 Hz, H1), 7.73 (1H, app s, H2), 3.66 (2H, s, H5); δ_C (101 MHz, CD_3OD): 166.4 (C7), 138.5 (C2), 132.6 (C1), 131.6 (C3), 123.3 (C6), 81.0 (C4), 79.2 (C5); ν_{max} : 3282 (C≡C, s), 1682 (C=O, s); **HRMS** (ESI+): m/z found $[M+H]^+$ 171.0444, $C_{11}H_7O_2$ required 171.0441 (Δ 1.9 ppm).

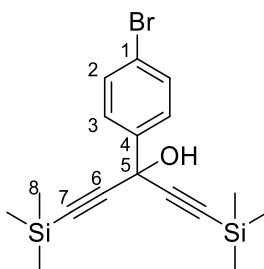
Characterisation data in accordance with literature.²²⁰

1,5-bis(Trimethylsilyl)penta-1,4-diyne-3-ol (C6-1)



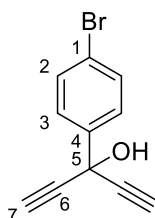
Prepared following *general method 9* using *n*BuLi (1.6 M in hexane, 3.15 mL, 0.100 mmol), trimethylsilylacetylene (0.700 mL, 0.100 mmol), THF (15.0 mL), 3-(trimethylsilyl)propionaldehyde (0.500 mL, 0.610 mmol). After the work up, the crude residue was purified by preparative TLC (5% EtOAc in toluene) to give **C6-1** as an orange oil (136 mg, 0.610 mmol, quantitative).

R_f = 0.3 (100% hexane); δ_H (400 MHz, $CDCl_3$): 5.10 (1H, s, H1), 3.49 (1H, br s, OH), 0.20 (18H, s, H4); δ_C (101 MHz, $CDCl_3$): 101.8 (C2), 89.4 (C3), 52.8 (C1), -0.4 (C4); ν_{max} : 3295 (O-H, br, w), 2961 (C≡C-H, m); **HRMS** (ESI+): m/z found $[M+H]^+$ 225.1121, $C_{11}H_{21}Si_2$ required 225.1131 (Δ -4.4 ppm).

3-(4-Bromophenyl)-1,5-bis(trimethylsilyl)penta-1,4-diyne-3-ol (**C6-6**)

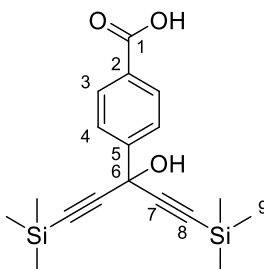
Prepared following *general method 9* using trimethylsilylacetylene (0.950 mL, 7.00 mmol) in THF (5.50 mL), *n*BuLi (1.6 M in hexane, 4.30 mL, 7.00 mmol), ethyl 4-bromo benzoate (300 μ L, 2.30 mmol) in THF (2.00 mL). After the work-up, the crude residue was purified by column chromatography on silica gel (100% hexane) to yield **C6-6** as a white solid (800 mg, 2.13 mmol, 93%).

R_f = 0.2 (100% hexane); **Mp** = 87.0-88.5°C; **δ_{H}** (400 MHz, CDCl₃): 7.67 (2H, d, *J* = 8.6 Hz, H₂), 7.53 (2H, d, *J* = 8.6 Hz, H₃), 2.97 (1H, br s, OH), 0.23 (18H, s, H₈); **δ_{C}** (101 MHz, CDCl₃): 140.7 (C₁), 131.5 (C₂), 127.8 (C₃), 122.8 (C₄), 104.1 (C₆), 90.5 (C₇), 65.0 (C₅), -0.4 (C₈); **ν_{max}** : 2960 (C \equiv C, m), 838 (C=C, s), 760 (C=C, s); **HRMS** (ESI⁺): *m/z* found [M+Na]⁺ 401.0367, C₁₇H₂₃ON⁷⁹BrNa required 401.0363 (Δ 0.9 ppm).

3-(4-Bromophenyl)penta-1,4-diyne-3-ol (**C6-7**)

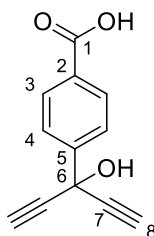
Prepared following *general method 8* using aqueous 6 M KOH (0.500 mL, 2.40 mmol), **C6-6** (100 mg, 0.260 mmol) and MeOH (0.500 mL). After the work-up, the crude material was purified by flash chromatography on silica gel (0 to 10% EtOAc in hexane) to yield **C6-7** as a yellow oil (33.0 mg, 0.140 mmol, 54%).

R_f = 0.11 (10% EtOAc/Hexane); **δ_{H}** (400 MHz, CDCl₃): 7.69 (2H, d, *J* = 8.6 Hz, H₂), 7.55 (2H, d, *J* = 8.6 Hz, H₃), 3.04 (1H, br s, OH), 2.82 (2H, s, H₇); **δ_{C}** (101 MHz, CDCl₃): 139.8 (C₁), 131.7 (C₂), 127.6 (C₃), 123.2 (C₄), 83.0 (C₆), 74.0 (C₇), 64.2 (C₅); **ν_{max}** : 3283 (C \equiv C, s), 944 (C=C, s), 826 (C=C, s); **HRMS** (ESI⁺): *m/z* found [M-H]⁻ 232.9602, C₁₁H₆O⁷⁹Br required 232.9602 (Δ 0.0 ppm).

4-(3-Hydroxy-1,5-bis(trimethylsilyl)penta-1,4-diyne-3-yl)benzoic acid (**C6-9**)

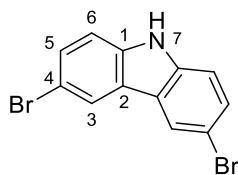
Prepared following *general method 9* using trimethylsilylacetylene (5.00 mL, 34.7 mmol) in THF (50.0 mL), n BuLi (1.6 M in hexane, 25 mL, 36.0 mmol) and methyl-4-carboxybenzoate (2.50 g, 13.8 mmol) in THF (10.0 mL). After the work-up, the crude residue was purified by flash chromatography on silica gel (100% CH_2Cl_2) to yield **C6-9** as an off white solid (2.20 g, 6.38 mmol, 46%).

R_f = 0.02 (0.5% MeOH/ CH_2Cl_2); **Mp** = 199.8-200.6 °C δ_H (400 MHz, CD_3OD): 8.05 (2H, d, J = 8.4 Hz, H3), 7.84 (2H, d, J = 8.4 Hz, H4), 0.22 (18H, s, H9); δ_C (101 MHz, CD_3OD): 168.0 (C1), 147.4 (C2), 130.4 (C5), 129.3 (C3), 125.6 (C4), 105.1 (C7), 88.6 (C8), 64.3 (C6), -1.7 (C9); ν_{max} : 3340 (O-H, br, w), 1683 (C=O, m); **HRMS** (ESI+): m/z found $[\text{M}+\text{H}]^+$ 345.1336, $\text{C}_{18}\text{H}_{25}\text{O}_3\text{Si}_2$ required 345.1342 (Δ -1.7 ppm).

4-(3-Hydroxypenta-1,4-diyne-3-yl)benzoic acid (**C6**)

Prepared following *general method 8* using aqueous 6 M KOH (5.00 mL, 29.0 mmol), **C6-9** (1.00 g, 2.84 mmol) and MeOH (6.00 mL). After the work-up, **C6** was yielded as a yellow solid (350 mg, 1.75 mmol, 62%).

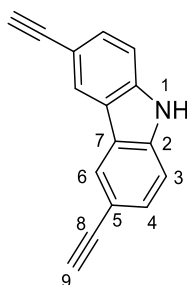
R_f = 0.4 (20% CH_2Cl_2 /MeOH); **Mp** = 154.4-155.6 °C; δ_H (400 MHz, CD_3OD): 8.07 (2H, d, J = 8.4 Hz, H3), 7.88 (2H, d, J = 8.4 Hz, H4), 3.22 (2H, s, H8); δ_C (101 MHz, CD_3OD): 167.9 (C1), 147.2 (C2), 130.5 (C5), 129.3 (C3), 125.6 (C4), 83.6 (C7), 73.2 (C8), 63.5 (C6); ν_{max} : 3275 ($\text{C}\equiv\text{C}$, m), 1658 (C=O, s); **HRMS** (ESI+): m/z found $[\text{M}+\text{Na}]^+$ 223.0369, $\text{C}_{12}\text{H}_8\text{O}_3\text{Na}$ required 223.0366 (Δ 1.7 ppm).

3,6-Dibromo-9*H*-carbazole (**C8-1**)

A solution of *N*-bromosuccinimide (1.17 g, 6.60 mmol) in DMF (66.0 mL) was added dropwise to an ice-cold suspension of carbazole (500 mg, 3.00 mmol) in toluene (2.50 mL). The reaction mixture was warmed to rt, stirred for 30 minutes then poured onto H₂O (100 mL). The precipitate formed was then washed with H₂O (20 mL) and cold MeOH (20 mL). The crude product was triturated in cold MeOH/hexanes (1:1) to give the desired product as an off-white solid (673 mg, 2.10 mmol, 69%).

R_f = 0.30 (30% CH₂Cl₂/PE 40-60); **Mp** = 250-256 °C (lit. 210-211 °C); **δ_H** (400 MHz, DMSO-*d*₆): 11.57 (1H, s, H7), 8.44 (2H, app. d, *J* = 1.44 Hz, H3), 7.55-7.47 (4H, m, H5, H6); **δ_C** (101 MHz, DMSO): 139.3 (C1), 129.2 (C3), 123.8 (C5), 123.8 (C4), 113.7 (C6), 111.4 (C2); **ν_{max}**: 3420 (N-H, s), 800 (C-Br, s); **HRMS** (ESI+): *m/z* found [M+H]⁺ 323.9012, C₁₂H₈N⁷⁹Br₂ required 323.9024 (Δ - 3.7 ppm).

Characterisation data in accordance with literature.^{252,253}

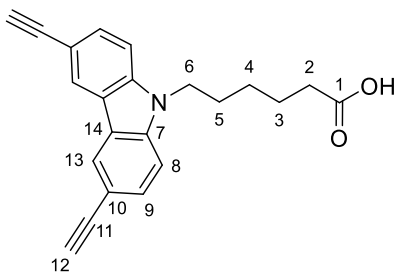
3,6-Diethynyl-9*H*-carbazole (**C8**)

A suspension of **C8-1** (5.00 g, 15.5 mmol), Pd(PPh₃)₂Cl₂ (500 mg, 0.775 mmol), CuI (100 mg, 0.465 mmol), ethynyltrimethylsilane (10.0 mL, 69.8 mmol), and PPh₃ (100 mg, 0.388 mmol) in NEt₃ (160 mL) was refluxed for 48 hours. The reaction mixture was filtered through Celite, washed with H₂O (50 mL), brine (50 mL) and dried (MgSO₄). The mixture was concentrated under reduced pressure and the residue resuspended in 500 mL of MeOH. K₂CO₃ (14.1 g, 101 mmol) was added and the suspension stirred at rt for 18 hours. The reaction mixture was evaporated under reduced pressure and the residue was purified by flash column chromatography on silica gel (30% CH₂Cl₂/PE 40-60) to yield the desired product as a dark orange solid (2.69 g, 12.5 mmol, 81%).

R_f = 0.28 (20% EtOAc/hexanes); **Mp** = 210 °C decomp. (lit. Mp = 212-213 °C); δ_H (400 MHz, DMSO- d_6): 11.71 (1H, s, H1), 8.37 (2H, s, H6), 7.50 (4H, app. s, H3, H4), 4.04 (2H, s, H9); δ_C (101 MHz, DMSO- d_6): 140.5 (C2), 130.2 (C4), 125.2 (C6), 122.4 (C7), 112.6 (C5), 112.0 (C3), 85.3 (C9), 78.9 (C8); ν_{max} : 3404 (NH s), 3269 (C \equiv C-H, m), 2103 (C \equiv C, s), **HRMS** (ESI): m/z found [M+H]⁺ 216.0818, C₁₆H₁₀N required 216.0813 (Δ 2.3 ppm).

Data in accordance with the literature.²⁴⁴

6-(3,6-Diethynyl-9H-carbazol-9-yl)hexanoic acid (**C9**)



Prepared following a literature procedure.²⁵⁴ To a solution of 3,6-diethynyl-9H-carbazole (1.00 g, 2.78 mmol) in DMF (5.60 mL) was added powdered KOH (1.23 g, 22.0 mmol). The reaction mixture was stirred at rt for 20 minutes. After this time 6-bromohexanoic acid (1.08 g, 5.56 mmol) was added and the reaction was irradiated at 37 kHz ultrasonic waves at 35 °C for 2 hours. The reaction was acidified to pH 5 with conc HCl, portioned with Et₂O and H₂O and the organic phase washed with brine. The organic extract was dried (MgSO₄) and the solvent removed under reduced pressure. The crude product was purified by flash chromatography on silica gel (0-50% EtOAc/hexane) to yield **C9** as a gummy yellow oil (880 mg, 1.86 mmol, 67%).

R_f = 0.20 (20% EtOAc/hexane); δ_H (400 MHz, CDCl₃): 8.22 (2H, d, J = 1.0 Hz, H13), 7.61 (2H, dd, J = 8.4, 1.00 Hz, H9), 7.32 (2H, J = 8.4 Hz, H8), 4.27 (2H, t, J = 9.4 Hz, H6), 3.11 (2H, s, H12), 2.34 (2H, t, J = 7.4 Hz, H2), 1.88 (2H, app quint., J = 7.4 Hz, H5), 1.68 (2H, app quint., J = 6.8, H3), 1.46-1.39 (2H, m, H4); δ_C (101 MHz, CDCl₃): 179.6 (C1), 140.6 (C7), 130.2 (C13), 124.8 (C9), 122.3 (C14), 112.8 (C10), 108.9 (C8), 84.7 (C11), 75.6 (C12), 43.0 (C6), 33.7 (C2), 28.6 (C5), 26.6 (C4), 24.3 (C3); ν_{max} : 3260 (C \equiv C, m), 1698 (C=O, s); **HRMS** (ESI+): m/z found [M+H]⁺ 330.1491, C₂₂H₂₀O₂N required 330.1494 (Δ -0.9 ppm).

6.1.2. Peptides

General method 10: Manual peptide synthesis

Manual peptide synthesis was performed on Merck LL MHBA Rink amide resin (0.33 mmol/g, 1 equiv). Couplings were carried out by adding HATU (4 equiv) to a solution of the Fmoc-protected amino acid (4 equiv) in DMF (~0.4 M). After 10 seconds, DIPEA (8 equiv) was added to the mixture. This pre-activated mixture was then added to the resin in DMF and shaken for 3 minutes. The coupling time was extended in the case of N-terminal capping with **C5** and **C9** (1 hour), for coupling of Arg and unnatural amino acids (30 minutes). The side chain protecting groups used were: ^tBu for Asp, Glu, Ser, Thr, Tyr; Boc for Lys, Trp; Pbf for Arg; Trt for Asn, Gln, His. Fmoc-Lys(dddve)-OH was used for conjugation of FITC with Lys. Fmoc-Gly(Dmb)-OH was used for the synthesis of peptide **P7**.

Fmoc deprotection was carried out with 20% piperidine in DMF (3 x 3 minutes).

N-terminal capping with FITC and Ac₂O (2 equiv) was achieved using DIPEA (4 equiv) in CH₂Cl₂ overnight (FITC) or for 1 hour (Ac₂O).

On-resin attachment of FITC *via* Lys was achieved by orthogonal deprotection of the Lys(dddve) with 5% NH₂NH₂ in DMF (2 x 10 minutes) followed by conjugation with FITC (2 equiv) in the presence of DIPEA (4 equiv) overnight.

Completion of amide couplings and Fmoc deprotection was determined by a chloranil test, in which acetaldehyde (200 μL) and a saturated solution of chloranil in toluene (50 μL) were added to a small amount of resin swelled in CH₂Cl₂. After 10 seconds shaking at rt, no change in colour indicated complete coupling, whilst green colouration of the resin indicated presence of a free amine. Any incomplete couplings was submitted to a second round of coupling.

Side chain deprotection and cleavage from the resin was achieved with TFA containing 2.5% TIPS and 2.5% H₂O for 3 hours at rt or 1 hour at 42 °C. In case of methionine and cysteine-containing peptides, cleavage was achieved with TFA containing 5% EDT, 5% H₂O and 2.5% TIPS. After cleavage, the mixture was filtered through a sintered funnel, the beads washed with MeOH and the filtrate was concentrated under a stream of N₂. The crude residue was triturated with cold Et₂O before purification by preparative HPLC.

General method 11: Automated Fmoc solid-phase peptide synthesis

Automated peptide synthesis was carried out on a CEM Liberty Automated Microwave Peptide Synthesiser using Merck LL MHBA Rink Amide resin (0.33 mmol/g, 1 equiv). All peptide couplings were performed with Fmoc-protected amino acids (5 equiv), Oxyma pure (10 equiv) and DIC (5 equiv) in DMF. Arg was coupled using double couplings for 15 min each without

microwave irradiation. All other amino acids were coupled with 25 W power at 75 °C over 15 min.

Fmoc deprotection was achieved with a solution of 20% piperidine in DMF, using 45 W power at 75 °C over 3 min. N-terminal capping, cleavage and HPLC purification of peptides were carried out as previously described for manual SPPS (general method 10).

General method 12: Peptide stapling *via* Copper-catalysed azido-alkyne click (CuAAC).³⁸

A solution of diazido peptide (1 equiv) and dialkynyl linker (1 equiv) in 1:1 *t*BuOH/H₂O (0.8 mL/mg peptide) was degassed with N₂ for 15 min, followed by the addition of CuSO₄ · 5H₂O (1 equiv), THPTA (1 equiv), and sodium ascorbate (3 equiv). Peptides bearing sulfur atoms required CuSO₄ · 5H₂O (2 equiv), THPTA (2 equiv), and sodium ascorbate (6 equiv). All the reactions were stirred under N₂ and monitored by LCMS. When no starting material could be detected by LCMS, the reaction mixture was diluted with H₂O and lyophilised prior to purification. The absence of azido peak on IR (~ 2100 cm⁻¹) was checked for all the purified, dried peptide.

General method 13: Peptide macrocyclisation *via* disulphide bridge formation.²¹⁵

To a solution of the linear peptide in aqueous AcOH (50%) was added 2 mM I₂ in MeOH dropwise. After 5 minutes the reaction was quenched by adding ascorbic acid (1 M). The crude mixture was directly purified on preparative HPLC.

General method 14: Peptide macrocyclisation *via* ring-closing metathesis (RCM).⁴⁶

RCM of the peptides was carried out on resin. After N-terminus capping, the resin was de-swollen in MeOH, then washed with CH₂Cl₂ and resuspended in the minimum amount of CH₂Cl₂. Grubb's II catalyst (20 mol%) was dissolved in CH₂Cl₂ and added to the resin under bubbling N₂. The reaction was agitated for 2 hours. The resin was then washed with CH₂Cl₂ and the process repeated. The peptide was then cleaved from the resin and purified as described above (*general method 10*).

6.1.2.1. Conversion of CuAAC macrocyclisation reactions

The conversions of the peptides that underwent macrocyclisation *via* CuAAC 2C PS refer to LCMS conversion of the crude material (Table 18). All the reactions were quenched when no starting material could be detected.

Table 18 - LCMS conversion of peptides that underwent CuAAC cyclisation. CK2 peptides are shown in the left column, BH3 peptides in the right column.

Peptide	Conversion (%)	Peptide	Conversion (%)
P0-C1	82	P9-C5	58
P1-C2	65	P9-C7	81
P1-C3	62	P9-F4C5	59
P1-C4	79	P9-F5C5	87
P1-C5	92	P11-F4C5	NA
P1-C6-7	52	P14-C8	NA
P1-C6	85	P15-C8	90
FITC-P1-C5	56	P16-C8	60
P1-F1C5	79	P17-C5	92
P1-F2C5	54	P18-C5	68
P1-F3C5	87	P19-C5	97
P2'-C5	67	P17-F1C5	92
P2''-C5	NA	P18-F1C5	77
P3-C5	53	P19-F1C5	72
P4-C5	60	FITC-Ahx-P9-F4C4	74
P5'-C5	53	FITC-Ahx-P9-F5C5	90
P5''-C5	47	FITC-Ahx-P11-F4C4	79
P6-C5	88		
P7-C5	83		
P7-F1C5	60		
P7-F2C5	72		
P8-F1C5	72		

NA = not available due to complicated chromatogram.

6.1.2.2. LCMS and purity of CK2 peptides

CK2 peptides sequence, mass observed on LCMS, purity and retention time (Rt) by analytical HPLC are shown in Table 19.

Table 19- Sequence, mass, purity and retention time of CK2 peptides

Peptide	Sequence	Mass	m/z found	m/z calcul.	Species	Purity	Rt* (min)
Pc	GCRLYGFKIHGCG(S-S)	1448.7	1449.5	1449.7	M+H	87%	7.26
Pc linear	GCRLYGFKIHGCG	1450.7	1451.49	1451.7	M+H	99%	9.62
Short Pc linear	CRLYGFIHGC	1336.6	1337.3	1337.7	M+H	90%	9.92
Short Pc	CRLYGFKIHGC (S-S)	1334.6	1335.4	1335.6	M+H	84%	14.32
P0	XRLYGFKIHGX	1297.7	1298.9	1298.7	M+H	> 99%	10.16
P0-C1	X _{C1} RLYGFKIHXC ₁	1376.7	1377.5	1377.7	M+H	97%	6.96
P1	GXRLYGFKIHGXGG	1468.7	1470	1469.8	M+H	91%	7.29
P1-C2	GXC ₂ RLYGFKIHXC ₂ GG	1594.8	1595.61	1595.8	M+H	91%	7.78
P1-C3	GXC ₃ RLYGFKIHXC ₃ GG	1532.8	1533.6	1533.8	M+H	97%	6.98
P1-C4	GXC ₄ RLYGFKIHXC ₄ GG	1423.7	1424.5	1424.7	M+H	97%	7.85
P1-C5	GXC ₅ RLYGFKIHXC ₅ GG	1638.9	1639.4	1639.9	M+H	89%	7.46
P1-C6-7	GXC ₆₋₇ RLYGFKIHXC ₆₋₇ GG	1702.7	568.6	568.3	M+3H	> 99%	7.74
P1-C6	GXC ₆ RLYGFKIHXC ₆ GG	1671.0	836.2	836.2	M+2H	92%	7.14
FITC-P1	FITC-Ahx-GXRLYGFKIHGXGG	1929.7	644.6	644.3	M+3H	62%	8.96
FITC-P1-C5	FITC-Ahx-GXC ₅ RLYGFKIHXC ₅ GG	1709.7	1710.1	1710.7	M+H	94%	7.89
P1-F1C5	GXF _{1C5} RLYGFKIHXF _{1C5} GG	2334.3	1168.1	1168.1	M+2H	>99%	6.96
P1-F2C5	GXF _{2C5} RLYGFKIHXF _{2C5} GG	2851.4	1427.3	1426.7	M+2H	98%	7.69
P1-F3C5	GXF _{3C5} RLYGFKIHXF _{3C5} GG	1191.1	1192.7	1192.1	M+2H	89%	8.44
P2'	GXRLYG(L-3-CI-F)KIHGXGG	1502.7	752.3	752.4	M+2H	74%	7.57
P2''	GXRLYG(3-CI F)KIHGXGG	1502.7	752.3	752.4	M+2H	91%	7.50
P2'-C5	GXC ₅ RLYG(L-3-CI F)KIHXC ₅ GG	1674.7	1675	1675.7	M+H	90%	7.46
P2''-C5	GXC ₅ RLYG(D-3-CI F)KIHXC ₅ GG	1674.7	1675.5	1675.7	M+H	85%	7.24
P3	GXRLYG(4-CI-F)KIHGXGG	1502.7	752.3	752.4	M+2H	87%	7.71
P3-C5	GXC ₅ RLYG(4-CI-F)KIHXC ₅ GG	1677.8	1676.9	1676.8	M-H	92%	7.33
P4	GXRLYG(3-CI phegly)KIHGXGG	1490.7	1491.1	1491.7	M+H	>99%	7.56
P4-C5	GXC ₅ RLYG(3-CI phegly)KIHXC ₅ GG	1659.8	1659.6	1658.4	M-H	92%	8.26
P5	GXRLYG(4-CI phegly)KIHGXGG	1490.7	1491.2	1491.7	M+H	>99%	7.61
P5'-C5	GXC ₅ RLYG(4-CI phegly)KIHXC ₅ GG	1659.8	1661.3	1660.8	M+H	92%	7.25
P5''-C5	GXC ₅ RLYG(4-CI phegly)KIHXC ₅ GG	1659.8	1661.3	1660.8	M+H	97%	7.38
P6	GXRLPGFKIHGXGG	1403.7	1402.1	1402.7	M-H	89%	7.15
P6-C5	GXC ₅ RLPGFKIHXC ₅ GG	1573.6	1574.7	1573.7	M+H	98%	6.95
P7	GXRLYGFKWHGXGG	1543.7	1544	1544.7	M+H	95%	7.48
P7-C5	GXC ₅ RLYGFKWHXC ₅ GG	1713.6	1714.7	1714.6	M+H	>99%	7.29
P7-F1C5	GXF _{1C5} RLYGFKWHXF _{1C5} GG	2407.3	1205	1204.5	M +2H	>99%	7.22
P7-F2C5	GXF _{2C5} RLYGFKWHXF _{2C5} GG	2929.5	1462.2	1463.7	M+2H	95%	7.62

P8-F1C5	GX _{F1C5} RLYGFKIH _X _{F1C5} GG	2146.1	1074.2	1074.1	M+2H	86%	6.27
e1F2β	MSGDEMIFDPTMS(K)8PNH2	1311.7	1312.9	1312.7	M+2H	90%	6.85

*rt (retention time) on a 5 to 95 % B over 15 minutes run on analytical HPLC. X = Aza-alanine. All the peptides feature an amide at the C-terminus and an acetyl capping at the N-terminus

6.1.2.3. LCMS and purity of CPPs

CPPs sequence, mass observed on LCMS, purity and retention time (Rt) by analytical HPLC are shown in Table 20.

Table 20-Sequence, mass, purity and retention time of cell-penetrating peptides.

Peptide	Sequence	Mass	m/z found	m/z calcul.	Species	Purity	Rt* (min)
F1C5	C5-(Ahx) ₂ +[(D)R] ₃	863.5	864.9	864.5	M+H	99%	7.47
F2C5	C5-Ahx ₂ [(D)R] ₃ K-FITC	1381.7	1382.4	1382.7	M+H	83%	9.18
F3C5	C5-(Ahx) ₂ +K+FITC	911.3	912.4	911.3	M+H	97%	7.18
F4C4	C5-RRR	637.4	638.7	638.4	M+H	93%	6.6
F5C5	C5-(Ahx) ₂ -PKKKRKV	1259.8	1261.2	1260.9	M+H	99%	7.3

*rt (retention time) on a 5 to 95 % B over 15 minutes run on analytical HPLC.

6.1.2.4. LCMS and purity of BH3 peptides

BH3 peptides sequence, mass observed on LCMS, purity and retention time (Rt) by analytical HPLC are shown in Table 21.

Table 21-Sequence, mass, purity and retention time of BH3 peptides.

Peptide	Sequence	Mass	m/z found	m/z calcul.	Species	Purity	Rt* (min)
P9	IWIAQELRX _{F5C5} IGDX _{F5C5} FNAYYARR	2677.4	1339.7	1337.6	M+2H	94%	13.7
P9-C5	IWIAQELRX _{C5} IGDX _{C5} FNAYYARR	2846.4	1424.9	1424.2	M+2H	93%	9.92
P9-F4C5	IWIAQELRX _{F4C5} IGDX _{F4C5} FNAYYARR	3315.2	1658.1	1658.1	M+2H	96%	14.32
P9-F5C5	IWIAQELRX _{F5C5} IGDX _{F5C5} FNAYYARR	3940.0	1314.1	1314.3	M+3H	> 99%	8.49
P9-C7	IWIAQELRX _{C7} IGDX _{C7} FNAYYARR	2975.2	1487.6	1487.6	M+2H	99%	10.09
FITC-P9	FITC-Ahx-IWIAQELRXIGDXFNAYYARR	3136.5	1046.6	1046.2	M+3H	>99%	11.73
FITC-P9-F4C5	FITC-Ahx-IWIAQELRX _{F4C5} IGDX _{F4C5} FNAYYARR	3773.8	1887.3	1887.9	M+2H	83%	9.96
FITC-P9-F5C5	FITC-Ahx-IWIAQELRX _{F5C5} IGDX _{F5C5} FNAYYARR	4397.3	1465.3	1466.4	M+3H	>99%	9.82
FITC-P9-C7	FITC-Ahx-IWIAQELRX _{C7} IGDX _{C7} FNAYYARR	3228.6	1075.7	1075.5	M-3H	89%	12.14
P10	IWIAQELRRIGDEFNAYYARR	2682.1	1341.6	1341.2	M +2H	95%	6.16 ^a
FITC-P10	FITC-Ahx-IWIAQELRRIGDEFNAYYARR	3141.5	1629.86	1629.2	(M+TFA)	88%	9.9
P11-F4C5	IWIAQELDX _{F4C5} IGDX _{F4C5} FNAYYARR	3272.7	1638.4	1638.3	M+2H	98%	8.98
FITC-P11	FITC-Ahx-IWIAQELDXIGDXFNAYYARR	3095.4	1548.7	1548.7	M+2H	97%	12.27
FITC-P11-F4C5	FITC-Ahx-IWIAQELDX _{F4C5} IGDX _{F4C5} FNAYYARR	3731.8	1866.9	1866.4	M+2H	90%	10.11
SAHBa	IWIAQELRX _{AH} IGDX _{AH} FNAYYARR	2646.4	1324.24	1324.2	M+2H	91%	11.13
FITC-SAHBa	FITC-Ahx-IWIAQELRX _{AH} IGDX _{AH} FNAYYARR	3106.5	1554.8	1554.2	M+2H	93%	11.91
P12	RYGRELRRMSDEFVDSF	2204.6	2205.7	2205.7	M+H	87%	7.81

Chapter 6: Chemistry Experimental

P13	IIRNIARHLAQVGDSDMSDRS	2192.2	1098	1098.1	M+2H	96%	8.66
P14	IAXELRRIGDEFNXYAA	2151.1	2152.4	2152.4	M+H	86%	9.21
P14-C8	IAX _{C8} ELRRIGDEFN _{C8} YAA	2366.1	1182.6	1182.2	M-2H	92%	9.95
P15	XYGRELRRMSDXFVDSF	2199.6	2200.5	2200.6	M+H	75%	8.79
P15-C8	X _{C8} YGRELRRMSDX _{C8} FVDSF	2414.0	2415.2	2415	M+H	75%	9.59
P16	IIRNIAXHLAQVGDSDMXS	2160.4	2161.8	2161.4	M+H	85%	9.68
P16-C8	IIRNIAX _{C8} HLAQVGDSDMX _{C8} S	2375.5	1189.2	1188.7	M+2H	90%	9.45
P17	IAQXLRRIGDXFNAYAA	2092.1	1047.7	1047	M+2H	75%	10.65
P17-C5	IAQX _{C5} LRRIGDX _{C5} FNAYAA	2262.1	2263.8	2263.1	M+H	88%	10.1
P17-F1C5	IAQX _{F1C5} LRRIGDX _{F1C5} FNAYAA	2955.6	1479.2	1478.8	M+2H	88%	9.42
P18	YGRXLRRMSDXFVDSF	2069.0	1035.6	1035.5	M+2H	80%	9.2
P18-C5	YGRX _{C5} LRRMSDX _{C5} FVDSF	2240.7	1120.0	1120.0	M+2H	85%	8.74
P18-F1C5	YGRX _{F1C5} LRRMSDX _{F1C5} FVDSF	2933.0	1468.4	1466.5	M+2H	>99%	8.59
P19	IIRXIARHLAXVGDSDMSDRS	2230.2	1117.1	1116.1	M+2H	75%	9.3
P19-C5	IIRX _{C5} IARHLAX _{C5} VGDSDMSDRS	2400.2	1202.3	1201.1	M+2H	98%	9.52
P19-F1C5	IIRX _{F1C5} IARHLAX _{F1C5} VGDSDMSDRS	3097.0	1548.8	1548.5	M+2H	90%	9.09

*Unless otherwise specified, rt (retention time) refers to a 5 to 95 % B over 15 minutes run on analytical HPLC.

^a rt on a 30 to 100% solvent B over 15 minutes.

CHAPTER 7:
Computational Chemistry
Experimental

With the exclusion of the docking studies, all the experiments described in this dissertation were performed by Dr Yaw Sing Tan, A*STAR, Singapore.

7.1. Docking studies for CK2 fragments

All the docking studies herein reported were performed using Glide of the suite Maestro, produced by Schrodinger.²⁵⁵⁻²⁵⁷ The protein was prepared starting from the PDB file of the X-ray structures generated by Dr Paul Brear (Department of Biochemistry, Hyvönen Group) and using the PrepWinz feature of Maestro. To keep the conformation of the protein as close as possible to the X-ray structures, no modifications such as 'cap termini', 'filling loops' or 'side chain', 'original hydrogen deletion' were performed. Only the orientation of the water molecules was sampled, and the ionisation state of the protein was calculated at pH 7 ± 2 . Ligands were prepared with the LigPrep functionality, using OPLS_2005 as the force field. All other parameters were left as default. Conformational search of the ligands was performed after ligand preparation. The parent ligand of the crystal structure was used as the template for the grid generation and positional constraints were given to the benzylamine nitrogen of the ligand. All other parameters were left as default. Ligand input partial charges were used and, in addition to default parameters, the planarity of conjugated pi groups was enhanced. For the conformer generation, enhanced sampling was used, and the energy window for ring sampling was increased to 3.5 kcal mol⁻¹.

7.2. Computational chemistry for CK2 peptides

7.2.1 Molecular dynamics

Chains A and D from the crystal structure of human CK2 α in complex with a CK2 β -derived cyclic peptide called Pc (1-GCRLYGFKIHGCG-13) (PDB: 4IB5)²¹⁵ were used as the initial structures for molecular dynamics (MD) simulations. The unresolved CK2 α residue Met1 was added using PyMOL. CK2 α was capped at its C-terminus by *N*-methyl while Pc was capped by acetyl and amide groups. Crystallographic water molecules were retained. PDB2PQR²⁵⁸ was then used to determine the protonation states of residues. Using the LEaP program in the AMBER 14²⁵⁹ package, each complex was solvated with TIP3P²⁶⁰ water molecules in a periodic truncated octahedron box such that its walls were at least 10 Å away from the complex, followed by neutralisation of the system with either sodium or chloride ions.

Energy minimisations and MD simulations were carried out by the PMEMD module of AMBER 14, using the ff14SB²⁶¹ force field for protein residues and the generalised AMBER force field (GAFF)²⁶² for the stapled residues. Atomic charges for the stapled residues were derived using the R.E.D. Server,²⁶³ which fits restrained electrostatic potential (RESP) charges²⁶⁴ to a molecular electrostatic potential (MEP) computed by the Gaussian 09 program²⁶⁵ at the HF/6-31G* theory

level. A total of three independent explicit-solvent MD simulations using different initial atomic velocities were carried out. The SHAKE algorithm²⁶⁶ was applied to constrain all bonds involving hydrogen atoms, allowing for a time step of 2 fs. A cutoff distance of 9 Å was implemented for nonbonded interactions. The particle mesh Ewald method²⁶⁷ was used to treat electrostatic interactions with a grid spacing of 1.0 Å and the order of B-spline interpolation set to 4. Energy minimisation was performed for 500 steps with the steepest descent algorithm, followed by another 500 steps with the conjugate gradient algorithm. The system was then heated gradually to 300 K over 50 ps at constant volume before equilibration at a constant pressure of 1 atm for another 50 ps. During the minimisation and equilibration, weak harmonic positional restraints with a force constant of 2.0 kcal mol⁻¹ Å⁻² were imposed on the non-hydrogen atoms of the solute. These restraints were removed in a subsequent equilibration run (2 ns) and the production run (100 ns), which were carried out at 300 K and 1 atm. The Langevin thermostat²⁶⁸ was used to maintain the temperature with a collision frequency of 2 ps⁻¹. Pressure was maintained by a Berendsen barostat²⁶⁹ with a pressure relaxation time of 2 ps.

7.2.2 Ligand mapping simulations

Ten different distributions of chlorobenzenes around apo CK2α were created using Packmol.²⁷⁰ The LEaP module in the AMBER 14 package was then used to solvate each system with TIP3P water molecules in a periodic truncated octahedron box, such that its walls were at least 10 Å away from the protein, resulting in a final chlorobenzene concentration of ~0.15 M. Minimisation, equilibration and production (20 ns) MD simulations were carried out as described above for the CK2α complexes, for a cumulative sampling time of 200 ns. The GAFF6 force field was used to describe the chlorobenzenes during the simulations. Atomic charges for chlorobenzene were used as previously described.²⁷¹

The 10 individual runs were combined into a single trajectory for analysis. Chlorobenzene occupancy grids were generated using the cpptraj module of AMBER 14 to bin both carbon and chlorine atoms of chlorobenzenes into 1 Å × 1 Å × 1 Å grid cells. The cutoff isocontour value used for visualisation of chlorobenzene carbon and chlorine atom occupancies is five times the threshold bulk value, which is defined as the highest isovalue at which the respective atoms are detected in the bulk solvent. In order to compare the overlap of the chlorobenzene occupancy maps with known CK2α ligands, the respective ligand-bound CK2α structures were aligned using PyMOL²⁷² to the average protein structure sampled during the LMMD simulations.

7.2.3 Binding free energy decomposition

The contribution of each Pc peptide residue to the binding free energy of the complex was computed by applying the free energy decomposition method²⁷³ on 200 equally-spaced structures extracted from the last 40 ns of the MD simulations of the CK2α–Pc complex. Binding

free energies were calculated in AMBER 14²⁵⁹ using the molecular mechanics/generalised Born surface area (MM/GBSA) method.²⁷⁴ The molecular mechanical energies and polar contribution to solvation free energy were computed by the sander module and pbsa program using the modified GB model described by Onufriev *et al.*²⁷⁵ respectively. The nonpolar contribution to solvation free energy was estimated from the solvent accessible surface area (SASA) using the ICOSA method.²⁷⁶

7.2.4 Computational alanine scanning (CAS)

Computational alanine scanning was carried out on 200 equally-spaced structures extracted from the last 40 ns of the MD simulations of the CK2 α -Pc complex. The difference in the binding free energy ($\Delta\Delta G_{\text{bind}}$) of the wild-type and alanine mutants was calculated using the MM/GBSA method 18 with modules in AMBER 14.²⁵⁹ Molecular mechanical energies were calculated with the sander module. The polar contribution to the solvation free energy was calculated by the pbsa module²⁷⁷ using the modified GB model described by Onufriev *et al.*²⁷⁵ while the nonpolar contribution was estimated from the SASA using the linear combinations of pairwise overlaps method,²⁷⁸ with γ set to 0.0072 kcal mol⁻¹ Å⁻² and β to zero.²⁷⁸ The entropy term was not considered due to the high computational cost and the assumption that the entropy of the mutant does not differ considerably from that of the wild-type.²⁷⁹

7.2.5 Binding free energy calculations

Binding free energies for the CK2 α complexes were calculated using the molecular mechanics/generalised Born surface area (MM/GBSA) method²⁷⁴ implemented in AMBER 14.²⁵⁹ Two hundred equally-spaced snapshot structures were extracted from the last 40 ns of each of the trajectories, and their molecular mechanical energies calculated with the sander module. The polar contribution to the solvation free energy was calculated by the pbsa²⁷⁷ module using the modified generalised Born (GB) model described by Onufriev *et al.*²⁷⁵ while the nonpolar contribution was estimated from the solvent accessible surface area using the molsurf²⁸⁰ program with $\gamma = 0.0072$ kcal Å⁻² and β set to zero. Entropies were estimated by normal mode analysis²⁸¹ using the nmode program. Due to its computational expense, only 50 equally-spaced snapshots from the last 40 ns of the trajectories were used for entropy calculations.

7.3. Computational chemistry for BH3 peptides

7.3.1 Preparation of structures

The structure of Bcl-x_L (Δ 45-84) in complex with Bim BH3 (residues 141-166) (PDB: 4QVF)²⁴⁶ was used as the initial structure for MDs. Bim BH3 was truncated to residues 146-166. The unresolved Bim residues 165 and 166 were then added using PyMOL to give peptide **P9-C2**. Bcl-x_L was capped at its *N*- and *C*-termini by acetyl and *N*-methyl groups respectively while peptide **P9-C2** was capped at its *N*- and *C*-termini by acetyl and amide groups respectively. Peptide **P9-C2** was modified into the stapled peptide by replacing residues 154 and 158 with a two-component triazole staple formed by a double-click reaction between two azido-ornithine residues and 1,3-diethylnylbenzene. PDB2PQR²⁵⁸ was used to determine the protonation states of residues. Each Bcl-x_L complex was solvated with TIP3P water molecules²⁶⁰ in a periodic truncated octahedron box, such that its walls were at least 9 Å away from the complex, and neutralised with sodium ions.

7.3.2 Molecular dynamics

Energy minimisations and MD simulations were performed with the sander and PMEMD modules of AMBER 14²⁵⁹ respectively. Three independent MD simulations were carried out on each of the Bcl-x_L complexes using the ff14SB²⁶¹ and GAFF. Atomic charges for the stapled residues were derived using the R.E.D. Server,²⁶³ which fits RESP charges²⁶⁴ to a MEP computed by the Gaussian 09 program²⁶⁵ at the HF/6-31G* theory level. All bonds involving hydrogen atoms were constrained by the SHAKE algorithm,²⁶⁶ allowing for a time step of 2 fs. Nonbonded interactions were truncated at 9 Å, while the particle mesh Ewald method²⁶⁷ was used to account for long range electrostatic interactions under periodic boundary conditions. Weak harmonic positional restraints with a force constant of 2.0 kcal mol⁻¹ Å⁻² were placed on the protein and peptide non-hydrogen atoms during the minimisation and equilibration steps. Energy minimisation was carried out using the steepest descent algorithm for 500 steps, followed by the conjugate gradient algorithm for another 500 steps. The systems were then heated gradually to 300 K over 50 ps at constant volume before equilibration at a constant pressure of 1 atm for another 50 ps. Subsequent unrestrained equilibration (2 ns) and production (100 ns) runs were carried out at 300 K using a Langevin thermostat²⁶⁸ with a collision frequency of 2 ps⁻¹, and 1 atm using a Berendsen barostat²⁶⁹ with a pressure relaxation time of 2 ps.

7.3.3 Binding free energy calculations

Binding free energies for the Bcl-x_L complexes were calculated using the molecular mechanics/generalised Born surface area (MM/GBSA) method²⁷⁴ implemented in AMBER 14.²⁵⁹

Two hundred equally-spaced snapshot structures were extracted from the last 40 ns of each of the trajectories, and their molecular mechanical energies calculated with the sander module. The polar contribution to the solvation free energy was calculated by the pbsa program²⁷⁷ using the modified GB model described by Onufriev *et al.*²⁷⁵ while the nonpolar contribution was estimated from the solvent accessible surface area using the molsurf program²⁸⁰ with $\gamma = 0.0072$ kcal Å⁻² and β set to zero. Entropies were estimated by normal mode analysis²⁸¹ using the nmode program. Due to its computational expense, only 50 equally-spaced snapshots from the last 40 ns of the trajectories were used for entropy calculations.

CHAPTER 8:
Biophysics Experimental

8.1. Biophysics experimental for CK2 fragments and peptides

8.1.1. Protein expression and purification

8.1.1.1. CK2 α

Three constructs of CK2 α were used in this study. For kinase activity assays and competition experiments, CK2 α _WT was used (residues 2-329). For ITC CK2 α _KA construct was used whilst CK2 α _FP10 was used for crystallisation purposes. CK2 α _KA (residues 2-329) contained four mutations designed to aid crystallisation by reducing the overall charge of the protein; R21S, K74A, K75A and K76A. CK2 α _FP 10 contained one mutation (R21S) and an *N*-terminal extension GSMDIEFDDDDADDDGSGSGSGSGS aimed at mimicking a substrate peptide for CK2 α . CK2 α _FP10 was cloned into pHAT4 vector and CK2 α _KA was cloned into pHAT2 vector to give constructs with cleavable His6-tags. Recombinant plasmids containing one of the three constructs (CK2 α _WT/ CK2 α _KA/ CK2 α _FP10) were introduced into *Escherichia coli* BL21(DE3) for protein production. Single colonies of the cells were grown in 6 x 1L of 2 x TY with 100 μ g/mL ampicillin at 37°C. Isopropylthio- β -D-galactopyranoside (IPTG) was added to a final concentration of 0.4 mM to induce expression when the optical density at 600 nm reached 0.6. The cells were incubated overnight at 25°C then harvested by centrifugation at 4,000 g for 20 minutes. The same extraction and purification procedure were used for all three constructs, with the exception that CK2 α _KA used 350 mM NaCl in the buffer, whereas, CK2 α _WT and CK2 α _FP10 required 500 mM NaCl. The cell pellets were suspended in 20 mM Tris, 350/500 mM NaCl, pH 8.0) and lysed using a high-pressure homogeniser. Protease inhibitor cocktail tablets (one tablet per 50 mL extract; Roche Diagnostics) and DNase I were then added. The crude cell extract was then centrifuged at 10,000 g for 45 minutes, the supernatant was filtered with a 0.22 μ m filter. The soluble supernatant was applied on a Ni Sepharose Fast Flow6 column at pH 8.0, washed and eluted in 20 mM Tris pH 8.0, 350/500 mM NaCl, 200 mM imidazole. After overnight dialysis into 20 mM Tris, pH 8.0, 350/500 mM NaCl the *N*-terminal His6-Tag was cleaved overnight by TEV protease and passed through a second metal affinity column to remove uncleaved protein and the protease. The cleaved protein was further purified on a Sepharose Q HP anion-exchange column and the main peak fraction from this column was further purified by gel filtration on a Superdex 75 16/60 HiPrep column equilibrated with Tris 20 mM, pH 8.0, 350/500 mM NaCl. Pure protein was concentrated to 15 mg/mL and flash frozen in liquid N₂.

8.1.1.2. CK2 β

pGEX-CK2 β construct (1-198) obtained from Victor Bolanos-Garcia (Prof. Tom Blundell's lab) was introduced into *Escherichia coli* BL21 (DE3) for protein production. Single colonies of the cells were grown in 6x1 L of 2 x TY with 100 μ g/mL ampicillin at 37 °C. Isopropyl thio- β -D-galactopyranoside (IPTG) was added to a final concentration of 0.4 mM to induce expression when

the optical density at 600 nm reached 0.6. The cells were incubated overnight at 25 °C then harvested by centrifugation at 4,000 g for 20 minutes. The cell pellets were suspended in 20 mM Tris, 500 mM NaCl, pH 8.5) and lysed using a high-pressure homogeniser.

Protease inhibitor cocktail tablets (one tablet per 50 mL extract; Roche Diagnostics) and DNase I were then added. The crude cell extract was then centrifuged at 10,000 g for 45 minutes, the supernatant was filtered with a 0.22 µm filter. The soluble supernatant was applied on a Glutathione Sepharose column and washed with 5 column volumes of loading buffer (20 mM Tris, 500 mM NaCl, pH 8.5) followed by washing with 10 column volumes of cleavage buffer (20 mM Tris 500 mM NaCl, 1mM DTT, 1mM EDTA, pH 8.5). 100µL of the precision protease was loaded onto the column and incubated for 5 hours at 4°C and eluted in the cleavage buffer. The cleaved protein was further purified on a Sepharose Q HP anion-exchange column (gradient 0-500 mM NaCl) and the main peak fraction from this column was further purified by gel filtration on a Superdex 75 16/60 HiPrep column equilibrated with Tris 20 mM, pH 8.5, 500 mM NaCl. Pure protein was concentrated to 15 mg/mL and flash frozen in liquid N₂.

8.1.2. Fluorescent Polarisation

Approximate % inhibition of the holoenzyme assembly was determined using a PHERAstar FS plate reader (BMG labtech). The fluorescein probe was measured using 485 nm excitation and 530 nm emission. The fluorescein probe was covalently linked to the *N*-terminal of the linear CK2β-based peptide RLYGFKIHPMAYQLQ (CK2β_{pep}). Inhibition was measured using 15 µM and 0 µM of the test compounds at a constant concentration of 3% DMSO. The experiments were performed in a 384 well plate with final concentrations of 450 nM CK2α_{KA}, 7.4 nM CK2β_{pep}, 350 mM NaCl, 20 mM MES pH 6.5. The plates were read after a 30 min incubation period. The experiment was ran in triplicates.

8.1.3. Isothermal Calorimetry Titration

Direct binding assay

All ITC experiments were performed at 25 °C using a MicroCal ITC-200 (GE Healthcare). CK2α_{KA} (20 mg/mL, 20 mM tris pH 8.0, 500 mM NaCl) was diluted in Tris buffer (200 mM, NaCl 300 mM, 10% DMSO) and concentrated to 20-50 µM. Compounds in 100× stock solutions were diluted into the same buffer. In a typical experiment CK2α (25 µM) was loaded into the sample cell and 19 injections (2 µL each) with a 2 second duration were performed at 150 second intervals. The syringe was loaded with 200-250 µM peptides or with 0.4-2 mM fragments and rotated at 750 rpm. Control titrations were performed, and the data fitting was performed with a single site binding model using Origin software.

Competition assay

Experiments were performed at 25 °C using a MicroCal ITC-200 (GE Healthcare). CK2 α (0.2 mg/mL, 20 mM Tris pH 8.0, 500 mM NaCl) was diluted in Tris buffer (200 mM, NaCl 300 mM, 10% DMSO) and concentrated to 4-6 μ M. CK2 β (9.3 mg/mL, 20 mM Tris pH 8.5, 500 mM NaCl) was diluted in Tris buffer (200 mM, NaCl, 300 mM, 10% DMSO) and concentrated to 40 μ M. In a typical experiment, CK2 α was loaded into the sample cell and 19 injections (2 μ L each) with a 2 second duration were performed at 150 second intervals. The syringe was loaded with CK2 β and rotated at 750 rpm. The same experiment was repeated in the presence of the peptides: compounds in 10 mM DMSO stock solutions were diluted to 1 mM and added to the solutions of CK2 α and CK2 β (prepared as described above) to a final concentration of 100 μ M. Control titrations were performed, and the data fitting was performed with a single site binding model using Origin software.

8.1.4. Kinase assay

The kinase assays were performed using the ADP-Glo™ kinase assay kit (Promega). 50 nM CK2 α _WT was incubated in the kinase reaction buffer (40 mM Tris pH 7.5, 200 mM NaCl, 20 mM MgCl₂, 0.1 mg/mL BSA, 25 μ M ATP, 50 μ M substrate peptide (RRRADDSDDDD, Enzo Life Sciences Inc. or eIF2 β peptide, MSGDEMIFDPTMSKKKKKKKKP), 5% (v/v) DMSO) in the presence of different concentrations of the inhibitor at 25 °C for 120 min. In the kinase assay using eIF2 β substrate 50 nM CK2 β _WT was added to the reaction mixture. 5 μ L aliquots of the kinase reaction were quenched with 5 μ L of ADP-glo™ solution. After 45 min 10 μ L of the kinase detection reagent was added and maintained at 25 °C for 20 minutes. The luminescence was recorded using a PHERAstar FS plate reader (BMG LABTECH) with an integration time of 1 s. Percentage inhibition was calculated relative to a DMSO control and a baseline measurement without substrate. All measurements were performed in duplicates. The IC₅₀ curves were fitted using GraphPad Prism software.

8.1.5. X-ray crystallography

X-ray crystallography was performed by Dr Paul Brear, Department of Biochemistry, University of Cambridge.

For fragment crystallisation the following conditions were used: CK2 α _KA at 5 mg/mL in 20 mM Tris, pH 8.0, 350 mM NaCl, 1 mM DTT, and 25 mM ATP was crystallised with 112.5 mM MES pH 6.5, 35% glycerol ethoxylate and 180 mM ammonium acetate in a 1:1 ratio with a total volume of 2 μ L by the hanging drop vapour-diffusion method. The fragments were soaked as singletons at 2-100 mM into these crystals for 15–20 h in 107 mM MES pH 6.5, 35% glycerol ethoxylate and 1.04 M ammonium acetate after which the crystals were cryo-cooled in liquid nitrogen for data collection. CK2 α _FP10 at 10 mg/mL in 20 mM Tris, pH 8.0, 500 mM NaCl, 4 mM DTT, 13 mM

ATP, 2 mM phytic acid was crystallised with 107 mM MES, pH 6.5, 29% glycerol ethoxylate, 1.04 M ammonium acetate in a 1:1 ratio with a total volume of 2 μ L by the hanging drop vapour-diffusion method. The fragments were soaked into the crystals of CK2 α _FP10 for 15–20 h at 100 mM in 107 mM MES pH 6.5, 29% glycerol ethoxylate and 1.04 M ammonium acetate.

Co-crystals of CK2 α and **P1-C5** were generated by screening CK2 α _FP10 at 10 mg/mL in 20 mM Tris, pH 8.0, 500 mM NaCl and 500 μ M peptide with the JCSG+ screen (molecular dimensions). Drops were set up at 0.2 μ L protein solution 0.2 μ L screen using the sitting drop vapour-diffusion method. Crystals were observed in a number of conditions in the JCSG+ screen. The condition that yielded the crystals from which the final data set was collected grew in 0.1 M Hepes pH 7.5, 10%(w/v) PEG 8K, 8% v/v Ethylene glycol. The crystals were cryo-cooled in liquid nitrogen in the same solution for data collection.

Crystals of **P2'-C5** and **P7-C5** were generated using matrix seeding from the co-crystals grown of **P1-C5**. Seeds of CK2 α were generated using Micro seed beads (Molecular Dimensions). Co-crystals of CK2 α and **P2'-C5** or **P7-C5** were generated by screening CK2 α _FP10 at 10 mg/mL in 20 mM Tris, pH 8.0, 500 mM NaCl and 500 μ M peptide with the JCSG+ screen (Molecular Dimensions) and the seed stocks obtained from **P1-C5**. Drops were set up at 0.2 μ L protein solution + 0.2 μ L screen +0.01 μ L seed stock using the sitting drop vapour-diffusion method. Crystals were observed in a number of conditions in the JCSG+ screen. The condition that yielded the crystals from which the final data set was collected grew in 0.16 M calcium acetate, 0.08 M sodium cacodylate, 14.4% PEG 8K, 20% glycerol.

The crystals were cryo-cooled in liquid nitrogen in the same solution for data collection. The crystals were cryo-cooled in liquid nitrogen in the same solution for data collection.

X-ray diffraction data was collected at the Diamond synchrotron radiation source, then processed using the pipedream package by Global Phasing Ltd; structures were solved by using programs from the CCP4 package. Models were iteratively refined and rebuilt by using AutoBuster and Coot programs. Ligand coordinates and restraints were generated from their SMILES strings using the Grade software package.

8.2. Biophysics experimental for BH3 peptides

8.2.1. Protein expression and purification of Bcl-x_L

Bcl-x_L protein was expressed and purified by Jha Rupam at AstraZeneca. The His6-TEV-Bcl-x_L construct was expressed in *Escherichia coli* (BL21 Gold DE3) by induction with 0.2 mM IPTG for 16 h at 18 °C and purified by affinity purification followed by gel filtration. The pellets from 3 L culture were thawed and resuspended in lysis buffer (50 mM Hepes, pH 8.0, 500 mM NaCl, 20 mM imidazole, 5% glycerol, 1 mM TCEP) supplemented with protease inhibitors (Complete-EDTA Free, Roche Applied Science), Benzonase, and 2.5 mg/mL lysozyme. The lysate was clarified by centrifugation (15000 rpm, 60 min, 4 °C) and incubated with 8 mL of Talon Supeflow resin (Clontech) for 1 hour whilst rotating. The lysate was then passed through an Econocolumn (BioRad) and washed with 200 mL of lysis buffer. The protein was eluted by elution buffer (50 mM Hepes pH 8, 500 mM NaCl, 250 mM imidazole, 1 mM TCEP, 5% glycerol), and dialysed overnight against 5 L of dialysis buffer (50 mM Hepes pH 8, 300 mM NaCl, 1 mM TCEP). The dialysed protein was concentrated to 4 mL volume using centrifugal 10K MWCO concentrator (Millipore). The concentrated protein was loaded on to HiLoad 16/60 Superdex 75 PG (GE Healthcare) pre-equilibrated in the storage buffer (25 mM Hepes pH 7.4, 150 mM NaCl, 1 mM TCEP). The fractions containing Bcl-x_L protein from this size exclusion chromatography step were analysed on SDS-PAGE, pooled, snap frozen, and stored at -80 °C.

8.2.2. Surface plasmon resonance (SPR)

Biacore™ T200 (GE Healthcare) was used to conduct all experiments reported herein. Sensor surface preparation and all interaction analyses experiments were performed at 25 °C utilising a data collection rate of 10 Hz. Reagents were purchased from GE Healthcare. Running buffer containing 10 mM Hepes, pH 7.4, 150 mM sodium chloride, 1 mM DTT, 1% DMSO and 0.05% polysorbate 20 were utilised throughout surface preparation and all interaction analysis experiments. Histidine tagged Bcl-x_L protein was diluted to 5 µg/mL and captured onto Sensor chip NTA *via* the following sequence of injections to achieve a target Bcl-x_L surface density of 700 R.U. (response units). The carboxymethyl dextran surface of Sensor chip NTA was activated by injection of an aqueous solution containing 50 mM *N*-hydroxysuccinimide (NHS) and 200 mM *N*-ethyl-*N'*-(dimethylaminopropyl) carbodiimide (EDC). 500 µM nickel sulfate (NiSO₄) was subsequently injected for one minute and utilised to capture Bcl-x_L from a 5 µg/mL solution injected for one minute. A further one-minute injection of 1 M ethanolamine, pH 8.5 was performed to deactivate any unreacted carboxymethylesters.²⁸² The flow-rate for all injections during surface derivatisation was 10 µL/min. A blank flow-cell was similarly treated with the exception of injection of Bcl-x_L and served as a reference surface in the direct binding interaction analyses. Interaction analyses were performed by first equilibrating each sample within a 7-

point 2-fold peptide dilution series in the range 33.3 nM to 1.03 nM for 30 minutes during instrument start-up procedures. nM peptide concentrations were used to accommodate potential solubility issues for the panel screening assay. Running buffer samples (0 nM peptide) were injected following each cycle and later used to facilitate double-referencing procedures during data analysis. Each peptide sample was injected over each peptide surface 90 seconds at a flow-rate of 80 $\mu\text{L}/\text{min}$ to monitor peptide association, and peptide dissociation was subsequently monitored for 300 seconds. Data analyses were carried out using Biacore™ T200 evaluation software v2.0 to validate assay quality, perform double-referencing (blank buffer sample and reference surface data subtraction) and evaluate steady state affinity plots. Briefly, equilibrium R.U. levels (R_{eq}) were collected 5 seconds before the end of the sample injection. R.U. levels at this time-point were plotted versus sample concentration and the resultant binding isotherm fitted using the following steady state equation:

$$R_{\text{eq}} = \text{Conc} \cdot R_{\text{max}} / (\text{Conc} + K_{\text{d}})$$

R_{eq} refers to the equilibrium binding response (R.U.), R_{max} is the total surface binding capacity (R.U.) and K_{d} is the apparent equilibrium dissociation constant, a parameter subsequently utilised to provide a relative ranking for the peptides studied in the current panel.

8.2.3. Circular dichroism experiments

CD spectra of selected peptides were recorded on an Applied Photo-physics Chirascan circular dichroism spectro-polarimeter (**P9-C5** and **P10**) or on an AVIV 410 circular dichroism spectro polarimeter using a 1 mm path length quartz cuvette. CD measurements were performed at 298 K over a range of 185-260 nm using a response time of 0.5 s, 1 nm pitch and 0.5 nm bandwidth. The recorded spectra represent a smoothed average of three scans, zero-corrected at 260 nm and normalised against the solvent used (Mean Residue Ellipticity θ_{MRE} is quoted in $\text{deg}\cdot\text{cm}^2\cdot\text{dmol}^{-1}\cdot\text{residue}^{-1}$ and defined as the ratio between the Molar Ellipticity and the number of residues in the peptide). Peptides were dissolved in a 1:1 mixture of MQ water and MeCN to a final concentration of 50-100 μM .

Percentage helicity was calculated based on mean residue ellipticity at 222 nm compared to the theoretical maximum helicity:

$$\text{maximum } MRE_{222} = 40000 \times [1 - (2.5/n)]$$

where n is the number of amide bonds, as previously reported.²⁹⁰

CHAPTER 9:

Biology Experimental

9.1. Biology experimental for CK2 peptides

9.1.1. Serum stability test

500 μL of PBS buffer supplemented with 20% (v/v) of human serum was allocated into an Eppendorf tube and temperature kept at 37 °C for 15 minutes before commencing the experiment. 5 μL of the peptide from 10 mM stock solution in DMSO was added. Caffeine was added as an internal standard (10 μL of a 15 mg/mL solution in MQ water). At specific intervals, 50 μL of the reaction mixture was taken and quenched with 100 μL of a 1:1 mixture of 96% Ethanol:DMSO. The suspension was spun at 13400 g for 10 minutes. 100 μL of the supernatant was analysed using C-18 HPLC with an eluting gradient 5-95% MeCN (0.05% TFA) in water (0.05% TFA) over 15 minutes (90 μL injection volume). Percentage of intact starting peptide was monitored over 24 h (calculated as the ratio of the area of the peak corresponding to the intact peptide to the area of the peak of caffeine). The experiment was performed in duplicates.

9.1.2. Tissue culture

All cell lines used were supplied by AstraZeneca cell bank as mycoplasma free. U2OS bone osteosarcoma and HCT116 colon carcinoma cells were maintained in RPMI-1640 (1x, Sigma Aldrich, R0883) supplemented with 2 mM *L*-glutamine (Gibco, 25030-149) and fetal bovine serum (FBS, Gibco Life Technologies, 10270-106) at a final concentration of 10%. All cells were grown at 37°C / 5% CO₂ in a humidified environment and all the assays were performed using these culturing conditions.

9.1.3. Proliferation assay

HCT116 cells were seeded at 2000 cells per well into two flat-bottomed tissue 384-well plates (PerkinElmer CellCarrier Ultra™) in a volume of 40 μL of growth medium. After 24 hours, the peptides dissolved in DMSO (10 mM) were added to the cells (to final concentrations of 100, 75, 50, 32, 25, 16, 10, 7.7, 5, 3.2, 0 μM) using HP Tecan dispenser and DMSO normalised to a final concentration of 1% (v/v). Cells were then incubated in the presence of the compounds for 4 days and the rate of growth monitored with IncuCyte Zoom™ (plate *day 4*). To one plate (*day 0*), 5 μL of Saponin (2.5% w/v in 5 mM EDTA in Tris buffer) and 10 μL of Sytox green™ reagent (2 μM Tris buffer containing 5 mM EDTA) were added after dosing. The plate was left in the dark at rt for 4 hours before imaging with Thermo Scientific™ CellInsight™ CX5 High Content Screening (HCS) Platform using a 10X lens. The same procedure was repeated for plate *day 4* after 4 days of incubation.

Percentage of growth inhibition was calculated relative to DMSO controls, normalised against day 0 and GI₅₀ values were calculated using Graphpad Prism. The results are the average of at least 4 independent repeats.

9.1.4. Viability assay

HCT116 cells were seeded at 5000 cells per well into a flat-bottomed tissue 384-well plate (PerkinElmer CellCarrier Ultra™) in a volume of 40 µL of growth medium. After 24 hours, the compounds (10 mM stock in DMSO) were added to the cells (to final concentrations of 100, 75, 50, 32, 25, 16, 10, 7.7, 5, 3.2, 0 µM) using HP Tecan dispenser and DMSO normalised to a final concentration of 1% (v/v). After 4 hours, 20 µL of CytoTox-Glo™ Cytotoxicity Assay Reagent (Promega) were added to all well. After 15 minutes at room temperature, luminescence was read on a multimode plate reader (EnVision™, PerkinElmer). 40 µL of Lysis Reagent (prepared using 33 µL Digitonin in 5 mL of assay buffer) were added to all the wells, mixed, and incubated at room temperature for 15 minutes to cause lysis of all the cells. Luminescence of total dead cells was measured and used as normalisation. The results are the average of at least three independent repeats.

9.1.5. Co-localisation experiments

Confocal imaging of fixed U2OS cells was conducted using a Yokogawa Cell Voyager CV8000™ confocal microscope with a 40X water immersion objective. Images were acquired with excitation at 488, 561 and 405 nm and emissions detected with a 525/50, 600/37, 445/460 nm BP filter for the green, red and blue channel respectively.

The following primary antibodies were used:

Antibody	Supplier and catalogue number	Working concentration
EEA1	Abcam, ab2900	1:4000
Rab7	Abcam, ab50533	1:4000
LAMP1	Cell Signalling, 9091	1:4000
TGN46	Abcam, ab50595	1:750
ZFPL1	Sigma, HPA014909	1:500
Calnexin	Invitrogen, PA5-34665	1:750

Secondary antibodies goat anti-rabbit IgG (H+L) AlexaFluor 568 and goat anti-mouse IgG (H+L) AlexaFluor 568 were used at a working concentration of 1:500. Hoechst nuclei stain was used to a working concentration of 1:5000. FITC-labelled peptides were used to 1.25 µM final concentration.

U2OS cells were seeded at 2500 cell per well into a flat-bottomed tissue 384-well plate (PerkinElmer CellCarrier Ultra™) in a volume of 40 µL of growth medium and cultured for 24 h before commencing the experiment. After 24 hours, FITC-labelled compounds dissolved in

CHAPTER 9: Biology Experimental

DMSO (1 mM) were added to the cells using HP Tecan™ dispenser and DMSO normalised to a final concentration of 0.3% (v/v). Cells were fixed after 360, 180, 120, 60, 30, 15, and 5-minute incubation using 40 µL of 8% PFA (final PFA concentration 4%). Cells were fixed for 15 minutes, washed with PBS (3x) and blocked with 3% BSA + 0.1 % Triton X-1000 for 5 minutes. The blocking solution was then removed and 40 µL of the primary antibodies in BSA added. The plate was stored in the dark, at 4 °C overnight. The primary antibodies were washed with PBS (3x) and 40 µL of the secondary antibodies and Hoechst nuclei stain in BSA added. The plate was kept at 4 °C for 1 hour, washed with PBS (3x) and imaged as described above. Images were analysed using Fiji (ImageJ) software.

9.2. Biology experimental for BH3 peptides

Ethical approval was obtained from the Faculty Research Ethics Committee at Anglia Ruskin University, Cambridge, UK where the experiments were carried out. Unless otherwise stated, the experiments were performed on no fewer than three separate occasions using platelets from different donors. Data were analysed using AccuriC6 BD Software and GraphPad Prism.

9.2.1. Preparation of washed platelet suspension

Human blood was collected from healthy volunteers, who had not taken medication for two weeks, following informed consent in accordance with the Declaration of Helsinki. Blood was collected into 11 mM sodium citrate and washed platelets were prepared as follows: Platelet-rich plasma (PRP) was obtained by centrifugation (240 g, 15 min). Prostaglandin E1 (PGE₁, 2 μM) was added to prevent premature platelet activation, and the plasma was centrifuged at 640 g for 15 min. Platelets were suspended in calcium free Tyrode's buffer (CFT buffer, containing: 140 mM NaCl, 5 mM KCl, 10 mM Hepes, 5 mM Glucose, 0.42 mM NaH₂PO₄, 12 mM NaHCO₃, titrated to pH 7.4 with NaOH) to a final concentration of 2x10⁸ platelet/mL and rested at 37 °C for 1 hour prior to experimentation.

9.2.2. Flow cytometry

Treated washed platelet suspensions (1x10⁷/mL) were analysed by flow cytometry using a C6 Accuri Flow Cytometer (Beckton Dickinson, UK), in the presence or absence of Annexin-V-PE (BD Biosciences, UK), anti-PAC-1 (BD Biosciences, UK), anti-CD62P (BD Pharmingen, UK), or anti-CD63 (BD Pharmingen, UK). Peptides were used to a final concentration of 10 μM (from 1 mM DMSO stock solutions). At least 10,000 events were acquired per experiment. In all the experiments, the entire platelet population was primarily gated by FSC. Untreated platelets (no fluorescent markers, no compounds) were analysed by flow cytometer on the laser of interest and the measurement used as *zero*. The shift of the peak of treated platelets towards the right was normalised against untreated platelets (Figure 72).

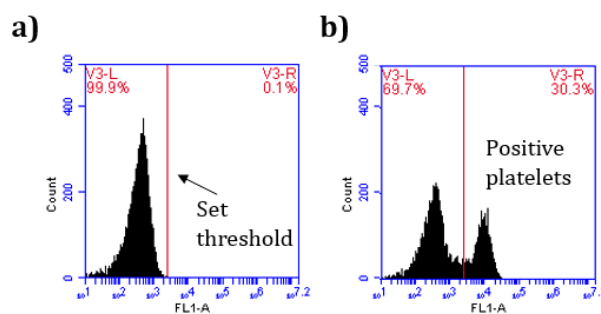


Figure 72 – Example of flow cytometry data normalisation. a) The fluorescence associated with untreated platelets is used to set the threshold for future measurements. b) After treatment, the platelet population that gives a shift towards the right of the threshold in the fluorescent signal is considered as positive platelets.

9.2.2.1. Peptide uptake experiments in a washed platelet suspension

250 μL of washed platelet suspension was incubated with 2.5 μL of the fluorescently labelled peptide. The suspension was kept in the dark at 37 °C and measurements taken at the designed time points (1, 2, 3 hours). For real time measurements, the peptides were added to the 250 μL of washed platelet suspension after events had been recorded for 1 minute and then event were monitored for a further 4 minutes.

9.2.2.2. Peptide uptake experiments in platelet rich plasma (PRP)

The PRP was rested for 30 minutes prior experimentation. 120 μL of PRP was added to 1.2 μL of the fluorescently labelled peptide (1 mM DMSO stock) and incubated in the dark at 37 °C for 1 h prior analysis by flow cytometry.

9.2.2.3. PS exposure and activation markers

PS exposure was assessed after incubation of 50 μL of washed platelet suspensions at 37 °C in 445 μL of Tyrode's solution (pH 7.4) with the peptide (5 μL of 1 mM stock solution in DMSO). At the designed time point 25 μL of the suspension was added to 25 μL of Annexin V (10% Annexin V in Tyrode's solution) under the protection from direct light and analysed by flow cytometry.

Platelet activation markers (PAC-1, CD62P and CD63 binding) were assessed after incubation of 3 μL of washed platelet suspensions at 37 °C in 105 μL of CFT buffer (pH 7.4) with 1.2 μL of the desired antibody and 1.1 μL peptide (1 mM DMSO stock). The suspensions were analysed by flow cytometry.

9.2.3. Light Transmission Aggregometry

Platelet aggregation was monitored using an AggRam™ aggregometer (Helena Biosciences, UK). 250 μL of washed platelet suspensions ($1 \times 10^8/\text{mL}$) were stimulated with 10 μM peptide under stirring conditions at 37 °C for 15 minutes and the percentage aggregation was acquired from the aggregation traces using proprietary software (Helena Biosciences, UK).

9.2.4. Confocal microscopy of live platelets

Peptides were used to a final concentration of 10 μM . Confocal imaging of live washed platelet suspensions ($2 \times 10^8/\text{mL}$) were conducted using a Zeiss 510 confocal microscope with a Plan-APOCHROMAT 63x/1.4NA oil immersion objective, and a confocal aperture of 60 μm . Images of TAMRA-labelled model peptide stained platelets were acquired after 1-hour incubation using with excitation at 565 nm and emission was detected with a 560-615 nm BP filter. Images of

FITC-peptide stained platelets were acquired after 15-minute incubation³⁸ using excitation at 488 nm and emission was detected with a 505-550 nm BP filter.

9.2.5. Serum stability test

One mL of RPMI-1640 media supplemented with 25% (v/v) of human serum was allocated into an Eppendorf tube and temperature kept at 37 °C for 15 minutes before commencing the experiment. 40 µL of 10 mM peptide in DMSO were added to make a final peptide concentration of 100 µg/mL. At specific intervals, 100 µL of the reaction mixture was taken and quenched with 200 µL of a 1:1 mixture of 96% Ethanol:DMSO. The suspension was cooled to 4 °C for 15 minutes and then spun at 13400 g for 4 minutes.²⁸³ Caffeine (0.5 µL of 7 mg/mL solution in MQ water) was then added to 100 µL of the supernatant and used as a reference. The supernatant was analysed using C-18 HPLC with an eluting gradient 5-95% MeCN (0.05% TFA) in water (0.05% TFA) over 15 minutes. Percentage of intact starting peptide was monitored over time (calculated as the ratio of the area of the peak corresponding to the intact peptide to the area of the peak of caffeine). The results are the average of three independent repeats.

³⁸ Difference in incubation times are due to the fact that the model peptides do not activate platelets while the BH3 peptides do. Therefore, to avoid complication in the imaging due to platelet aggregation or activation images were acquired after 15 minutes incubation.

CHAPTER 10:

Bibliography

- 1 D. A. Erlanson, S. W. Fesik, R. E. Hubbard, W. Jahnke and H. Jhoti, *Nat. Rev. Drug Discov.*, 2016, **15**, 605–619.
- 2 C. W. Murray and D. C. Rees, *Nat. Chem.*, 2009, **1**, 187–192.
- 3 E. Valeur, S. M. Guéret, H. Adihou, R. Gopalakrishnan, M. Lemurell, H. Waldmann, T. N. Grossmann and A. T. Plowright, *Angew. Chemie - Int. Ed.*, 2017, **56**, 10294–10323.
- 4 R. A. E. Carr, M. Congreve, C. W. Murray and D. C. Rees, *Drug Discov. Today*, 2005, **10**, 987–992.
- 5 D. E. Scott, A. G. Coyne, S. A. Hudson and C. Abell, *Biochemistry*, 2012, **51**, 4990–5003.
- 6 J. K. Kranz and C. Schalk-Hihi, *Methods Enzymol.*, 2011, **493**, 277–298.
- 7 I. Navratilova and A. L. Hopkins, *ACS Med. Chem. Lett.*, 2010, **1**, 44–48.
- 8 M. J. Harner, A. O. Frank and S. W. Fesik, *J. Biomol. NMR*, 2013, **56**, 66–75.
- 9 H. Jhoti, A. Cleasby, M. Verdonk and G. Williams, *Curr. Opin. Chem. Biol.*, 2007, **11**, 485–493.
- 10 L. Hoffer, J-P. Renaud and D. Horvath, *Comb. Chem. High Throughput Screen.*, 2011, **14**, 500-520.
- 11 A. Ciulli and C. Abell, *Curr. Opin. Biotechnol.*, 2007, **18**, 489–496.
- 12 E. H. Mashalidis, P. Śledź, S. Lang and C. Abell, *Nat. Protoc.*, 2013, **8**, 2309–2324.
- 13 P. D. Leeson and B. Springthorpe, *Nat. Rev. Drug Discov.*, 2007, **6**, 881–890.
- 14 O. Ichihara, J. Barker, R. J. Law and M. Whittaker, *Mol. Inform.*, 2011, **30**, 298–306.
- 15 M. Nazaré, H. Matter, D. W. Will, M. Wagner, M. Urmann, J. Czech, H. Schreuder, A. Bauer, K. Ritter and V. Wehner, *Angew. Chemie - Int. Ed.*, 2012, **51**, 905–911.
- 16 W. P. Jencks, *Proc. Natl. Acad. Sci. U. S. A.*, 1981, **78**, 4046–4050.
- 17 M. I. Page and W. P. Jencks, *Proc. Natl. Acad. Sci.*, 1971, **68**, 1678–1683.
- 18 Practical fragments blog,
<http://practicalfragments.blogspot.com/search?q=+fragments+in+the+clinic>, (accessed January 2019).
- 19 G. Bollag, J. Tsai, J. Zhang, C. Zhang, P. Ibrahim, K. Nolop and P. Hirth, *Nat. Rev. Drug Discov.*, 2012, **11**, 873–886.
- 20 G. Del Poeta, M. Pastorino, L. Pupo, M. I. Del Principe, M. Dal Bo, F. Buccisano, B. Mariotti, E. Iannella, L. Maurillo, A. Venditti, V. Gattei, P. De Fabritis, M. Cantonetti and S. Amadori, *Drugs Today (Barc.)*, 2016, **52**, 249–260.
- 21 A. M. Petros, J. Dinges, D. J. Augeri, S. A. Baumeister, D. A. Betebenner, M. G. Bures, S. W. Elmore, P. J. Hajduk, M. K. Joseph, S. K. Landis, D. G. Nettesheim, S. H. Rosenberg, W. Shen, S. Thomas, X. Wang, I. Zanze, A. H. Zhang and S. W. Fesik, *J. Med. Chem.*, 2006, **49**, 656–663.
- 22 E. Marsault and M. L. Peterson, *J. Med. Chem.*, 2011, **54**, 1961–2004.

- 23 E. M. Phizicky and S. Fields, *Microbiol. Rev.*, 1995, **59**, 94–123.
- 24 T. A. F. Cardote and A. Ciulli, *ChemMedChem*, 2016, **11**, 787–794.
- 25 D. J. Craik, D. P. Fairlie, S. Liras and D. Price, *Chem. Biol. Drug Des.*, 2013, **81**, 136–147.
- 26 L. D. Fader, E. Malenfant, M. Parisien, R. Carson, F. Bilodeau, S. Landry, M. Pesant, C. Brochu, S. Morin, C. Chabot, T. Halmos, Y. Bousquet, M. D. Bailey, S. H. Kawai, R. Coulombe, S. Laplante, A. Jakalian, P. K. Bhardwaj, D. Wernic, P. Schroeder, M. Amad, P. Edwards, M. Garneau, J. Duan, M. Cordingley, R. Bethell, S. W. Mason, M. Bös, P. Bonneau, M. A. Poupart, A. M. Faucher, B. Simoneau, C. Fenwick, C. Yoakim and Y. Tsantrizos, *ACS Med. Chem. Lett.*, 2014, **5**, 422–427.
- 27 K. G. McLure, E. M. Gesner, L. Tsujikawa, O. A. Kharenko, S. Attwell, E. Campeau, S. Wasiak, A. Stein, A. White, E. Fontano, R. K. Suto, N. C. W. Wong, G. S. Wagner, H. C. Hansen and P. R. Young, *PLoS One*, 2013, **8**, e83190.
- 28 B. B. Lao, I. Grishagin, H. Mesallati, T. F. Brewer, B. Z. Olenyuk and P. S. Arora, *Proc. Natl. Acad. Sci.*, 2014, **111**, 7531–7536.
- 29 K. Busschots, L. A. Lopez-Garcia, C. Lammi, A. Stroba, S. Zeuzem, A. Piiper, P. M. Alzari, S. Neimanis, J. M. Arencibia, M. Engel, J. O. Schulze and R. M. Biondi, *Chem. Biol.*, 2012, **19**, 1152–1163.
- 30 O. Mirguet, R. Gosmini, J. Toum, C. A. Clément, M. Barnathan, J. M. Brusq, J. E. Mordaunt, R. M. Grimes, M. Crowe, O. Pineau, M. Ajakane, A. Daugan, P. Jeffrey, L. Cutler, A. C. Haynes, N. N. Smithers, C. W. Chung, P. Bamborough, I. J. Uings, A. Lewis, J. Witherington, N. Parr, R. K. Prinjha and E. Nicodème, *J. Med. Chem.*, 2013, **56**, 7501–7515.
- 31 S. He, T. J. Senter, J. Pollock, C. Han, S. K. Upadhyay, T. Purohit, R. D. Gogliotti, C. W. Lindsley, T. Cierpicki, S. R. Stauffer and J. Grembecka, *J. Med. Chem.*, 2014, **57**, 1543–1556.
- 32 L. Otvos, and J. D. Wade, *Front. Chem.*, 2014, **2**, 1–4.
- 33 T. Uhlig, T. Kyprianou, F. G. Martinelli, C. A. Oppici, D. Heiligers, D. Hills, X. R. Calvo and P. Verhaert, *EuPA Open Proteomics*, 2014, **4**, 58–69.
- 34 L. Diao and B. Meibohm, *Clin. Pharmacokinet.*, 2013, **52**, 855–868.
- 35 M. A. Abdalla and L. J. McGaw, *Molecules*, 2018, **23**, 2080.
- 36 D. S. Nielsen, N. E. Shepherd, W. Xu, A. J. Lucke, M. J. Stoermer and D. P. Fairlie, *Chem. Rev.*, 2017, **117**, 8094–8128.
- 37 C. J. White and A. K. Yudin, *Nat. Chem.*, 2011, **3**, 509–524.
- 38 Y. H. Lau, Y. Wu, P. de Andrade, W. R. J. D. Galloway and D. R. Spring, *Nat. Protoc.*, 2015, **10**, 585–594.
- 39 K. D. R. J. N. Lambert, J. P. Mitchell, *J. Chem. Soc., Perkin Trans.*, 2001, **1**, 471–484.
- 40 T. A. Hill, N. E. Shepherd, F. Diness and D. P. Fairlie, *Angew. Chemie - Int. Ed.*, 2014, **53**, 13020–13041.
- 41 J. Tang, Y. He, H. Chen, W. Sheng and H. Wang, *Chem. Sci.*, 2017, **8**, 4565–4570.

- 42 A. Rietsch and J. Beckwith, *Annu. Rev. Genet.*, 1998, **32**, 163–184.
- 43 H. E. Blackwell and R. H. Grubbs, *Angew. Chemie - Int. Ed.*, 1998, **37**, 3281–3284.
- 44 H. E. Blackwell, J. D. Sadowsky, R. J. Howard, J. N. Sampson, J. A. Chao, W. E. Steinmetz, D. J. O’Leary and R. H. Grubbs, *J. Org. Chem.*, 2001, **66**, 5291–5302.
- 45 G. H. Bird, N. Madani, A. F. Perry, A. M. Princiotta, J. G. Supko, X. He, E. Gavathiotis, J. G. Sodroski and L. D. Walensky, *Proc. Natl. Acad. Sci.*, 2010, **107**, 14093–14098.
- 46 C. E. Schafmeister, J. Po and G. L. Verdine, *J. Am. Chem. Soc.*, 2000, **122**, 5891–5892.
- 47 P. M. Cromm, J. Spiegel and T. N. Grossmann, *ACS Chem. Biol.*, 2015, **10**, 1362–1375.
- 48 A. M. Felix, E. P. Heimer, C-T Wang, T. J. Lambros, A. Fournier, T. F. Mowles, S. Maines, R. M. Campbel, B. B. Wegrzynski, V. Toome, D. Fry and V. S. Madison, *Int. J. Pept. Protein Res.*, 1988, **32**, 441–454.
- 49 N. E. Shepherd, H. N. Hoang, G. Abbenante and D. P. Fairlie, *J. Am. Chem. Soc.*, 2005, **127**, 2974–2983.
- 50 Y. H. Lau, P. de Andrade, Y. Wu and D. R. Spring, *Chem. Soc. Rev.*, 2015, **44**, 91–102.
- 51 A. A. Aimetti, R. K. Shoemaker, C-C. Lin and K. S. Anseth, *Chem. Commun.*, 2010, **46**, 4061–4063.
- 52 S. Cantel, A. Le Chevalier-Isaad, M. Scrima, J. J. Levy, R. D. Di Marchi, P. Rovero, J. A. Halperin, A. M. Ursi, A. M. Papini and M. Chorev, *J. Org. Chem.*, 2008, **73**, 5663–5674.
- 53 M. Scrima, A. Le Chevalier-Isaad, P. Rovero, A. M. Papini, M. Chorev and A. M. D’Ursi, *European J. Org. Chem.*, 2010, **3**, 446–457.
- 54 S. A. Kawamoto, A. Coleska, X. Ran, H. Yi, C. Y. Yang and S. Wang, *J. Med. Chem.*, 2012, **55**, 1137–1146.
- 55 L. Mendive-Tapia, S. Preciado, J. García, R. Ramón, N. Kielland, F. Albericio and R. Lavilla, *Nat. Commun.*, 2015, **6**, 1–9.
- 56 F. M. Brunel and P. E. Dawson, *Chem. Commun.*, 2005, **0**, 2552–2554.
- 57 C. M. Haney, M. T. Loch and W. S. Horne, *Chem. Commun.*, 2011, **47**, 1915–1917.
- 58 M. M. Madden, A. Muppidi, Z. Li, X. Li, J. Chen and Q. Lin, *Bioorg. Med. Chem. Lett.*, 2011, **21**, 1472–1475.
- 59 J. Iegre, J. S. Gaynord, N. S. Robertson, H. F. Sore, M. Hyvonen, D. R. Spring, *Adv. Ther.*, 2018, **1**, 1800052.
- 60 S. L. Kuan, T. Wang and T. Weil, *Chem. - A Eur. J.*, 2016, **22**, 17112–17129.
- 61 D. P. Fairlie and A. Dantas de Araujo, *Biopolymers*, 2016, **106**, 843–852.
- 62 F. Brotzel and H. Mayr, *Org. Biomol. Chem.*, 2007, **5**, 3814–3820.
- 63 O. Koniev and A. Wagner, *Chem. Soc. Rev.*, 2015, **44**, 5495–5551.
- 64 H. Jo, N. Meinhardt, Y. Wu, S. Kulkarni, X. Hu, K. E. Low, P. L. Davies, W. F. Degrado and D.

- C. Greenbaum, *J. Am. Chem. Soc.*, 2012, **134**, 17704–17713.
- 65 L. E. St. Louis, T. M. Rodriguez and M. L. Waters, *Bioorg. Med. Chem.*, 2018, **26**, 1203–1205.
- 66 L. E. J. Smeenk, N. Dailly, H. Hiemstra, J. H. Van Maarseveen and P. Timmerman, *Org. Lett.*, 2012, **14**, 1194–1197.
- 67 N. Assem, D. J. Ferreira, D. W. Wolan and P. E. Dawson, *Angew. Chemie - Int. Ed.*, 2015, **54**, 8665–8668.
- 68 S. Sun, I. Compañón, N. Martínez-Sáez, J. D. Seixas, O. Boutureira, F. Corzana and G. J. L. Bernardes, *ChemBioChem*, 2018, **19**, 48–52.
- 69 Z. Li, R. Huang, H. Xu, J. Chen, Y. Zhan, X. Zhou, H. Chen and B. Jiang, *Org. Lett.* 2017, **19**, 4972–4975.
- 70 Y. Wang and D. H. C. Chou, *Angew. Chemie - Int. Ed.*, 2015, **54**, 10931–10934.
- 71 J. Guy, R. Castonguay, N. B. Campos-Reales Pineda, V. Jacquier, K. Caron, S. W. Michnick and J. W. Keillor, *Mol. Biosyst.*, 2010, **6**, 976–987.
- 72 A. M. Spokoyny, Y. Zou, J. J. Ling, H. Yu, Y. S. Lin and B. L. Pentelute, *J. Am. Chem. Soc.*, 2013, **135**, 5946–5949.
- 73 S. Kalhor-Monfared, M. R. Jafari, J. T. Patterson, P. I. Kitov, J. J. Dwyer, J. M. Nuss and R. Derda, *Chem. Sci.*, 2016, **7**, 3785–3790.
- 74 C. M. Grison, G. M. Burslem, J. A. Miles, L. K. A. Pilsel, D. J. Yeo, Z. Imani, S. L. Warriner, M. E. Webb and A. J. Wilson, *Chem. Sci.*, 2017, **8**, 5166–5171.
- 75 S. P. Brown and A. B. Smith III, *J. Am. Chem. Soc.*, 2015, **137**, 4034–4037.
- 76 E. Y.-L. Hui, B. Rout, Y. S. Tan, C. S. Verma, K.-P. Chan and C. W. Johannes, *Org. Biomol. Chem.*, 2018, **1**, 389–392.
- 77 J. C. Phelan, N. J. Skelton, A. C. Braisted and R. S. McDowell, *J. Am. Chem. Soc.*, 1997, **119**, 455–460.
- 78 O. Torres, D. Yüksel, M. Bernardina, K. Kumar and D. Bong, *ChemBioChem*, 2008, **9**, 1701–1705.
- 79 L. Zhang, T. Navaratna and G. M. Thurber, *Bioconjug. Chem.*, 2016, **27**, 1663–1672.
- 80 P. T. Tran, C. Ø. Larsen, T. Røndbjerg, M. De Foresta, M. B. A. Kunze, A. Marek, J. H. Løper, L. E. Boyhus, A. Knuhtsen, K. Lindorff-Larsen and D. S. Pedersen, *Chem. - A Eur. J.*, 2017, **23**, 3490–3495.
- 81 Y. H. Lau, P. de Andrade, S.-T. Quah, M. Rossmann, L. Laraia, N. Sköld, T. J. Sum, P. J. E. Rowling, T. L. Joseph, C. Verma, M. Hyvönen, L. S. Itzhaki, A. R. Venkitaraman, C. J. Brown, D. P. Lane and D. R. Spring, *Chem. Sci.*, 2014, **5**, 1804–1809.
- 82 Y. Wu, F. Villa, J. Maman, Y. H. Lau, L. Dobnikar, A. C. Simon, K. Labib, D. R. Spring and L. Pellegrini, *Angew. Chemie - Int. Ed.*, 2017, **56**, 12866–12872.
- 83 M. M. Wiedmann, Y. S. Tan, Y. Wu, S. Aibara, W. Xu, H. F. Sore, C. S. Verma, L. Itzhaki, M. Stewart, J. D. Brenton and D. R. Spring, *Angew. Chemie - Int. Ed.*, 2017, **56**, 524–529.

- 84 W. Xu, Y. H. Lau, G. Fischer, Y. S. Tan, A. Chattopadhyay, M. De La Roche, M. Hyvönen, C. Verma, D. R. Spring and L. S. Itzhaki, *J. Am. Chem. Soc.*, 2017, **139**, 2245–2256.
- 85 Y. H. Lau, P. De Andrade, G. J. McKenzie, A. R. Venkitaraman and D. R. Spring, *ChemBioChem*, 2014, **15**, 2680–2683.
- 86 Y. Wu, L. B. Olsen, Y. H. Lau, C. H. Jensen, M. Rossmann, Y. R. Baker, H. F. Sore, S. Collins and D. R. Spring, *ChemBioChem*, 2016, **17**, 689–692.
- 87 L. Zhang, T. Navaratna, J. Liao and G. M. Thurber, *Bioconjug. Chem.*, 2015, **26**, 329–337.
- 88 A. Zorzi, K. Deyle and C. Heinis, *Curr. Opin. Chem. Biol.*, 2017, **38**, 24–29.
- 89 S. C. Deresinski and D. A. Stevens, *Clin. Infect. Dis.*, 2003, **36**, 1445–1457.
- 90 J. M. Balkovec, D. L. Hughes, P. S. Masurekar, C. A. Sable, R. E. Schwartz and S. B. Singh, *Nat. Prod. Rep.*, 2014, **31**, 15–34.
- 91 A. Laupacis, P. A. Keown, R. A. Ulan, N. McKenzie and C. R. Stiller, *Can. Med. Assoc. J.*, 1982, **126**, 1041–1046.
- 92 P. Kirkpatrick, A. Raja, J. LaBonte and J. Lebbos, *Nat. Rev. Drug Discov.*, 2003, **2**, 943–944.
- 93 J. A. Vasquez, *Therapy*, 2006, **3**, 39–54.
- 94 S. Jain and J. Zain, *J. Blood Med.*, 2011, **2**, 37–47.
- 95 I. M. Modlin, M. Pavel, M. Kidd and B. I. Gustafsson, *Aliment. Pharmacol. Ther.*, 2010, **31**, 169–188.
- 96 T. Liu, S. H. Joo, J. L. Voorhees, C. L. Brooks and D. Pei, *Bioorg. Med. Chem.*, 2009, **17**, 1026–1033.
- 97 L. B. Giebel, R. T. Cass, D. L. Milligan, D. C. Young, R. Arze and C. R. Johnson, *Biochemistry*, 1995, **34**, 15430–15435.
- 98 M. Krook, C. Lindbladh, J. A. Eriksen and K. Mosbach, *Mol. Divers.*, 1998, **3**, 149–159.
- 99 T. Czömpöly, Á. Lábadi, M. Balázs, P. Németh and P. Balogh, *Biochem. Biophys. Res. Commun.*, 2003, **307**, 791–796.
- 100 S. C. Meyer, T. Gaj and I. Ghosh, *Chem. Biol. Drug Des.*, 2006, **68**, 3–10.
- 101 C. Heinis, T. Rutherford, S. Freund and G. Winter, *Nat. Chem. Biol.*, 2009, **5**, 502–507.
- 102 S. Chen, J. Morales-Sanfrutos, A. Angelini, B. Cutting and C. Heinis, *ChemBioChem*, 2012, **13**, 1032–1038.
- 103 T. M. Kinsella, C. T. Ohashi, A. G. Harder, G. C. Yam, W. Li, B. Peelle, E. S. Pali, M. K. Bennett, S. M. Molineaux, D. A. Anderson, E. S. Masuda and D. G. Payan, *J. Biol. Chem.*, 2002, **277**, 37512–37518.
- 104 A. Tavassoli and S. J. Benkovic, *Angew. Chemie - Int. Ed.*, 2005, **44**, 2760–2763.
- 105 S. W. Millward, S. Fiacco, R. J. Austin and R. W. Roberts, *ACS Chem. Biol.*, 2007, **2**, 625–634.
- 106 S. W. Millward, T. T. Takahashi and R. W. Roberts, *J. Am. Chem. Soc.*, 2005, **127**, 14142–

- 14143.
- 107 A. Wada, *Front. Immunol.*, 2013, **4**, e224.
- 108 F. Tian, M.-L. Tsao and P. G. Schultz, *J. Am. Chem. Soc.*, 2004, **126**, 15962–15963.
- 109 T. Kawakami and H. Murakami, *J. Nucleic Acids*, 2012, **2012**, e713510.
- 110 R. Obexer, L. J. Walport and H. Suga, *Curr. Opin. Chem. Biol.*, 2017, **38**, 52–61.
- 111 Y. Hayashi, J. Morimoto and H. Suga, *ACS Chem. Biol.*, 2012, **7**, 607–613.
- 112 Y. Yamagishi, I. Shoji, S. Miyagawa, T. Kawakami, T. Katoh, Y. Goto and H. Suga, *Chem. Biol.*, 2011, **18**, 1562–1570.
- 113 Y. Yamagishi, H. Ashigai, Y. Goto, H. Murakami and H. Suga, *ChemBioChem*, 2009, **10**, 1469–1472.
- 114 R. A. Houghten, C. Pinilla, S. E. Blondelle, J. R. Appel, C. T. Dooley and J. H. Cuervo, *Nature*, 1991, **354**, 84–86.
- 115 K. Fosgerau and T. Hoffmann, *Drug Discov. Today*, 2015, **20**, 122–128.
- 116 J. L. Lau and M. K. Dunn, *Bioorg. Med. Chem.*, 2018, **83**, 2700–2707.
- 117 A. M. Davis, A. T. Plowright and E. Valeur, *Nat. Rev. Drug Discov.*, 2017, **16**, 681–698.
- 118 C. Morrison, *Nat. Rev. Drug Discov.*, 2018, **17**, 531–533.
- 119 A. Ricardo, M. Arata, S. DeMarco, K. Dhamnaskar, R. Hammer, M. Fridkis-Hareli, V. Rajagopal, K. Seyb, G-Q. Tang, S. Tobe and D. Treco, *Blood*, 2014, **124**, e2936.
- 120 Bicycle Therapeutics, <https://www.bicycletherapeutics.com/beyond-oncology>, (accessed January 2019).
- 121 Polyphor, <https://www.europeanpharmaceuticalreview.com/news/67983/polyphor-antibiotic-murepavadin>, (accessed January 2019).
- 122 L. Portt, G. Norman, C. Clapp, M. Greenwood and M. T. Greenwood, *Biochim. Biophys. Acta*, 2011, **1813**, 238–259.
- 123 W. R. Sellers and D. E. Fisher, *J. Clin. Invest.*, 1999, **104**, 1655–1661.
- 124 M. Hassan, H. Watari, A. Abualmaaty, Y. Ohba and N. Sakuragi, *Biomed Res. Int.*, 2014, **2014**, e150845.
- 125 P. C. Rath and B. B. Aggarwal, *J. Clin. Immunol.*, 1999, **19**, 350–364.
- 126 S. Nowsheen and E. S. Yang, *Exp. Oncol.*, 2012, **34**, 243–254.
- 127 R. S. Whelan, V. Kaplinskiy and R. N. Kitsis, *Annu. Rev. Physiol.*, 2010, **72**, 19–44.
- 128 A. Rami, I. Bechmann and J. H. Stehle, *Prog. Neurobiol.*, 2008, **85**, 273–296.
- 129 T. A. Yacoubian and D. G. Standaert, *Biochim. Biophys. Acta*, 2009, **1792**, 676–687.
- 130 R. Palacios-Pelaez, W. J. Lukiw and N. G. Bazan, *Mol. Neurobiol.*, 2010, **42**, 367–374.

- 131 K. Eguchi, *Intern. Med.*, 2001, **40**, 275–284.
- 132 K. B. Storey, *Gerontology*, 2010, **56**, 220–230.
- 133 D. R. Green and G. Kroemer, *J. Clin. Invest.*, 2005, **115**, 2610–2617.
- 134 J. H. Trembley, G. Wang, G. Unger, J. Slaton and K. Ahmed, *Cell. Mol. Life Sci.*, 2009, **66**, 1858–1867.
- 135 K. A. Ahmad, G. Wang, G. Unger, J. Slaton and K. Ahmed, *Adv. Enzyme Regul.*, 2008, **48**, 179–187.
- 136 J. Zhang, P. L. Yang and N. S. Gray, *Nat. Rev. Cancer*, 2009, **9**, 28–39.
- 137 R. T. Nitta, S. Gholamin, A. H. Feroze, M. Agarwal, S. H. Cheshier, S. S. Mitra and G. Li, *Oncogene*, 2015, **34**, 3688–3699.
- 138 K. Niefind, B. Guerra, I. Ermakowa and O. G. Issinger, *EMBO J.*, 2001, **20**, 5320–5331.
- 139 A. J. Siddiqui, D. Drygin, N. Streiner, P. Chua, F. Pierre, S. E. O'Brien, J. Bliesath, M. Omori, N. Huser, C. Ho, C. Proffitt, M. K. Schwaebe, D. M. Ryckman, W. G. Rice, K. Anderes, *Cancer Res.*, 2010, **70**, 10288–10299.
- 140 K. Niefind, J. Raaf and O. G. Issinger, *Cell. Mol. Life Sci.*, 2009, **66**, 1800–1816.
- 141 A. D. Ferguson, P. R. Sheth, A. D. Basso, S. Paliwal, K. Gray, T. O. Fischmann and H. V. Le, *FEBS Lett.*, 2011, **585**, 104–110.
- 142 E. Papinutto, A. Ranchio, G. Lolli, L. A. Pinna and R. Battistutta, *J. Struct. Biol.*, 2012, **177**, 382–391.
- 143 J. Raaf, E. Brunstein, O.-G. Issinger and K. Niefind, *Protein Sci.*, 2008, **17**, 2180–2186.
- 144 D. W. Litchfield, *Biochem. J.*, 2003, **369**, 1–15.
- 145 G. Poletto, J. Vilardell, O. Marin, M. A. Pagano, G. Cozza, S. Sarno, A. Falqués, E. Itarte, L. A. Pinna and F. Meggio, *Biochemistry*, 2008, **47**, 8317–8325.
- 146 J. H. Trembley, Z. Chen, G. Unger, J. Slaton, B. T. Kren, C. Van Waes and K. Ahmed, *Biofactors.*, 2010, **36**, 187–195.
- 147 I. Dominguez, G. E. Sonenshein and D. C. Seldin, *Cell. Mol. Life Sci.*, 2009, **66**, 1850–1857.
- 148 F. Piazza, S. Manni, M. Ruzzene, L. A. Pinna, C. Gurrieri and G. Semenzato, *Leukemia*, 2012, **26**, 1174–1179.
- 149 K. A. Ahmad, G. Wang and K. Ahmed, *Mol. Cancer Res.*, 2006, **4**, 331–338.
- 150 D. Hanahan and R. A. Weinberg, *Cell*, 2000, **100**, 57–70.
- 151 R. A. Faust, S. Tawfic, A. T. Davis, L. A. Bubash and K. Ahmed, *Head Neck*, 2000, **22**, 341–346.
- 152 R. Prudent and C. Cochet, *Chem. Biol.*, 2009, **16**, 112–120.
- 153 M. A. Pagano, M. Andrzejewska, M. Ruzzene, S. Sarno, L. Cesaro, J. Bain, M. Elliott, F. Meggio, Z. Kazimierczuk and L. A. Pinna, *J. Med. Chem.*, 2004, **47**, 6239–6247.

- 154 F. Meggio, M. A. Pagano, S. Moro, G. Zagotto, M. Ruzzene, S. Sarno, G. Cozza, J. Bain, M. Elliott, A. D. Deana, A. M. Brunati and L. A. Pinna, *Biochemistry*, 2004, **43**, 12931–12936.
- 155 S. Sarno, E. De Moliner, M. Ruzzene, M. A. Pagano, R. Battistutta, J. Bain, D. Fabbro, J. Schoepfer, M. Elliott, P. Furet, F. Meggio, G. Zanotti and L. A. Pinna, *Biochem. J.*, 2003, **374**, 639–646.
- 156 J. E. Dowling, M. Alimzhanov, L. Bao, C. Chuaqui, C. R. Denz, E. Jenkins, N. A. Larsen, P. D. Lyne, T. Pontz, Q. Ye, G. A. Holdgate, L. Snow, N. O’Connell and A. D. Ferguson, *ACS Med. Chem. Lett.*, 2016, **7**, 300–305.
- 157 Z. Fang, C. Grütter and D. Rauh, *ACS Chem. Biol.*, 2013, **18**, 58–70.
- 158 Y. Perera, H. G. Farina, I. Hernández, O. Mendoza, J. M. Serrano, O. Reyes, D. E. Gómez, R. E. Gómez, B. E. Acevedo, D. F. Alonso and S. E. Perea, *Int. J. Cancer*, 2008, **122**, 57–62.
- 159 V. Martel, O. Filhol, P. Colas and C. Cochet, *Oncogene*, 2006, **25**, 7343–7353.
- 160 B. Laudet, V. Moucadet, R. Prudent, O. Filhol, Y. S. Wong, D. Royer and C. Cochet, *Mol. Cell. Biochem.*, 2008, **316**, 63–69.
- 161 B. Laudet, C. Barette, V. Dulery, O. Renaudet, P. Dumy, A. Metz, R. Prudent, A. Deshiere, O. Dideberg, O. Filhol and C. Cochet, *Biochem. J.*, 2007, **408**, 363–373.
- 162 J. Raaf, E. Brunstein, O. G. Issinger and K. Niefind, *Chem. Biol.*, 2008, **15**, 111–117.
- 163 C. Nienberg, C. Garmann, A. Gratz, A. Bollacke, C. Götz and J. Jose, *Pharmaceuticals*, 2017, **10**, e6.
- 164 B. Bestgen, Z. Belaid-Choucair, T. Lomberget, M. Le Borgne, O. Filhol and C. Cochet, *Pharmaceuticals*, 2017, **10**, e16.
- 165 J. Marie Hardwick and L. Soane, *Cold Spring Harb. Perspect. Biol.*, 2013, **5**, a008722.
- 166 A. M. Petros, E. T. Olejniczak and S. W. Fesik, *Biochim. Biophys. Acta*, 2004, **1644**, 83–94.
- 167 S. N. Willis, J. I. Fletcher, T. Kaufmann, M. F. van Delft, L. Chen, P. E. Czabotar, H. Ierino, E. F. Lee, W. D. Fairlie, P. Bouillet, A. Strasser, R. M. Kluck, J. M. Adams and D. C. S. Huang, *Science*, 2007, **315**, 856–859.
- 168 S. Willis, C. L. Day, M. G. Hinds and D. C. S. Huang, *J. Cell Sci.*, 2003, **116**, 4053–4056.
- 169 K. W. Yip and J. C. Reed, *Oncogene*, 2008, **27**, 6398–6406.
- 170 C. Billard, *Mol. Cancer Ther.*, 2013, **12**, 1691–1700.
- 171 X. Liu, S. Dai, Y. Zhu, P. Marrack and J. W. Kappler, *Immunity*, 2003, **19**, 341–352.
- 172 C. Tse, A. R. Shoemaker, J. Adickes, M. G. Anderson, J. Chen, S. Jin, E. F. Johnson, K. C. Marsh, M. J. Mitten, P. Nimmer, L. Roberts, S. K. Tahir, Y. Xiao, X. Yang, H. Zhang, S. Fesik, S. H. Rosenberg and S. W. Elmore, *Cancer Res.*, 2008, **68**, 3421–3428.
- 173 A. J. Souers, J. D. Levenson, E. R. Boghaert, S. L. Ackler, N. D. Catron, J. Chen, B. D. Dayton, H. Ding, S. H. Enschede, W. J. Fairbrother, D. C. S. Huang, S. G. Hymowitz, S. Jin, S. L. Khaw, P. J. Kovar, L. T. Lam, J. Lee, H. L. Maecker, K. C. Marsh, K. D. Mason, M. J. Mitten, P. M. Nimmer, A. Oleksijew, C. H. Park, C. M. Park, D. C. Phillips, A. W. Roberts, D. Sampath, J. F. Seymour,

- M. L. Smith, G. M. Sullivan, S. K. Tahir, C. Tse, M. D. Wendt, Y. Xiao, J. C. Xue, H. Zhang, R. A. Humerickhouse, S. H. Rosenberg and S. W. Elmore, *Nat. Med.*, 2013, **19**, 202–208.
- 174 C. L. Oliver, M. B. Miranda, S. Shangary, S. Land, S. Wang and D. E. Johnson, *Mol. Cancer Ther.*, 2005, **1**, 23–31.
- 175 M. Nguyen, R. C. Marcellus, A. Roulston, M. Watson, L. Serfass, S. R. Murthy Madiraju, D. Goulet, J. Viallet, L. Belec, X. Billot, S. Acoca, E. Purisima, A. Wiegmanns, L. Cluse, R. W. Johnstone, P. Beauparlant and G. C. Shore, *Proc. Natl. Acad. Sci.*, 2007, **104**, 19512–19517.
- 176 L. D. Walensky, K. Pitter, J. Morash, K. J. Oh, S. Barbuto, J. Fisher, E. Smith, G. L. Verdine and S. J. Korsmeyer, *Mol. Cell*, 2006, **24**, 199–210.
- 177 J. L. LaBelle, S. G. Katz, G. H. Bird, E. Gavathiotis, M. L. Stewart, C. Lawrence, J. K. Fisher, M. Godes, K. Pitter, A. L. Kung and L. D. Walensky, *J. Clin. Invest.*, 2012, **122**, 2018–2031.
- 178 M. A. Debrincat, I. Pleines, M. Lebois, R. M. Lane, M. L. Holmes, J. Corbin, C. J. Vandenberg, W. S. Alexander, A. P. Ng, A. Strasser, P. Bouillet, M. Sola-Visner, B. T. Kile and E. C. Josefsson, *Cell Death Dis.*, 2015, **6**, e1721.
- 179 K. McArthur, S. Chappaz and B. T. Kile, *Blood*, 2018, **131**, 605–610.
- 180 C. N. Morrell, A. A. Aggrey, L. M. Chapman and K. L. Modjeski, *Blood*, 2014, **123**, 2759–2769.
- 181 L. J. Gay and B. Felding-Habermann, *Nat. Rev. Cancer*, 2011, **11**, 123–134.
- 182 M. Gawaz, H. Langer and A. E. May, *J. Clin. Invest.*, 2005, **115**, 3378–3384.
- 183 S. H. Yun, E. H. Sim, R. Y. Goh, J. I. Park and J. Y. Han, *Biomed Res. Int.*, 2016, **2016**, e9060143.
- 184 M. Dittrich, I. Birschmann, S. Mietner, A. Sickmann, U. Walter and T. Dandekar, *Arterioscler. Thromb. Vasc. Biol.*, 2008, **28**, 1326–1331.
- 185 D. Boyanova, S. Nilla, I. Birschmann, T. Dandekar and M. Dittrich, *Blood*, 2012, **119**, 22–34.
- 186 D. Ren, H-C. Tu, H. Kim, G. X. Wang, G. R. Bean, O. Takeuchi, J. R. Jeffers, G. P. Zambetti, J. J-D. Hsieh and E. H-Y. Cheng, *Science*, 2010, **330**, 1390–1393.
- 187 S. Cory and J. M. Adams, *Nat. Rev. Cancer*, 2002, **2**, 647–656.
- 188 M. Vogler, H. A. Hamali, X. M. Sun, E. T. W. Bampton, D. Dinsdale, R. T. Snowden, M. J. S. Dyer, A. H. Goodall and G. M. Cohen, *Blood*, 2011, **117**, 7145–7154.
- 189 B. T. Kile, *Br. J. Haematol.*, 2014, **165**, 217–226.
- 190 S. M. Schoenwaelder, Y. Yuan, E. C. Josefsson, M. J. White, Y. Yao, K. D. Mason, L. A. O'Reilly, K. J. Henley, A. Ono, S. Hsiao, A. Willcox, A. W. Roberts, D. C. S. S. Huang, H. H. Salem, B. T. Kile and S. P. Jackson, *Blood*, 2009, **114**, 663–666.
- 191 T. L. Nero, C. J. Morton, J. K. Holien, J. Wielens and M. W. Parker, *Nat. Rev. Cancer*, 2014, **14**, 248–262.
- 192 J. Ware, *Thromb. Haemost.*, 2004, **92**, 478–485.

- 193 J. Iegre, N. S. Ahmed, J. S. Gaynord, Y. Wu, K. M. Herlihy, Y. S. Tan, M. E. Lopes-Pires, R. Jha, Y. H. Lau, H. F. Sore, C. Verma, D. H O'Donovan, N. Pugh, D. R. Spring, *Chem. Sci.*, 2018, **9**, 4638–4643.
- 194 Y. Vugmeyster, *World J. Biol. Chem.*, 2012, **3**, 73–92.
- 195 B. J. Bruno, G. D. Miller and C. S. Lim, *Ther. Deliv.*, 2013, **4**, 1443–1467.
- 196 C. Stubbs, PhD thesis, University of Cambridge, 2015.
- 197 K. Hadje Georgiou, PhD thesis, University of Cambridge, 2015.
- 198 P. Brear, C. De Fusco, K. Hadje Georgiou, N. J. Francis-Newton, C. J. Stubbs, H. F. Sore, A. R. Venkitaraman, C. Abell, D. R. Spring and M. Hyvönen, *Chem. Sci.*, 2016, **7**, 6839–6845.
- 199 T. Kinoshita, T. Nakaniwa, Y. Sekiguchi, Y. Sogabe, A. Sakurai, S. Nakamura and I. Nakanishi, *J. Synchrotron Radiat.*, 2013, **20**, 974–979.
- 200 C. De Fusco, P. Brear, J. Iegre, K. H. Georgiou, H. F. Sore, M. Hyvönen and D. R. Spring, *Bioorg. Med. Chem.*, 2017, **25**, 3471–3482.
- 201 V. Moucadel, R. Prudent, C. F. Sautel, F. Teillet, C. Barette, L. Lafanechere, V. Receveur-Brechot, C. Cochet, V. Moucadel, R. Prudent, C. F. Sautel, F. Teillet, C. Barette, L. Lafanechere, V. Receveur-Brechot and C. Cochet, *Oncotarget*, 2011, **2**, 997–1010.
- 202 P. Brear, A. North, J. Iegre, K. Hadje Georgiou, A. Lubin, L. Carro, W. Green, H. F. Sore, M. Hyvönen and D. R. Spring, *Bioorg. Med. Chem.*, 2018, **26**, 3016–3020.
- 203 M. R. C. Yang, R. Edsall, H. A. J. Harris, X. Zhang and E. S. Manas, *Bioorg. Med. Chem. Lett.*, 2004, **12**, 2553–2570.
- 204 M. I. Dawson, Z. Xia, G. Liu, M. Ye, J. A Fontana, L. Farhana, B. B. Patel, S. Arumugarajah, M. Bhuiyan, X.-K. Zhang, Y.-H. Han, W. B. Stallcup, J.-I. Fukushi, T. Mustelin, L. Tautz, Y. Su, D. L. Harris, N. Waleh, P. D. Hobbs, L. Jong, W. R. Chao, L. J. Schiff and B. P. Sani, *J. Med. Chem.*, 2007, **11**, 2622–2639.
- 205 S. Kotha, K. Lahiri and D. Kashinath, *Tetrahedron*, 2002, **58**, 9633–9695.
- 206 J. Iegre, P. Brear, C. De Fusco, M. Yoshida, S. L. Mitchell, M. Rossmann, L. Carro, H. F. Sore, M. Hyvönen and D. R. Spring, *Chem. Sci.*, 2018, **9**, 3041–3049.
- 207 N. Clauson-Kaas, *Acta. Chem. Scand.*, 1952, **6**, 667–670.
- 208 W. D. Schmitz, I. E. Whitney, A. P. Degnan and J. J. Bronson, US App. 12169874, 2009.
- 209 M. F. Francis S. Wekesa, N. Phadke, C. Jahier and D. B. Cordes, *Synthesis*, 2014, **46**, 1046–1051.
- 210 J. Wells, A. R. Renslo, D. Wolan and J. Zorn, PCT Int. App. WO2009089508, 2009.
- 211 C. A. Lipinski, F. Lombardo, B. W. Dominy and P. J. Feeney, *Adv. Drug Deliv. Rev.*, 2001, **46**, 3–26.
- 212 G. Bold, J. Frei, M. Lang, P. Traxler and P. I. Furet, PCT Int. App. WO1998014451A1, 1998.
- 213 A. M. Birch, S. Groombridge, R. Law, A. G. Leach, C. D. Mee and C. Schramm, *J. Med. Chem.*,

- 2012, **55**, 3923–3933.
- 214 A. F. Abdel-Magid, K. G. Carson, B. D. Harris, C. A. Maryanoff and R. D. Shah, *J. Org. Chem.*, 1996, **61**, 3849–3862.
- 215 J. Raaf, B. Guerra, I. Neundorf, B. Bopp, O. G. Issinger, J. Jose, M. Pietsch and K. Niefind, *ACS Chem. Biol.*, 2013, **8**, 901–907.
- 216 Y. H. Lau, P. De Andrade, N. Sköld, G. J. McKenzie, A. R. Venkitaraman, C. Verma, D. P. Lane and D. R. Spring, *Org. Biomol. Chem.*, 2014, **12**, 4074–4077.
- 217 L. Zhang, G. S. Kauffman, J. A. Pesti and J. Yin, *J. Org. Chem.*, 1997, **62**, 6918–6920.
- 218 N. Fischer, E. D. Goddard-Borger, R. Greiner, T. M. Klapötke, B. W. Skelton and J. Stierstorfer, *J. Org. Chem.*, 2012, **77**, 1760–1764.
- 219 B. Förster, J. Bertran, F. Teixidor and C. Viñas, *J. Organomet. Chem.*, 1999, **587**, 67–73.
- 220 Y. Tobe, N. Utsumi, K. Kawabata, A. Nagano, K. Adachi, S. Araki, M. Sonoda, K. Hirose and K. Naemura, *J. Am. Chem. Soc.*, 2002, **124**, 5350–5364.
- 221 A. Yaron, F. Naider and S. Scharpe, *Crit. Rev. Biochem. Mol. Biol.*, 2008, **28**, 31–81.
- 222 A. B. M. Abdel-Aal, G. Papageorgiou, M. Quibell and J. Offer, *Chem. Commun.*, 2014, **50**, 8316–8319.
- 223 P. Lönn, A. D. Kacsinta, X. S. Cui, A. S. Hamil, M. Kaulich, K. Gogoi and S. F. Dowdy, *Sci. Rep.*, 2016, **6**, e32301.
- 224 H. Zhang, P. M. Nimmer, S. K. Tahir, J. Chen, R. M. Fryer, K. R. Hahn, L. A. Iciek, S. J. Morgan, M. C. Nasarre, R. Nelson, L. C. Preusser, G. A. Reinhart, M. L. Smith, S. H. Rosenberg, S. W. Elmore and C. Tse, *Cell Death Differ.*, 2007, **14**, 943–951.
- 225 Y. Wu, A. Kaur, E. Fowler, M. M. Wiedmann, R. Young, W. R. J. D. Galloway, L. Olsen, H. F. Sore, A. Chattopadhyay, T. T.-L. Kwan, W. Xu, S. J. Walsh, P. De Andrade, M. Janecek, S. Arumugam, L. S. Itzhaki, Y. H. Lau and D. R. Spring, *ACS Chem. Biol.*, 2019, in press.
- 226 S. Futaki, *Adv. Drug Deliv. Rev.*, 2005, **57**, 547–558.
- 227 M. Gooding, S. Tudzarova, R. J. Worthington, S. R. Kingsbury, A. S. Rebstock, H. Dube, M. I. Simone, C. Visintin, D. Lagos, J. M. F. Quesada, H. Laman, C. Boshoff, G. H. Williams, K. Stoeber and D. L. Selwood, *Chem. Biol. Drug Des.*, 2012, **79**, 9–21.
- 228 E. M. Kolonko and L. L. Kiessling, *J. Am. Chem. Soc.*, 2008, **130**, 5626–5627.
- 229 D. S. Goldfarb, A. H. Corbett, D. A. Mason, M. T. Harreman and S. A. Adam, *Trends Cell Biol.*, 2004, **14**, 505–514.
- 230 M. Okuyama, H. Laman, S. R. Kingsbury, C. Visintin, E. Leo, K. L. Eward, K. Stoeber, C. Boshoff, G. H. Williams and D. L. Selwood, *Nat. Methods*, 2007, **4**, 153–159.
- 231 B. R. Lentz, *Prog. Lipid Res.*, 2003, **42**, 423–438.
- 232 A. V. Gyulkhandanyan, A. Mutlu, D. J. Allen, J. Freedman and V. Leytin, *Thromb. Res.*, 2014, **133**, 73–79.

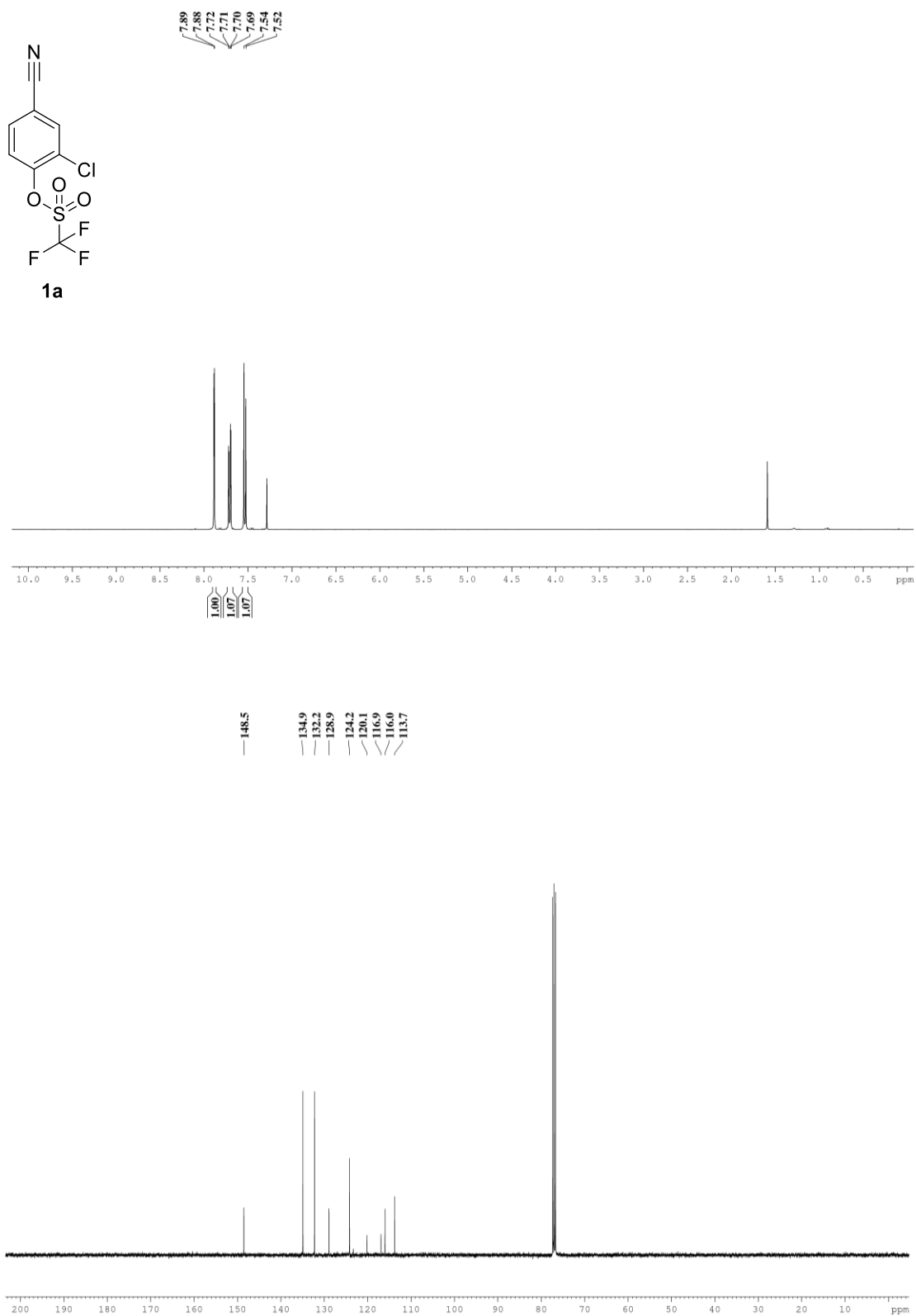
- 233 E. Gavathiotis, D. E. Reyna, J. A. Bellairs, E. S. Leshchiner and L. D. Walensky, *Nat. Chem. Biol.*, 2012, **8**, 639–645.
- 234 P. E. Czabotar, P. M. Colman and D. C. S. Huang, *Cell Death Differ.*, 2009, **16**, 1187–1191.
- 235 Y. H. Lau and D. R. Spring, *Synlett*, 2011, **13**, 1917–1919.
- 236 S. J. Shattil, J. A. Hoxie, M. Cunningham and L. F. Brass, *J Biol Chem*, 1985, **260**, 11107–11114.
- 237 M. L. Taylor, N. L. Misso, G. a Stewart and P. J. Thompson, *Platelets*, 1995, **6**, 394–401.
- 238 S. J. Shattil, M. Cunningham and J. Hoxie, *Blood*, 1987, **70**, 307–315.
- 239 M. L. Stewart, E. Fire, A. E. Keating and L. D. Walensky, *Nat. Chem. Biol.*, 2010, **6**, 595–601.
- 240 Y. H. Lau, PhD thesis, University of Cambridge, 2013.
- 241 T. Okamoto, K. Zobel, A. Fedorova, C. Quan, H. Yang, W. J. Fairbrother, D. C. S. S. Huang, B. J. Smith, K. Deshayes and P. E. Czabotar, *ACS Chem. Biol.*, 2013, **8**, 297–302.
- 242 A. M. Petros, D. G. Nettesheim, Y. Wang, E. T. Olejniczak, R. P. Meadows, J. Mack, K. Swift, E. D. Matayoshi, H. Zhang, C. B. Thompson and S. W. Fesik, *Protein Sci.*, 2000, **9**, 2528–2534.
- 243 J. A. Miles, D. J. Yeo, P. Rowell, S. Rodriguez-Marin, C. M. Pask, S. L. Warriner, T. A. Edwards and A. J. Wilson, *Chem. Sci.*, 2016, **7**, 3694–3702.
- 244 S. Shanmugaraju, A. K. Bar, K. W. Chi and P. S. Mukherjee, *Organometallics*, 2010, **29**, 2971–2980.
- 245 P. Palladino and D. A. Stetsenko, *Org. Lett.*, 2012, **14**, 6346–6349.
- 246 S. Rajan, M. Choi, K. Baek and H. S. Yoon, *Proteins Struct. Funct. Bioinforma.*, 2015, **83**, 1262–1272.
- 247 J. Wu and C. Yue, *Synth. Commun.*, 2006, **36**, 2939–2947.
- 248 M. Zhong and S. A. Strobel, *J. Org. Chem.*, 2008, **73**, 603–611.
- 249 R. Pal, R. J. Clark, M. Manoharan and I. V. Alabugin, *J. Org. Chem.*, 2010, **75**, 8689–8692.
- 250 G. Primofiore, S. Taliani, F. Da Settimo, A. M. Marini, C. La Motta, F. Simorini, M. P. Patrizi, V. Sergianni, E. Novellino, G. Greco, B. Cosimelli, V. Calderone, M. Montali, F. Besnard and C. Martini, *J. Med. Chem.*, 2007, **50**, 1627–1634.
- 251 F. Giordanetto, J. D. Revell, L. Knerr, M. Hostettler, A. Paunovic, C. Priest, A. Janefeldt and A. Gill, *ACS Med. Chem. Lett.*, 2013, **4**, 1163–1168.
- 252 C. H. Ku, C. H. Kuo, C. Y. Chen, M. K. Leung and K. H. Hsieh, *J. Mater. Chem.*, 2008, **18**, 1296–1301.
- 253 W. E. Lu, X. Z. Dong, W. Q. Chen, Z. S. Zhao and X. M. Duan, *J. Mater. Chem.*, 2011, **21**, 5650–5659.
- 254 S. Zhao, J. Kang, Y. Du, J. Kang, X. Zhao, Y. Xu, R. Chen, Q. Wang and X. Shi, *J. Heterocycl. Chem.*, 2014, **51**, 683–689.

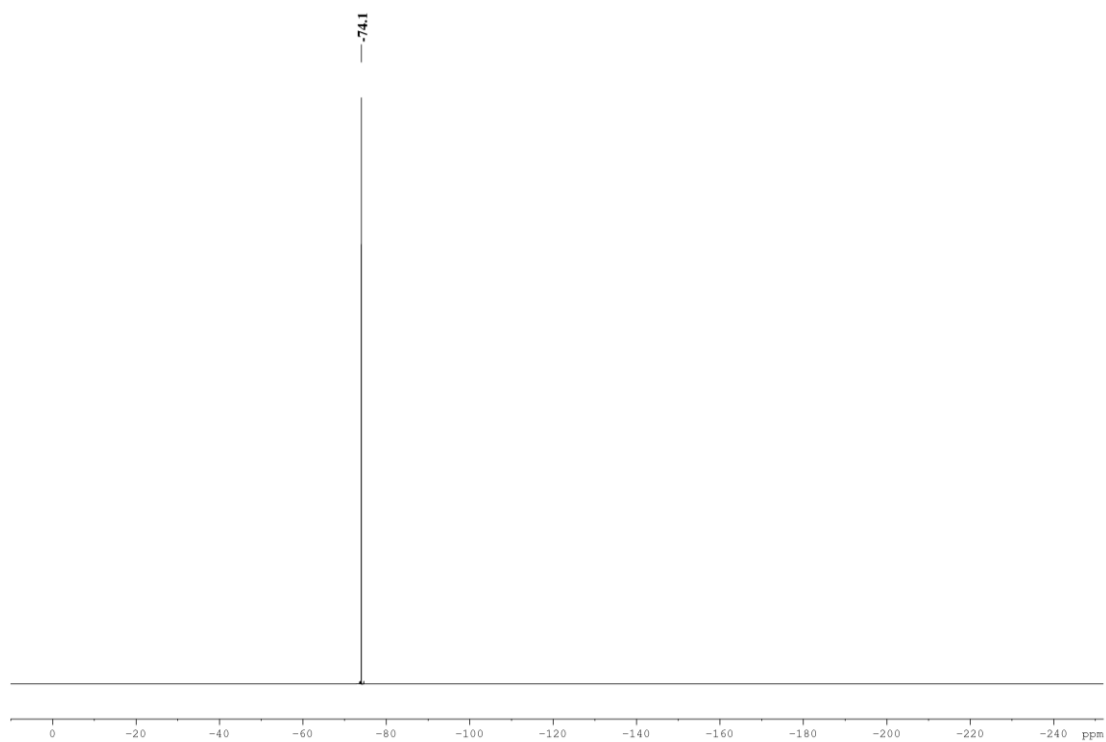
- 255 R. A. Friesner, R. B. Murphy, M. P. Repasky, L. L. Frye, J. R. Greenwood, T. A. Halgren, P. C. Sanschagrin and D. T. Mainz, *J. Med. Chem.*, 2006, **49**, 6177–6196.
- 256 R. A. Friesner, J. L. Banks, R. B. Murphy, T. A. Halgren, J. J. Klicic, D. T. Mainz, M. P. Repasky, E. H. Knoll, M. Shelley, J. K. Perry, D. E. Shaw, P. Francis and P. S. Shenkin, *J. Med. Chem.*, 2004, **47**, 1739–1749.
- 257 T. A. Halgren, R. B. Murphy, R. A. Friesner, H. S. Beard, L. L. Frye, W. T. Pollard and J. L. Banks, *J. Med. Chem.*, 2004, **47**, 1750–1759.
- 258 T. J. Dolinsky, J. E. Nielsen, J. A. McCammon and N. A. Baker, *Nucleic Acids Res.*, 2004, **32**, 665–667.
- 259 D.A. Case, V. Babin, J.T. Berryman, R.M. Betz, Q. Cai, D.S. Cerutti, T.E. Cheatham, III, T.A. Darden, R.E. Duke, H. Gohlke, A.W. Goetz, S. Gusarov, N. Homeyer, P. Janowski, J. Kaus, I. Kolossvary, A. Kovalenko, T.S. Lee, S. LeGrand, T. Luchko, R. Luo, B. Madej, K.M. Merz, F. Paesani, D.R. Roe, A. Roitberg, C. Sagui, R. Salomon-Ferrer, G. Seabra, C.L. Simmerling, W. Smith, J. Swails, R.C. Walker, J. Wang, R.M. Wolf, X. Wu and P.A. Kollman, AMBER 14, University of California, San Francisco, 2014.
- 260 W. L. Jorgensen, J. Chandrasekhar, J. D. Madura, R. W. Impey and M. L. Klein, *J. Chem. Phys.*, 1983, **79**, 926–935.
- 261 J. A. Maier, C. Martinez, K. Kasavajhala, L. Wickstrom, K. E. Hauser and C. Simmerling, *J. Chem. Theory Comput.*, 2015, **11**, 3696–3713.
- 262 J. Wang, R. M. Wolf, J. W. Caldwell, P. A. Kollman and D. A. Case, *J. Comput. Chem.*, 2004, **25**, 1157–1174.
- 263 E. Vanquelef, S. Simon, G. Marquant, E. Garcia, G. Klimerak, J. C. Delepine, P. Cieplak and F. Y. Dupradeau, *Nucleic Acids Res.*, 2011, **39**, 511–517.
- 264 W. D. Cornell, P. Cieplak, C. I. Bayly and P. A. Kollman, *J. Am. Chem. Soc.*, 2002, **115**, 9620–9631.
- 265 M. J. Frisch, G. W. Trucks, H. B. Schlegel, G. E. Scuseria, M. A. Robb, J. R. Cheeseman, G. Scalmani, V. Barone, G. A. Petersson, H. Nakatsuji, X. Li, M. Caricato, A. V. Marenich, J. Bloino, B. G. Janesko, R. Gomperts, B. Mennucci, H. P. Hratchian, J. V. Ortiz, A. F. Izmaylov, J. L. Sonnenberg, D. Williams-Young, F. Ding, F. Lipparini, F. Egidi, J. Goings, B. Peng, A. Petrone, T. Henderson, D. Ranasinghe, V. G. Zakrzewski, J. Gao, N. Rega, G. Zheng, W. Liang, M. Hada, M. Ehara, K. Toyota, R. Fukuda, J. Hasegawa, M. Ishida, T. Nakajima, Y. Honda, O. Kitao, H. Nakai, T. Vreven, K. Throssell, J. A. Montgomery, Jr., J. E. Peralta, F. Ogliaro, M. J. Bearpark, J. J. Heyd, E. N. Brothers, K. N. Kudin, V. N. Staroverov, T. A. Keith, R. Kobayashi, J. Normand, K. Raghavachari, A. P. Rendell, J. C. Burant, S. S. Iyengar, J. Tomasi, M. Cossi, J. M. Millam, M. Klene, C. Adamo, R. Cammi, J. W. Ochterski, R. L. Martin, K. Morokuma, O. Farkas, J. B. Foresman, and D. J. Fox, GAUSSIAN 16 (Revision B.01), Gaussian, Inc., Wallingford CT, 2016.
- 266 J. P. Ryckaert, G. Ciccotti and H. J. C. Berendsen, *J. Comput. Phys.*, 1977, **23**, 327–341.
- 267 T. Darden, D. York and L. Pedersen, *J. Chem. Phys.*, 2003, **98**, e10089.
- 268 J. A. Lzaguirre, D. P. Catarello, J. M. Wozniak and R. D. Skeel, *J. Chem. Phys.*, 2001, **114**,

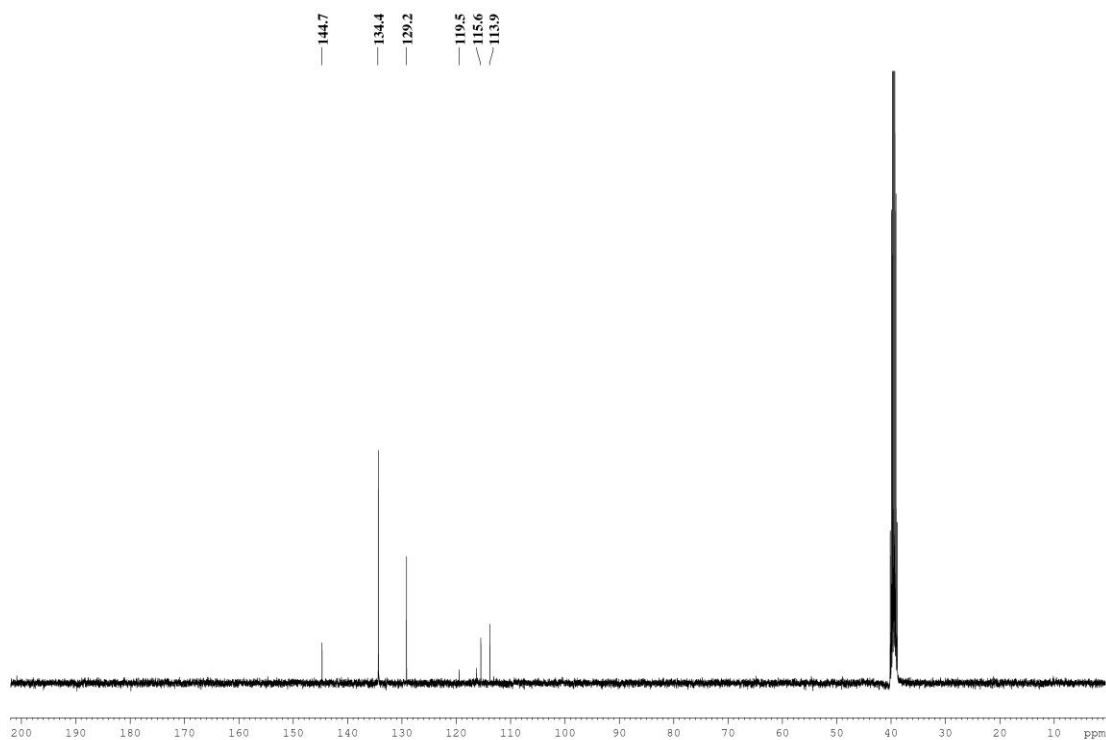
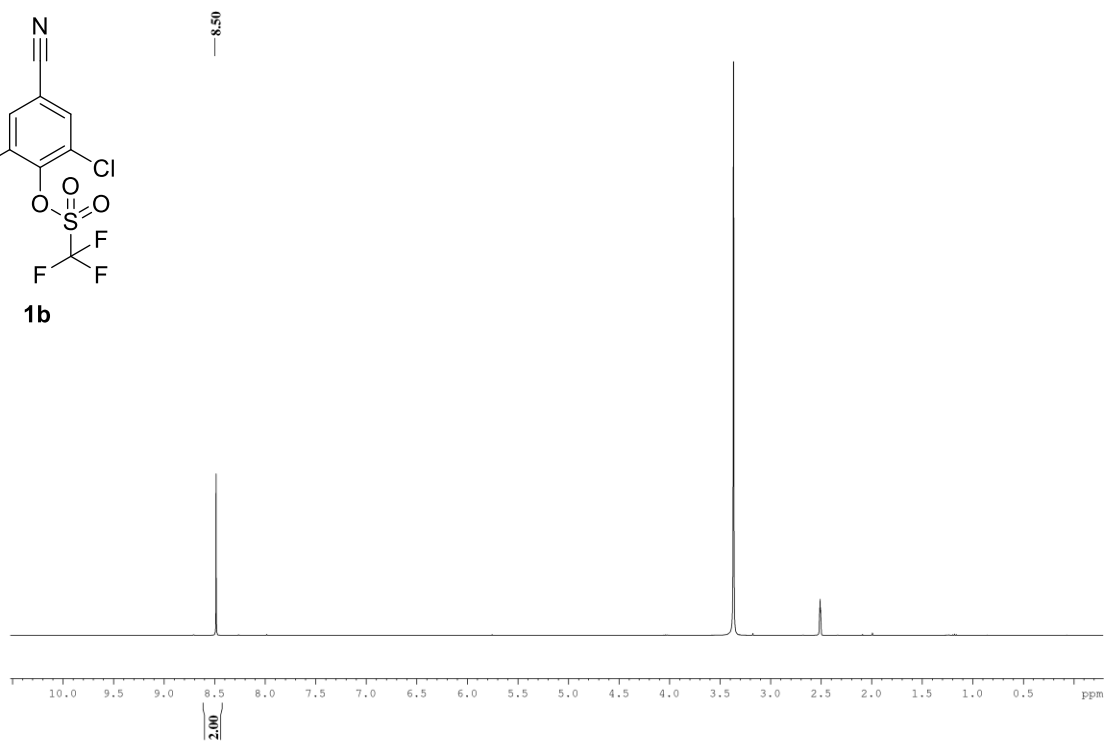
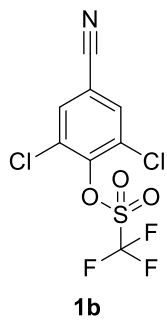
- e2090.
- 269 H. J. C. Berendsen, J. P. M. Postma, W. F. Van Gunsteren, A. Dinola and J. R. Haak, *J. Chem. Phys.*, 1984, **81**, e3684.
- 270 L. Martinez, R. Andrade, E. G. Birgin and J. M. Martínez, *J. Comput. Chem.*, 2009, **30**, 2157–2164.
- 271 Y. S. Tan, D. R. Spring, C. Abell and C. Verma, *J. Chem. Inf. Model.*, 2014, **54**, 1821–1827.
- 272 W. L. De Lano, *The PyMOL Molecular Graphics System*, DeLano Scientific, San Carlos, CA, 2002.
- 273 H. Gohlke, C. Kiel and D. A. Case, *J. Mol. Biol.*, 2003, **330**, 891–913.
- 274 J. Srinivasan, T. E. Cheatham, P. Cieplak, P. A. Kollman and D. A. Case, *J. Am. Chem. Soc.*, 1998, **120**, 9401–9409.
- 275 A. Onufriev, D. Bashford and D. A. Case, *Proteins Struct. Funct. Genet.*, 2004, **55**, 383–394.
- 276 M. Rarey, B. Kramer, T. Lengauer and G. Klebe, *J. Mol. Biol.*, 1996, **261**, 470–489.
- 277 R. Luo, L. David and M. K. Gilson, *J. Comput. Chem.*, 2002, **23**, 1244–1253.
- 278 J. Weiser, P. S. Shenkin and W. C. Still, *J. Comput. Chem.*, 1998, **20**, 217–230.
- 279 I. Massova and P. A. Kollman, *J. Am. Chem. Soc.*, 1999, **121**, 8133–8143.
- 280 M. L. Connolly, *J. Appl. Crystallogr.*, 1983, **16**, 548–558.
- 281 B. R. Brooks, D. Janežič and M. Karplus, *J. Comput. Chem.*, 1995, **16**, 1522–1542.
- 282 A. J. Kimple, R. E. Muller, D. P. Siderovski and F. S. Willard, *Methods Mol. Biol.*, 2010, **627**, 91–100.
- 283 H. Jenssen and S. I. Aspmo, *Methods Mol. Biol.*, 2008, **494**, 177–186.
- 284 A. L. Hopkins, C. R. Groom and A. Alex, *Drug Discov. Today*, 2004, **9**, 430–431.
- 285 M. Congreve, R. Carr, C. Murray and H. Jhoti, *Drug Discov. Today*, 2003, **8**, 876–877.
- 286 D. F. Veber, S. R. Johnson, H. Cheng, B. R. Smith, K. W. Ward, K. D. Kopple and K. D. Veber, *J. Med. Chem.*, 2002, **45**, 2615–2623.
- 287 J. W. Scott, S. Galic, K. L. Graham, R. Foitzik, N. X. Y. Ling, T. A. Dite, S. M. A. Issa, C. G. Langendorf, Q. P. Weng, H. E. Thomas, T. W. Kay, N. C. Birnberg, G. R. Steinberg, B. E. Kemp and J. S. Oakhill, *Chem. Biol.*, 2015, **22**, 705–711.
- 288 J. Iegre, P. Brear, D. J. Baker, Y. S. Tan, E. L. Atkinson, H. F. Sore, D. H. O' Donovan, C. S. Verma, M. Hyvönen and D. R. Spring, *Chem. Sci.*, 2019, **10**, in press.
- 289 J. M. Collins, in *Microwaves in Organic Synthesis, Third Edition.*, Wiley-VCH Verlag GmbH & Co. KGaA, Third., 2012, 897–959.
- 290 G. H. Bird, F. Bernal, K. Pitter and L. D. Walensky, *Methods Enzymol.*, 2008, **446**, 369–386.

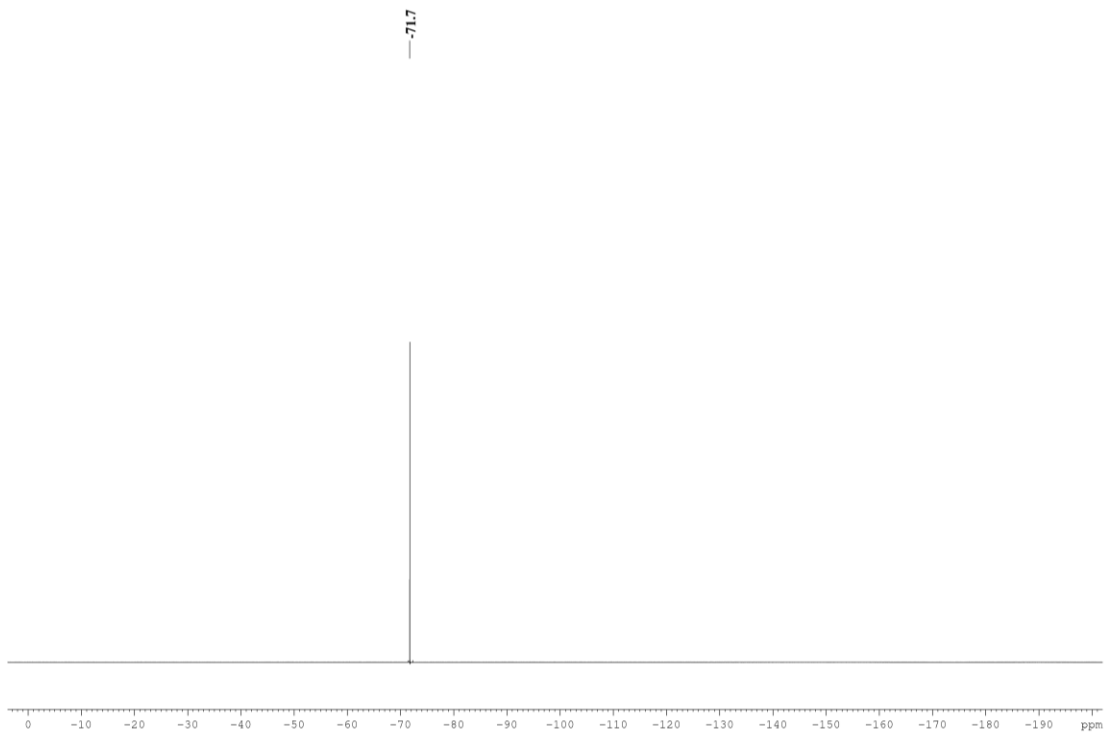
Appendices

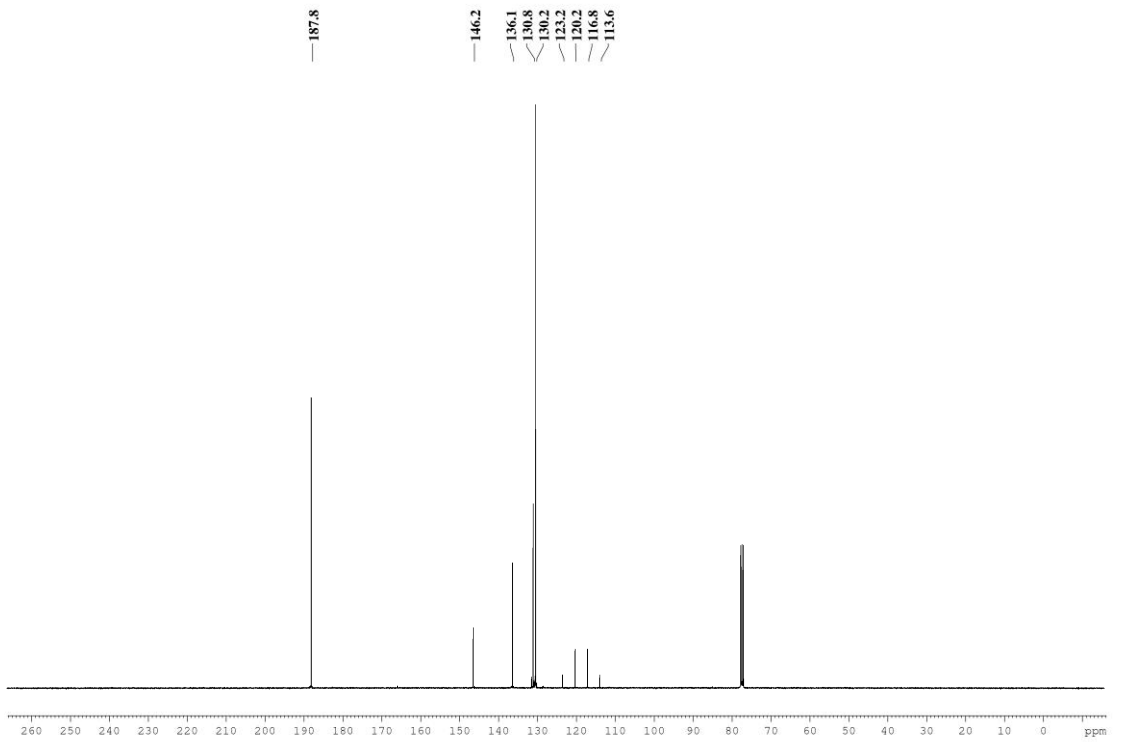
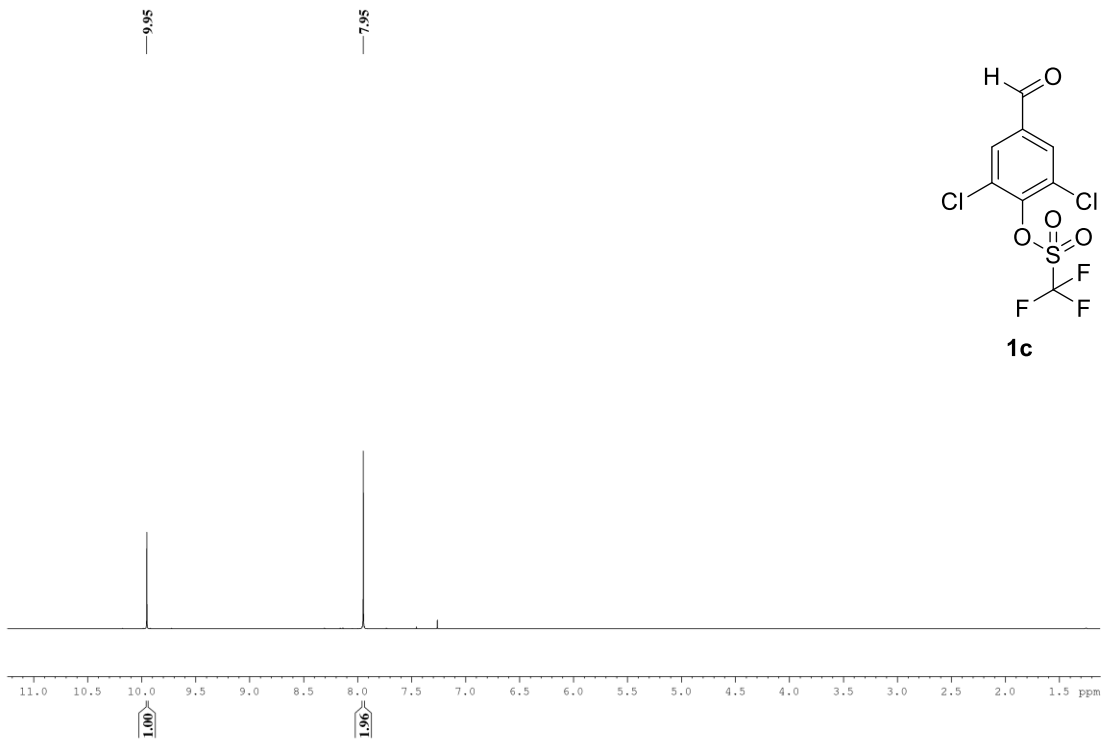
A.1. ^1H , ^{19}F and ^{13}C NMR spectra

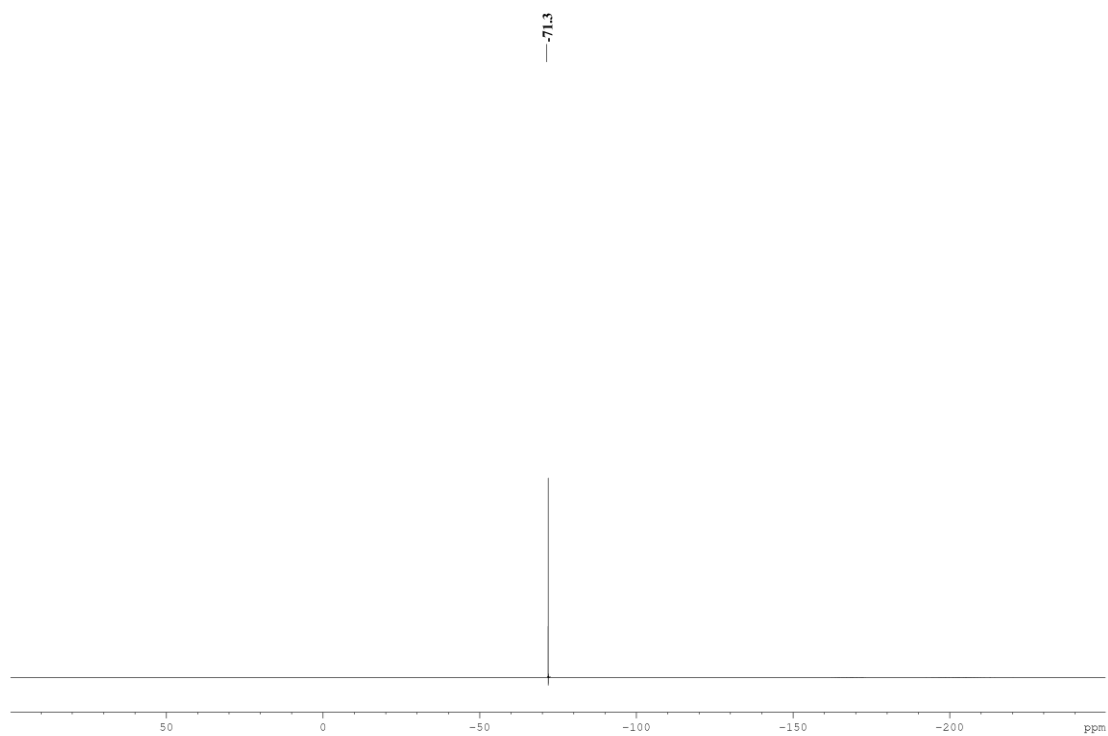


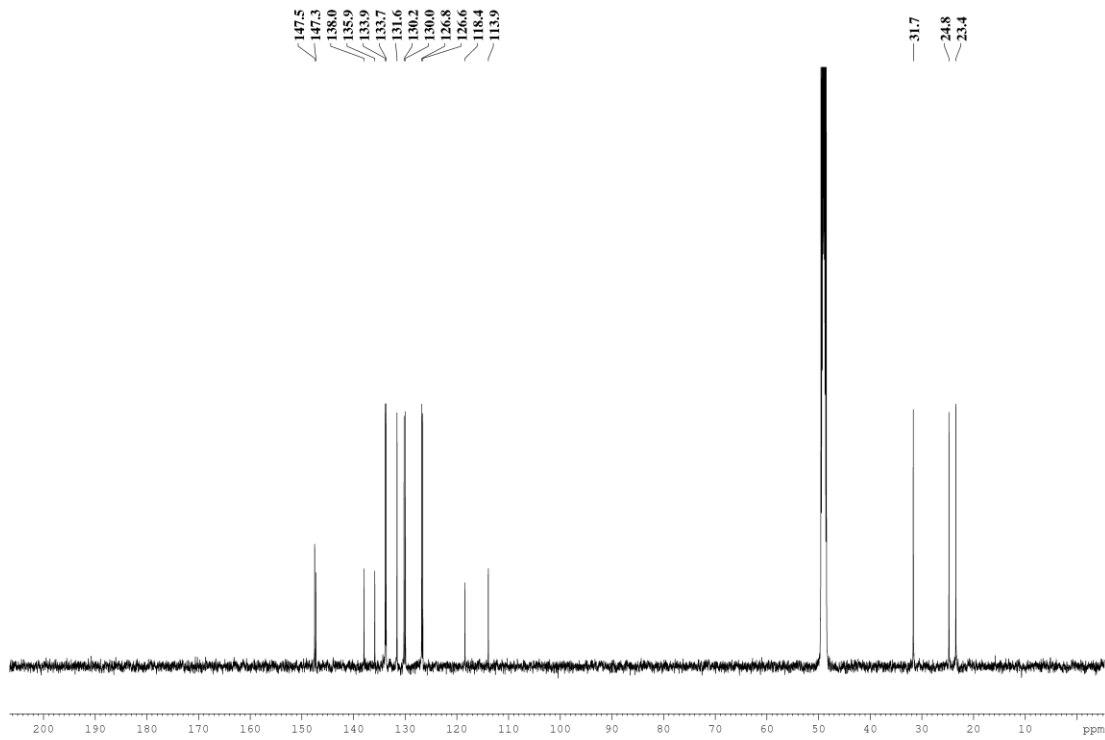
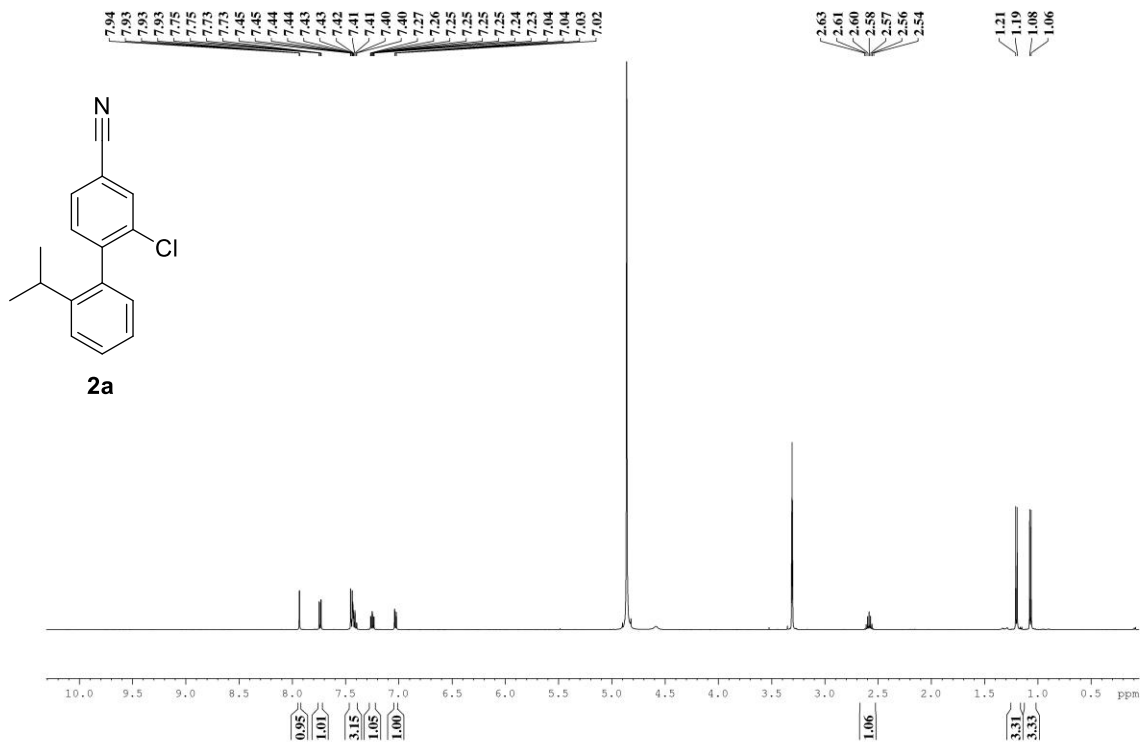


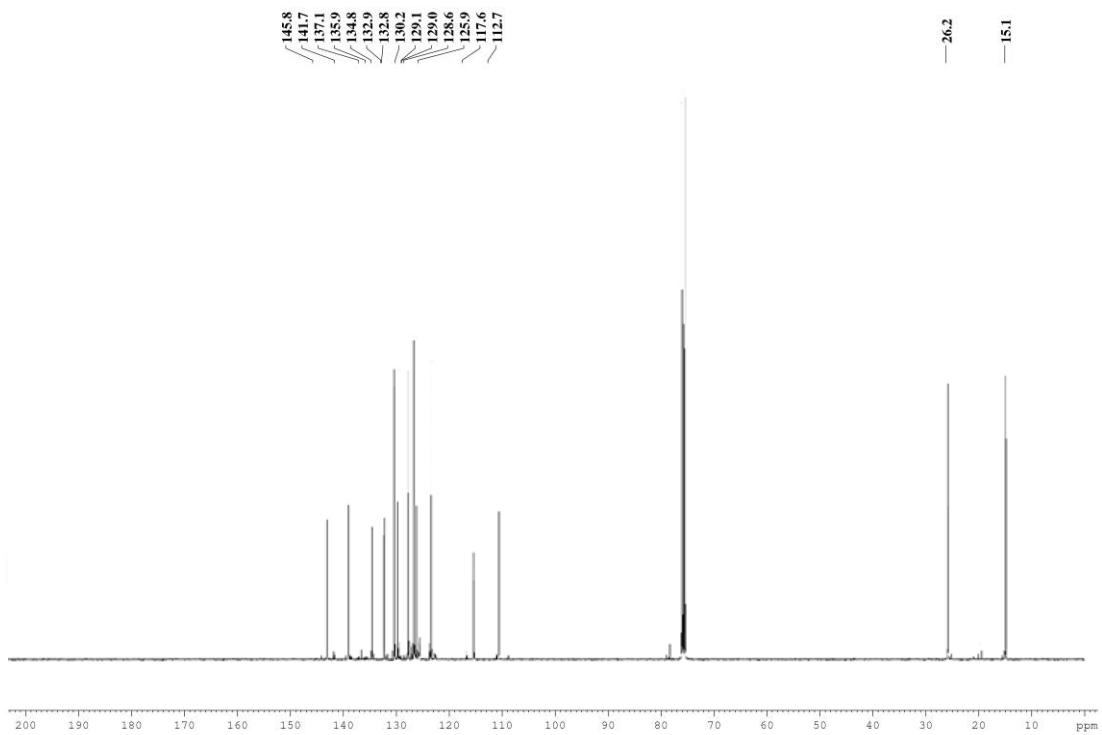
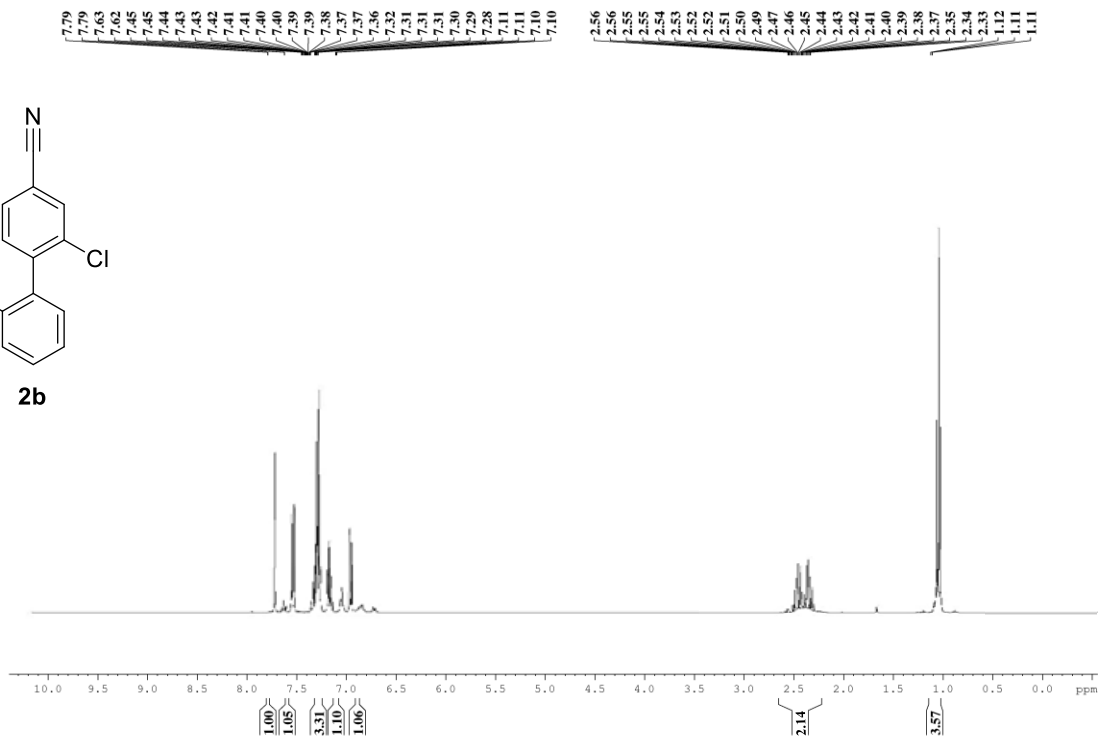
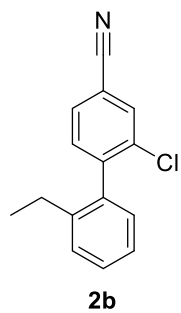


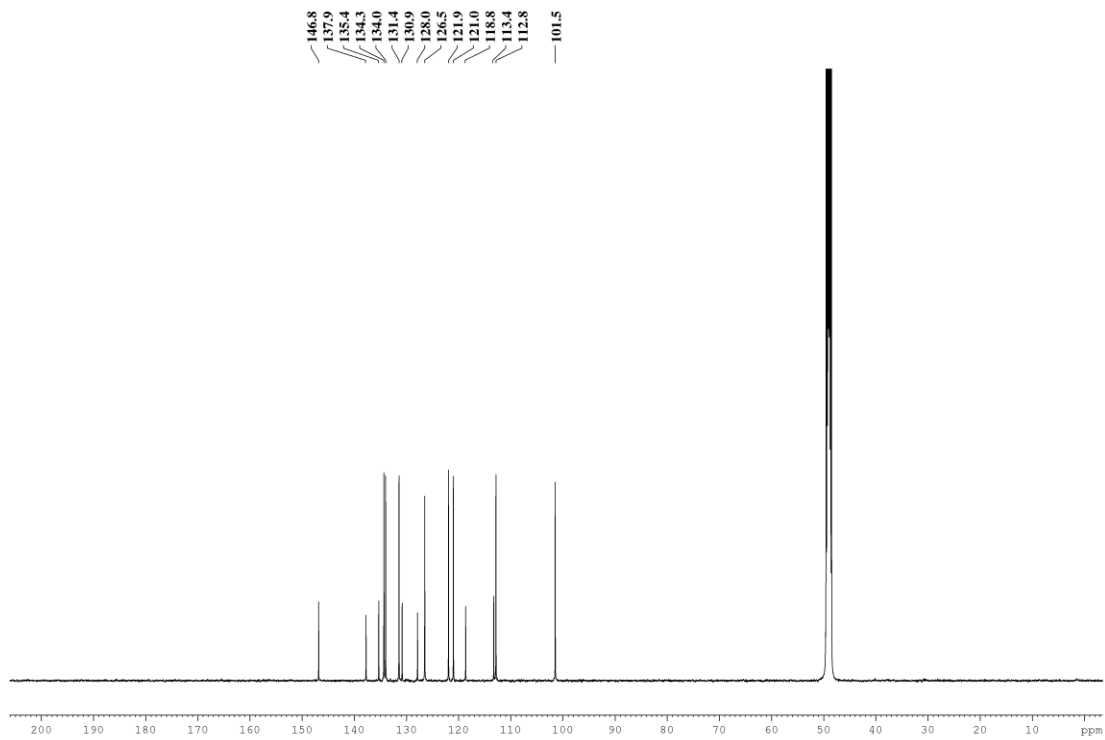
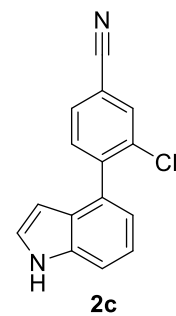
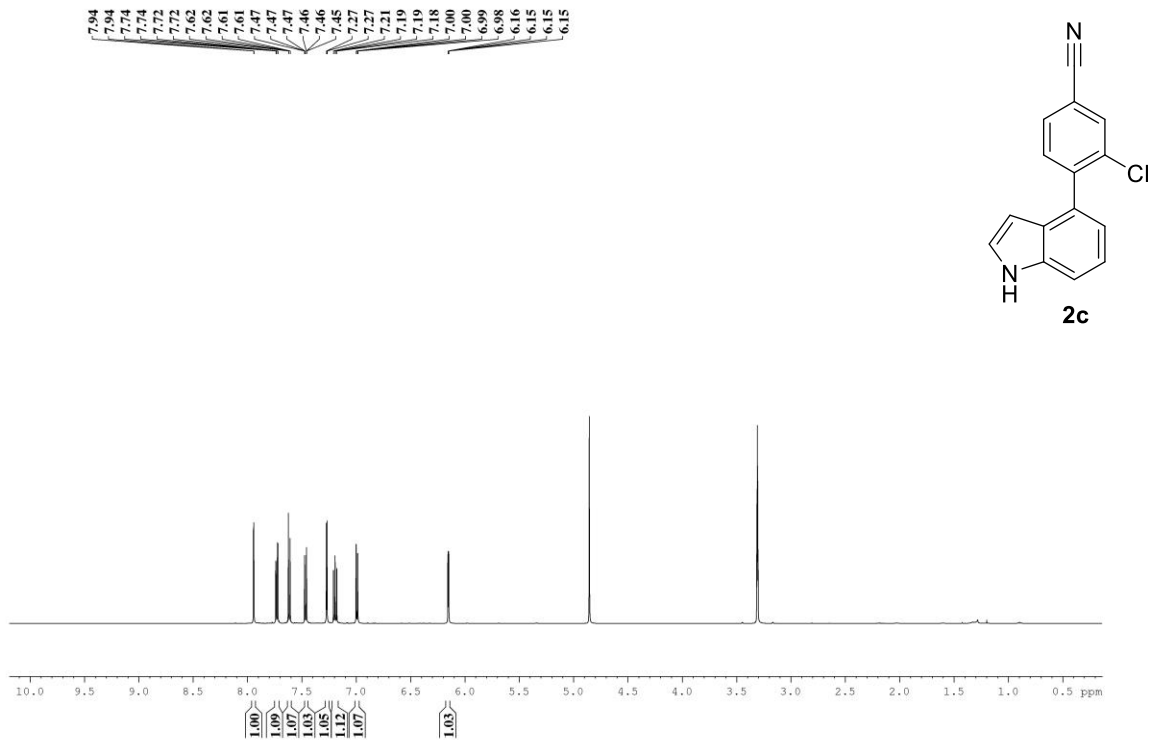


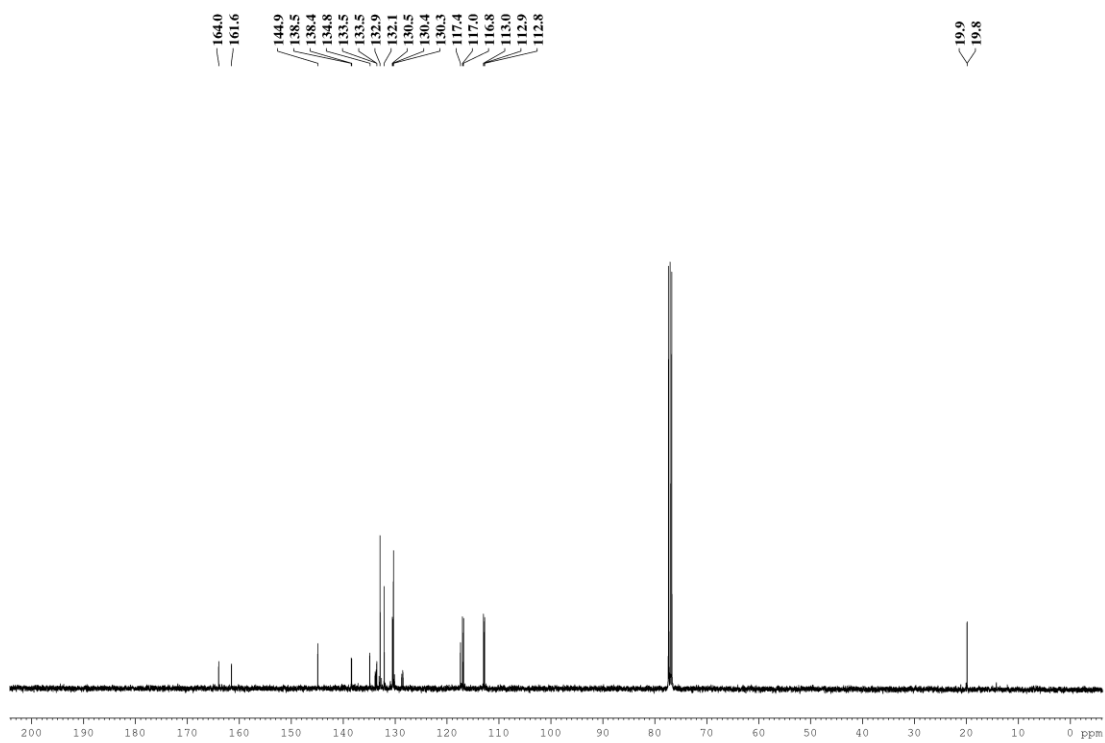
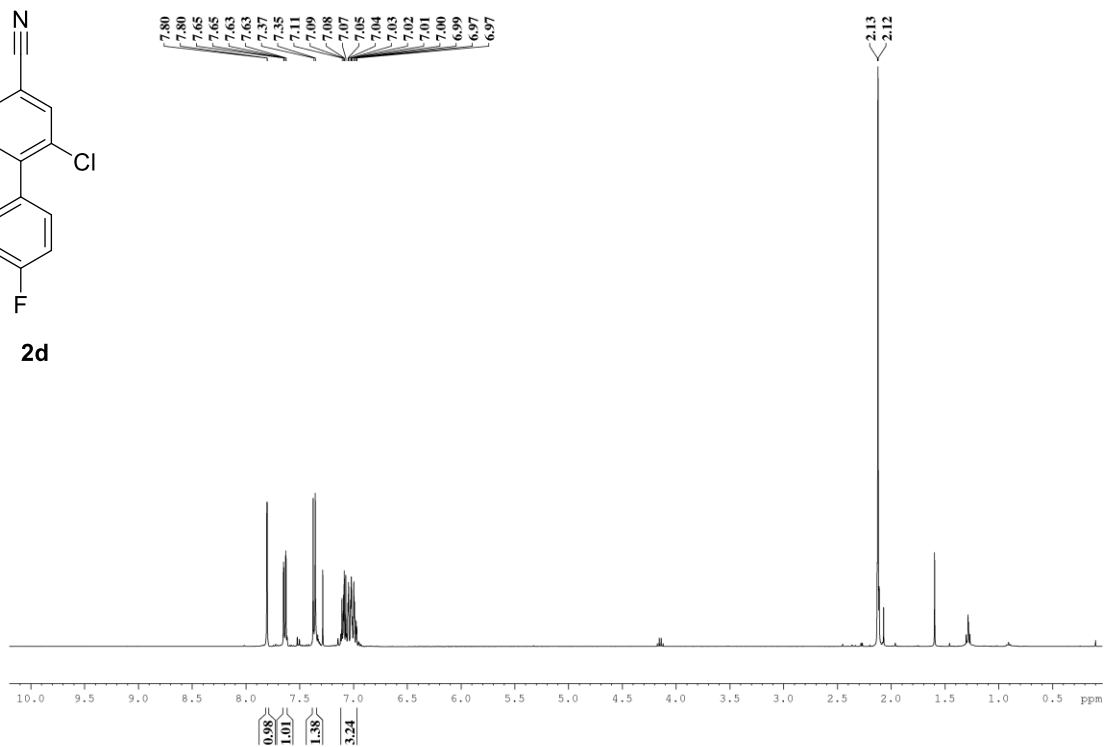
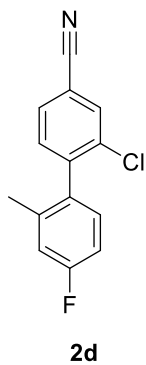


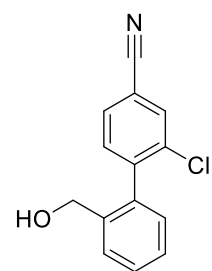
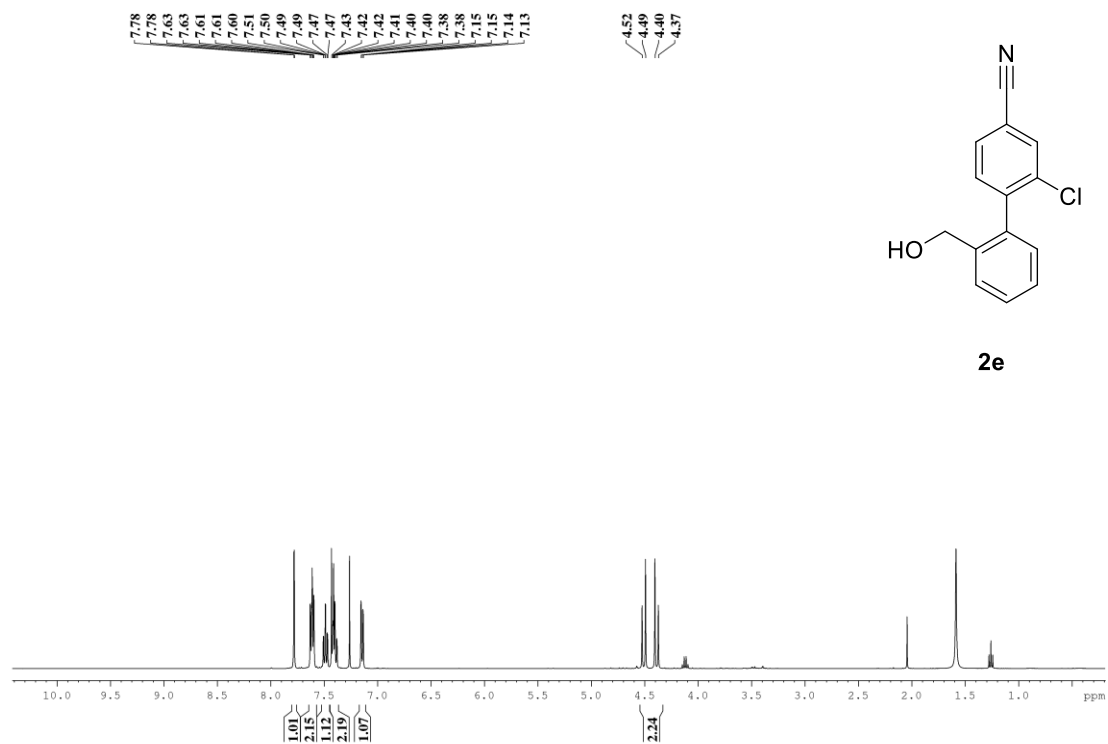




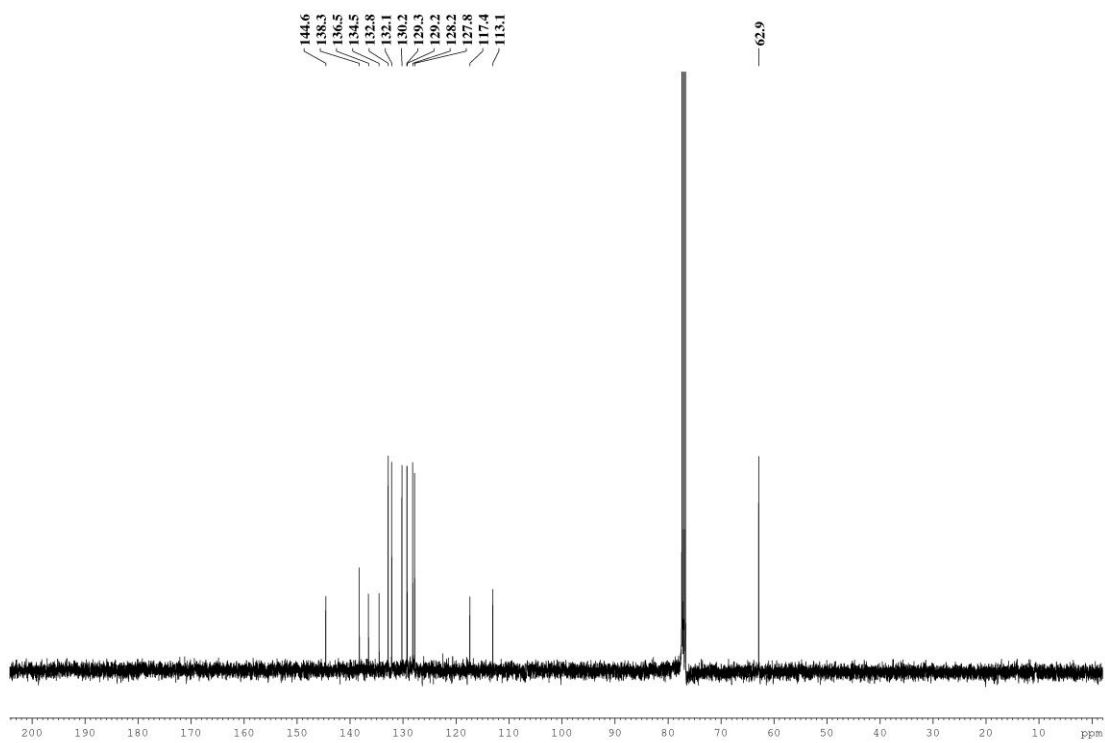


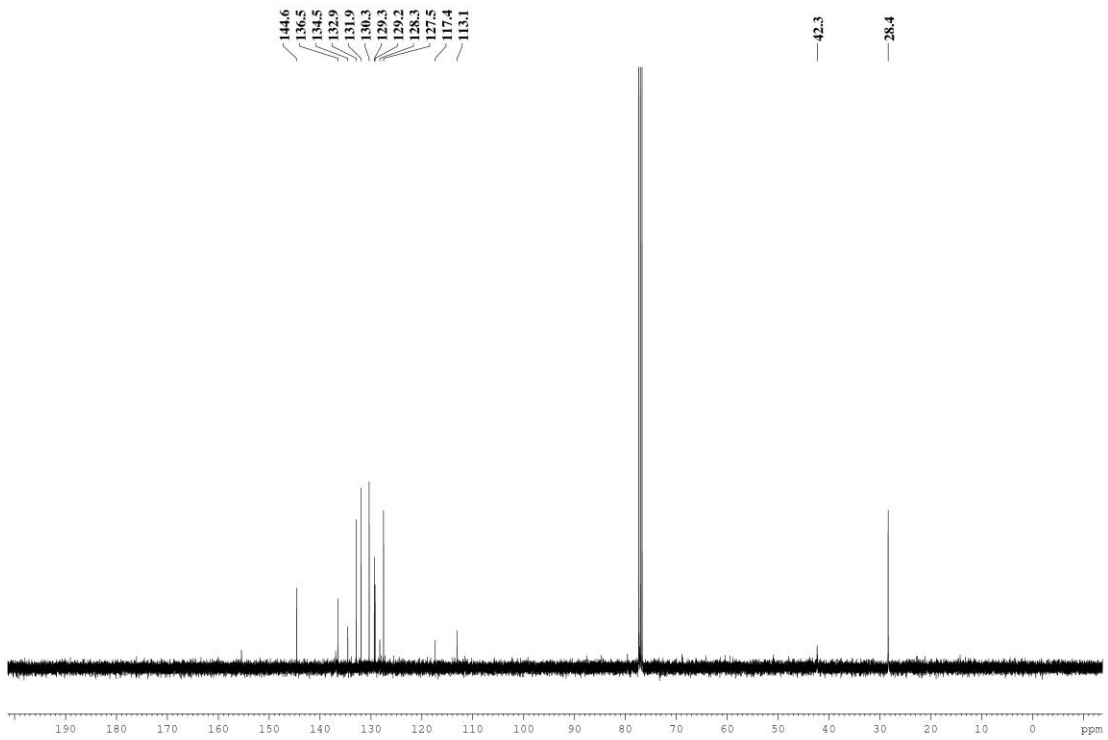
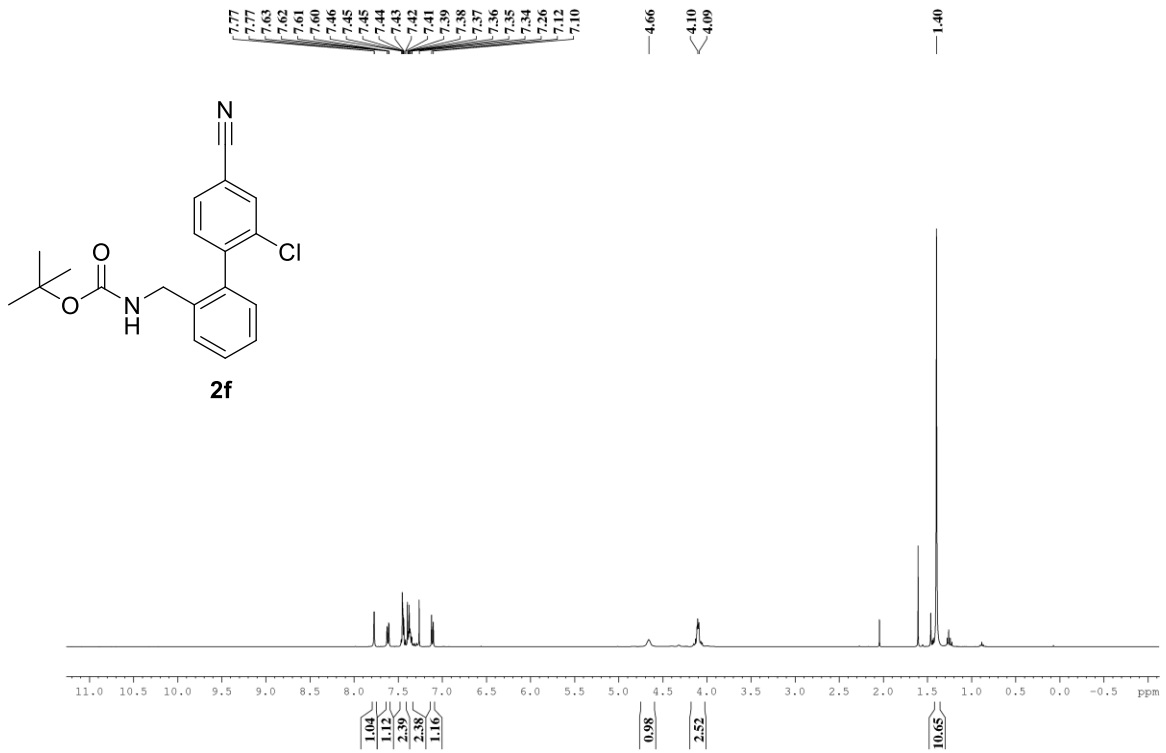


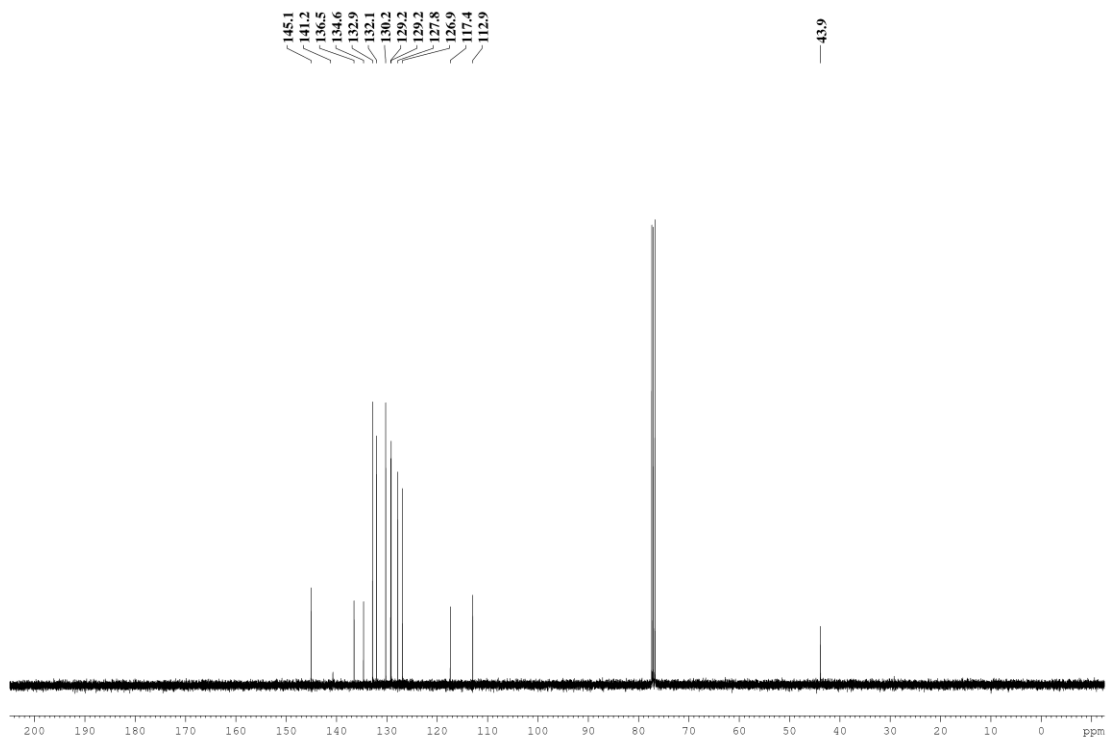
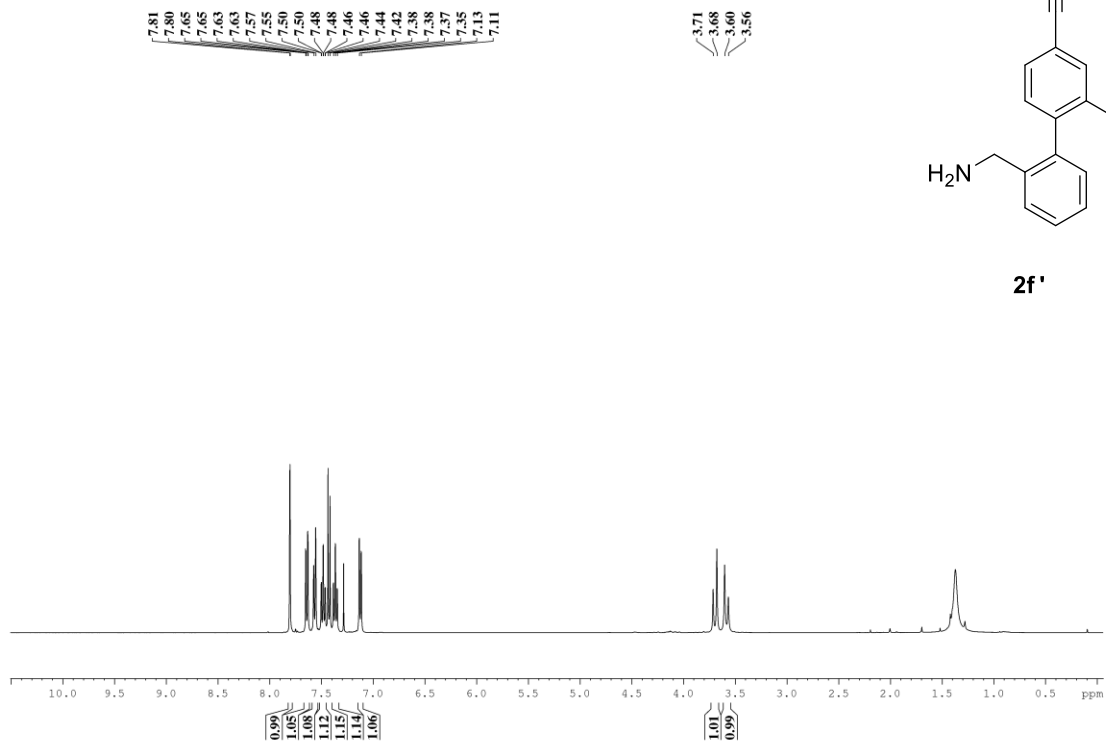
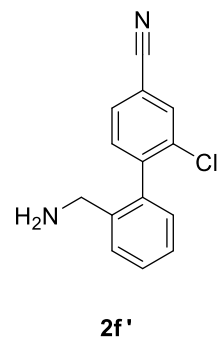


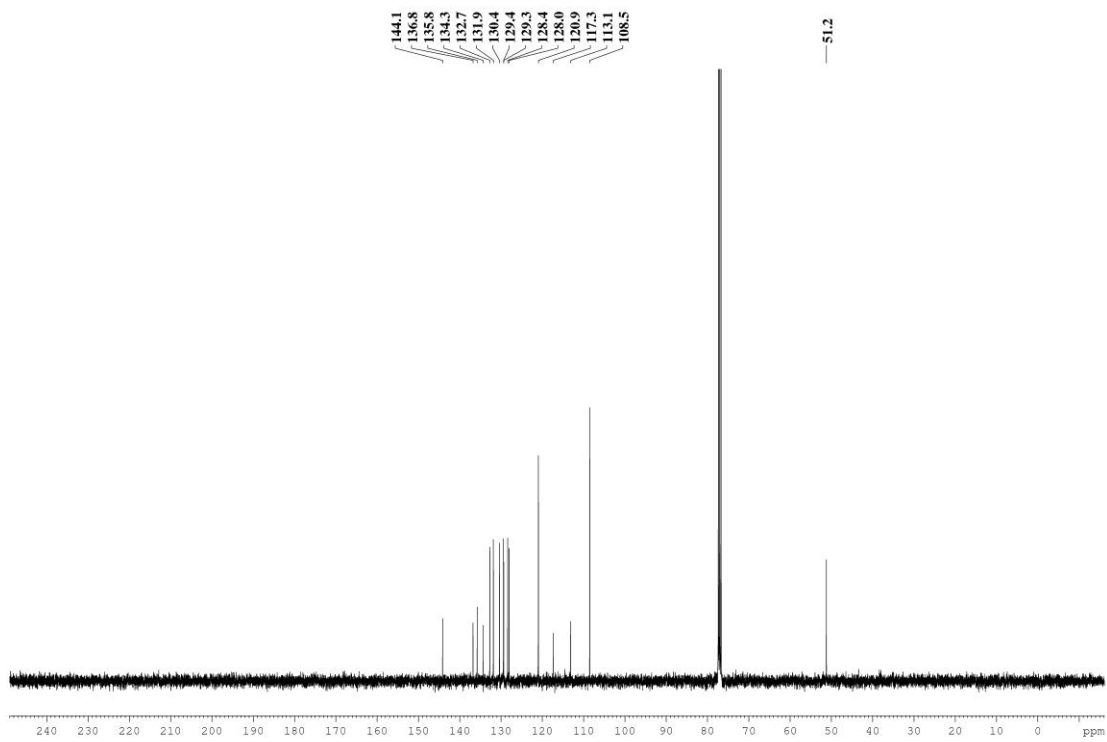
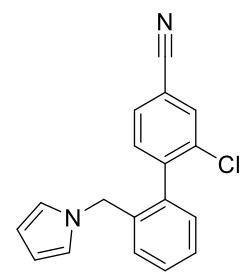
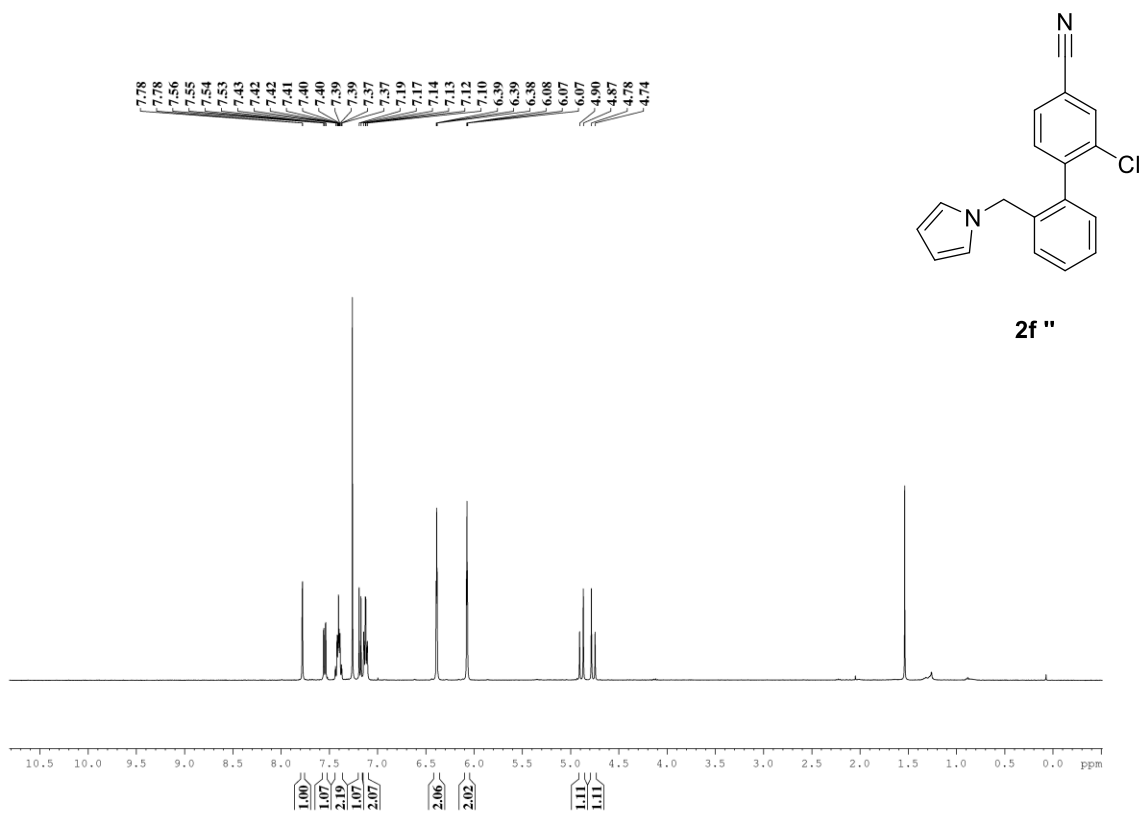


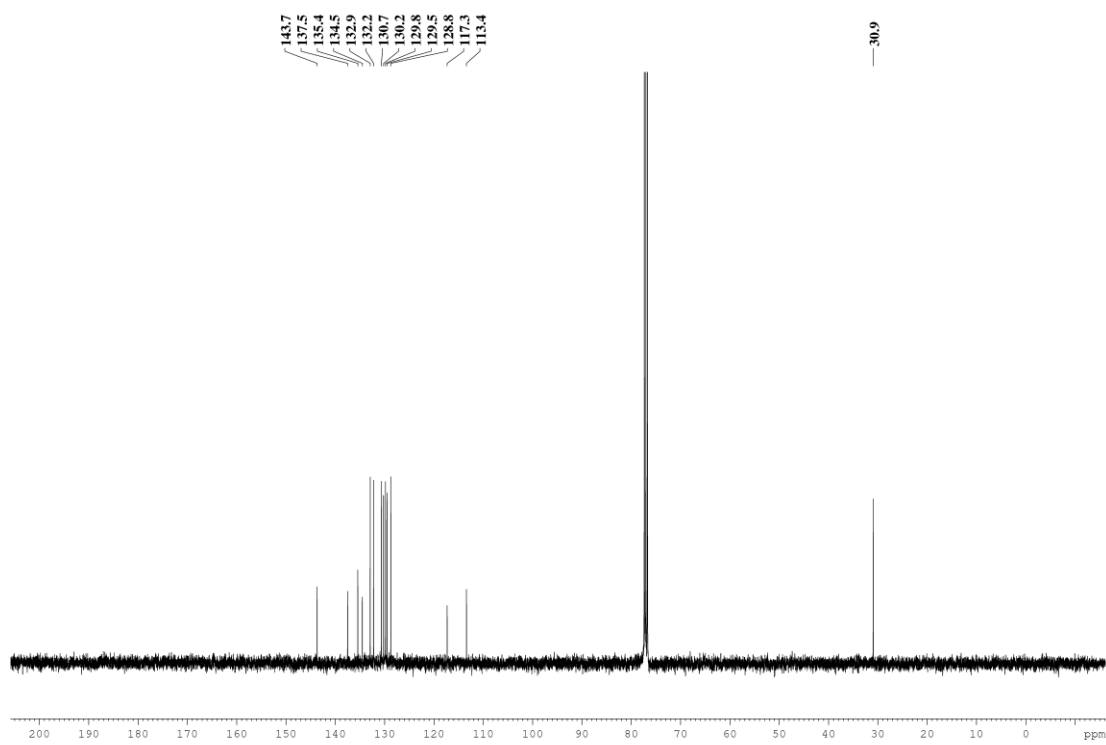
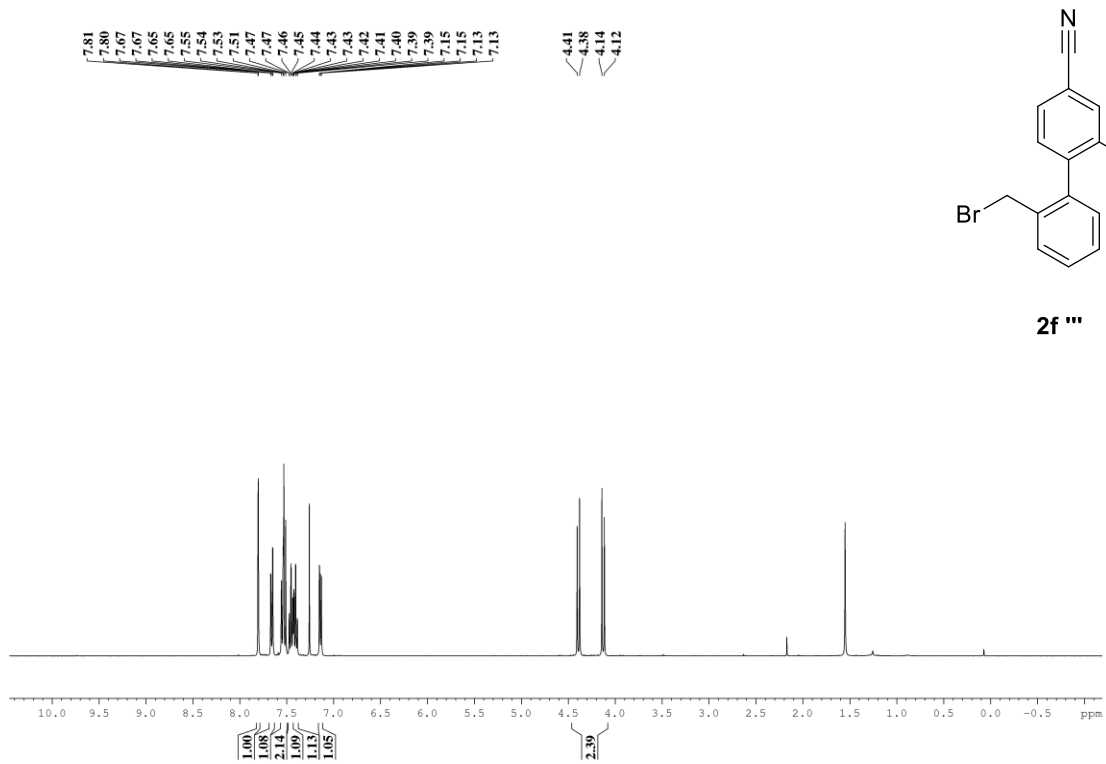
2e

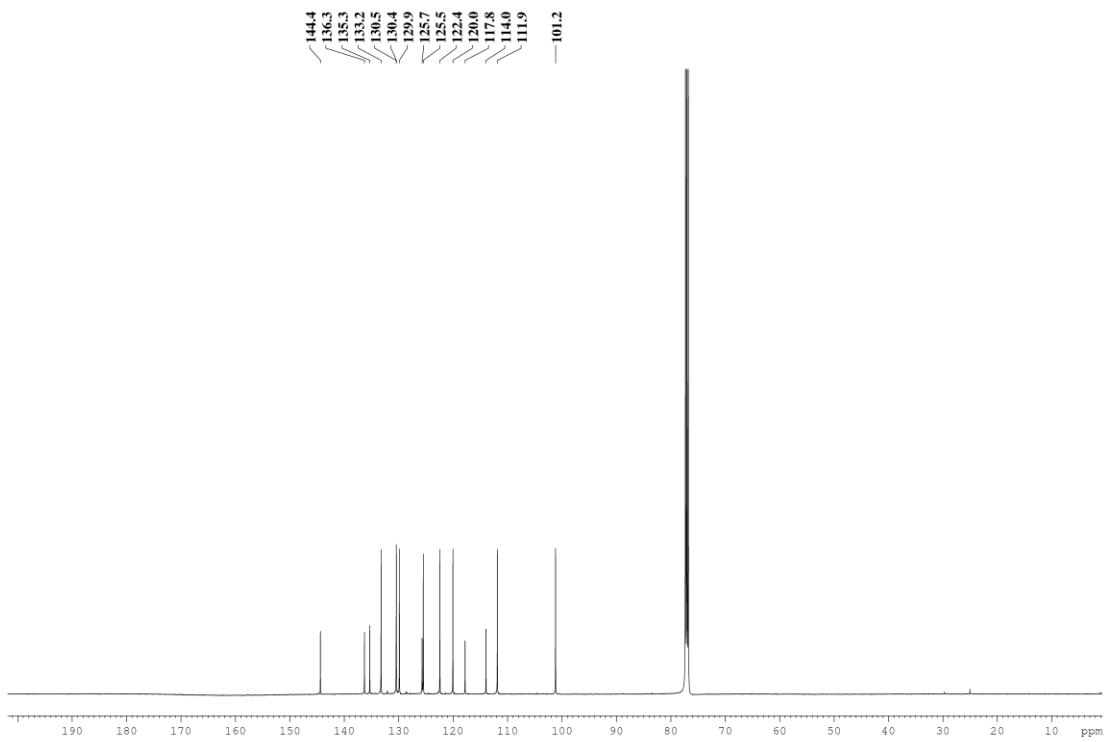
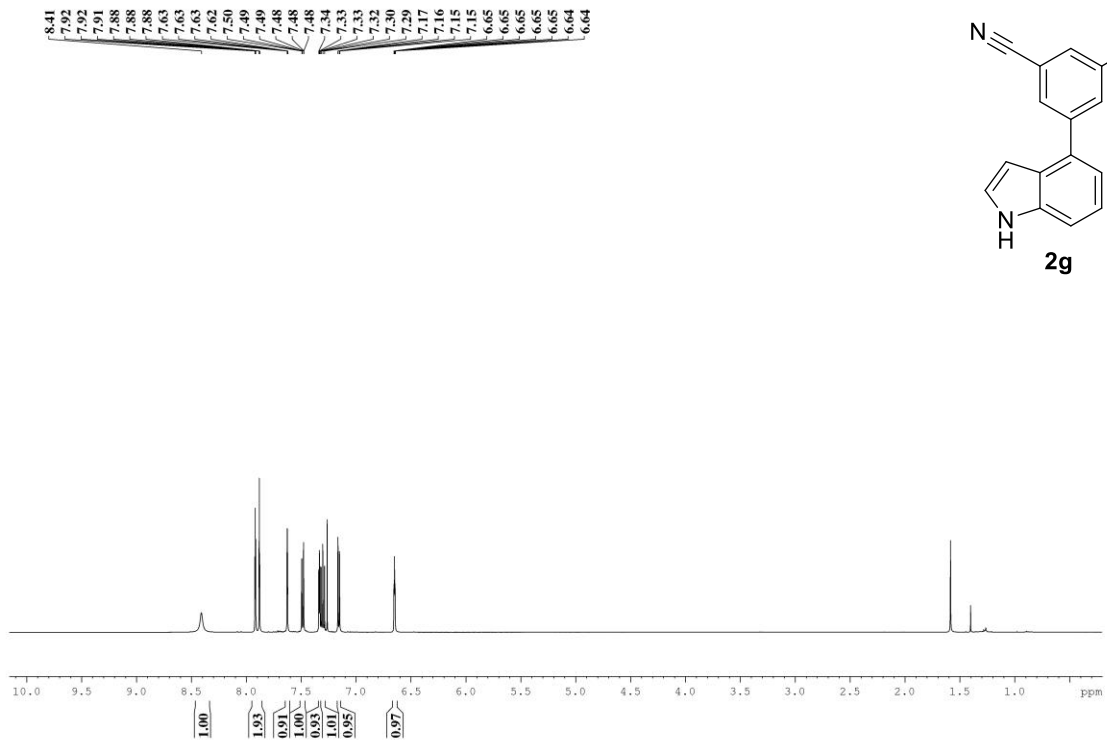


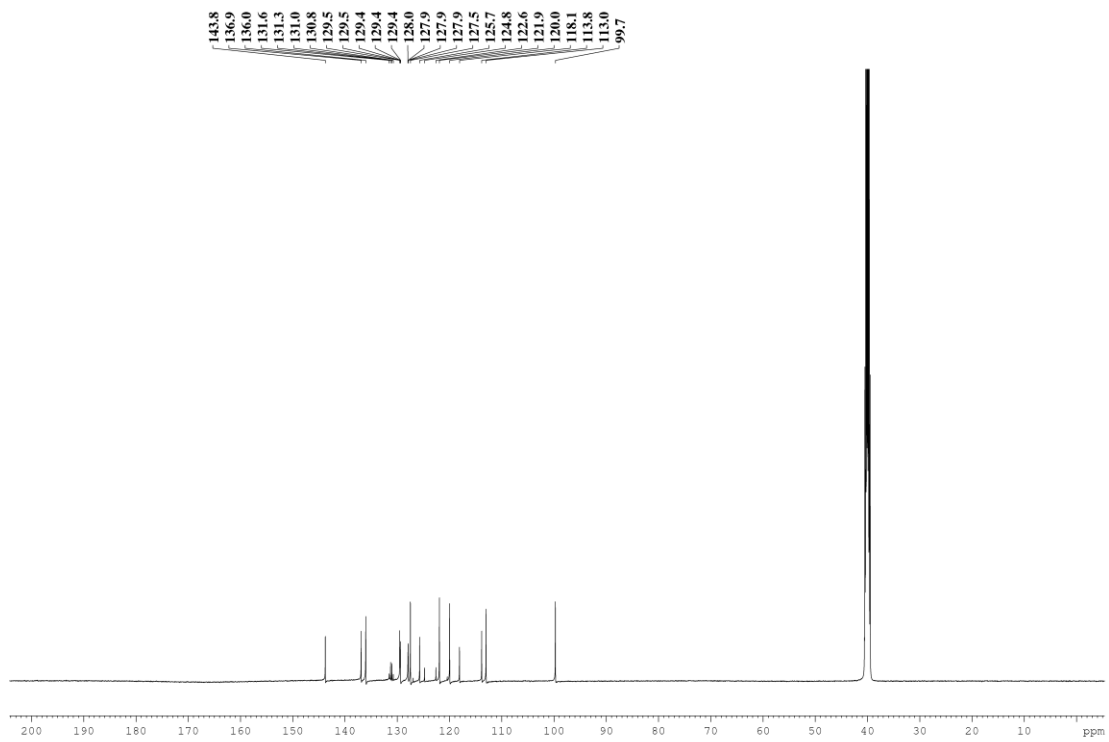
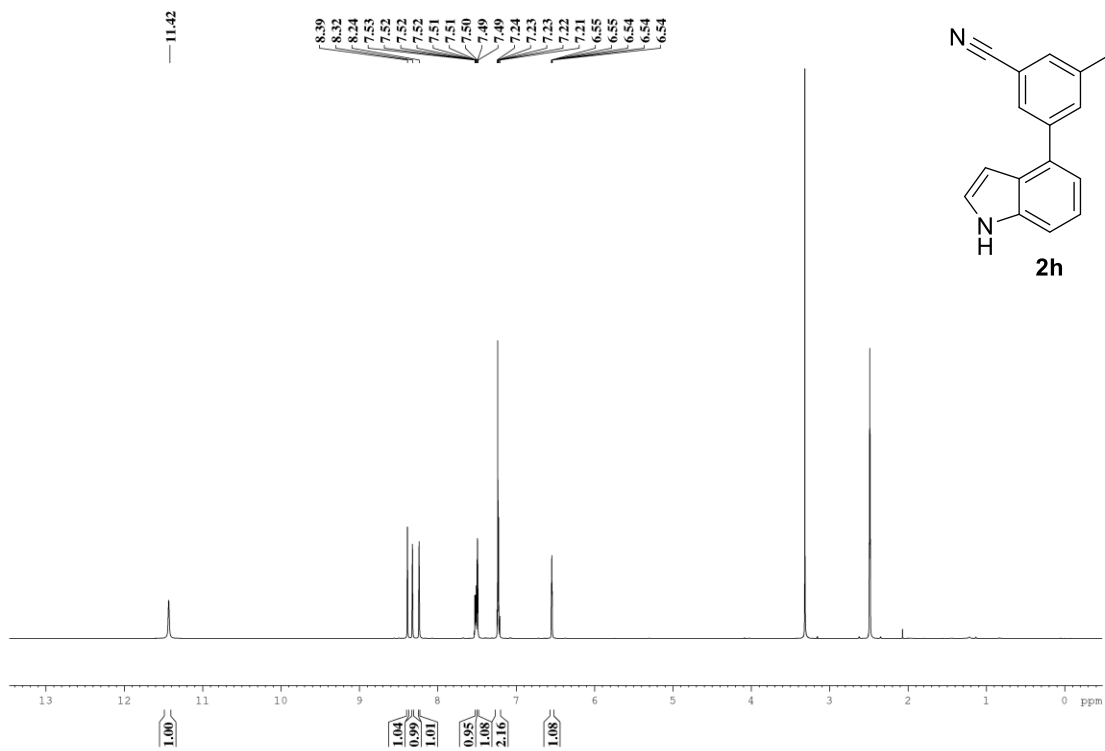


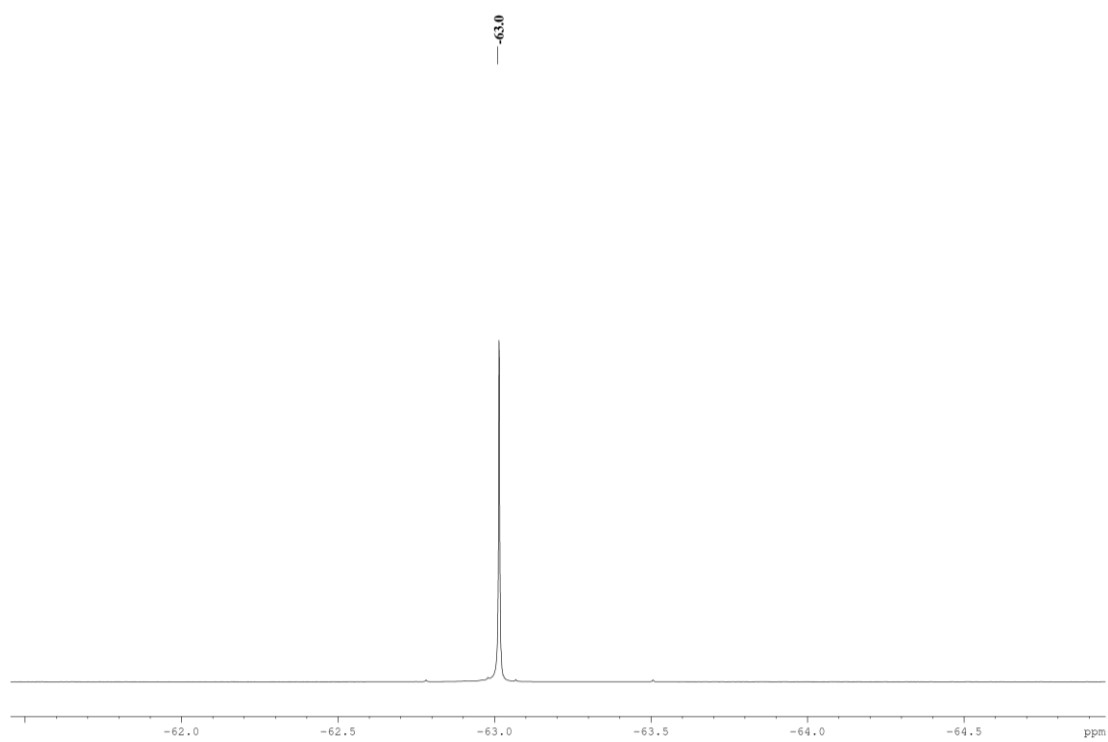


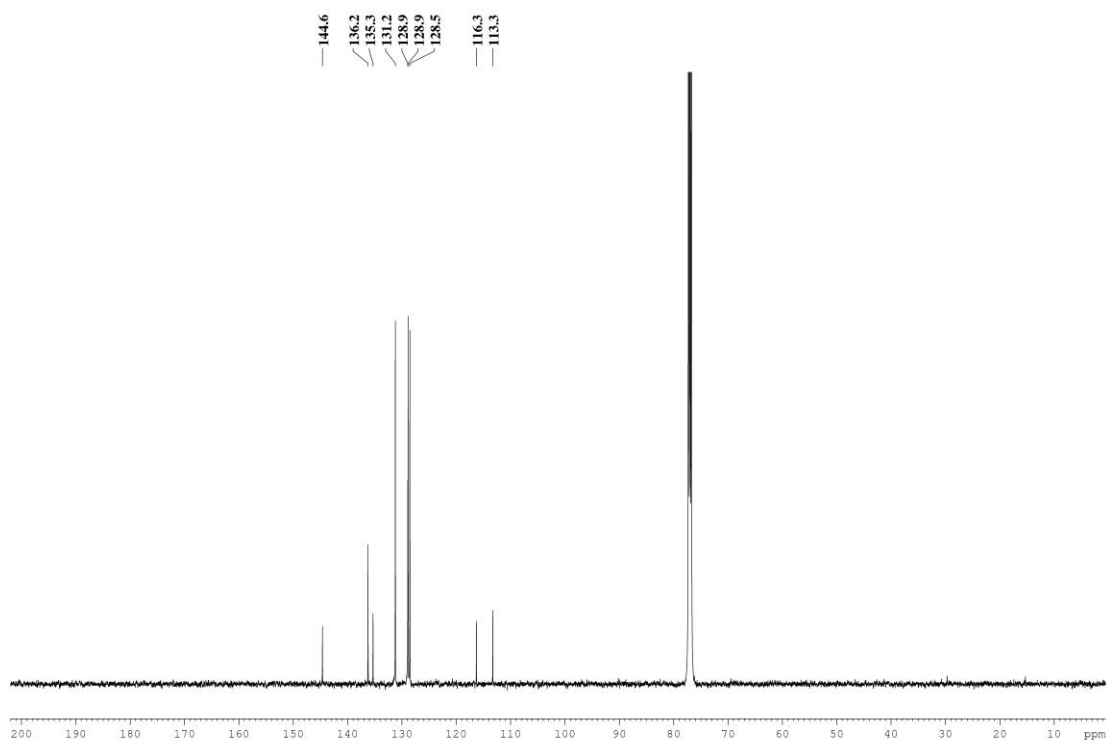
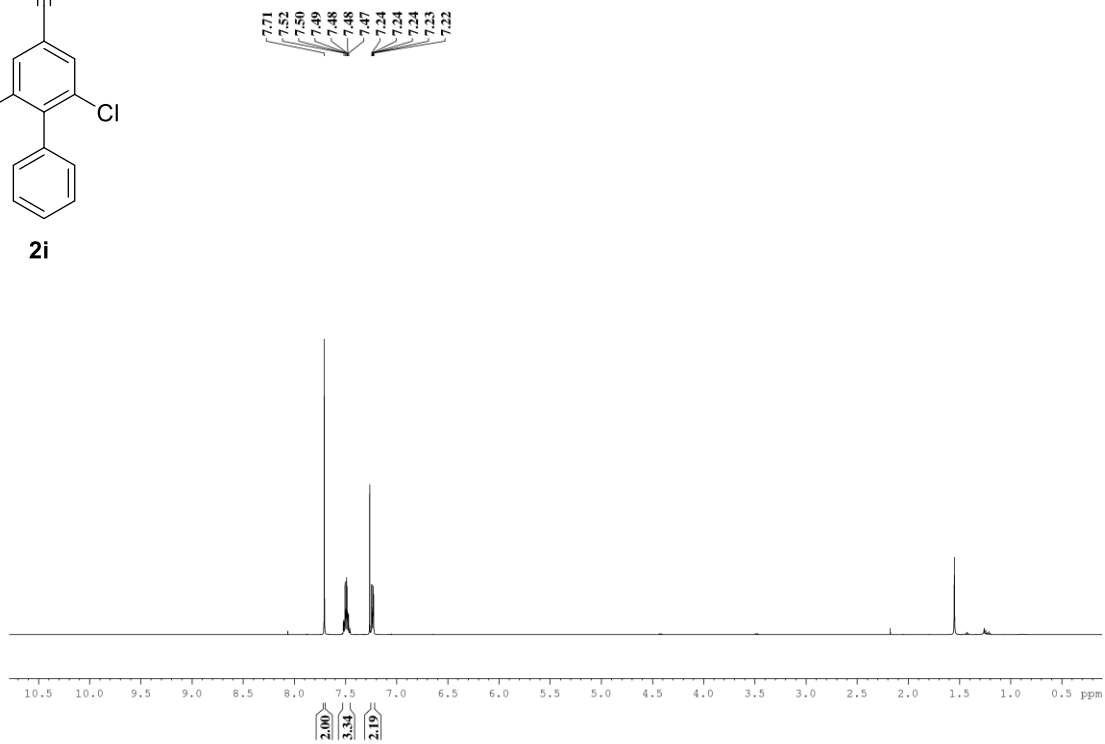
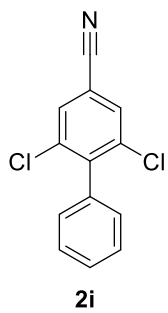


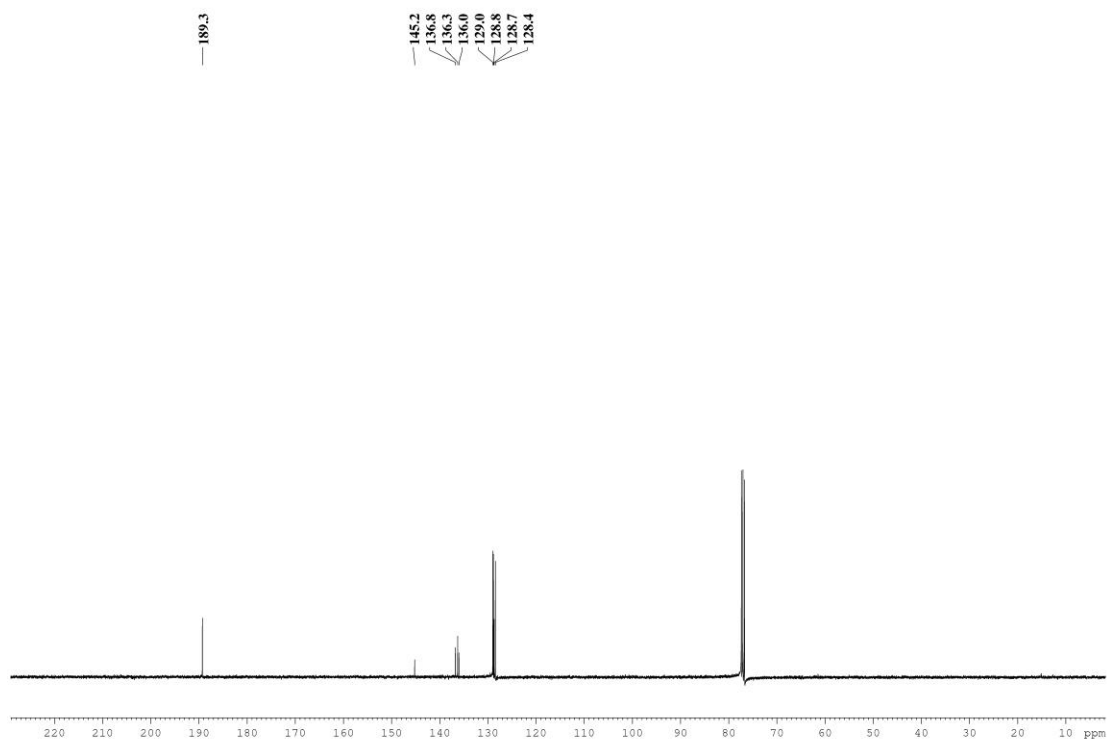
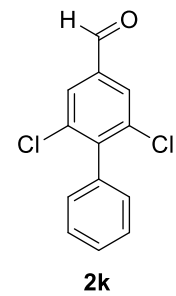
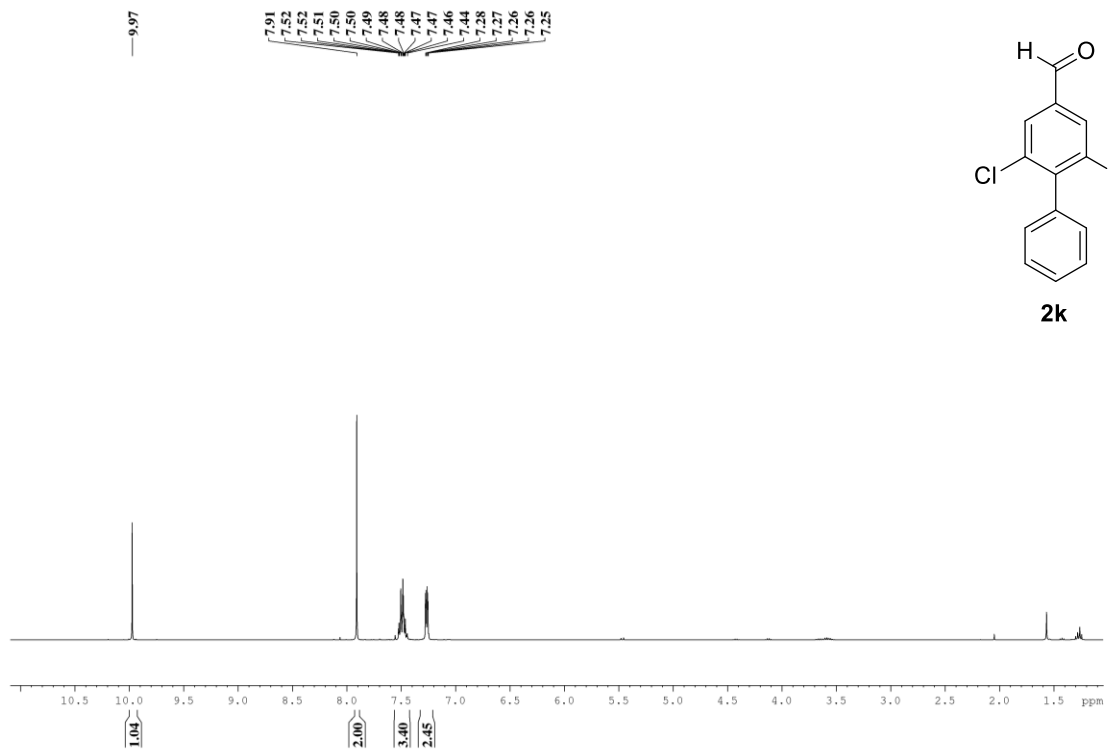


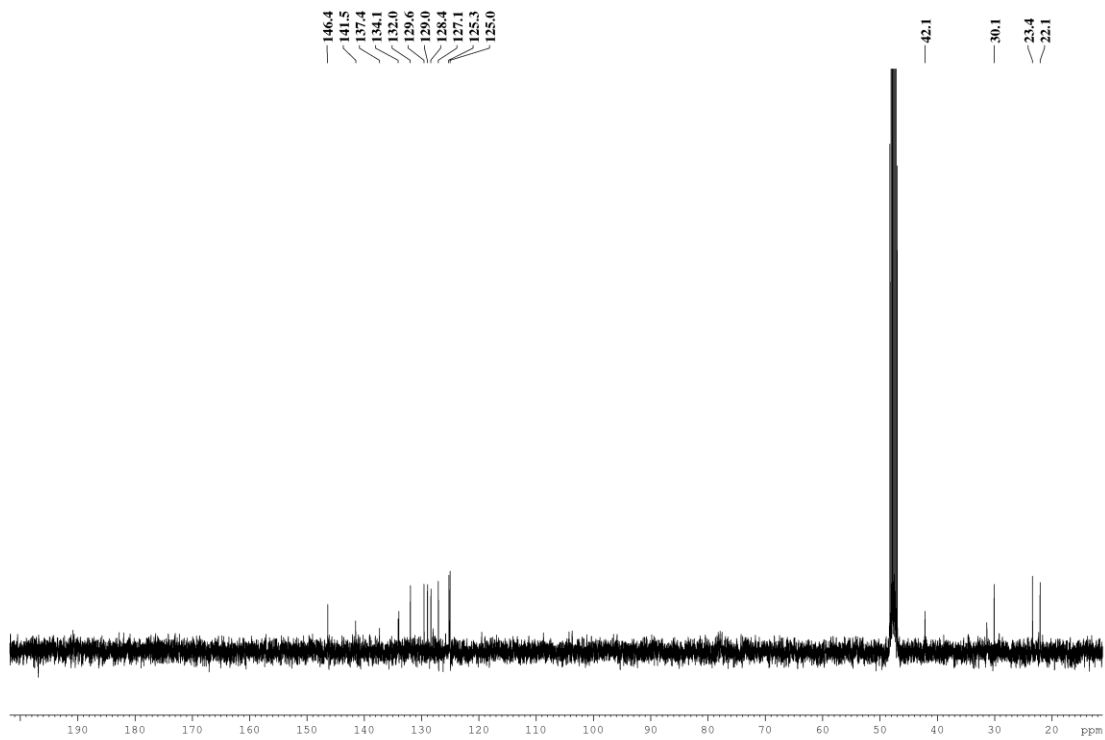
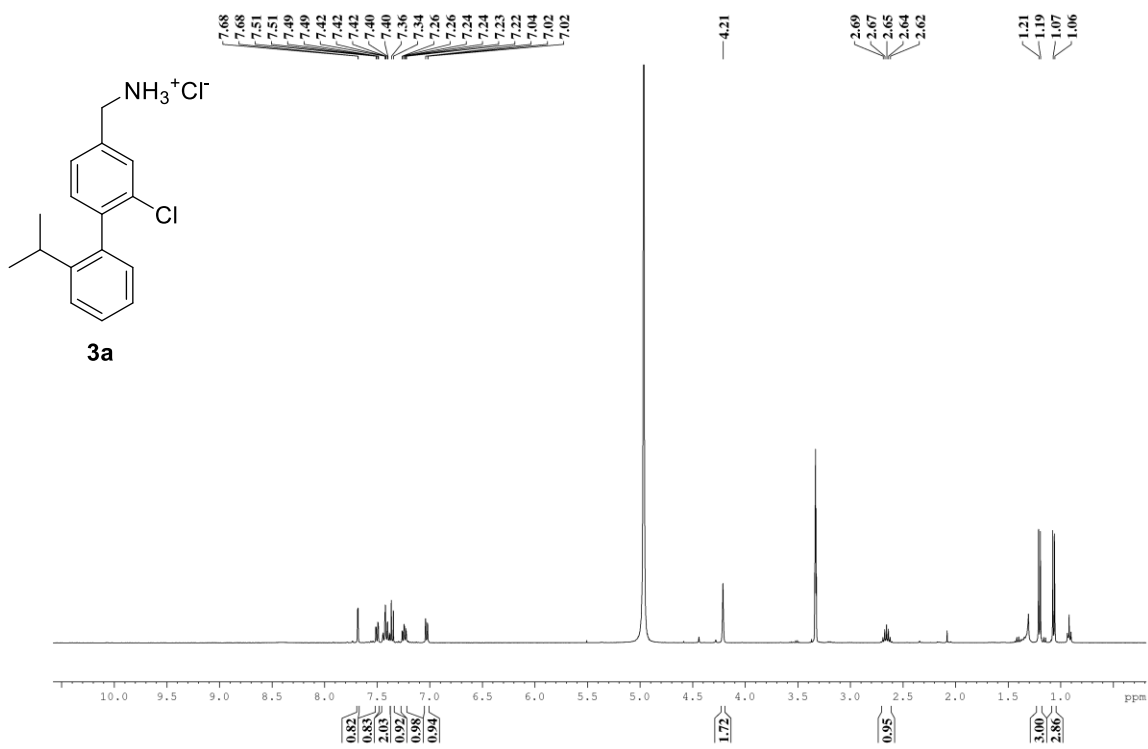


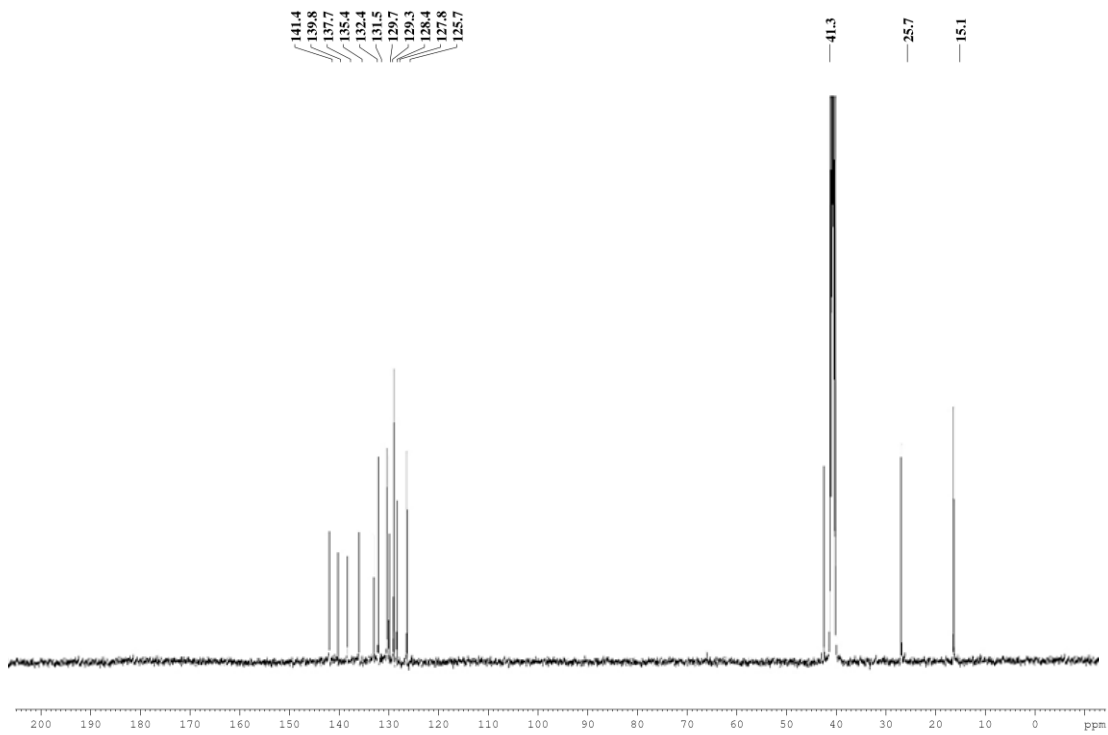
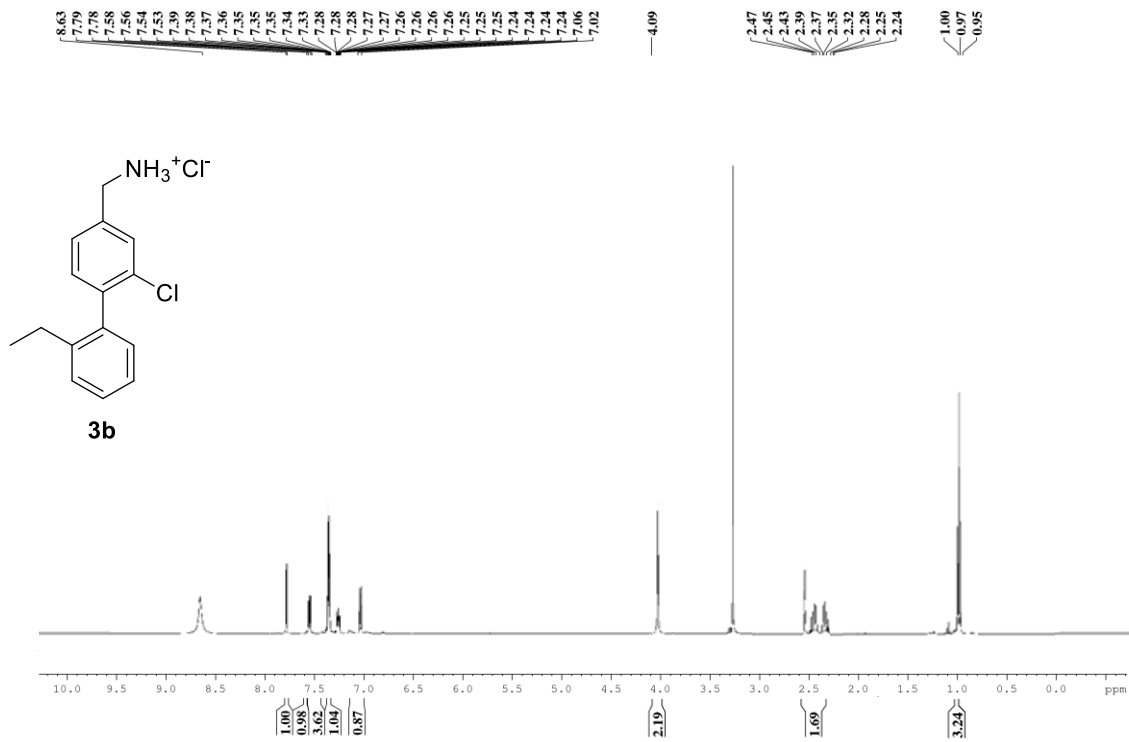


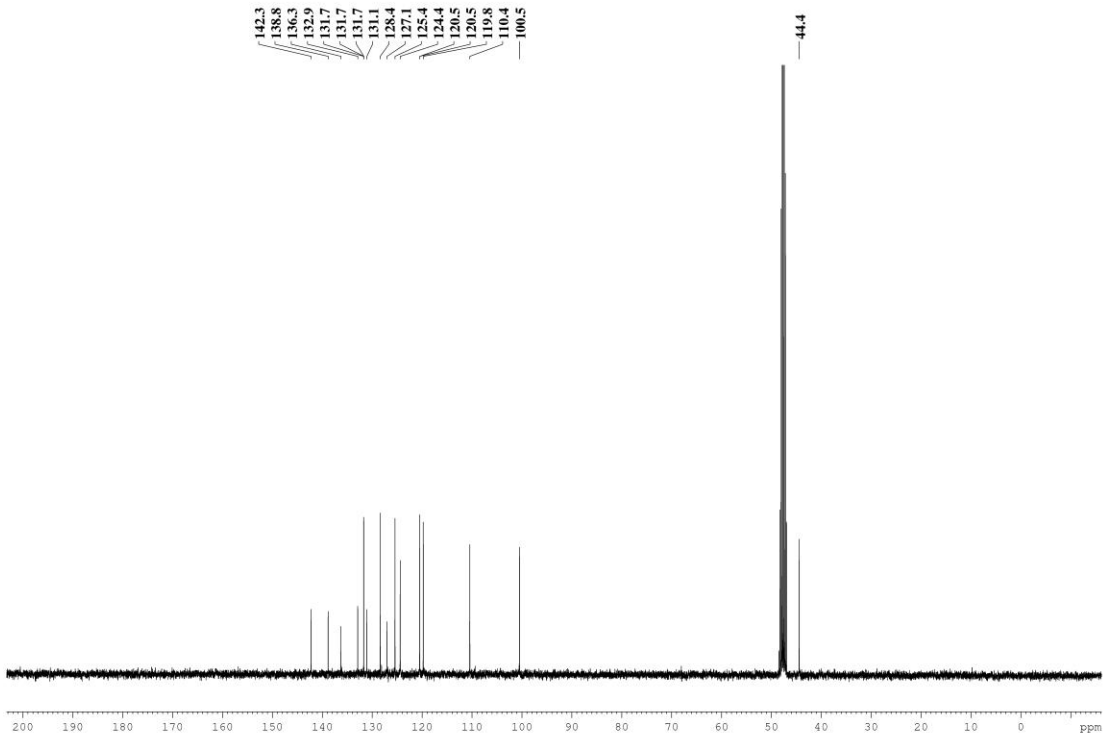
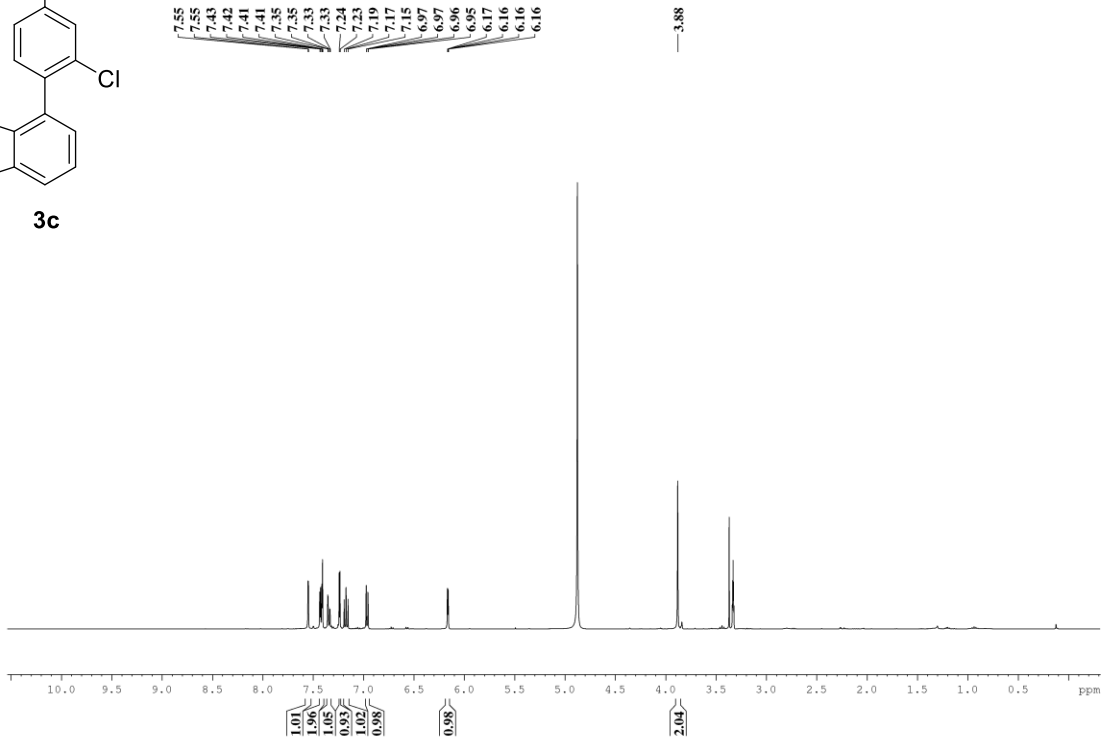
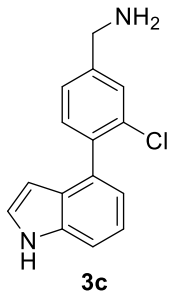


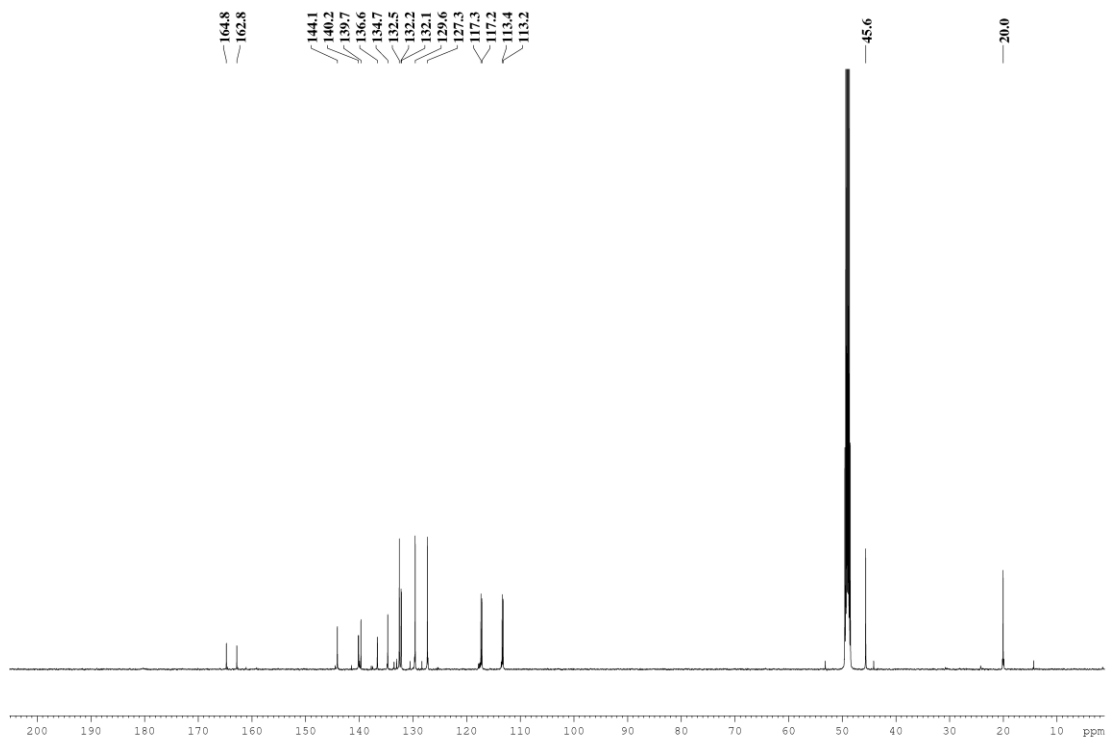
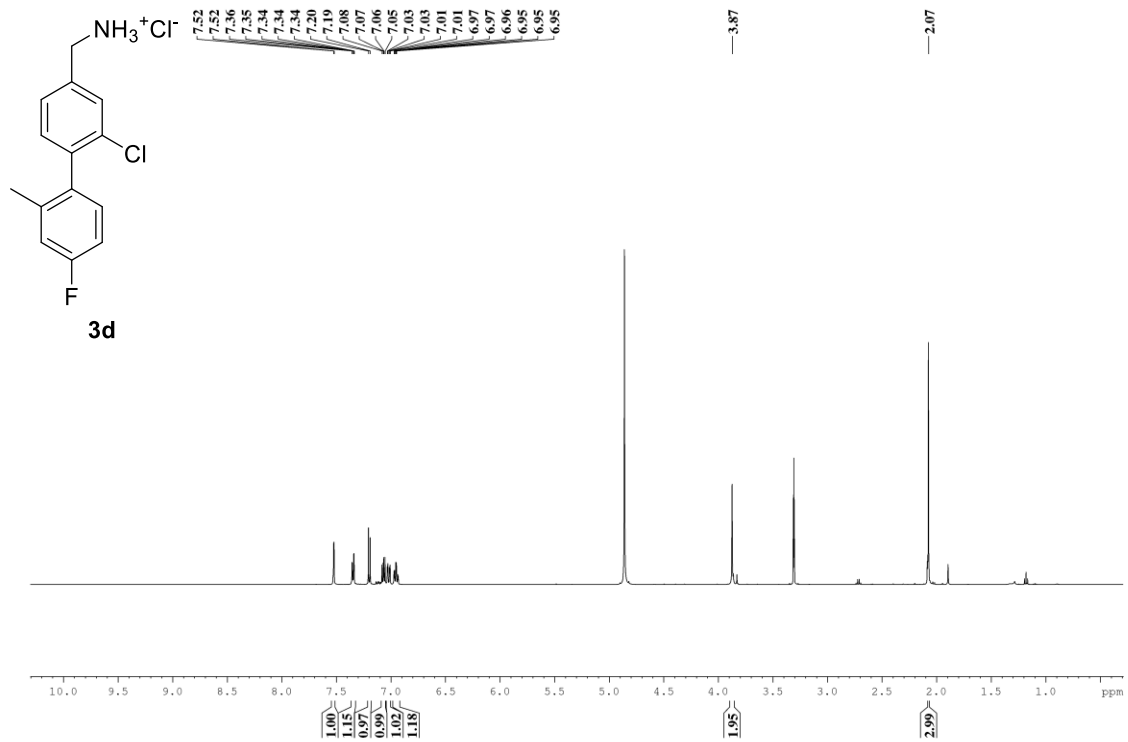


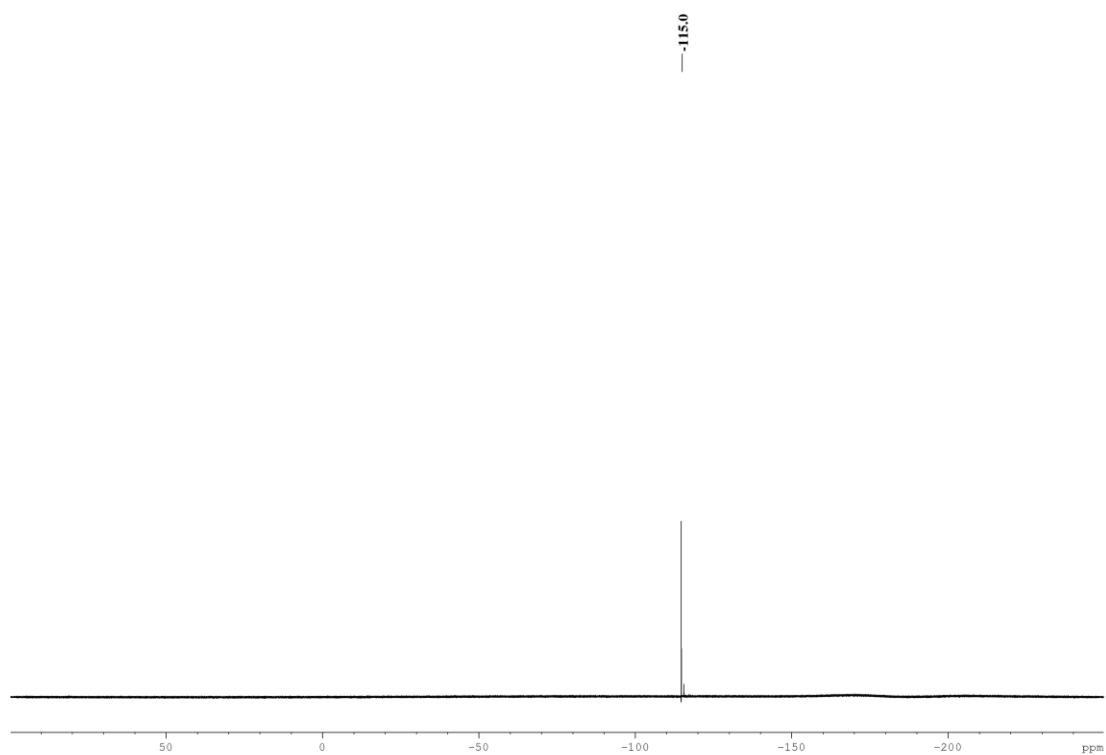


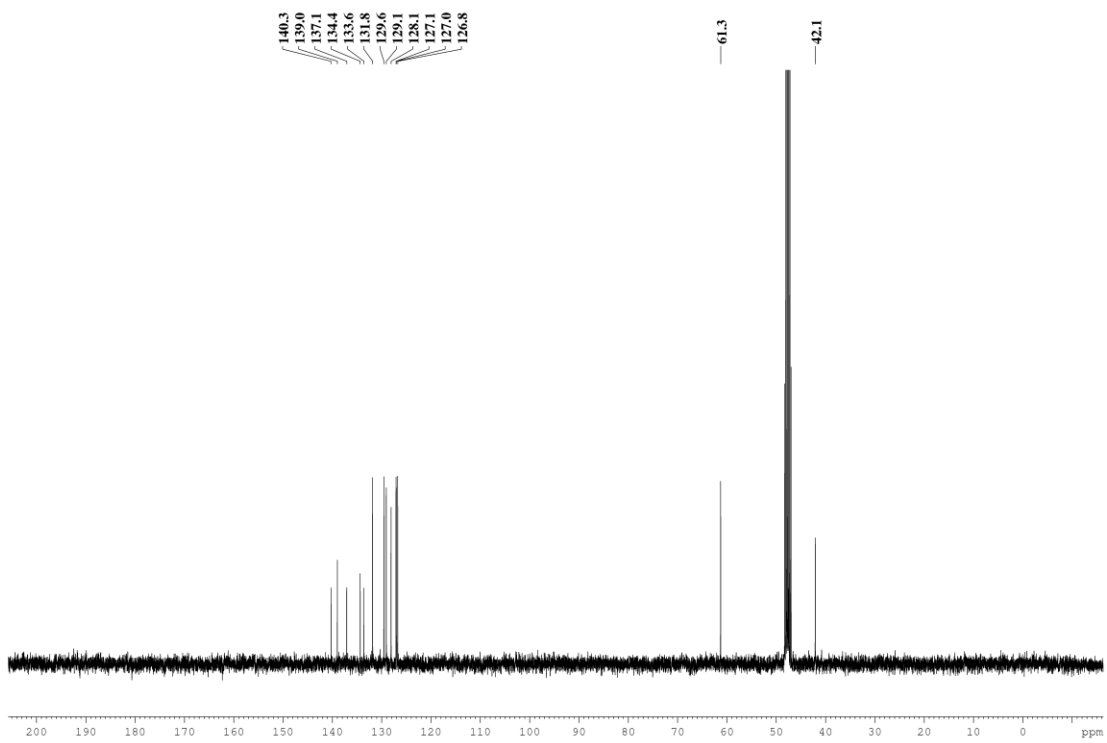
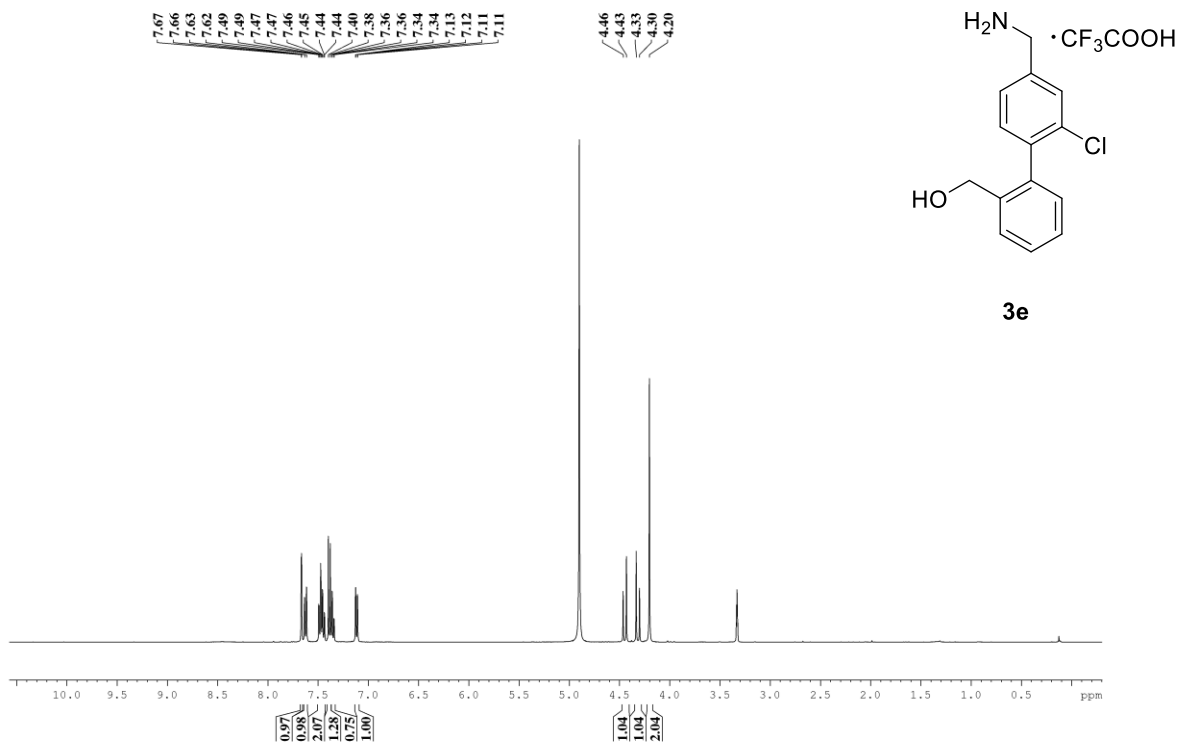


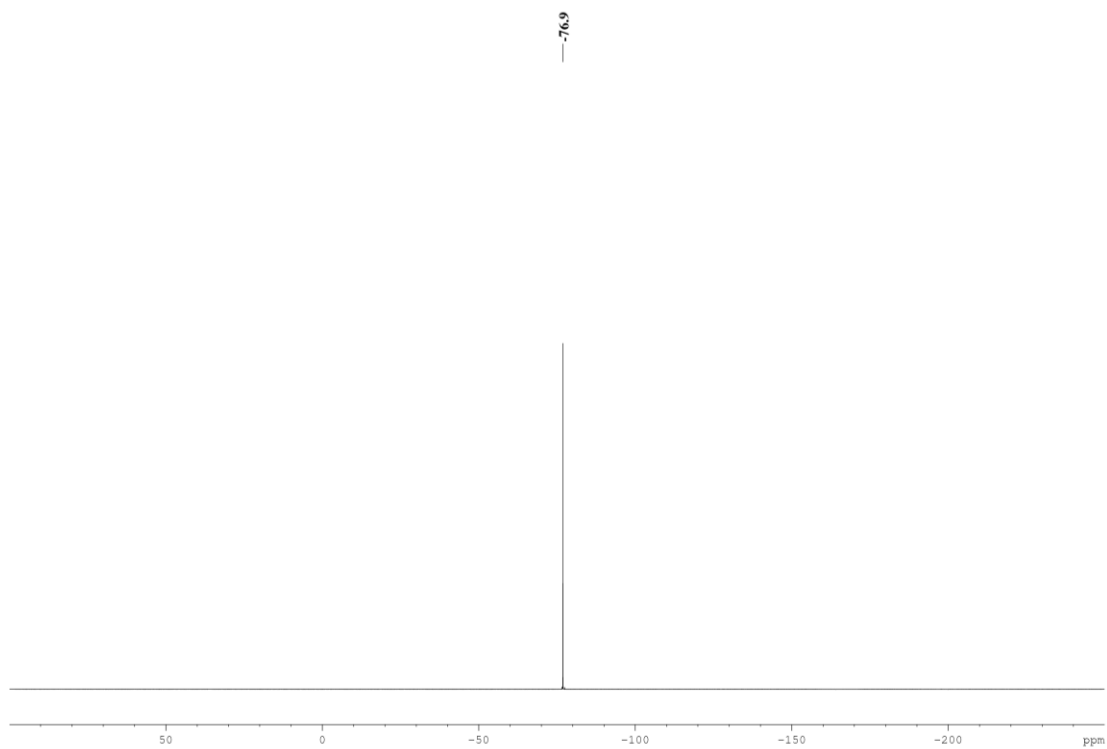


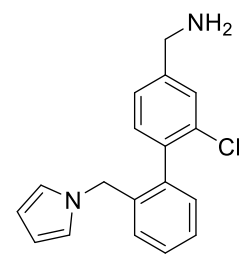




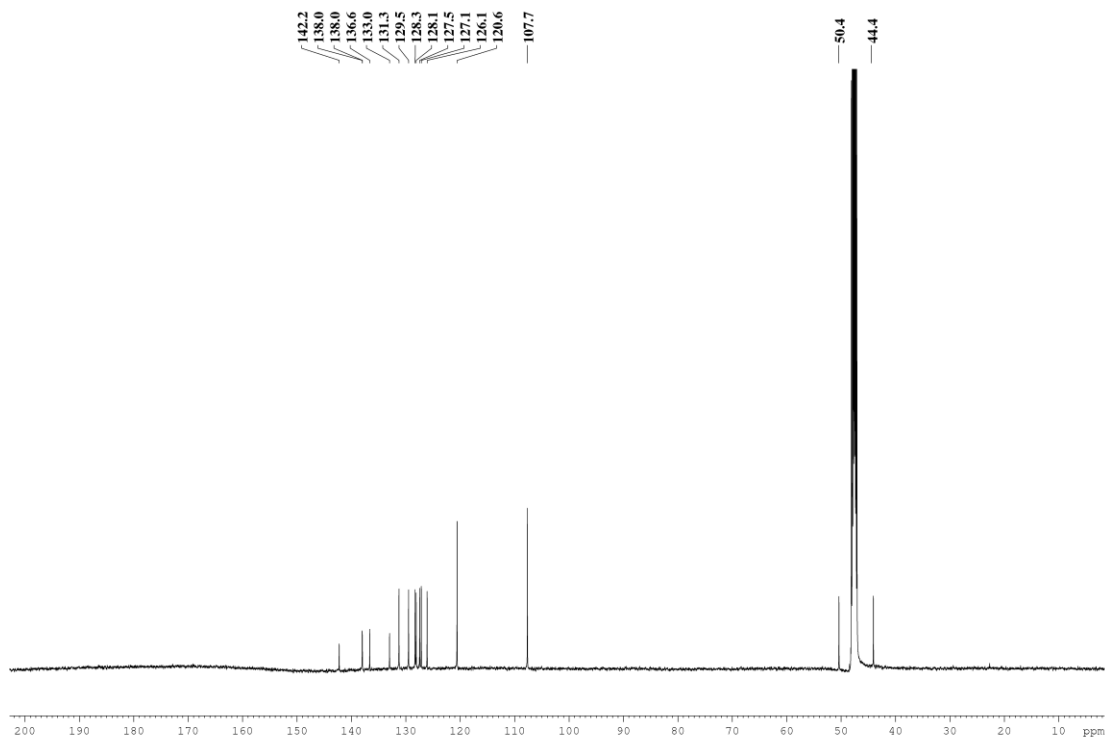
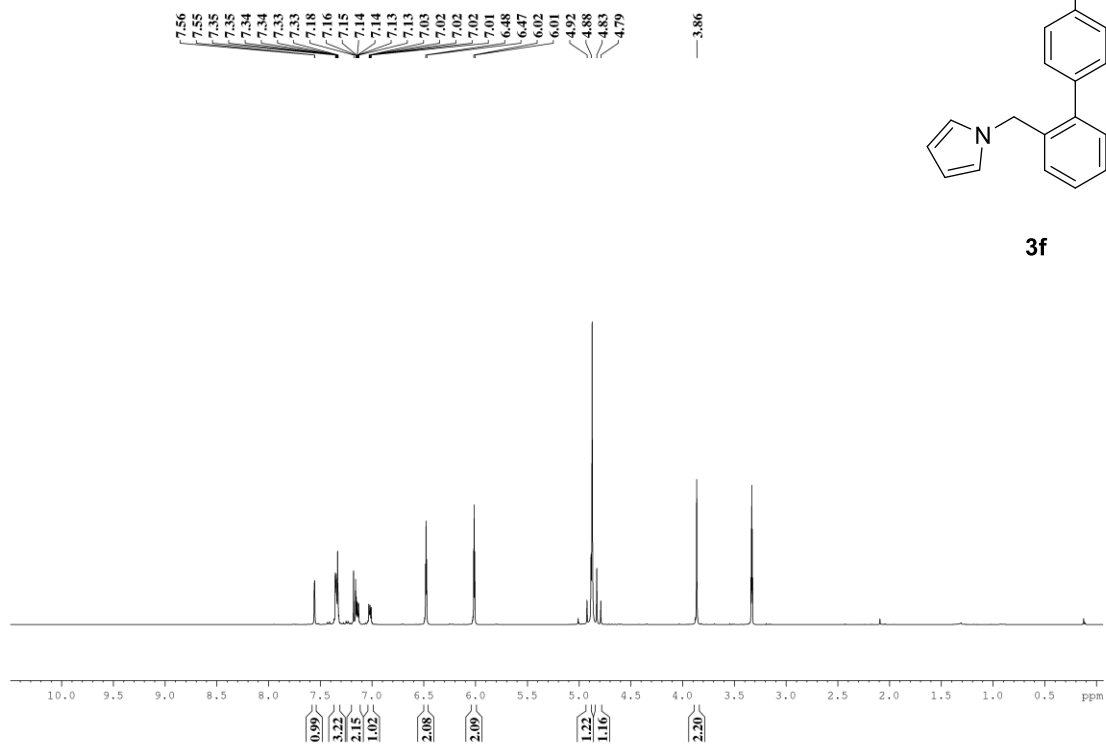


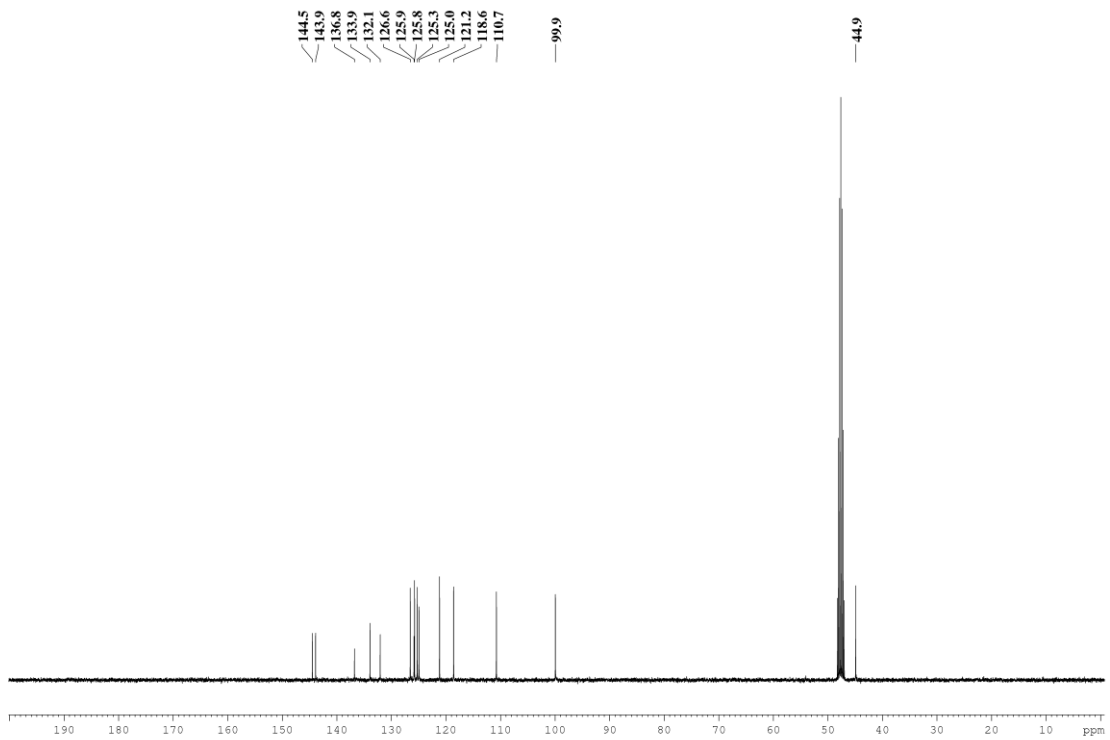
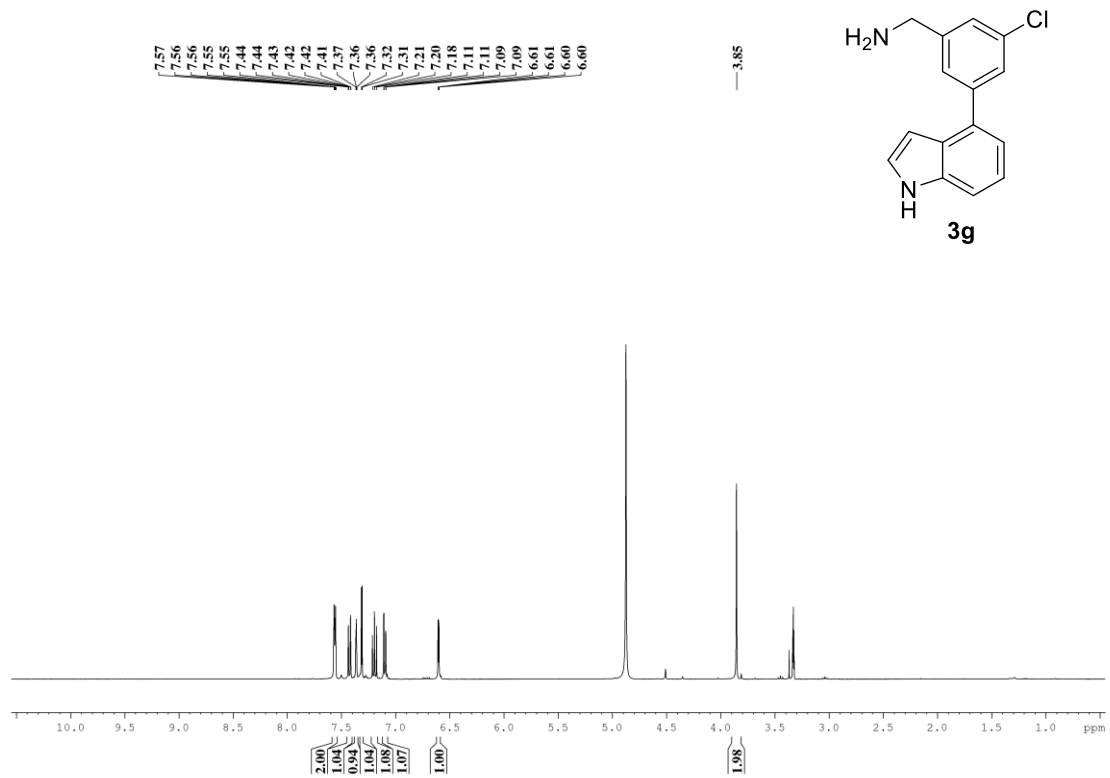


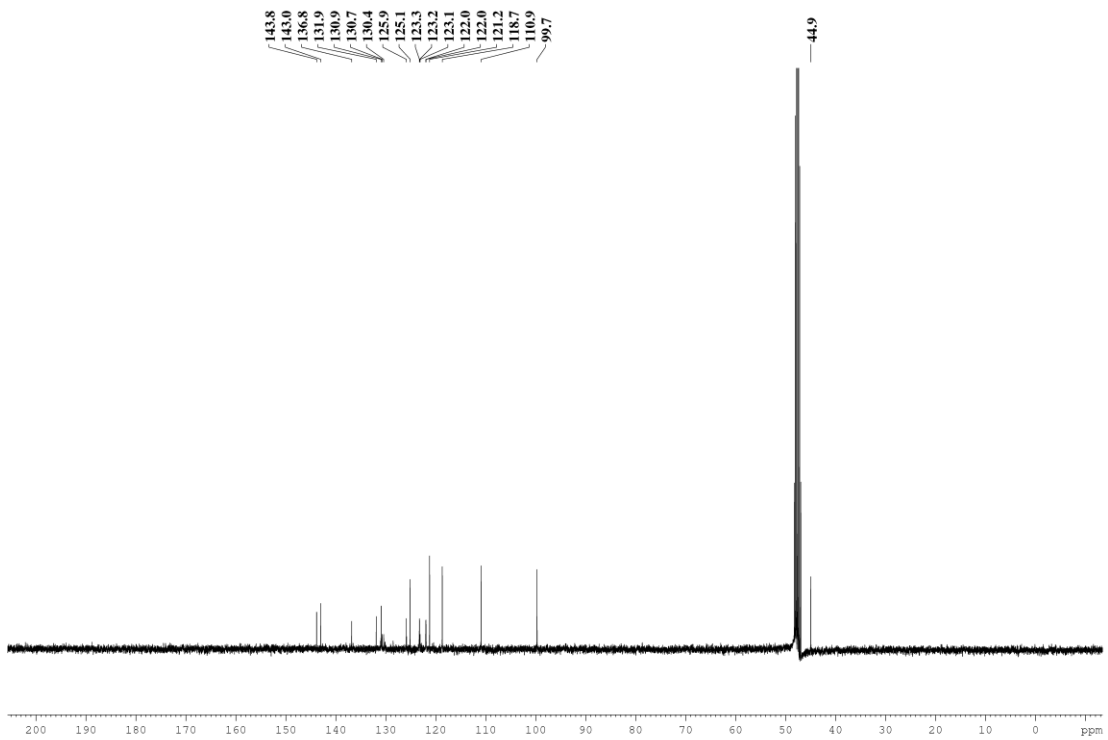
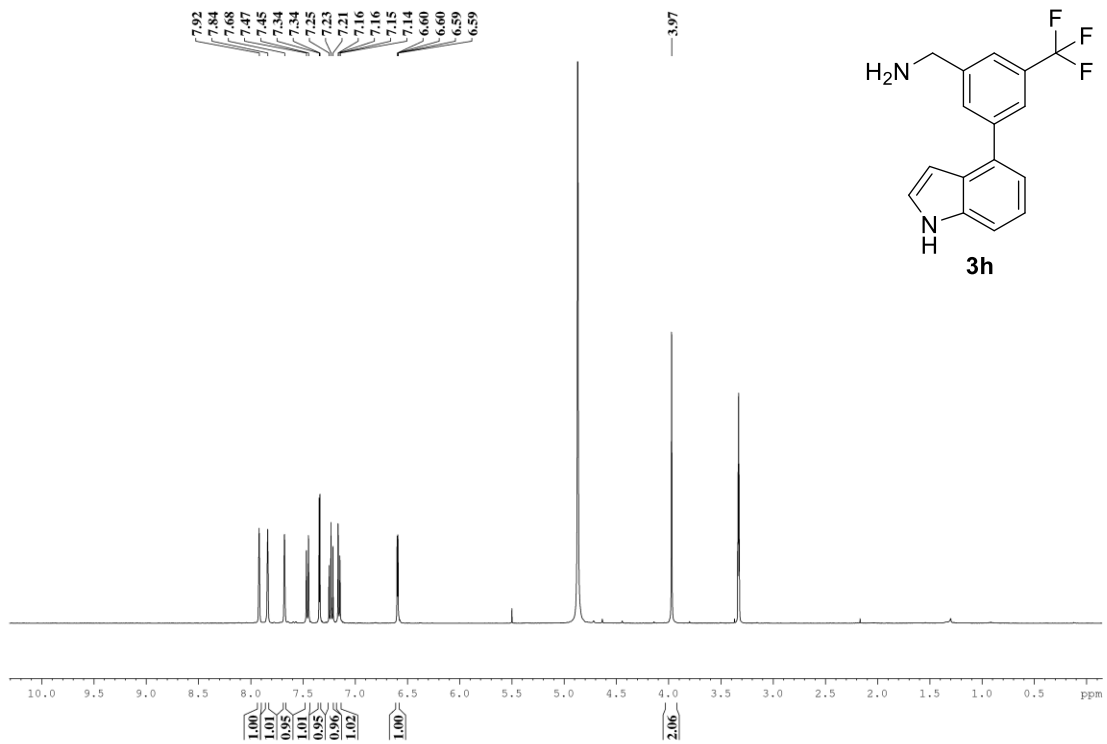


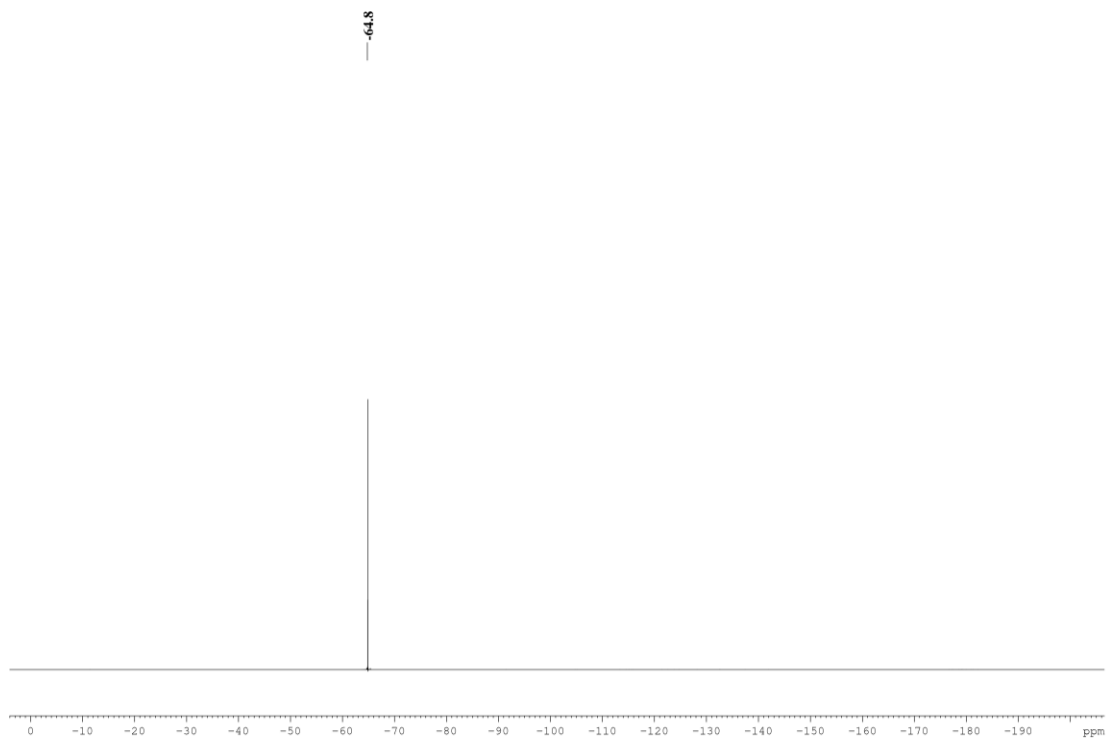


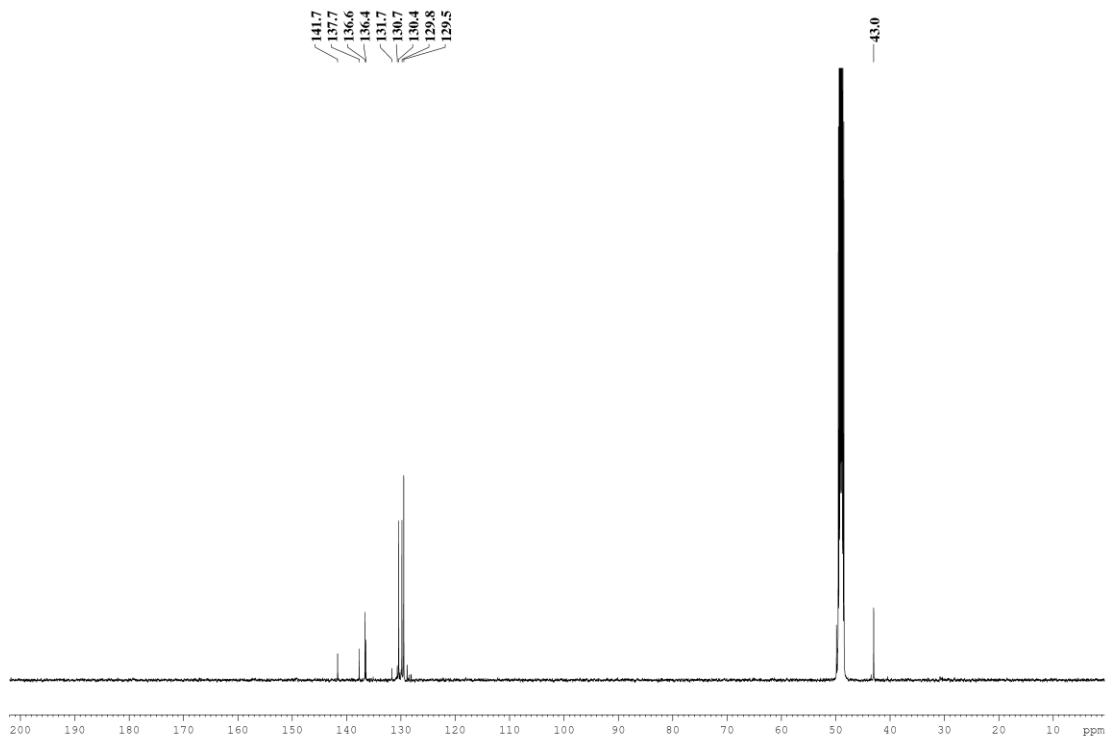
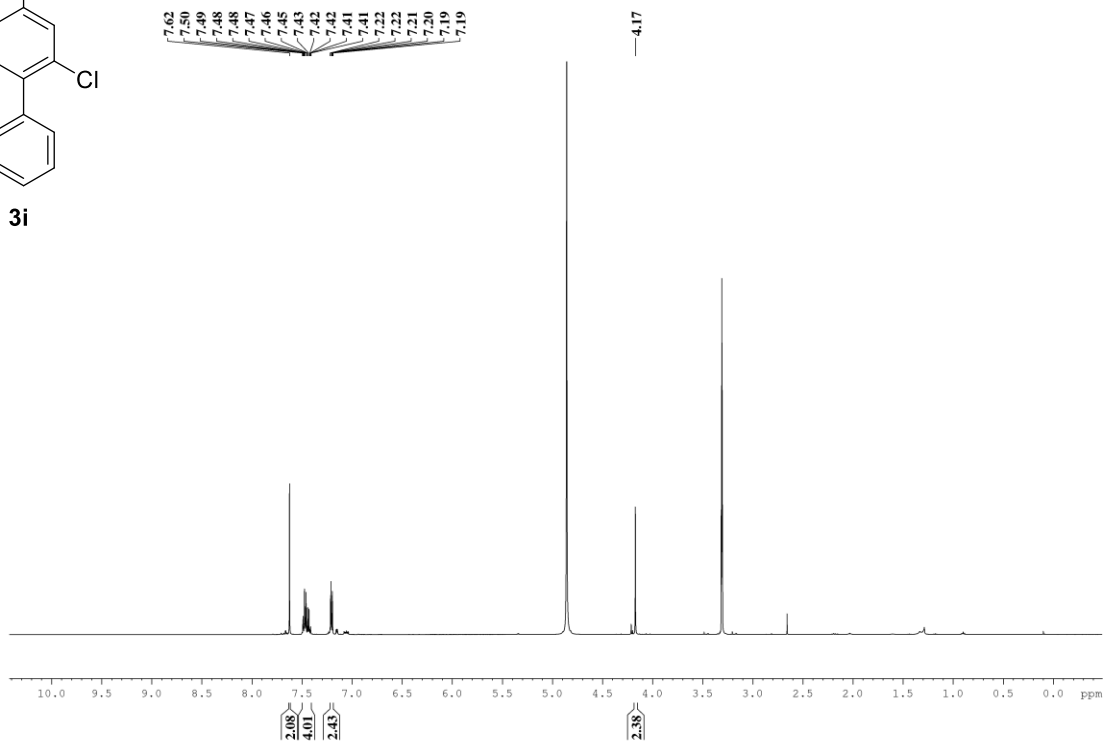
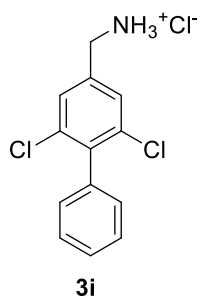
3f

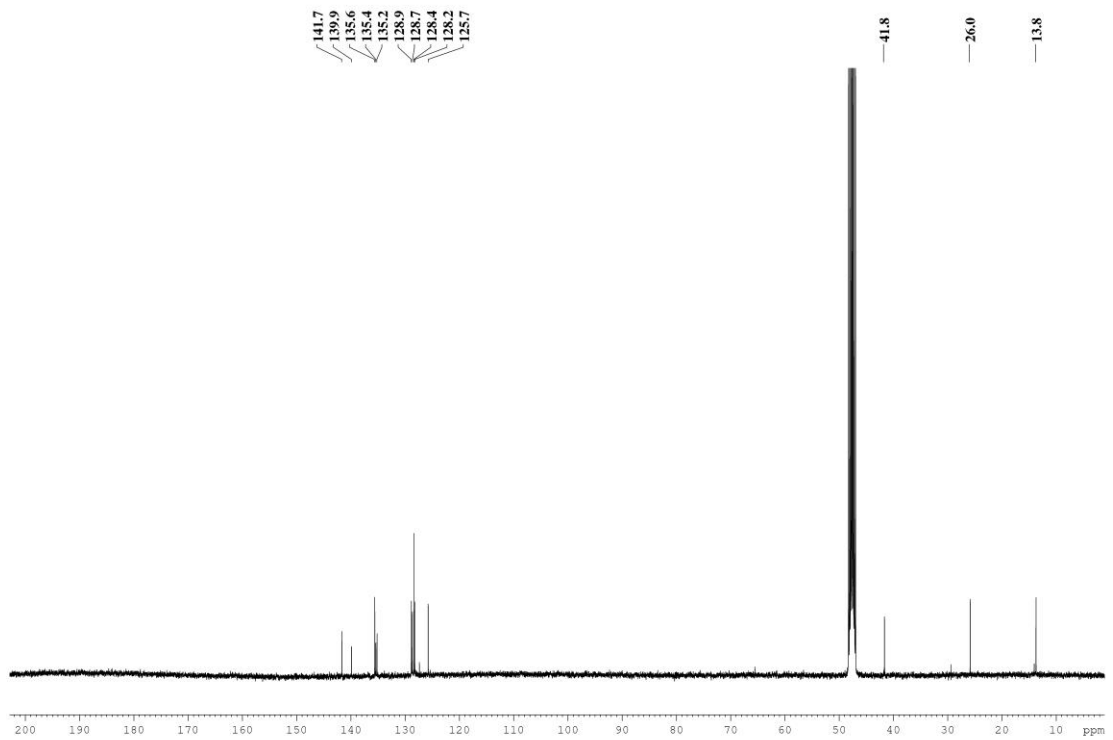
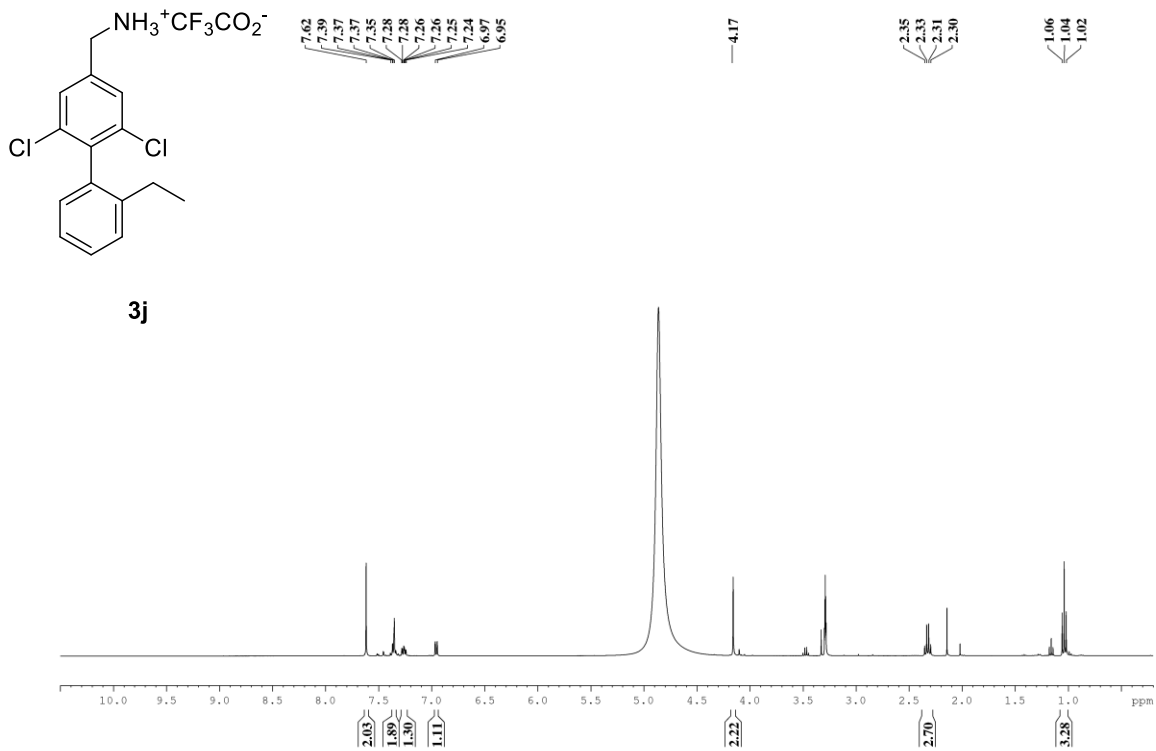


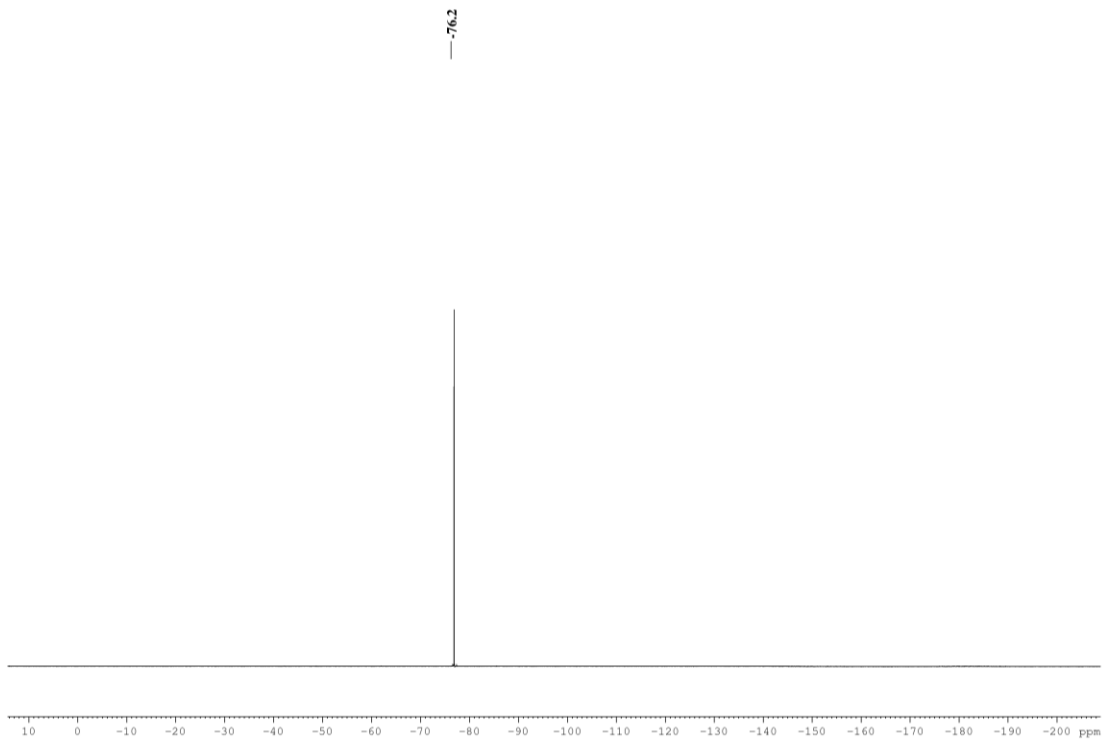


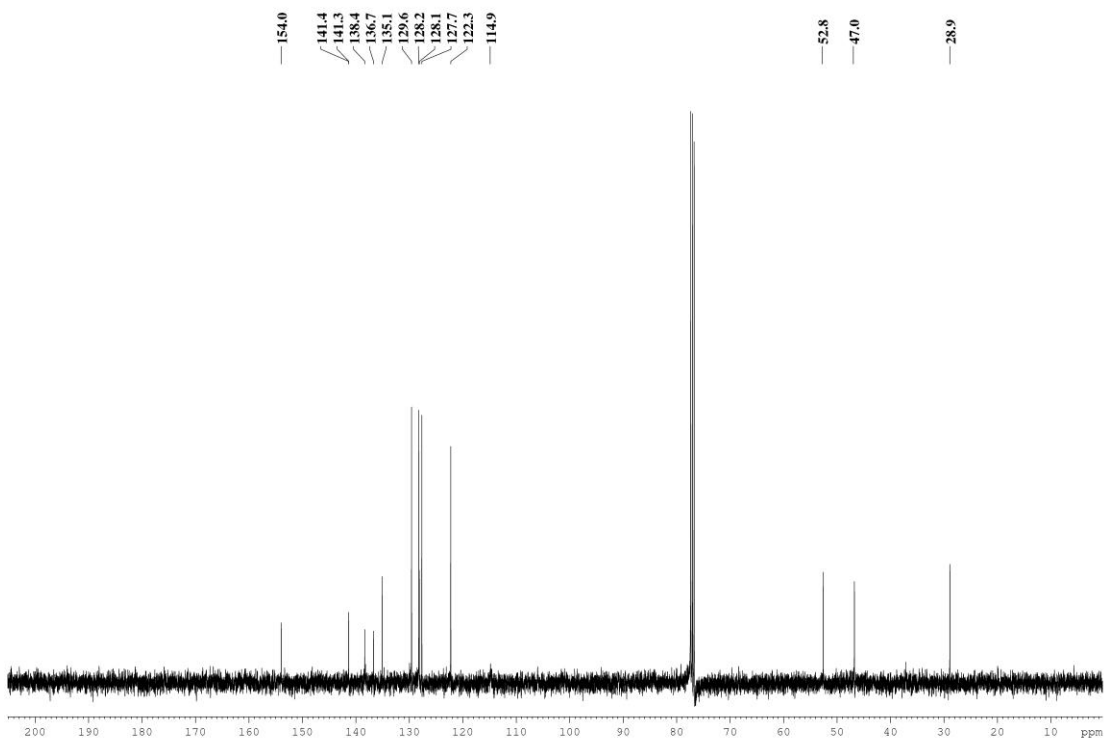
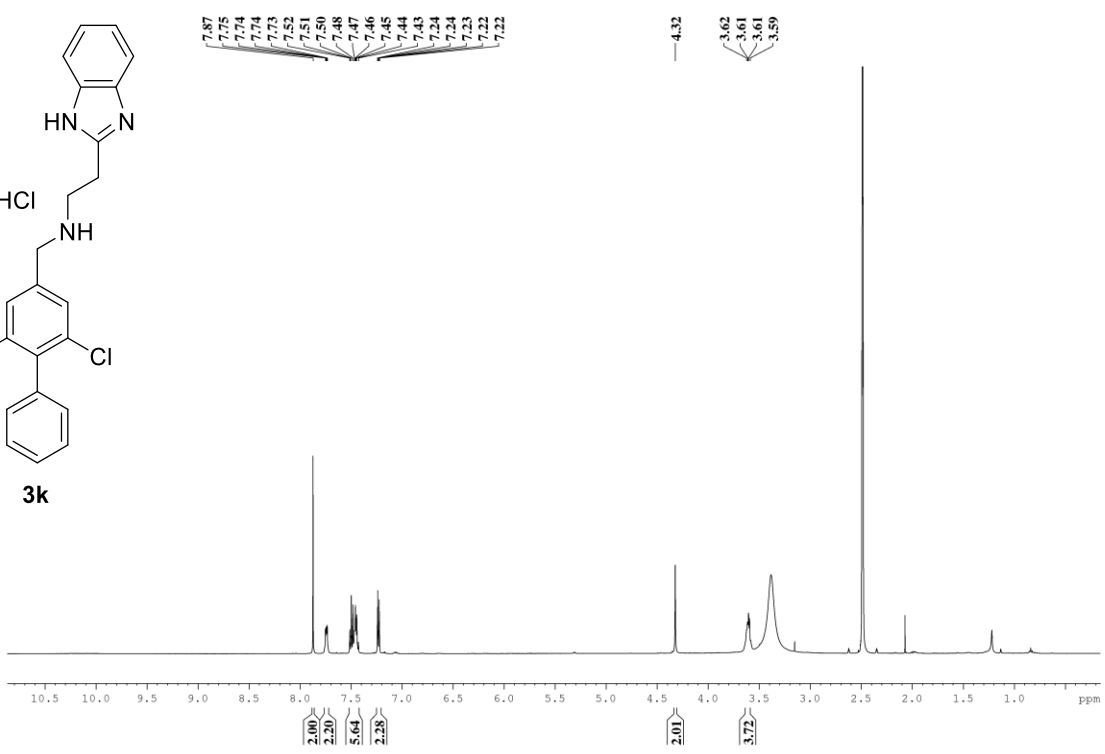
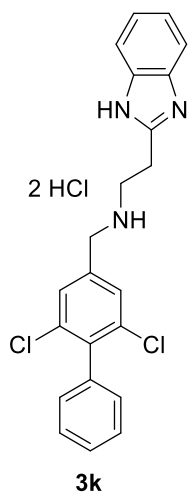


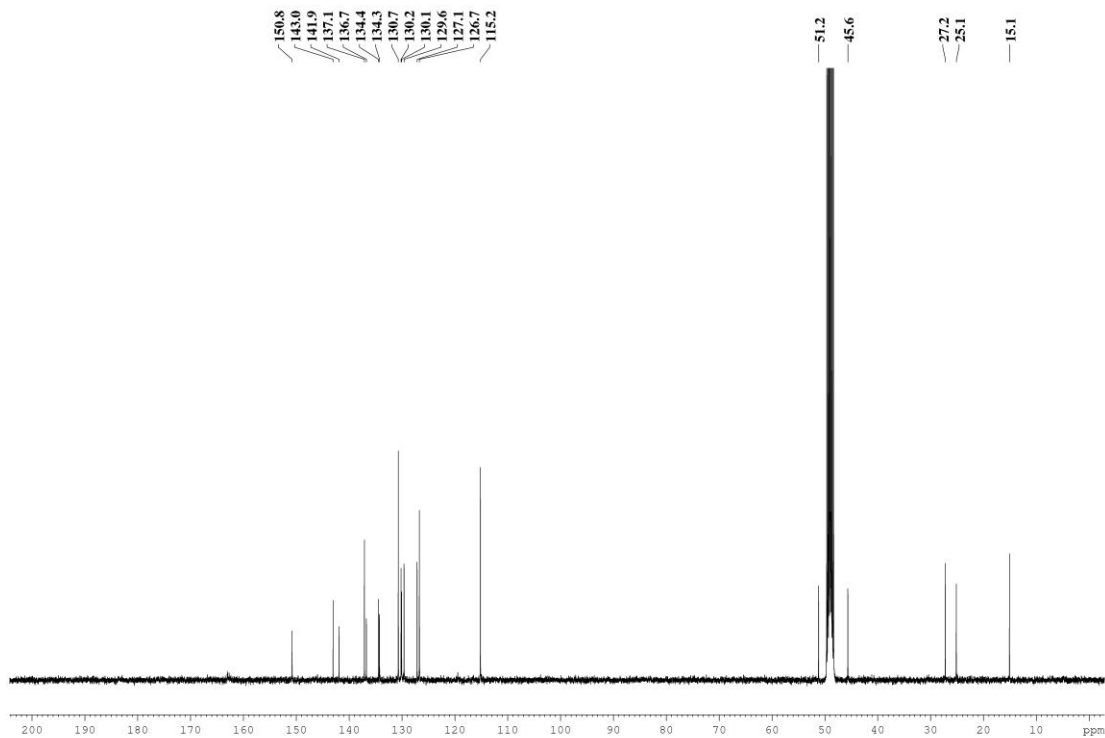
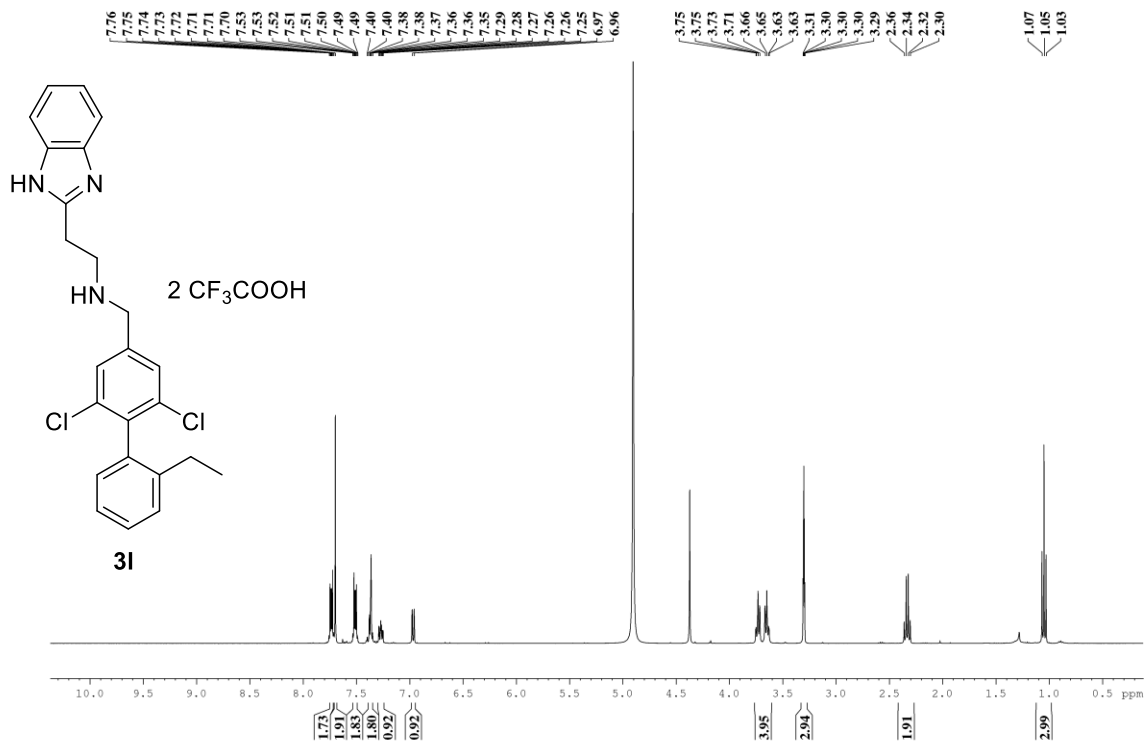


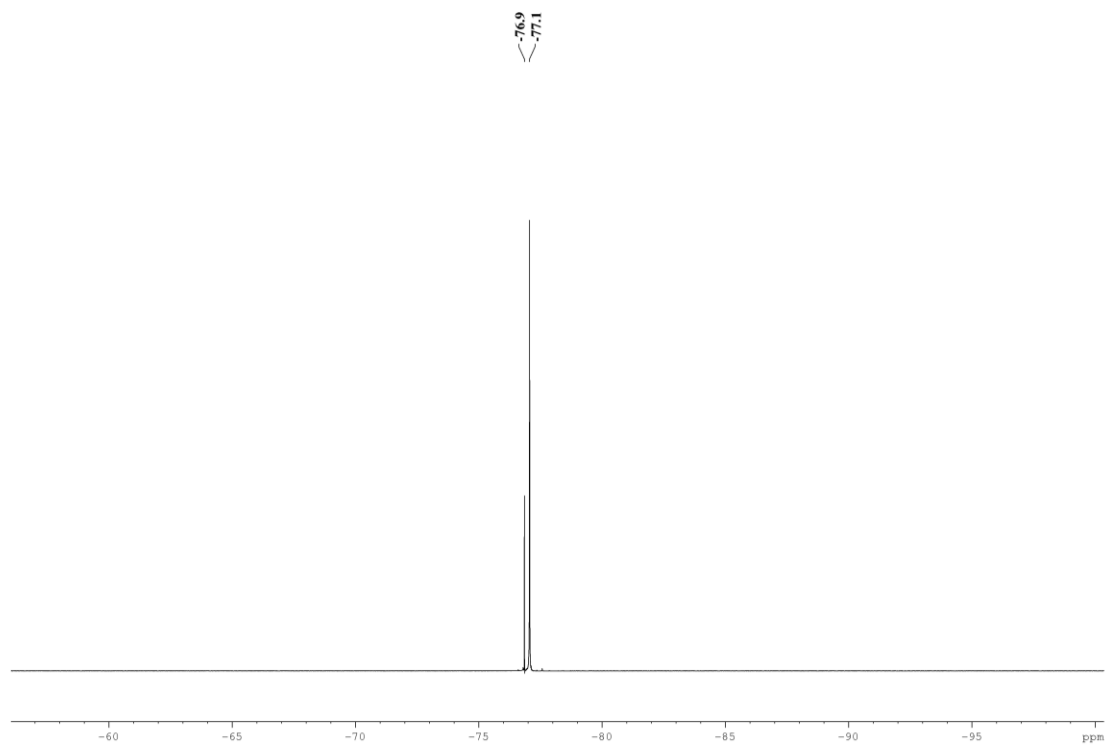


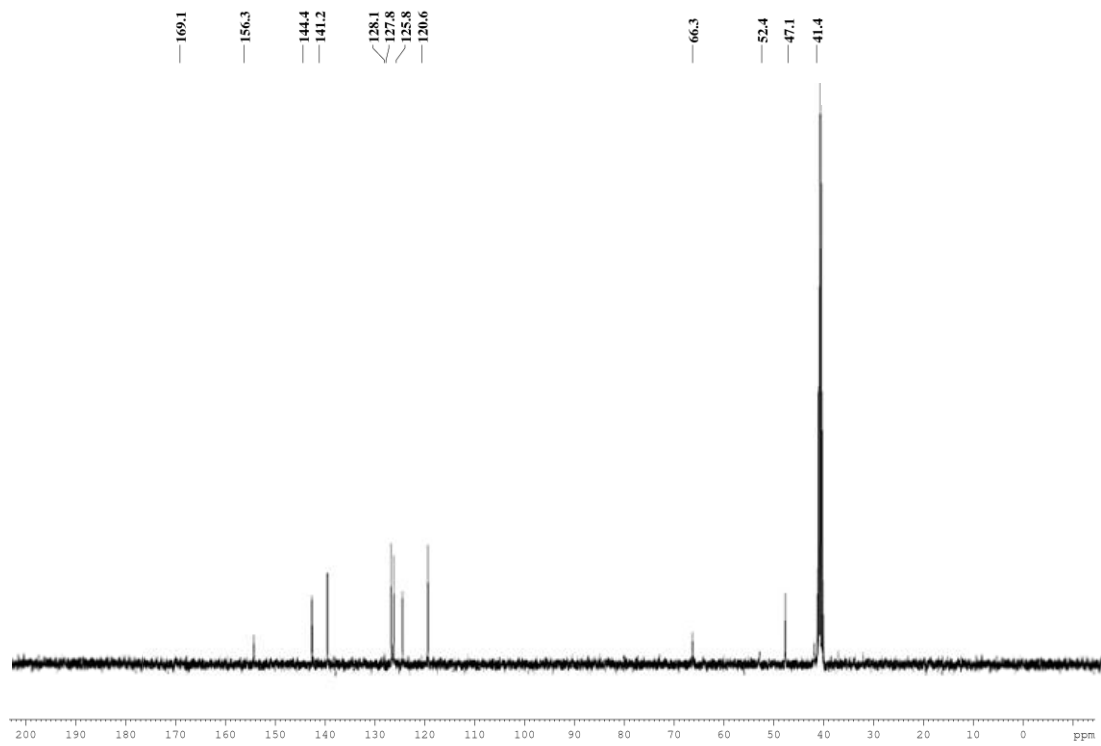
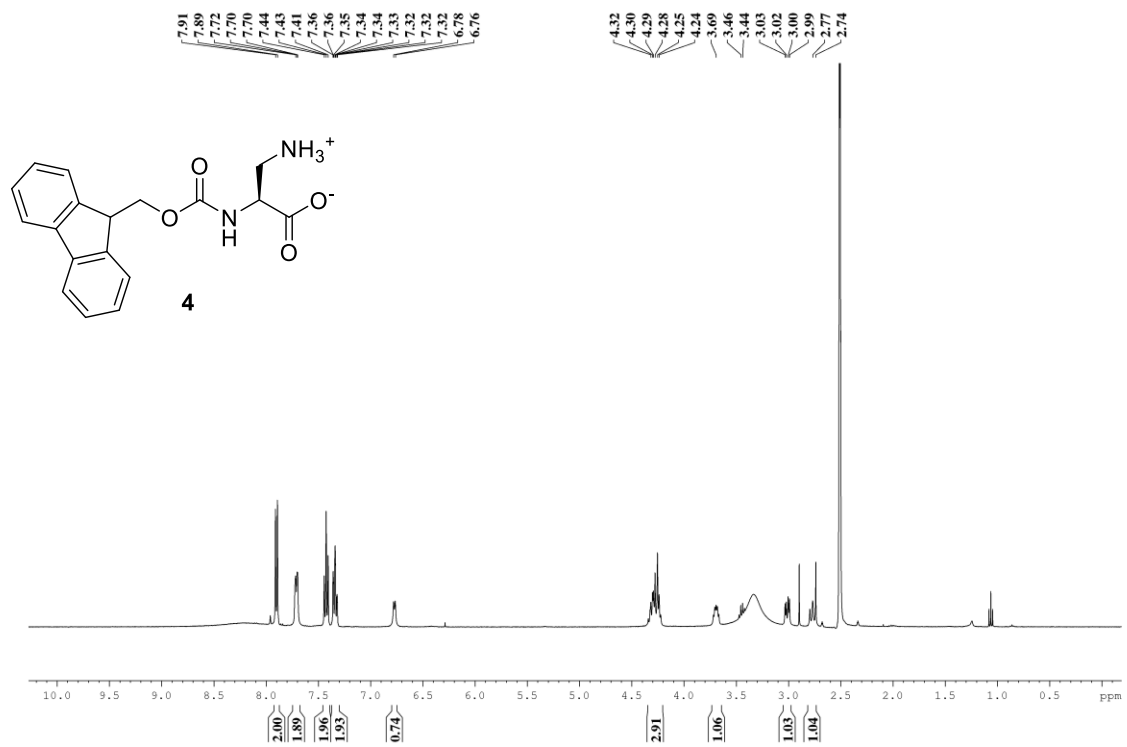






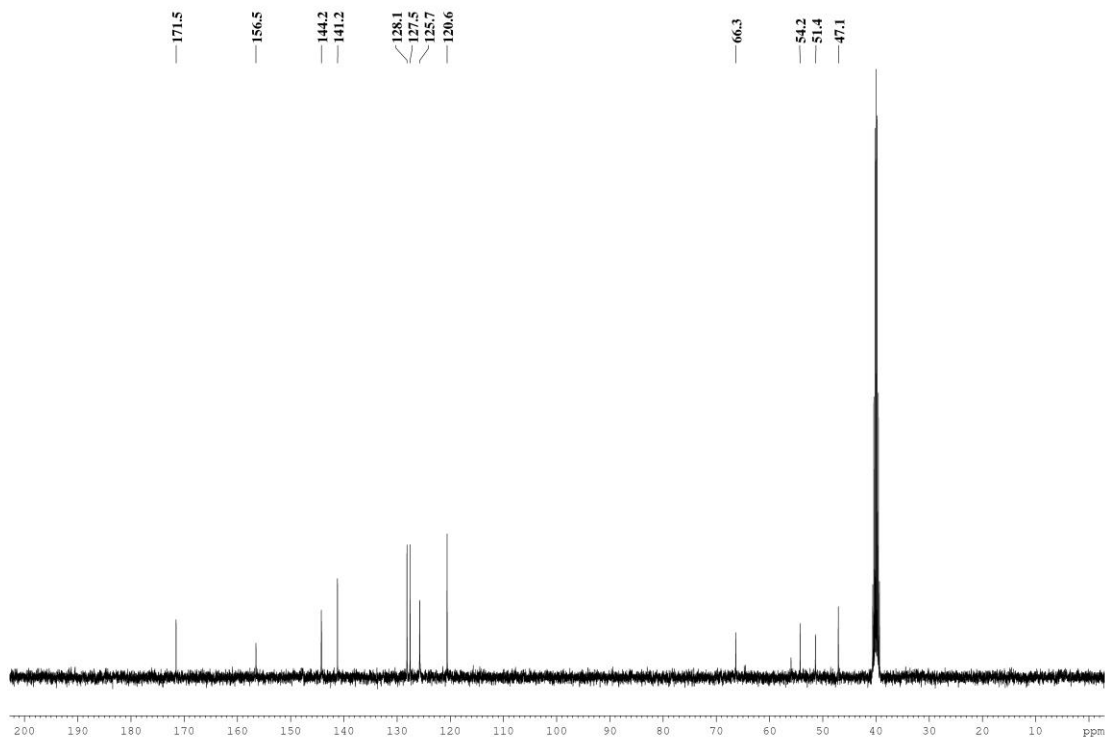
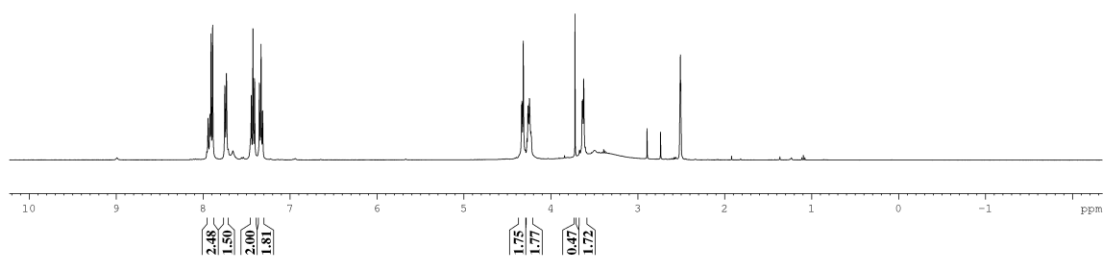
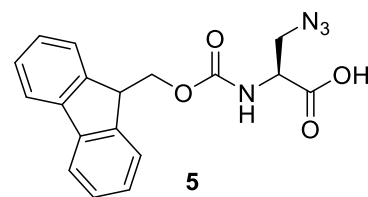


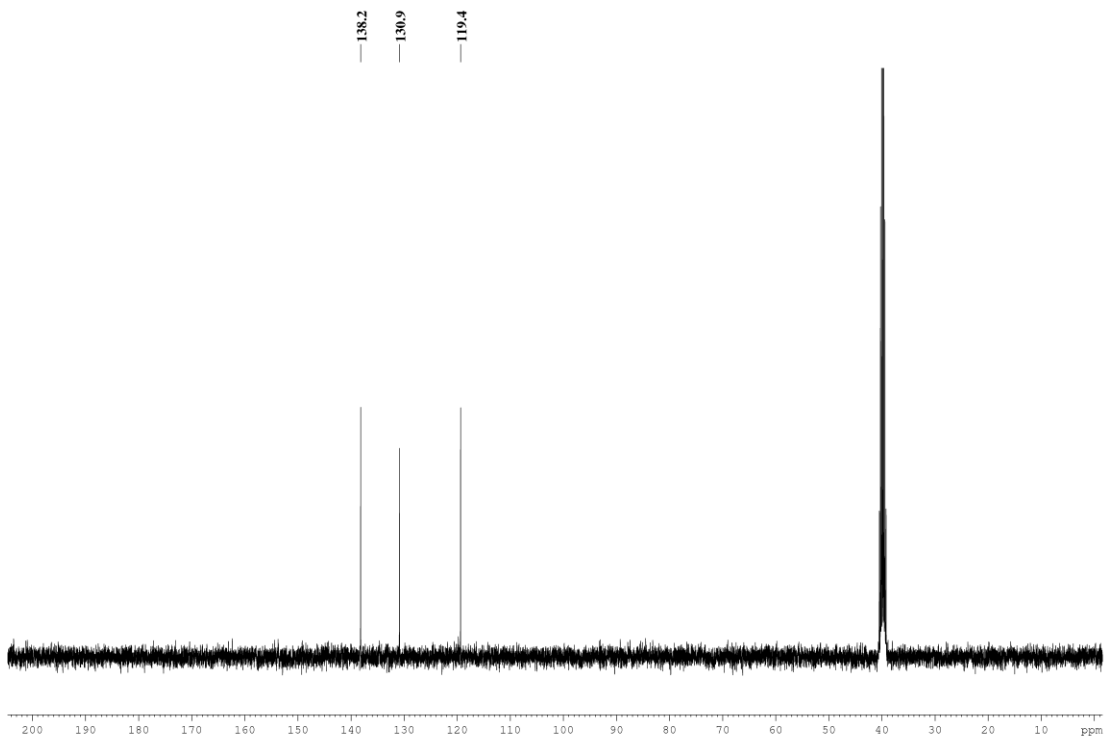
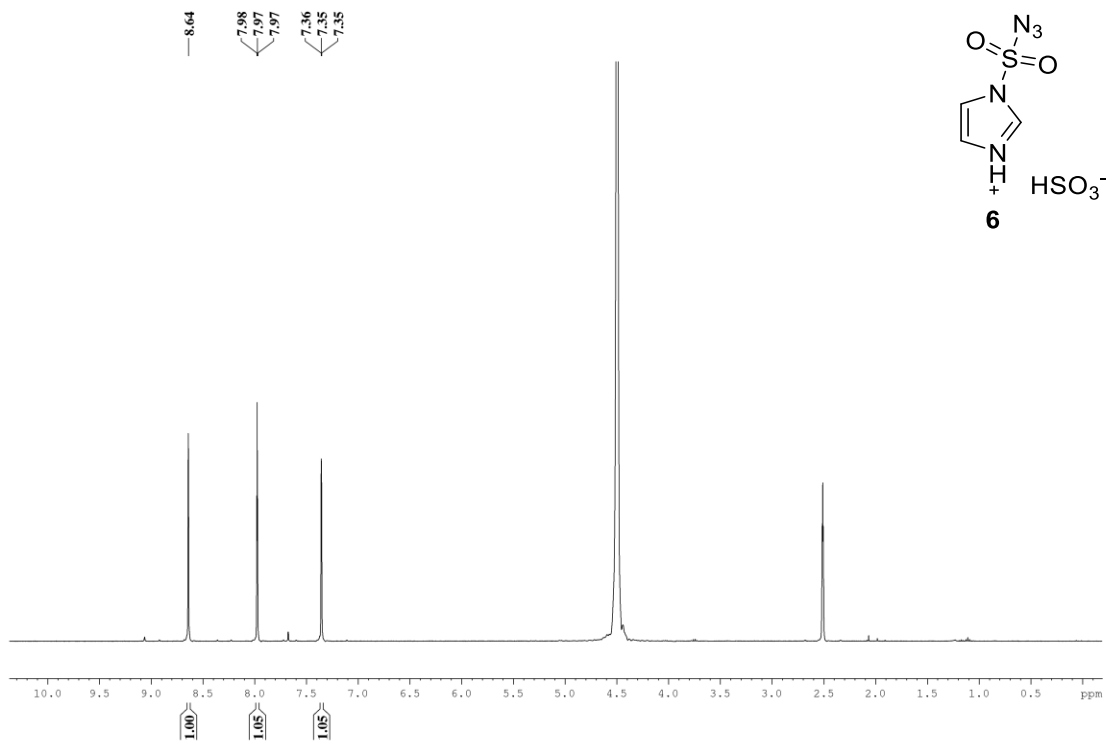


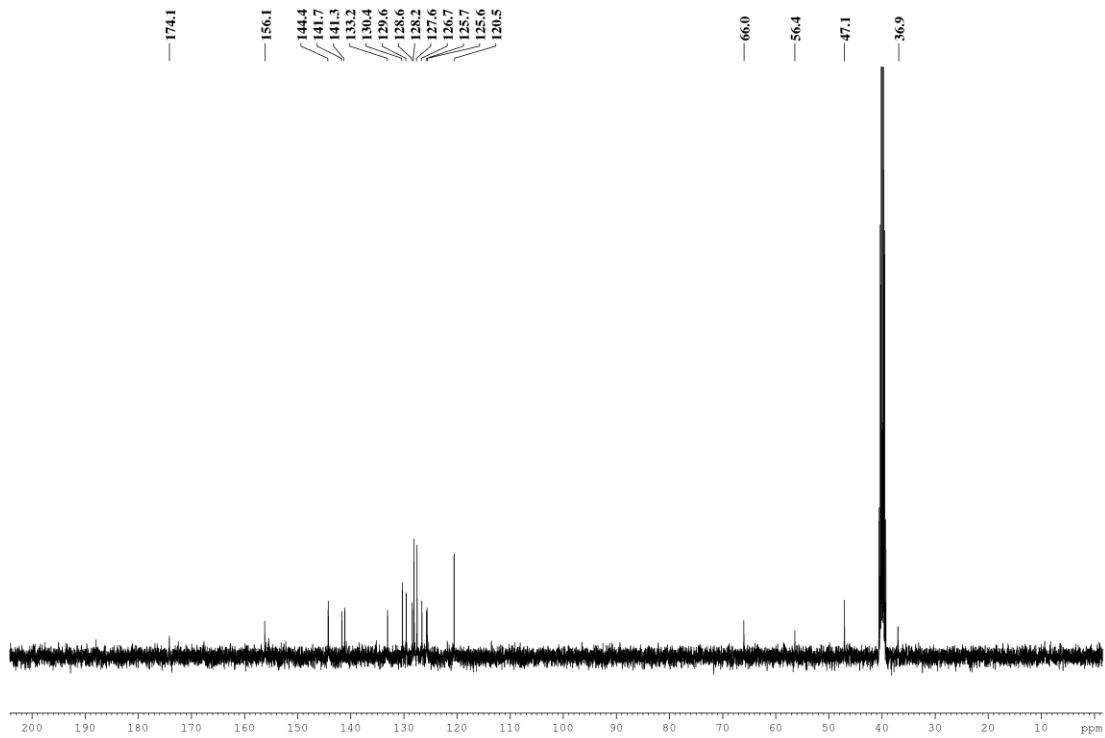
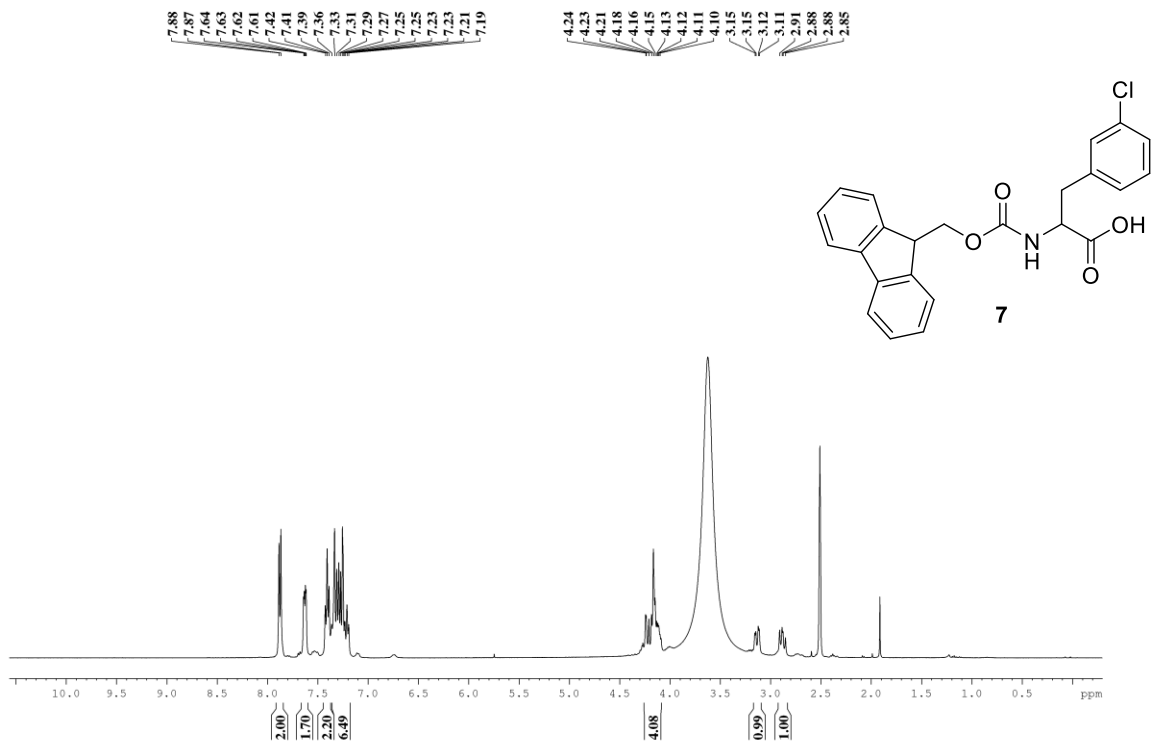


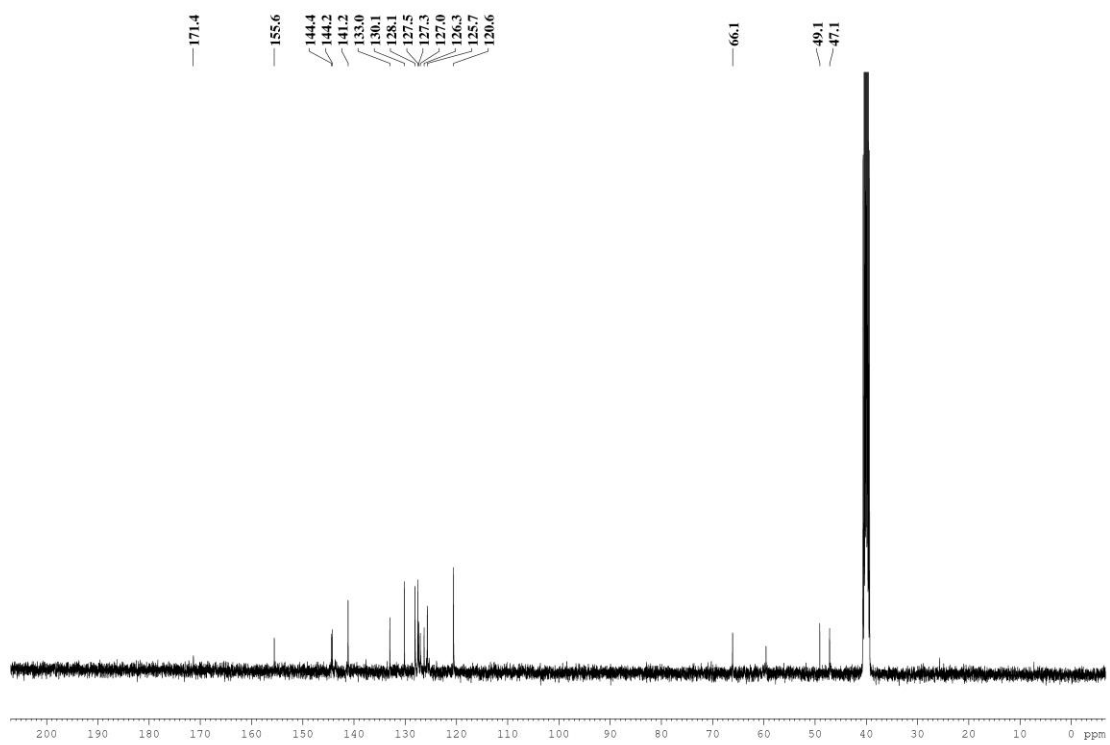
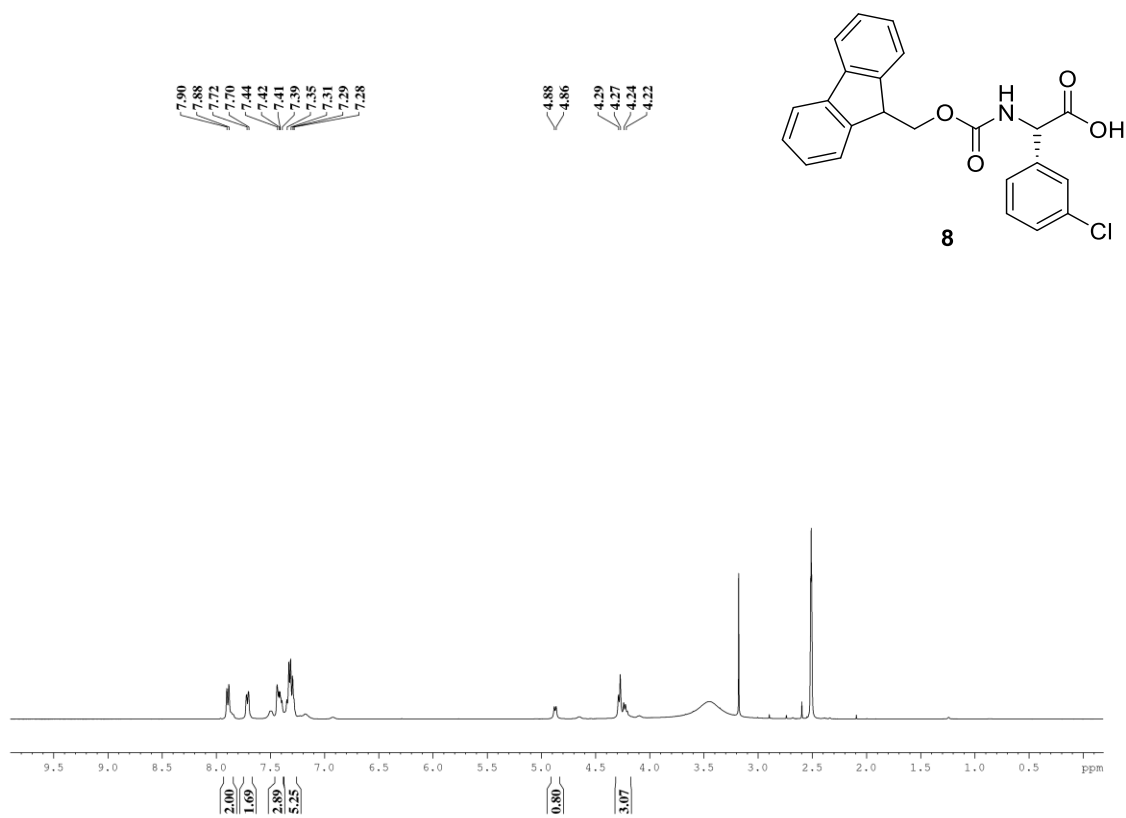
7.94
7.92
7.91
7.89
7.75
7.73
7.44
7.43
7.41
7.35
7.33
7.31

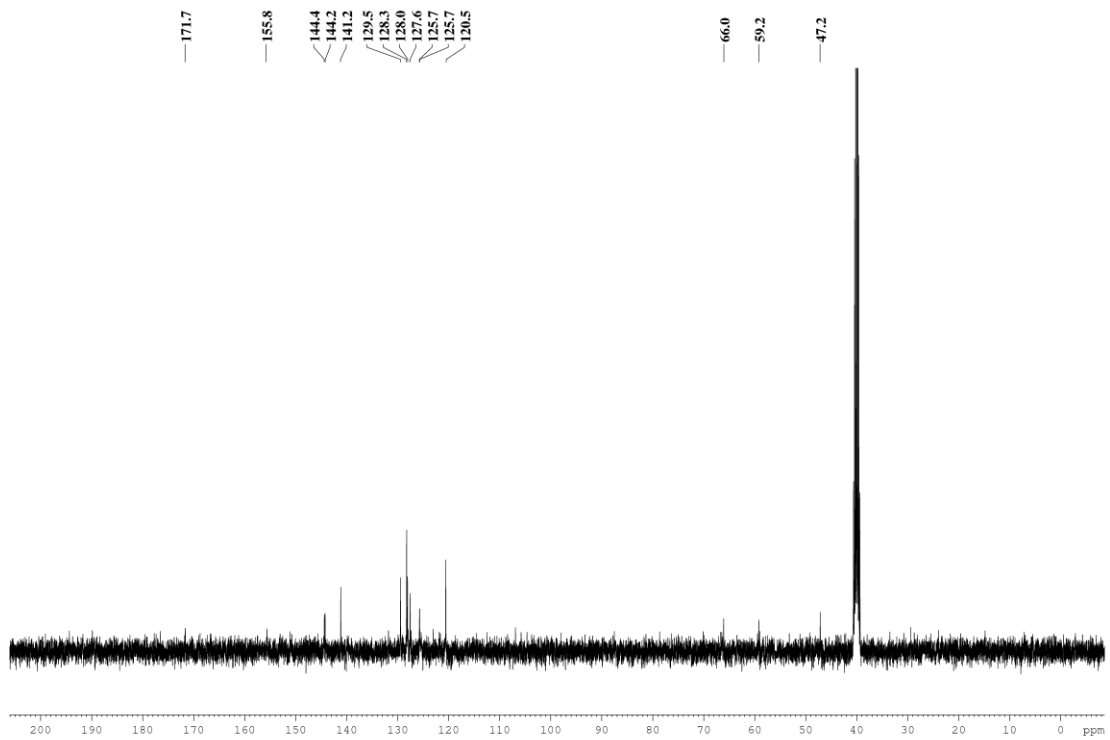
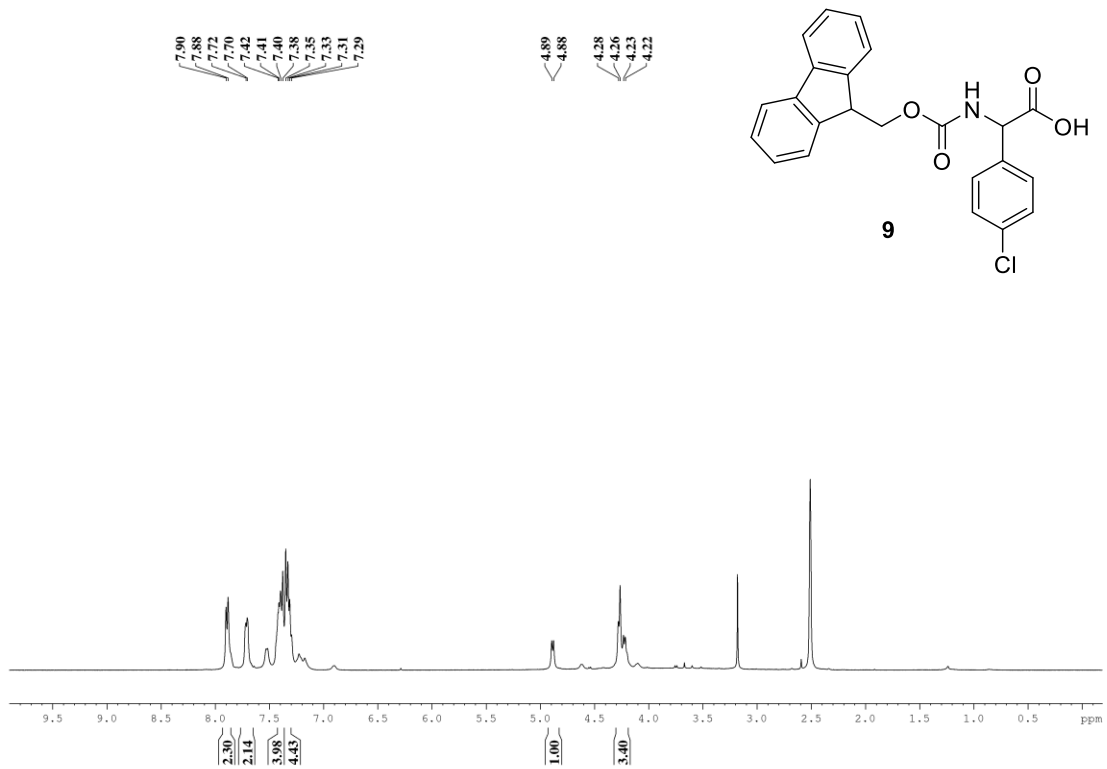
4.34
4.33
4.32
4.27
4.26
4.24
4.23
4.22
3.64
3.63
3.62

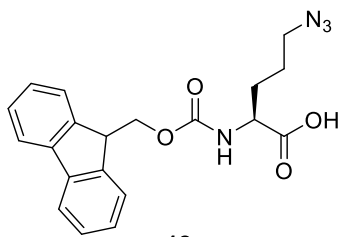




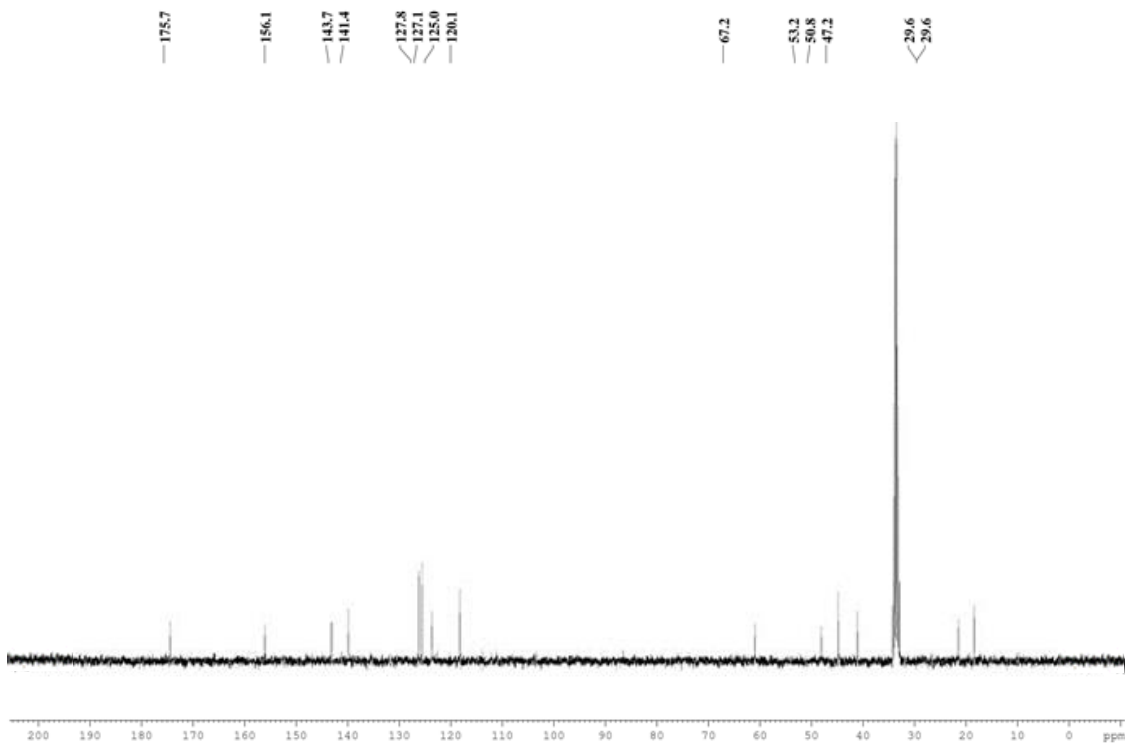
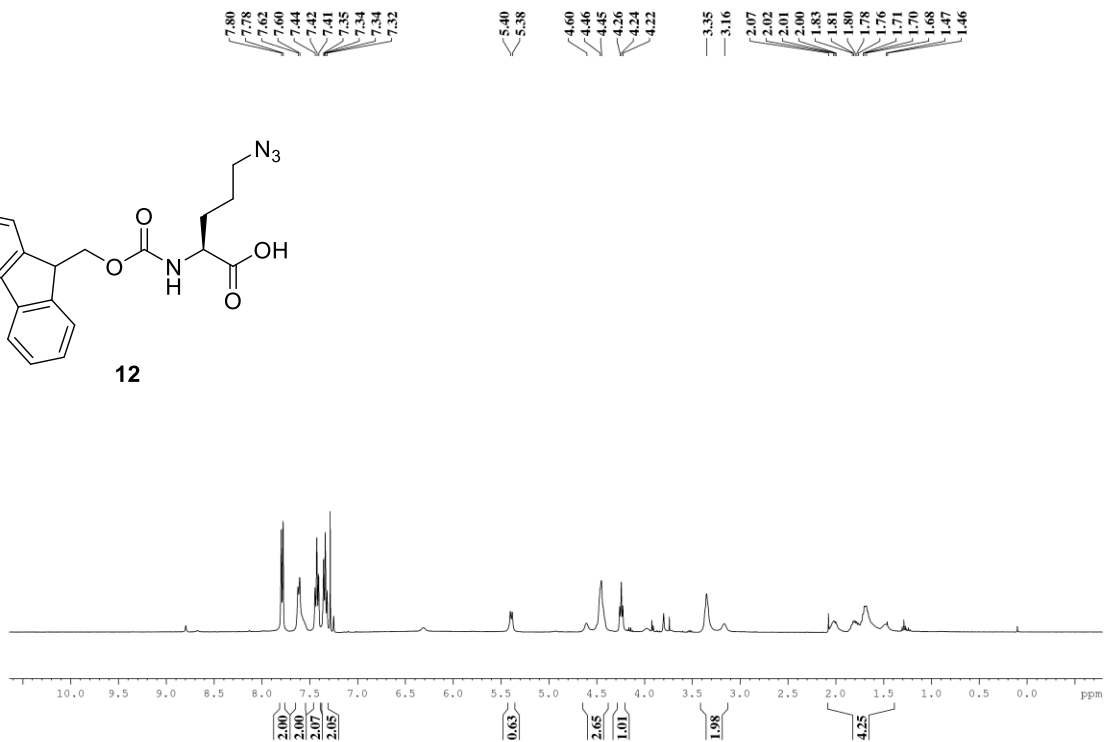


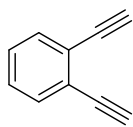




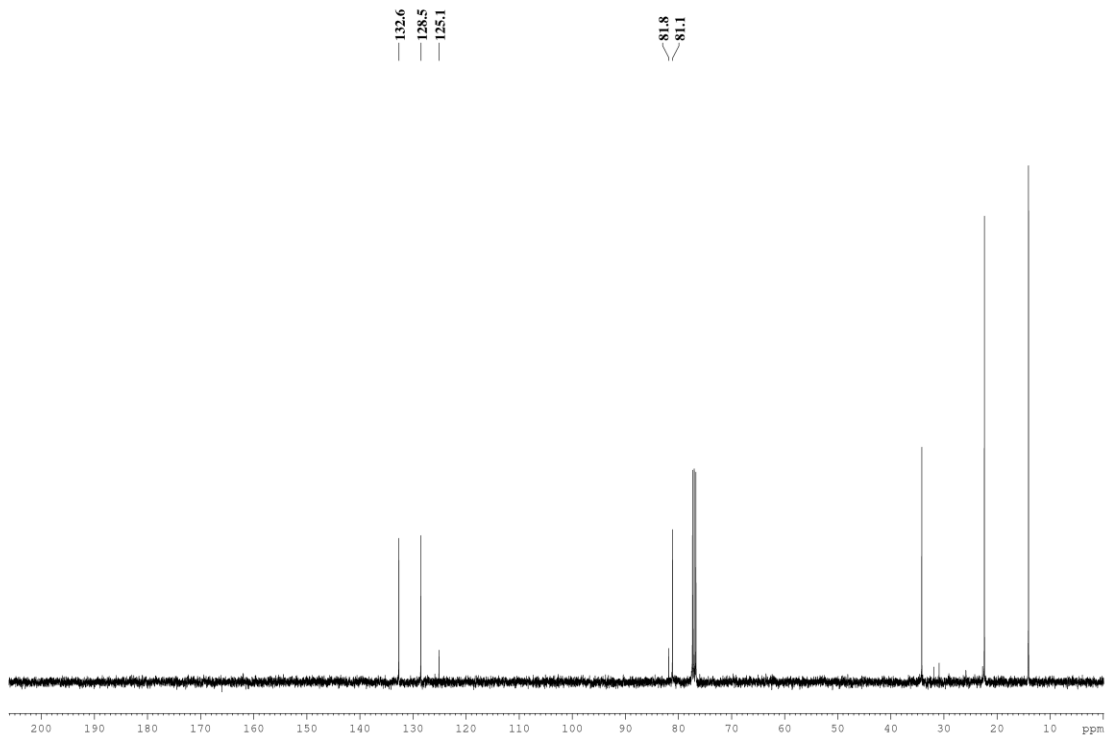
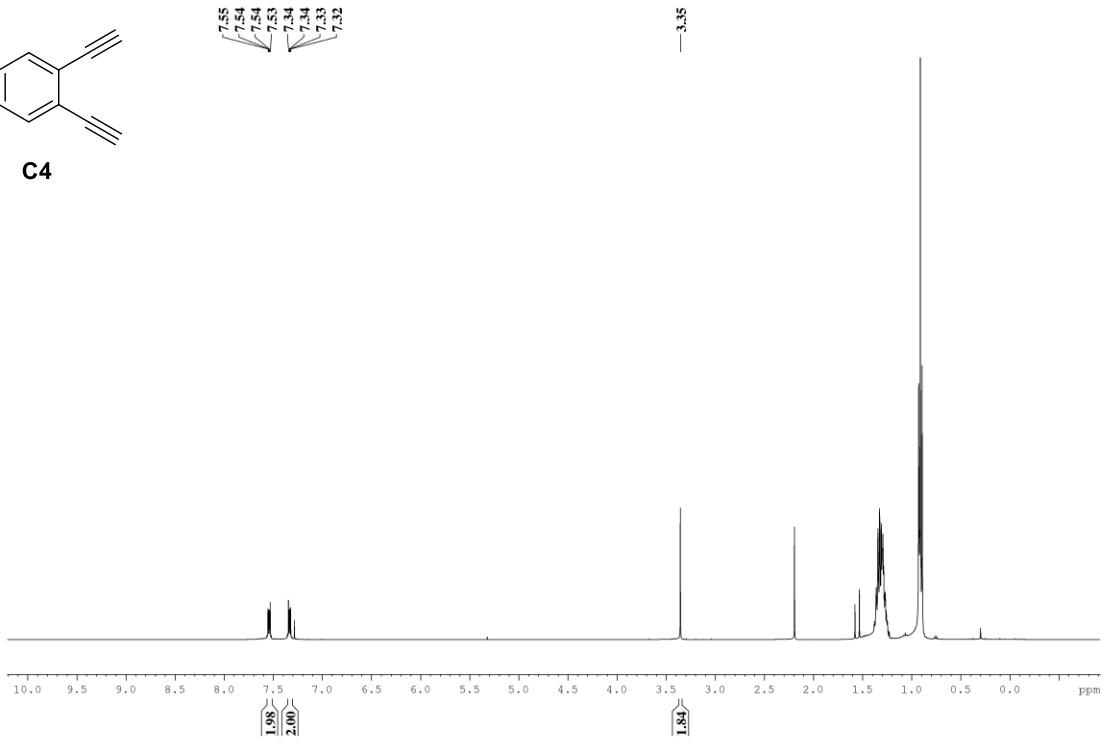


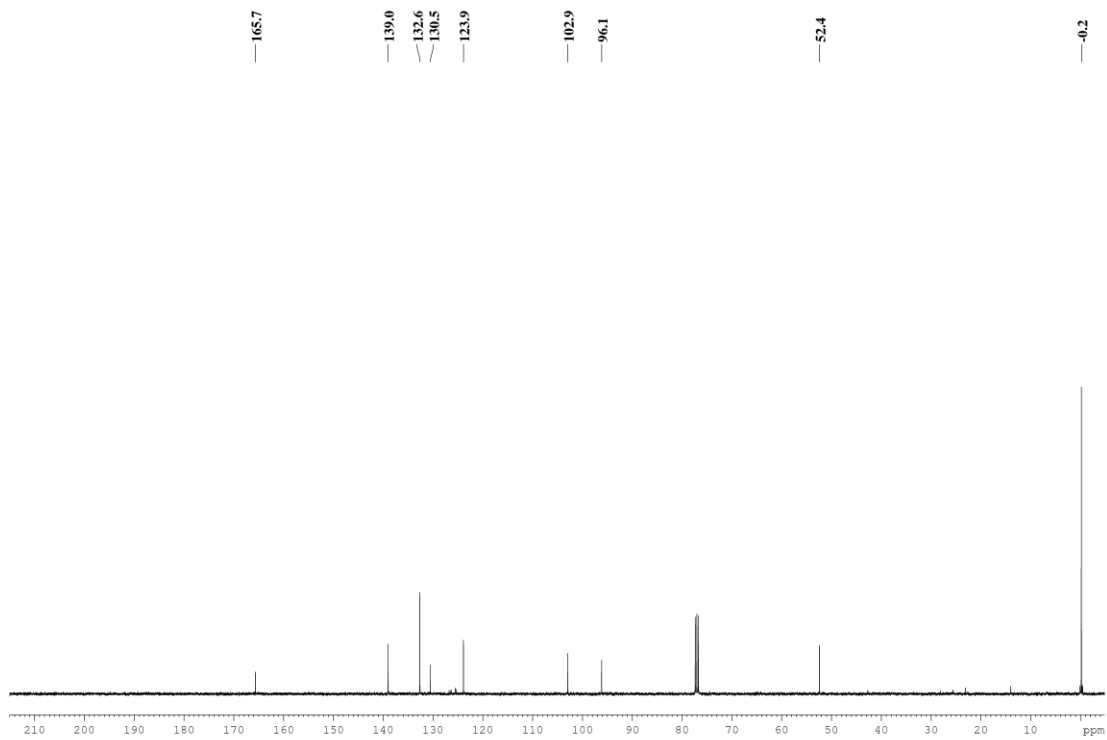
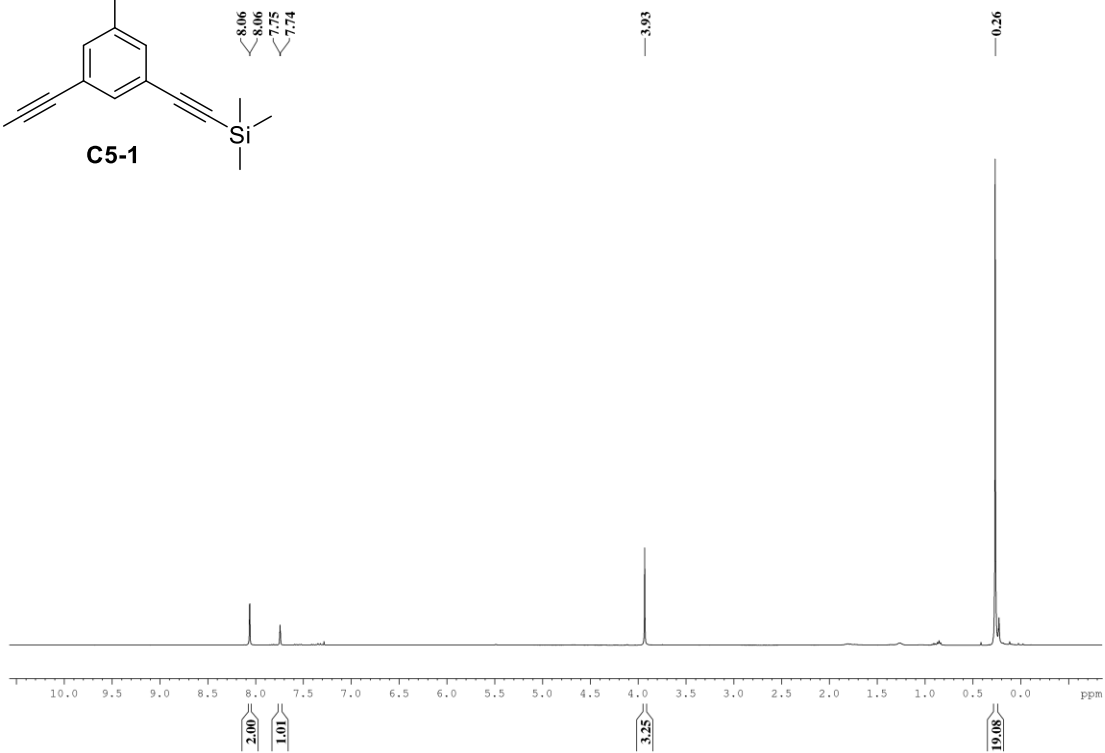
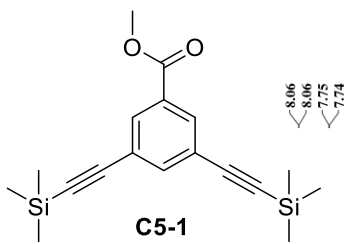
12

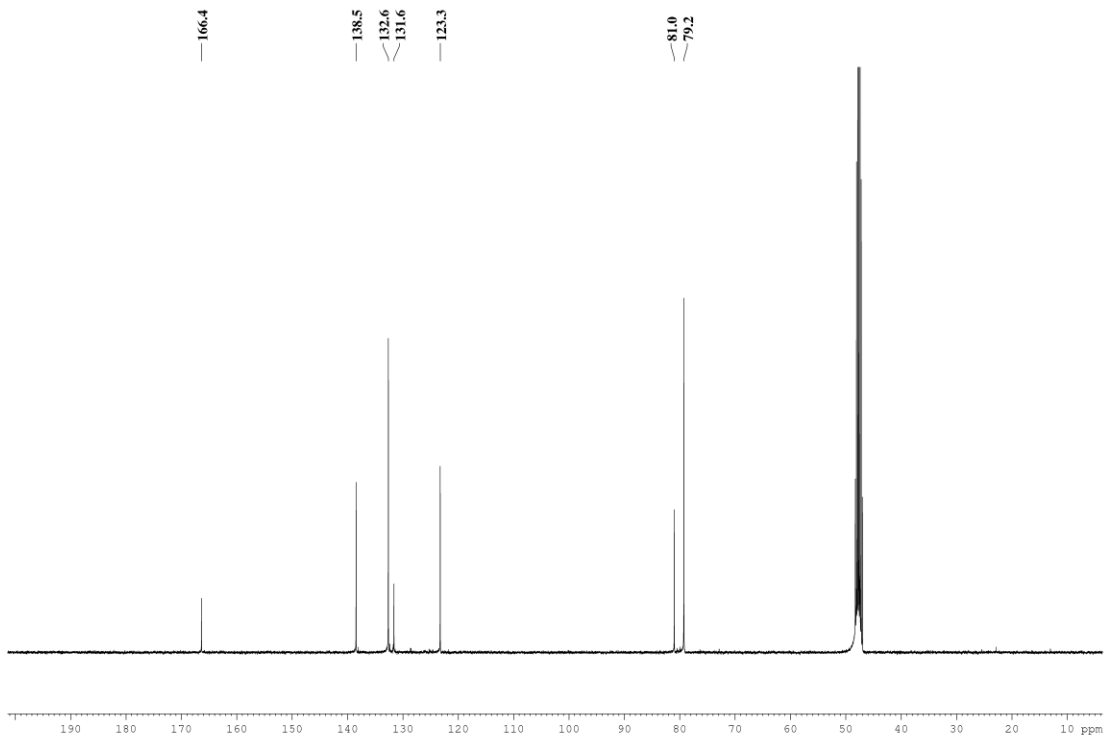
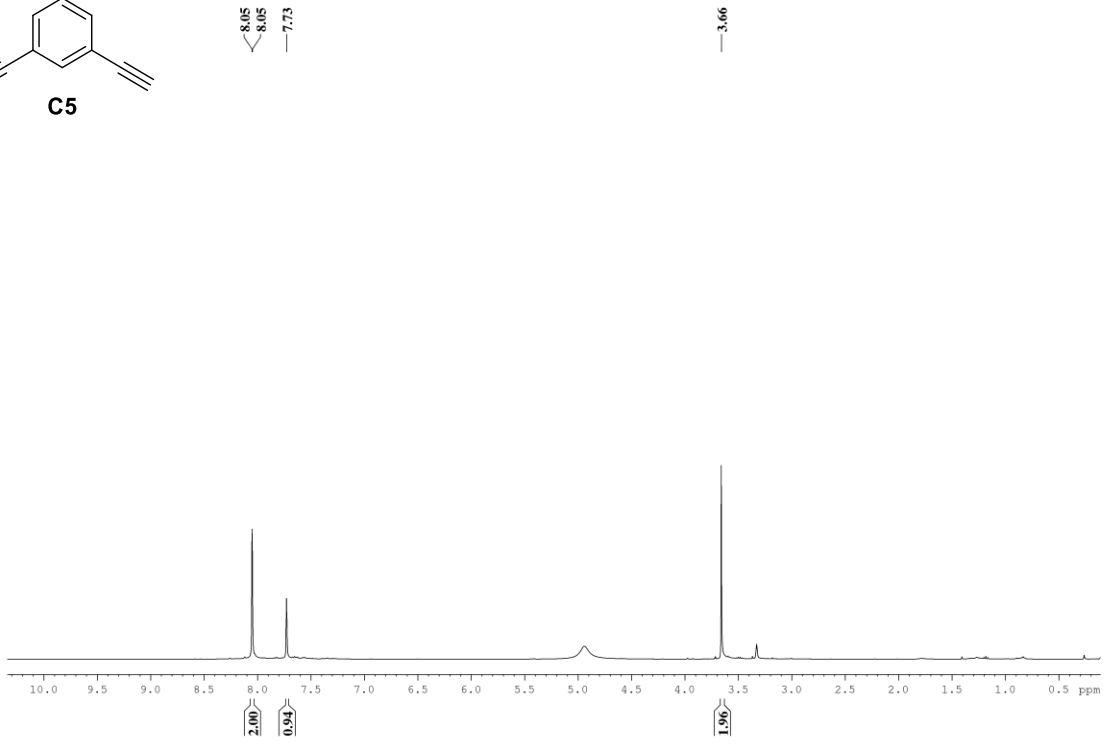
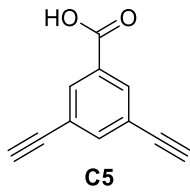


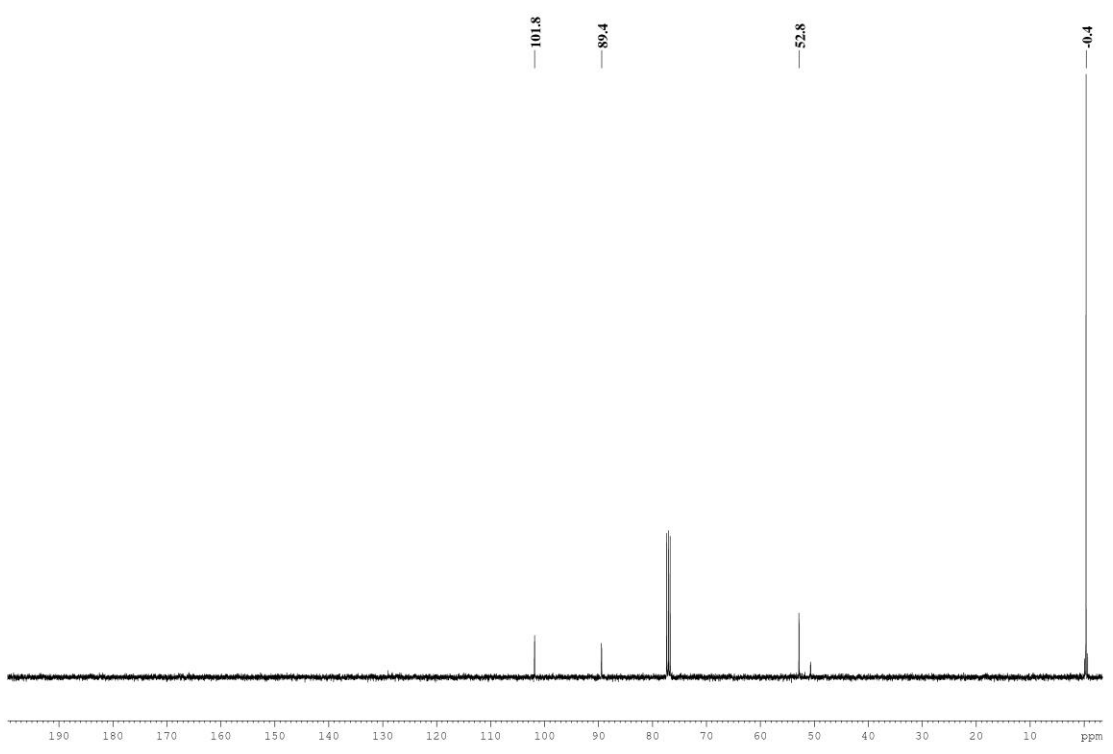
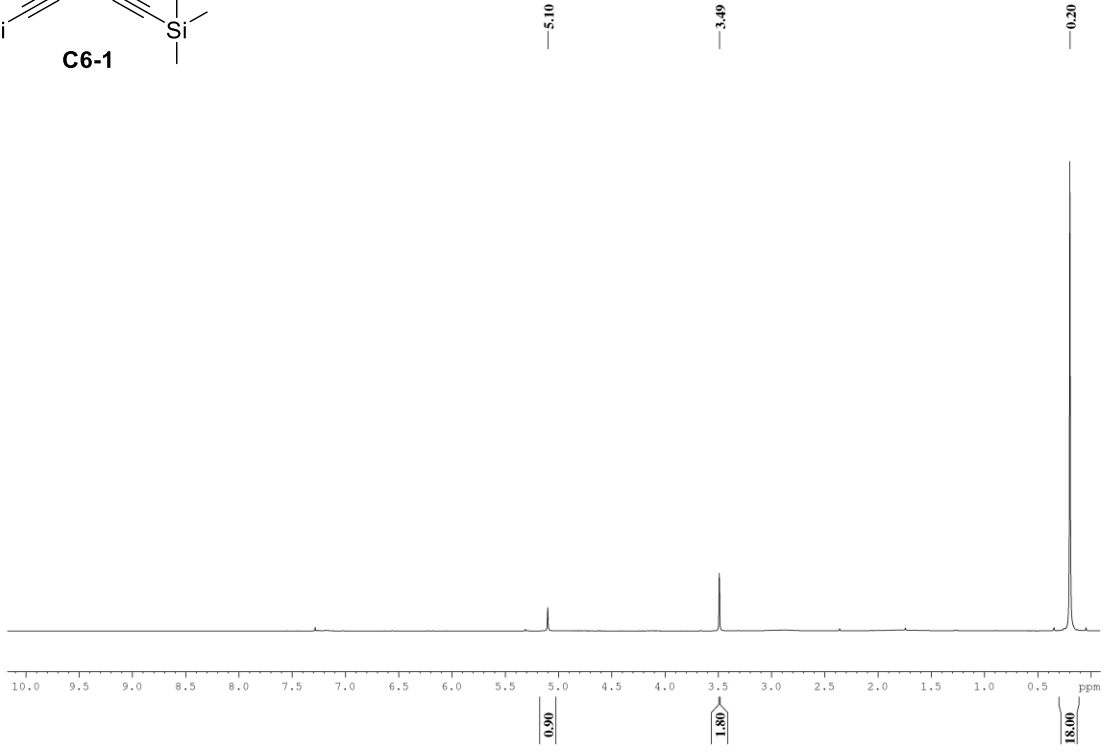
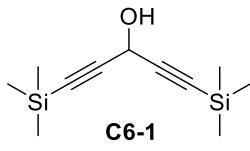


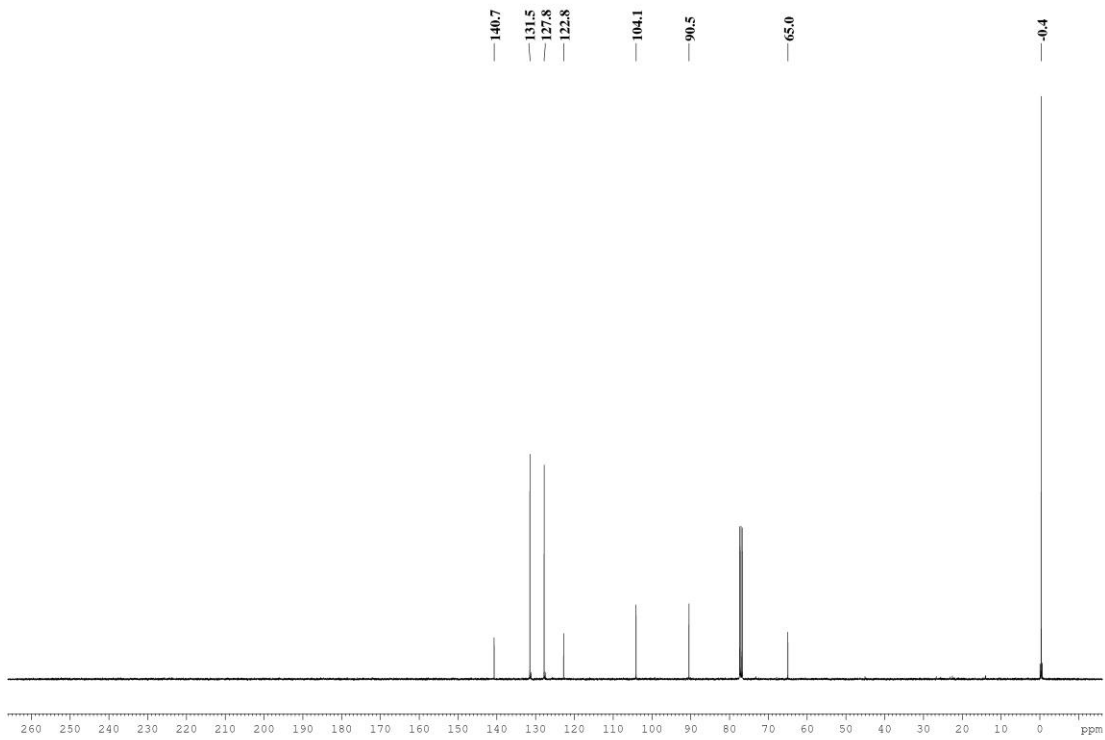
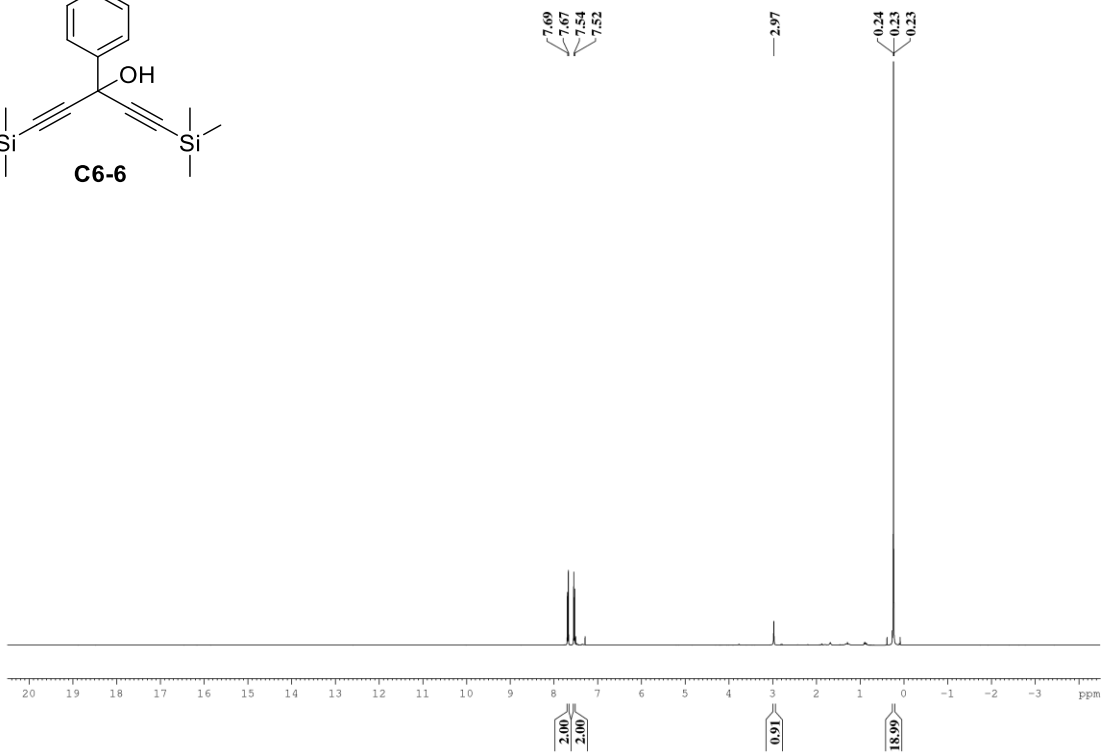
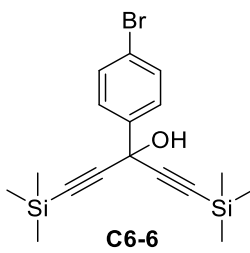
C4

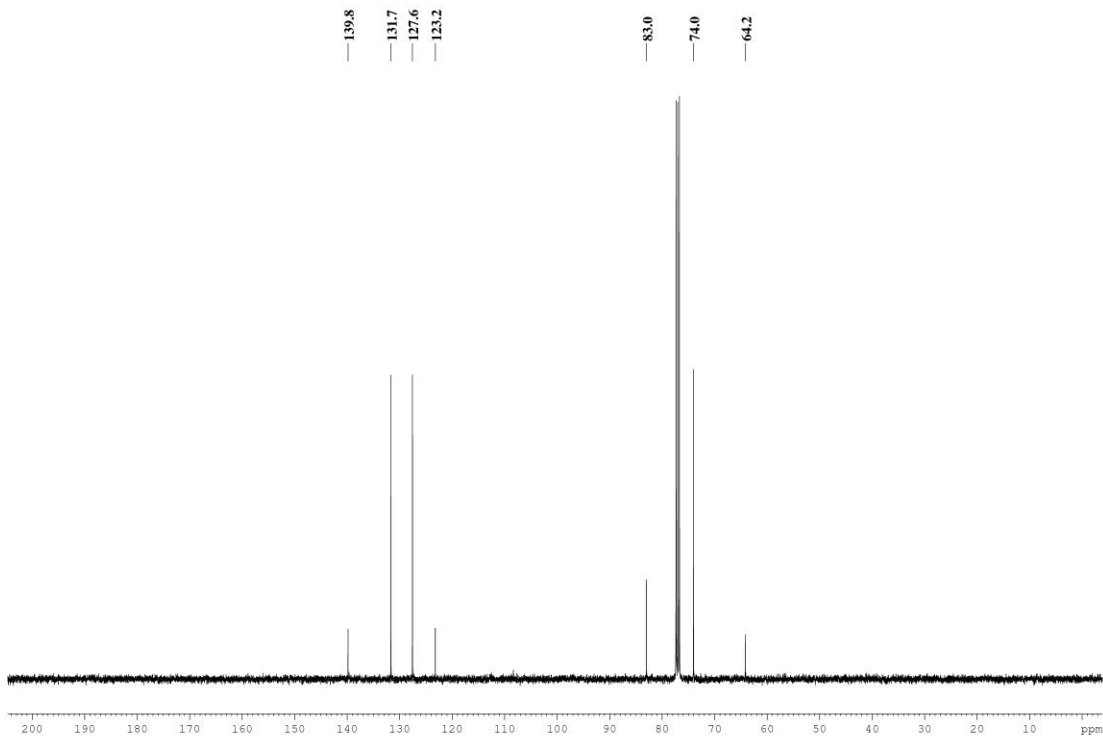
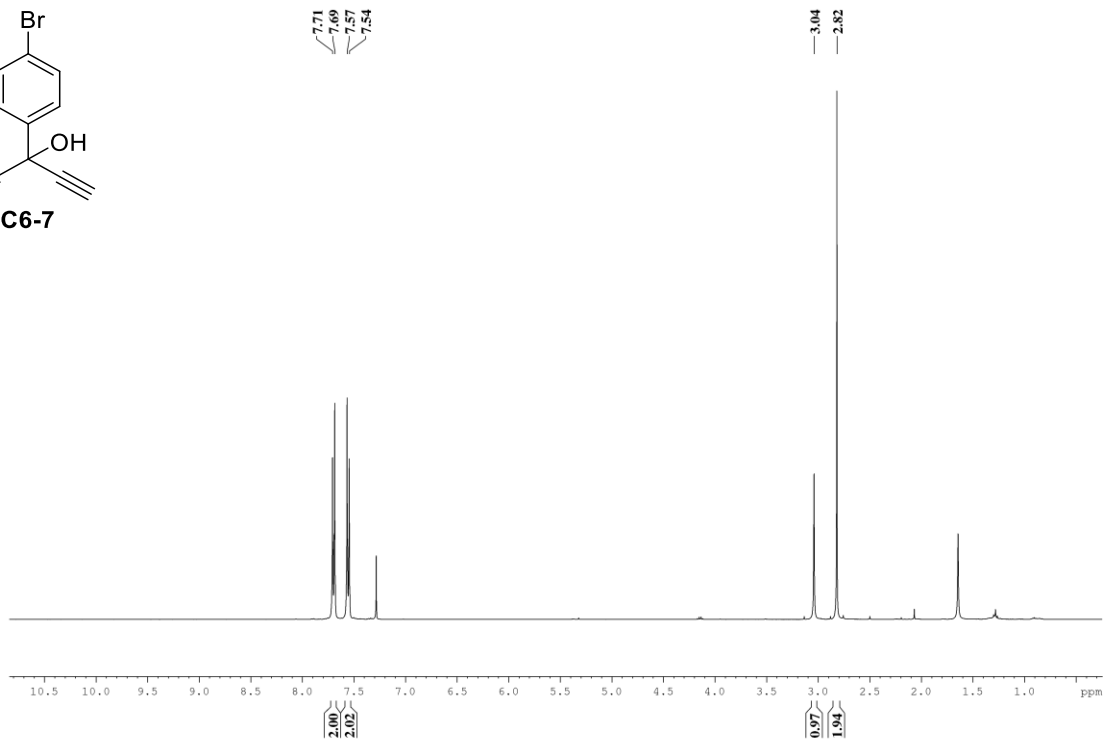
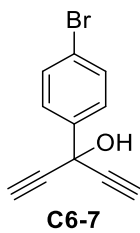


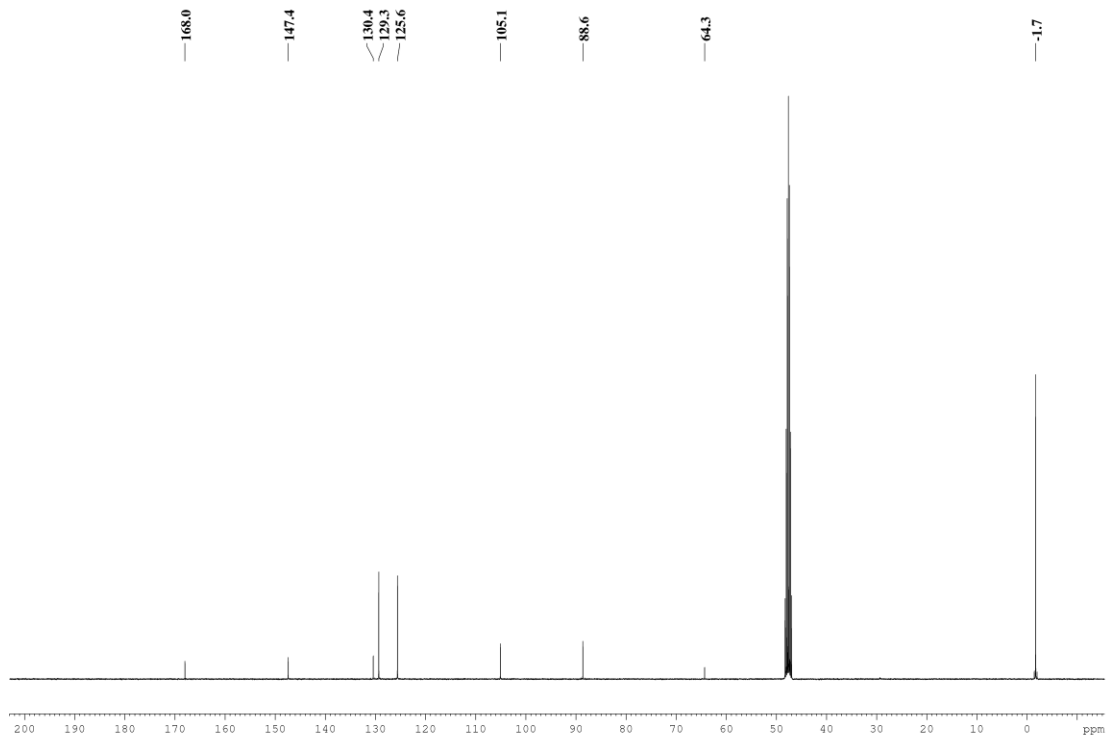
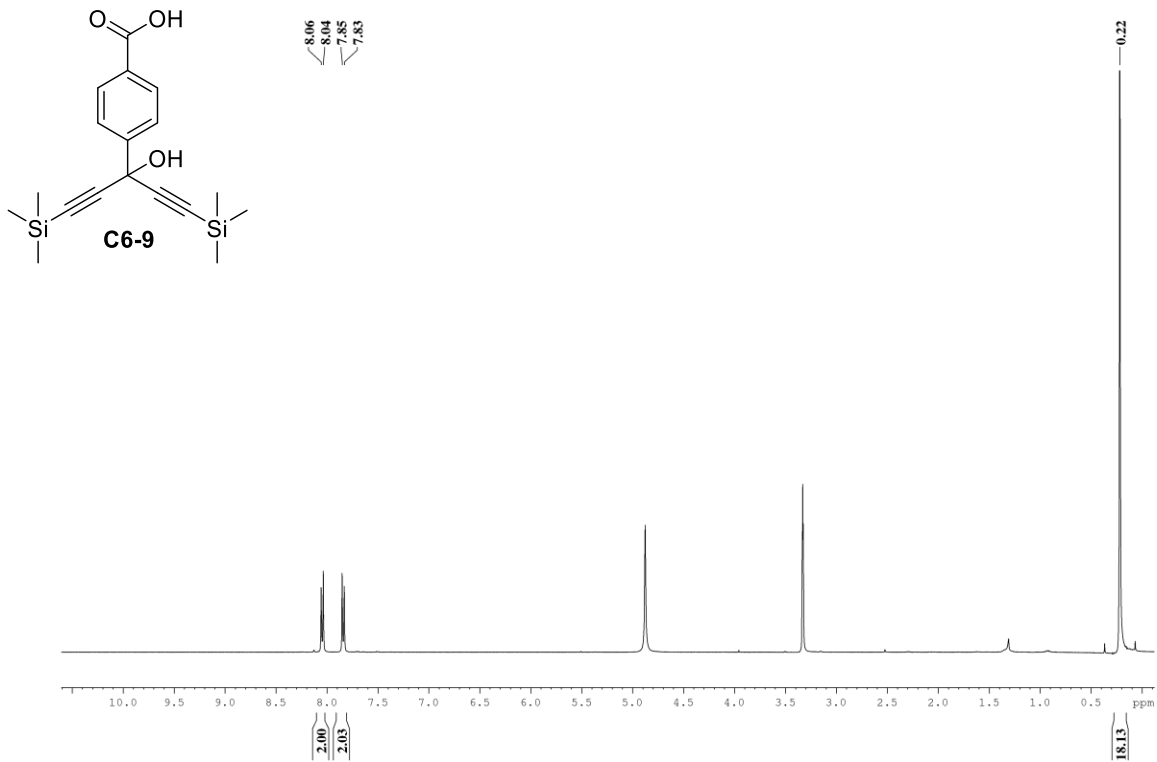


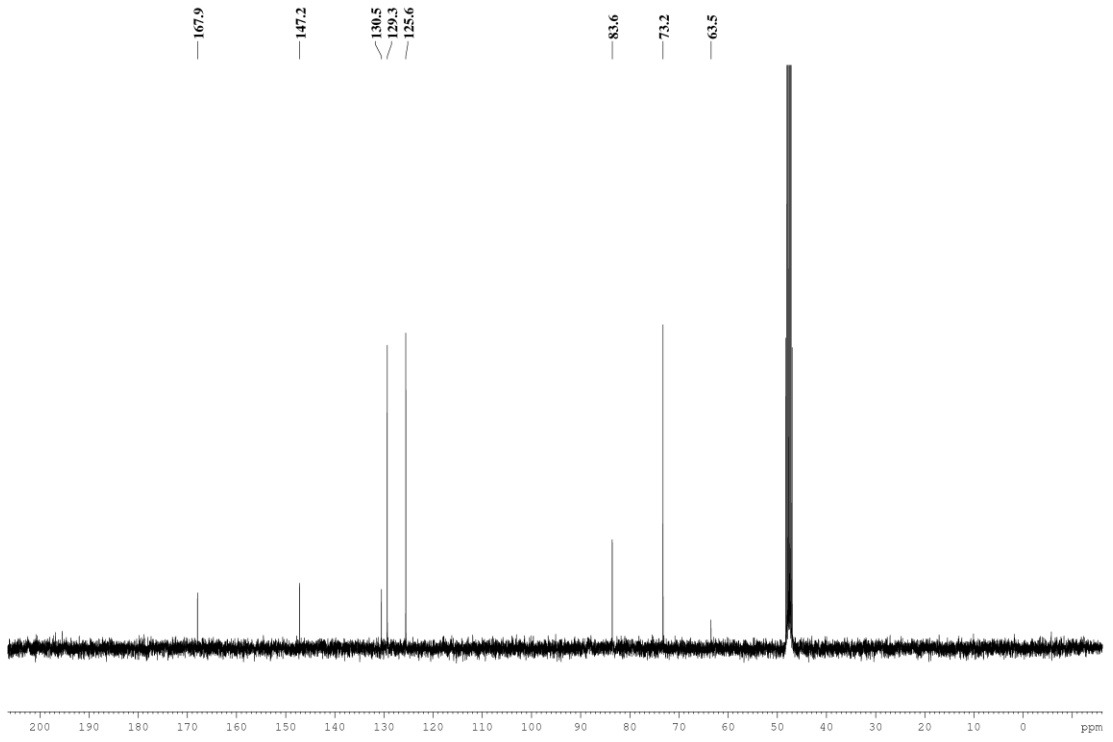
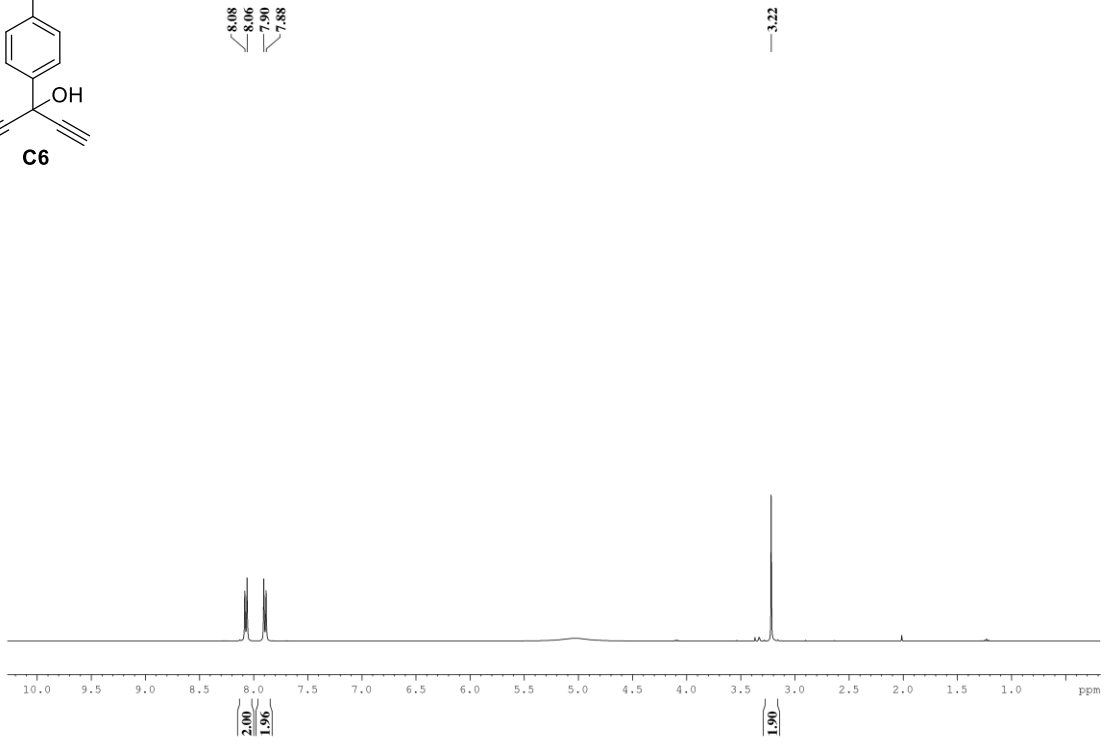
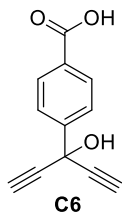


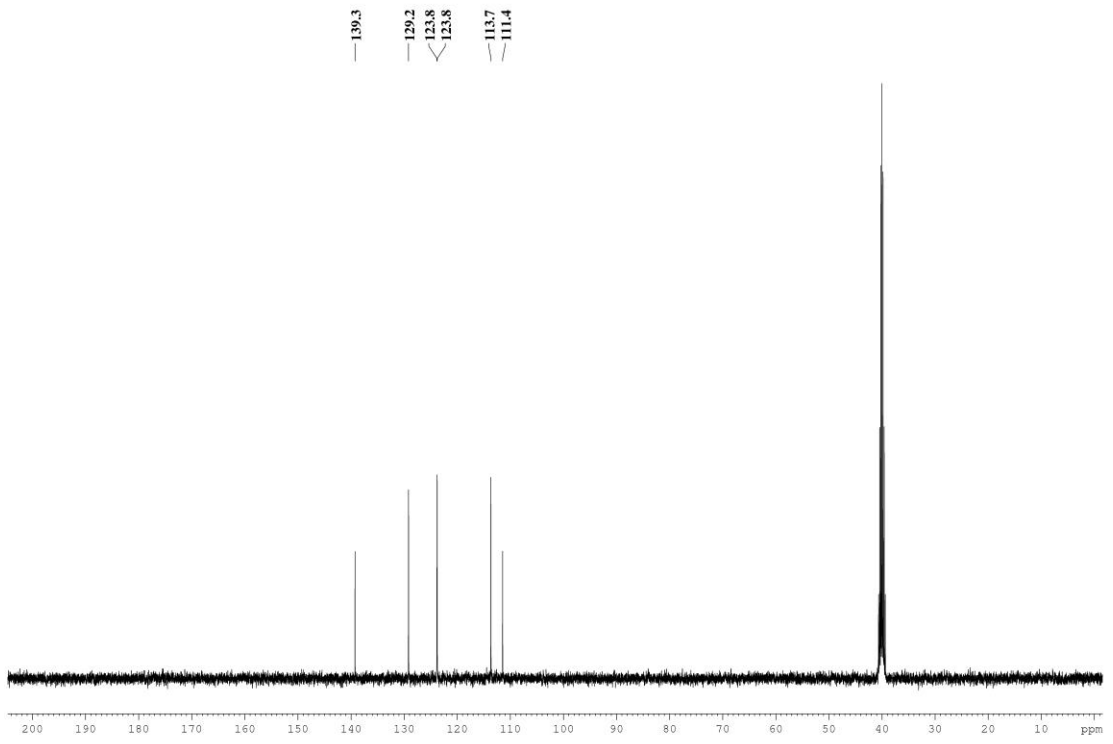
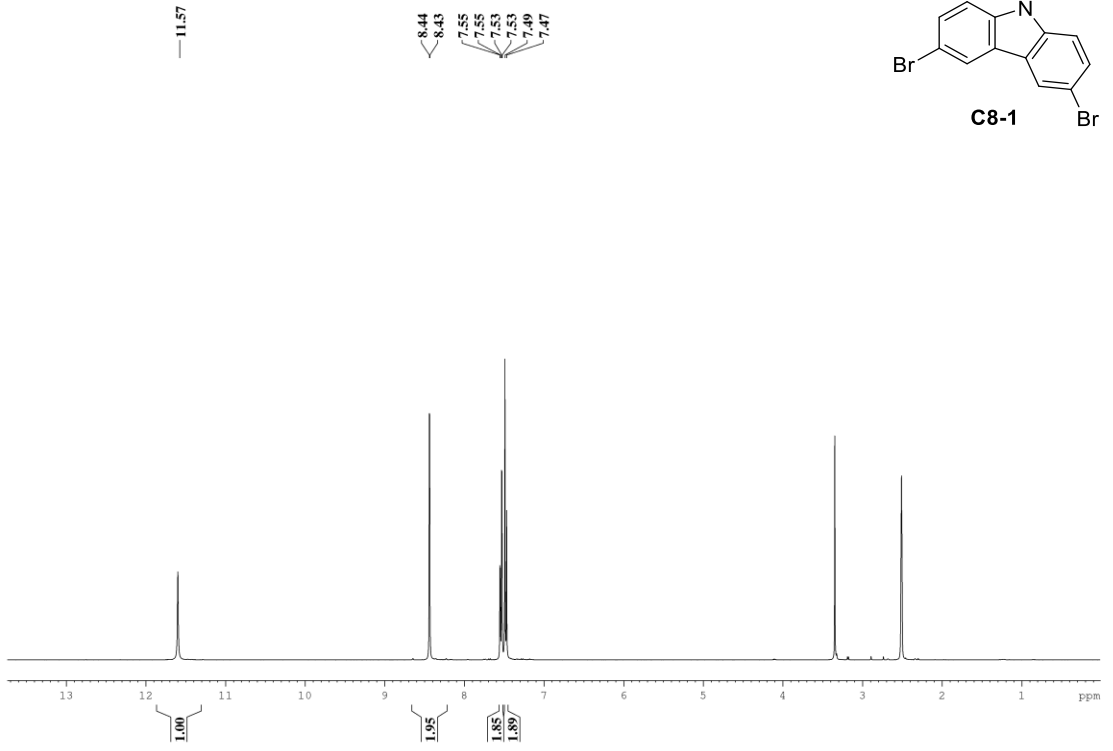
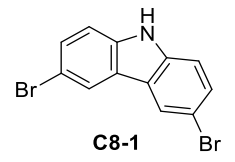


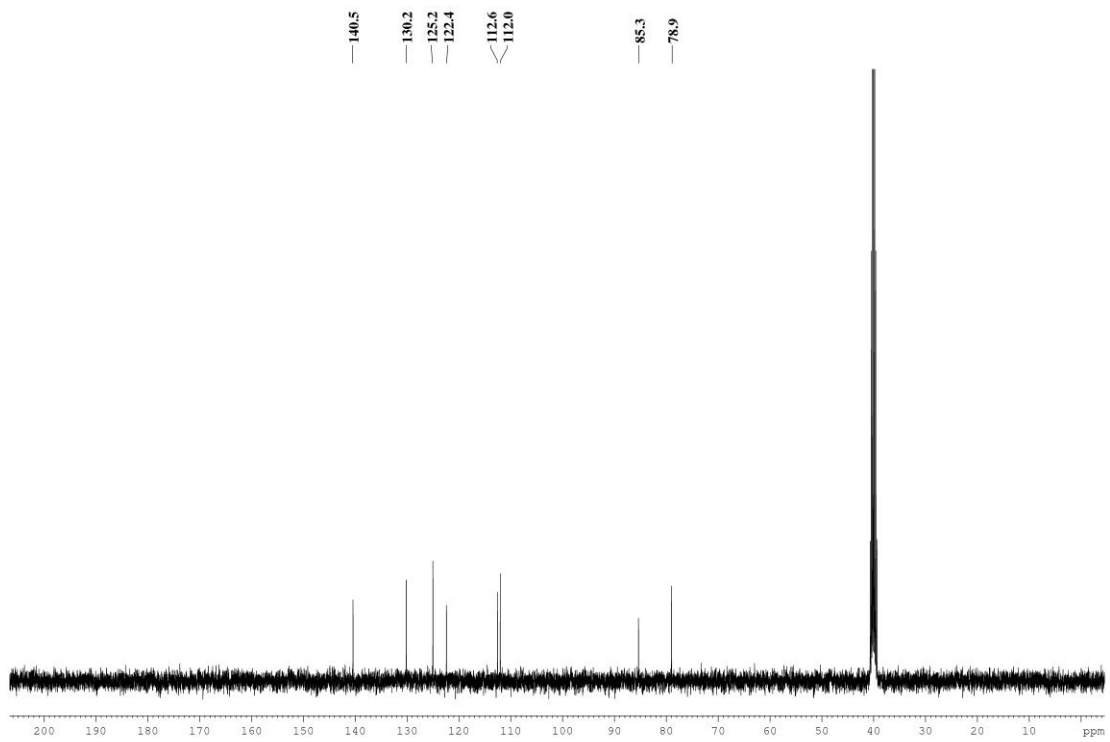
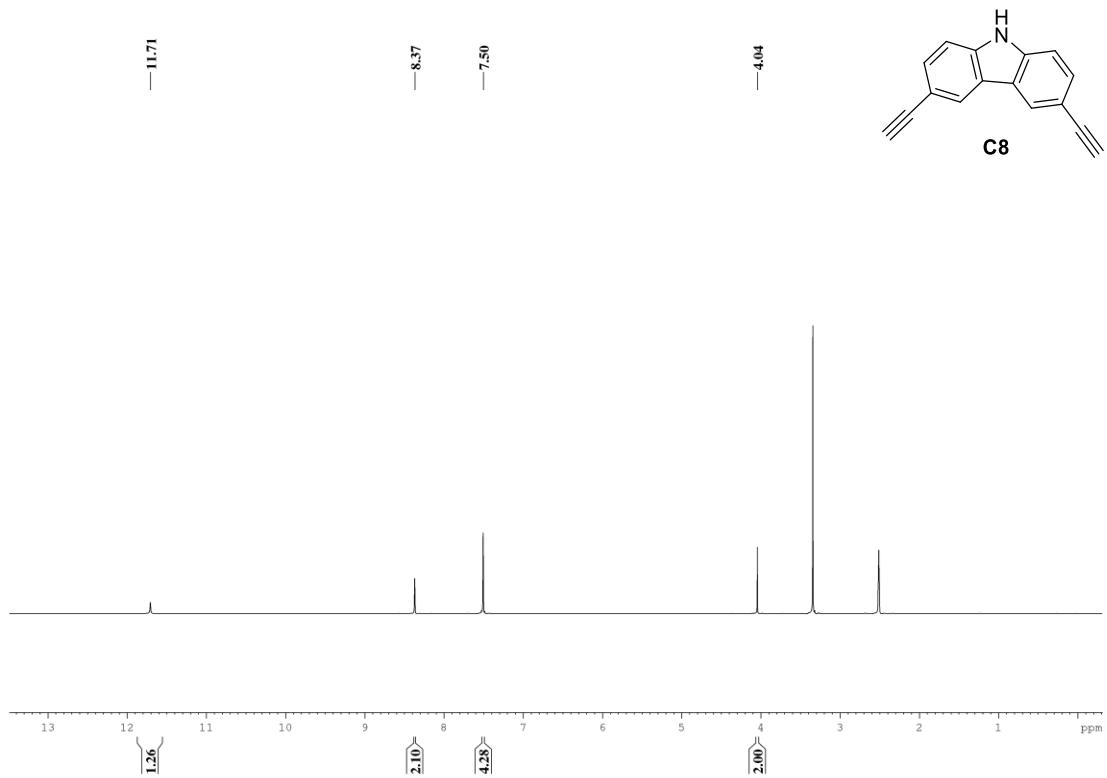


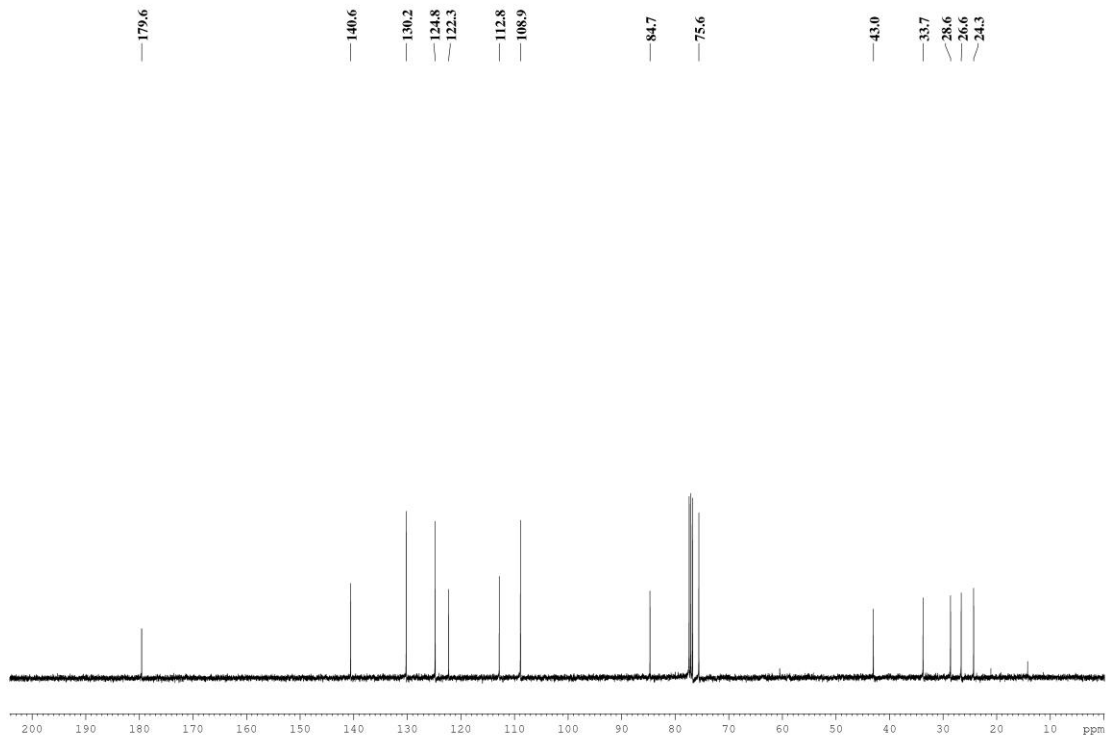
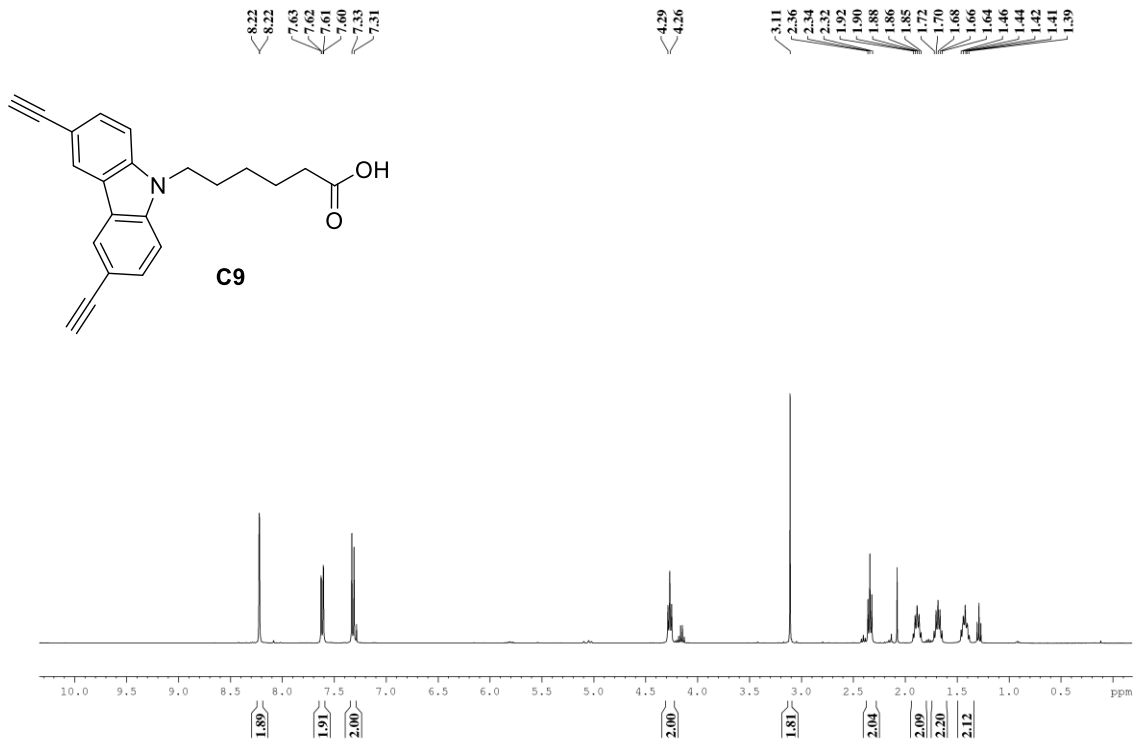








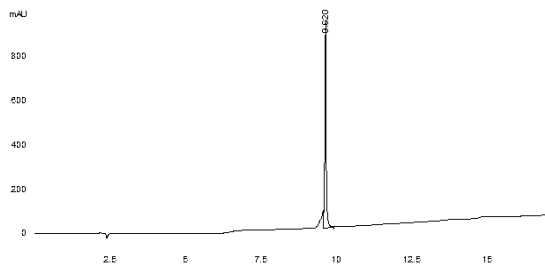




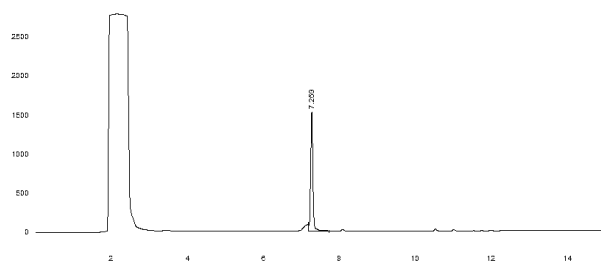
A.2. HPLC traces of selected compounds

CK2 peptides

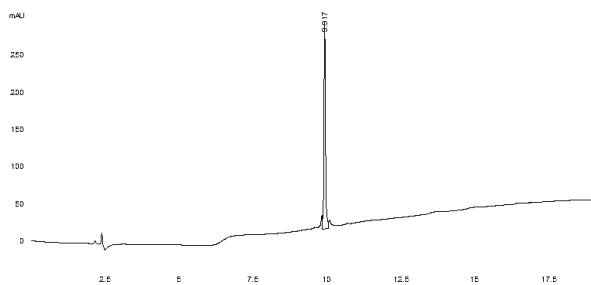
Pc linear



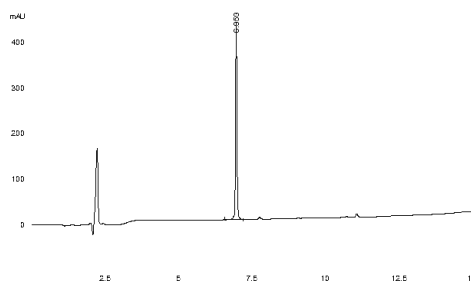
Pc cyclic



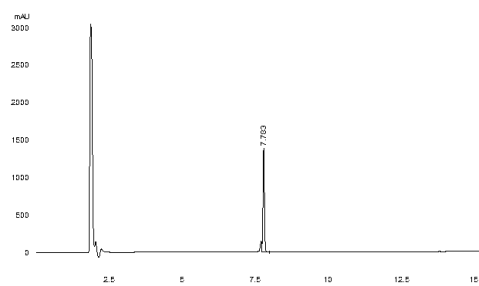
Pc cyclic short



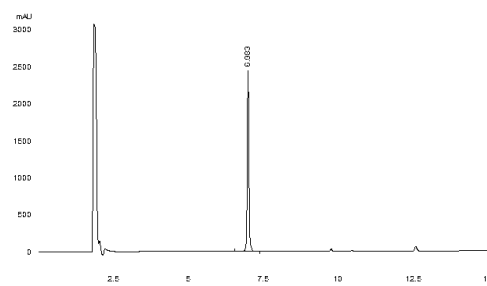
P0-C1



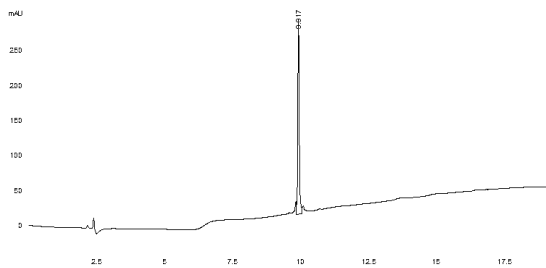
P1-C2



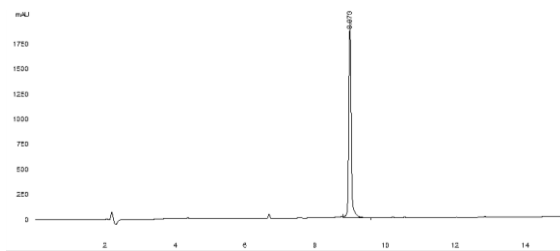
P1-C3



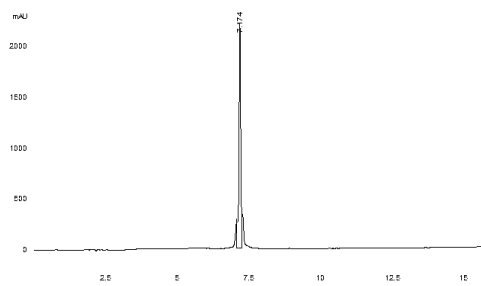
P1-C4



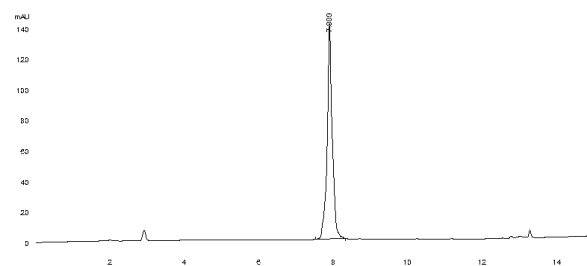
P1-C5



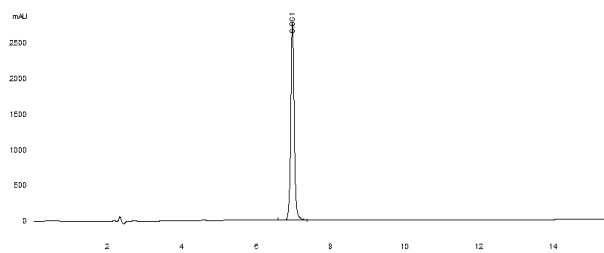
P1-C6



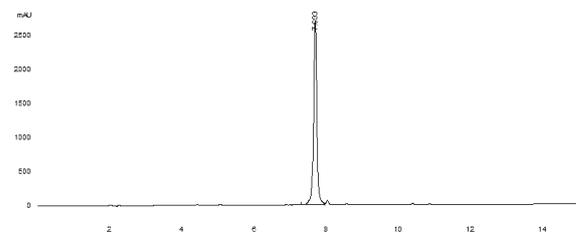
FITC-P1-C5



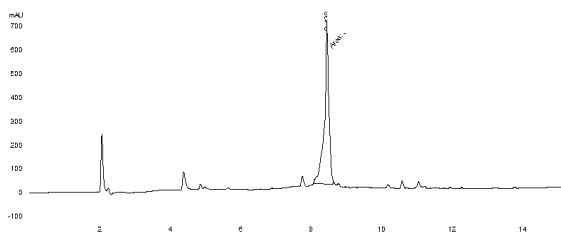
P1-F1C5



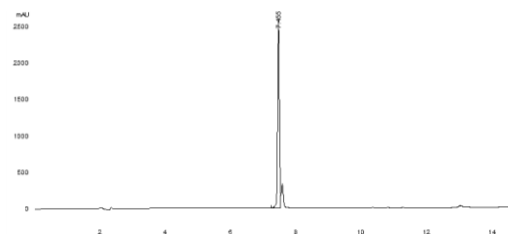
P1-F2C5



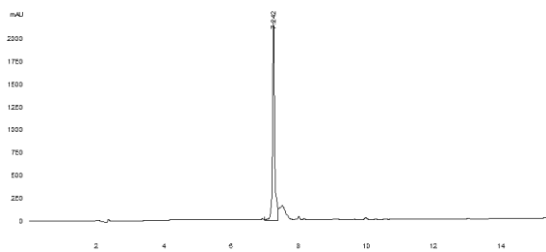
P1-F3C5



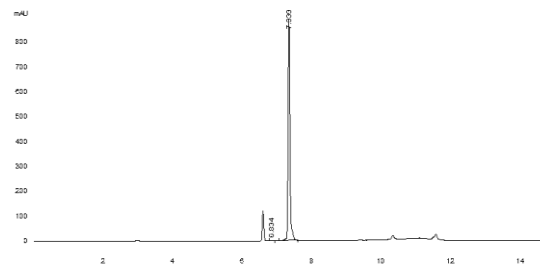
P2'-C5



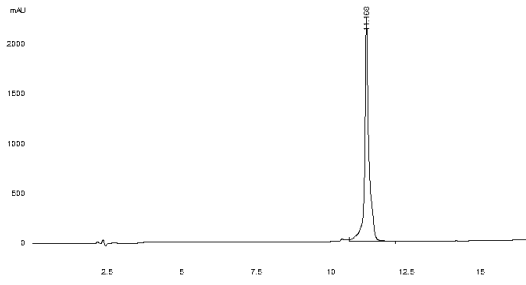
P2''-C5



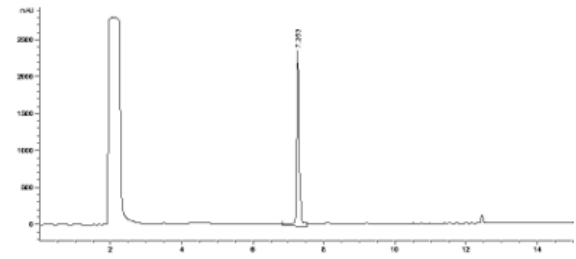
P3-C5



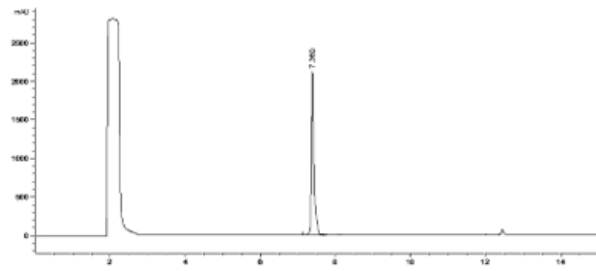
P4-C5



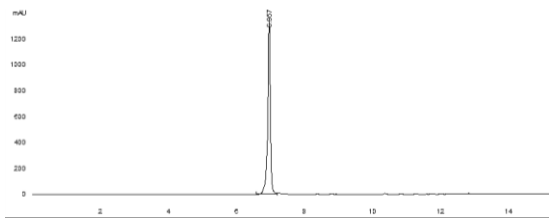
P5'-C5



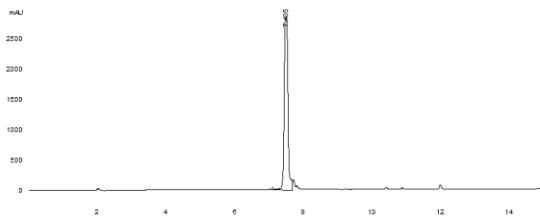
P5''-C5



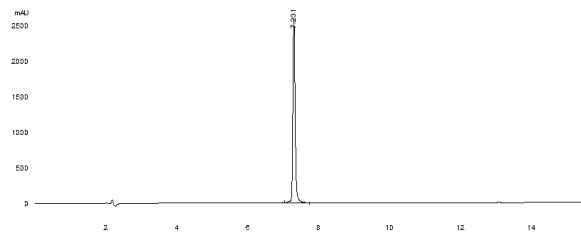
P6-C5



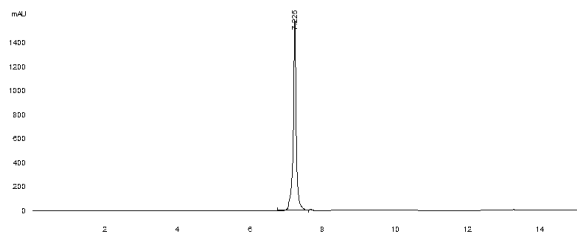
P7



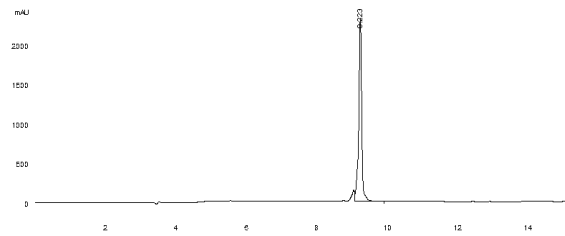
P7-C5



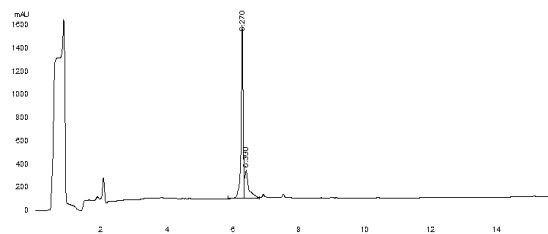
P7-F1C5



P7-F2C5

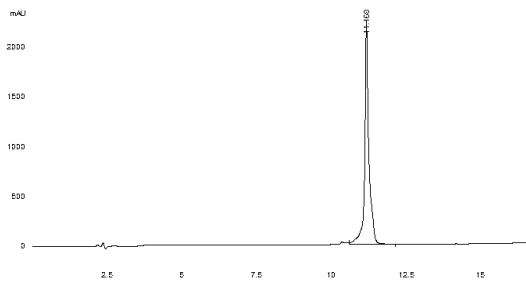


P8-F1C5

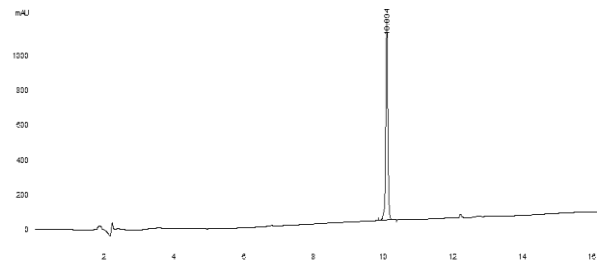


BH3 peptides

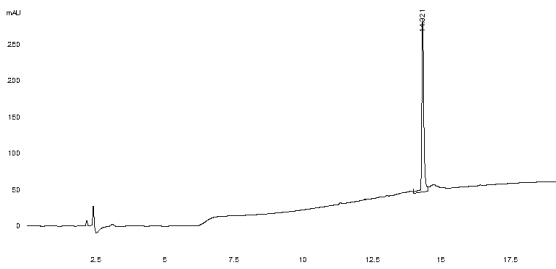
P9-C5



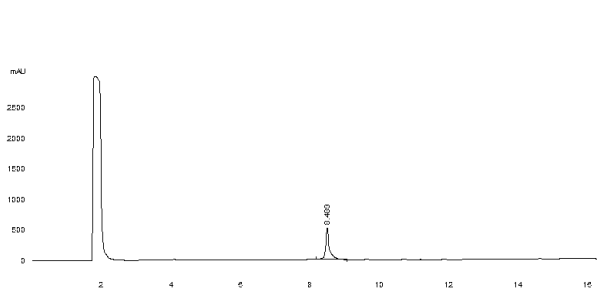
P9-C7



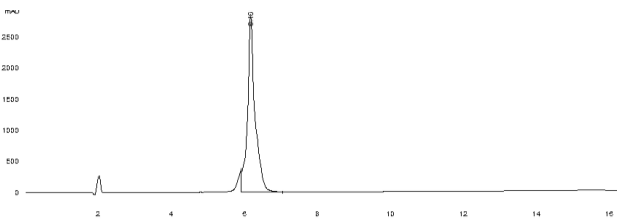
P9-F4C5



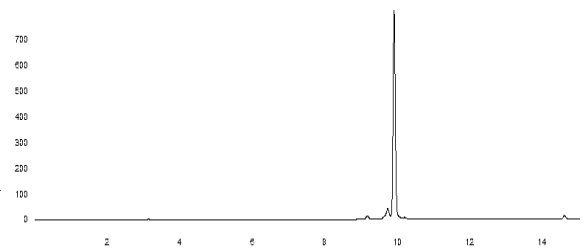
P9-F5C5



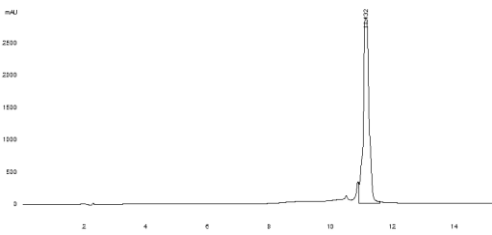
P10



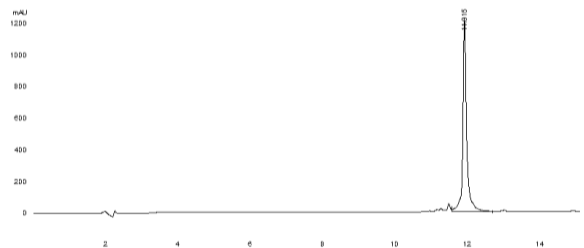
FITC-P10



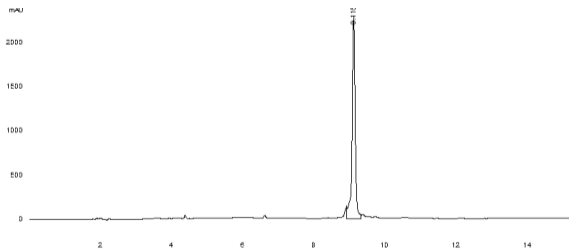
SAHBa



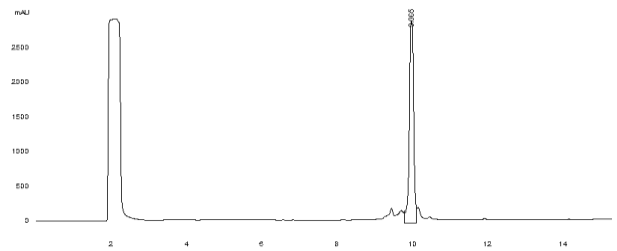
FITC-SAHBa



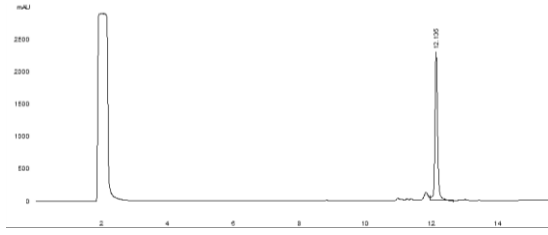
FITC-P9-F4C5



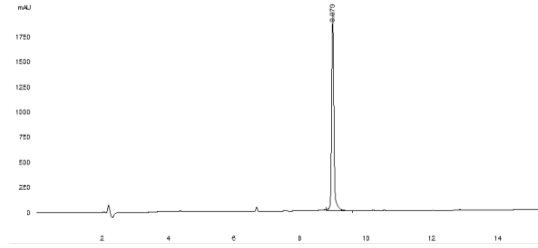
FITC-P9-F5C5



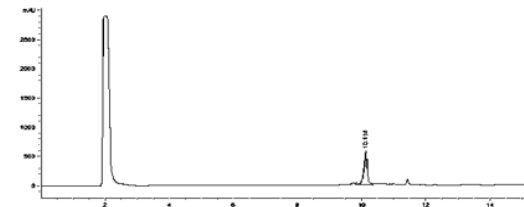
FITC-P9-C7



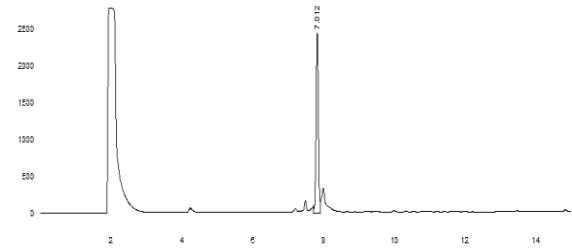
P11-F4C5



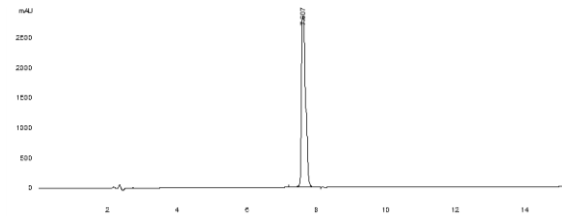
FITC-P11-F4C5



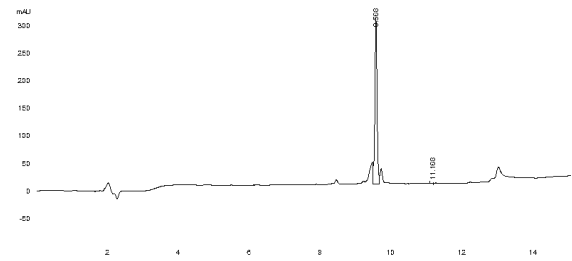
P12



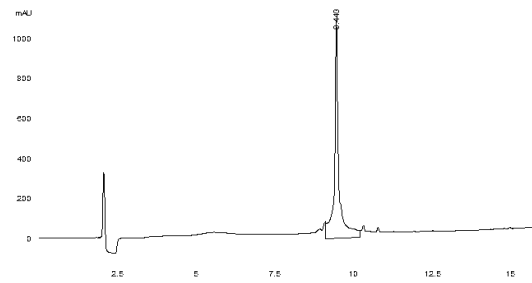
P13



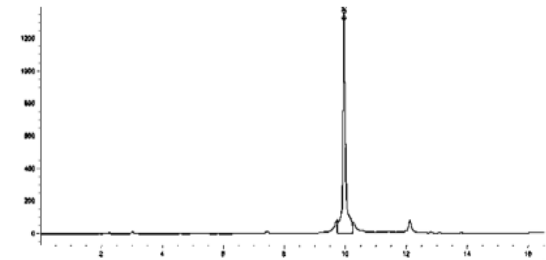
P14-C8



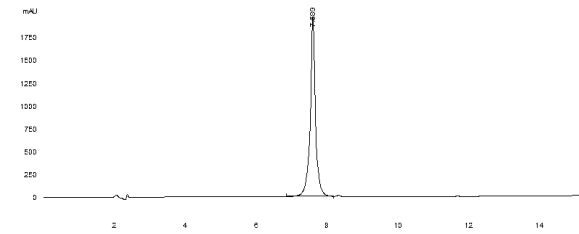
P15-C8



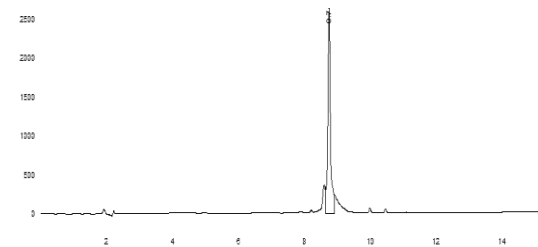
P16-C8



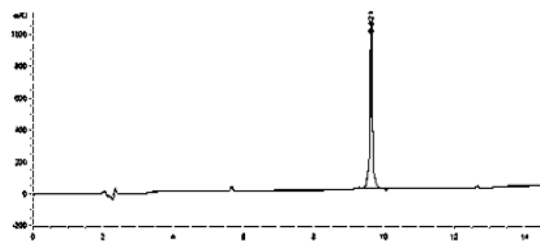
P17-C5



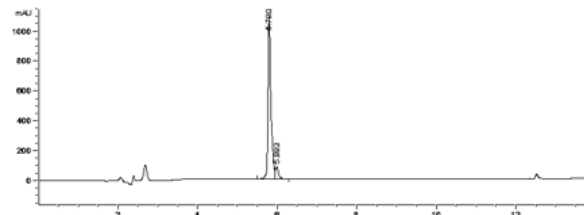
P18-C5



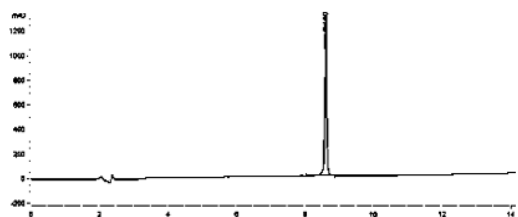
P19-C5



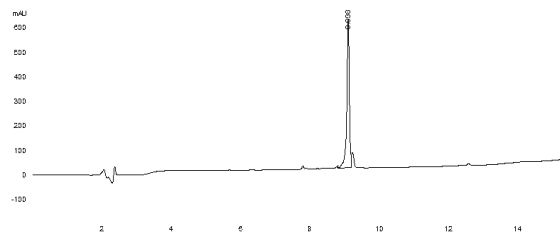
P17-F1C5



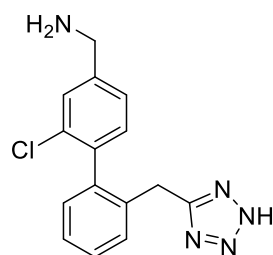
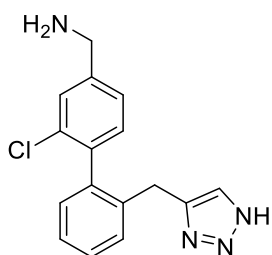
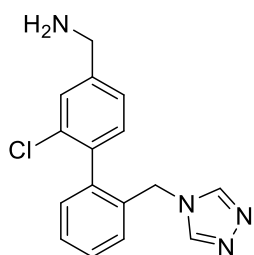
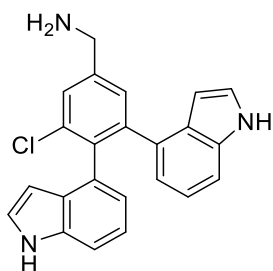
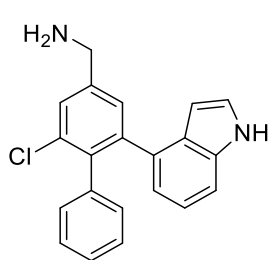
P18-F1C5



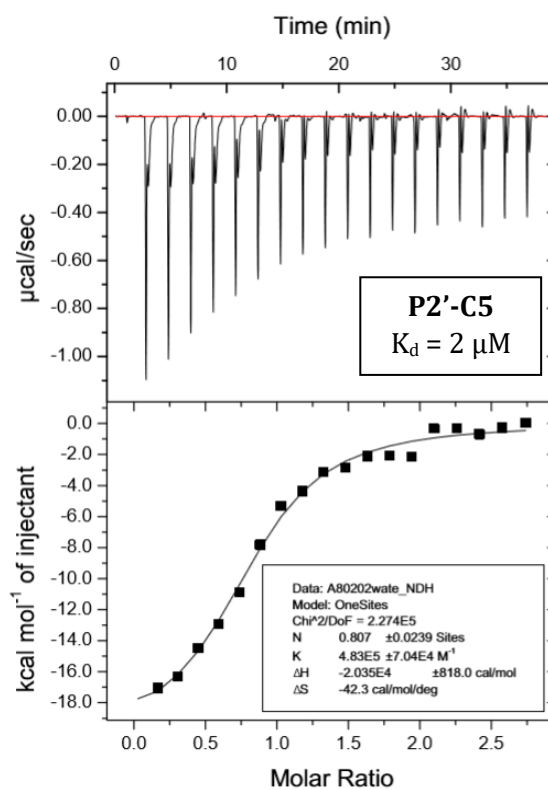
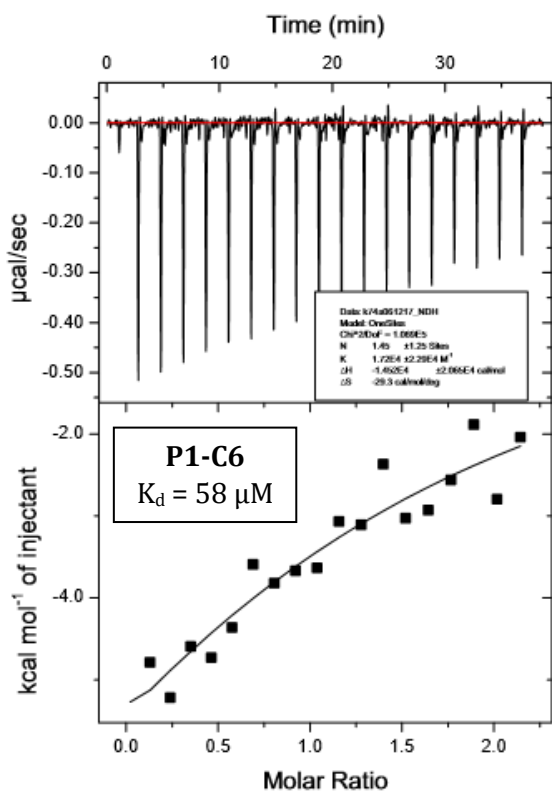
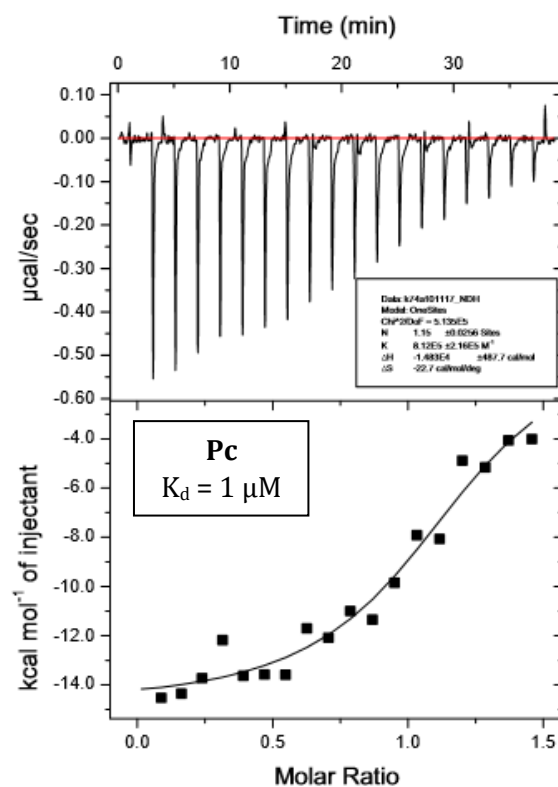
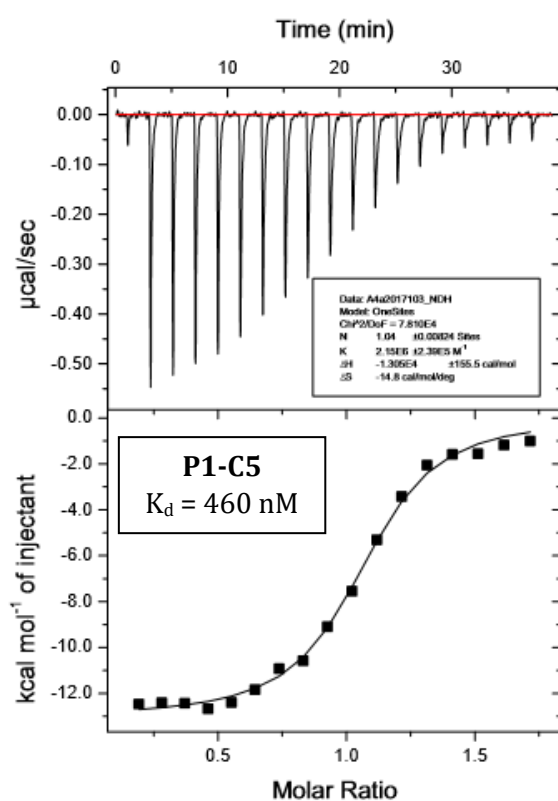
P19-F1C5

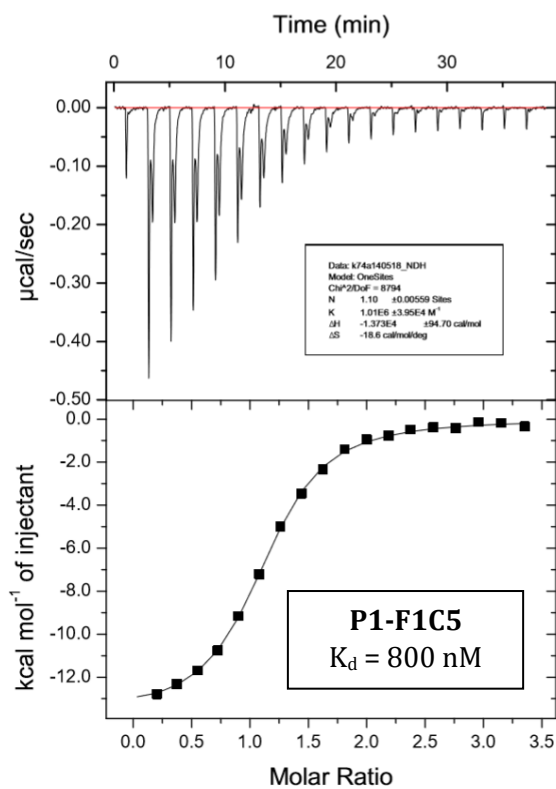
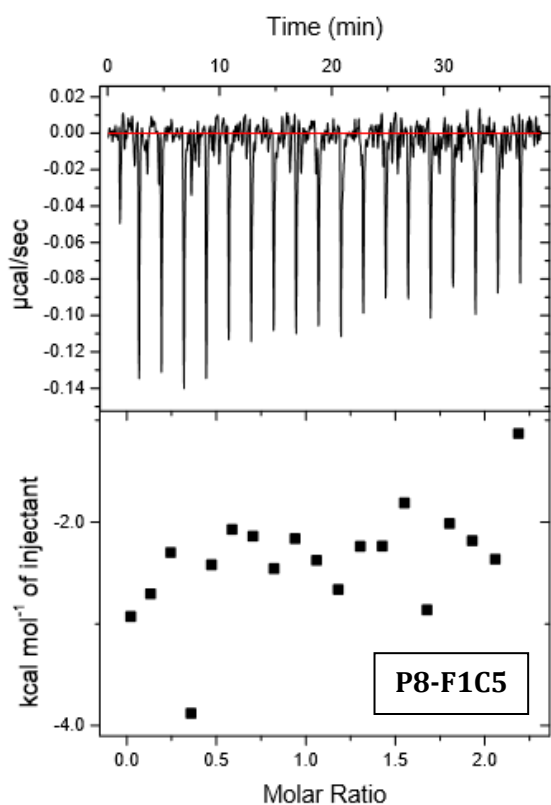
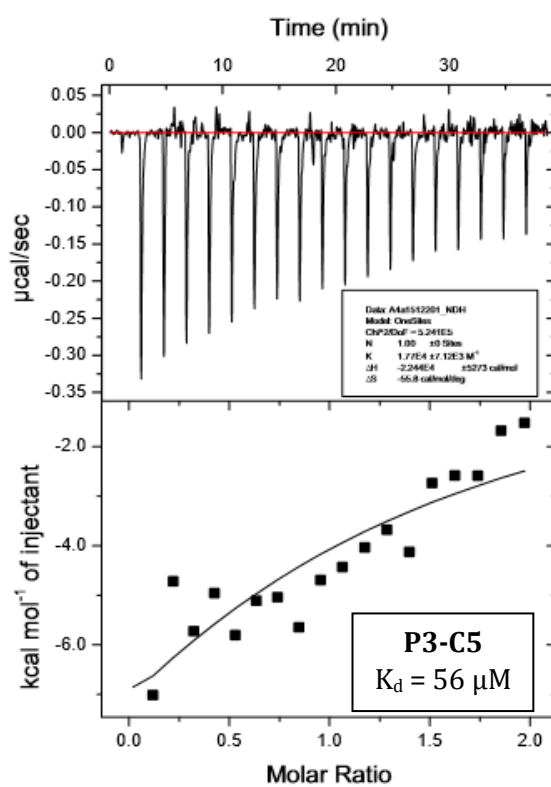
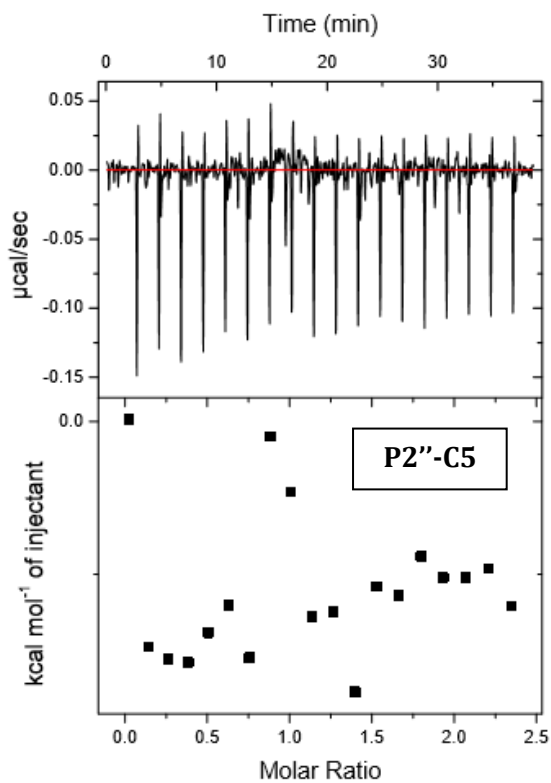


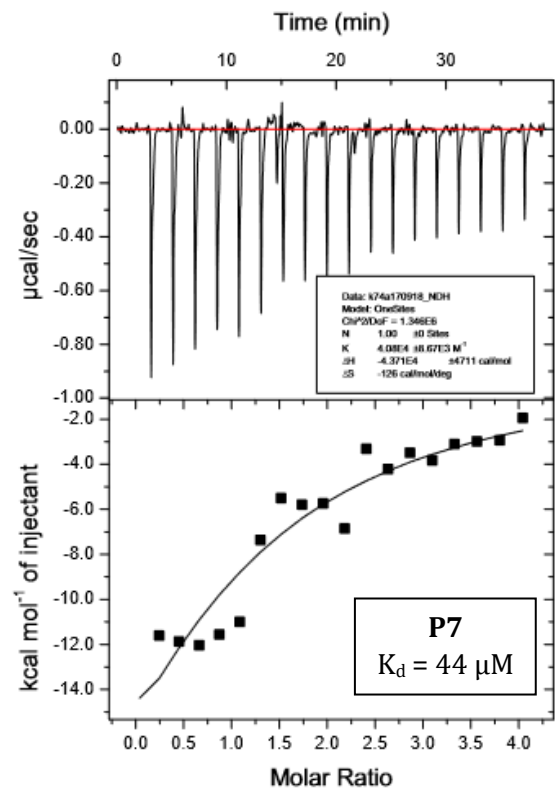
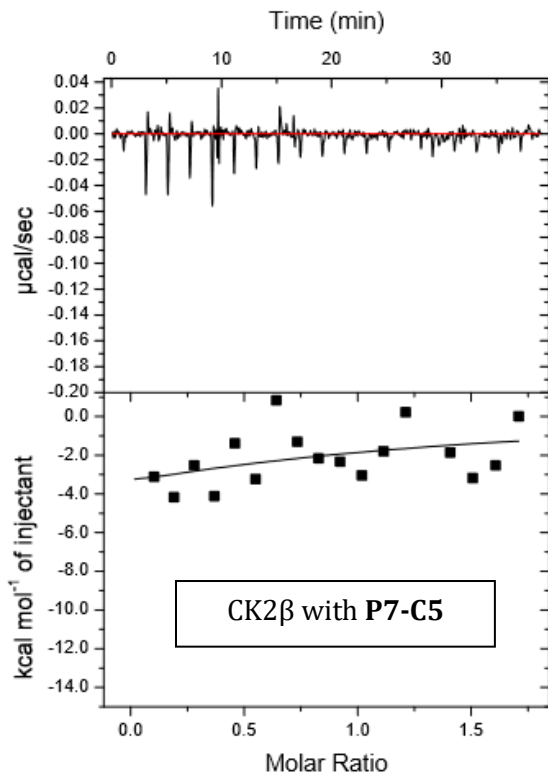
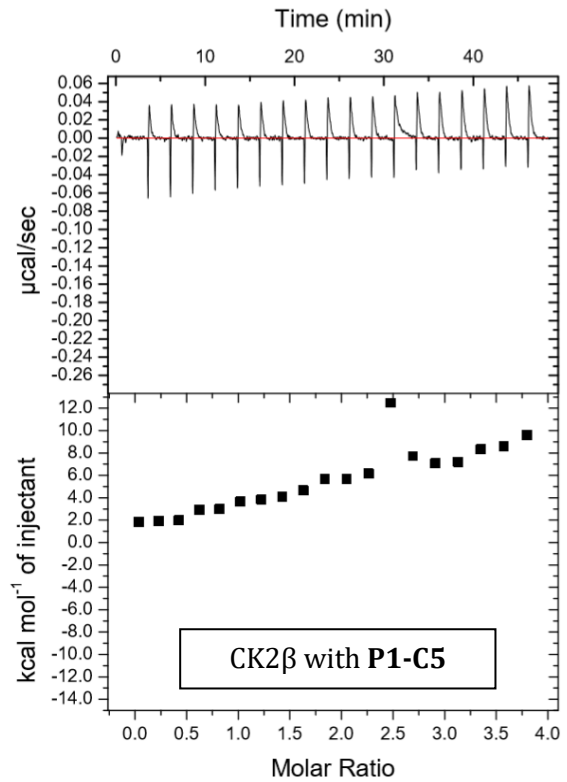
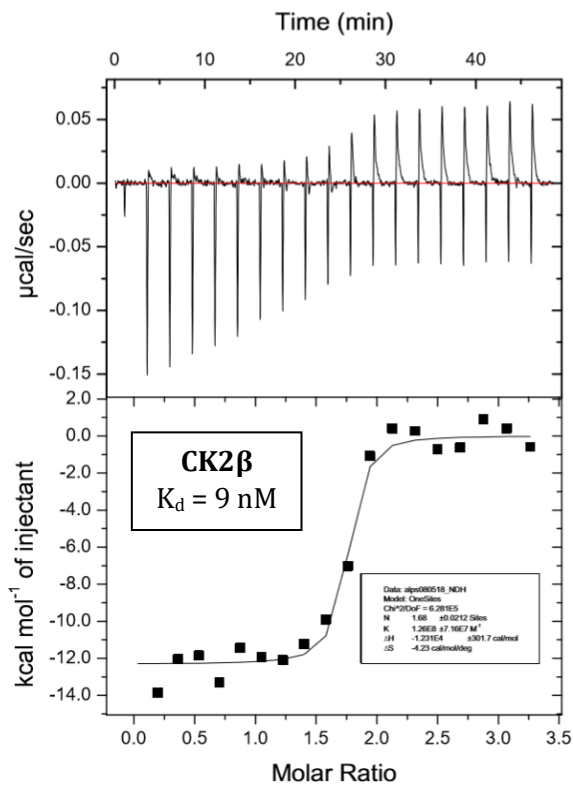
A.3. Structures of additional fragments docked

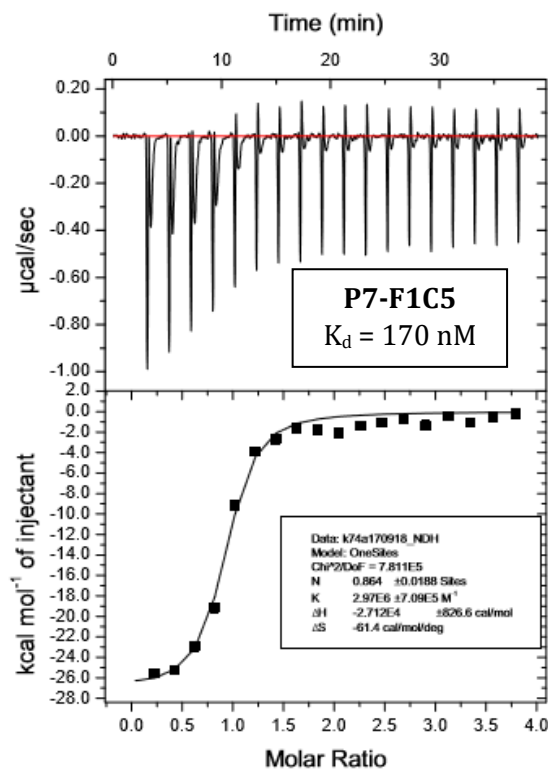
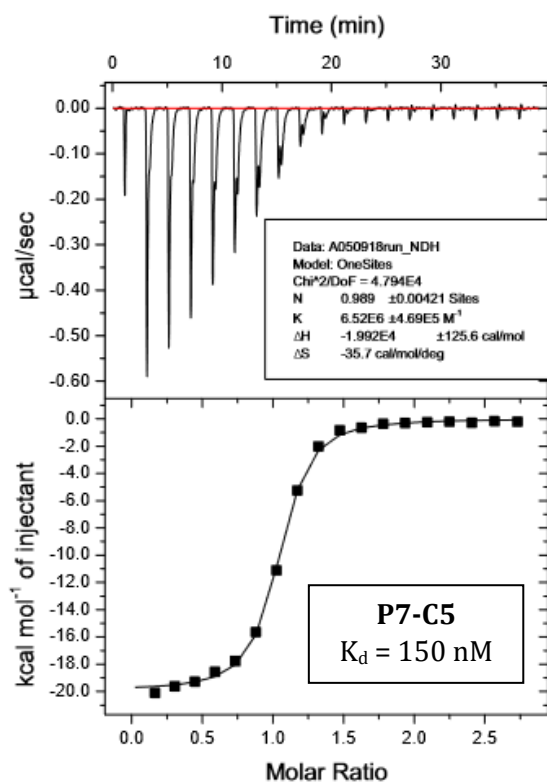


A.4. Selected ITC binding curves









Thermodynamic data

Peptide	K_D μ M	ΔH cal/mol	ΔS cal/mol/deg	Stoichiometry
Pc	1	$-1.483E4 \pm 487.7$	-22.7	1.15 ± 0.0256
P1-C5	0.46	$-1.305E4 \pm 155.5$	-14.8	1.04 ± 0.00824
P1-C6	58	$-1.452E4 \pm 2.06 E4$	-29.3	1.45 ± 1.25
P2'-C5	2	$-2.035E4 \pm 818.0$	-42.3	0.807 ± 0.0239
P3-C5	56	$-2.244E4 \pm 5273$	-55.8	1.00 ± 0
P1-F1C5	0.8	$-1.373E4 \pm 94.70$	-18.6	1.10 ± 0.00559
CK2 β	0.01	$-1.231E4 \pm 301.7$	-4.23	1.68 ± 0.0212
P7-C5	0.15	$-1.992E4 \pm 125.6$	-35.7	0.989 ± 0.00421
P7	44	$-4.372E4 \pm 4711$	-126	1.00 ± 0
P7-F1C5	0.34	$-2.712E4 \pm 826.6$	-61.4	0.864 ± 0.0188

A.5. Unsuccessful crystallisation attempts of CK2 peptides and CK2 α

Crystallisation technique	Protein construct	Conditions	Results
Soaking	WT, K74A	No ATP 10 μ M peptide	Crystals of the protein
		Conditions from Brear <i>et al.</i> ¹⁹⁸	
Soaking	WT, K74A	No ATP 100 μ M peptide	Crystals of the protein
		Conditions from Brear <i>et al.</i> ¹⁹⁸	
Soaking	WT, K74A	No ATP 1 mM peptides	Crystals of the protein
		Conditions from Brear <i>et al.</i> ¹⁹⁸	
Co-crystallisation	WT, K74A	Conditions from Raaf <i>et al.</i> ²¹⁵	No crystals
Co-crystallisation	WT, K74A	No ATP JCSG+™ screen	No crystals
		100 μ M peptide	
Co-crystallisation	WT, K74A	ATP JCSG+™ screen	No crystals
		10 to 100 μ M peptide	
Co-crystallisation	K74A	No ATP JCSG+™ screen	No crystals
		10 to 100 μ M peptide	
Co-crystallisation	FP_10, K74A, WT	ATP JCSG+™ screen	No crystals
		50 μ M peptide	
Co-crystallisation	FP_10, K74A, WT	ATP Proplex™ screen	No crystals
		1 mM peptide	

A.6. Papers published on this work